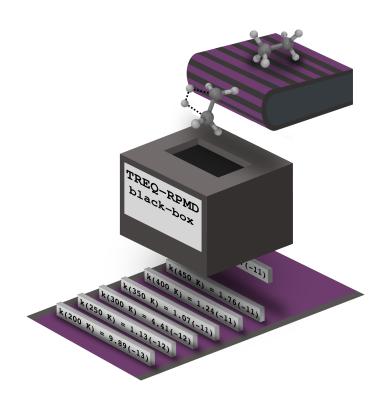# Towards High-Quality Black-Box Chemical Reaction Rates with System-Specific Potential Energy Surfaces

Dissertation

in partial fulfillment of the requirements for the degree

Dr. rer. nat.

of the Faculty of Mathematics and Natural Sciences at Kiel University

submitted by

Julien Steffen

Kiel, December 2019

**Towards High-Quality Black-Box Chemical Reaction Rates
with System-Specific Potential Energy Surfaces**
Dissertation, submitted by Julien Steffen
Kiel, December 03, 2020

First referee:	Prof. Dr. Bernd Hartke
Second referee:	Prof. Dr. Carolin König

Date of the oral examination:	20.02.2020
Approved for publication:	20.02.2020

Meiner Mutter

Abstract

The calculation of highly-accurate reaction rate constants (k(T)) is one of the central topics in theoretical chemical kinetics. Two approaches for doing this are dominant in literature: application of heuristic corrections of the transition state theory (TST) and wave packet propagation with the aim to represent exact quantum mechanical dynamics. While the first approach is easy to handle but suffers from intrinsic approximations and limited accuracy, the second approach enables convergence towards the exact result, but at the expense of a complex handling and massive costs. This limits its application to a small circle of highly-specialized theoreticians.

A new method that might be able to bridge the gap between easy application and convergence towards the exact result is the ring polymer molecular dynamics (RPMD) method. It is based on the isomorphism between quantum statistical mechanics and classical statistical mechanics of a fictitious ring polymer. With this, configurational state sums and free energy surfaces can be obtained from probabilistic samplings of the system's accessible phase space with classical MD of ring polymers. Based on these free energy surfaces reaction rate constants can be obtained that converge towards the results of wave packet propagations, if the size of the ring polymer is adequate.

In order to conduct RPMD calculations, a sufficiently accurate representation of the thermally accessible potential energy surface (PES) of the system on which the ring polymers are propagated is needed. In principle, this surface could be represented by *ad hoc* calculations of energies and gradients based on quantum chemical methods like density functional theory (DFT) or second order Møller-Plesset perturbation theory (MP2). However, since many millions of single gradient calculations are needed to converge a free energy surface and the associated k(T) value, this approach is impractical. Instead, analytical representations of PESs that are fitted to DFT or MP2 results are commonly used. The parametrization of these representations is quite demanding, though, thus being a task for experts.

The present thesis deals with new methods for the automated parametrization of analytical PES representations of reactive systems and the successive k(T) calculations based on RPMD. These representations are built on a combination of the quantum mechanical derived force field (QMDFF) method by Grimme and the empirical valence bond method (EVB) by Warshel, being plugged together recently by Hartke and Grimme (EVB-QMDFF). In line with this thesis a crucial improvement of this combination of methods was done, complementing it with newly developed EVB concepts. For practical usage a new program package was developed, which enables the automated generation of an EVB-QMDFF-PES representation and calculations of RPMD-free-energy surfaces, recrossing corrections as well as k(T) values and Arrhenius parameters for comparison with experimental data, based on the preoptimized reaction path of an arbitrary thermal ground state system.

The abilities of the new methods and the associated implementation were thoroughly benchmarked in different kinds of applications. These are calculations of k(T) values and Arrhenius parameters of arbitrary systems from a reaction data base and their comparison to literature values, theoretical molecular force experiments with quantitative investigations of force-dependent reactivities for different systems, a thorough study of urethane synthesis being part of our cooperation with Covestro AG and finally a combination of calculated rate constants of several elementary reactions for describing the dynamics of larger systems based on the kinetic Monte Carlo (KMC) method.

Kurzzusammenfassung

Die Berechnung von hochgenauen Reaktionsgeschwindigkeitskonstanten (k(T)) ist eines der zentralen Themenfelder in der theoretisch-chemischen Kinetik. Bisher dominieren zwei Ansätze in der Literatur: die Anwendungen von heuristischen Korrekturen der Übergangszustandstheorie (TST) und die Wellenpaketpropagation mit dem Ziel der exakten Darstellung von quantenmechanischer Dynamik. Während der erste Ansatz leicht anzuwenden ist, aber dafür mit intrinsischen Näherungen und Genauigkeitsbeschränkungen zu kämpfen hat, ist es mit dem zweiten Ansatz möglich, Konvergenz zum exakten Resultat zu erreichen, allerdings mittels einer sehr komplexen Handhabung und immenser Kosten, die ihn letzten Endes auf einen Kreis hochspezialisierter Theoretiker beschränkt.

Eine neue Methode mit dem Potential die Lücke zwischen leichter Anwendbarkeit und Konvergenz zum exakten Resultat zu überbrücken, ist die Ringpolymer-Moleküldynamik (RPMD). Sie basiert of dem Isomorphismus zwischen quantenmechanischer Statistik und der klassischen Mechanik eines fiktiven Ringpolymers. Damit können Zustandssummen und Flächen freier Energie unter Berücksichtigung quantenmechanischer Effekte aus probabilistischen Erkundungen des thermisch zugänglichen Phasenraums eines Systems mittels klassicher MD von Ringpolymeren erhalten werden. Aus den Flächen freier Energie werden wiederum chemische Reaktionsgeschwindigkeitskonstanten erhalten, welche bei genügender Größe der zugrundeliegenden Ringpolymere zum Ergebnis von Wellenpaketpropagationsrechnungen konvergieren.

Zur Durchführung von RPMD-Rechnungen ist eine möglichst präzise Darstellung der thermisch zugänglichen Potentialenergiefläche (PES) des Systems notwendig, auf welcher die Ringpolymere propagiert werden können. Prinzipiell könnte diese durch *ad-hoc*-Berechnungen von Energien und Gradienten auf Basis quantenchemischer Methoden wie Dichtefunktionaltheorie (DFT) oder Møller-Plesset Störungstheorie 2. Ordnung (MP2) dargestellt werden. Da jedoch viele Millionen einzelner Gradientenberechnungen zur Konvergenz der erhaltenen Fläche freier Energie und eines zuverlässigen k(T)-Wertes notwendig sind, ist diese Herangehensweise zeitlich nicht zu bewerkstelligen. Stattdessen greift man für gewöhnlich auf analytische Darstellungen der PES zurück, die an DFT- oder MP2-Resultate gefittet wurden. Die Parametrisierung solcher Darstellungen für neue Systeme ist jedoch erneut eine äußerst anspruchsvolle Aufgabe für Experten.

Die vorliegende Arbeit beschäftigt sich mit neuartigen Verfahren zur automatisierten Parametrisierung analytischer PES-Darstellungen von reaktiven System und daran anschließende k(T)-Berechnungen auf Basis von RPMD. Die Darstellungen beruhen auf einer Verknüpfung der quantenmechanisch-abgeleiteten Kraftfeldmethode (QMDFF) von Grimme und der empirischen Valenzbindungsmethode (EVB) von Warshel, welche unlängst von Hartke und Grimme entwickelt wurde (EVB-QMDFF). Im Rahmen dieser Arbeit wurde diese Methodenkombination entscheidend weiterenwickelt und um neuentwickelte EVB-Konzepte ergänzt. Zur praktischen Handhabung wurde ein neues Programmpaket verfasst, welches automatisiert auf Basis des voroptimierten Reaktionspfades eines beliebigen thermischen Grundzustandsssystems eine PES-Darstellung mit der EVB-QMDFF-Methode erstellt und auf dieser mittels RPMD Flächen freier Energe, Rückkreuzungskorrekturen und k(T)-Werte, sowie Arrheniusparameter berechnet, welche direkt mit experimentellen Resultaten verglichen werden können.

Die Fähigkeiten der neuen Methoden und der sie enthaltenden Implementation wurden anhand verschiedener Anwendungen ausführlich getestet. Enthalten sind hierbei Berechnungen von k(T)-Werten und Arrheniusparametern zufällig ausgewählter Systeme aus einer Reaktionsdatenbank und deren Vergleich mit Literaturwerten, theoretische Molekularkraftexperimente mit quantitativer Untersuchung der Reaktivität von Systemen abhängig von angelegten Kräften, ausführliche Untersuchungen von Urethanbildungsreaktionen als Teil unserer Zusammenarbeit mit der Covestro AG und schließlich die Kombination von berechneten Geschwindigkeiten einzelner Teilreaktionen zur Dynamik größerer Systeme auf Basis der kinetischen-Monte-Carlo-Methode (KMC).

Contents

12 Bibliography   259

Curriculum Vitae   I

Acknowledgements   V

Declaration   VII

List of Acronyms

AFM	**A**tomic **F**orce **M**icroscope
AIMD	**A**b **I**nitio **M**olecular **D**ynamics
AO	**A**tomic **O**rbital
BJ	**B**ecke-**J**ohnson
COM	**C**enter **O**f **M**ass
CUS	**C**anonical **U**nified **S**tatistical Model
CV	**C**ollective **V**ariable
CVT	**C**anonical **V**ariational **T**heory
DFT	**D**ensity **F**unctional **T**heory
DG	**D**istributed **G**aussian
EHT	**E**xtended **H**ückel **T**heory
EVB	**E**mpirical **V**alence **B**ond
FCI	**F**ull **C**onfiguration **I**nteraction
FF	**F**orce **F**ield
GA	**G**enetic **A**lgorithm
GUI	**G**raphical **U**ser **I**nterface
GVB	**G**eneralized **V**alence **B**ond
HF	**H**artree-**F**ock
HL	**H**eitler-**L**ondon
ICVT	**I**mproved **C**anonical **V**ariational **T**heory
IRC	**I**ntrinsic **R**eaction **C**oordinate
KMC	**K**inetic **M**onte **C**arlo
k(T)	Chemical Reaction Rate Constant
LCAO	**L**inear **C**ombination of **A**tomic **O**rbitals
LCT	**L**arge **C**urvature **T**unneling
LEPS	**L**ondon-**E**yring-**P**olanyi-**S**ato
LM	**L**evenberg-**M**arquardt
LQA	**L**ocal **Q**uadratic **A**pproximation
MC	**M**onte **C**arlo
MCSI	**M**ulti-**C**onfiguration **S**hepard-**I**nterpolation
MDI	**M**ethylene **D**iphenyl **I**socyanate
MM	**M**olecular **M**echanics
MO	**M**olecular **O**rbital
MOF	**M**etal **O**rganic Framework
MP2	**M**øller-**P**lesset Perturbation Theory 2nd. Order
MPI	**M**essage **P**assing Interface
MS	**M**ulti-**S**tate
MSLS	**M**ulti-**S**tart **L**ocal **S**earch
μVT	**M**icrocanonical **V**ariational **T**heory
NDI	1,5-**N**aphtyl-**D**i**I**socynaate
NEB	**N**udged **E**lastic **B**and
NN	**N**eural **N**etwork
NR	**N**ewton-**R**aphson

PES	**P**otential **E**nergy **S**urface
PI	**P**ath **I**ntegral
PIMC	**P**ath **I**ntegral **M**onte **C**arlo
PIMD	**P**ath **I**ntegral **M**olecular **D**ynamics
PMF	**P**otential of **M**ean **F**orce
QM	**Q**uantum **M**echanics
QMDFF	**Q**uantum **M**echanically **D**erived **F**orce **F**ield
QTST	**Q**uantum **T**ransition **S**tate **T**heory
RF	**R**eactive **F**lux
RP	**R**eaction **P**ath
RPMD	**R**ing **P**olymer **M**olecular **D**ynamics
SC	**S**olvent **C**omplex
SCT	**S**mall **C**urvature **T**unneling
STM	**S**canning **T**unneling **M**icroscope
SVD	**S**ingular **V**alue **D**ecomposition
TDI	**T**oluene **D**i**I**socynaate
TDSE	**T**ime-**D**ependent **S**chrödinger **E**quation
TISE	**T**ime-**I**ndependent **S**chrödinger **E**quation
TREQ	**T**ransition **R**egion Corrected **R**P-EVB-**Q**MDFF
TS	**T**ransition **S**tate
TST	**T**ransition **S**tate **T**heory
UFF	**U**niversal **F**orce **F**ield
UI	**U**mbrella **I**ntegration
US	**U**nified **S**tatistical Model
VB	**V**alence **B**ond
VTST	**V**ariational **T**ransition **S**tate **T**heory
WHAM	**W**eighted **H**istogram **A**nalysis **M**ethod
ZCT	**Z**ero **C**urvature **T**unneling

List of Figures

List of Tables

Introduction

> This is your last chance. After this, there is no turning back. You take the blue pill – the story ends, you wake up in your bed and believe whatever you want to believe. You take the red pill – you stay in Wonderland and I show you how deep the rabbit-hole goes.
>
> (*Morpheus*)

The description of time-dependent processes is an important part of chemistry. There is a bunch of quite different phenomena that can be described time-dependently, e.g., phase changes, changes of protein tertiary structures, reactions facilitated by collisions between reactive partners (mostly bimolecular reactions) or reactions inside one single molecule, such as decompositions or rearrangements, also called unimolecular reactions.

Most of them can be described either in terms of thermodynamics, by looking at different equilibria and chemical potentials, or in terms of kinetics, i.e., investigating what the particles do during the reactive processes. The field of kinetics itself can be further subdivided into *continuum kinetics* and *particle kinetics* [1]. In continuum kinetics time-dependent partial pressures or concentrations of different species are measured. The aim of the theoretical description is then to find a suitable model consisting of different rate constants that describes the apparent changes by simultaneously giving some insight into the interplay of various involved reactions. In particle kinetics, we want to calculate rate constants based on simulations of what single atoms and molecules actually do during their reactions. Since reaction rate constants appear in both pictures, they provide a link between these two concepts. It is, e.g., possible to calculate rate constants for various processes on the particle level and parametrize macroscopic continuum equations with them.

An important utility for kinetical descriptions of processes are therefore *chemical reaction rate constants* (k(T)). Since chemical reactions are mostly *rare events*, they can be described at a level in which surrounding processes like thermal vibrations only enter as averages without any atomistic details. These averages are narrowly associated with the temperature of the system [2].

Historically, the systematic calculation of rate constants was made possible with the development of *transition state theory* (TST) [3–5]. Based on TST, two opposite approaches of calculating chemical reaction rates were developed in the last couple of decades. The first direction constitutes the field of *parametric TST corrections*. These are heuristic methods that try to overcome different TST-limitations with as simple as possible correction schemes [6], e.g., by trying to add a correction factor that accounts for quantum effects like tunneling. The second direction is to do *quantum TST*

(QTST) based on wave-packet propagations of the atomic nuclei [7–9]. QTST is able to deliver exact rate constants if the propagations are done on exact *potential energy surfaces* (PES) with arbitrary high resolution of the wave functions in terms of spatial basis functions. This is of course never the case, but QTST calculations converge to the exact result if the propagation is done for instance only in a significant subspace of the system's internal coordinates or with a coarser grid of spatial basis functions on a PES representation of high quality.

The exact QTST approach, however, is very demanding both in terms of computational power and intellectual expense needed for its setup, such that it is usually performed only by a rather small group of designated experts in the field. The average chemist instead who, for instance, wants to compare his or her experimental results to theory will almost always rely on parametric improved TST models (unless he or she knows colleagues who are able to calculate QTST rates), which are, e.g., implemented in the popular POLYRATE program [10].

These simple methods perform surprisingly well in many cases and are therefore often used as a quasi-*black-box* tool if rate constants need to be calculated. However, many of these authors might underestimate the underlying approximations within those methods that usually assume that the system to be calculated obeys some crucial requirements. There are, e.g., many different tunneling correction schemes, whose actual choice should depend on the curvature of the reaction path. The method used in almost all cases, however, is the one which only should be used for small curvatures. There are certainly many authors who will scrutinize themselves if the "nine to five"-method requiring small reaction curvature is really appropriate, but the temptation to simply repeat what others do might be large. When doing this, the researcher always is on the line to catch a case where the method spectacularly fails. Even moving to related methods not always equals salvation. Furthermore, it is not possible to invest more computational power and come closer to the exact result. One has to rely on the available methods whose underlying assumptions cannot be simply overcome by, for instance, adding more frequencies along the reaction path.

This gap between the domain of exact theory and more or less vulnerable correction schemes for the masses seems to be unbridgeable. Fortunately, a new method indeed has emerged that could be able to do so. *Ring polymer molecular dynamics* (RPMD) [11] is based on the proven theorem that quantum behavior of a system can be modeled by several classical instances of it connected together by harmonic forces, building a ring polymer of replicas or *beads*. With this, classical *molecular dynamics* (MD) can be calculated in an extended ring-polymer phase space in order to reproduce QTST results (e.g., simultaneously perform 8 classical MD samplings whose atoms are connected to their counterparts in other instances by harmonic forces, resulting in 8-bead RPMD). Thus, the exact quantum wave-packet representation of the system's nuclei is replaced by a collection of classical particles that mimic the quantum-delocalization by scattering in space, hold together by their ring-polymer interactions.

RPMD is much less costly than wave packet propagation because the degree of quantumness can be fine-tuned by varying the number of beads, i.e., the number of replicas each atom has and thus the exactness of the portrayal of quantum reality. If exact reproduction of QTST is desired[1], the number of beads needs to go to infinity, however, exactness is pointless anyway: Both wave packages and classical trajectories connected to form RPMD must be propagated on representations of the system's PES[2].

This PES can be obtained by solving the *time-independent Schrödinger equation* (TISE) for each point in coordinate space of the system. In the case of wave packet propagation this refers to

---

1 It should be noted that RPMD only converges to exact QTST results in the high-temperature limit and for barriers of harmonic shape. However, very good agreements between RPMD and QTST are achieved for other cases as well, such that errors introduced by RPMD are usually much smaller than that of, e.g., the underlying PES representation.

2 The picture of propagating wave packages on a parametrized PES originates in the Born-Oppenheimer approximation that the much lighter electrons are reacting instantly on a positional change of the nuclei. If we restrict ourselves to thermal ground-state reactions, this picture works quite well, however, to be really exact (in the regime of the Schrödinger equation) we should propagate both electrons and nuclei as *pari passu* quantum particles.

an uniform grid of coordinate values, in the case of RPMD this refers to each point one of the replicas visits during their propagation. Unless the rather pointless H+H$^+$-reaction is treated it is impossible to solve the TISE analytically. Instead, numerical approximation methods, describing the field of time-independent quantum chemistry, are needed. If we still want to get the exact solution of the TISE, the *full configuration interaction* (FCI) method within a complete basis set must be used, which is impossible as well for all but some two- to three-atomic systems. Underneath FCI, a wide variety of methods has emerged in the last decades, ranging from cheap but poor or good only at special cases (e.g., semiempirical methods), to very expensive and almost exact at least for non-pathological cases (e.g., CCSDTQ) [12].

Usually, we would use methods delivering a reasonable compromise between quality and cost, like *density functional theory* (DFT) or *second order Møller-Plesset perturbation theory* (MP2). By using these methods, our claim to be exact must be abandoned. We then should make a similar choice for the quality of our dynamics, i.e., to wisely choose a number of RPMD-beads between one (classical description) and towards infinity (exact quantum treatment). Fortunately, the method usually converges rapidly towards almost full inclusion of quantum effects such that a limited number of RPMD beads (e.g., 16-32) is adequate for inclusion of almost all relevant quantum effects.

Is this the final answer? Unfortunately such an *ab-initio MD* (AIMD) is infeasible for the type of calculations we need. Even for very small three- to four atomic systems, DFT or MP2 calculations usually need at least some tenth of seconds for a single energy calculation. Calculating a rate constant with RPMD needs a thorough sampling of the system's available phase space, requiring millions of energy and gradient calculations. In contrast to parametric TST calculations, where some dozens of *ab-initio* gradient and Hessian calculations are enough for the setup of even the most expensive methods, RPMD samplings with direct calls to *ab-initio* methods are virtually infeasible.

A loophole out of this scaling issue are *analytical PES representations*. These are built by optimization of mathematical functions with respect to *ab-initio* energies or gradients at several points in coordinate space relevant for the reactions of interest. If such an analytical surface is available, the computational expense for a single energy and gradient calculation on it becomes a tiny fraction (usually several orders of magnitudes smaller) than the direct DFT or MP2 calculation. Almost all computational expense is transferred to the *initial setup* of the surface. All what the average chemist needs to do is to search online if someone has already built an analytical PES for his or her system. If this is true, he or she downloads it, links it to the RPMD program and starts the calculation [13]. If this is not the case, though, a giant problem exists. Building a new analytical PES is again a field where a high degree of expertise is needed, certainly out of reach for the average chemist. There are universal approaches that can provide, at least in principle, descriptions of almost all reactive systems [14], but these usually need much effort to *reparametrize* them for the system of interest, especially since, due to the exponential dependence of rate constants on the barrier height, this must be represented with a high degree of accuracy.

This thesis tries to give a solution to that kind of problem. We have seen so far that RPMD is a convenient method to calculate rate constants of high quality based on rather simple methodologies like classical MD. If we would have a way to build a reasonable PES representation for a new system of interest that is easy enough to convince the average chemist to apply it, RPMD really could replace parametric TST corrections as default method for rate constant calculations, then solving the problem of obscure approximations and subsequent pitfalls in its application.

Origin for the new approach presented in this thesis is the *quantum mechanically derived force field* (QMDFF) by Grimme [15]. It is a *black-box* force field that can be set up for an arbitrary chemical system if a preset, very small batch of quantum chemical reference data has been calculated for it. The parameters of the QMDFF are optimized based on this reference data, giving a force field that is able to describe the complete torsional configuration space of the molecule of interest, further, all possible dissociations and decompositions of the system are included with reasonable quality. It

cannot, however, describe the formation of new bonds that have not already existed in the reference structure.

Since a large fraction of chemical reactions are bond dissociations directly followed by building of new bonds, QMDFF alone is not yet the answer for our PES setup problem. The path to this answer was found by HARTKE and GRIMME in 2015 [16]. They combined two QMDFFs describing reactants and products, respectively, by using the *empirical valence bond* (EVB) method, resulting in EVB-QMDFF. EVB was developed by WARSHEL in 1980. Its underlying idea is to couple two (or more) diabatic surfaces which are described by force fields in order to get a smooth transition between them along a reaction path.

The exact parametrization of this coupling described by an either energy- or coordinate-dependent function is crucial for the whole EVB-QMDFF approach, since the transition region between two minima has by far the largest influence on the quality of rate constants describing reactions from one minimum to the other. Starting from the simple energy-dependent coupling term introduced in the paper by HARTKE and GRIMME, its design was improved gradually in line with this thesis, resulting in two additional publications [17, 18]. The developments described within this thesis have two main objectives: First, enhancing the ability of the EVB-coupling to describe the transition region of a reaction as good as possible, i.e., reproducing its quantum chemical reference data. Second, decreasing the amount of work needed for the applicant as far as possible, such that an easy to use *black-box* method with high accuracy usable for RPMD rate constant calculations by the average chemist can be established. It will be shown throughout this thesis that the development of such a method was indeed successful, opening a new chapter for reliable and easy to perform rate constant calculations.

This thesis can be divided into three parts.

In the *first part*, consisting of chapters 2 and 3, the theoretical foundations of rate constant calculations are presented, culminating in a detailed derivation and description of the RPMD-methodology. Then, PES construction methods in general and the QMDFF and EVB methodologies in particular are explained. The necessary translation of those mathematical details into working program code, namely our EVB-QMDFF program package, is then described in chapter 3.

In the *second part* (chapters 4-5), the two publications which developed the EVB-QMDFF-RPMD *black-box* rate constant calculation methodology are reprinted, showing both thorough benchmarks and application examples of the new approaches.

Finally, the developed methods are applied to several fields of chemical theory in the *third part*. Shown are *black-box* calculations of chemical reactions chosen from the literature, with EVB-QMDFF-RPMD rate constants compared to experimental values (chapter 6), simulations of mechanochemical reactions, where influences of forces attached to molecules with respect to their stability and resulting rate constants are investigated (chapter 7), results of our ongoing cooperation with Covestro AG, where urethane synthesis is described theoretically with EVB-QMDFF (chapter 8) and finally a connection of single rate constant calculations to large-scale simulations of more realistic systems, made possible by the *kinetic Monte Carlo* (KMC) method (chapter 9).

A final evaluation of my work, in the form of questions asked by a fictional reader and hopefully satisfactorily answered, is made in chapter 10. Supervised projects as well as details concerning theory, implementation and calculated results can be found in the appendix (chapter 11).

Theoretical Background

> A philosopher once said, "It is necessary for the very existence of science that the same conditions always produce the same results". Well, they don't!

(Richard Feynman)

2.1 Chemical Reaction Rates

As will be shown in this thesis, chemical reaction rates can be calculated for a whole range of molecular systems and situations, and in connection with methods like KMC, much larger systems of almost real-world size can be simulated with manageable usage of resources but nevertheless high accuracy.

Since a comprehensive review of the rich field of quantitative reaction dynamics culminating in the calculation of reaction rates would need several volumes of textbooks, it cannot be given even approximately in the scope of this thesis.

Nevertheless, I will try to lead through a little theorist's journey starting from the foundations like TST, continuing through improved transition state theory as well as sampling methods of the relevant configuration space and exact quantum mechanical treatments, and finally ending at methods of calculating reaction rates with quantum corrections using classical trajectory sampling, which will be used extensively in the presented applications throughout this work.

Of course this journey cannot admit any claim to give a representative overview of the field, we will essentially focus on all what is needed to calculate the results presented in the course of this thesis. Further, mathematical foundations of TST, lying in *flux-flux autocorrelations* and others, are treated rather shortly and at later stages, which could irritate some designated experts of the field. In order to understand ordinary TST as an average chemist, this background is not needed; it is needed, however, to understand why RPMD can be used to calculate k(T) values with quantum corrections.

Since only gas phase reactions[1] of rather small systems in their electronic ground state are investigated in this thesis, the whole treatment will focus on this subtopic, ignoring the rich variety of methods designed for the description of, for instance, reactions in solutions or surrounded by

---

1 In chapter 9 rate constants for diffusions on surfaces are calculated and fitted into KMC-schemes. However, their rate constants are also calculated on the assumption of a gas phase reaction, treating the surface atom and the subjacent surface slab as a single molecule.

protein backbones influencing the reaction mechanism. A better overview of the whole topic is presented, e.g., in the book by PETERS [1].

2.1.1 Transition State Theory

Perhaps one of the earliest quantitative observations in the field of chemical kinetics was that the rates of most chemical reactions roughly double if the system's temperature is increased by a certain amount, e.g., 10 K. More precisely, it was noticed that chemical reaction rates usually show *exponential dependence* on the temperature. This behavior is also known as *Arrhenius' law* [19], and the respective mathematical formulation is usually:

$$k(T) = A \exp\left[\frac{-E_a}{RT}\right],$$
(2.1)

where A is the *preexponential factor*, E_a is the *activation energy* of the reaction, T is the *temperature* and R is the *universal gas constant*.

If we take the logarithm of rate constants measured at different temperatures and plots them against the reciprocal temperatures, both A and E_a can be obtained from a linear fit[2]. Since A can be interpreted as the number of collisions between possible reactants per time unit and the exponential term picks the fraction of collisions that lead to reactions (depending on the height of the activation barrier), we are able to determine information on the molecular level from macroscopic experiments.

Surprisingly, in spite of its simplicity, Arrhenius law, i.e., exponential increase of reaction rates with temperature, is valid to a high degree of accuracy in the largest fraction of systems and reactions, even if they were treated with much more elaborate methods as is shown in subsequent chapters.

In principle, we could go along the opposite direction: calculate the collision number via kinetic theory of gases to get A and the energy barrier E_a *via* quantum chemistry and insert it to calculate the reaction rate [20]. Unfortunately, in most cases the results will be rather poor [3].

In the 1930s, efforts to get more rigorous formulations of microscopic chemical rate theory lead to transition-state theory, as formulated by EYRING, EVANS and POLANYI [4, 5].

Derivation

We look at a standard second order reaction of two molecules **A** and **B**, reacting to one or more product molecules **P** without any detailed specification of them [1]. Reactive trajectories pass through *transition states* (TSs) ‡, being located at the barrier between reactant and product basins. Just for mathematical reasons it is assumed that these transition states are located within an interval $\delta\zeta$ centered at a central position $\zeta_{\ddagger}$ with respect to the *reaction coordinate* $\zeta(\mathbf{q})$ (where $\mathbf{q}$ is a suitable set of *internal coordinates*), defining a a transition region at $\zeta_{\ddagger} - \frac{\delta\zeta}{2} < \zeta(\mathbf{q}) < \zeta_{\ddagger} + \frac{\delta\zeta}{2}$. It is further supposed that an equilibrium exists between reactants and transition states but not between transition states and products, i.e., no products can react back to transition states. Hence, the mechanism is:

$$\mathbf{A} + \mathbf{B} \rightleftharpoons \ddagger \rightarrow \mathbf{P}.$$
(2.2)

Since no equilibrium exists between transition states and products all trajectories headed to the products in the transition region will have no chance of coming back and contribute to the reaction rate. These are half of the trajectories in the transition region, since they are in equilibrium with

---

2 It should be noted that the *van't Hoff equation* emerged even before the approach by Arrhenius. Its differential form is $\left(\frac{\partial ln K_c}{\partial T}\right)_P = \frac{\Delta U^o}{RT^2}$, where K_c is the *concentration equilibrium constant* and ΔU^o is the standard *internal energy* change upon reaction. Similar to Arrhenius, a logarithmic plot can be done to determine the unknown quantities.

the reactants and are moving into both directions with equal probability. With this, the *frequency of transition states exiting to the product region* $\nu_{\ddagger}$ and contributing to the reaction rate can be expressed as:

$$\nu_{\ddagger} = \frac{1}{2\delta\xi}\langle|\dot{\xi}|\rangle_{\ddagger},\tag{2.3}$$

where $\langle|\dot{\xi}|\rangle_{\ddagger}$ is the average velocity along the reaction coordinate at position ξ. In order to get an absolute rate, the concentration of transition states to be multiplied with their exit-frequency needs to be calculated. According to the *law of mass action*, this concentration can be obtained from eq. 2.2, being:

$$[\ddagger] = K'_{\ddagger}[\mathbf{A}][\mathbf{B}].\tag{2.4}$$

As it is well known from statistical mechanics [21], chemical equilibria can be expressed in terms of the *partition functions Q* of their participants:

$$K'_{\ddagger} = \frac{\delta\xi}{\lambda_{T,\xi}}\frac{Q_{\ddagger}}{Q_{\mathbf{A}}Q_{\mathbf{B}}}\exp\left(\frac{-\Delta E_a}{RT}\right),\tag{2.5}$$

where ΔE_a is the activation energy (e.g., the zero point energy difference between reactants and TS), $Q_{\mathbf{A}}$, $Q_{\mathbf{B}}$ are the partition functions of both reactants and $\frac{\delta\xi}{\lambda_{T,q}}Q_{\ddagger}$ is the partition function of the TS. The latter is separated into two factors since the reaction coordinate ξ plays a special role: Unlike all other bound vibrational modes at the TS, it plays the role of a translation from reactants to products[3]. Hence, its contribution to the total partition sum needs to be that of a translation, which can be expressed in terms of a *de Broglie wavelength*:

$$\lambda_{T,\xi} = \frac{h}{\sqrt{2\pi\mu_{\xi}k_BT}},\tag{2.6}$$

with μ_{ξ} being the *reduced mass* for the motion along ξ, h the *Planck constant* and k_B the *Boltzmann constant*. The total rate of the reaction in eq. 2.2 is the product of the TS concentration expressed as in eq. 2.4 and the conversion frequency (eq. 2.3):

$$
\begin{aligned}
k_{TST}[\mathbf{A}][\mathbf{B}] &= K'_{\ddagger}\nu_{\ddagger}[\mathbf{A}][\mathbf{B}]\\
k_{TST} &= K'_{\ddagger}\nu_{\ddagger}\\
&= \frac{\delta\xi}{\lambda_{T,\xi}}\frac{Q_{\ddagger}}{Q_{\mathbf{A}}Q_{\mathbf{B}}}\exp\left(\frac{-\Delta E_a}{RT}\right)\frac{1}{2\delta\xi}\langle|\dot{\xi}|\rangle_{\ddagger}\\
&= \frac{1}{2}\frac{\langle|\dot{\xi}|\rangle_{\ddagger}}{\lambda_{T,\xi}}\frac{Q_{\ddagger}}{Q_{\mathbf{A}}Q_{\mathbf{B}}}\exp\left(\frac{-\Delta E_a}{RT}\right).
\end{aligned}\tag{2.7}
$$

The average velocity along the reaction coordinate at the TS $\langle|\dot{\xi}|\rangle_{\ddagger}$ can be calculated by means of the *Maxwell-Boltzmann velocity distribution*:

$$\langle|\dot{q}|\rangle_{\ddagger} = \frac{\int_{-\infty}^{\infty}\exp\left(-\frac{\beta\mu_{\xi}\dot{\xi}^2}{2}\right)|\dot{\xi}|d\dot{\xi}}{\int_{-\infty}^{\infty}\exp\left(-\frac{\beta\mu_{\xi}\dot{\xi}^2}{2}\right)d\dot{\xi}} = \sqrt{\frac{2k_BT}{\pi\mu_{\xi}}}.\tag{2.8}$$

---

[3] Partition functions of ideal gases with internal degrees of freedom usually contain translational, rotational, electronic and vibrational contributions as well as the zero-point potential energy $V_{zp}^{\mathbf{X}}$, resulting in $Q_{\mathbf{X}} = Q_{trans}^{\mathbf{X}}Q_{rot}^{\mathbf{X}}Q_{el}^{\mathbf{X}}Q_{vib}^{\mathbf{X}}\exp(-\frac{1}{k_BT}V_{zp}^{\mathbf{X}})$. The vibrational mode of the reaction coordinate at the TS is treated as a translation in TST, therefore contributing to $Q_{trans}^{\mathbf{X}}$ instead of $Q_{vib}^{\mathbf{X}}$.

This expression and eq. 2.6 can be inserted into eq. 2.7, resulting in:

$$k_{TST} = \frac{1}{2}\sqrt{\frac{2k_B T}{\pi\mu_\xi}} \frac{\sqrt{2\pi\mu_\xi k_B T}}{h} \frac{Q_\ddagger}{Q_{\mathbf{A}} Q_{\mathbf{B}}} \exp\left(\frac{-\Delta E_a}{RT}\right)$$
$$= \frac{k_B T}{h} \frac{Q_\ddagger}{Q_{\mathbf{A}} Q_{\mathbf{B}}} \exp\left(\frac{-\Delta E_a}{RT}\right).$$

$$(2.9)$$

It can be seen that neither the width of the transition region $\delta\xi$ nor the reduced mass of the translation along the reaction coordinate μ_ξ remain. Now we have obtained the TST rate expression. Usually, an additional prefactor κ containing additional corrections (as will be explained below) is added, resulting in the famous *statistical formulation* of TST:

$$k(T) = \kappa \frac{k_B T}{h} \frac{Q_\ddagger}{Q_A Q_B} \exp\left[\frac{-\Delta E_a}{RT}\right].$$

$$(2.10)$$

Thus, by knowing the partition functions of reactants and TS as well as the potential energy barrier of the reaction, we can directly calculate the rate of the whole reaction, without knowing anything about other areas in configuration space at all. This fact is quite impressive given that the whole available coordinate space of the system scales *exponentially* with the number of particles, thus quickly becoming huge. Then the vicinities of the two points needed for TST shrink to a tiny section of the whole space, ignoring almost everything else of it. Nevertheless at least qualitative estimates of reaction rates can be obtained for most systems if only this two tiny regions are included in the description. Besides the statistical formulation of TST, the perhaps even more renowned *thermodynamic* formulation (also termed *Eyring-Polanyi equation*) can be used [22]:

$$k(T) = \frac{k_B T}{h} K^0 \exp\left[\frac{-\Delta G^{\ddagger,0}}{RT}\right] = \frac{k_B T}{h} K^0 \exp\left[\frac{-\Delta S^{\ddagger,0}}{R}\right] \exp\left[\frac{-\Delta H^{\ddagger,0}}{R}\right],$$

$$(2.11)$$

with K^0 the *reciprocal standard concentration* and $\Delta G^{\ddagger,0}$, $\Delta S^{\ddagger,0}$ and $\Delta H^{\ddagger,0}$ the *free energy*, *entropy* and *enthalpy* barriers at standard conditions, respectively. Now, transition state theory is again quite similar to the Arrhenius equation (eq. 2.1), however, the potential energy barrier E_a is replaced by the free energy barrier $\Delta G^{\ddagger,0}$, indicating the fact that entropic effects are also needed if a reliable description of reaction rates shall be achieved[4].

Shortcomings

Reviewing the derivation of TST shown above some of its limitations are becoming obvious. In the underlying model (eq. 2.2) reactants and TS are assumed to be equilibrated, whereas only reactions in the direction TS to products are possible. The second assumption is deficient in practice: trajectories going through the TS region on their way to the products might turn back, e.g., due to thermal fluctuations and recross to reactants, in opposition to the assumption made in eq. 2.3. It is therefore called the *no recrossing* assumption. Even without thermal fluctuations recrossings are quite common if we look at the underlying PES of the system. For the simple case of a system with a linear or near-linear reaction path and negligible coupling between the reaction path and other vibrational modes, successful reactive trajectories will pass the TS and accomplish the reaction by reaching the products basin. Then, however, the story is not finished. If coupling between reaction coordinate and other vibrations is low, there will be almost no vibrational energy distribution such that the system performs a pendulum motion through the products minimum, climbs the other side and then turns back to the TS. Due to the small coupling the energy in the reaction coordinate will often be still high enough to cross the TS again, now directed to the reactants, thus generating

---

4 The thermodynamic formulation of TST builds the base for *Eyring-plots* well known in experimental (and theoretical) kinetics. They are conducted similar to Arrhenius-plots with the distinction that the parameters $\Delta G^{\ddagger,0}$, $\Delta S^{\ddagger,0}$ and $\Delta H^{\ddagger,0}$ for the actual reaction can be obtained from them. Eyring-plots are used in chapter 8

a recrossing event. If the reaction coordinate is *curved* near the TS, a reactive trajectory will usually climb up the potential wall beyond the TS after it has reacted. If it comes back, the probability is large that it recrosses the TS in a pendulum motion unless vibrational couplings will guide the trajectory from this hillslope straight into the product region.

Moreover, the reaction coordinate ξ plays an exceptional role in the whole TST-concept. Its partition function is treated separately (eq. 2.6) and its time derivative is used to calculate the turnover frequency at the TS (eq. 2.3). In reality, it is difficult to treat a single internal coordinate of a molecule independently from all others, since the vibrational modes are usually coupled during internal motions.

The TS-region, in which all motions towards the products are assumed to be reactive, is located around the TS position $\xi_{\ddagger}$ and has a width $\delta\xi$. Since $\delta\xi$ does not appear in the final TST rate expression, its actual extent does not play any role. It is therefore possible to make it infinitesimal, then resulting in a $N-1$ *dimensional hypersurface* perpendicular to the reaction coordinate, incorporating the full space of all other coordinates at the actual TS-position. This surface is called *dividing surface*, since all trajectories that cross it are classified as reactive in TST, thus effectively dividing the coordinate space in reactants and products sections. This surface is located at $\xi_{\ddagger}$, the point along the reaction coordinate with the highest potential energy, hence the TS with respect to *potential energy*. We will see below that the position must actually be determined with respect to the *free energy* along the reaction coordinate, hence showing the deficiency of the location in TST.

As it can be seen from eq. 2.10, only information about the reactants minimum and the TS is needed for the whole theory. Usually, the *harmonic approximation* is used to calculate these partition functions, thus anharmonic shapes of the PES, as they always exist in real systems, are not recognized.

Further, the derivation of TST uses classical trajectories moving along the system's PES as underlying model, hence ignoring all quantum mechanical effects such as tunneling or zero point energies[5]. This leads to five major pitfalls of TST, also shown in fig. 2.1.

1. Separability of the reaction coordinate from all others.

2. No recrossing of the dividing surface.

3. The diving surface is always located at the TS of the potential energy.

4. Harmonic approximation in the calculation of partition functions.

5. Classical behavior of the system is assumed.

In practice, the significance of these shortcomings strongly depends on the chosen system and the temperature, e.g., tunneling will get more important at lower temperatures, whereas the no-recrossing assumption is less valid at higher temperatures. For systems that approximately obey all TST-assumptions and thus circumvent all its pitfalls, very accurate k(T) values can be obtained, whereas the theory might fail spectacularly for others [23, 24].

2.1.2 Handling of TST-Problems

Since its foundation in the 1930s, TST has become a widely used tool for k(T) calculations. In parallel, several authors tried to solve or at least diminish TST's intrinsic problems listed above [6].

---

5 Interestingly, quantum mechanical models like the harmonic oscillator (for vibrations), the rigid rotator (for rotations) and the particle in the box (for translations) are used for the calculation of the partition sums for the reactants and the TS, thus incorporating quantum mechanics indirectly.
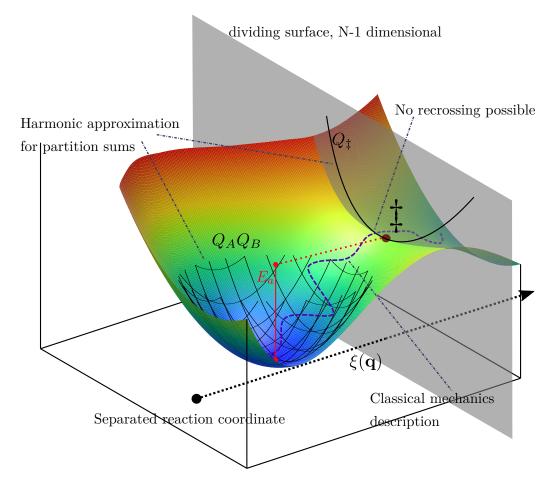
Figure 2.1: Schematic overview of the inherent approximations of TST, for a two-dimensional model system. The reaction coordinate $\xi(\mathbf{q})$ is shown in the base plane, the dividing surface is perpendicular to it, positioned at the potential energy TS (large scarlet dot). The partition sums of reactants (2 dimensional) as well as the TS (one dimensional, due to the separated reaction coordinate) are calculated with the harmonic approximation. Reactive trajectories show no recrossing and end always on the products side of the dividing surface.

Variational TST

The first important improvement is the *variational TST* (VTST), also called *canonical variational theory* (CVT) [25, 26]. Conventional TST as discussed above leads usually to an *overestimation* of the rate constant. The reason is that in eq. 2.10 the dividing surface, representing the bottleneck the system must overcome during a reaction, is placed at the potential energy maximum along the reaction coordinate.

In reality, however, the activation criterion is not the potential energy but the *free energy*, since entropic effects play a significant role during reactions (what is already included in thermodynamic TST (eq. 2.11), but not with the correct position of the free energy barrier).

Therefore, the free energy maximum along the reaction coordinate needs to be taken as position of the dividing surface (fig. 2.2 (a)). Usually this is viewed from another perspective: Since the rate constant depends exponentially on the free energy activation barrier (eq. 2.11), the resulting rate constant (or the *reactive flux*) needs to be *minimized*, with respect to the reaction coordinate ξ. In line with that, the number of recrossings becomes minimal at the correct TS-position, thus maximizing the effective reactive flux[6]:

$$k^{CVT}(T) = \min_{\xi}(k^{TST}(T, \xi)). \tag{2.12}$$

The minimum can be determined variationally, i.e., by setting the first derivative with respect to ξ to zero:

$$\frac{\partial}{\partial \xi}[k^{TST}(T, \xi)] \stackrel{!}{=} 0. \tag{2.13}$$

Since TST and CVT provide an *upper bound* for the exact k(T) value in case of classical systems and known PES functions [27], CVT is always an improvement over TST[7]. The drawback of this improvement is that much more calculation effort is needed. Instead of only three frequency calculations (TST, first and second reactant) a number of additional frequency calculations along the interpolated reaction path is needed in order to parametrize a free energy surface based on partition sums and then determine $k(T, \xi)$ as well as the minimum of its derivative [10, 29].

In spite of the larger computational expense, CVT rate constants are usually calculated besides TST rates in present publications (chapter 6). Though CVT/VTST is an important step forward and frequently used, it has only solved issue 3 of the TST shortcomings!

Recrossing

The issues of recrossing and quantum effects are usually handled together by inserting a single prefactor in the TST or CVT rate constants: The *transmission coefficient* κ.

As stated in the last section, TST assumes that trajectories crossing the dividing surface always end in the product region. In reality, the system can be pushed back, for instance, by thermal or geometric effects such it only stays a short time in the product side before returning to the

---

6 The VTST method presented here is still an approximation since only the position of the dividing surface with respect to the reaction coordinate is altered, but not the shape of the surface itself. In reality, the correct dividing surface (i.e., the one that corresponds to the "global minimum" of the rate constant and thus also the global minimum for the recrossing) might have a complicated rugged shape, depending on the couplings between the different internal coordinates of the system. Of course, such an exact parametrization of the dividing surface is impossible at least analytically for all but the smallest systems [1]. Even if it is known, recrossings still can happen.

7 Besides usual CVT, where the free energy needs to be calculated along the reaction coordinate, some improved but also more tedious approaches are known in the literature: *microcanonical variational theory* (μVT) [28] uses a microcanonical ensemble instead of a canonical one for optimization of ξ, which involves calculations of accessible states depending on the path progress and the total energy (phase space integration), *improved canonical variational theory* (ICVT) uses a mixture of canonical and microcanonical optimizations depending on threshold energies [22], which reduces the phase space integration effort.

reactants. This effect is called *recrossing*. Since TST ignores it by construction, its rate constant value will be always too large (the effective reactive flux should be diminished by recrossing). It can be shown that the location of the dividing surface at maximum free energy of activation minimizes the recrossing, i.e., recrossing appears more often if the dividing surface is placed at the potential energy bottleneck instead of the free energy one. If the exact dividing surface would be known, the recrossing could be diminished further (see above).

For real systems, recrossing can still be an important factor, especially if reactions with broad barriers are calculated, where the trajectories remain a significant amount of time in the transition region and high temperatures are used, where, e.g., thermal motions can push the system back through the bottleneck more easily.

Exact calculations of classical transmission coefficients (i.e., exclusion of quantum effects) require actual sampling of trajectories and calculation of correlation functions, as it will be shown in the next section. For static calculations, though, a bunch of approximate models was developed. Two of them are the *unified statistical model* (US) for TST [30] and the *canonical US* (CUS) [31] for CVT calculations.

The general assumption for US and CUS is that recrossing becomes important if more than one bottleneck, i.e., local free energy maximum, is located along the reaction path. If two local maxima are present, the dividing surface will be located at the higher one for CVT (since the global maximum of free energy is used as the position), but the system might be trapped in the high energy region between this and the slightly lower second maximum some amount of time, such that it could oscillate back and forth, increasing the possibility for recrossings (fig. 2.2 (b)).

The partition function for the bound degrees of freedom (excluding the reaction coordinate) at a certain value ξ of the reaction path progress can be expressed as:

$$q(T, \xi) = e^{-\beta V_{MEP}(\xi)} Q(T, \xi),\tag{2.14}$$

where $\beta = \frac{1}{k_B T}$ is the *inverse temperature*, $Q(T, \xi)$ denotes the partition function of a dividing surface located at ξ and the exponential provides an energy shift with respect to the reactants minimum.

If we calculate the partition function for the global free energy maximum $q_{CVT}(T)$, for the second local maximum $q_{max}(T)$ and for the local minimum between both maxima $q_{min}(T)$, the CUS recrossing coefficient can be expressed as:

$$\kappa^{CUS}(T) = \frac{q_{max}(T) q_{CVT}(T)}{q_{max}(T) + q_{CVT}(T) - \frac{q_{max}(T) q_{CVT}(T)}{q_{min}(T)}}.\tag{2.15}$$

This empirical correction delivers good results for some cases, but it cannot describe situations, where recrossing occurs even if the free energy profile only has one maximum (which is the case in most reactions). In those cases κ_{CUS} becomes unity [31]. In general, analytical recrossing corrections are rarely used.

Tunneling Corrections

More common are *tunneling corrections* to TST or CVT. In contrast to recrossing, which typically imposes a correction factor between 0.99 and 0.6 to reaction rates, slightly growing in importance with raising temperature, tunneling can enhance reactions even more radical, up to more than ten orders of magnitude for proton transfers at very low temperatures [6, 23, 32–34][8].

---

8 In general, tunneling and recrossing corrections can be seen to be of similar importance, since recrossings always influence the rate constant, where tunneling only causes the huge accelerations over many orders of magnitude if it is favored and the classical rate is extremely small, what is usually the case for very low temperatures and systems were hydrogen or deuterium are transferred (see chapter 9).

One of the simplest but still widely known tunneling models is the semiclassical *Wigner correction* [35]. Here, the shape of the potential barrier is modeled as an inverted parabola, i.e., a Taylor series at the TS of the reaction coordinate, truncated after the second term:

$$\kappa^W(T) = 1 + \frac{1}{24} \left| \beta \hbar \omega^\ddagger \right|, \tag{2.16}$$

with $\omega^\ddagger$ being the imaginary frequency of the (potential energy) transition state, i.e., the curvature of the reaction coordinate, and $\hbar$ the *reduced Planck constant* ($\frac{h}{2\pi}$). Unsurprisingly, this model hardly delivers quantitative results, if at all it should be used for barriers with near parabolic shape at temperatures where the expected tunneling coefficient is small (less than 1.2) [22]. Nevertheless, it can serve as a first rule-of-thumb estimate for the importance of tunneling: If the temperature is small and $\omega^\ddagger$ is large, i.e., the barrier is sharp, large tunneling contributions can be expected and more sophisticated tunneling corrections should be applied.

If rate constants are calculated with corrected TST nowadays, two tunneling approximations are the most popular ones: *zero curvature tunneling* (ZCT) [36] and *small curvature tunneling* (SCT) [37].

As the terminology may indicate, the actual choice of the method depends on the *curvature* of the reaction path. It is the second derivative of the *cartesian geometry* $\mathbf{x}(\xi)$ with respect to the *reaction coordinate* ξ:

$$\gamma(\xi) = \frac{d^2 \mathbf{x}}{d\xi^2}. \tag{2.17}$$

If the curvature is low, i.e., the reaction path appears nearly linear in the coordinate space under consideration, the ZCT method can be applied. Both ZCT and SCT are *one-dimensional* models. Their common assumption is that the motion along the reaction coordinate can be separated from the motion of the bound degrees of freedom orthogonal to them, i.e., similar to TST. The motion along the reaction coordinate is considered as slow with respect to the bound degrees of freedom, due to the similarity to quantum dynamics this is also called the *vibrationally adiabatic model*.

In the resulting one-dimensional system, the transmission coefficient for CVT is then evaluated by integration over all energies present in the thermal ground state, populated according to a *Boltzmann distribution* (the largest part of the derivation is identical for ZCT and SCT):

$$\kappa(T) = \frac{\int_0^\infty P(E) e^{\beta E} dE}{\int_0^\infty P_C(E) e^{\beta E} dE}. \tag{2.18}$$

Both numerator and denominator are essentially calculating *transmission probabilities* $P(E)$ for all energies E, weighted by the actual population, expressed with the Boltzmann factor. In the numerator, the approximated *quantum mechanical* transmission probabilities are integrated, whereas in the denominator, the *classical* transmission probabilities as already included into usual CVT are integrated. Therefore, the division accounts for the remaining transmission prefactor not already included into CVT itself[9].

In the classical picture, the system can only overcome the barrier if its energy is higher than the barrier height:

$$P_c(E) = \Theta \left\{ E - (V_{MEP}(\xi*) + E_{ZPE}(\xi*)) \right\}, \tag{2.19}$$

where Θ is the *Heaviside function*, $\xi*$ is the variationally corrected position of the dividing surface, V_{MEP} is the potential energy of the reaction path and E_{ZPE} are the vibrational ground state energies of the bound degrees of freedom.

---

9 This point might get clearer if we recall that the definition of the transmission coefficient can be written as the relation between the CVT rate constant ($k_{CVT}(T)$) and the desired exact one ($k(T)$): $\kappa = \frac{k(T)}{k_{CVT}(T)}$.

An approximate expression for the quantum mechanical transmission probability is a semiclassical one:

$$P(E) \approx \begin{cases} 0 & E < E_0 \\ \{1 + \exp{[2\theta(E)]]\}}^{-1} & E_0 \leq E \leq V_{max} \\ 1 - \{1 + \exp{[2\theta(E)]]\}}^{-1}(2V_{max} - E) & V_{max} \leq E \leq 2V_{max} - E_0 \\ 1 & 2V_{max} - E_0 < E \end{cases}. \quad (2.20)$$

Here, E_0 is the maximum of the reactants and products energies (i.e., the lowest energy value existent on both sides of the TS), V_{max} is the highest potential energy along the reaction path under consideration of zero point vibrational energies of bound degrees of freedom and $\theta(E)$ is the *imaginary action integral* defined as:

$$\theta(E) = \frac{1}{\hbar} \int_{\xi_E}^{\xi_P} \sqrt{2\mu[V(s) - E]} d\xi, \quad (2.21)$$

where ξ_E and ξ_P are the reaction coordinate values of reactant and product asymptotes and μ the reduced mass of the system. Equation 2.20 is distinguishing four cases. No transmission can occur at all if the reactant energy is *lower* than the lowest energy on the product side. For all other energies up to the TS, transmission probabilities can be calculated with imaginary action-integrals, as it is done for tunneling in common. Note that no transmission can occur in the classical case here (eq. 2.19). Above the barrier, non-classical *reflection* can occur, which leads to lower quantum mechanical than classical transmission coefficients in this area. By assuming a parabolic shape of the barrier, case three calculates the influence of this effect. In order to hold the calculation effort manageable, the transmission is set to one beyond a certain limit ($2V_{max} - E_0$). This can be seen in fig. 2.2 (c).

The ZCT transmission coefficient is calculated with eq. 2.18. If the SCT coefficient shall be calculated, the reaction path curvature needs to be included explicitly. As stated above, the central assumption is that the reaction coordinate is *decoupled* from all coordinates orthogonal to it, i.e., the path is linear. For curved paths, some coupling between the coordinates will happen, therefore seriously damaging the underlying assumptions of ZCT. For paths with small (and medium) curvature a small correction is thought to be sufficient: The effective reduced mass of the system (as needed for eq. 2.21) is altered:

$$\mu(\xi) = \mu \prod_{m=1}^{N-1} \min \begin{cases} \exp\left(-2\overline{a_m}(\xi) - [\overline{a_m}(\xi)]^2 + \left[\frac{d\overline{t_m}(\xi)}{d\xi}\right]^2\right) \\ 1 \end{cases}, \quad (2.22)$$

with the product running over all bound $N-1$ normal coordinates. $\overline{t_m}(\xi)$ is the average value of the mass-scaled normal coordinate m on its zero-energy turning point on the concave side of the reaction path [22], and $\overline{a_m}(\xi)$ includes the respective coordinate of the reaction-path curvature via:

$$a_m(\xi) = -\gamma_m(\xi)t_m(\xi). \quad (2.23)$$

This corrected mass is the consequence of *corner-cutting*-effects due to tunneling, i.e., shortening the reaction path by going through classically forbidden regions at corners (fig. 2.2 (d)). The larger the curvature of the respective modes, the lower becomes the effective mass in these dimensions, increasing the quantum mechanical transmission coefficient.

If the curvature of the reaction path is too large, the SCT assumption of the corrected mass can implode. For these situations, the *large curvature tunneling* (LCT) model was developed. More details to it can be found in the respective papers [22, 36]. As one may suspect from the triad of ZCT, SCT and LCT (there are actually also different versions of LCT!), the handling of tunneling in TST calculations is far from straightforward. Although CVT with SCT correction (usually termed

(a) CVT: variational optimization

(b) CUS: recrossing correction

(c) ZCT: one-dimensional tunneling

(d) SCT: corner cutting
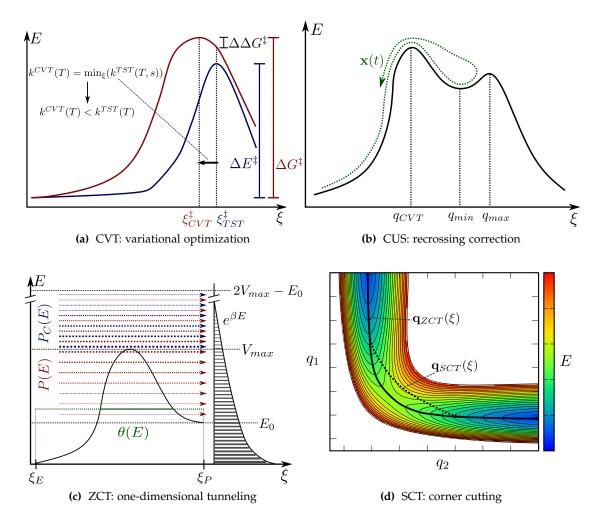
Figure 2.2: Overview of different TST-correction schemes. (a) The CVT method minimizes the rate constant by optimization of the dividing surface position. The barrier is corrected by $\Delta\Delta G^{\ddagger}$. (b) The CUS recrossing correction considers cases where two local minima in free energy space are neighbored and trajectories tend to recross. (c) The ZCT tunneling scheme calculates classical $P_C(E)$ as well as semiclassical $P(E)$ transmission probabilities and integrates over the Boltzmann distribution. (d) The SCT tunneling scheme considers the coupling to other coordinates, e.g., through *corner cutting* [22].

as CVT/SCT) is by far the most commonly used corrected TST descendant (see theory references in chapter 6), it is dangerous to simply use it for all reactions as a *black-box*-method since there are many cases where the method can fail.

In addition, the effort for doing a calculation raises significantly if we move from simple TST to, e.g., CVT/SCT. The former only needs two frequency calculations and can be done with pen and paper for small systems, the latter needs a large number of frequency calculations along the reaction path (also for the correct optimization of the dividing surface position in CVT) and significant postprocessing of the data (like evaluations of Boltzmann- and imaginary-action integrals) with programs like POLYRATE [10]. This is far from *black-box*, since, e.g., an appropriate set of internal coordinates needs to be specified manually in order to get useful results[10].

Besides these drawbacks the maybe most severe one is that *no convergence* to exact results can be expected when moving to more complicated methods. There is no guarantee that CVT/SCT or CVT/LCT are even near to the exact (classical or quantum) result, since, e.g., the handling of recrossing is complicated or the shape of the surface might be so far from harmonic that simple anharmonic corrections for the partition sums are not sufficient.

Therefore, corrected parametric TST calculations are only used in chapter 4 in this thesis for comparison, otherwise methods based on sampling of the configuration space are employed. It will be shown in the next sections that these methods can indeed accomplish convergence to the exact quantum mechanical result if used correctly.

2.1.3   Configurational Samplings

As we have seen so far, parametric models for rate constant calculations based on TST have numerous disadvantages. They are complicated both in understanding and usage, they have no guarantee to converge to the exact result and they require the user to gather tons of knowledge of the topic if he or she wants to judge which type of method is best suited for the current problem. Of course there are many papers where the authors simply used TST, CVT, CVT/ZCT and CVT/SCT to calculate rates and compare them to experiment, but this approach might fail spectacularly if the reaction of interest is somewhat different from the "standard case", e.g., having large curvature of the reaction path or no near-parabolic shape of the activation barrier.

Back in the golden era of parametric TST-corrections in the early 80s, quantitative trajectory samplings or even wave packet calculations as discussed in the following were practically out of reach for most systems greater than 4 to 6 atoms. Today, the limits especially for trajectory samplings have been greatly broadened. As will be shown in chapter 8, rate constants for systems of fourty atoms or more can be calculated to a high degree of accuracy with configurational samplings. The future range of applicability for parametric TST corrections could therefore be shifted to the calculations of very large systems (hundreds of atoms)[11], leaving small and medium sized systems to trajectory methods.

---

10 There are a plenty of other methods for the correction of TST deficiencies, for instance, usage of anharmonic frequencies, reduced dimensionality and microcanonical corrections. They are skipped here to keep this section manageable, since they are used rarely in practice. Details to these methods and relative importances of them are explained elsewhere [6, 22, 38].

11 Another problem are the frequency calculations needed for the parametric methods. If very large systems are treated, these will become very expensive, if an *ab-initio* method with good quality is used. This problem becomes even more urgent if no analytical frequencies are available for the method of choice. Therefore in practice the range of applicability is also limited for parametric models.

Statistical Definition of Free Energy

The connection between parametric and sampling methods is the free energy[12]. As seen in eqs. 2.10-2.11, the TST rate constant can be calculated either with respect to the partition functions of reactants and the transition state or with respect to the free energy difference between them.

The *canonical partition function* of a system can be integrated above its full coordinate space [39]:

$$Q = \int e^{-\beta E(\mathbf{q})} d^N \mathbf{q}, \tag{2.24}$$

with N being the number of degrees of freedom in the system. Here and in the following, the integrals are meant to run over all space, corresponding to limits of $-\infty$ to $+\infty$ in all N dimensions. This is assumed also in the following.

The *Helmholtz free energy*[13] can be calculated directly from this partition function:

$$A = -k_B T \ln Q. \tag{2.25}$$

This definition is valid for each system but has no use in rate constant calculations since it includes all coordinate space, i.e., the whole reactive process and it is not possible to calculate reaction barriers.

The solution is to include a reaction coordinate ξ, also called *collective variable* (CV). Now all degrees of freedom but ξ can be integrated out, resulting in a ξ-dependent partition function:

$$Q(\xi) = \frac{\int \delta \left[\xi(\mathbf{q}) - \xi \right] e^{\beta E} d^N \mathbf{q}}{\int e^{\beta E} d^N \mathbf{q}}, \tag{2.26}$$

with $\delta \left[\xi(\mathbf{q}) - \xi \right]$ being the *Dirac delta function*, thus for each value of $\xi(\mathbf{q})$ only contributions with the exact value of ξ are included into the partition sum. Now a free energy profile along ξ can be calculated as needed for VTST[14]:

$$A(\xi) = -k_B T \ln Q(\xi). \tag{2.27}$$

Unfortunately it is still impossible to calculate the integrals over space as needed in eq. 2.26, since an infinite number of potential energy calculations would be needed. The loophole and also the step towards trajectory samplings is the assumption that the system of interest is *ergodic* i.e., that every point in space is visited during a MD simulation if the simulated time interval goes to

---

12 This equivalence is only approximate, since the *reactive flux* formulation of TST is the basis for TST rates calculated from trajectory samplings. Within this formulation, a number of trajectories originating at the reactants basin are propagated and those who get beyond the dividing surface contribute to the actual rate. More details are shown in the recrossing section and further below in the RPMD section. However, in practice, this conceptual difference only affects the TST prefactor.

13 It is important to distinct between the *Gibbs* free energy G, the *Helmholtz* free energy A and the *Landau* free energy F. The Helmholtz free energy can be calculated as $F = U - TS$ with U being the internal energy and S being the entropy, whereas the Gibbs free energy can be calculated as $G = U + PV - TS$, where PV is the pressure-volume product. Thus the Gibbs free energy describes a system with constant pressure and temperature (the common case for chemical reactions in test tubes), whereas the Helmholtz free energy describes a system with constant volume and temperature. In the forthcoming of this work, only gas phase systems are treated and it is assumed that $G \approx F$, i.e., that the pressure-volume product PV can be neglected. The Landau free energy parametrically depends on a reaction coordinate but is calculated in the same way as the Helmholtz free energy in practice. Therefore, the letters G, A and F are used here as synonyms, unless noted explicitly, depending in which community with type of free energy is used conventionally.

14 TST-correction methods like CVT calculate the free energy surface by means of interpolation between a number of frequency calculations along the given reaction path. In the case of sampling methods, this surface is obtained from exploration of the thermally accessible coordinate space of the system.

infinity. An equivalent expression is that in the limit of infinite simulation time the *time average* $P(\xi)$ becomes equal to the *ensemble average* $Q(\xi)$:

$$\lim_{t \mapsto \infty} (P(\xi)) = Q(\xi). \tag{2.28}$$

Of course, infinite simulations are impossible, therefore finite simulations are done and canceled after some time. Then, eq. 2.28 is still approximately true. If the PES of the system would be flat in the interesting area, a probabilistic sampling could indeed result in a representative description of it. In the usual case of a PES with local minima and high-energy transitions between them, this approach is much less convenient, since the probability that a trajectory visits a certain area in coordinate space decreases exponentially with the energy of the respective space section. It is said that visits of these regions with high energy like transition areas between minima are *rare events*. In order to do a meaningful sampling also at those areas, extremely long MD runs would be needed.

Umbrella Sampling

To overcome the rare-event-problem, several *enhanced sampling* techniques were developed [40]. For our application of sampling a one-dimensional reaction path $\xi((q)$ the *umbrella sampling* method [41] is the best suited one. In order to enforce samplings at a certain value of the CV ξ (we could say of the dividing surface orthogonal to ξ), a *bias potential* only depending on the reaction coordinate is added to the potential energy function of the system:

$$E_b(\mathbf{q}) = E(\mathbf{q}) + w(\xi), \tag{2.29}$$

where E_b is the biased potential energy, E is the unbiased potential energy and $w(\xi)$ is the bias potential, usually of parabolic shape:

$$w(\xi) = K(\xi - \xi_0)^2, \tag{2.30}$$

with K being the applied *bias force constant*. We can now, for instance, add a bias potential at the transition state and get a reliable sampling distribution $P^b(\xi)$[15], what would have needed enormous amount of calculation time if only rare events were used to sample the critical region (fig. 2.3). Of course this biased distribution cannot simply be plugged into eq. 2.26 since then the free energy of the transition state could be lower than that of the minima.

Fortunately, the effect of the umbrella potential can be integrated out. First, the bias potential $w(\xi)$ can be added directly to the energy expressions appearing in the time average, resulting in the *biased average*:

$$P_b(\xi) = \frac{\int \delta \left[\xi(\mathbf{q}) - \xi\right] \exp \left[\beta(E(\mathbf{q}) + w(\xi(\mathbf{q})))\right] d^N \mathbf{q}}{\int \exp \left[\beta(E(\mathbf{q}) + w(\xi(\mathbf{q})))\right] d^N \mathbf{q}}. \tag{2.31}$$

By disassembling the exponential in the numerator into two factors, the one solely depending on the bias potential (and not the actual energy) can be factored out and set before the integral:

$$P_b(\xi) = e^{\beta w(\xi(\mathbf{q}))} \cdot \frac{\int \delta \left[\xi(\mathbf{q}) - \xi\right] e^{\beta E(\mathbf{q})} d^N \mathbf{q}}{\int \exp \left[\beta(E(\mathbf{q}) + w(\xi(\mathbf{q})))\right] d^N \mathbf{q}}. \tag{2.32}$$

---

15 A time average $P(\xi)$ can also be seen as a probability distribution with respect to ξ. This enables practical calculations of the time average and thus the desired free energy profile $A(\xi)$.

(a) unbiased sampling   **(b)** biased sampling
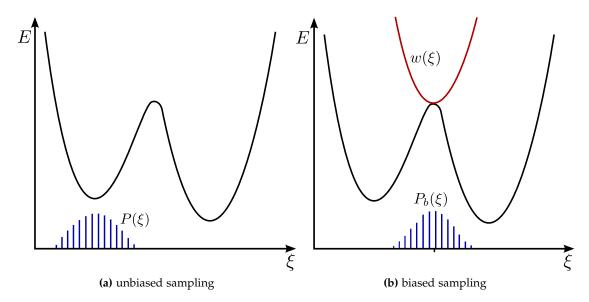
Figure 2.3: Effect of the umbrella bias potential on a MD sampling trajectory. Without any bias, a sampling trajectory started at one minimum would be trapped in it until it might escape to the right minimum by a rare event, resulting in the probability distribution $P(\xi)$ (a). When a bias located at the transition state is applied, a sampling trajectory starting from one minimum will be pulled towards the TS and then be trapped there, resulting in $P_b(\xi)$ (b).

The objective is now to express the wanted unbiased distribution $P(\xi)$ in terms of the biased one $P_b(\xi)$ and a correction depending on the bias potential $w(\xi)$. If we compare eqs. 2.26 and 2.31, the following expression can be obtained:

$$
\begin{aligned}
P(\xi) &= P_b(\xi)e^{\beta w(\xi(\mathbf{q}))} \cdot \frac{\displaystyle\int \exp\left[-\beta(E(\mathbf{q}) + w(\xi(\mathbf{q})))\right] d^N\mathbf{q}}{\displaystyle\int e^{\beta E(\mathbf{q})} d^N\mathbf{q}} \\
&= P_b(\xi)e^{\beta w(\xi(\mathbf{q}))} \cdot \frac{\displaystyle\int e^{-\beta E(\mathbf{q}))} e^{-\beta w(\xi(\mathbf{q}))} d^N\mathbf{q}}{\displaystyle\int e^{\beta E(\mathbf{q})} d^N\mathbf{q}}
\end{aligned}
\tag{2.33}
$$

The fraction can be integrated out to an ξ-independent *Boltzmann-average* $\left\langle e^{\beta w(\xi)} \right\rangle$ of the bias potential, leading to a significant simplification of the whole expression:

$$
P(\xi) = P_b(\xi)e^{\beta w(\xi)} \left\langle e^{\beta w(\xi)} \right\rangle.
\tag{2.34}
$$

To get rid of the exponentials, the logarithm can be taken on both sides, leading to the free energy through eq. 2.27:

$$
A(\xi) = -k_B T \ln(P_b(\xi)) - w(\xi) + \mathfrak{F},
\tag{2.35}
$$

where $\mathfrak{F} = -k_B T \ln\left\langle e^{\beta w(\xi)} \right\rangle$ is an additional constant independent of ξ. Since we are only interested in *relative* free energy values, $\mathfrak{F}$ can be ignored and we must just take the logarithm of the sampled bias probability distribution for each (discrete) value of ξ and subtract the value of the additional potential at this position. Thus, evaluating an umbrella sampling is surprisingly simple.

However, by closer inspection of fig. 2.3 (b) a new problem becomes apparent: In fact the transition region that was problematic is now well sampled, but therefore the minimum regions

are almost completely neglected! Hence the rare event problem only has *shifted* from the transition state to the minima. Of course we could argue that the strength of the potential simply needs to be reduced such that also regions farther away from the TS are sampled more often. But then the effect of the potential in the direct vicinity of the TS might become too loose, so that the original problem returns. It might be possible in certain cases to find an ideal bias potential (either in terms of the force constant or the mathematical expression of the term itself) such that the whole region of interest is sampled with similar probability. At least if more than one barrier is present in the coordinate space of interest this ansatz becomes impractical. In general, another strategy is used: connection of several independent umbrella samplings scattered along the reaction coordinate.

WHAM

One quite prominent method for combining umbrella samplings at different positions along a reaction coordinate is the *weighted histogram analysis method* (WHAM) [42]. It constructs a total unbiased probability distribution $\mathfrak{P}(\xi)$ as a sum of weighted histograms obtained from the single samplings conducted with different positions of the biasing potential (also called *umbrella windows*):

$$\mathfrak{P}(\xi) = \sum_i^W p_i(\xi) P_i(\xi), \tag{2.36}$$

where W is the number of sampled distributions to combine, $P_i(\xi)$ and $p_i(\xi)$ the i'th sampling distribution and its ξ-dependent weighting factor, respectively. For each distribution, the i'th unbiased free energy surface can be calculated as:

$$A_i(\xi) = -k_B T \ln(P_{b,i}(\xi)) - w_i(\xi) + \mathfrak{F}_i, \tag{2.37}$$

which is identical to eq. 2.35, apart from the indices i. However, now $\mathfrak{F}_i$ cannot be simply ignored as it was done for the single sampling because this constant is different for each sampling and due to this different offsets the correct weighting of the single distributions is not obvious. Hence, if different samplings shall be combined, the $\mathfrak{F}_i$'s need to be determined somehow. It is practically impossible to explicitly integrate the average values they represent, but fortunately an iterative method exists: WHAM.

In order to understand how this method works it is useful to translate the rather abstract formulation used so far into the language of applied numerics. As already explained and indicated in fig. 2.3, the needed time averages or probability functions ($P_i(\xi)$) are obtained by trajectory samplings from which the number of hits in different *bins* along the reaction coordinate are counted, i.e., the full ξ-range is divided into a number of sections and for each sampled structure the actual ξ-value is assigned to the correct section or bin. This results in multiple ξ-dependent *histograms*, one for each umbrella sampling. After some derivation [42], the WHAM equations are obtained:

$$\mathfrak{P}(\xi_j) = \frac{\sum_{i=1}^N P_i(\xi_j)}{\sum_{i=1}^N n_i \exp\left[\beta(\mathfrak{F}_i - w_i(\xi_j))\right]}, \tag{2.38}$$

$$\mathfrak{F}_i = -k_B T \ln\left[\sum_{j=1}^M \mathfrak{P}(\xi_j) e^{-\beta w_i(\xi_j)}\right]. \tag{2.39}$$

Here, N is the total number of individual umbrella samplings with i being the actual sampling, M the total number of bins per sampling with j being the actual bin and n_i the total number of sampling steps per umbrella window. Equation 2.38 calculates the total unbiased probability distribution $\mathfrak{P}(\xi)$ for each discrete ξ-value by summing up all single biased distributions, divided through an $\mathfrak{F}_i$-dependent term. Equation 2.39 calculates the needed $\mathfrak{F}_i$-terms by summing over the total unbiased distribution and weighting it by the i'th bias term. Both $\mathfrak{F}_i$ and $\mathfrak{P}(\xi)$ are unknown and are itself needed to calculate the other. Therefore, an *iterative procedure* is needed to solve these

(a) sampling in coordinate space   **(b)** resulting distributions
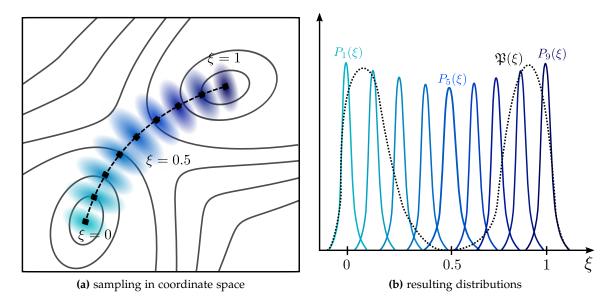
Figure 2.4: Combination of several umbrella sampling trajectories to a large probability distribution. The different samplings result in thousands of points in coordinate space, distributed around the central position of the bias (a). By sorting these points with respect to their ξ position, probability distributions $P_1(\xi)$ to $P_9(\xi)$ are obtained. These can be combined to a summarized distribution $\mathfrak{P}(\xi_j)$ with WHAM (b) or directly integrated to $A(\xi)$ with UI (not shown).

two equations to *self-consistency*. In practice, the initial guess for the $\mathfrak{F}_i$ is unity and the iterations are conducted until the change in the $\mathfrak{F}_i$-values falls below a suited threshold.

If convergence was reached, the resulting free energy surface $A(\xi)$ can be calculated by simply inserting $\mathfrak{P}(\xi_j)$ into eq. 2.27.

The WHAM method was implemented in the EVB-QMDFF program package, however it has a serious drawback: the calculations are quite expensive, especially if a large number of structures was sampled and many bins are used to subdivide the reaction path. During the umbrella samplings, each sampled structure needs to be assigned to one bin and at the end, the large expressions in eqs. 2.38-2.39 are calculated until convergence is reached. Unfortunately the convergence behavior gets worse the more bins are used, such that several hundreds or thousands iterations and in each iteration sums over millions to trillions of single sampling structures are needed for high quality k(T) calculations.

Although the calculation effort for the free energy profile is usually negligible in comparison to the sampling trajectories themselves, WHAM was only used for benchmarking in the line of this thesis. The idea of combining several independent umbrella samplings with WHAM is also illustrated in fig. 2.4.

Umbrella Integration

A much more practical method is the *umbrella integration* (UI) algorithm by Kästner and Thiel [43]. The idea of this method is to calculate the *derivatives* of the different samplings $P_i(\xi)$, weight them by a certain method to create the derivative of the full free energy profile and finally integrate this resulting curve.

By looking at eq. 2.37 the problematic part are the $\mathfrak{F}_i$. We have seen that the whole iterative procedure of WHAM is needed due to the unknown different $\mathfrak{F}_i$ which made it impossible to directly build a weighted sum of the different $P_i(\xi)$.

However, since the $\mathfrak{F}_i$ are constant and thus do not depend on ξ they vanish if the derivative of eq. 2.37 is taken with respect to ξ:

$$\frac{\partial A_i}{\partial \xi} = -k_B T \frac{\partial \ln(P_i^b(\xi))}{\partial \xi} - \frac{dw_i(xi)}{d\xi}. \tag{2.40}$$

This derivative is exact and independent of the unknown $\mathfrak{F}_i$. Unfortunately, a new problem has been introduced: The sampled probability distributions $P_i^b(\xi)$ have no analytic derivatives but should be derived numerically. This in turn can introduce numerical artifacts and instabilities, if they have, e.g., rugged shapes. Therefore the UI inventors had the idea of *approximating* the sampled distributions as normal distributions[16]:

$$P_i^b(\xi) = \frac{1}{\sigma_i^b \sqrt{2\pi}} \exp\left[-\frac{1}{2} \left(\frac{\xi - \overline{\xi_i^b}}{\sigma_i^b} \right)^2 \right], \tag{2.41}$$

where $\overline{\xi_i^b}$ is the *mean* and $(\sigma_i^b)^2$ is the *variance* of each window as calculated from the trajectory. In practice, the $P_i^b(\xi)$-distributions are not calculated if UI is used. Instead of that, $\overline{\xi_i^b}$ and $(\sigma_i^b)^2$ are calculated *on the fly* from each umbrella sampling trajectory. Thus, instead of a large array with bin population numbers in the case of WHAM, only two values are returned in the case of UI from each umbrella window, making the whole method much more comfortable.

In the next step, the logarithmic derivatives of the approximated probability distributions can be calculated analytically, leading directly to the desired derivatives of the free energy, where eq. 2.30 is used:

$$\frac{\partial A_i}{\partial \xi} = k_B T \frac{\xi - \overline{\xi_i^b}}{(\sigma_i^b)^2} - K(\xi - \xi_0). \tag{2.42}$$

In the penultimate step, the derivative of the desired free energy surface is obtained by building the weighed average of the single derivatives:

$$\frac{\partial A(\xi_j)}{\partial \xi} = \sum_i^N \frac{n_i P_i^b(\xi_j)}{\sum_k^N n_i P_k^b(\xi_j)} \left(\frac{\partial A_i(\xi_j)}{\partial \xi} \right). \tag{2.43}$$

The appearing parameters are basically the same as for the WHAM equations (eqs. 2.38-2.39). N is the number of umbrella windows, n_i is the total number of steps sampled for window i. The first factor calculates the normalized weight for the actual derivative: Near the maximum of its probability distribution $P_i^b(\xi)$, the corresponding free energy derivative i has by far the largest weight. Hence, no iterative procedure is needed anymore, all in all only some parameters are stuck together.

All what is left to do now is to integrate $\frac{\partial A(\xi_j)}{\partial \xi}$ numerically over all bins, such that the free energy curve $A(\xi)$ for the whole reaction is obtained.

A disadvantage is that UI is less accurate than WHAM by construction. That is due to the fact that the actual single probability distributions $P_i(\xi)$ are approximated by normal distributions and thus smeared out. If a large number of time steps is used for each umbrella trajectory, the resulting $P_i(\xi)$ are converging indeed to normal distributions, but if only rather few, e.g., some hundred points are used for the trajectories, it might be better to evaluate the actual distributions themselves with WHAM.

As a rule of thumb it can be formulated that WHAM should be used for "cheap" samplings with a low number of umbrella windows and short trajectories, whereas UI can be used for very

---

16 It can be shown that the normal distribution approximation is equivalent to a power series of $A_i(\xi)$ (i.e., the logarithm of $P_i^b(\xi)$), truncated at second order or to the truncation of the *cumulant expansion* of $P_i^b(\xi)$ after the second cumulant [43].

expensive samplings with many long trajectories[17]. Since thoroughly calculations are needed to converge the free energy curves to the level of accuracy needed for reliable k(T) values, UI will be used for all rate constant calculations reported in this thesis. If, on the other hand, simulations of large proteins or solvent boxes are desired where samplings are expensive and thus rather short, WHAM will certainly be the method of choice.

Recrossing Calculations

Looking back at section 2.1.1, it turns out that trajectory-based calculations are able to solve the inherent TST-problems 1,3 and 4. Although the reaction coordinate ξ is somewhat exceptional for umbrella samplings as the biasing potentials $w_i(\xi)$ only depend on it, couplings between ξ and all other bound coordinates are included automatically by the free sampling in coordinate space, such that the restricting assumption of no coupling to other modes is solved.

The correct location of the dividing surface is quite trivial for sampled free energy surfaces: it can be located at the maximum of the obtained $A(\xi)$ surface.

Assuming that the exact or at least a very good approximated PES is used for the umbrella samplings, the problem of harmonic approximations is solved as well: Instead of Taylor approximations around some significant points along the reaction path the shape of the whole thermally accessible PES relevant for the actual reaction is sampled and included for the free energy calculation.

The remaining two problems of no recrossing and neglection of quantum effects are still not solved, though. As mentioned in section 2.1.2, recrossing is important especially for high temperatures and broad barriers. There are parametric methods like US and CUS for the incorporation of recrossing but these act on certain rather particular assumptions and are not suited in general, further, they are unable of converging to the exact result.

Trajectory calculations are able to do so. It is possible to converge the recrossing coefficient κ to the exact (classical) value for the given PES if enough trajectories are sampled for enough time steps[18].

The basis for the exact formulation of recrossing is an alternative expression for the TST rate constant expressed in eqs. 2.10-2.11, namely the *reactive flux* (RF) formulation. The forward TST rate constant can be expressed as the instantaneous flux through the transition state dividing surface from reactants to products, divided by the number of reactants [2,44]:

$$k^{TST}(T) = \frac{\left\langle \Theta\left[\xi(0)\right] \dot{\xi}(0) \Theta\left[\dot{\xi}(0)\right]\right\rangle}{\left\langle \Theta\left[-\xi(0)\right]\right\rangle}, \tag{2.44}$$

with Θ being the Heaviside step function, ξ the time dependent reaction coordinate, $\dot{\xi}$ its time derivative and $\langle...\rangle$ describing Boltzmann averages (see eq. 2.34). The zero argument indicates that all quantities are measured at one single time, here at $t = 0$.

As already stated above, the TST equation is able to deliver fairly good results, but the assumption of no time-dependence of the flux leads to an overestimation of the rate, namely because all transitions are assumed to lead to a product state and thus recrossings are neglected (all what is headed to the products by $\frac{\partial \xi(0)}{\partial t}$ is assumed to end there).

---

17 As it is explained also in section 3.3.7, many short trajectories starting with randomized positions and momenta are sampled in each umbrella window and subsequently summed up for analysis as if it was one large trajectory in the EVB-QMDFF program. This is due to the fact that the used RPMD method seriously harms the ergodicity of a single long sampling trajectory, since the springs between the RPMD beads are very stiff especially if many beads are used (see below) [11].

18 We might expect that the effects of recrossing are already included if the free energy surface is generated by free trajectory samplings, which itself will recross the dividing surface many times. However, the applied samplings result in a free energy surface that plays the same role as the parametrized free energy surface used in CVT calculations, which itself are based on TST and its assumptions. Therefore, recrossing must be accounted for still separately.

Recrossing can be considered if the flux in eq. 2.44 is calculated time dependently and not instantaneous:

$$k^{RF}(T,t) = \frac{\langle \Theta\left[\xi(0)\right] \dot{\xi}(0)\Theta\left[\xi(t)\right]\rangle}{\langle \Theta\left[-\xi(0)\right]\rangle}.$$

(2.45)

Now, the reactive flux is considered to have explicit time dependence via $\xi(t)$ such that the value of the reaction coordinate at time t decides if the system is on the reactant or product side and not only its direction at time 0, i.e., the system is allowed to recross ($\xi(t)$ could be become lower than zero at some time t). This description is also called the *reactive flux method*[19] [45].

We could calculate the rate constant with eq. 2.45 by starting a large ensemble of trajectories at the reactants valley and look how many of them are reaching the products valley after some time t. However, this becomes very costly since reactions are rare events and thus only a very small fraction of the started trajectories will actually reach the product valley.

Fortunately, the reactive flux rate constant can be factored out into two contributions: the usual TST rate constant and a *transmission coefficient* $\kappa(T,t)$:

$$k^{RF}(T,t) = \kappa(T,t)k^{TST}(T).$$

(2.46)

Due to the significant contribution of CHANDLER to the development of the reactive flux method [45] this is also called the *Chandler-factorization* of the TST-rate.

The idea is to calculate first the usual TST rate constant (either with corrected parametric or trajectory sampling methods) and then to do a separate recrossing calculation. For this calculation, we only look at the events happening directly after crossing the dividing surface, which shall be located at $\xi = 0$ for this derivation. Instead of assuming that all trajectories are reacting to products, we start a number of trajectories at $\xi = 0$ and look after a number of times t how many of them have reached the product region or went back to the reactants. This can be expressed as (note the time derivatives $\dot{\xi}(...)$!):

$$\kappa(T,t) = \frac{\langle \delta\left[\xi(0)\right]\dot{\xi}(0)\Theta\left[\xi(t)\right]\rangle}{\langle \delta\left[\xi(0)\right]\dot{\xi}(0)\Theta\left[\dot{\xi}(t)\right]\rangle} = \frac{\langle \dot{\xi}(0)\Theta\left[\xi(t)\right]\rangle_\xi}{\langle \dot{\xi}(0)\Theta\left[\dot{\xi}(0)\right]\rangle_\xi},$$

(2.47)

where in the second step the condition that all trajectories start at $\xi = 0$ at $t = 0$ ($\delta\left[\xi(0)\right]$) is denoted as a *conditional* Boltzmann average $\langle...\rangle_\xi$ over the constrained ensemble in which all trajectories start at $\xi = 0$. In practice, a constrained *parent trajectory* is sampled a certain amount of time exactly at $\xi = 0$ but with free thermal movement orthogonal on the dividing surface. At some interval, bunches of *child trajectories* are started from the current position of the parent trajectory. Their momenta are set as random pairs according to the thermostat in usage, whereas the first trajectory gets $\mathbf{p}(0)$ and the second gets $-\mathbf{p}(0)$.

From these momentum vectors, the initial time derivatives of the reaction coordinate $\dot{\xi}(0)$ are determined. Of each pair of child trajectories, only one will be included in the actual recrossing calculation, since $\Theta\left[\dot{\xi}(0)\right]$ will be zero for the other (with the momentum directed to the reactants). With this procedure, it can be ensured that all child trajectories considered for the $\kappa(T,t)$ calculation are starting headed to the product valley (such that they can be considered *reactive* in the traditional TST picture).

The child trajectories are then started without any restraint, such that they will evolve freely (only under influence of the thermostat) either to the reactant or to the product valley. Only if the trajectory is still in the product side $\xi \geq 0$, it will be counted for the transmission coefficient. Since

---

19 In section 11.2.2 it is shown that the recrossing coefficient appears if we look at flux-side correlation functions. Instead of calculating the long time limit we can restrict the evaluation to the short time limit and correct the resulting rate by a separate recrossing factor, which is analogous to the approach shown here.

the average is taken over all trajectories, $\kappa(T,t)$ will only be one if all child trajectories directed initially to the product region are still on the product side at time t.

Since for most reactions $\xi = 0$ is located on or near to a potential barrier, most child trajectories will decay quite rapidly either to the products or to the reactants region. Therefore recrossing events are becoming increasingly improbable the more time is elapsed. Only a few molecular vibrations after starting the systems will be still near the TS such that thermal hits or redistribution of internal vibrations might lead to recrossings back above the barrier. Therefore a typical time-dependent plot of $\kappa(T,t)$ decays rapidly after some femtoseconds. However, since reactions are rare events, it is still possible that child trajectories already arrived at the product valley might come back above the barrier, affecting $\kappa(T,t)$. Thus, $\kappa(T,t)$ does converge to a final result $\kappa(T)$ but increasingly slowly with advancing time.

This procedure of calculating $\kappa(T,t)$ is illustrated in fig. 2.5 for a small ensemble of child trajectories in order to further clarify the concept. In reality, several thousands to hundreds of thousands of trajectories are needed to really converge to the exact value of $\kappa(T)$ for the given PES.

2.1.4 Rigorous Quantum Theories

The original TST-formulation by EYRING is an approximation, sometimes a good one, sometimes a poor one. The different parametric corrections presented here lead to better qualities of the calculated rate constants, however, they are still not exact, even in the classical regime. With recrossing corrected sampling methods, formally exact classical rate constants can be obtained. However, real systems always impose *quantum effects*, especially if light atoms and/or low temperatures are coming into play.

Cumulative Reaction Probabilities

Fortunately, it is possible to formulate an exact[20] quantum theory for reaction rate calculations [7]. The canonical rate constant for a bimolecular chemical reaction can be expressed as:

$$k(T) = \frac{1}{2\pi\hbar Q_r(T)} \int_{\infty}^{\infty} dE \exp\left[\frac{-E}{kT}\right] N(E), \qquad (2.48)$$

with Q_r being the reactants partition function per unit volume. Similarly, we can calculate the microcanonical (i.e., energy-dependent) rate constant, as it is usually done for unimolecular systems:

$$k(E) = \frac{1}{2\pi\hbar \rho_r(E)} N(E), \qquad (2.49)$$

where $\rho_r(E)$ is the *density of reactant states* per unit energy.

For both canonical and microcanonical rate constants, the *cumulative reaction probability $N(E)$* is needed. This quantity can in general be obtained from the *S-matrix* of the reaction:

$$N(E) = \sum_{n_r n_p} \left| S_{n_p,n_r}(E) \right|^2. \qquad (2.50)$$

---

20 In practice, a rate constant is considered to be *exact* if the exact value with respect to the used potential energy surface is obtained. Of course there is still no guarantee that these "exact" results are even near to the experimental ones, because deficiencies of the used potential energy surface are passed on the calculated rate (see chapter 5). Further, the quantum dynamics calculations are performed numerically in practice, thus the number of used grid basis functions also affects the quality of the result. At least it is possible to obtain the exact quantum mechanical result if a hypothetical perfect PES is used and the number of basis functions goes to infinity. In practice it is possible however to obtain results of spectroscopic accuracy at least for small systems if a parametrized PES and a good basis is used.
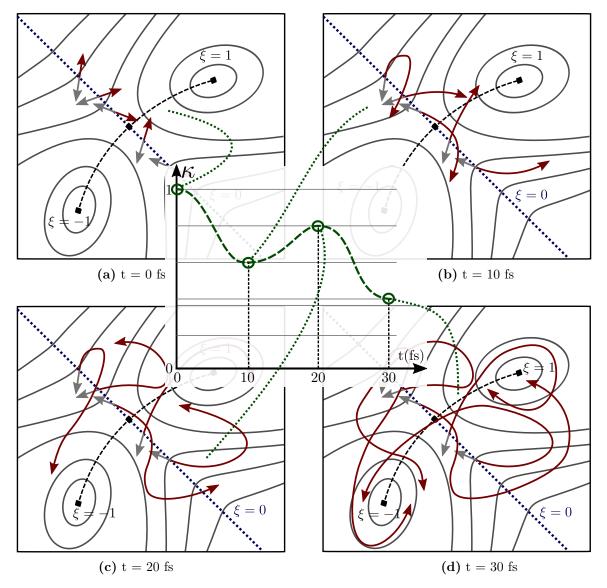
Figure 2.5: Simplified illustration of a recrossing calculation. Five pairs of child trajectories are started at the TS dividing surface with opposite momenta. Only the trajectories headed to the product well are propagated. At the beginning, the transmission κ is one since all trajectories are located at $\xi = 0$ (a). After 10 fs, two trajectories inverted their direction and recrossed the dividing surface, $\kappa = 0.6$ (b). After 20 fs, one recrossed trajectory has again turned back, such that four of five are on the product side, $\kappa = 0.8$ (c). After 30 fs, two trajectories have reached the products minimum and three the reactants minimum, leading to a converged value of $\kappa = 0.4$ (d). The obtained transmission time profile is shown in the middle.

The S-matrix expresses the probabilities for the transition from a reactant state n_r to a product state n_p.

This matrix can essentially be calculated if we propagate each single reactant state as a wave packet to the product region and analyze the distribution of product states. With this method, one row or column of the S-matrix is calculated for each propagation (one reactant state to all product states).

A Simple Example

In the case of a simple collinear three-atomic reaction like F+H$_2$, the S-matrix can be calculated as follows [46]: The *Jacobi coordinates* for the reactants valley can be taken as the distance between the F-atom and the H$_2$-molecule ($R_{\text{F-H}_2}$) and the distance between both H's into the H$_2$-molecule ($R_{\text{H-H}}$).

Then, the initial wave packet describing a certain vibrational state v of the H$_2$-molecule (no rotation considered) can be expressed as:

$$\Psi(R_{\text{F-H}_2}, R_{\text{H-H}}, t=0) = \phi_v(R_{\text{H-H}}) \exp[-\alpha(R_{\text{F-H}_2} - R_{\text{F-H}_2}^0)^2]$$
$$\exp[-ik(R_{\text{F-H}_2} - R_{\text{F-H}_2}^0)], \tag{2.51}$$

where the first factor is the vibrational wave function for the isolated *H$_2$*-molecule at vibrational state v, the second factor defines the Gaussian shape of the overall wave packet and the last factor enables the motion of the packet along the reaction coordinate (via the imaginary exponential and the *momentum k*).

Before the actual dynamics of the wave packet can be calculated, it should be considered that the Jacobi coordinates of the products are different (HF-H-distance $R_{\text{H-HF}}$ and H-F-distance $R_{\text{H-F}}$) than that of the reactants. In order to avoid any topological difficulties, the initial wave packet is directly transformed into the product coordinates and all propagation is done in these.

During the propagation, the forthcoming wave packet is analyzed with respect to the vibrational states of the product, i.e., the wave packet is projected onto all vibrational states v' of the H-F-molecule to be analyzed:

$$C_{v'}(R_{\text{H-HF},\infty}, t) = \int_0^\infty \phi_{v'}(R_{\text{H-F}})\Psi(R_{\text{F-H}_2}, R_{\text{H-H}}, t)dR_{\text{H-F}}. \tag{2.52}$$

The ∞-subscripts indicate that this analysis is done at the product asymptote, whereas in reality a dividing surface is chosen on which the interactions between H and H-F are negligible.

By looking at eq. 2.50 an energy-dependent S-matrix is needed for k(T) calculations. In order to get there, the obtained *time-dependent* coefficients $C_{v'}(R_{\text{H-HF},\infty}, t)$ need to be transformed to *energy-dependent* coefficients $A_{v'}(R_{\text{H-HF},\infty}, E)$ by Fourier transform:

$$A_{v'}(R_{\text{H-HF},\infty}, E) = \frac{1}{2\pi} \int_{t=0}^\infty \exp\left(\frac{iEt}{\hbar}\right) C_{v'}(R_{\text{H-HF},\infty}, t)dt. \tag{2.53}$$

After some derivation it is possible to calculate the desired S-matrix for the F+H$_2$-reaction directly from the energy-dependent coefficients of the product states:

$$\left|S_{v',v}(E)\right|^2 = \frac{64\pi^2 h^2}{\mu'^2} k_{v'} k_v \left|\frac{A_{v'}(R_{\text{H-HF},\infty}, E)}{f(|k_v|)}\right|^2, \tag{2.54}$$

with μ' the reduced mass of the HF-molecule, v' and v the vibrational states of products and reactants, respectively and $f(|k_v|)$ the momentum distribution of the initial wave packet.

In order to get the full quadratic $S_{v',v}$-matrix, initial wave packets (eq. 2.51) need to be started for an equal number of vibrational states v of the H$_2$-molecule as states v' of the HF-molecule are included into the analysis for eq. 2.52. After completing this analysis, the canonical rate constant k(T) could be calculated for F+H$_2$ with eqs. 2.48 and 2.50.

Practical Considerations

In spite of its ostensible simplicity the "direct" method of calculating $S_{n_p,n_r}(E)$ has a serious drawback: In the example presented above, a simple three-atomic collinear reaction without any rotation was considered, resulting in only one vibrational quantum number for the reactants and the products, respectively.

In real applications of somewhat larger molecules all energetically favorable combinations of the system's normal modes with consideration of rotational splitting must be included, resulting in hundreds to tens of thousands of different initial conditions. Each of these states must be propagated and analyzed according to the scheme above, resulting in very expensive calculations.

In quantum dynamics, the time-dependent wave functions like eq. 2.51 are usually expanded in basis functions located at a regular grid in coordinate space (therefore called grid functions). If very large asymptotic areas should be described (such that $R_{H-HF,\infty}$ is reached) the number of used basis functions will increase rapidly.

Unlike time-independent quantum mechanics, where, e.g., simple *Hartree-Fock* (HF) calculations scale with N_b^4 with N_b the number of basis functions, time-dependent calculations scale less than N_g^2, where N_g is the number of grid functions. However, since the number of such grid points scales exponentially with the number of used coordinates (in contrast to three spatial coordinates in HF), exact treatments are becoming infeasible even for systems of 6 atoms or more, unless approximations such as reduced coordinate sets are used.

One way of getting cheaper methods is to consider the fact that the full *S*-matrix contains much more information (all what is needed to calculate every possible quantum mechanical observable relating to the reaction of interest) than necessary in order to calculate the cumulative reaction probability $N(E)$.

Several methods were developed that aim at the calculation of $N(E)$ but without explicit consideration of the *S*-matrix itself [8].

Reactive Flux Calculations and QTST

Real-time-correlation functions play an important role for calculations of dynamical properties of systems [11]. The general expression for the real time correlation $c_{AB}(t)$ of two quantities A and B is:

$$c_{AB}(t) = \frac{1}{Q}\text{tr}\left[e^{-\beta\hat{H}}\hat{A}(0)\hat{B}(t)\right],\tag{2.55}$$

with Q the canonical partition function of the system, which can be calculated in terms of the trace of the *Boltzmann operator*[21]:

$$Q = \text{tr}\left[e^{-\beta\hat{H}}\right].\tag{2.56}$$

Both $\hat{A}(0)$ and $\hat{B}(t)$ are *Heisenberg-evolved* operators of the general form:

$$\Xi(t) = \exp\left(\frac{i\hat{H}t}{\hbar}\right)\hat{\Xi}\exp\left(\frac{-i\hat{H}t}{\hbar}\right).\tag{2.57}$$

Depending on the kind of operators chosen, different quantities of interest can be calculated, for instance, the diffusion coefficient from the velocity operator $\hat{A} = \hat{B} = \hat{\mathbf{v}}$, an infrared spectrum from the dipole operator $\hat{A} = \hat{B} = \hat{\boldsymbol{\mu}}$ or, most interesting for our case, chemical reaction rates for the reactive flux operator $\hat{A} = \hat{B} = \hat{F}$.

---

21 This operator is the quantum mechanical analogue to the classical Boltzmann average integrals introduced for the derivation of umbrella samplings (e.g., in eq. 2.34).

In order to calculate them, the *flux-flux autocorrelation* time profile needs to be integrated for all times [47]:

$$k(T) = \frac{1}{Q_r(T)} \int_0^\infty \text{tr} \left[e^{-\beta \hat{H}} \hat{F} \exp\left(\frac{i\hat{H}t}{\hbar}\right) \hat{F} \exp\left(\frac{-i\hat{H}t}{\hbar}\right) \right] dt. \tag{2.58}$$

Since this method closely resembles the reactive flux formulation of TST given in eq. 2.44, it is also called *quantum transition state theory* (QTST) [9]. An important difference is, however, that QTST is at least formally exact, in contrast to classical TST. In practice, these calculations work similar to trajectory recrossing calculations. Wave packets are started in the TS region (whereas their delocalization in phase space is considered by the quantum Boltzmann operator $e^{-\beta \hat{H}}$) and propagated some time, whereas the flux-flux-correlation time-profile is recorded [48]. By integrating this profile, the rate constant can be obtained. Since the correlation function reaches an asymptotic value quite fast, almost no propagations into the reactants/product valleys are needed, instead, absorbing potentials are placed in their directions in order to avoid artifacts. The total number of grid points to set up is greatly reduced to the TS area, which of course lowers the costs significantly.

Further, as it will be seen below, this method of calculating k(T) values plays a pivotal role for the conceptual ground of the RPMD-approach used throughout this thesis[22].

There are a plenty of other methods that aim at reducing the computational expense of wave packet k(T)-calculations, either in the way the rate is calculated or the way the propagation itself is done, but even a short description of them would blow up the extent of this thesis. The interested reader is referred to the respective literature [7, 8, 49].

2.1.5 Path Integral Formulation of Quantum Mechanics

In order to bridge the gap between cheap classical calculations that are unable to include quantum effects and (at least in principle) exact but too expensive exact quantum calculations, the *path integral* (PI) formulation of *quantum mechanics* (QM) turned out to be quite useful. Developed by FEYNMAN and others, it is an alternative formulation of quantum mechanics that can be shown to be equivalent to the usual Schrödinger picture and turns out to be quite advantageous for developing approximate time-dependent QM-calculations based on classical trajectory samplings.

After giving a short introduction to the field, we will see in the next section how PIs can be used to develop the RPMD-method, which is able to consider quantum effects yet is based on classical dynamics.

It is of course not my demand to give a comprehensive review of PI-QM, thus I will only show the very basics needed for understanding RPMD. For a deeper treatment of the field the famous book of FEYNMAN and HIBBS [50] is recommended.

Foundations

In our days, quantum mechanics is usually treated within the Schrödinger picture, i.e., by solving the Schrödinger equation for different situations, either analytically or, especially in theoretical chemistry, numerically in order to get the wave function of a system[23]. Because the *time-dependent*

---

22 A closer look at the relation between RPMD and QTST is made in the derivation of the bimolecular RPMD reaction rate shown in section 11.2.2. There, we switch from flux-flux-autocorrelation functions to flux-side-correlation functions, by retention of the concept of looking at time-dependent correlation profiles of wave packets started in the TS region (fig. 11.2).

23 In fact, there are several different formulations of quantum mechanics, which all can be shown to be equivalent. Some of the most important ones are [51]:

    1. The *Schrödinger picture*, or wave mechanics.

    2. The *Heisenberg representation*, also called *matrix mechanics*.

    3. The *Feynman path integral formulation*, as it will be presented here.

Schrödinger equation (TDSE) is a partial differential equation, this description is also called the *differential formulation* of quantum mechanics.

Besides this, it is as well possible to describe quantum mechanics in an *integral formulation*. There, instead of differential equations integral equations need to be solved in order to obtain descriptions and predictions for certain systems. This integral formulation is also called the path-integral formulation of quantum mechanics.

In classical mechanics, similar correspondences exist. Besides the Newtonian equations of motion, which are differential equations, we can, e.g., solve the motion of a one-dimensional particle between two points *a* and *b* by calculating its *action*:

$$\mathcal{S}[b,a] = \int_{t_a}^{t_b} L(\dot{x}, x, t) dt, \tag{2.59}$$

with t_a and t_b start and end points of the time interval to be examined and *L* the *Lagrangian* of the system, defined as:

$$L = \frac{m}{2}\dot{x}^2 - V(x,t), \tag{2.60}$$

with *m* the mass of the system, for the case if an arbitrary time-dependent potential energy $V(x,t)$ is existent.

We can now calculate the path the system will tread between t_a and t_b ($x(t)$) by applying the *principle of least action*: The quantity $\mathcal{S}[b,a]$ has a minimum value for the classical motion of the system in the time interval of interest. This can also be expressed variationally: $\mathcal{S}[b,a]$ should have an extremum for the *extremum path* $\overline{x}(t)$:

$$\delta\mathcal{S} = \mathcal{S}[\overline{x} + \delta x] - \mathcal{S}[\overline{x}] = 0, \tag{2.61}$$

i.e., the action remains unchanged to first order if the extremum path is changed infinitesimally. If this condition is inserted into eq. 2.59, we obtain:

$$\mathcal{S}[\overline{x} + \delta x] = \int_{t_a}^{t_b} L(\dot{x} + \delta\dot{x}, x + \delta x, t) dt = \int_{t_a}^{t_b} \left[L(\dot{x}, x, t) + \delta\dot{x}\frac{\partial L}{\partial \dot{x}} + \delta x\frac{\partial L}{\partial x} \right] dt. \tag{2.62}$$

The resulting integral can be split up into the action and its variation:

$$\mathcal{S}[\overline{x} + \delta x] = \mathcal{S}[x] + \int_{t_a}^{t_b} \left[\delta\dot{x}\frac{\partial L}{\partial \dot{x}} + \delta x\frac{\partial L}{\partial x} \right] dt. \tag{2.63}$$

The remaining integral can be evaluated by integration of parts, resulting in the expression for the variation in $\mathcal{S}$:

$$\delta\mathcal{S} = \left[\delta x\frac{\partial L}{\partial \dot{x}} \right]_{t_a}^{t_b} - \int_{t_a}^{t_b} \delta x \left[\frac{d}{dt}\left(\frac{\partial L}{\partial \dot{x}}\right) - \frac{\partial L}{\partial x} \right] dt. \tag{2.64}$$

The first term becomes zero since all possible paths have the same starting and ending points, respectively. Therefore, the derivative of *L* is zero at t_a and t_b. All what remains is the second factor in the integral. If the whole expression for δS should be zero, it leads to the condition:

$$\frac{d}{dt}\left(\frac{\partial L}{\partial \dot{x}}\right) - \frac{\partial L}{\partial x} = 0. \tag{2.65}$$

This expression is well known in classical mechanics, namely it is the classical *Lagrangian equation of motion*.

---

4. The *Dirac representation*, or the interaction picture.

5. The *phase space formulation*, also called *Wigner representation*.

The quintessence of this derivation is that in the classical picture exactly *one single path* describes the motion of a particle between two endpoints for given potential and kinetic energy, hence position and momentum are known exactly during the whole motion.

In quantum mechanics this is of course no longer the case. Here, not only the single path of least action is important for the motion of the particle, but all possible paths contribute to the actual motion, corresponding to a smeared-out time-dependent probability distribution between the points a and b. The probability to go from point a to b in space can be expressed as:

$$P(b,a) = |K(b,a)|^2, \tag{2.66}$$

where $K(b,a)$ is the *amplitude* to go from a to b, obtained if all possible paths $x(t)$ (no matter how absurd they might appear) the system could take are summed up:

$$K(b,a) = \sum_{\text{all } x(t) \text{ from } a \text{ to } b} \phi[x(t)] \tag{2.67}$$

As for the classical case, the action $\mathcal{S}$ is an important measure for each path $x(t)$, but now it infects only the *phase* of each possible path:

$$\phi[x(t)] = C \exp\left(\frac{i}{\hbar} S[x(t)]\right), \tag{2.68}$$

with C being a suitable normalization constant. At first sight, we could think that all possible paths contribute equally to the total amplitude, since their prefactors are equal and only their phases are different. However, in practice all paths will be integrated and especially for large values of S far offside the classical extremum path neighbored paths will cancel out each other due to their heavily fluctuating phases. In the classical limit, with $\hbar$ going to zero, the phases will oscillate significantly for neighbored paths for all but the direct vicinity of the classical optimum $\overline{x}$, where the change in S and thus of the phase is zero in first order. Thus, the single classical optimum path is obtained if either S is becoming large or $\hbar$ is going to zero[24].

So far, the amplitude for a certain quantum mechanical motion is given only qualitatively in eqs. 2.67-2.68. How does this work in practice? Even in the simplest case of one dimension x we have an *infinite* number of possible paths, each of it needs to be integrated from a to b.

One way of doing this is to divide each path into a finite number of linear slices connected together. If the number of these discrete steps per path is N, we can integrate over all paths for each of the obtained x_i values[25]. Because all paths are identical for the first x_i at a and the last at b, we get:

$$K(b,a) \sim \int \ldots \int \int \phi[x(t)] dx_1 dx_2 \ldots dx_{N-1}, \tag{2.69}$$

where the first (x_0) and the last (x_N) are omitted. At this stage, the result is far from exact, because we only have a finite number of steps on which the different paths are evaluated. In order to get the exact limit, the number of intersections must go to infinity, which corresponds to the distances ϵ between them going to zero. Further, the whole integral needs to be normalized, where A is a suitable normalization constant, depending on ϵ:

$$K(b,a) = \lim_{\epsilon \to 0} \frac{1}{A} \int \ldots \int \int \exp\left(\frac{i}{\hbar} \int_{t_a}^{t_b} L(\dot{x}, x, t) dt\right) \frac{dx_1}{A} \frac{dx_2}{A} \ldots \frac{dx_N}{A}. \tag{2.70}$$

---

24 The value of the action will become large for all possible paths if, e.g., a large particle (heavy atoms or molecules) is considered, since the $\frac{m}{2}$ part of L will become huge in units of $\hbar$.

25 Considering all possible paths means that for each time, every point in space is part of one path. Therefore, for each slice considered, the integral must be taken over the whole space, i.e., here the x dimension in which the particle can move.

$$\mathcal{S}[b,a] = \frac{i}{\hbar} \sum_{i=0}^{7} L(\dot{x}(t_i), x(t_i), t_i) \Delta t \qquad\qquad \mathcal{S}[b,a] = \frac{i}{\hbar} \int_{t_a}^{t_b} L(\dot{x}(t), x(t), t) dt$$

(a) Finite number of intersections　　　　　**(b)** Limit of infinite intersections
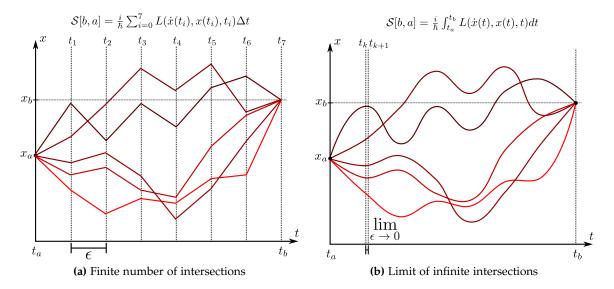
Figure 2.6: Process of the derivation of eq. 2.70 for the exact path integral. We can intersect the time axis into a number of slices of length ϵ and calculate the Lagrangians of the path at each of these sections. For each section, all points in space need to be integrated (a). To obtain the exact path integral, the number of slices needs to go to infinity (or ϵ needs to go to zero), such that an infinite number of integrals need to be evaluated, one at each infinitesimal slice. Now, the action can be integrated over time as well (b). Of course, also an infinite number of paths needs to be considered in the reality.

With this equation, we can calculate the quantum mechanical amplitude for going from a to b in the one-dimensional case with a given Lagrangian $L(\dot{x}, x, t)$ and $\int_{t_a}^{t_b} L(\dot{x}, x, t) dt = \mathcal{S}[b,a]$ being a line-integral passing through all x_i along a certain curve. The process of obtaining the exact limit of infinite integrations is shown in fig. 2.6. Equation 2.70 does not only look terrible, it is almost impossible to evaluate for all but the simplest cases where analytical tricks can be applied to get rid of the infinite-dimensional integral. This is the main reason why the path integral formulation is rarely used in, e.g., quantum chemistry.

Usually, a shortened notation for the amplitude is used:

$$K(b,a) = \int_a^b \exp\left(\frac{i}{\hbar}\mathcal{S}[b,a]\right) \mathfrak{D}x(t), \qquad\qquad (2.71)$$

where $\mathfrak{D}x(t)$ denotes the integration over the limit of infinite subsections between a and b over all paths. $K(b,a)$ is hence called the *path integral* between a and b, sometimes it is also called the *kernel* for describing the motion between a and b or the *propagator*, since it essentially propagates from a to b.

Path Integrals and Differential Formulations

In order to explore the usefulness of PI QM to get an approximate description of QM-effects based on classical trajectories it is helpful to show the equivalence between the path integral and the Schrödinger picture of QM. In section 11.2.1 in the appendix this equivalence is exemplified by the derivation of the TDSE from the path integral propagator.

The time propagation of a wave function can be described in the Schrödinger picture as a time-dependent superposition of the eigenstates of the respective Hamiltonian[26]:

$$\psi(x,t) = \sum_{n=1}^{\infty} c_n \exp\left(-\frac{i}{\hbar} E_n t\right) \phi_n(x). \tag{2.72}$$

It can be shown that a kernel can be expressed in terms of *eigenstates* as well, but now of the respective states of the origin (x_a, t_a) and the endpoint (x_b, t_b):

$$K(x_b, t_b; x_a m t_a) = \sum_{n=1}^{\infty} \phi_n(x_b)\phi_n^*(x_a) \exp\left(-\frac{i}{\hbar} E_n(t_b - t_a)\right), \tag{2.73}$$

where $t_b > t_a$. Now, the kernel representing a path integral is expressed in terms of solutions of the TISE, a differential equation! It will be seen that this differential representation plays an important role for the following derivations.

2.1.6 Ring Polymer Molecular Dynamics

As shown so far, exact quantum treatment of dynamics is expensive and almost impossible for all but quite small systems unless some subtle tricks are used. We also have seen that the PI formulation of quantum mechanics is even more expensive than the differential treatment, which is the foundation for all direct quantum dynamics methods. It seems to be ridiculous to even try to develop a numerical method based on path integrals.

However, as will become clear in the next section, the path integral approach is well suited for the analytical calculations of *quantum mechanical partition functions*. As we have seen for example in eq. 2.27, the free energy is defined in terms of the system's partition function. Similarly, all other thermodynamical observables of a system can be calculated in terms of the partition function, which is discussed in larger detail in textbooks on statistical thermodynamics [21].

For our purpose, the determination of free energy profiles turned out to be essential for chemical reaction rate calculations. We will now see how it is possible to obtain a quantum mechanical procedure of calculating partition functions and next how this can be approximated in a classical manner.

Path Integrals and Partition Functions

Physical systems are rarely isolated in nature. In fact, if we want to get a physical description of realistic systems containing large numbers of particles a *statistical* description is needed. This implies that the actual state of the system is not known but several states could occur with different probabilities. The probability of a state to occur depends on its energy:

$$p_n = \frac{1}{Q} e^{-\beta E_n}, \tag{2.74}$$

where the normalization constant is itself the *partition sum* of the system:

$$Q = \sum_n e^{-\beta E_n}. \tag{2.75}$$

Thus, a sum over all states with exponential weighting of their energies is done. In order to switch to the quantum mechanical picture, the definition of a *state* needs to be clarified: If a

---

26 These eigenstates are the solution of the TISE of the system: $H\phi_n(x) = E_n\phi_n(x)$.

one-dimensional particle is considered, the probability of finding the particle at x is the sum over all of its possible states, taken as absolute square:

$$P(x) = \frac{1}{Q} \sum_n \phi_n^*(x) \phi_n(x) e^{-\beta E_n}. \tag{2.76}$$

In the general case, the expectation value of an arbitrary operator $\mathfrak{A}$ shall be described statistically. Then, its expected value can be given as:

$$\overline{A} = \frac{1}{Q} \sum_n A_n e^{-\beta E_n} = \frac{1}{Q} \sum_n \int \phi_n^*(x) \mathfrak{A} \phi_n(x) dx e^{-\beta E_n}. \tag{2.77}$$

In general, the expected value depends on a function called the *statistical density matrix*, or *density matrix* in short:

$$\rho(x', x) = \sum_n \phi_n(x') \phi_n^*(x) \exp\left(-\beta E_n\right). \tag{2.78}$$

In order to calculate the probability to find the system at x, the density matrix can be used:

$$P(x) = \frac{1}{Q} \rho(x, x). \tag{2.79}$$

The partition sum can now be calculated to normalize the total probability distribution to 1, then we get its expression:

$$Q = \int \rho(x, x) dx \equiv \mathrm{tr}(\rho). \tag{2.80}$$

Thus, we need to calculate the *trace* of the density matrix of a system in order to get its partition sum. But where are the path integrals? If we compare eqs. 2.78 and 2.73, we see that they are surprisingly similar. The density matrix expression has the exponent βE_n, the eigenfunction representation of the kernel has the exponent $-\frac{i}{\hbar} E_n (t_b - t_a)$, whereas the rest is identical.

We can expand this similarity if the density matrix element $\rho(x, x')$ is expressed as a "pseudo kernel", a kernel working in *imaginary time*:

$$k(x_b, u_b, x_a, u_a) = \sum_n \phi_n(x_b) \phi_n^*(x_a) \exp\left(-\frac{u_b - u_a}{\hbar} E_n\right), \tag{2.81}$$

with $x_b = x'$, $x_a = x$, $u_b = \hbar\beta$ and $u_a = 0$. Now, we have transformed the Boltzmann factor of the density matrix into an imaginary time difference between 0 and $\hbar\beta$. Starting at this expression, it can be shown that the whole density matrix element $\rho(x_b, x_a)$ is equivalent to a path integral over the imaginary time variable u. This results in:

$$\rho(x_b, x_a) = \int \exp\left[-\frac{1}{\hbar} \int_0^{\beta\hbar} \left(\frac{m}{2} \dot{x}^2(u) + V(x(u))\right) du\right] \mathfrak{D}x(u). \tag{2.82}$$

Now, we can evaluate partition functions in terms of path integrals! In contrast to the general PI expression given in eq. 2.70, no imaginary unit i appears in the exponent. Therefore, neighbored paths do not cancel out another like for real dynamics, instead, paths of high potential and/or kinetic energy also add to the partition function but only with small amounts, since the (negative) exponential becomes small for large values in the bracket.

As the calculation of partition functions only needs the diagonal elements of the density matrix, $x_a = x_b$ can be set. This means that start and end points of all paths calculated by eq. 2.82 are *identical*. To calculate the coordinate-dependent partition function of the system we evaluate all possible paths or motions the system can make at any point in coordinate space to start, travel for an imaginary time $\hbar\beta$ and come back before this interval has ended. The longer these cyclic paths are, the larger the kinetic energy will be and hence the lower this path's contribution. Further, if the

(a) Imaginary time path integrals

(b) Cyclic paths in coordinate space
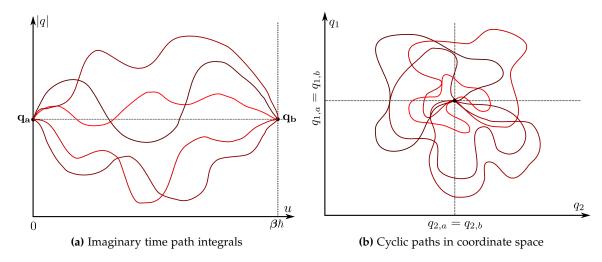
Figure 2.7: Calculation of partition functions with path integrals for a two-dimensional example [52]. In imaginary time u with the interval 0 to $\beta\hbar$, usual path integrals are calculated, where start and end points are identical (a). In coordinate space, each of these integrals is represented by a cyclic parametric curve depending on the dimensionless parameter u (b).

temperature gets lower and lower, $\hbar\beta$ gets large and thus longer paths are possible, the particles get smeared out.

Path Integral Molecular Dynamics

We already got some basic understanding why "ring polymers" might play an important role if the PI-based calculation of partition functions shall be approximated, since cyclic path integrals need to be evaluated.

However, the actual derivation of the working *path integral molecular dynamics* (PIMD) Hamiltonian is still quite lengthy [51]. To hold the equations as short as possible, we will now switch to the *Dirac notation*. In this notation, the kernel according to eq. 2.70 can be expressed as:

$$K(x, t, x', t') = \left\langle x \left| \exp\left(-\frac{it\mathfrak{H}}{\hbar}\right) \right| x' \right\rangle, \tag{2.83}$$

with $\mathfrak{H}$ being the Hamiltonian of the system and $\exp\left(-\frac{it\mathfrak{H}}{\hbar}\right)$ the time propagation operator. The density matrix according to eq. 2.82 can now be expressed similarly:

$$\rho(x, x') = \left\langle x' \left| e^{-\beta\mathfrak{H}} \right| x \right\rangle, \tag{2.84}$$

where $\exp(-\beta\mathfrak{H})$ is called the *Boltzmann operator* [11]. The Hamiltonian of the system $\mathfrak{H}$ is the sum of its potential and kinetic energy operators $\hat{V}$ and $\hat{T}$:

$$\mathfrak{H} = \frac{m}{2}\dot{x}^2 + V(x) = \hat{T} + \hat{V}. \tag{2.85}$$

Unfortunately, the effect of the propagator on the states cannot be evaluated directly, because the $\hat{T}$ and $\hat{V}$ operators do not commute. Fortunately, there is a way to circumvent this problem. The *Trotter theorem* can be used to rewrite an exponent of two non-commuting operators [51]:

$$\exp[-\beta(\hat{T} + \hat{V})] = \lim_{P \to \infty} \left[\exp\left(\frac{\beta\hat{V}}{2P}\right) \exp\left(\frac{\beta\hat{T}}{P}\right) \exp\left(\frac{\beta\hat{V}}{2P}\right) \right]^P, \tag{2.86}$$

with P being the *Trotter number*. The evaluated propagator can now be reinserted into the density matrix expression:

$$\rho(x,x') = \lim_{P\to\infty} \left\langle x' \left| \left[\exp\left(\tfrac{\beta\hat{V}}{2P}\right) \exp\left(\tfrac{\beta\hat{T}}{P}\right) \exp\left(\tfrac{\beta\hat{V}}{2P}\right) \right]^P \right| x \right\rangle. \tag{2.87}$$

Now, we have single exponential operators that could be evaluated, however, there is still an infinite product of them:

$$\rho(x,x') = \lim_{P\to\infty} \left\langle x' \left| \prod_{k=1}^{P} \exp\left(\tfrac{\beta\hat{V}}{2P}\right) \exp\left(\tfrac{\beta\hat{T}}{P}\right) \exp\left(\tfrac{\beta\hat{V}}{2P}\right) \right| x \right\rangle. \tag{2.88}$$

It is possible to introduce the *identity operator* expressed in the space of possible position eigenstates $\hat{I} = \int |x\rangle \langle x| \, dx$, here we write them between each pair of operators, resulting in an $P-1$ dimensional integral:

$$\rho(x,x') = \lim_{P\to\infty} \int \prod_{k=1}^{P} \left\langle x_{k+1} \left| \exp\left(\tfrac{\beta\hat{V}}{2P}\right) \exp\left(\tfrac{\beta\hat{T}}{P}\right) \exp\left(\tfrac{\beta\hat{V}}{2P}\right) \right| x_k \right\rangle dx_2 \ldots dx_P, \tag{2.89}$$

where $x_1 = x$ and $x_{P+1} = x'$. Each of the brackets can be evaluated separately. The potential energy operator takes effect on the actual position and calculates its potential, therefore, they can be evaluated on both positional states:

$$\left\langle x_{k+1} \left| \exp\left(\tfrac{\beta\hat{V}}{2P}\right) \exp\left(\tfrac{\beta\hat{T}}{P}\right) \exp\left(\tfrac{\beta\hat{V}}{2P}\right) \right| x_k \right\rangle =$$
$$\exp\left(-\tfrac{\beta V(x_{k+1})}{2P}\right) \left\langle x_{k+1} \left| \exp\left(\tfrac{\beta\hat{T}}{P}\right) \right| x_k \right\rangle \exp\left(-\tfrac{\beta V(x_k)}{2P}\right). \tag{2.90}$$

Thus, only the kinetic energy operators remain to be evaluated. Its energy operator can be expressed in terms of the momentum operator: $\hat{T} = \tfrac{\hat{p}^2}{2m}$, with m the mass of the system. Now, similar to eq. 2.89, the identity operator expressed in the space of possible momentum eigenstates $\hat{I} = \int |p\rangle \langle p| \, dp$ can be inserted:

$$\left\langle x_{k+1} \left| \exp\left(\tfrac{\beta\hat{T}}{P}\right) \right| x_k \right\rangle = \int \langle x_{k+1}|p\rangle \langle p| \exp\left(\tfrac{\beta\hat{T}}{P}\right) |x_k\rangle \, dp$$
$$= \int \exp\left(-\tfrac{\beta p^2}{2mP}\right) \langle x_{k+1}|p\rangle \langle p|x_k\rangle, \tag{2.91}$$

where the kinetic energy operator was applied on the momentum eigenstate from the left. The overlap between a position and a momentum eigenstate can be expressed as:

$$\langle x|p\rangle = \frac{1}{\sqrt{2\pi\hbar}} \exp\left(-\tfrac{ipx}{\hbar}\right). \tag{2.92}$$

Now, the kinetic energy operator can finally be evaluated:

$$\left\langle x_{k+1} \left| \exp\left(\tfrac{\beta\hat{T}}{P}\right) \right| x_k \right\rangle = \int \exp\left(-\tfrac{\beta p^2}{2mP}\right) \frac{1}{2\pi\hbar} \exp\left(-\tfrac{ipx_{k+1}}{\hbar}\right) \exp\left(\tfrac{ipx_k}{\hbar}\right) dp$$
$$= \frac{1}{2\pi\hbar} \int \exp\left(\tfrac{ip(x_{k+1}-x_k)}{\hbar}\right) \exp\left(-\tfrac{\beta p^2}{2mP}\right) dp. \tag{2.93}$$

The integral over the momentum is solvable, if some tricks concerning the Gaussian form of the second factor are done [27], which results in:

$$\left\langle x_{k+1} \left| \exp\left(\frac{\beta \hat{T}}{P}\right) \right| x_k \right\rangle = \sqrt{\frac{mP}{2\pi\beta\hbar^2}} \exp\left(-\frac{mP}{2\beta\hbar^2}(x_{k+1} - x_k)^2\right). \tag{2.94}$$

Now, all state vectors disappear, the remaining expressions are simple functions of the single points in space! This result can be inserted into eq. 2.90, such that the expectation values of the single multiplied operators can now be noted. These can be inserted into eq. 2.89 where the integral over the whole coordinate space x is calculated over a product of P approximated operators. Since all of these are themselves products of exponentials, all can be summarized into one large exponential, with the exponents being summed up:

$$\rho(x, x') = \lim_{P \to \infty} \left(\frac{mP}{2\pi\beta\hbar^2}\right) \int \exp\left\{-\frac{1}{\hbar}\sum_{k=1}^{P}\left[\frac{mP}{2\beta\hbar^2}(x_{k+1} - x_k)^2 + \right.\right.$$
$$\left.\left. \frac{\beta\hbar}{2P}[V(x_{k+1}) + V(x_k)]\right]\right\} dx_2 \dots dx_P, \tag{2.95}$$

with $x_{P+1} = x'$ and $x_1 = x$. At this stage, we can return to the initial expression for the partition sum given in eq. 2.80:

$$Q = \lim_{P \to \infty} \left(\frac{mP}{2\pi\beta\hbar^2}\right)^{\frac{P}{2}} \int \exp\left\{-\frac{1}{\hbar}\sum_{k=1}^{P}\left[\frac{mP}{2\beta\hbar^2}(x_{k+1} - x_k)^2 + \right.\right.$$
$$\left.\left. \frac{\beta\hbar}{P}V(x_k)\right]\right\} dx_1 \dots dx_P, \tag{2.96}$$

where now the integration is also over all points x, x' of real space included into the density matrix expression of eq. 2.80, with $x_1 = x = x'$. Since in eq. 2.89 the states x and x' are included once, the states x_2 to x_{P-1} are included twice and $x = x'$ for our special case, each state appears twice in the potential energy term. Therefore, the sum runs over $V(x_k)$, with an additional prefactor of two, where $x_1 = x_P$.

In practice, the integrals needed for evaluation of the partition function can be evaluated by *path integral Monte Carlo* (PIMC) samplings. In order to perform PIMD, i.e., running trajectories in order to sample the coordinate space, *momenta* need to be added to the effective potential in eq. 2.96. Then, integration must also be done in momentum space, thus being extended to the full phase space of the system. Thereafter, also kinetic energy contributions of all particles can be added, with $T = \frac{p^2}{2m}$ [8]. With this, we get an effective classical partition function, being an approximation to the exact path integral one, which can be evaluated by PIMD samplings:

$$Q = \lim_{P \to \infty} \left(\frac{mP}{2\pi\beta\hbar^2}\right)^{\frac{P}{2}} \int e^{-\beta\mathfrak{H}_{\text{eff}}(\mathbf{x},\mathbf{p})} d\mathbf{x} d\mathbf{p}, \tag{2.97}$$

---

[27] Equation 2.93 can be rewritten such that only one exponential depends on the momentum: $\left\langle x_{k+1} \left| \exp\left(\frac{\beta \hat{T}}{P}\right) \right| x_k \right\rangle = \frac{1}{2\pi\hbar}\int \exp\left(-\frac{\beta}{2mP}\left[p - \frac{imP}{\beta\hbar}(x_{k+1} - x_k)\right]\right)^2 dp \exp\left(-\frac{mP}{2\beta\hbar^2}(x_{k+1} - x_k)^2\right)$. The integral needs only to be done over the first factor, where a substitution can be made: $p' = p - \frac{imP(x_{k+1} - x_k)}{\beta\hbar}$. The resulting simple Gaussian integral can be solved similar to eq. 11.18. Then, the second exponential remains, whereas the integration over momentum gives a constant prefactor.
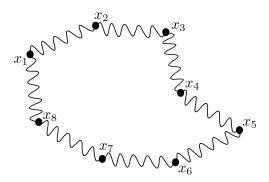
Figure 2.8: Schematic picture of an approximated imaginary time path integral. A fictitious ring polymer of 8 beads is considered. In the one-dimensional case considered so far all beads would be located on the x-axis.

with **x** and **p** denoting all position and momentum variables, respectively and $\mathfrak{H}_{\text{eff}}$ being the effective classical PIMD-Hamiltonian defined as:

$$\mathfrak{H}_{\text{eff}}(\mathbf{x}, \mathbf{p}) = \sum_{k=1}^{P} \left[\frac{p_i^2}{2m} + \frac{1}{2} m\omega_P^2 (x_{k+1} - x_k)^2 + \frac{1}{P} V(x_k) \right], \tag{2.98}$$

with $\omega_P = \frac{\sqrt{P}}{\beta\hbar}$. This can be interpreted as follows: The Hamiltonian of a system located at point x can be calculated by considering $P-1$ *additional points* in phase space. All P points contribute equally to the total kinetic energy. The potential energy is simply the average of potential energies at all points, as indicated by the $\frac{1}{P}$-prefactor. But an additional contribution exists, that of *harmonic spring* potentials with force constants ω_P between each pair of neighbored points x_{k+1} and x_k. Thus, in addition to a global potential energy surface in which the points might exist, an *intrinsic* potential energy resulting from their relative positions is added. Since $x_1 = x_{P+1}$, the first and last points are also stuck together by these springs, resulting in a *string of beads* held together by springs. This is shown in fig. 2.8.

We see that the Trotter number introduced to approximate the sum of kinetic and potential operators in eq. 2.86 has turned out to be the number of beads in the ring polymer. Thus, if we want to get the exact treatment of the imaginary time propagator, the number of beads must go to infinity, according to eq. 2.86.

PIMD and RPMD

In PIMD, the masses m in eq. 2.98 can be set arbitrarily, since they are only used to explore the potential energy surface in order to calculate the static partition function Q of the system, which was the objective of all our PI derivations fo far. However, our actual objective is to calculate the chemical reaction rate constant k(T) of the system of interest. This is of course a *dynamical* quantity. Thus, the fictitious *points* in phase space need to be treated as real *particles* with atomic masses, beads of a real ring polymer, connected via harmonic spring potentials [8].

This slight modification is then called RPMD. In practice, we want to calculate rate constants for reactions of molecules in the gas phase. For this situation, each atom of the reactive system is translated into a ring polymer of P beads. The ring polymers are interacting only beadwise, i.e., only bead number k of atom A is seen from bead number k of atom B and thus integrated into its part of the Hamiltonian. This is visualized in fig. 2.9.

(a) The water molecule   (b) 8 bead RPMD representation
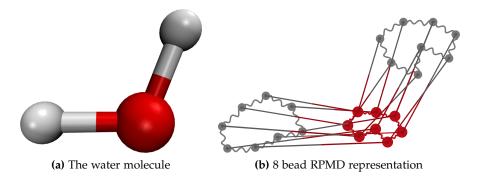
Figure 2.9: Example for the actual implementation of the RPMD Hamiltonian. Shown is the water molecule (a). It shall be described by RPMD with 8 beads. Therefore, each atom is represented by a ring polymer with 8 beads, whereas beach k of each atom is interacting with the corresponding bead of the others (b).

With this, the RPMD-Hamiltonian of a system with N atoms and n beads can be expressed as [53]:

$$\mathfrak{H}_n(\mathbf{p}, \mathbf{q}) = \sum_{i=1}^{N} \sum_{j=1}^{n} \left(\frac{|p_i^{(j)}|^2}{2m_i} + \frac{1}{2}m_i\omega_n^2|\mathbf{q}_i^{(j)} - \mathbf{q}_i^{(j-1)}|^2 \right) + \sum_{j=1}^{n} V(\mathbf{q}_1^{(j)}, \ldots, \mathbf{q}_N^{(j)}), \tag{2.99}$$

where $\mathbf{q}$ and $\mathbf{p}$ are the position and momentum vectors of the full reactive system, m is the atomic mass of atom N and $\omega_n = \frac{1}{\beta_n \hbar}$ ($\beta_n = \frac{\beta}{n}$) is again the force constant connecting the neighbored beads. Note also that the potential energy is no longer divided by the number of beads, since each bead is treated as an fully-fledged copy of the classical atom.

In order to calculate the RPMD rate constant for a MD calculation it is useful to remember that both TST and QTST, i.e., the classical and the exact quantum mechanical rate equations, can be expressed by means of the reactive flux through a dividing surface (eq. 2.44 and 2.58). Indeed it is possible to formulate the QTST rate constant in terms of a flux-side correlation function with respect to the dividing surface:

$$k(T) = \frac{1}{Q_r^{(n)}(T)} \lim_{t \to \infty} \tilde{c}_{fs}^{(n)}(t), \tag{2.100}$$

with $\tilde{c}_{fs}^{(n)}$ being the Kubo-transformed flux-side correlation function:

$$\tilde{c}_{fs}(t) = \frac{1}{(2\pi\hbar)^N} \int \int e^{-\beta H_n(\mathbf{p}_0, \mathbf{q}_0)} \delta(\bar{\mathbf{q}}_0 - \mathbf{q}_{\ddagger}) \frac{\bar{\mathbf{p}}_0}{m} \Theta(\bar{\mathbf{q}}_t - \mathbf{q}_{\ddagger}) d^N \mathbf{p}_0 d^N \mathbf{q}_0, \tag{2.101}$$

where $\delta(\bar{\mathbf{q}}_0 - x_{\ddagger})$ takes only trajectories located at the dividing surface at $t = 0$ into account and $\Theta(\bar{\mathbf{q}}_t - \mathbf{q}_{\ddagger})$ accounts for all trajectories located at the product side at time t. At this point, an *approximation* is made. Instead of averaging the flux side operator along the ring polymers, only the *average positions* $\bar{\mathbf{q}}$ and momenta $\bar{\mathbf{p}}$ of all beads for each atom are considered:

$$\bar{\mathbf{q}}_i = \frac{1}{n} \sum_{j=1}^{n} \mathbf{q}_i^{(j)},$$

$$\bar{\mathbf{p}}_i = \frac{1}{n} \sum_{j=1}^{n} \mathbf{p}_i^{(j)}. \tag{2.102}$$

These averaged values are called *centroid variables*. All observables are therefore calculated only indirectly from the ring polymer. They depend on its centroid variables, what effectively

retains the classical one-particle picture. These centroid particles are, however, affected from the motion of the whole ring polymer by eqs. 2.102 and 2.99. In practice, it could be shown that this *centroid-approximation* hardly affects the results of rate constant calculations although it is only *exact* in the high-temperature and short-time limits and for a simple harmonic-oscillator-PES [11]. In fig. 2.10 it is shown that the centroid particle is able to tunnel through barriers thanks to it average definition.

Similar to classical trajectory calculations (section 2.1.2) it is possible to reformulate the reactive flux expression into two factors: Instead of sampling many trajectories from the reactants to the product region, which will need huge amounts of them due to the rare-event problem, the free energy surface is calculated by *biased sampling* methods (section 2.1.3), the TS dividing surface is located on its maximum value and a bunch of recrossing trajectories is started in order to calculate a transmission coefficient κ. In the case of QTST this is called the *Bennett-Chandler factorization* of the reaction rate expression [53].

Further details concerning the samplings and dividing surface constructions are skipped here in order to hold this section manageable. They are described in section 3.3.7 of the program description.

In the most prominent case of a bimolecular reaction, the RPMD QTST rate constant can be shown to be given as [53]:

$$k_{RPMD}(T) = \kappa 4\pi R_\infty^2 \sqrt{\frac{1}{2\pi\beta\mu_R}} e^{-\beta\Delta F}, \qquad (2.103)$$

where ΔF is the free energy activation barrier calculated from umbrella integration, R_∞ is the assumed *asymptotic distance* between the reactants, μ_R is the reduced mass of them and κ is the transmission coefficient calculated by a recrossing calculation (fig. 2.5). The derivation of this rate expression is shown in section 11.2.2 of the appendix, where also the function of the dividing surfaces and the connection to reactive-flux QTST is deepened.

In practice, free energy calculations as well as recrossings depend only on the centroid variables: The umbrella bias is applied to them as well as the constraint applied for recrossing parent trajectories. The averages and expectation values of the reaction coordinate ξ for eq. 2.42 are calculated as well solely from the centroids. It should be mentioned that RPMD, although much cheaper than "true" wave packet dynamics calculations, is itself much more expensive than classical trajectory samplings, since the potential energy of the system as well as its gradient needs to be evaluated for *each bead*, separately. Bead number k of each atom only interacts with the same index of all other atoms, thus it is straightforward to do n separate potential energy calculations. Hence, a RPMD calculation is n times more expensive than a classical trajectory sampling. It is therefore important to find a compromise between accuracy (more beads) and feasibility (less beads). Usually, the k(T) value will converge at 8 to 32 beads, unless very low temperatures (below 200 K) are calculated.

2.2 Potential Energy Surfaces

We have seen how chemical reaction rates with consideration of quantum effects can be calculated by classical trajectory samplings using RPMD. In practice, the potential energy as well as its gradient need to be calculated and included into the RPMD Hamiltonian (eq. 2.99). This could be done by AIMD, where for each structure the potential energy and gradient is calculated, e.g., by DFT or MP2[28]. However, if we consider that at least several millions of sampling steps are needed

---

28 I renounced to give any theoretical background of quantum mechanical methods in line with this thesis since this would extend its scope too far. There are several well-known books that can be considered by the interested reader [12,54,55]. Basic knowledge of quantum chemical methods is assumed in the following.

(a) Classical dynamics

(b) RPMD centroid dynamics

(c) Free energy profiles
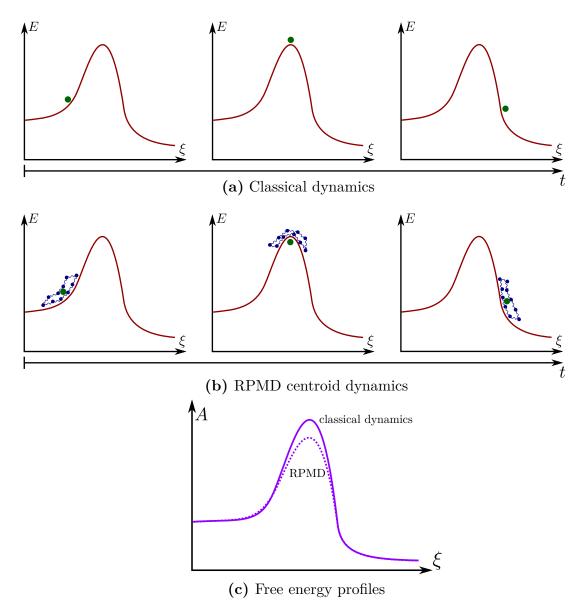
Figure 2.10: Comparison between classical and RPMD dynamics for the sampling of a reaction barrier. In the classical picture, the particles moves above the barrier (a). In the RPMD picture, the particle is a centroid of RPMD beads, therefore it is able to tunnel trough the barrier if the ring polymer is spread over the barrier (b). Due to this behavior, the calculated free energy barrier of the reaction will be lower in the RPMD case, which corresponds to a larger k(T) value (c).

to converge the free energy profile of medium-sized systems, it becomes clear that this approach is unfeasible, even if semiempirical methods are used.

Therefore, reaction rate constants are usually calculated with parametrized potential energy surfaces, whose potential energies and gradients can be calculated very fast. The usual procedure is to set up a function defining the potential energy and its gradient in the region of interest for the reactive system under consideration. Since the description should be as accurate as possible, several schemes were developed to calculate high-level *ab-initio* reference data and fit empirical functions to them and sometimes also to experimental data.

In line with this thesis, the EVB-QMDFF method founded by HARTKE and GRIMME [16] was used to express the potential energy surfaces of the reactions. Since the overall aim is to develop reliable high-quality *black-box* methods for reaction rate calculations of arbitrary systems, it will be explained why EVB-QMDFF is at least one of the best PES representations to be used in this context. To make this point clear, a short review of popular approaches for setting up reactive PESs will be given, by describing their advantages and disadvantages the path to EVB-QMDFF will be depicted.

In order to do a fair and comprehensible judgment, three conditions will be applied:

1. Simple parametrization (both intellectual and computational)

2. General applicability

3. High quality in the vicinity of the reaction path

Our method of choice should fulfill all three. Therefore, all approaches that are shortly explained in the following will be evaluated with respect to these conditions. In order to make things clearer, the methods are assigned to a number of categories and subcategories. In reality there is of course a methodological continuum such that the assignment of a method to a category is not definite.

2.2.1 System-Specific Parametrizations

The idea of parametrizing PESs of molecular systems in order to avoid direct *ab-initio* calculations for dynamics or other purposes was recognized already in the early days of computational chemistry[29]. Perhaps the first usable PES representation was built for the $H + H_2$-reaction in 1955: The *London-Eyring-Polanyi-Sato* (LEPS) surface [56, 57]. It is based on the *Heitler-London* (HL) method (eq. 2.122) for the H_2-molecule, when the third H-atom is in infinite separation to them. Within HL, the bonding energy is given by a simple Morse function, whereas the antibonding energy is expressed by a slightly changed Morse function. To obtain the whole surface, essentially three HL-type surfaces (for each permutation of H-pairs) are combined and weighted according to the actual $H_i - H_j$-distances.

Early Approaches

Though originally designed for $H + H_2$-systems, generalized LEPS-surfaces can be built for arbitrary three-atomic systems and advanced versions of them are still in use today [58, 59]. Since its origins until the early 90s, the field of PES-publications for new systems has grown steadily [60]. Those old but still frequently used surfaces can be classified into three branches:

(a) System-specific static global expressions with individual functions, fitted to *ab-initio* reference data. Since the intellectual effort for this individual construction of PES-functions steeply increases with system size, very small systems are the main area of application. For three-atomic systems, they are often based on the LEPS surface type, e.g., the H+H$_2$-surface by TRUHLAR and HOROWITZ [61] as it is used in chapter 5.

---

29 The essentials of this first section are also included in the introduction of chapter 5.

(b) Full-dimensional *spline-interpolation* of regularly scattered *ab-initio* reference energies. This approach is possibly the simplest one to think of but imposes an exponential scaling with the number of internal coordinates. If, e.g., a system with five atoms or $3 \cdot 5 - 6 = 9$ internal coordinates shall be parametrized with a quite rough grid of ten points per dimension, a total amount of one billion *ab-initio* reference energies would be needed! Therefore, only systems with 3 to 4 atoms can be described by this method. An example is the HCO-PES by Bowman, Bittman and Harding [62].

(c) *Many-body expansions* of the potential energy. Depending on the distances between atom i and j (r_{ij}), the PES can be expressed as:

$$V(\mathbf{q}) = \sum_{i<j} V_2(r_{ij}) + \sum_{i<j<k} V_3(r_{ij}, r_{ik}, r_{jk}) + ..., \tag{2.104}$$

where V_2 is the two body potential and V_3 the three body potential. In practice, this series is terminated after third, fourth or sometimes fifth order. With this method, a polynomial scaling (dependent on the highest body-multiplicity in usage) is realized, which enables the usage on much larger systems than with (a) and (b). If the n-body potentials are cleverly formulated, the scaling can even be brought to less than quadratic. The traditional nonreactive force field potential function (eq. 2.105) is also a many-body expansion, where V_2 is built of the bond as well as noncovalent energy terms and V_3 is the bond angle energy. Examples (in the field of specific PES parametrizations) are: $H+C_2H_2$ (White and Schatz) [63], $SiH_2 + SiH_2 \rightarrow Si_2H_4$ (Agrawal *et. al.*) [64].

For our purpose, approaches (a) and (b) are inappropriate. The heavy scaling permits the usage for larger systems, which makes further investigations of them unnecessary. In contrast, approach (c) is much cheaper and the generalized functional expression of eq. 2.104 could enable a system-independent approach. We will see below that QMDFF itself is essentially a many-body expansion method.

Machine Learning Approaches

Much more subtle are *machine learning* (ML) based surfaces, as they have emerged since the 1990s [65]. As for ML in general, PES functions generated by it do not have any direct physical meaning, they become meaningful and accurate if a sufficient amount of *ab-initio* reference data is used as a *training set*.

They are system-independent methods due to the fact that the underlying functions could be used for every possible chemical system. However, usually a quite large amount of effort is needed to set up a new ML-based PES, such that ML can be seen as at least partial system-specific.

One example are the *Shepard-interpolation*-based methods [66]. Here, the QM-reference PES is approximated by a number of Taylor series expansions scattered in the configuration space relevant for the reaction of interest. Those independent Taylor-expansions are then connected via Shepard interpolation. Energy and gradient on each point of the PES is expressed as a weighted sum of the different Taylor expansions, whereas the nearest expansion has the largest weighting factor. This approach is similar to the distributed Gaussian EVB method explained in section 2.4.5. It is possible to construct a *black-box* Shepard interpolation method, we could run short AIMD trajectories and place new Taylor expansion points in the visited PES areas. This is realized in the GROW algorithm by Collins *et al.* [67]. With growing number of Taylor expansions, the PES quality increases. The Shepard-interpolation methods are closely related to the full-dimensional spline interpolations listed in (b) above and can be seen as another branch of them. Only if the Taylor-expansions are cleverly distributed in space, such that an exponential scaling can be avoided, as it is done, for instance, in the GROW algorithm, the Shepard-interpolation methods are superior.

A bunch of other ML-based methods exists. The interpolating moving least-squares method [68] can be seen as a generalization of Shepard interpolation, which is its zeroth order. Higher orders differ mainly in the interpolation functions in usage, enhancing the quality of the PES but also the calculation effort, since the interpolation needs to be done numerically by means of matrix diagonalizations. In the Gaussian processes method [69], which is a non-parametric model, no interpolation functions exist, instead all PES information is expressed statistically by a multivariate Gaussian distribution depending on the internal coordinates of the system. *Neural networks* (NN) [70] finally connect actual configurations to potential energies and gradients by training a number of interconnected artificial NN-layers with a bunch of QM reference data.

All those methods have in common that the PES quality can be raised arbitrarily if more and more QM reference is thrown in during the training process. With this, a number of problems appear. How much reference data shall be calculated? Which type of reference data shall be added at a certain point to get a balanced description of the whole relevant area? With this, criterion 1 seems to be violated. Further, the actual process of QM-data selection and model training might depend strongly on the system under consideration, which makes it almost impossible to formulate a general, system-independent algorithm for parametrization, contrary to criterion 2.

2.2.2 Generalized Potential Functions

An alternative way is to define a flexible framework of potential terms whose final composition is determined from the topology of the system under consideration. This can be done by means of a many-body expansion (see above), i.e., by including terms that depend on the *relative positions* of two atoms, of three atoms etc.

The most popular variant of those generalized PESs are the traditional non-reactive *force fields* (FFs). A compelling variety of them has been emerged since the 1970s [71, 72]. It would be prohibitive to give even an abbreviated review, however, the general construction of the potential function is similar for most of them[30]:

$$E_{\text{ff}} = E_{\text{bonds}} + E_{\text{ang}} + E_{\text{dihed}} + ... + E_{\text{disp}} + E_{\text{coul}} + E_{\text{rep}} + ... \tag{2.105}$$

The first three terms are many-body potentials and describe the covalent energy: bonds (E_{bonds}), angles (E_{ang}) and dihedrals (E_{dihed}). The last three are of noncovalent nature and affect all pairs of atoms in the system unless bound directly or too far away (*cutoff*): dispersion (E_{disp}), Coulomb interactions (E_{coul}) and repulsions (E_{rep}). Up-to-date force field functions usually contain much more terms, such as crossterms or for consideration of particular chemical phenomena (e.g., hydrogen bonds); however, the terms listed in eq. 2.105 are still building the foundation.

In contrast to the system-specific PESs described above, force fields are able to describe arbitrarily large systems, such as enzymes or biochemical membranes since no *ab-initio* reference data of those systems is needed. Even today it is practically impossible to calculate *ab-initio* energies for systems of thousands of atoms, but if we consider that these are many small instances (e.g., amino acids, aliphatic chains, aromatic rings) plugged together it becomes clear that only *ab-initio* references for those subunits are needed in order to parametrize a force field that is able to describe the whole system.

So far, it should be obvious that force fields fulfill criterion 2, a single popular force field such as MM3 [73] can be used for thousands or millions of different simple organic molecules, whereas each of them would have needed an exhausting parametrization procedure in the case of, e.g., ML-methods. Unfortunately, there is a serious drawback: MM3 (and others) raise the claim that they are able to describe half the periodic table (or more). To ensure such a claim, reference data

---

30 This statement is only true if just *all-atom* force fields are taken under consideration. Especially for very large biomolecular systems, *coarse-graining*, i.e., combining reactive groups to effective particles, is quite usual [12]. Their potential functions are of course different, and are skipped here.

for all chemically stable combinations of elements should be included somehow in the force field potential. In reality, for example, the energy profile of a rotation depends on the three involved atoms but as well on the bonding partners of those atoms and their bonding partners etc.. An angle constructed with three carbon atoms will behave totally different with benzene rings or metal clusters bound to it as it would be with hydrogen atoms. Nevertheless only one or a handful of different C-C-C-angles are defined in usual force fields. Even more radical in the sense of generality is the *universal force field* (UFF) [74]. It is able to describe systems containing arbitrary compositions of all stable elements in the periodic table. However, the degree of specification is even lower than in MM3, only one atom type is used per element, thus neglecting almost any composition-specific phenomena.

Therefore it can be stated that the generality is achieved at the expense of its specific quality, criterion 3 is not fulfilled. Further, as the name "nonreactive" already reveals, those FFs are unable to describe reactions with breaking and forming bonds. The FF potential function contains a set of terms that is determined before the actual calculation (e.g., MD) is started. For example, a fixed set of bond terms is used, depending on the bonds present in the system as it was generated. No new bonds can be build subsequently because it is impossible to delete the old bond term and add a new one during a trajectory. Only conformational changes can be described, which is insufficient for our demand.

The problem of nonreactivity is tackled with *reactive force fields*. Their most prominent example is the ReaxFF force field [75]. Its central idea is the inclusion of geometry-dependent *bond orders*. It is well known that double bonds are shorter than single bonds, triple bonds are even shorter than double bonds, etc. Therefore, instead of defining the bonding pattern of the system manually at the beginning, the location of all bonds is determined solely based on the actual geometry of the system (i.e., of its atoms). The order of the bond between two atoms i and j is calculated as:

$$
\begin{aligned}
BO'_{ij} = \exp\left[p_{\text{BO},1} \cdot \left(\frac{r_{ij}}{r_0^\sigma} \right)^{p_{\text{BO},2}} \right] + \exp\left[p_{\text{BO},3} \cdot \left(\frac{r_{ij}}{r_0^\pi} \right)^{p_{\text{BO},4}} \right] + \\
\exp\left[p_{\text{BO},5} \cdot \left(\frac{r_{ij}}{r_0^{\pi\pi}} \right)^{p_{\text{BO},6}} \right]'
\end{aligned}
\tag{2.106}
$$

where r_0^σ, r_0^π, $r_0^{\pi\pi}$, $p_{\text{BO},1-6}$ are element-pair specific force field parameters. Based on this scheme it is possible to form and break bonds during trajectories, thus describing reactions. It turns out, however, that this feature comes at the expense of a much more complicated potential energy function, containing much more element specific parameters than traditional nonreactive force fields. Therefore, ReaxFF has no universal parameter set for the whole periodic table but is usually reparametrized for the system of interest containing, e.g., 5 different elements.

One might think that ReaxFF could be the method of choice for our demands, since it can be generally applied (the mathematical system remains the same for all elements) and is of high quality (due to its specific parametrization). The only criterion remaining is the simple parametrization. Since ReaxFF is able by construction to represent the whole global PES of a system, all possible (but maybe unapparent) reactions of the systems should be explicitly considered with *ab-initio* reference data in order to avoid unphysical artifacts. Fortunately part of the possible chemistry is already included into the underlying potential functions such that less reference data is needed than, e.g., for ML-methods where no physics is contained in the underlying model.

A closer look at eq. 2.106 might arouse suspicion that many parameters are needed in ReaxFF. Indeed, the number of interdependent parameters easily grows to several hundreds for systems with a handful of different elements, especially if elements from lower regions of the periodic table should be included. The resulting optimization problem is by far too complicated to solve it with a simple local optimization, especially since the parameters show complicated interdependencies and are not directly connected to individual bunches of reference data. The optimization can be done with the usage of *genetic algorithms* (GAs), e.g., with the OGOLEM package [76–79], however, this is

no genuine *black-box* process since the user must check if the obtained set is physically reliable, even if it is the best one to fit to the reference data set.

To be fair it should be said that such a ReaxFF reparametrization is able to do much more than we need. The resulting force field is able to describe the whole chemistry of the chosen element combination, maybe with a certain bias towards the reactions of interest. In order to calculate the k(T) value of a certain reaction, we only need the thermally accessible PES of both reactants and products as well as the reaction path between them and not between others.

Therefore, ReaxFF is somewhat incompatible with our desires, resulting in a failure to fulfill criterion 1.

2.2.3   Black-Box Approaches

So far, the issue of parametrization seems to be the largest one. No matter if system-specific PES functions, ML-approaches or reactive force fields are used, all of them require a significant amount of (re-)parameterization (at least if good PES qualities shall be achieved). This problem has inspired some workgroups to design force field functions that are system-specific but have a predefined standard way of parametrizing them, such that the process of parametrization can be translated into a number of programmable steps. These approaches can be termed as *black-box*, since no user-sided creative thinking is needed for their setup. In the ideal case, only one button must be clicked and after some time the completed force field will be ejected.

A popular field for those approaches is the FF-description of *metal organic frameworks* (MOFs). The MOF-FF [80] and QuickFF [81] approaches impose standard schemes for the construction of those functions. Within MOF-FF, the potential function is a modified MM3 FF, where the atomic charges are taken from a separate Gaussian calculation. The force field parameters are fitted with a GA to a set of reference data. Unfortunately, the convergence behavior of the GA cannot be predicted, it might become necessary to enlarge the set of reference data during the optimization process if convergence problems arise. This problem is tackled by QuickFF. Here, force field constant are first fitted to Hessian calculations of one or more equilibrium structures and are then refined by simulation of perturbation trajectories along each internal coordinate. With this refinement, manual interventions during a GA optimization can be diminished. Of course, these force fields are not suitable for our needs, since they are specialized for the use with MOFs, thus violating criterion 2.

Besides this, (partial) *black-box* methods for the optimization of traditional nonreactive force fields were developed [82]. MM3-parameters can be optimized to a given set of QM reference data (e.g., to describe a certain molecule particularly well) by applying local *Newton-Raphson* (NR) optimization. Those methods are no true *black-boxes* since user-sided selection of the reference is still needed.

Quantum-guided molecular mechanics (Q2MM) [83] is a method specialized on the description of *transition states* with high quality. In metal-catalyzed reactions, a bunch of TSs similar in energy can exist, depending on the ligand conformations. In order to calculate their relative free energy barriers and thus their importance for actual reactions (stereoselectivity), *Monte Carlo* (MC) samplings of their vicinity can be done. In Q2MM, the PES around the different TS-structures is expressed by a quadratic force field based on MM3 fitted to the TS Hessian matrix. Additional QM-reference can be directly calculated from the Q2MM program by applying calls to Gaussian. Unfortunately we need a description of the whole reaction path vicinity, not only of the TS.

All methods discussed in this section can be applied generally or to broad fields of chemistry like MOFs (depending on the system for which the reference data is generated) and their quality can be expected to be quite high for this particular system. However, though they all claim (at least indirectly) to be *black-box* methods, in all of them at least some user-sided cooperation (mainly in the selection of QM reference) is needed, therefore violating criterion 1.

2.3 Quantum Mechanically Derived Force Field

In 2014, GRIMME published a new type of *black-box* semireactive force field, called *quantum mechanically derived force field* (QMDFF)[31] [15]. Semireactive means that QMDFF is able to describe breaking bonds by using asymptotic bonding terms, but is unable to allow for newly formed bonds. Much more importantly, it is indeed a *black-box* method. Unlike all methods mentioned so far, a fixed set of QM-reference is needed to set it up, such that the parametrization can be (and actually is) automated, the user only needs to execute a single command for a new FF[32]!

2.3.1 Idea

In order to set up a QMDFF for a molecular structure, no matter which of the 92 stable elements are contained, its geometry needs to be minimized by a QM-method of choice, followed by a frequency calculation.

Four ingredients are needed to parametrize a new QMDFF:

1. Geometry

2. Hessian matrix

3. Wiberg-Mayer bond orders [87,88]

4. CM5-charges [89]

The geometry is determined by the preceding structure optimization, the other three pieces of information can be obtained in line with a frequency calculation from most of the standard QM-packages. When the whole data is present, the QMDFF-optimization can be started. First, all force field terms that shall be part of the Hamiltonian are determined from the Wiberg-Mayer bond orders. Each pair of bound atoms (with a bond order of 0.5 or higher) contributes a bond term. Each pair of directly neighbored bond terms contributes a bond angle term and each triplet of neighbored bond terms contributes a dihedral term.

In addition, noncovalent terms are added between each pair of atoms that has at least three bonds between them or belong to different fragments. The Coulomb terms are parametrized from the CM5-charges, dispersions and others are set up from several element-specific global parameters contained into the program. Finally, the force constants are fitted by minimizing the difference between the QMDFF-Hessian and its reference counterpart.

All this is being done in *black-box* fashion, i.e., all the user needs to do is to start the QMDFF-optimization program with the reference data as input and after a few seconds the QMDFF force field file is ejected from it.

---

31 In order to avoid confusion it should be noted that a method named *quantum mechanical derived force field* (QMD-FF) was published in 2007 by CACELLI and PRAMPOLINI [84,85]. This method enables the parametrization of intramolecular force fields based on energy, gradient and Hessian information from a number of configurations of the respective molecule. It constructs a traditional-nonreactive force field and is no *black-box* method (and thus of no interest for us), since the number and locations of the reference points need to be picked by the user.

32 For some special cases where the *black-box* approach might run into difficulties (e.g., low bond orders in the case of transition metal complexes) the user can add specific command line parameters to the program call that adjust default settings (like the threshold for the bond orders above which a covalent bond is assumed). Details can be found on the QMDFF website [86]. In the reimplemented version of QMDFF contained in `qmdffgen.x` these command line parameters are deactivated so far.

2.3.2 The QMDFF Potential Function

The QMDFF-energy can be subdivided into three contributions:

$$E_{\text{QMDFF}} = E_{e,\text{QM}} + E_{\text{intra}} + E_{\text{inter}}, \tag{2.107}$$

where $E_{e,\text{QM}}$ is the *reference* energy for the minimum geometry, E_{intra} are the bounded *intramolecular* contributions and E_{inter} are the noncovalent *intermolecular* energy contributions (or intramolecular with three or more bonds between the atoms, see above). In general, $E_{e,\text{QM}}$ could be chosen arbitrarily, since it is an additional constant for the QMDFF-PES. However, if two or more QMDFFs shall be combined as it is done in the EVB-QMDFF method, this shift plays a crucial role (see section 3.3.1).

Intramolecular Energy

The intramolecular energy is itself a sum of different terms[33]:

$$E_{\text{intra}} = \sum_{\text{bonds}} V_{\text{str}}^{12} + \sum_{1,3} V_{\text{str}}^{13} + \sum_{\text{angles}} V_{\text{ang}} + \sum_{\text{torsions}} V_{\text{tors}} + \sum_{\text{inversions}} V_{\text{inv}}. \tag{2.108}$$

This composition is quite similar to that of traditional nonreactive force fields (eq. 2.105). The usual directly bounded (V_{str}^{12}) and bridged (V_{str}^{13}) bond terms are considered as well as bond angles (V_{ang}), dihedrals (V_{tors}) and inversions (V_{inv}).

It should be mentioned that the QMDFF terms in general work different than that of traditional force fields: Instead of predefined bonding configurations that need to be given by the user in line with the structure input file, the lists of force field interaction terms are generated automatically during the QMDFF optimization and are then written to the force field file (section 3.3.1).

Further, there are no globally defined optimum bond lengths or bond angles that are loaded for the respective bonding configurations, instead all energies are calculated by consideration of differences between the actual coordinate value and that of the reference minimum geometry. As already noted, the force constants are also determined individually during the optimization of the force field. Therefore, no compromises between different systems are needed, all parameters are optimized solely for the actual structure, thus significantly enhancing the force field quality with respect to the reference.

The *bond energy* terms are expressed by a polynomial potential:

$$V_{\text{str}} = k_{\text{str},AB} \left[1 + \left(\frac{r_{e,\text{AB}}}{r_{\text{AB}}} \right)^a - 2 \left(\frac{r_{e,\text{AB}}}{r_{\text{AB}}} \right)^{\frac{a}{2}} \right], \tag{2.109}$$

with $k_{\text{str},AB}$ being the force constant, $r_{e,\text{AB}}$ the coordinate value of the reference structure and a an atom pair specific parameter, defined as:

$$a = k_a(\text{A})k_a(\text{B}) + k_{\text{EN}} \left| \Delta\text{EN}(\text{AB}) \right|^2. \tag{2.110}$$

Here, $\Delta\text{EN}(\text{AB})$ is the electronegativity-difference of the involved elements and $k_a(\text{A})$ is an element-specific global parameter. Details of the fitting scheme for obtaining the different parameters used in the potential function can be found in the QMDFF paper itself [15].

Similar to a Morse potential, the polynomial potential allows for dissociations to happen at the correct dissociation limits (heat of formation)[34]. Since no new bond can be built due to the

---

[33] The following description of the different QMDFF energy contributions will give all essential information and some computational details but will shorten some of its explanations. These can be found in the original publication by GRIMME [15].

[34] As stated by GRIMME, he originally tried Morse potentials as bond terms, but they lead to problems in the force constant fitting scheme explained below [15].

predefined bonding pattern, QMDFF can be termed as a *semireactive force field*. The 1,3-interactions are also calculated by a polynom potential, with slight changes of the prefactors.

For the *bond angles*, a distinction is made between close-to-linear angles and all others. For a triplet of bound atoms ABC with A in the center, the bond angle energy for the near-linear case is a cheaper parabolic expression:

$$V_{\text{bend}}(\text{ABC}, \theta) = k_{\text{bnd}} f_{\text{dmp}} (\theta_{e,\text{ABC}} - \theta)^2, \tag{2.111}$$

whereas in all other cases the more expensive double-minimum form which allows for inversion of the angle is used:

$$V_{\text{bend}}(\text{ABC}, \theta) = k_{\text{bnd}} f_{\text{dmp}} (\cos \theta_{e,\text{ABC}} - \cos \theta)^2. \tag{2.112}$$

In both cases a damping function $f_{\text{dmp}} = f_{\text{dmp}}(\text{AB}) f_{\text{dmp}}(\text{AC})$, is applied to correct the force constant k_{bnd}. In cases where bond dissociations have occurred, the angle potential should of course also vanish. This is realized by applying the damping with respect to the lengths of both involved bonds:

$$f_{\text{dmp}}(\text{AB}, r) = \frac{1}{a + k_{\text{dmp}} \left(\frac{r_{\text{AB}}}{r_{\text{cov,AB}}} \right)}. \tag{2.113}$$

Note that this formula works similarly to the bond potential in eq. 2.109, with the distinction that the force constant k_{dmp} is a global parameter uniquely defined for all elements.

The *torsional potential* constitutes a special case within the QMDFF-description. Its energy is expressed as:

$$
\begin{aligned}
V_{\text{tors}}(\text{CABD}, \psi) = f_{\text{dmp}} \sum_n k_{\text{tors}}^n \{ f_{\text{chiral}}(\psi) \cdot [1 + \cos(n(\psi - \psi_e) + \pi)] \\
+ (1 - f_{\text{chiral}}(\psi)) \cdot [1 + \cos(n(\psi + \psi_e - 2\pi) + \pi)] \}
\end{aligned}
\tag{2.114}
$$

where f_{dmp} is a product of damping factors of all involved bonds (C-A, A-B, B-D) according to eq. 2.113, ψ_e is the reference dihedral value, f_{chiral} is used for correct description of both enantiomers (if involved atoms are asymmetric), k_{tors}^n are the torsional force constants. In contrast to bonds and bond angles, more than one of such force constants are needed for the construction of a dihedral, since torsional profiles usually contain more than one minimum. Here, n is the number of those minima (or: the multiplicity of the torsion), i.e., each minimum contributes one term in the sum.

This characteristic imposes a serious problem for the QMDFF-construction: So far, each force constant could be obtained from the Hessian of the given reference structure. In the case of the torsions, however, Hessians of all conformational minima of the system would be needed in principle to do this fit of all force constants. Such a proceeding of course contradicts the initial idea of only one minimum structure as reference. Therefore, an approximation is made: The rotational force constants are obtained by means of *extended Hückel theory* (EHT) calculations. After replacing their substituents by hydrogen atoms, scans are made for all dihedrals in the system. From those profiles, the number of minima n is determined as well as their force constants.

EHT calculations are cheap but nevertheless known to give quite reasonable rotational profiles. With this, a meaningful rotational landscape for the reference system can be obtained.

In some cases, the EHT fails to produce useful results. Then, the Hessian fit is reintroduced. Basically, all n force constants (where n is taken from the EHT calculation) are fitted to the frequency reference (which of course diminishes their expressiveness).

Noncovalent Interactions

For all but the smallest systems, the noncovalent interactions constitute the largest fraction of force field terms. The QMDFF-description of those terms is partially based on an intermolecular force field designed for gas adsorptions in microporous organic crystals developed by GRIMME in 2012 [90]. The following terms are considered:

$$E_{\text{inter}} = E_{\text{disp}} + E_{\text{rep}} + E_{\text{ES}} + E_{\text{hbnd}} + E_{\text{xbond}} + E_{\text{pol}}, \tag{2.115}$$

where E_{disp} and E_{rep} are dispersion and repulsion energy terms, E_{ES} includes electrostatics, E_{hbnd} and E_{xbond} are designed for hydrogen and halogen bonds and E_{pol} considers possible polarization effects.

For the *dispersion energy*, the D3-dispersion scheme as developed by GRIMME himself and broadly used for DFT dispersion correction is used in combination with the *Becke-Johnson* (BJ) damping [91]:

$$E_{\text{disp}} = -\sum_{\text{AB}} \epsilon_{\text{rep/disp}}(AB) \left[\frac{C_6^{\text{AB}}}{r_{\text{AB}}^6 + f(R_{\text{AB}}^0)^6} + s_8 \frac{C_8^{\text{AB}}}{r_{\text{AB}}^8 + f(R_{\text{AB}}^0)^8} \right]. \tag{2.116}$$

All parameters (global scaling factor s_8 as well as element pair specific C_6 and C_8 coefficients) are stored globally in the QMDFF program. Further, $f(R_{\text{AB}}^0)$ is the BJ-damping function which circumvents potentially divergent behavior of the dispersion term for short distances. Since D3 is atom *pair* specific in contrast to usual FF dispersion schemes that are usually atom *type* specific, the QMDFF dispersion is superior to that of most other FFs, but also more expensive for large molecules due to missing cutoff distances. For our applications to rather small gas phase systems, this disadvantage is irrelevant.

The short-range *Pauli-repulsion* is treated by a separate energy term:

$$E_{\text{rep}} = \sum_{\text{AB}} \epsilon_{\text{rep/disp}}(AB) \frac{Z_{\text{eff}}(\text{A})Z_{\text{eff}}(\text{B})}{r_{\text{AB}}} \exp\left(\frac{-\beta_{\text{rep}} r_{\text{AB}}}{R_{0,\text{D3}}^{3/2}} \right), \tag{2.117}$$

with Z_{eff} being effective nuclear charges, $R_{0,\text{D3}}$ standard D3 pair-cutoff-radii (distances below them dispersion is turned off in the D3-scheme) and β_{rep} global fit parameters. All those quantities are again stored within the program.

The *electrostatic energy* contribution is expressed as a standard Coulomb term with a topological screening prefactor $\epsilon_{\text{ES}}(\text{AB})$:

$$E_{\text{ES}} = \sum_{\text{AB}} \epsilon_{\text{ES}}(\text{AB}) \frac{q(\text{A})q(\text{B})}{r_{\text{AB}}}. \tag{2.118}$$

The $\epsilon_{\text{ES}}(\text{AB})$ deactivates all 1,2- and 1,3-electrostatic interactions and applies an element pair specific damping to 1,4-interactions, such that only atom pairs separated by four or more bonds are fully considered for Coulomb interactions. The partial charges $q(\text{A})$ and $q(\text{B})$ are the respective CM5-charges of the atoms that are part of the reference data, scaled by an empirical factor of 1.15.

Last but not least, particular terms are included for consideration of hydrogen and halogen bonds in the system. *Hydrogen bonds* can be built between two atoms of the elements N, O, F, S or Cl with a hydrogen between them, halogen bonds are of the form D-X-Y, with D being the donor (N or O), X the halogen and Y an arbitrary atom. Here, only the hydrogen bond energy term is shown:

$$E_{\text{hbnd}} = -\sum_{\text{AHB}} f_{\text{dmp}}^{\text{AHB}} f_{\text{dmp}}^{\text{hbnd}} \frac{c_{\text{AB}}^{\text{hbnd}}}{r_{\text{AB}}^3}, \tag{2.119}$$

where c_{AB}^{hbnd} is the atom pair specific interaction strength, f_{dmp}^{hbnd} turns off the hydrogen bond interaction for long distances and f_{dmp}^{AHB} is an angular damping term of the form:

$$f_{dmp}^{AHB} = \left(\frac{1}{2} (\cos \theta_{AHB} + 1) \right)^6. \tag{2.120}$$

It ensures that hydrogen bonds are only relevant for linear or near-linear arrangements.

In addition to the covalent and noncovalent terms described here, several special situations as coordinated metal atoms or ring-systems of different sizes are explicitly considered with separate energy terms (their description is skipped here). QMDFF was benchmarked against several standard sets of small molecules up to large metal complexes and proteins and can thus be considered as being quite general.

2.3.3 Optimization of Parameters

In the first step of the QMDFF-generation, the geometry of the reference is analyzed. The list of noncovalent interactions is set up by considering all atom-pairs separated by three or more bonds in between (dispersion, Coulomb) or between triplets of appropriate elements (hydrogen and halogen bonds). Whereas the list of all covalent interactions is generated based on the Wiberg-Mayer bond orders, their equilibrium values ($r_{e,AB}$, $\theta_{e,ABC}$, ...) are calculated subsequently from the given structure.

If torsions (i.e chains of four bound atoms) are present in the system, their energy profiles are calculated by means of EHT-calculations and the force constants are fitted to these, subsequently. Sometimes, the EHT-calculations give insufficient results, for instance, unnatural barrier heights. Then, the respective force constants are transferred to the next step.

Finally, the fit of all covalent force constants (k_{str}, k_{bnd}, insufficient k_{tors}) is done. For this, the difference between the FF Hessian (calculated numerically from FF gradients) and the reference Hessian as given by the user is minimized by means of the *Levenberg-Marquardt* (LM) algorithm:

$$\sum_{ij} (H_{ij}^{QM} - H_{ij}^{FF}(\mathbf{k}, [\mathbf{k'}]))^2 \to \min, \tag{2.121}$$

where $\mathbf{k}$ denotes the set of force constants to be optimized and $\mathbf{k'}$ the remaining ones that will not be changed during the procedure (noncovalent interactions, torsions optimized from EHT).

Usually, the fit converges within a few cycles.

The different origins of the QMDFF force constants and their optimization are shown in fig. 2.11.

2.3.4 Properties

As already noted above, a QMDFF is generated for a certain structure (containing one or more separate molecules) and is able to describe the region around the reference minimum as well as its torsional profile with high quality. If only covalent interactions would be considered, the reference structure would be obtained exactly from a QMDFF geometry optimization starting near to it. However, some noncovalent terms contain global parameters that might vary slightly from the exact reference case. Therefore, the global QMDFF minimum will usually slightly deviate from the reference. Similar effects can be seen by inspection of the energy and gradient (the QMDFF-energy will not be exactly zero at the reference minimum, even if $E_{e,QM}$ is set to zero). In practice, this can be neglected since the reproduction is still of outstanding quality, especially in comparison to traditional force fields.

QMDFF is further able to describe the whole set of torsional and noncovalent (for clusters of several molecules used as reference) minima the system can explore without bond-breaking. Here,

+0.385

−0.557

−0.039

−0.165

+0.375

Charges and geometry

$r_{e,AB}, r_{e,BC}, ...$
$\theta_{e,ABC}, \theta_{e,BCD}, ...$
$\psi_{e,CABD}, ...$
$q(A), q(B), ...$

Cutoff-radii $R_{0,D3}(A, B), ...$

```
r0ab(  1:  70)=(/
.    2.1823,  1.8547,  1.7347,  2.9086,  2.5732,  3.4956,  2.3550
.,   2.5095,  2.9802,  3.0982,  2.5141,  2.3917,  2.9977,  2.9484
```

Allen-electronegativities $EN(A), EN(B), ...$

```
data en/ 2.300,4.160,0.912,1.576,2.051,2.544,3.066,3.610,4.193
.         ,4.789,0.869,1.293,1.613,1.916,2.253,2.589,2.869,3.242
```

Atomic masses

```
data  ams /  1.00790d0,   4.00260d0,   6.94000d0,   9.01218d0,
.10.81000d0, 12.01100d0, 14.00670d0, 15.99940d0, 18.99840d0,
```

Grimme-C6 dispersion parameters

```
pars(      1:     100)=(/
.  0.30267000D+01,0.100D+01,0.100D+01,0.91180000D+00,0.91180000D+00
.,0.20835000D+01,0.200D+01,0.100D+01,0.00000000D+00,0.91180000D+00
```

etc. p.p.

$a_1, a_2, s_8, k_D, k_Z, k_{hbnd}, \beta_{rep}, kq, ...$

Global and element specific parameters from database

Input:
Energy, geometry,
CM5-charges,
Wiberg-Mayer
bond orders
Hessian matrix

$k_{str,AB}, k_{str,BC}, ...$
$k_{bnd,ABC}, k_{bnd,BCD}, ...$
$(k^n_{tors,CABD}, ...)$

Fit of FF Hessian to
QM reference for covalent
force constants

Torsional force constants
from extended Hückel
calculation

$k^n_{tors,CABD}, ...$

Fit too bad or rotational
barrier too high

$\min \left[\sum_{ij} (\mathbf{H}^{QM}_{ij} - \mathbf{H}^{FF}_{ij}(\mathbf{k}, [\mathbf{k'}]))^2 \right]$

$H_{ij} = \frac{1}{2} K (H_{ii} + H_{jj}) S_{ij}$

Figure 2.11: Overview of the QMDFF generation from the needed reference data. There are four sources for QMDFF force field parameters (clockwise): Reference geometry and CM5 charges, global parameters, EHT torsional fit and fit to reference Hessian matrix.

the QMDFF quality is slightly worse in comparison to the direct vicinity of the reference minimum but still very good in comparison to traditional force fields.

With this, we can state that QMDFF fulfills criteria 1 and 2, i.e., it is generally applicable and can be optimized in a *black-box* fashion. It further partly fulfills criterion 3: The quality of QMDFF in reproducing the reference PES is very encouraging for the whole configuration space of either the reactants or products area. All what remains is the region between them, i.e., the reaction channel[35]. This challenge is tackled in the next section.

2.4 Empirical Valence Bond

We have learned so far that QMDFF is perhaps the single PES description method that deserves the label *black-box* more than all others. Unfortunately it is semireactive, thus unable to represent PESs of reactive systems (disregarding simple diffusions, *cis-trans* isomerizations or other purely noncovalent reactions). To make QMDFF reactive, *empirical valence bond* (EVB) is the method of choice.

Originally formulated by Warshel in 1980 [92], the EVB-method is a surprisingly simple way of constructing reactive force fields by connecting traditional nonreactive force fields or even simpler formulations with an individually designed coupling term. Since its invention, a multiplicity of EVB-coupling terms has been emerged in the literature. Since the implementation and construction of EVB-coupling terms was one of my main working fields, a thorough review of those terms will be given, culminating in the description of those that are best suited for construction of high-quality *black-box* PESs.

2.4.1 Valence Bond or Molecular Orbital Theory?

Looking back to the origins of modern applied quantum mechanics, two concurring theories were in play many decades. *Molecular orbital* (MO) and *valence bond* (VB) theory. Since the 50s and especially since computer power has raised significantly such that quantum chemical calculations of large molecular systems became routine, MO theory is the dominant theory in practice [93].

VB still serves an important role for understanding of chemical bonding situations and molecular structures, mainly due to the localized VB orbitals, resembling bonds or resonance in π-systems. However, although quantum chemical programs based on VB are available [94], modern computational chemistry almost exclusively relies on MO.

The differences of VB- and MO-concepts can be explained quite well in the simplest possible case of the H_2-molecule [95]: It consists of (at least) two atomic orbitals (AO), one located at each H atom: χ_a and χ_b.

In the VB-picture, the wave function of H_2 is made of a linear combination of both the covalent and the possible ionic structures. The covalent structure is expressed by:

$$|\chi_a \overline{\chi_b}| - |\overline{\chi_a} \chi_b|. \tag{2.122}$$

Each term in this Heitler-London [96] wave function consists of a Slater determinant:

$$|\chi_a \overline{\chi_b}| = \frac{1}{\sqrt{2}} [\chi_a(1)\alpha(1)\chi_b(2)\beta(2) - \chi_a(2)\alpha(2)\chi_b(2)\beta(1)],$$

$$|\overline{\chi_a} \chi_b| = \frac{1}{\sqrt{2}} [\chi_a(1)\beta(1)\chi_b(2)\alpha(2) - \chi_a(2)\beta(2)\chi_b(2)\alpha(1)]. \tag{2.123}$$

---

35 In chapter 7 it is shown that a single QMDFF is able to deliver a PES-description that can be used to do accurate covalent mechanochemistry simulations, since there only bond dissociations must be described with high quality.

It becomes clear that the linear combination consists of all possibilities to distribute the α and β spin electrons on both AOs. However, it is also possible that both electrons are located in the same AO, leading to the ionic contributions $|\chi_a\overline{\chi_a}|$ and $|\chi_b\overline{\chi_b}|$.

The total VB wave function consists of four determinants, two covalent and two ionic ones:

$$\Psi_{VB} = \lambda(|\chi_a\overline{\chi_b}| - |\overline{\chi_a}\chi_b|) + \mu(|\chi_a\overline{\chi_a}| + |\chi_b\overline{\chi_b}|), \tag{2.124}$$

where the two parameters λ and μ are to be optimized variationally. For small bond distances near the equilibrium value, the covalent part is dominant, corresponding to a large λ-value. During bond breaking, μ increases, since ionic configurations are needed for its description. If the bond is broken homolytically and the atoms were moved far away, λ will converge to one, corresponding to two separated H radicals [55].

In the case of MO-theory, the molecular orbitals are built by *linear combination of atomic orbitals* (LCAO):

$$\begin{aligned} \phi_1 &= \chi_a + \chi_b, \\ \phi_2 &= \chi_a - \chi_b. \end{aligned} \tag{2.125}$$

In the simplest case, both electrons are located in the bonding orbital ϕ_1. Building the Slater determinant results in:

$$\Psi_{MO} = |\phi_1\overline{\phi_1}| = (|\chi_a\overline{\chi_b}| - |\overline{\chi_a}\chi_b|) + (|\chi_a\overline{\chi_a}| + |\chi_b\overline{\chi_b}|). \tag{2.126}$$

If we compare Ψ_{MO} to Ψ_{VB}, both wave functions are almost identical with the exception of λ and μ in the VB case. Therefore the VB wave function is much more *flexible* than the MO one, which consists of always 50 % covalent and ionic components.

This deficiency of MO theory can also be seen in many dissociation curves calculated with HF, which show qualitatively wrong shapes [12, 55]. To correct this deficiency, inclusion of *electron correlation* is needed.

In the simple H_2-case, *configuration interaction* (CI) needs to be applied, i.e., the wave function is itself a linear combination of two Slater determinants, the ground state and the exited state:

$$\Psi_{MO-CI} = c_1|\phi_1\overline{\phi_1}| - c_2|\phi_2\overline{\phi_2}|. \tag{2.127}$$

Evaluating both Slater determinants and simplifying, the wave function can be expressed depending on the atomic orbitals:

$$\Psi_{MO-CI} = (c_1 + c_2)(|\chi_a\overline{\chi_b}| - |\overline{\chi_a}\chi_b|) + (c_1 - c_2)(|\chi_a\overline{\chi_a}| + |\chi_b\overline{\chi_b}|). \tag{2.128}$$

Now, additional prefactors $c_1 + c_2$ and $c_1 - c_2$ are present. Compared to the VB expression, it is clear that $\lambda = c_1 + c_2$ and $\mu = c_1 - c_2$. The surprising result is that in this simple system a FCI MO wave function is needed to reproduce the VB wave function.

Further, it can be seen that both VB- and MO-theory come to the same result, if all configurations are included and all electron correlation is considered.

Why MO theory is still superior in practice?

The main reason is that the VB orbitals are *nonorthogonal*, which raises the needed computational amount significantly in comparison to MO, where the molecular orbitals are orthogonal [97]. Further, for larger systems, the number of needed configurations, especially ionic ones similar to eq. 2.124, grows heavily, which leads to both large computational demand and obscured conceptual clarity. Another important aspect is that in VB CI- and MO-coefficients are always optimized simultaneously (corresponding to a FCI calculation in the H_2-example). This apparent advantage was indeed a huge disadvantage in the early days of computational chemistry. Then, calculations of reactions involving bond dissociations where out of reach for most systems and usual applications

were restricted to near-equilibrium geometries, where a single electronic configuration is sufficient. Methods like HF are of satisfying quality for those regions by simultaneously being much chapter than VB. Even if today's computational resources are enough to perform VB-calculations for many systems, this historical mortgage constitutes another inhibiting factor.

Since the 1980s, a small but nevertheless visible renaissance of VB can be seen, at least in the eyes of VB enthusiasts[36]. This is mainly due to new implementations like *Generalized Valence Bond* (GVB) [98], which can, e.g., also be used with the Gaussian program suite [99]. In GVB, some simplifications are introduced in order to accelerate both user sided setup and computational time of a calculation. The wave function is expressed as a product of the HL function type (eq. 2.122) with the condition that two different of such functions are orthogonal to each other. With this prerequisite, the demand of calculating overlap integrals is reduced significantly.

There are many other published VB-methods, which makes it quite cumbersome to know which one could be needed for a specific situation. Therefore, MO-methods are still widely superior in terms of high quality (near-)*black-box* calculations of arbitrary molecules executed by the average chemist [94].

2.4.2 EVB-Foundations

What is needed to go from VB to EVB? One central advantage of VB is that the wave function is a superposition of orbitals that can be constructed by chemical intuition. In the H_2-example presented above these orbitals are the covalent HL wave function and the two ionic configurations.

During the (homolytic) dissociation of the H_2-bond the relative weights of these configurations change, from roughly 3 to 1 covalent to ionic at equilibrium distance over almost equal distribution at intermediary distances up to exclusively covalent at long distances.

The concept of expressing a reaction as a coordinate-dependent superposition of different chemical configurations can also be used apart from wave-function methods like VB. For the H_2-example, we could equally well describe both the covalent and the ionic states with fitted potential energy surfaces like force fields, if the parameters are chosen such that they reproduce the quantum mechanical energies and gradients.

Now, the total PES of the system could be expressed again as a superposition of these force fields, resulting in a superposition FF. This is the central idea of the EVB approach first developed by Warshel in his groundbreaking paper [92].

All concepts shown in this first publication are still valid for all EVB applications, therefore they will be shown here in some detail. The simplest (and mostly used) case is a superposition of *two configurations,* like the covalent and one of the ionic ones at the H_2 example. This closely resembles the famous *two-state problem* of quantum mechanics [100]. For this, the EVB-energy can be expressed as:

$$\mathbf{H} = \begin{pmatrix} F_1(\mathbf{q}) & C(\mathbf{q}) \\ C(\mathbf{q}) & F_2(\mathbf{q}) \end{pmatrix}. \tag{2.129}$$

Here, $F_1(\mathbf{q})$ and $F_2(\mathbf{q})$ are the coordinate-dependent potentials of both configurations and $C(\mathbf{q})$ is the *resonance integral* or *coupling term*. If no coupling is present, the EVB energy would be always the energy of the lower lying state, without any smooth transition between them. Of course this is not true for nearly any real system, therefore the exact formulation of this coupling term becomes a central aspect in EVB, as will be shown below.

The general idea of 2x2-EVB is also illustrated in fig. 2.12.

---

36 Reason for the success of some new invented VB-methods is also the partial mixing with MO-concepts. In order to at least partially avoid the problem of nonorthogonal orbitals, the VB orbitals are allowed in some approaches to delocalize somehow such that orthogonality of neighbored orbitals can be achieved. More details to this can be found in [94].
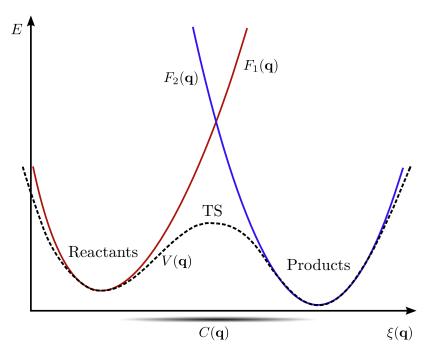
Figure 2.12: Illustration of the general EVB-concept. Reactant and product states are represented by their diabatic surfaces $F_1(\mathbf{q})$ and $F_2(\mathbf{q})$ that perform well in the vicinity of their minima but get qualitatively wrong in the TS-region. A coupling term $C(\mathbf{q})$ is needed to reproduce the reference energy $V(\mathbf{q})$ in all areas relevant for a reaction.

In most applications, the potentials of both states, also named *diabatic surfaces*, are simple harmonic potentials or traditional nonreactive force fields.

The energy of the 2x2-EVB system (sometimes named *adiabatic state* in reminiscence to VB) is obtained by solving the usual two-state problem, i.e., diagonalizing the EVB-Hamiltonian and take its lower eigenvalue:

$$V(\mathbf{q}) = \frac{1}{2}(F_1(\mathbf{q}) + F_2(\mathbf{q})) \pm \sqrt{\left[\frac{1}{2}(F_1(\mathbf{q}) - F_2(\mathbf{q}))\right]^2 + C(\mathbf{q})^2}. \tag{2.130}$$

For more than two states, EVB can be used equally well, however no analytical solution is available for such NxN-systems, the EVB-matrix needs to be diagonalized numerically. For the applications shown in this thesis, a 2x2-EVB was always the method of choice, which it is in all cases of usual chemical reactions from reactants to products (without bifurcations). Therefore, if EVB is mentioned in the remainder of this thesis, always 2x2-EVBs are meant, unless noted specifically.

In the first EVB-paper by WARSHEL [92], basically the same type of reaction as treated in the VB-section was looked at: A dissociation of a single bond into two charged fragments. The simplest case would be again H_2, where the heterolytic fission is treated. The general reaction is:

$$X - Y \rightarrow X^- + Y^+, \tag{2.131}$$

where it is assumed that X is more electronegative than Y. Both X and Y are allowed to have substituents or they might be even part of larger molecules. The first diabatic surface, describing the bonded, neutral molecule, can be expressed as:

$$F_1(r_{X-Y}) = \frac{-e^2}{r_{X-Y}} + V_{\mathrm{nb}}(r_{X-Y}), \tag{2.132}$$

where $\frac{-e^2}{r_{X-Y}}$ is the Coulomb force between both (partially) charged atoms and $V_{nb}(r_{X-Y})$ are additional nonbonded interactions like dispersion forces.

The second diabatic surface is similar to the first, however it is shifted by the formation-energy of X^-Y^+ from $X \cdot Y \cdot$ at infinite separation (Δ)[37]:

$$F_2(r_{X-Y}) = \frac{-e^2}{r_{X-Y}} + V_{nb}(r_{X-Y}) + \Delta. \tag{2.133}$$

The EVB resonance integral can be constructed by looking back at eq. 2.130. If this equation is solved for $C(\mathbf{q})$, the result is:

$$C(\mathbf{q})^2 = [F_1(\mathbf{q}) - V(\mathbf{q})][F_2(\mathbf{q}) - V(\mathbf{q})]. \tag{2.134}$$

Applied to our simple two-atom problem, the only relevant internal coordinate is the separation of both atoms r_{X-Y}:

$$C(r_{X-Y})^2 = [F_1(r_{X-Y}) - V(r_{X-Y})][F_2(r_{X-Y}) - V(r_{X-Y})]. \tag{2.135}$$

Warshel and Weiss assumed that the "true" potential energy surface of the reacting system can be modeled by a simple Morse-oscillator, depending solely on the bond length between atoms X and Y:

$$V(\mathbf{q}) = M(r_{X-Y}). \tag{2.136}$$

The total EVB-surface is obtained by inserting $F_1(r_{X-Y})$, $F_2(r_{X-Y})$ and $C(r_{X-Y})^2$ (calculated from eq. 2.135) into eq. 2.130. In the transition-region between both diabatic surfaces, the coupling term dominates the shape of the whole EVB-surface. Therefore, if $C(r_{X-Y})^2$ is constructed such that the whole EVB-term resembles a Morse-oscillator, this will actually be the case for the surface itself in the critical region. Near the covalent and ionic minima, the usual shapes of $F_1(r_{X-Y})$ and $F_2(r_{X-Y})$ will be resembled, but in the transition region they both will converge to the desired Morse-oscillator shape.

An important feature of EVB is the (near) independence of the coupling term $C(\mathbf{q})$ from the molecular environment[38]. With this, is is possible to parametrize the coupling term with gas phase calculations (especially if methods like distributed Gaussian EVB (see below), where the costs of QM-reference calculations are important are utilized) and use it in solutions or protein environments. Only the diabatic states need to be set up with inclusion of the whole environment. Since these states are force fields in most cases, the total expense of the EVB calculation should be affected only slightly (i.e., with modest scaling).

Having this property of partial solvent-independence, EVB is well suited for *multiscale* calculations, i.e., combinations of a small reactive system with the environment that – although passive with respect to the actual reaction – might have a significant influence on it. Warshel received his Nobel prize of 1992 together with Karplus and Lewitt "for the development of multiscale models for complex chemical systems" [104].

---

37 The gas phase formation-energy of X^-Y^+ from $X \cdot Y \cdot$ can be expressed in terms of the electron affinity of X (EA_X) and the ionization potential of Y (I_Y): $\Delta = I_Y - EA_X$.

38 This independence of the coupling term from the molecular environment was proven numerically in a paper by Warshel *et al.* [101]. There, the $Cl^- + CH_3Cl$ symmetric nucleophilic substitution was taken as benchmark reaction. Energies of diabatic states as well as the adiabatic state were calculated with frozen density functional theory (FDFT) both in presence and absence of solvents calculated with QM/MM methods. Using eq. 2.134 it could be shown that the needed coupling was almost identical for the whole reaction path with and without solvent. Similar tests were done in [102] and [103].

2.4.3   Simple EVB Coupling Terms

Since the invention of EVB in 1980 a huge number of publications spanning a large range of applications has been published. I will give no comprehensive review of EVB in a whole, this is done elsewhere [95, 105]. However, especially the construction of the resonance integral $C(\mathbf{q})$ is of central importance and a wide range of concepts for it is known, therefore it seems to be useful to give a short overview of successful approaches, starting with the most simple ones and successively going to quite comprehensive ideas.

The simplest case would be a *constant coupling* term:

$$C(\mathbf{q}) = a. \tag{2.137}$$

This quite primitive formulation leads indeed to a significant improvement over no coupling at all but it is nevertheless not suited for real applications with desired quantitative accuracy [106]. The reason is that the reactant and product areas are usually described well by their diabatic surfaces (i.e., force fields). If a coupling disturbs the diabatic surfaces in those areas, their description will often become worse although there is a general tendency that a global constant coupling usually disturbs the areas near the minima less than the transition region[39]. Even if the influence on the minima can be made small, one single parameter is usually not sufficient to guarantee a high-level quantitative description of the transition region. Hence, to the best of my knowledge, the constant coupling was so far never used for actual EVB-applications. However, in the supplementary information of the first EVB-QMDFF paper [16] (section 11.6.1), one example for this term is shown.

The next step on the path to better EVB coupling terms is the *energy-gap reaction coordinate* [107–109]. In this case, the coupling itself is dependent on the energies of both diabatic surfaces:

$$C(\mathbf{q}) = g(F_1(\mathbf{q}) - F_2(\mathbf{q})). \tag{2.138}$$

Here, g might be any kind of useful functional expression. An obvious choice is a Gaussian located at zero energy difference [108]:

$$C(\mathbf{q}) = a \exp\left(-b(F_1(\mathbf{q}) - F_2(\mathbf{q}))^2\right). \tag{2.139}$$

In this case, the coupling has maximum strength in the TS region (where both diabatic surfaces usually cross) and decays to zero in the reactant and product areas. Then, the diabatic energies in those regions are preserved. This is illustrated in fig. 2.12. The actual functional expressions used for energy gaps in this thesis are listed in table 3.1 of the program chapter.

Another formulation is by far the most common one: the *coordinate-dependent coupling*. This type was already used in the original paper by WARSHEL, there it was a Morse potential dependent on the length of the broken bond (eqs. 2.135, 2.136).

Since a large part of chemical reactions consists essentially of breaking or formation of one or more bonds, this type of coordinate-dependence, despite being quite simple, has been applied to many published systems. The general formula for the coupling term is:

$$C(\mathbf{q}) = a g_1(q_1) g_2(q_2) ... g_n(q_n). \tag{2.140}$$

One famous application is the *multistate* (MS)-EVB model by VOTH *et al.* [102, 110], which was constructed to simulate alternating hydrogen bond networks between water molecules with excess protons. Since each bonding configuration can be represented by its own diabatic surface, more

---

[39] This behavior can be explained by looking back at eq. 2.130. There, the square root consists of two summands: the squared difference between both diabatic energies and the squared coupling. Near the TS-region, the first term is nearly zero, such that the coupling determines the square root term almost exclusively. Near the reactants and products, however, the difference between both diabatic surfaces becomes large, marginalizing the effect of the coupling in the argument of the root.

than two of these surfaces are needed. In practice, for each oxygen atom in the system, one additional EVB is needed. Reactions with more than 30 states (corresponding to a 30x30-EVB term) were done [111].

In spite of this rather general nxn-EVB approach, the used type of coupling term is also well suited for our case of 2x2-EVB terms:

$$C(\mathbf{q})_{ij} = (V_{const}^{ij} + V_{ex}^{ij})f(R_{OO})g(q), \tag{2.141}$$

where $V_{ex}^{ij} = \sum_{m=1}^{7} \sum_{k=1}^{N_{H_2O}-1} \sum_{n_k=1}^{3} \frac{q_{n_k, H_2O} q_m^{ex}}{R_{mn_k}}$ represents the electrostatic interactions with nearby point charges of $H_5O_2^+$ dimers (R_{mn_k} is the cartesian distance to the atoms of such structures), $f(R_{OO})$ is an oxygen-oxygen distance-dependent damping function and $g(q) = \exp(-\gamma q^2)$ with $q = \frac{R_{OO}}{2} - R_{OH}$ is an asymmetric stretch coordinate of the actual $H_5O_2^+$-dimer.

In spite of the rather complicated functional expressions, all depends on distances between the H- and O-atoms, therefore the MS-EVB coupling term is a prominent example of the coordinate-dependent coupling.

Very similar to MS-EVB is the approach by VILLEUMIER and BORGIS [112, 113], which also handles the description of excess protons in hydrogen bonding networks. A special feature of this approach is that the diabatic surfaces participating in the nxn-EVB matrix are updated in each dynamic step during a proton transport trajectory. Thus, only neighbored water molecules will be included into the EVB-description. The coupling term is much simpler than in the MS-EVB case:

$$C(\mathbf{q})_{ij} = V_{12} \exp\left(\alpha R_{OO} - \gamma q^2\right). \tag{2.142}$$

Here, $q = q_H - \frac{1}{2}(q_{O_1} + q_{O_2})$ is the distance between the position of the transferred proton and the middle of the actual O-O bond. The coordinate-dependent coupling terms used in this thesis are listed in table 3.3 of the program chapter.

2.4.4 Chang-Miller EVB

All EVB coupling methods discussed so far are quite successful in their specific applications but they lack general applicability as it is needed for our desired *black-box* method. The MS-EVB formulation by VOTH *et al.* is, although the name sounds quite general, only applicable to excess-protons solved in water. Even small variations of the system of interest, e.g., if water should be replaced by ethanol, are not possible without at least partial rethinking of the whole mathematical structure.

The energy-gap couplings are much simpler, but, as will be shown below, they often give quite bad results for larger systems or asymmetric reaction paths.

Additionally, the concrete parametrization of the coupling terms listed above is not clear from the beginning. Are prefactors chosen such that a compromise between several reaction paths is reached or shall one specific path be optimized such that a bunch of reference energies are reproduced as well as possible?

A solution for this problems of either no general applicability or bad quality is already given implicitly in the original EVB-paper by WARSHEL (eq. 2.134). We can calculate the *needed* coupling for reproduction of a certain energy at $\mathbf{q}$ by inserting this reference energy and the energies of both diabatic surfaces in eq. 2.134.

Starting from this idea, CHANG and MILLER developed their Taylor expansion of reference data around the TS, the so called *Chang-Miller coupling term* [114].

We know that the coupling can be expressed as:

$$C(\mathbf{q})^2 = [F_1(\mathbf{q}) - V(\mathbf{q})][F_2(\mathbf{q}) - V(\mathbf{q})]. \tag{2.143}$$

Near the transition state, we can develop the reference energy in a Taylor series up to second order, with $\Delta\mathbf{q} = \mathbf{q} - \mathbf{q}_0$:

$$V(\mathbf{q}) = V_0 + \frac{1}{2}\Delta\mathbf{q} \cdot \frac{\partial^2 V(\mathbf{q})}{\partial\mathbf{q}^2} \cdot \Delta\mathbf{q}, \tag{2.144}$$

where only the constant and quadratic terms appear since the gradient at a saddle point is zero.

Similarly, the energies of both diabatic states can be expressed in Taylor series. Now, the linear term (generally) does not vanish because the diabatic states usually have no stationary point at the saddle point of the reference. Their expressions are:

$$F_i(\mathbf{q}) = F_i + \frac{\partial F_i(\mathbf{q})}{\partial\mathbf{q}} \cdot \Delta\mathbf{q} + \frac{1}{2}\Delta\mathbf{q} \cdot \frac{\partial^2 F_i(\mathbf{q})}{\partial\mathbf{q}^2} \cdot \Delta\mathbf{q}, \tag{2.145}$$

where i is 1 or 2, depending on the actual diabatic state.

These Taylor series can be inserted into the formula for the squared coupling (eq. 2.143), resulting in a quite lengthy expression:

$$C(\mathbf{q})^2 = (F_1 - V)(F_2 - V) + (F_2 - V)\frac{\partial F_1(\mathbf{q})}{\partial\mathbf{q}} \cdot \Delta\mathbf{q} + (F_1 - V)\frac{\partial F_2(\mathbf{q})}{\partial\mathbf{q}} \cdot \Delta\mathbf{q} +$$
$$\frac{1}{2}(F_1 - V)\Delta\mathbf{q} \cdot \left(\frac{\partial^2 F_2(\mathbf{q})}{\partial\mathbf{q}^2} - \frac{\partial^2 V(\mathbf{q})}{\partial\mathbf{q}^2}\right) +. \tag{2.146}$$
$$\frac{1}{2}(F_2 - V)\Delta\mathbf{q} \cdot \left(\frac{\partial^2 F_1(\mathbf{q})}{\partial\mathbf{q}^2} - \frac{\partial^2 V(\mathbf{q})}{\partial\mathbf{q}^2}\right) + \left(\frac{\partial F_1(\mathbf{q})}{\partial\mathbf{q}} \cdot \Delta\mathbf{q}\right)\left(\frac{\partial F_2(\mathbf{q})}{\partial\mathbf{q}} \cdot \Delta\mathbf{q}\right)$$

Now, the coupling near the TS can be described with this expression of combined Taylor series, if energies, gradients of Hessians of both the reference and the diabatic states at the TS are known. However, it has been shown that a *cumulant resummation*[40] gives better extrapolation properties. Applying this, a *generalized Gaussian* is obtained:

$$C(\mathbf{q})^2 = \mathcal{A}\exp\left(\mathbf{B} \cdot \Delta\mathbf{q} - \frac{1}{2}\Delta\mathbf{q} \cdot \mathbf{C} \cdot \Delta\mathbf{q}\right). \tag{2.147}$$

Here, the constant $\mathcal{A}$ is similar to the initial coupling strength expression:

$$\mathcal{A} = (F_1 - V)(F_2 - V), \tag{2.148}$$

the vector $\mathbf{B}$ depends on the energies and gradients of reference and diabatic states:

$$\mathbf{B} = \frac{1}{F_1 - V}\frac{\partial F_1(\mathbf{q})}{\partial\mathbf{q}} + \frac{1}{F_2 - V}\frac{\partial F_2(\mathbf{q})}{\partial\mathbf{q}} \tag{2.149}$$

and the matrix $\mathbf{C}$ depends on the Hessians, gradients and energies of all three potentials:

$$\mathbf{C} = \frac{1}{(F_1 - V)^2}\left(\frac{\partial F_1(\mathbf{q})}{\partial\mathbf{q}}\right)^2 + \frac{1}{(F_2 - V)^2}\left(\frac{\partial F_2(\mathbf{q})}{\partial\mathbf{q}}\right)^2 +$$
$$\frac{1}{F_1 - V}\left(\frac{\partial^2 V(\mathbf{q})}{\partial\mathbf{q}^2} - \frac{\partial^2 F_1(\mathbf{q})}{\partial\mathbf{q}^2}\right) + \frac{1}{F_2 - V}\left(\frac{\partial^2 V(\mathbf{q})}{\partial\mathbf{q}^2} - \frac{\partial^2 F_2(\mathbf{q})}{\partial\mathbf{q}^2}\right). \tag{2.150}$$

---

40 Cumulant resummations are well known in mathematical statistics [115]. A probability density function can be characterized by its *moments*, where the zeroth moment is the mean, the first is the variance, the second is the skewness and so forth. Depending on moments, the density function can be developed in a Taylor series (where the n'th Taylor expansion term depends on the n'th moment of the distribution). A cumulant resummation links this Taylor expansion to the more common Gaussian-shape density function.

This type of coupling performs quite well for reactions with simple reaction paths, where the TS-region converges fast to the reactants- and products-regions. However, other small and simple systems are described much worse. The reason is that the Taylor expansions around the TS are valid only close to it. If the distance between TS and reactant/product valleys is larger or the reference PES exposes significant anharmonicity, the whole approach fails (fig. 2.13).

CHANG and MILLER themselves proposed a fairly self-evident way to improve their coupling term: inclusion of higher-order Taylor series elements [116]. Of course the coupling term would be exact in the limit of an infinite number of Taylor series elements, but even inclusion of third or fourth order becomes very expensive. It would be no big deal to calculate numerical third and fourth derivatives of the diabatic terms represented by force fields, but calculation of such derivatives with the quantum chemical reference is nearly impossible in terms of computational expense, considering the fact that they must be calculated numerically based on Hessians or even gradients.

Further, eqs. 2.147 to 2.150 need to be evaluated for each energy calculation. With the initial version, this scales with N^2, where N is the number of internal coordinates used to express the coupling. Adding, for instance, up to fourth order, a scaling of N^4 with system size would be achieved, which is the same scaling as for, e.g., HF!

2.4.5 Distributed Gaussian (DG)-EVB

A way to solve this problem of the insufficient Taylor expansion was proposed by SONNENBERG and SCHLEGEL in 2006 [117]. Their ansatz is to *combine* several Taylor expansions in the relevant areas of the PES such that the whole accessible surface might be covered. Similar to eq. 2.147, the single Taylor series can be expressed by Gaussians. Thus, instead of using one giant expansion, an arbitrary large number of modest expansions distributed along, e.g., the reaction path is employed[41]. This idea is illustrated in fig. 2.13 with schematic energy plots which are similar to actual results obtained during the work on this thesis.

In order to translate this idea into a valid mathematical structure, the expression for the coupling (eq. 2.147) needs to be partially reformulated. Instead of a generalized Gaussian with all gradient and Hessian parameters in the exponent and thus coordinate-dependent decay behavior, a much simpler *spherical Gaussian* times a polynomial prefactor is used:

$$C(\mathbf{q})^2 = \mathcal{A} \left[1 + \mathbf{B} \cdot \Delta\mathbf{q} + \frac{1}{2}\Delta\mathbf{q} \cdot (\mathbf{C} + \alpha\mathbf{I}) \cdot \Delta\mathbf{q} \right] \exp\left[-\frac{1}{2}|\Delta\mathbf{q}|^2 \right], \qquad (2.151)$$

where $\mathbf{I}$ is the unit matrix. The $\mathcal{A}$ and $\mathbf{B}$ parameters are the same as for Chang-Miller, but $\mathbf{C}$ is slightly altered:

$$\mathbf{C} = \frac{1}{\mathcal{A}} \left(\frac{\partial F_1(\mathbf{q})}{\partial \mathbf{q}} \cdot \frac{\partial F_2(\mathbf{q})}{\partial \mathbf{q}}^T + \frac{\partial F_2(\mathbf{q})}{\partial \mathbf{q}} \cdot \frac{\partial F_1(\mathbf{q})}{\partial \mathbf{q}}^T \right) + \frac{1}{F_1 - V} \frac{\partial^2 F_1(\mathbf{q})}{\partial \mathbf{q}^2} + \frac{1}{F_2 - V} \frac{\partial^2 F_2(\mathbf{q})}{\partial \mathbf{q}^2}. \qquad (2.152)$$

Eq. 2.151 can be seen as a Taylor expansion with Gaussian-damping applied, i.e., for larger distances the coupling decays to zero (if $\alpha > 0$). Another way of seeing it is to factorize the

---

41 A similar approach is the *multiconfigurational Shepard interpolation* (MCSI) method by TRUHLAR et al. [118, 119], which itself is closely related to the Shepard interpolation methods for PES construction discussed in section 2.2.1. Here, several quadratic Taylor expansions are located in the transition region of the PES of interest. The relevant coupling is constructed applying a Shepard interpolation between those reference points such that a smooth coupling surface is constructed. In spite of its similarity to DG-EVB, TRUHLAR claimed that he has invented a new method superior to EVB, which lead to a public argument with WARSHEL [120].

(a) Chang Miller second order

(b) Chang Miller fourth order

(c) DG-EVB with three points
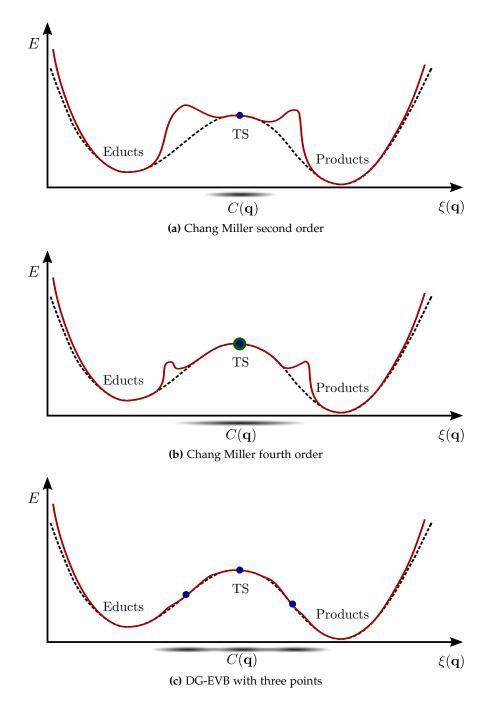
Figure 2.13: Comparison between the Chang-Miller and the DG-EVB coupling terms. In most cases the standard Chang-Miller approach performs well in the TS vicinity but tends to diverge between TS and educt/product asymptotes (a). If up to fourth derivatives of the reference are included into the Chang-Miller approach, the area of reliable coupling is expanded, but might still be too small (b). In the case of DG-EVB, two additional reference points can be located in the problematic regions, resulting in reliable behavior in spite of using only up to second derivatives of the reference (c).

polynomial prefactor. Then, we get three Gaussians, with prefactors $\mathcal{A}$ (constant), $\mathcal{A}\mathbf{B} \cdot \Delta\mathbf{q}$ (linear) and $\mathcal{A}\frac{1}{2}\Delta\mathbf{q} \cdot (\mathbf{C} + \alpha\mathbf{I}) \cdot \Delta\mathbf{q}$ (quadratic). This can be compared to Gaussian-type basis functions as used in quantum chemistry. Those are usually expressed in cartesian coordinates:

$$G_{i,j,k}(\mathbf{x}, \alpha, \mathbf{a}) = x_{\mathbf{a}}^i y_{\mathbf{a}}^j z_{\mathbf{a}}^k e^{-\alpha r_{\mathbf{a}}^2}, \tag{2.153}$$

where $\mathbf{x}$ is the actual position in cartesian space, α the exponential prefactor, $\mathbf{a}$ the position and $L = i + j + k$ the angular momentum of the basis function. As it is well known from quantum chemistry, functions with $L = 0$ are s-functions, those with $L = 1$ are p-functions etc. .

In quantum chemistry, the MOs are expressed as LCAO, which themselves are simply the Gaussian basis functions or fixed linear combinations of them.

For this *distributed Gaussian* (DG)-EVB, the same idea can be utilized. Instead of MOs we want to express the coupling term $C(\mathbf{q})$ as linear combination of the basis functions. The MOs are located in the three dimensional cartesian space, but $C(\mathbf{q})$ depends on all N chosen internal coordinates[42]. Therefore, the number of basis functions for a given angular momentum value L is different, it depends on the used set of internal coordinates. In quantum chemistry, there are one s-function, three p-functions and five/six d-functions[43], for DG-EVB, there are one s-function, N p-functions and $\frac{N(N-1)}{2}$ d-functions per reference point. The s-functions in DG-EVB are defined as:

$$g(\mathbf{q}, \mathbf{q}_K, 0, 0, \alpha_K) = \left[1 + \frac{1}{2}\alpha_K|\Delta\mathbf{q}_K|^2\right] \exp\left[\frac{1}{2}\alpha_K|\Delta\mathbf{q}_K|^2\right], \tag{2.154}$$

where $\mathbf{q}$ is the actual point in internal coordinate space, $\mathbf{q}_K$ the position of the basis function, $\Delta\mathbf{q}_K = \mathbf{q} - \mathbf{q}_K$ and α_K the exponential prefactor of the function. Instead of simply using 1 as global prefactor, the squared distance is taken in order to improve the behavior of the coefficient matrix (see below).

p-functions are defined as:

$$g(\mathbf{q}, \mathbf{q}_K, i, 0, \alpha_K) = (\Delta\mathbf{q}_K)_i \exp\left[\frac{1}{2}\alpha_K|\Delta\mathbf{q}_K|^2\right], \tag{2.155}$$

with i being the internal coordinate whose angular momentum is 1. In the case of d-functions, the unit matrix from eq. 2.151 is applied:

$$g(\mathbf{q}, \mathbf{q}_K, i, j, \alpha_K) = \left(1 - \frac{1}{2}\delta_{ij}\right)(\Delta\mathbf{q}_K)_i(\Delta\mathbf{q}_K)_j \exp\left[\frac{1}{2}\alpha_K|\Delta\mathbf{q}_K|^2\right]. \tag{2.156}$$

A general linear combination consists of s-, p- and d-functions at different points in coordinate space, the DG-coupling term can be expressed as:

$$C(\mathbf{q})^2 = \sum_K^M \sum_{i \geq j \geq 0}^N b_{ijK} g(\mathbf{q}, \mathbf{q}_K, i, j, \alpha_K), \tag{2.157}$$

with M being the number of DG-EVB points. By comparing eq. 11.109 with eq. 2.151, one can see that the parameters $\mathcal{A}$, $\mathbf{B}$ and $\mathbf{C}$ were exchanged with the b_{ijk}-coefficients that are so far unknown.

---

42 In principle, DG-EVB could also be implemented with usage of cartesian coordinates. However, since the molecular system will move and rotate during MD simulations, the coupling needs to be independent of overall translations and rotations, which is achieved with internal coordinates. The actual choice of internals for DG-EVB is far from trivial (see chapter 4 and section 11.6.2). Detailed descriptions of the internal coordinates used within the EVB-QMDFF program packages are presented in section 11.3.2.

43 According to eq. 2.153, s-functions are uniquely defined by $i = j = k = 0$, for p-functions one of the prefactors is 1, with all others zero (x, y, z), for d-functions there are 9 possible permutations. Imposing symmetry, 6 of them remain $(x^2, y^2, z^2, xy, xz, yz)$. These are used for some basis sets. Others use linear combinations $(x^2 - y^2$ instead of $x^2, y^2)$, reducing the total number of d-functions to 5 [12]

If we would simply combine several Gaussians based on eq. 2.151, wrong results would be obtained. The reason is that Gaussians at different locations in space are not independent from each other, at least if they show significant overlap. Then, the coupling at $\mathbf{q}_1$ is not only determined by Gaussian 1, but also of all other $M-1$ Gaussians. Therefore, the b_{ijK}-expansion coefficients must be determined such that the sum of all Gaussians (the one located at the point and the tails of all others) exactly reproduces the coupling values, gradients and Hessians at all M reference points.

Mathematically, this can be done by solving a system of linear equations:

$$\mathbf{Db} = \mathbf{f}, \tag{2.158}$$

where $\mathbf{b}$ is the vector of the b_{ijK} expansion coefficients, $\mathbf{f}$ is the vector of coupling values, gradients and Hessians at all reference points and $\mathbf{D}$ is a matrix of Gaussian function values, gradients and Hessians, based on eqs. 2.154-2.156 and their derivatives.

To go into some detail, the $\mathbf{f}$-vector looks like [121]:

$$\mathbf{f} = \begin{pmatrix} C^2(\mathbf{q}_1) \\ \vdots \\ C^2(\mathbf{q}_M) \\ \partial C^2(\mathbf{q}) / \partial \mathbf{q}|_{\mathbf{q}=\mathbf{q}_1} \\ \vdots \\ \partial C^2(\mathbf{q}) / \partial \mathbf{q}|_{\mathbf{q}=\mathbf{q}_M} \\ \partial^2 C^2(\mathbf{q}) / \partial^2 \mathbf{q}|_{\mathbf{q}=\mathbf{q}_1} \\ \vdots \\ \partial^2 C^2(\mathbf{q}) / \partial^2 \mathbf{q}|_{\mathbf{q}=\mathbf{q}_M} \end{pmatrix}. \tag{2.159}$$

First, the coupling values at all M reference points are listed, then, the coupling gradient vectors are listed (M times N derivative values) and finally the second derivatives are listed as M one-dimensional arrays, consisting of $\frac{N(N-1)}{2}$ elements. In total, the $\mathbf{f}$ vector has a dimension of $M\left(1 + N + \frac{N(N-1)}{2}\right)$.

The $\mathbf{D}$-matrix is somewhat more complicated:

$$\mathbf{D} = \begin{pmatrix} g(\mathbf{q}_1,\mathbf{q}_1,i,j,\alpha_1) & \cdots & g(\mathbf{q}_1,\mathbf{q}_M,i,j,\alpha_1) \\ \vdots & \ddots & \vdots \\ g(\mathbf{q}_M,\mathbf{q}_1,i,j,\alpha_M) & \cdots & g(\mathbf{q}_M,\mathbf{q}_M,i,j,\alpha_M) \\ \partial g(\mathbf{q}_1,\mathbf{q}_1,i,j,\alpha_1)/\partial \mathbf{q}|_{\mathbf{q}=\mathbf{q}_1} & \cdots & \partial g(\mathbf{q}_1,\mathbf{q}_M,i,j,\alpha_1)/\partial \mathbf{q}|_{\mathbf{q}=\mathbf{q}_1} \\ \vdots & \ddots & \vdots \\ \partial g(\mathbf{q}_M,\mathbf{q}_1,i,j,\alpha_M)/\partial \mathbf{q}|_{\mathbf{q}=\mathbf{q}_M} & \cdots & \partial g(\mathbf{q}_M,\mathbf{q}_M,i,j,\alpha_M)/\partial \mathbf{q}|_{\mathbf{q}=\mathbf{q}_M} \\ \partial^2 g(\mathbf{q}_1,\mathbf{q}_1,i,j,\alpha_1)/\partial^2 \mathbf{q}|_{\mathbf{q}=\mathbf{q}_1} & \cdots & \partial^2 g(\mathbf{q}_1,\mathbf{q}_M,i,j,\alpha_1)/\partial^2 \mathbf{q}|_{\mathbf{q}=\mathbf{q}_1} \\ \vdots & \ddots & \vdots \\ \partial^2 g(\mathbf{q}_M,\mathbf{q}_1,i,j,\alpha_M)/\partial^2 \mathbf{q}|_{\mathbf{q}=\mathbf{q}_M} & \cdots & \partial^2 g(\mathbf{q}_M,\mathbf{q}_M,i,j,\alpha_M)/\partial^2 \mathbf{q}|_{\mathbf{q}=\mathbf{q}_M} \end{pmatrix}. \tag{2.160}$$

Here, the values as well as first and second derivatives of all basis functions are listed. Each *column* contains the data of one single basis function at all M reference points: its values, first and second derivatives, similar to eq. 2.159. In the general case, there are, as explained above, one s, N p and $\frac{N(N-1)}{2}$ d basis functions located at each reference point. Each of these functions is located in one column, such that each *row* consists of the values of all basis functions for the current property, e.g., a coupling value or a specific coupling Hessian element at a distinct reference point. Hence, the dimension of the $\mathbf{D}$ coefficient matrix is $M\left(1 + N + \frac{N(N-1)}{2}\right) \times M\left(1 + N + \frac{N(N-1)}{2}\right)$.
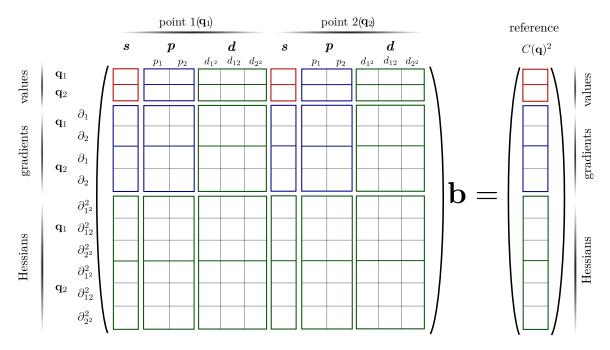
Figure 2.14: Illustration of the system of linear equations in eq. 2.158 for two reference points and two internal coordinate in usage. The axis above the matrix shows the list of Gaussian basis functions. On each reference point, one s-, two p- and three d-functions are located, such that there are 12 distributed Gaussians in total. The axis on the left shows the values of all basis functions as well as their gradients and Hessians on the reference points. The different colors indicate the possibility of choosing the available reference data. If only coupling strengths shall be optimized, the red block is sufficient, for strengths and gradients, the blue elements need to be added and for strengths, gradients and Hessians, the green elements are also added. In order to reproduce one of the vector entries in the right, a row of the matrix times the coefficient vector **b** needs to be evaluated as a linear combination of the respective basis functions.

The whole structures of **D** and **f** are illustrated further in fig. 2.14 for the simplest possible model case of two reference points and two internal coordinates. As it can be seen there, DG-EVB is somewhat flexible with respect to the choice of basis functions. We might only use s-functions, resulting in 1 Gaussian per reference point that is able to reproduce the energy in this point (also termed as *mode1*) or s- and p-functions, resulting in $N+1$ functions per reference point that are able to reproduce energy and gradient (*mode2*) as well as the full machinery (*mode3*).

Mathematical details like the derivatives of coupling reference and distributed Gaussian functions can be found in section 11.4 of the appendix.

It should be noted that it is *not* possible to use different qualities of basis functions at different points, e.g., only s- functions at $\mathbf{q}_1$ and s-, p- and d- functions at $\mathbf{q}_2$ due to the symmetric structure of eq. 2.158.

By solving eq. 2.158 we get the full **g**-vector containing the g_{ijK}-parameters needed for eq. 11.109. However, by looking at this equation it is obvious that the exponential prefactors α_K are still unknown. As indicated by their label, all basis functions located on one reference point share the same exponential prefactor, resulting in M α_K-values in total.

In the original DG-EVB-publications [117, 121, 122] no systematic way for determination of these parameters was given, instead they were chosen more or less by rule of thumb, such that smooth EVB-surfaces were obtained.

In line with this thesis, the α_i's were optimized systematically for the first time using *multi-start local search* (MSLS) methods. Using energies along the reaction path as reference and taking the error sum of EVB- and reference energies as objective function, the optimizations are straightforward.

More details concerning this procedure and the general DG-EVB-methodology can be found in chapter 4.

The DG-EVB-method is one of the central topics in this thesis. In chapters 4 and 5, further experiments done with DG-EVB are presented.

2.4.6   Reaction Path (RP)-EVB with Corrections

The DG-EVB method as exposed in the last section in connection with QMDFF as diabatic surfaces has been shown to be quite a reliable foundation for partially automated generations of PESs suitable for chemical rate constant calculations [17].

It was indeed the hope that DG-EVB-QMDFF could be a suitable method for general automated k(T) calculations as it is the overall aim of this thesis. However, unexpected problems arose shortly after it became established. Details of the problems are shown in upcoming chapters but in short it seems that the connection of several Taylor expansions along the reaction path is still not sufficient in many cases where the convergence radii of the Taylor series are too small and/or the diabatic surfaces (i.e., the QMDFFs) show bad behavior, largely reducing the viability of eq. 2.143.

In line with the efforts to solve those problems, a new EVB coupling term was developed in the scope of this thesis [18]. Theoretical background as well as benchmarking results are presented in chapter 5 with great detail. Therefore, only a short-as-possible overview of the method is given here.

The main idea is to make the *reaction path* itself, a one-dimensional curve in the N-dimensional space of internal coordinates, the central part for the description of the coupling. Since we are interested in the calculation of k(T)-values and other properties related to them, an as-good-as possible description of this path and its accessible vicinity is crucial for the method of choice.

In DG-EVB, a good description of the reaction path can be achieved by optimizing the α_K-values in order to minimize the error sum with respect to a reference path. In combination with the distributed Gaussians themselves, quite a good description of the relevant regions is possible in many cases. But a good description of regions between two DG-EVB points and only slightly away from the optimized path cannot be guaranteed. Therefore, the method fails in many seemingly simple cases: The system's trajectory could, for instance, be trapped in holes or chasms existent in the PES near the reaction path.

In *reaction path* (RP)-EVB this path becomes a central part of the coupling formulation. Essentially, a given reference reaction path is modeled via *cubic spline interpolation* and then a Taylor expansion is built around it:

$$C(\mathbf{q})^2 = C(s)^2 + \Delta\mathbf{q}\frac{\partial C(s)^2}{\partial\mathbf{q}} + \frac{1}{2}\Delta\mathbf{q}\frac{\partial^2 C(s)^2}{\partial\mathbf{q}^2}\Delta\mathbf{q}. \tag{2.161}$$

There, $C(s)$ is the coupling strength along the reaction path, dependent on the parameter s of the cubic spline curve. In practice, internal coordinates of the path structures as well as coupling strengths calculated according to eq. 11.109 are interpolated as a one-dimensional parametric curve in $N+1$-dimensional space. The gradients $\frac{\partial C(s)^2}{\partial\mathbf{q}}$ and Hessians $\frac{\partial^2 C(s)^2}{\partial\mathbf{q}^2}$ of the coupling are also interpolated between a smaller number of energy-, gradient- and Hessian-reference points on the path, based on the s-parameter. This is illustrated in fig. 2.15.

During a MD calculation, the value of the s-parameter has to be calculated first, this is done by numerical minimization of the distance between the current structure and the reaction path curve, such that the current structure is projected on the reaction path. With the known value of s, the nearest structure on the reaction path curve as well as its coupling value $C(s)$ can be calculated. With this information, the projection vector $\Delta\mathbf{q}$ from the current structure to the path can be determined and finally $C(\mathbf{q})$ is calculated with eq. 2.161.
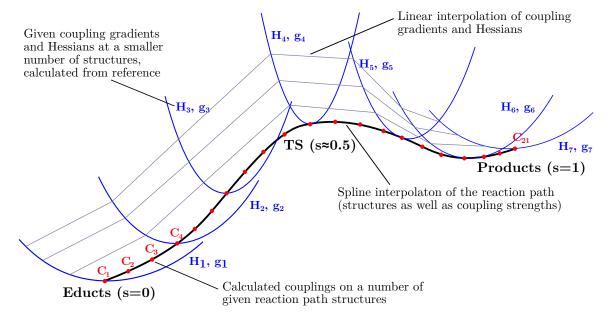
Figure 2.15: Schematic presentation of the RP-EVB method. The structures and coupling strengths at a number of points (e.g., 21) along the optimized reaction path are interpolated via cubic spline interpolation of a parametric curve, resulting in a description dependent on the curve parameter *s*. At a usually much smaller number of structures (e.g., 7), gradients and Hessians are calculated with the the reference method and coupling gradients and Hessians are calculated from them. These are interpolated linearly along the path. In reality, the coupling surface is also smooth offside the reaction path due to the shift with the path coupling itself.

Unfortunately, this generic ansatz has some deficiencies in practice. The Taylor expansion of the coupling tends to diverge in some regions, where the reference surface or the diabatic surfaces show significant nonlocal behavior, similar to the Chang-Miller coupling term.

The solution is inspired by DG-EVB (eq. 11.109). The divergencies of the Taylor series can be at least partially removed if the whole coupling is *damped* with a Gaussian:

$$C(\mathbf{q})^2 = \left[C(\mathbf{q}(s)^2) + (\mathbf{q} - \mathbf{q}(s)) \frac{\partial C(s)^2}{\partial \mathbf{q}} + \frac{1}{2}(\mathbf{q} - \mathbf{q}(s)) \frac{\partial^2 C(s)^2}{\partial \mathbf{q}^2}(\mathbf{q} - \mathbf{q}(s)) \right] . \\ \exp\left[-\alpha(\mathbf{q} - \mathbf{q}(s))^2 \right] \qquad (2.162)$$

Now an additional parameter α is introduced. This parameter could be *s*-dependent, such that the damping varies along the path, however its influence is much smaller than of the α_K-parameters in DG-EVB because only regions far distant from the minimum energy path are influenced and not the path itself (what is the case between reference points in DG-EVB).

With this correction the range of applications for the new method is enlarged significantly. Though, there are still cases where the RP-EVB surface imposes divergencies or holes especially in the transition region near the TS. This is presumably due to problematic behavior of the QMDFF diabatic surfaces in this region, where they tend to have huge gradients, diminishing the size of the area where the Taylor approximations are still valid.

The fix to this problem is to *replace* the whole EVB energy term in the problematic areas around the TS with a *direct interpolation* of the reference, which is done equivalent to the coupling in eq. 2.161:

$$V(\mathbf{q}) = V(\mathbf{q}(s)) + (\mathbf{q} - \mathbf{q}(s)) \frac{\partial V(s)}{\partial \mathbf{q}} + \frac{1}{2}(\mathbf{q} - \mathbf{q}(s)) \frac{\partial^2 V(s)}{\partial \mathbf{q}^2}(\mathbf{q} - \mathbf{q}(s)). \qquad (2.163)$$

Now, *two quantities* are interpolated together with the internal coordinates along the reaction path: the coupling $C(\mathbf{q})$ and the energies of the reference $V(\mathbf{q})$. The idea is now to represent the area around the TS with the direct interpolation of eq. 2.163, switch to the usual damped RP-EVB in the intermediate areas between TS region and minima and finally converge to the QMDFF surfaces as it can be managed by EVB.

We might think that an immediate transition between direct interpolation in the TS region and QMDFFs at the minima should suffice as well. However, the coordinate space of the reactants/products regions is huge, including whole landscapes of torsional minima. In contrast, near the TS usually only a narrow multidimensional tube around the reaction path is accessible. The transition between both worlds is problematic if they are interpolated directly. Adding the intermediary RP-EVB coupling term ensures a valid and smooth transition and thus a reliable PES-description.

The resulting *transition region corrected (TRC)-RP-EVB-QMDFF* (TREQ) coupling term can be expressed in a single formula:

$$
V(\mathbf{q}(s)) = \begin{cases}
F_1(\mathbf{q}) & s = 0 \\
\Sigma F(\mathbf{q}) - \sqrt{\Delta F(\mathbf{q}) + \frac{1}{2}(\sin(s\eta - \frac{\pi}{2} + 1)C(\mathbf{q})^2} & 0 < s \leqslant s_1 \\
\Sigma F(\mathbf{q}) - \sqrt{\Delta F(\mathbf{q}) + C(\mathbf{q})^2} & s_1 < s \leqslant s_2 \\
\zeta_1(s)\left[V(\mathbf{q})_{\text{intp}}\right] + [1 - \zeta_1(s)]\left[\Sigma F(\mathbf{q}) - \sqrt{\Delta F(\mathbf{q}) + C(\mathbf{q})^2}\right] & s_2 < s \leqslant s_3 \\
V(\mathbf{q})_{\text{intp}} & s_3 < s \leqslant s_4 \ , \\
[1 - \zeta_2(s)]\left[V(\mathbf{q})_{\text{intp}}\right] + \zeta_2(s)\left[\Sigma F(\mathbf{q}) - \sqrt{\Delta F(\mathbf{q}) + C(\mathbf{q})^2}\right] & s_4 < s \leqslant s_5 \\
\Sigma F(\mathbf{q}) - \sqrt{\Delta F(\mathbf{q}) + C(\mathbf{q})^2} & s_5 < s \leqslant s_6 \\
\Sigma F(\mathbf{q}) - \sqrt{\Delta F(\mathbf{q}) + \frac{1}{2}(\sin(s\eta - (\eta + \frac{\pi}{2}) + 1)C(\mathbf{q})^2} & s_6 < s < 1 \\
F_2(\mathbf{q}) & s = 1
\end{cases} \quad (2.164)
$$

with $\Sigma F(\mathbf{q}) = \frac{1}{2}(F_1(\mathbf{q}) + F_2(\mathbf{q}))$, $\Delta F(\mathbf{q}) = \left[\frac{1}{2}(F_1(\mathbf{q}) - F_2(\mathbf{q}))\right]^2$, $\zeta_1(s) = \frac{s-s_2}{s_3-s_2}$, $\zeta_2(s) = \frac{s-s_4}{s_5-s_4}$ and s_1 to s_6 borders of different PES regions along the reference reaction path. This is illustrated in fig. 2.16, much more details are located in chapter 5.

2.4.7 Summary or Jacob's Ladder of EVB

As we had seen in the previous sections, a variety of different coupling methods has been emerged since the dawn of EVB in 1980. Besides the ones explicitly mentioned here there are several others, varying in publicity and success, presented in the past.

In order to clarify the picture of confusing diversity surrounding the practical applications of EVB, I tried to sort the available methods in different sections. These are ordered similar to the famous "Jacobs ladder" notation in density functional theory, where subsequent improvements and/or sophistications of the exchange correlation descriptions are seen as subsequent rugs on the path to the "heaven of chemical accuracy" [123].

There is of course no ubiquitous rating for the different EVB-couplings and some of the respective authors might argue that their method can be considered as superior to others in practice even if its functional description is rather simple.

However, if two criteria, *flexibility* in the actual description for a certain system and *scalability* in the sense that the coupling term can be further improved by adding more data and/or calculation effort, are used, the ranking can be made quite convincing, at least in my eyes.
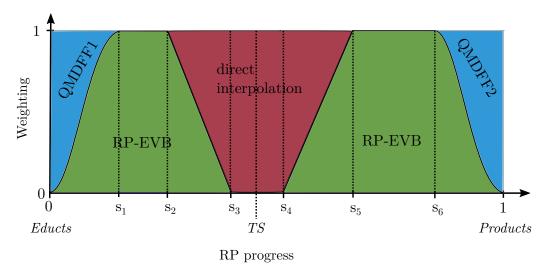
Figure 2.16: Illustration of the different regions along the reaction path as represented by eq. 2.164. Around the TS, the direct interpolation is applied, followed by the RP-EVB coupling in the intermediate regions and the QMDFFs at the minima. The shapes of the transitions indicate the used switching functions. Figure taken from [17] and slightly changed.

The simplest and most primitive method is of course the *constant* coupling. Only one single number can be varied and no quantitative description of the system can be expected in most cases. The next is the *energy gap* or *dE* coupling (eqs. 2.138, 2.139). Here, the functional form can be varied quite broadly, see table 3.1. However, all used functions still depend on the *same coordinate*, the energy difference between both diabatic surfaces. If these behave somehow asymmetric or pathological, the coupling method will give bad results independent of the used function (at least if no ingenious mathematical formulation can be found).

This absent flexibility with respect to the used set of coordinates is realized for the *geometry-dependent* coupling. Here, an arbitrary set of internal coordinates, from single reactive bond lengths up to quite subtle sets of bonds, angles and others, can be taken and different functions depending on this set that describe the coupling can be used.

With geometry-dependent coupling, EVB-surfaces of good quality can be obtained in many cases, which makes it the most popular coupling variant in literature. However, for some cases it is very difficult or even impossible to get a chemically accurate description of certain regions, e.g., for very sharp barriers [124]. Further, neither the set of used coordinates nor the used coupling functions are clear from the beginning, which leads to quite elaborate work if a completely new reaction shall be handled.

The *Taylor expansion* coupling method provides a different perspective. Its original and still most prominent representative is the Chang-Miller coupling term as described in section 2.4.4. Here, an exact (up to second order) reproduction of the reference surface is achieved at the TS, with decreasing quality when moving from it to the minima. In principle (but not in practice), this coupling term can be improved arbitrarily, by adding more and more Taylor expansion terms. However, the scaling exponent is incremented by one for each added term.

Finally, DG-EVB as well as the newly invented TRE(Q) methods are able to reproduce the regions of the surface relevant for description of a reaction with arbitrary high quality (up to second order), if a huge number of expansion points is used (and still quite well for a rather small number). Therefore, these two terms (together with TRUHLAR's MCSI) constitute in my opinion the fifth and highest ladder. The given argument is summarized in table 2.1.

Table 2.1: List of different EVB coupling term approaches ("Jacobs ladder of EVB"), ordered based on the criteria of flexibility and scalability for actual applications.

Order	method	examples
1	constant	-
2	energy-gap	WARSHEL (1982) [107], E_{GAP}-EVB [108, 109]
3	geometry-dependent	MS-EVB [102, 110, 111], VILLEUMIER-BORGIS-EVB [112, 113], TROBRO-ÅQVIST-Peptide-EVB [125, 126]
4	One Taylor expansion	Chang-Miller-EVB [114]
5	Combined expansions	MCSI (TRUHLAR) [118, 119], Distributed Gaussian [107, 108], TREQ [17]

Program Development

In line with this thesis, a program package named EVB-QMDFF was developed to be used for the calculations presented in the following sections.

Before going to concrete applications, the general structure of this program package shall be outlined. A detailed discussion of all contained subroutines is impractical, since it would probably need several hundred pages, while no real insight for the average reader can be gained.

Therefore a rather coarse description will be given, first outlining the history, general structure and idea of the whole package, then going into some detail concerning the different programs that are designed to perform a number of frequently needed tasks with EVB-QMDFF.

3.1 History

Before turning to a comprehensive description of the actual implementation and its handling in practice, a short history of EVB-QMDFF programming shall be givenin order to clarify some peculiarities that might irritate the reader at some point.

I have subdivided the program development into four stages. Of course, the changes were done successively during my work, some improvements were made as deficiencies became apparent at certain applications or as colleagues or my supervisor had ideas to make things easier.

Nevertheless, four milestones can be clearly identified, without them the applications presented within this thesis would have been simply impossible to do. An overview of this four development milestones is given in fig. 3.1.

3.1.1 Version 1: The Origins

EVB-QMDFF was invented by HARTKE [16], who also wrote its first implementation. He obtained the QMDFF program by GRIMME which itself was able to calculate energies and gradients as well as performing geometry optimizations and MD with QMDFF. HARTKE wrote a new program which called the internal energy and gradient routines of QMDFF (Up to three instances of them, since 2x2- and 3x3-EVB could be used) and coupled them with EVB. Two simple coupling terms were available: constant coupling (eq. 2.137) as well as the Gaussian energy-gap coupling (eq. 2.139).

The parameters of the coupling terms were given by the user in the input file. This program could calculate energies and gradients for a trajectory of structures, e.g., in order to perform surface scans. Before doing the EVB-calculation, both QMDFFs needed to be set up with the QMDFF optimization program, their relative energies were calculated from the QM reference energies of the reactants/products minima, corrected by the QMDFF energy deviation, introduced by noncovalent interactions (section 2.3.4).

With this first version, the general concept of coupling two QMDFFs with simple EVB terms was introduced, however, it was unable to do more sophisticated tasks like running MD, doing k(T) calculations, optimize more complicated EVB terms and so forth.

3.1.2   Version 2: EVB-QMDFF-Tinker

During my Master's thesis [124], the next program version was developed. Originally, the aim was to check whether EVB-QMDFF is able to represent the PES also offside the reaction path used for parametrization of EVB in the transition region. There is no guarantee at all that regions slightly offside this path are reproduced even qualitatively if the simple constant or energy-gap EVB methods are used. The first step of investigating this was to perform two-dimensional scans for several combinations of internal coordinates. This was done with the first version of EVB-QMDFF ([16], supporting information (section 11.6.1)).

For three-atomic systems, a three-dimensional coordinate scan would be needed in order to fully discover the configuration space and hence get a complete picture of the EVB-QMDFF quality. Even in the case of still quite small four- or five-atomic systems, this approach of full-dimensional scanning becomes infeasible due to its exponential scaling. Furthermore, a large fraction of the scanned coordinate-space is needless as only regions of low energy are relevant in practice. An alternative is to utilize the ergodic theorem and perform coordinate samplings. From those, free-energy profiles can be obtained (section 2.1.3) and compared with AIMD samplings (at least where a sufficiently cheap *ab-initio* method is used).

However, in order to simulate biased sampling trajectories, new program code had to be added. Instead of writing it myself, I chose to utilize existent program packages.

This led to the EVB-QMDFF-Tinker program package. The existing EVB-QMDFF program was coupled to the well known Tinker FF-MD program package [127], which is also written in Fortran. The gradient routine in Tinker was replaced by the EVB-QMDFF gradient routine such that a couple of Tinker features, for instance, molecular dynamics, geometry optimization, TS optimization and many others, could be applied for EVB-QMDFF.

Because biased samplings are not included in Tinker, a MD addon particularly designed for those tasks was added: Plumed [128]. It enables a whole range of different collective variables (CV) for application of bias potentials.

Finally, free energy profiles were calculated by combination of several biased samplings. Again, a separate program was used: WHAM by Grossfield [129]. As the name says, it applies the WHAM-equations (eqs. 2.38-2.39) for calculation of free energy surfaces.

In order to investigate the overall quality of EVB-QMDFF, free energy surfaces were calculated with AIMD (by implementing a call to an Orca [130, 131] gradient calculation in the modified Tinker program) as well as with EVB-QMDFF and compared to each other. Since information of the whole thermally accessible surface is accumulated in both cases, a good agreement of the free energy surfaces implies an EVB-QMDFF of high quality.

Besides the ability of calculating free energy surfaces, different energy-gap as well as simple coordinate-dependent EVB-coupling terms were implemented, with automated optimization of their parameters. The quadratic Chang-Miller coupling term (section 2.4.4) was implemented as well for benchmark purposes (no dynamics was possible since this coupling term was constructed based on cartesian coordinates). Further, the relative energy-adjustment of both QMDFFs previous to the EVB-optimization was automated.

(a) EVB-QMDFF Prototype (March 2015)

(b) EVB-QMDFF-Tinker (September 2015)

(c) EVB-QMDFF+RPMDrate (May 2017)

(d) Unified *black-box* (February 2019)
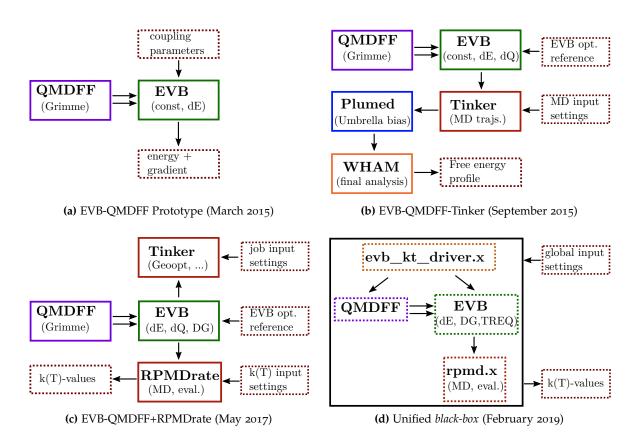
Figure 3.1: The four major program development steps since the invention of EVB-QMDFF. First, manually parametrized EVB was connected to the QMDFF-program by Grimme, being able to calculate energies and gradients (a). After connection with some other programs (Tinker, Plumed, WHAM), it became possible to perform biased MD and to calculate free energy profiles (b). In order to calculate k(T)-values with consideration of QM-effects, RPMDrate was connected to the EVB-QMDFF energy and gradient routine, DG-EVB was added as coupling method (c). Finally, all separate parts were merged into one *black-box* program being able to do all tasks in one step. RPMD k(T) calculations became possible for several reaction types, the TREQ PES representation was implemented (d).

3.1.3   Version 3: EVB-QMDFF+RPMDrate

In the Master's thesis, the ability of EVB-QMDFF to reproduce all relevant areas along a reaction path with at least acceptable quality was verified for two example reactions. The next step was to make the method useful in practice.

Free energy profiles are used to calculate several quantities, for small gas phase systems up to large solvated enzymes or metal clusters. As explained in section 2.1, chemical reaction rate constants are of central importance for the quantification of reactions.

Therefore, it was the objective to implement a method for the calculation of k(T)-values based on trajectory samplings.

Fortunately, we discovered the RPMDrate program [13] which is designed to calculate bimolecular reaction rate constants based on RPMD samplings (eq. 2.103). Its concept is suited almost perfectly to EVB-QMDFF: A potential function expressed as Fortran subroutine needs to be supplied by the user such that RPMDrate is able to request energy and gradient for each dynamics step.

Instead of the rather complicated combination of EVB-QMDFF, Tinker, Plumed and WHAM, only EVB-QMDFF and RPMDrate are needed to perform the whole calculation. In addition, quantum effects can be considered with the RPMD method (section 2.1.6).

Shortly after establishing k(T)-calculations, it became clear that the rather simple EVB-coupling methods used so far were mostly unable to provide the degree of accuracy needed to obtain reasonable rate constants. Due to the exponential dependence of the free energy barrier in the case of k(T)-calculations, small errors in the EVB-QMDFF representation are magnified into large k(T)-errors. Therefore, an EVB-coupling method located much higher on the Jacobs ladder of EVB (table 2.1) was needed. DG-EVB was the method of choice. Its quality can be raised arbitrarily high if enough reference points with gradient and Hessian reference information are taken into account. The method was implemented in the EVB-QMDFF code, further, an automated optimization of the α_i-parameters (eq. 11.109) was introduced in order to make the whole process more convenient.

With this program version, the results presented in the second EVB-QMDFF paper [17] (chapter 4) were produced.

3.1.4   Version 4: Unification

The initial point for the next program development step was the cooperation with Covestro initiated in 2017 (chapter 8). During this cooperation the kinetics of polyurethane systems should be studied. Polyurethanes are formed by a polyaddition reaction of isocyanates and alcohols.

The program structure so far, i.e., k(T)-calculations by RPMDrate based on the EVB-QMDFF PES, was unable to deliver such rate constants: RPMDrate is designed to calculate only rates of bimolecular reactions with *two* reactants and *two* products, whereas in a polyadditon *two* reactants are merged into *one* product. Another disadvantage of RPMDrate was that it is based on Python code, which lead to problems with the needed Python-libraries on the computer clusters used for high-throughput calculations of k(T)-values.

In order to solve these problems, I decided to reimplement the RPMD code similar to RPMDrate but with the capability of handling a broader range of reaction types and to lower the dependency on external libraries. Therefore, the RPMD code was rewritten in Fortran90. In parallel, the remaining parts of the Tinker code were eliminated (apart from the input section). Finally, also the QMDFF code by GRIMME was reimplemented into Fortran90, mainly to improve the convenience of generating new QMDFFs.

With these changes, the program was able to calculate rate constants for the polyaddition processes of interest. However, the quality of those rate constants (especially their degree of convergence, i.e., the difference between k(T) values of several independent runs) was rather bad. The reason was the DG-EVB coupling used to represent the PESs. At this time, I got the idea for

constructing a new coupling term named TREQ (section 2.4.6) which was able to improve the convergence and reliability of the k(T) calculations significantly.

Since TREQ needs no parameter optimization (apart from the α-damping factor of the RP-EVB part (eq. 2.162), where a default value works well in many cases), it became clear that a *black-box* calculation of reaction rates was possible with it. All calculations, from the QMDFF- and EVB-parametrizations up to the k(T)-calculations, are done with the same program package, only a master program (or driver) was needed to call the different programs with the correct parameters. The latest significant change of the program code was therefore the addition of such a driver program, named `evb_kt_driver.x`.

Over the years, the initial collection of several independent programs needed for the calculation of free energy profiles therefore merged to one large program package which is able to do all tasks conducted in this thesis. Another advantage is that the user only needs to compile one large bunch of Fortran programs, subroutines and functions which is done by a single `make` command instead of installing several independent program packages from the literature.

3.2   General Statistics

Before going to a detailed description of the interactions between the several executables, subroutines and functions contained into EVB-QMDFF, it might be interesting to see its overall dimension in terms of some numbers (status: September 2019):

- No. of bytes (uncompiled): 6496256

- No. of bytes (compiled): 19992576

- No. of source code files: 331

- Source code lines (including comments): 133262

- No. of programs: 8

- No. of modules: 6

- No. of subroutines: 409

- No. of functions: 34

- No. of subroutine calls: 2337

Approximately 95% of this code is written in Fortran90, with Fortran77 code forming the other 5%. The Fortran77 subroutines are mainly the embedded PES functions for the analytical surfaces taken from the literature (see section 3.3.3).

In total, 148 functions and subroutines originate in the QMDFF program by GRIMME. They were translated from Fortran77 to Fortran90 and slightly changed in some parts concerning the read-in of QM reference data (see below). Another bunch of approx. 50 functions and subroutines is inspired from RPMDrate, concerning trajectory samplings, biasing potentials, as well as free energy and recrossing calculations. Here, the biasing part was altered to a more general form in order to make k(T)-calculations for a larger range of cases possible (more complex bimolecular as well as unimolecular reactions with almost arbitrary mechanisms). Further, WHAM calculations of free energy profiles were implemented in addition to the UI contained in RPMDrate. The parallelization was completely redone with usage of the *message passing interface* (MPI) instead of the original Python approach. The recrossing part was parallelized as well, which was not the case in RPMDrate, therefore further accelerating the rate constant calculations.

The method of reading user input was inspired by Tinker, yet almost no unaltered Tinker code remained in EVB-QMDFF.

All other functions and subroutines were implemented over the years, they are described in sec. 3.3 with some detail.

3.3   Program Descriptions

In the following, the eight different programs contained in the EVB-QMDFF package are inspected more closely. Details concerning the actual executions of calculations (list of all keywords as well as example input files) are presented in section 11.5 of the appendix. If a *black-box* k(T) calculation shall be done, only program `evb_kt_driver.x` (section 3.3.8) must be executed, which itself calls all other programs if needed.

3.3.1   qmdffgen

This program needs to be started first when a new system shall be investigated with EVB-QMDFF. It is able to generate up to three QMDFFs[1] and calculate their correct relative energy shift such that the EVB coupling can be applied in the next step.

Reference data calculated by four different QM-program packages can be used: Gaussian [99], Orca [130, 131], Turbomole [132] and CP2K [133, 134]. For all but Gaussian and CP2K, geometry optimization as well as calculation of all reference data can be done with one single program call, whereas Gaussian needs a separate geometry optimization[2] and CP2K only calculates CM5-charges for separate geometry optimizations. Besides these QM-programs, also EVB-QMDFF calculations can be done as reference. This is mainly for benchmark reasons (chapter 5).

After the QM-calculations are done, their logfiles should be copied into a QMDFF folder, then `qmdff.x` can be started.

After finishing, the QMDFF force field files (`name.qmdff`) as well as logfiles with detailed information about the parametrization processes (`name_qmdff.log`) are written. Further, a `qmdff.key` file is written which serves as initial point for all following calculations. In this file, the energy-shifts of both QMDFFs are noted. These can be calculated as

$$E_{\text{shift}} = E_{\text{ref}} - E_{\text{min,QMDFF}}, \tag{3.1}$$

with E_{ref} the QM reference energy of the structure and $E_{\text{min,QMDFF}}$ its (usually very small) QMDFF energy.

3.3.2   evbopt

For all EVB-methods but TREQ, coupling parameters need to be optimized before, e.g., a dynamic calculation can be done. Currently, four different EVB-methods are implemented for optimization: constant, energy-gap, coordinate-dependent and DG-EVB (table 2.1).

The aim of the parameter optimization is to minimize the *error sum* χ^2 between EVB-QMDFF and *ab-initio* reference energies for a number of structures:

$$\chi^2(\boldsymbol{\alpha}) = \sum_i \frac{(E_{\text{ref}}(\mathbf{x}_i) - E_{\text{EVB}}(\boldsymbol{\alpha}, \mathbf{x}_i))^2}{\sigma} \longmapsto \min, \tag{3.2}$$

---

1 For all applications presented in this thesis two QMDFFs were used, further, DG-EVB and TREQ (currently) only work for two QMDFFs, such that the possibility to parametrize three QMDFFs is of little use in practice.

2 According to the Gaussian manual it should be possible to do all this at a time. But unfortunately the cartesian Hessian itself is not printed to file (only the normal mode vibrations) in the case of combined optimization and frequency calculations.

Table 3.1: List of energy-gap (dE)-coupling terms as implemented in the EVB-QMDFF program. The short terms (inspired by QM basis functions), the number of parameters to be optimized as well as the functional expressions are given.

term	# params	functional expression
1g	2	$C(\Delta E) = \alpha_1 e^{-\alpha_2 \Delta E^2}$
2g	5	$C(\Delta E) = \alpha_1 e^{-\alpha_2 \Delta E^2} + \alpha_3 e^{-\alpha_4 (\Delta E + \alpha_5)^2}$
3g	8	$C(\Delta E) = \alpha_1 e^{-\alpha_2 E^2} + \alpha_3 e^{-\alpha_4 (\Delta E + \alpha_5)^2} + \alpha_6 e^{-\alpha_7 (\Delta E + \alpha_8)^2}$
sp	4	$C(\Delta E) = \alpha_1 e^{-\alpha_2 \Delta E^2} + \alpha_3 \Delta E e^{-\alpha_4 \Delta E^2}$
sd	4	$C(\Delta E) = \alpha_1 e^{-\alpha_2 \Delta E^2} + \alpha_3 \Delta E^2 e^{-\alpha_4 \Delta E^2}$
sp2	6	$C(\Delta E) = \alpha_1 e^{-\alpha_2 \Delta E^2} + \alpha_3 \Delta E e^{-\alpha_4 \Delta E^2} + \alpha_5 \Delta E e^{-\alpha_6 \Delta E^2}$
sd2	6	$C(\Delta E) = \alpha_1 e^{-\alpha_2 \Delta E^2} + \alpha_3 \Delta E^2 e^{-\alpha_4 \Delta E^2} + \alpha_5 \Delta E^2 e^{-\alpha_6 \Delta E^2}$
sp2d	8	$C(\Delta E) = \alpha_1 e^{-\alpha_2 \Delta E^2} + \alpha_3 \Delta E e^{-\alpha_4 \Delta E^2} + \alpha_5 \Delta E e^{-\alpha_6 \Delta E^2} + \alpha_7 \Delta E^2 e^{-\alpha_8 \Delta E^2}$
sp2d3	12	$C(\Delta E) = \alpha_1 e^{-\alpha_2 \Delta E^2} + \alpha_3 \Delta E e^{-\alpha_4 \Delta E^2} + \alpha_5 \Delta E e^{-\alpha_6 \Delta E^2} + \alpha_7 \Delta E^2 e^{-\alpha_8 \Delta E^2} + \alpha_9 \Delta E^2 e^{-\alpha_{10} \Delta E^2} + \alpha_{11} \Delta E^2 e^{-\alpha_{12} \Delta E^2}$

where $\boldsymbol{\alpha}$ is the vector of EVB-parameters and the sum runs over the selected pool of structures $\mathbf{x}_i$. The weighting factor σ is set to 1, which gave better results than e.g., prioritizing regions near the TS. In principle, arbitrary structures in the coordinate space of interest could be chosen to serve as reference. In line with this thesis, however, only structures along the reaction path of the system of interest were chosen as part of the training set, in order to make the whole process more systematic.

In practice the minimization is done with *multi-start local search* (MSLS): Initial values for $\boldsymbol{\alpha}$ are generated randomized from a predefined range, followed by local Levenberg-Marquardt [135, 136] optimizations. If a local optimization has reached a lower χ^2-value than before, the corresponding $\boldsymbol{\alpha}$-vector is stored as the actual optimum, until a new even better value is found. The optimum value after the maximum number of steps is taken as final result. We could of course also use much more powerful global optimization methods like GAs for the $\boldsymbol{\alpha}$-optimization problem. For the systems calculated so far the MSLS approach gave fairly good results and usually converged to similar values for separate optimization runs such that the algorithm was seen to be sufficient. If, however, larger systems with more internal coordinates and/or more DG-EVB reference points will be treated in the future, the implementation of, e.g., GA-based parameter optimization might become necessary.

For the energy-gap coupling, also called dE-coupling, a number of coupling terms as shown in table 3.1 were implemented into EVB-QMDFF.

The coordinate-dependent coupling (dQ) has similar functional expressions as dE, where here also a suitable set of internal coordinates for the measuring of the distance is needed (table 3.3). Usually, the TS is chosen as reference point, to which the distances are measured. Only three coupling functions were implemented for dQ since DG-EVB can be viewed as its superior generalization.

Table 3.3: List of the coordinate dependent (dQ)-coupling terms as implemented in the EVB-QMDFF program. The functions as well as the parameters are equivalent to the dE-coupling. The couplings are calculated with $\Delta Q^2 = \gamma \left(\mathbf{q} - \mathbf{q}_{\text{TS}}\right)^2$, where γ is a scaling factor (default value: 50).

term	# params	functional expression
1g	2	$C(\Delta Q) = \alpha_1 e^{-\alpha_2 \Delta Q^2}$
3g	8	$C(\Delta Q) = \alpha_1 e^{-\alpha_2 \Delta Q^2} + \alpha_3 e^{-\alpha_4(\Delta Q + \alpha_5)^2} + \alpha_6 e^{-\alpha_7(\Delta Q + \alpha_8)^2}$
sd2	6	$C(\Delta Q) = \alpha_1 e^{-\alpha_2 \Delta Q^2} + \alpha_3 \Delta Q^2 e^{-\alpha_4 \Delta Q^2} + \alpha_5 \Delta Q^2 e^{-\alpha_6 \Delta Q^2}$

For DG-EVB, the exponential damping factors α_i are optimized with evbopt.x. This case is special since the b_{ijk}-expansion coefficients are determined by solving eq. 2.158. The **D**-matrix appearing in the expression is itself dependent of the α_i-values. Thus we have a system of two coupled optimization procedures. In each LM-step, the **D**-matrix as well as the b_{ijk}-values need to be recalculated such that the new error sum can be evaluated with the updated coupling term[3]. This procedure is shown in fig. 3.2. For small to medium-sized systems, a quite well-converged value of the error sum and thus of the optimized α_i seems to be reached within 100 to 500 MSLS-steps. A special case needs to be considered: Since the optimized α_i-values are exponential prefactors of Gaussians (eq. 11.109), the coupling expression would diverge if one α_i becomes negative. Therefore, a manual penalty to the error sum is added if one of the α_i becomes negative in a LM-optimization run.

3.3.3 egrad

egrad.x formally resembles the function of the initial EVB-QMDFF-program by Hartke: It calculates energies and gradients for a trajectory file with an arbitrary number of structures in it. It can be used for, e.g., multidimensional surface scans or other time-independent investigations of the PES-quality.

Besides QMDFF and the different EVB coupling-terms, some other PES-functions are included into the EVB-QMDFF program package for benchmark and test reasons:

- A simple traditional nonreactive force field implementation: It is based on a slim version of the Tinker FF energy and gradient routine [127], with exclusion of exotic cross or coupling terms. Besides bond, angle, torsion and dispersion terms, bond-angle, angle-angle and angle-torsion cross terms are included. An additional input file with the bonding configuration and the atom types (in the Tinker coordinate input format) is needed for starting.

- The $H_2 + H \longrightarrow H + H_2$ surface by Truhlar and Horowitz [138]

- The $H + HBr \longrightarrow HBr + H$ surface by Clary [139]

- The $OH + H_2 \longrightarrow H_2O + H$ surface by Schatz and Elgersma [140]

- The $NH_3 + Cl \longrightarrow NH_2 + HCl$ surface by Corchado and Espinosa-Garcìa [141]

- The $H + CH_4 \longrightarrow H_2 + CH_3$ surface by Bravo and Espinosa-Garcìa [142]

- The $OH + NH_3 \longrightarrow H_2O + NH_2$ surface by Rangel and Espinosa-Garcìa [143]

- The $CH_4 + OH \longrightarrow CH_3 + H_2O$ surface by Espinosa-Garcìa and Corchado [144]

---

3 The detailed calculation of **D**-matrix elements is explained in section 11.4.2.
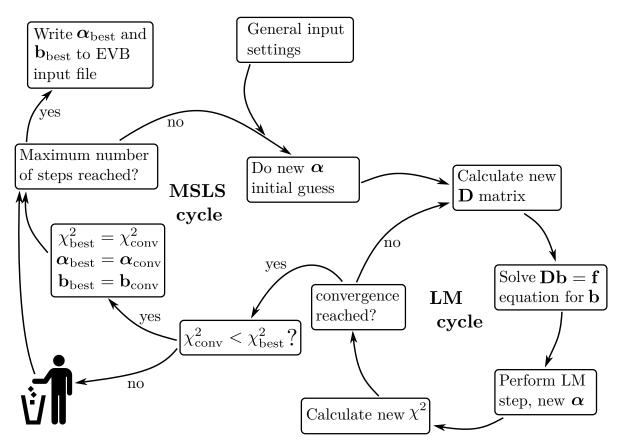
Figure 3.2: Illustration of the MSLS algorithm as used for DG-EVB parameter optimization in `evbopt.x`. dE- as well as dQ-parameters are optimized similarly. Initially, the user gives a number of settings (e.g., maximum number of MSLS- and LM-steps or ranges for the parameter initial guess), which enter the program at the main MSLS cycle. A new initial randomized guess for the $\boldsymbol{\alpha}$-vector is done. This enters the LM cycle, where the DG-coefficient matrix $\mathbf{D}$ needs to be calculated, the system of linear equations $\mathbf{DB} = \mathbf{f}$ is solved and after this, the LM-local optimization step can be done. New values for $\boldsymbol{\alpha}$ are obtained. The error sum χ^2 according to eq. 3.1 is calculated and compared to the previous cycle. If the change falls below the convergence threshold, the actual local search is considered successful and the program returns to the main MSLS-cycle. There it is checked if the obtained error sum χ^2_{conv} is lower than the result of the previous best local search χ^2_{best}. If this is the case, the error sum as well as the obtained $\boldsymbol{\alpha}$- and $\mathbf{b}$-vectors are stored as new best parameters, else they are discarded. Unless the maximum number of MSLS-steps is reached and the actual best parameters are written out, the next cycle is started with a new $\boldsymbol{\alpha}$ randomized guess. The vector image of the trash bin was downloaded from [137].

- The GeH$_4$+OH $\longrightarrow$ GeH$_3$+H$_2$O surface by Rangel and Espinosa-Garcìa [145]

- The CH$_4$+CN $\longrightarrow$ CH$_3$+HCN surface by Espinosa-Garcìa and Rangel [146]

- The H+C$_2$H$_6$ $\longrightarrow$ H$_2$+C$_2$H$_5$ surface by Chakraborty and Truhlar [147]

There is no difference in the handling of all other programs. We can, for instance, calculate gradients with egrad.x or rate constants with rpmd.x with EVB-QMDFF or with any of the surfaces mentioned above (calculations of chemical reactions involving bond breakings are of course not possible with the traditional nonreactive FF). Instead of the QMDFF energy shifts and EVB coupling parameters the keywords trad_ff or pot_ana with a descriptor of the desired surfaces must be given. No parameter optimization is needed.

We can, e.g., test the quality of an EVB-QMDFF surface by performing a k(T) calculation on one of the surfaces listed above, parametrize an EVB-QMDFF with the program itself as provider of reference information (performing Hessian calculations with evb_qmdff.x, charges and bond order calculations with a simple *ab-initio* method, optimizing the QMDFFs based on these data, optimize the IRC with irc.x, calculate additional reference data on it and run evbopt.x) and redo the k(T) calculation. Both reaction rates will be very similar if the relevant areas of the reference PES are reproduced well with EVB-QMDFF. This strategy was used for the benchmarking of TREQ presented in chapter 5.

3.3.4 evb_qmdff

evb_qmdff.x is able to calculate several quantities of a single structure provided by the user. Similar to, e.g., a quantum chemistry program package, the user can give keywords for the calculation of the energy, the gradient and the Hessian as well as to do a geometry optimization. The well known BFGS algorithm [148] was implemented and is used for geometry optimizations.

A special feature is that we can do the calculations as well for parts or fragments of the system. If, e.g., the EVB-QMDFF PES of a bimolecular reaction is given and we want to calculate frequencies of both separate reactants, e.g., in order to do a TST calculation based on their partition sums, the calc_frag keyword in combination with a file named fragment.inp that contains the atom indices of the desired fragments must be added (see table 11.2).

3.3.5 irc

Calculations of reaction paths using the *internal reaction coordinate* (IRC) algorithm [149] are integral parts of the QM reference calculations for EVB-QMDFF. Therefore, a separate program (irc.x) was written to perform such calculations with EVB-QMDFF or the other PES-descriptions provided by the EVB-QMDFF program package (section 3.3.3).

With this, EVB-QMDFF-benchmarks against other analytical PESs descriptions as mentioned above are possible. Alternatively, we could, for instance, check how good the reference RP is actually reproduced by the parametrized EVB-QMDFF surface.

In order to start irc.x, an initial guess structure of the TS along the desired IRC is needed. Since the IRC-calculation needs to be started from the imaginary TS-mode, a TS-structure must be optimized first. The simple NR-algorithm is implemented for TS-optimization.

NR converges always to the nearest stationary point on the PES, therefore a good initial guess of the structure is needed in order to converge to the correct TS (and not to, e.g., a local minimum). The method originates in a Taylor expansion around the current position on the PES:

$$V = V_0 + \mathbf{g}^t \mathbf{h} + \frac{1}{2}\mathbf{h}^t \mathbf{H} \mathbf{h} + ...,\qquad(3.3)$$

where **h** is the difference vector between the current and the desired points on the PES in cartesian coordinates, $\mathbf{g}^t$ the gradient and **H** the Hessian at the current position. Going the reverse direction, the step from an elongated structure to the extremum is:

$$\mathbf{h} = -\mathbf{H}^{-1}\mathbf{g}. \tag{3.4}$$

This simple algorithm is known to be unstable, since the inverse of the Hessian might be ill-defined due to translational and rotational as well as small vibrational eigenvalues. Therefore, the optimization is done in a suitable set of *internal coordinates*, and the step is expressed in terms of the eigenvectors (**V**) and -values (**b**) of the Hessian matrix **H**:

$$\mathbf{h} = \sum_i^N -\frac{F_i V_i}{b_i}, \tag{3.5}$$

with $\mathbf{F} = \mathbf{Vg}$. Only sufficiently large Hessian-eigenvalues are included into the sum. In practice, the same set of internal coordinates as later used for TREQ-couplings can be used for NR, at it was done in [17].

When the TS was found, the IRC can be calculated. Since all PES-descriptions in EVB-QMDFF are cheap, a simple but quite expensive IRC algorithm was implemented: the *Euler algorithm* in mass-weighted cartesian coordinates:

$$\mathbf{x}'_{k+1} = \mathbf{x}'_k - \Delta s \frac{\mathbf{g}_k}{||\mathbf{g}_k||}, \tag{3.6}$$

with Δs being the IRC step size chosen by the user and $\mathbf{g}_k$ the cartesian gradient at point $\mathbf{x}'_k$ and

$$x'_{\beta,i} = \sqrt{m_\beta} x_{\beta,i} \tag{3.7}$$

describes the mass-weighting of cartesian coordinate i of atom β.

The IRC can be followed in two directions (reactants and products), depending on the initial gradient. Both directions are started at the optimized TS-structure, where the gradient is the cartesian eigenvector of the imaginary TS-eigenmode **v** or its negative counterpart:

$$\mathbf{x}_0 = \mathbf{x}_{\text{TS}}, \qquad \mathbf{g}_0 = \mathbf{v}_1 \quad \vee \quad \mathbf{g}_0 = -\mathbf{v}_1. \tag{3.8}$$

All following IRC steps for both directions are simply calculated with eq. 3.6. Convergence is reached for both sides of the IRC, if $||\mathbf{g}_k||$ or the energy difference $E_k E_{k1}$ falls below a user given value.

In order to get a good description of the path, the step size Δs should be quite small. However, this results in IRCs containing thousands or tens of thousands of structures that are quite bulky in handling for, e.g., EVB optimizations. Therefore, a new step is only written after a covered distance of $\Delta \varsigma$, where $\Delta \varsigma$ is by default twenty times larger than the intrinsic Euler distance Δs. In practice, the optimization might fail in some cases because the energy increases for one direction after the first step in eq. 3.8. Presumably this happens because the respective TS optimization was not exact enough, such that the true TS is located near the optimized TS and the first eigenvector-following step "climbs the hill" of that true TS. In these cases, Δs of the first step is increased automatically in integer steps until the energy decreases for the reached second structure. After this, the usual step size is restored.

3.3.6 dynamic

This program performs single MD-trajectores, propagated with the usual *velocity Verlet* algorithm. Temperature can be applied via the *Andersen thermostat* [150]. In contrast to usual classical MD programs, RPMD trajectories with arbitrary bead numbers can be calculated as well.

If trajectories are run with RPMD (no matter if `dynamic.x` or `rpmd.x` are used), problems with the connected beads could arise. Since the force constants between the beads of an atom are much larger than force constants of usual chemical bonds (at least for temperatures around 300 K), much smaller Verlet time steps would be needed to ensure a reliable dynamics. This would of course make the whole calculation much more expensive. Fortunately, we can bypass this problem by translating the RPMD-bead propagation into the normal mode space of the harmonic interactions between the beads as it was done in the RPMDrate program as well [13]. This *free ring polymer* step is then calculated by intermediary fast Fourier transform, application of the harmonic interactions in normal mode space and finally transform back the updated bead positions.

`dynamic.x` was so far mainly used for benchmarks and stability tests of new EVB coupling terms. Alternatively, steered MD or *molecular force simulations* can be conducted (see chapter 7). The respective strategies and keywords are explained there.

3.3.7 rpmd

Main objective of this thesis is to calculate rate constants of chemical reactions, therefore `rpmd.x`, which is able to do this, is the most important part of EVB-QMDFF. The structure of `rpmd.x` is largely borrowed from the RPMDrate program by Suleymanov. However, a number of differences between those programs exist: RPMDrate is a Fortran/Python hybrid, whereas `rpmd.x` is pure Fortran90. The parallelization was implemented with MPI instead of the Python-specific parallel processing scheme. Now, also recrossing calculations can be done in parallel. Further, most importantly, only k(T) values of bimolecular substitutions with two separated products could be calculated with RPMDrate, whereas `rpmd.x` is able to calculate k(T)-values for arbitrary uni- and bimolecular reactions owing to a generalized dividing surface implementation[4].

Needed Input

What is needed to start a `rpmd.x` calculation? Essentially, five batches of information must be provided:

- The fully parametrized EVB-QMDFF surface

- Umbrella bias settings, depending on the type of the reaction

- Biased sampling settings, number of trajectories, time steps etc.

- Free energy evaluation settings: WHAM or UI, number of bins etc.

- Recrossing calculation settings: number and length of child trajectories

The reaction type and thus the dividing surface definitions as well as the biasing potentials can be determined based on three pieces of information: (1) How many reactant molecules are present (N_{ed}), (2) How many bonds are formed (N_f) and (3) how many bonds are broken (N_b) during the reaction. The classification of reaction types based on these criteria is listed in table 3.4.

---

4 The term *dividing surface* might be confusing if we look back to the TST-derivation in section 2.1.1, where the dividing surface was a central part of the whole formalism. For the RPMD k(T)-calculations, dividing surfaces play a double role: They can be seen simply as geometric constructions (lower dimensional subspaces orthogonal to the reaction coordinate located at certain values of it) needed for more convenient umbrella samplings or as conceptual ground for the derivation of the RPMD rate constant presented in section 11.2.2, similar to TST.

Table 3.4: List of reaction types that can be simulated with `rpmd.x`. The actual type can be determined uniquely if the number of reactants, forming and breaking bonds is known. The first type (atom-shift) represents a special case in which a single atom is moved a certain distance in cartesian space without any specification of formed or broken bonds. This type is needed for KMC simulations on metal surfaces (chapter 9). The last two types refer to solvent complex (SC) stabilized reactions. There, all but one reactant molecule are stabilized by a hydrogen bond complex, only the last reactant approaches from asymptotic distance.

Reaction type	No. of educts (N_{ed})	forming bonds (N_f)	breaking bonds (N_b)
atom-shift	1	n.A.	n.A.
dissociation	1	0	1
cycloreversion	1	0	2
rearrangement	1	1	1
elimination	1	1	2
merging	2	1	0
bimolecular substitution	2	1	1
addition	2	2	1
cycloaddition	2	2	0
3 reactant cyclic addition	3	3	2
4 reactant cyclic addition	4	4	3
3 reactant cyclic addition (SC)	2	3	2
4 reactant cyclic addition (SC)	2	4	3

Umbrella Sampling

The most time consuming part of a usual k(T) calculation are the biased sampling trajectories along the reaction coordinate. As we have seen in section 2.1.3 (eq. 2.30), umbrella samplings are conducted by adding a bias potential which depends solely on the reaction path variable ζ. In order so sample the whole relevant area from the reactants up to the TS and beyond, several umbrella samplings with force constants placed at different ζ values must be conducted.

But how are those reaction coordinates actually defined? There are several possibilities of constructing collective variables (CV) along which umbrella samplings can be done, the Plumed package [128] used within the second program version allows for a wide variability of them. For our task of doing reaction path samplings for several different reaction types (table 3.4) this approach of sampling along specific coordinates, e.g., placing the umbrella potential at different lengths of a certain bond in the system, is rather inappropriate since each reaction type would need its own CV definition.

Therefore, another concept based on dividing surfaces is used. As we have seen, e.g., in the TST derivation (section 2.1.1), we can define a subspace of reduced dimensionality orthogonal to the reaction path. For TST, the TS dividing surface was placed at the TS of the system and all trajectories that crossed this surface from the reactants to the products side were assumed to be reactive.

In the case of umbrella sampling, the system is restrained to a narrow range around a certain ζ-value by imposing a harmonic biasing potential depending on ζ. If ζ would be a single bond length and a certain sampling would be done with the biasing potential at $\zeta = 1$, the system would oscillate around this value, but all other coordinates, e.g., other bond lengths or angles, are unbiased and thus able to move freely. Thus, the accessible coordinate space of the system is narrowed in one dimension, by simultaneously maintaining its extent in all other dimensions. If we now strengthen the umbrella force constant, the accessible interval along ζ becomes narrower, in the limit case of an infinite force constant the *restraint* becomes a *constraint* which reduces the system's dimensionality by one.

In such a case, this reduced accessible space is called a dividing surface. Since the limit towards dividing surfaces exists for umbrella samplings, it is valid to define the biasing potential depending on those surfaces. One can define a TS dividing surface and a reactants dividing surface independently, for instance, by taking bond lengths of forming and breaking bonds at the TS as definition for the TS surface and taking the distance of both reactant molecules as definition for the reactants surface for bimolecular reactions. As shown in section 11.2.2 of the appendix, the additional definition of a reactants dividing surface is also needed to derive a simple expression for the bimolecular RPMD rate constant dependent on free energy differences. All the space between both surfaces can now be sampled by setting up a potential that depends on a *linear interpolation* between both dividing surfaces:

$$\zeta_{\text{act}}(\bar{\mathbf{q}}) = \frac{\zeta_0(\bar{\mathbf{q}})}{\zeta_0(\bar{\mathbf{q}}) - \zeta_1(\bar{\mathbf{q}})}, \tag{3.9}$$

where $\zeta_0(\bar{\mathbf{q}})$ and $\zeta_1(\bar{\mathbf{q}})$ are functions describing the distance of the actual systems RPMD centroid position $\bar{\mathbf{q}}$ (eq. 2.102) to the reactants and TS dividing surfaces, respectively[5]. If the system is located at the reactants dividing surface, the distance $\zeta_0(\bar{\mathbf{q}})$ becomes zero, as well as the numerator of eq. 3.9, thus resulting in $\zeta_{\text{act}} = 0$. If it is located at the TS, $\zeta_1(\bar{\mathbf{q}})$ becomes zero, resulting in $\zeta_{\text{act}}(\bar{\mathbf{q}}) = \frac{\zeta_0(\bar{\mathbf{q}})}{\zeta_0(\bar{\mathbf{q}})} = 1$, no matter what the value of ζ_0 is. Thus in the limiting case of very strong umbrella potentials the coordinate space would be sampled by cutting it into a number of thin slices orthogonal to the reaction path. This is illustrated in fig. 3.3. If, e.g., the sampling shall be

---

[5] If classical trajectories shall be calculated, one RPMD bead is used and thus $\bar{\mathbf{q}} = \mathbf{q}$. In the following, always the general case of more RPMD beads is assumed.
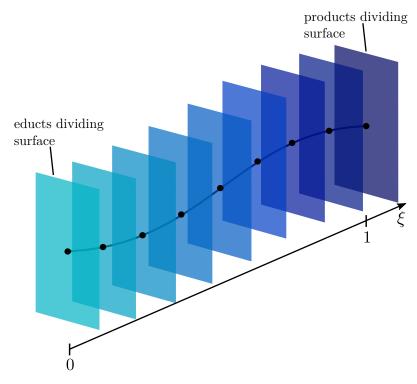
Figure 3.3: Illustration of the reaction coordinate expressed based on two dividing surfaces. If the reactants dividing surface defines $\xi = 0$ and the products dividing surface defines $\xi = 1$, all other ξ values and their respective dividing surfaces can be obtained by linear interpolation between both border cases.

done at the TS, the ideal ξ-value (ξ_{ideal}) is set to 1, whereas the actual ξ-value (ξ_{act}) is calculated by eq. 3.9 in each dynamics step. The umbrella potential is then imposed as $w(\xi_{\text{act}}) = K(\xi_{\text{act}} - \xi_{\text{ideal}})^2$.

The actual definitions of the dividing surface and the ξ_0- and ξ_1-functions depend on the reaction type. Within `rpmd.x` a more generalized framework for these surfaces was introduced.

For all reactions with two or more reactants, the reactants dividing surface is expressed in terms of the mutual distances of the reactants *center of masses* (COMs):

$$\xi_0(\bar{\mathbf{q}}) = \frac{2}{N_{\text{ed}}^2 - N_{\text{ed}}} \sum_{i=1}^{N_{\text{ed}}} \sum_{j=i+1}^{N_{\text{ed}}} (R_\infty - R_{ij}(\bar{\mathbf{q}})). \tag{3.10}$$

Here, $R_{ij}(\bar{\mathbf{q}})$ is the cartesian distance between the COMs of reactants i and j and R_∞ is a predefined asymptotic distance between the reactants where the asymptotic reactants valley is assumed to be. Thus, for $\xi = 0$ all reactant molecules are separated from all others by R_∞. With this formula, an arbitrary number of reactants could be calculated because umbrella potentials are applied between each pair of reactants. So far, only up to four reactants were considered (tab. 3.4).

The TS dividing surface for *bimolecular reactions* (or those with larger molecularity) is defined in terms of the forming and breaking bonds of the system during the reaction of interest:

$$\xi_1(\bar{\mathbf{q}}) = \frac{1}{N_{\text{b}}} \sum_{i=1}^{N_{\text{b}}} (r_i(\bar{\mathbf{q}}) - r_{i,\text{TS}}) - \frac{1}{N_{\text{f}}} \sum_{i=1}^{N_{\text{f}}} (r_i(\bar{\mathbf{q}}) - r_{i,\text{TS}}), \tag{3.11}$$

where $r_i(\bar{\mathbf{q}})$ are the actual values of the forming and breaking bonds and $r_{i,\text{TS}}$ their values at the TS (calculated at the beginning from the TS input structure).

In the case of *unimolecular reactions* (i.e., having one reactant molecule), the definition of ξ_1 is identical but ξ_0 is changed. Since we cannot calculate distances between reactants, this dividing surface is located at a certain structure, that of the reactants minimum ($r_{i,\text{ed}}$):

$$\xi_1(\bar{\mathbf{q}}) = \frac{1}{N_\text{b}} \sum_{i=1}^{N_\text{b}} (r_i(\bar{\mathbf{q}}) - r_{i,\text{ed}}) - \frac{1}{N_\text{f}} \sum_{i=1}^{N_\text{f}} (r_i(\bar{\mathbf{q}}) - r_{i,\text{ed}}). \tag{3.12}$$

For bimolecular reactions, such a definition would seriously damage the correct sampling of the reactants valley since there (almost) independent vibrations and rotations of the single reactant molecules will contribute a significant amount to its partition sum and thus its free energy. If several bond lengths are restraint at certain positions, this free rotations and vibrations would be seriously infected. In the case of unimolecular reactions, only one reactant exists such that this intermolecular contribution to the partition function drops out.

A special case are transitions of single atoms on metal surfaces, as investigated in chapter 9. If the system is rotated correctly, only a single cartesian coordinate is needed to perform the sampling. For example, one can simulate the diffusion of a H atom between two adsorption sites on a Cu-surface by placing the umbrella potential at certain values of the H_x-coordinate if both sites are located at identical y- and z-values. Then $\xi = H_x$. More details are given in chapter 9.

In order to actually apply the bias potential, its cartesian gradient needs to be added to the EVB-QMDFF gradient. This can be done by deriving the expressions from eqs. 3.9-3.12. The umbrella bias gradient itself is defined as:

$$\frac{\partial w(\xi_\text{act})}{\partial \bar{\mathbf{q}}} = K(\xi_\text{act} - \xi_\text{ideal}) \frac{\partial \xi_\text{act}}{\partial \bar{\mathbf{q}}}, \tag{3.13}$$

where $\frac{\partial \xi_\text{act}}{\partial \bar{\mathbf{q}}}$ the gradient of the actual reaction coordinate value can be calculated with:

$$\frac{\partial \xi_\text{act}}{\partial \bar{\mathbf{q}}} = \frac{\xi_0(\bar{\mathbf{q}}) \frac{\partial \xi_1(\bar{\mathbf{q}})}{\partial \bar{\mathbf{q}}} - \xi_1(\bar{\mathbf{q}}) \frac{\partial \xi_0(\bar{\mathbf{q}})}{\partial \bar{\mathbf{q}}}}{(\xi_0(\bar{\mathbf{q}}) - \xi_1(\bar{\mathbf{q}}))^2}. \tag{3.14}$$

The cartesian gradients of the dividing surfaces can be obtained by calculating the gradients of the involved distances and omitting all constant summands. In practice, the actual task of biased sampling is divided up into three single sections [13]:

1. *Start structure generation*: The initial structure is the TS as given by the user. Since usually an area of $\xi = -0.05$ to $\xi = 1.05$ or even larger is sampled in order to ensure that the reactants minimum and the TS maximum along the free energy surface are included[6], structures for both sides of the TS need to be calculated. The first umbrella trajectory is calculated with $\xi_\text{ideal} = 1$, the last structure of this trajectory is used as initial structure for the umbrella sampling at $\xi_\text{ideal} = 1.01$ (if the umbrella windows are placed at $\Delta\xi = 0.01$ intervals along the reaction path). The endpoint of this trajectory is used for the sampling at $\xi_\text{ideal} = 1.02$ and so forth until the highest ξ_ideal is sampled as well. Then, we return to the TS and move to smaller ξ_ideal-values in the same manner. The final structures of each sampling trajectory are written to file and will be used as initial points for the next step. For this first task, classical trajectories are run, i.e., only one RPMD-bead is used since only the rough position of the centroid shall be sampled. The actual dynamics is performed as in dynamic.x, i.e., by means of the velocity Verlet algorithm, where the temperature is simulated with the Andersen thermostat.

---

6 As mentioned in the discussion of the TST-limitations (section 2.1.2), the positions of the potential energy activation barrier and the free energy activation energy barrier usually do not exactly coincide. In order to be able to consider situations where the free energy activation barrier is moved towards the products (e.g., $\xi = 1.02$), the slightly prolonged range is calculated.

2. *Umbrella equilibration*: At this point, we switch from one bead to the number of beads given in the input. The initial structure for the actual umbrella window is loaded and each replica is given the same position-vector, such that they merge together. In order to get a more natural distribution of them and to avoid artifacts at the early stages being involved into the free energy calculation, some equilibration is needed. During this time, the ring polymers are untangled and spread out.

    For the sampling of classical trajectories, it would make no difference if one very long or several rather short trajectories are simulated. For RPMD, due to the stiff harmonic springs between the beads of each atom, it is much harder to explore the full phase space [11]. Therefore, the ergodicity of a long trajectory might be restricted. This can be circumvented if many rather short trajectories with randomized initial conditions are sampled for each umbrella window. The autonomous disentanglings of the beads at the numerous equilibration stages will lead to several different ring polymer configurations and thus relieve the problem of hindered ergodicity.

    Further, equilibrations as well as the following samplings can be done *in parallel*. In principle, an arbitrary number of sampling trajectories can be propagated simultaneously. In `rpmd.x`, this most time-consuming part is parallelized with MPI, such that hundreds or even thousands of cores might be used in parallel if an adequate machine is available.

3. *Umbrella samplings*: After equilibration, the actual sampling is started for each single equilibrated trajectory. Usually, samplings are set to be 5 to 10 times longer than the previous equilibrations. The only difference between equilibration and sampling is that in the latter, average and variance of ζ_{act} are calculated for the following UI (eq. 2.42). For this, ζ_{act} of each sampling step must be determined. Usually, we would set up a huge table with ζ_{act} values for each MD step and calculate the statistics at the end of the trajectory. Alternatively, average and variance (zeroth and first moment of the probability distribution) of umbrella window i can be incremented each time step:

$$\overline{\zeta_i^b} \mathrel{+}= \zeta_{\text{act}} \quad , \quad (\sigma_i^b)^2 \mathrel{+}= \zeta_{\text{act}}^2. \tag{3.15}$$

When the trajectory is complete, the obtained values are divided by the number of sampling time steps. Finally, after completion of all trajectories for an umbrella window, $\overline{\zeta_i^b}$ and $(\sigma_i^b)^2$ for it are calculated by averaging the values for the single trajectories.

All what is obtained from the time consuming umbrella sampling section in `rpmd.x` is a short file with averages and variances of the reaction coordinate for each umbrella window. These will be used for the following UI.

Error Handling

Before going on, an important feature of `rpmd.x` should be mentioned (which is not existent in the RPMDrate program): The systematic error handling which usually makes the manual intervention of the user unnecessary if something went wrong. For all potential energy surfaces in usage, erroneous propagation steps can occur, e.g., explosions of the molecular structure or unwanted dissociations of single bonds. This can happen due to bad behavior of the ring polymer or bumpy regions at the PES. Without any error handling, the calculation would simply progress with broken structures and finish some hours later giving rubbish as output.

In order to avoid that, each dynamics time step is checked for the following happenings:

- Undefined (NaN) values for energy or single coordinates of the system.

- Very high energies. The actual RPMD-energy is compared with the initial RPMD-energy for the TS. Since the TS has the highest energy along the reaction path and for usual temperatures

the system cannot go to areas offside the reaction path with much higher energy than this, an error is indicated if the energy per replica (containing all atoms of a certain bead) is more than 200 kJ/mol higher than the TS energy.

- ζ_{act} and ζ_{ideal} differ significantly. Usually, both values should be quite similar since usually a large number of 100 or more umbrella windows are used and the bias is sufficiently high to effectively avoid large distances from the bias position. If $|\zeta_{act} - \zeta_{ideal}| > 0.1$, it is assumed that something went wrong, e.g., an unwanted bond dissociation, and the error is thrown.

If an error is thrown during umbrella equilibrations or samplings, the actual trajectory as well as (in the case of sampling) their $\overline{\zeta_i^b}$ and $(\sigma_i^b)^2$ values are reset and restarted from the stored initial structure. Sometimes, this fix is insufficient. It might occur that the stored initial structure itself is already a bad one, even if no error could be associated with it. There might, for instance, be an early stage of an unwanted bond dissociation, which (almost) always leads to an explosion of the following samplings. In this case, the program would be trapped in an infinite loop (in practice: until the maximum number of errors is reached and the program is terminated). In order to break this, after five errors at the same stage the initial structures of both neighbored umbrella windows are taken one after another (if the error persists after the first one). If even this is insufficient, the structures of the next neighbored windows are taken and so on.

For the case that an error is thrown during the start structure generation stage, the current trajectory is restarted. If five restarts were unable to solve the problem, the whole structure generation is restarted from the TS. Since this is done with only one RPMD bead, the calculations are cheaper and the complete restart is justifiable in order to exclude "bequeathed errors".

PMF Calculation

After successful umbrella samplings, the largest part of the k(T) calculation is done. With the stored $\overline{\zeta_i^b}$ and $(\sigma_i^b)^2$ values of all umbrella windows, the free energy profile along the reaction path, also named *potential of mean force* (PMF), can be calculated. This is done by UI in the default case (eqs. 2.42-2.43). With numerical integration of the obtained $\frac{\partial A(\zeta_j)}{\partial \zeta}$, the calculation is done after some seconds.

Thereafter, the minimum (ζ_{min}) as well as maximum (ζ_{max}) positions of the obtained surface are calculated. WHAM is implemented as well, but this is connected with large amounts of calculation overhead and much more output for each umbrella trajectory. Further, it takes much more time to converge to a reasonable PMF profile. Therefore, UI is strongly recommended for real applications.

Transmission Coefficient

As explained in the theory section, recrossing is neglected within TST and QTST and thus must be calculated separately. The mechanism of such a calculation is illustrated in fig. 2.5. Each recrossing calculation consists of two interconnected sections: (1) propagation of a *parent trajectory* at the dividing surface located at ζ_{max} and (2) propagation of *child trajectories* that are started at regular intervals from the actual position of the parent trajectory.

As already mentioned above, trajectories can be sampled on a $N - 1$ dimensional dividing surface if they are constrained to a certain ζ value, here ζ_{max}. Within rpmd.x, this constraint is done with the iterative RATTLE algorithm [151].

The general expression for the classical transmission coefficient is given in eq. 2.47. For RPMD calculation, a slightly altered expression must be used [13]:

$$\kappa(t \to t_p; \xi^\ddagger) = \lim_{t \to t_p} \frac{\langle f_S(\overline{\mathbf{q}}_0)^{-1} v_s(\mathbf{p}_0, \mathbf{q}_0)\Theta[s_{\zeta_{max}}(\overline{\mathbf{q}}_t)]\rangle_{\zeta_{\zeta_{max}}}}{\langle f_S(\overline{\mathbf{q}}_0)^{-1} v_s(\mathbf{p}_0, \mathbf{q}_0)\Theta[v_s(\overline{\mathbf{q}}_0, \overline{\mathbf{p}}_0)]\rangle_{\zeta_{\zeta_{max}}}}. \tag{3.16}$$

The angular brackets denote canonical averages taken taken over the constrained ensemble at ζ_{max}, i.e., during the parent trajectory sampled at the corrected TS dividing surface, further, $v_\xi(\mathbf{p}_0, \mathbf{q}_0)$ denotes the initial velocity along the reaction coordinate for a child trajectory:

$$v_\xi(\mathbf{p}_0, \mathbf{q}_0) = \sum_{i=1}^{N} \sum_{j=1}^{n} \frac{\partial s_{\zeta_{max}}}{\partial \mathbf{q}_i^{(j)}} \frac{\mathbf{p}_i^{(j)}}{m_i} \Bigg|_{t=0}, \tag{3.17}$$

where the sum runs over all M atoms and all n beads, i.e., here the actual ring polymer itself instead of its centroid is considered, and $\mathbf{p}_i^{(j)}$ being the momentum of atom i, bead j. $f_\xi(\overline{\mathbf{q}}_0)$ is a metric tensor correction which is needed in order to consider the effect of the hard constraint applied to the parent trajectory:

$$f_\xi(\overline{\mathbf{q}}) = \sqrt{\sum_{i=1}^{N} \frac{1}{2\pi\beta m_i} \left| \frac{\partial \xi(\overline{\mathbf{q}})}{\partial \overline{\mathbf{q}}_i} \right|^2}. \tag{3.18}$$

Further, a slightly different definition of the reaction coordinate is needed. In order to correctly evaluate the Heaviside function, the $\xi_{\zeta_{max}}$-coordinate is zero on the reactant side and one of the product side of the chosen dividing surface:

$$\xi_{\zeta^\ddagger}(\overline{\mathbf{q}}) = \xi^\ddagger \xi_1(\overline{\mathbf{q}}) + (1 - \xi^\ddagger)\xi_0(\overline{\mathbf{q}}). \tag{3.19}$$

In practice, some thousands of child trajectories need to be started and sampled up to 1-2 picoseconds, until the κ-value converges.

Rate Constant Calculation

Finally, the reaction rate constant of the system at the given temperature can be calculated. For bimolecular reactions, the expression is [13] (for derivation, see section 11.2.2):

$$k_{\text{RPMD,bimol}}(T) = \sigma_{E1}\sigma_{E2}\kappa 4\pi R_\infty^2 \sqrt{\frac{1}{2\pi\beta\mu_R}} \exp\left(-\beta(F(\xi_{max}) - F(\xi_{min}))\right), \tag{3.20}$$

where σ_{Ei} are the symmetry numbers of both reactants, respectively and $\sigma_{E1}\sigma_{E2}$ the number of equivalent reaction channels (also known as the symmetry of the reaction)[7] and μ_R the reduced mass of the system at the reactants dividing surface. Depending on the system of interest, the free energy difference can either be taken between the maximum and the minimum along the PMF surface or between the maximum and the reactants asymptotic ($\xi = 0$). The former is done, e.g., in the case of cyclic urethane reactions (chapter 8), where it can be assumed that reactive processes start from an associated complex stabilized by noncovalent interactions which is represented by a minimum on the PMF surface.

Unimolecular reactions are calculated with [152]:

$$k_{\text{RPMD,unimol}}(T) = \kappa \frac{1}{\sqrt{2\pi\beta\mu}} \frac{e^{-\beta F(\text{max})}}{\int_{\xi_{min}}^{\xi_{max}} e^{-\beta F(\xi)} d\xi}, \tag{3.21}$$

where the integration is performed over the free energy surface from its minimum to its maximum value.

The actual implementation of `rpmd.x` is presented in fig. 3.4 by connecting all important subroutines that come into play. The picture is simplified, though, e.g., by neglecting that the recrossing subroutine calls the same Verlet dynamics subroutines as the sampling part.

---

7 If, e.g., a hydrogen abstraction reaction between ethane and a chloride radical is investigated, $\sigma_{E1} = 6$ and $\sigma_{E2} = 1$ since all six hydrogens of the ethane are identical and might react with the chloride but only one of this possibilities had been accounted for in the rate constant algorithm so far.
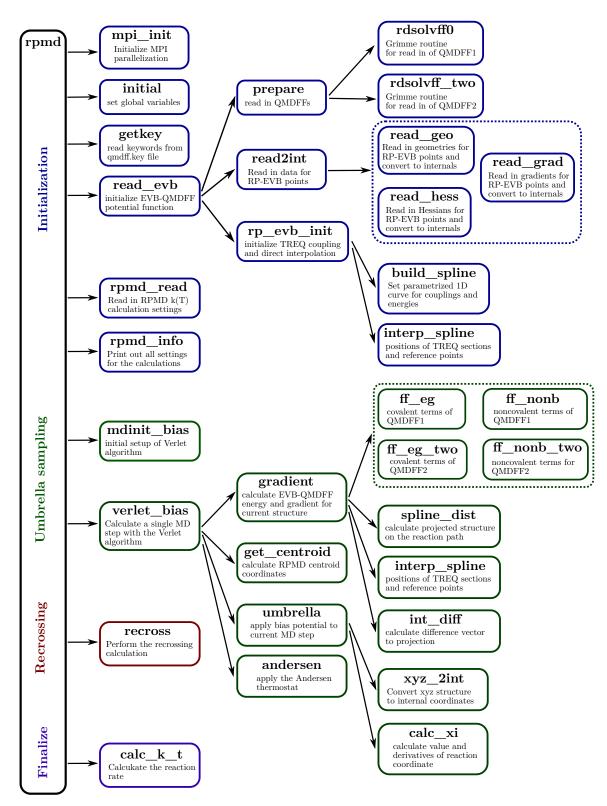
Figure 3.4: Simplified structure of the `rpmd.x` program. Shown are all important subroutine-calls and their respective sub-calls. Less important subroutines as well as functions are neglected, further, duplicate calls (such as for recrossing) are neglected as well.

3.3.8 evb_kt_driver

This program enables the *black-box* calculation of reaction rate constants. The underlying idea is that a specific elementary chemical reaction can be fully described if its minimum energy path has been calculated. Therefore it should be possible to calculate the rate constant of a reaction if this path is supplied by the user.

So far, a couple of steps was needed to go from the reaction path to a rate constant finally ejected from a RPMD calculation:

1. Optimize structures of both reactants and products minima, with the endpoints of the reaction path as origins.

2. Calculate sets of reference data needed for QMDFF generations.

3. Run the `qmdffgen.x` program for the generation of the QMDFF force field files.

4. If DG-EVB or TREQ shall be used as EVB-coupling method, calculate gradient and Hessian reference data for a manually chosen set of points along the reaction path.

5. Unless TREQ is used as EVB method, optimize the EVB-coupling term with `evbopt.x`

6. Determine settings needed for the following RPMD-run: reaction type, dividing surfaces, number of sampling steps etc. .

7. Execute `rpmd.x` for calculation of k(T)-value(s).

8. If the temperature-dependence of rate constants shall be investigated, e.g., by doing an Arrhenius or Eyring plot, calculate several k(T)-values and do the fit with a suitable script.

As will be shown in the following, all this can be fully automatized, under the condition that TREQ is used as EVB coupling method[8].

Needed Input

Since it is the aim that one single program execution shall be enough to do all steps depicted above, all information that might be needed at some point should be provided at the beginning (or calculated *on-the-fly* based on the results of preceding steps, if possible). Besides the reaction path structures and energies (provided in a xyz and an energy list file), only one additional input file (`qmdff.key`) is needed. Keywords were designed that allow the user to give all needed parameters:

- The used software package for *ab-initio* reference calculations (Currently, Gaussian and Orca are supported).

- The direction of the reaction (with respect to the IRC). Unless a symmetric reaction is considered, rate constants could be calculated for the forward and backward process.

- The used *ab-initio* reference method (as well as basis set and other settings such as DFT dispersion corrections etc.) for geometry optimizations, QMDFF reference calculations, TREQ reference calculations and an optional improvement of the path energies by a higher level method. Usually, all tasks except the last are done with the same method (e.g., MP2), whereas the last can be done with a much more expensive method (e.g., CCSD(T)) and possibly even with another software package.

---

8 Indeed, the *black-box* procedure can also be done with DG-EVB as coupling method, since no user intervention is needed for the DG-EVB parameter optimization in general. However, it turned out that the actual choice of DG-EVB coupling coordinates as well as the DG-EVB mode might affect the overall quality significantly. So far, no stringent method of predicting the best settings could be developed, thus excluding DG-EVB for usage within a true *black-box* approach.

- Calculation settings for the reference: Number of cores for QMDFF- as well as TREQ-reference calculations and the available memory per core. Further, *symlinks* to the program executables (QM program, `qmdffgen.x`, `rpmd.x`) must be given. With this, the calculations can be done on external calculation clusters as well.

- Number of TREQ gradient and frequency reference points along the reaction path (if no default values shall be used).

- Settings for RPMD calculations: temperatures as well as runs per temperature that shall be averaged.

All other settings (e.g., time steps for RPMD structure generation trajectories) are set by default from the program. If the user wants to change some of them manually, he or she can add the standard keywords with the preferred settings to the main `qmdff.key` input file.

QMDFF Generation

Depending on the choice regarding the direction of the reaction, the first and last structures of the reaction path are taken as initial points for reactants and products geometries, respectively. Starting from these structures, geometry optimizations are done with the chosen QM program package. Input files are generated in separate folders and the calculations are started, either serial or in parallel, depending on the total number of cores available and the chosen number of cores per calculation. The output files are monitored during the calculations, such that the main program waits until the program-package-dependent lines indicating a successful finishing appear. After this, the output files with the optimized structures are read in.

In the next step, new input files, now for QMDFF reference calculations, are written in separate folders. The program-package-specific keywords for frequency, CM5 charges etc. are added to the method and basis set chosen by the user. Now, the same procedure as with the geometry optimizations is repeated.

When all reference was calculated successfully, `qmdffgen.x` can be executed. Since this is also a *black-box* program, only one command is needed. After completion, the QMDFF-shift energies are slightly changed: Sometimes the QMDFF energy curves deviate quite significantly from the asymptotic *ab-initio* reference of the reaction path. Therefore, they are manually corrected such that the first and last energy of the RP are reproduced exactly by the reactants and products QMDFFs, respectively. This is illustrated in fig. 3.5 for the CF_3O+CH_4-reaction.

EVB Reference Calculations

Now, the EVB-part must be parametrized. No matter if DG-EVB or TREQ are used, gradient and Hessian reference information is needed on a number of points along the RP. The procedure of locating those points is usually far from *black-box*. So far, the user had to choose each point manually, usually by inspecting the RP energies and picking single points from them. It has turned out that better DG-EVB qualities (with respect to the reproduction of the reaction path) could be obtained if a denser grid of points was picked at regions with higher slope of the RP. Further, the TS was always chosen since the exact information of the RP turning point should be included. For TREQ, also the very first and very last point of the IRC must be chosen in order to make linear gradient and frequency interpolations along the whole path possible (chapter 5, section 2).

With these prerequisites, a heuristic algorithm for the automated location of those reference points was developed. First, the ideal total number of reference points M_{tot} should be determined. At least three points are needed (TS as being the structure along the RP with the highest energy and both ends of the RP), but of course much more are preferable in almost all cases. It was assumed that the number of needed reference points grows with system size since the accessible coordinate
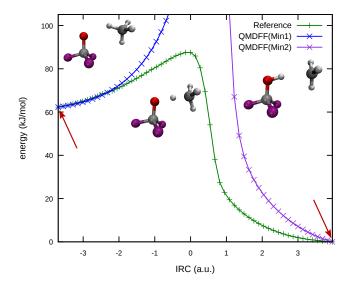
Figure 3.5: Illustration of the automated QMDFF energy shift correction applied during the *black-box* EVB generation.

space around the path grows as well and more information will be likely needed to represent it satisfactorily[9]. The used formula is:

$$M_{\text{tot}} = \min\left(M_{\text{base}} + \frac{N_{\text{at}}}{2}, \frac{n_{\text{RP}}}{2}\right), \tag{3.22}$$

with M_{base} being a minimum number of points (default: 10, might be changed by the user), N_{at} the number of atoms in the system and n_{RP} the number of energies along RP. Thus, M_{tot} grows with the number of atoms, until half of the RP energies is reached. This is done in order to avoid problems with the following steps.
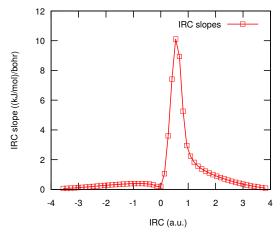
Reaction paths can be very asymmetric, for instance, in the case of a cycloaddition the way from the TS to the product is usually much shorter than to the reactants separated by a large distance. This effect is considered by inclusion of the path distances measured in mass-weighted coordinates of the left (d_{left}) and the right (d_{left}) part of the RP, measured from the TS:
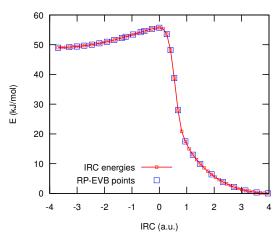
$$M_{\text{left}} = \frac{(M_{\text{tot}} - 3)d_{\text{left}}}{d_{\text{tot}}} \qquad M_{\text{right}} = \frac{(M_{\text{tot}} - 3)d_{\text{right}}}{d_{\text{tot}}}, \tag{3.23}$$

where the three fixed points (TS, first and last point) are excluded. With this, a useful distribution of the points to both sides can be achieved. But how shall the actual location of those points be determined? As mentioned above the slope of the RP should be considered. The spatial validity of a Taylor expansion (or its radius of convergence) depends on the steepness of the PES around its location. Flat areas such as reactants- or products-asymptotes will be described to a certain degree of accuracy by a thinner grid of Taylor expansions than the sharp barrier around the TS. Therefore, the RP-slope was included. It is calculated by building the numerical energy derivative along the RP: $\frac{\partial E}{\partial \xi}$ (fig. 3.6).

Now, a new reaction path progress parameter χ is introduced. Unlike ξ, the usual value of the RP-progress which depends only on the distance measured in mass weighted coordinates, χ also

---

9 Of course, the accessible configuration space of a molecular structures scales *exponentially* with the number of atoms in it, such that also the number of gradient/Hessian reference points might be needed to grow exponentially with the number of atoms. However, the number of structures along a RP is usually rather small and our method should of course not scale exponentially. Fortunately, it turned out that the *linear* growth with system size lead to good results in most cases.

(a) Derivative of the energy along the reaction path

(b) Selected positions of reference points

Figure 3.6: Example of the automated determination of TREQ gradient and Hessian reference points depending on the slope of the reaction path. First, the energy slope along the reaction path is calculated (a). Depending on this, a denser grid of reference points is located at areas where the path is steeper, here each point at the steep region to the left of the TS in contrast to each third point in the asymptotic regions (b).

depends on the RP-slope. For regions with high energy slope, χ will grow much faster than ξ, whereas their change is nearly equal in regions with almost constant energy. The values of χ left and right the TS can be calculated for all distinct points along the RP with:

$$\chi_{i,\text{right}} = \sum_{j=j_{TS}}^{i-1} [\chi_{j,\text{right}}] + \xi_i - \xi_{i+1} + \frac{1}{2} \left. \frac{\partial E}{\partial \xi} \right|_i \frac{\xi_{\text{right}}}{\sum_{j=1}^{p_{\text{tot}}} \left. \frac{\partial E}{\partial \xi} \right|_j}, \tag{3.24}$$

$$\chi_{i,\text{left}} = \sum_{j=1}^{j_{TS}} [\chi_{j,\text{left}}] + \xi_i - \xi_{i+1} + \frac{1}{2} \left. \frac{\partial E}{\partial \xi} \right|_i \frac{\xi_{\text{left}}}{\sum_{j=1}^{p_{\text{tot}}} \left. \frac{\partial E}{\partial \xi} \right|_j}. \tag{3.25}$$

On this *resized path*, the M_{left} and M_{right} points are then placed equidistantly[10]. After this is done, the input for the gradient/Hessian QM calculations is prepared in separate folders. Then, the calculations are started, where the number of parallel calculations depends again on the available processors and processors per run. When all calculations are finished, their results are read in and the `ref.input` file with energies, gradients and Hessians of the points to be used for EVB calculations is written.

TREQ enables the usage of a separate reference level for the RP-energies (*dual-level* approach). If the user wants to recalculate the path energies with a higher level of theory, he or she can add the respective keywords for QM level and basis set as well as desired program package and cores per calculation. The energies are then calculated and included into the EVB-parametrization.

EVB Coupling Parametrization

TREQ needs no separate parameter optimization, nevertheless some settings should be determined in a meaningful way. The main problem is the set of *internal coordinates*. Unlike DG-EVB, where a

---

10 In principle, we could interpolate the distinct RP-structures in order to get a smooth parametric curve, as it is done in TREQ and then pick structures that are exactly located at the desired χ-values. However, in the actual calculations, only RP structures obtained from the QM path were taken as reference points, such that the obtained χ-values were rounded to the value of the next RP structure.
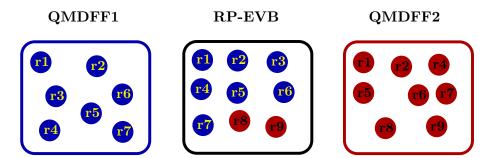
Figure 3.7: Exemplification of the automated choice of internal coordinates for the TREQ coupling term. Each bond or angular coordinate that is present either in the first or in the second QMDFF is chosen.

small number of coordinates important for the reaction is usually sufficient for a good quality of the coupling, in TREQ a *complete set* of coordinates is needed to avoid atom mergings at the direct interpolation region. If a single bonding configuration is to be parametrized, the z-matrix or other usual complete sets of internals could be used. However, here we always have reactions with built and broken bonds, therefore different ideal sets of internal coordinates along the RP. A simple but nevertheless quite successful solution was to go back to the Wiberg-Mayer bond orders used for the QMDFF parametrization. By comparing the sets of present chemical bonds in the reactants and products structures, all bonds that are present in *at least one* set are taken as internal coordinates for the coupling (fig. 3.7). Further, angle-coordinates are added to the set for all pairs of neighbored bonds in it.

All remaining parameters are the locations of the different TREQ regions along the RP (fig. 2.16) as well as the damping factor α offside the path (eq. 2.162). Fortunately, TREQ itself is a black-box method, the parameters are calculated in a standard way (chapter 5). Considering that most RPs are asymmetric, the relative positions of the transitions are adapted to the different lengths of both sides.

RPMD Calculations

With a complete PES-description, we can move on to the actual k(T)-calculations. As we have seen from section 3.3.7, a quite large number of parameters is needed for its setup. If the user should determine all those settings before an `evb_kt_driver.x` calculation, the black-box character would be seriously flawed. Therefore, default values for most of them are taken, unless the user indeed wants to set them manually (then, he or she simply adds the respective keywords to the `qmdff.key` file).

Some settings are system-dependent and thus must be determined based on the information gathered from the reaction path itself. First, the number of fragments in the reactants structure needs to be known. In the case of one fragment, the reaction is unimolecular, for two it is bimolecular etc. . This number can be read in from the QMDFF generation logfile, where this number is determined for the parametrization of noncovalent interactions. Second, the number of forming and breaking bonds must be known. If for example one bond is formed and one broken, the reaction is a rearrangement, if one bond is broken and two are formed, we have an addition and so forth. These numbers can be determined similar to the TREQ coupling coordinates, i.e., by comparison of the sets of chemical bonds in reactants and products QMDFFs (fig. 3.8). Then, all bonds that are present only in the reactants are broken bonds and all that are present only in the products are formed bonds.

As noted in table 3.4, the number of reactant fragments together with the number of formed and broken bonds determine the reaction type. Further, reactants- and TS-dividing surfaces as needed for the umbrella samplings are defined based on them.
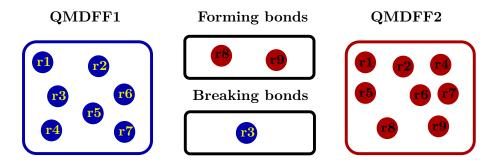
Figure 3.8: Automated determination of the reaction type: The numbers of built and broken bonds are determined by comparison of the bonds present in both QMDFFs. Each bond that is only present in QMDFF1 is depicted as *breaking* bond, each bond that is only present in QMDFF2 is depicted as *forming*.

Having determined those parameters, the RPMD calculations can be initiated. Depending on the user's choice, one single k(T) calculation or a larger number of calculations with averaging of the results is conducted. Further, one or more k(T)-values can be calculated at several different temperatures. In those cases, an Arrhenius-plot is done in the last step to determine activation energy and preexponential factor according to eq. 2.1. Further, an Eyring-plot is done and the parameters of eq. 2.11 are determined. Several results of calculations with `evb_kt_driver.x` are presented in chapter 6.

Publication: (DG-)EVB-QMDFF-RPMD

4.1 Scope of the Project

This project covers a significant period of the whole work for this thesis. As already explained in section 3.1.3 of the program chapter, it was our desire to enable reaction rate constant calculations on EVB-QMDFF surfaces. By coupling our EVB-QMDFF code with the RPMDrate program by Suleymanov [13] it became possible to calculate bimolecular rate constants with the RPMD formalism, such that also quantum effects could be considered in a MD based manner.

The present paper was designed to fulfill two purposes: First, it should show that the energy-gap (dE)-EVB as well as the distributed Gaussian (DG)-EVB coupling terms in connection with QMDFFs as diabatic surfaces are able to describe a reference PES based on an *ab-initio* reaction path in all regions relevant for a reactive sampling with good quality, shown by rate constants that coincide well with experimental references. Second, the much reduced effort for setting up an EVB-QMDFF PES description compared to traditional parametric surfaces should show that *black-box* calculations of reaction rate constants are already nearly possible and might become routine in the near future if the EVB-QMDFF formalism is further improved (with respect to the time the paper was written).

Three example reactions are presented, for which reaction rate constants were calculated with EVB-QMDFF-RPMD as well as with "traditional" parametric TST corrections in the POLYRATE [10] program package. A final comparison of both methods was made.

4.2   Publication Data and Reprint

Contribution Implementation of the EVB-QMDFF program, especially of the DG-EVB coupling term, connection with RPMDrate. Parametrization of the PES descriptions for the example reactions, running and evaluating the rate constant calculations. Further: Doing parametric rate constant calculations with POLYRATE in order to compare them with the EVB-QMDFF-RPMD values. Major Contributions to writing the article.

Publication: TREQ - Development and Benchmark

5.1 Scope of the Project

Shortly after the establishment of the DG-EVB method for rate constant calculations with RPMDrate it became clear that the provided PES description was insufficient for many even rather simple systems. The umbrella sampling trajectories became trapped in artificial minima offside the reaction path, leading to distorted free energy curves and absurd rate constants. Several approaches for solving these problems inside the DG-EVB network failed, such as optimization of internal coordinates and positions of DG-EVB reference points.

Therefore, the decision was made to develop an entirely new EVB coupling method, designed especially for high quality descriptions of reaction paths and their direct vicinity. The new coupling term was named Reaction Path (RP)-EVB. During first benchmarks, the new term, although superior to DG-EVB, showed problems in other examples.

This lead to the development of the Transition Region Corrected (TRC)-RP-EVB-QMDFF (TREQ) method, where the EVB-QMDFF construction is replaced by a direct Taylor series expansion of the QM-reference in the TS region. The presented publication shows the development and the (mathematical as well as algorithmic) construction of the TREQ method in great detail. Additionally, a thorough benchmark of the new method is conducted in order to prove its quality for relevant examples. For this, analytic potential energy functions from the literature for a number of small reactive systems were coupled to the EVB-QMDFF program package. The benchmark was then done as follows: On the analytic potential energy surfaces, reaction paths and the needed TREQ reference data were calculated similar to QM methods. Then, TREQ surfaces were parametrized based on this "pseudo-QM" reference. Finally, RPMD rate constant calculations were done both on the analytic surfaces and the TREQ surfaces derived from them, the results were compared thoroughly.

It turned out that TREQ is indeed able to provide quantitatively correct descriptions of reference surfaces, hence able to calculate high-quality rate constants. Additionally, TREQ was constructed such that no optimization procedure is needed for its setup which makes the development of a *black-box* algorithm for k(T) calculations possible (see chapter 6).

5.2   Publication Data and Reprint

Black-Box k(T) Calculations

We have seen in the last chapter that the TREQ method is well suited for performing *black-box* rate constant calculations since no ambiguous parameter optimization or system-specific choices by the user are needed for its setup. As explained in section 3.3.8 of the program chapter, this property was used to develop a program named `evb_kt_driver.x` that is able to calculate rate constants and Arrhenius parameters for an arbitrary elementary reaction if its reaction path is given by the user.

In this chapter, a first benchmark of `evb_kt_driver.x` is presented: Fifteen different reactions were chosen, their reaction paths were optimized and *black-box* rate constant calculations based on them were started. Then, the resulting rate constants and Arrhenius parameters were compared with (both theoretical and experimental) literature values as reference.

6.1 General Procedure

The first task was to find a suitable set of example reactions for the test of the program. In the ideal case, we should choose a wide variety of different system sizes, involved chemical elements and reaction mechanisms (uni- and bimolecular). In the reality, the desired reactions should further fulfill three requirements in order to be suited as easy-to-calculate *black-box* systems:

1. It should be a small to medium-sized thermally activated gas phase reaction in the ground state (due to the construction of the TREQ PES).

2. Experimental reference data for rate constants and Arrhenius parameters should be available.

3. To limit the effort for the QM-reference calculations, the reaction path needs to be of single-reference character.

A suitable place for the search of *gas-phase reactions* with available experimental data is the NIST Chemical Kinetics Database [153]. The idea was to randomly choose some handful of reactions from there and to calculate *black-box* rate constants. It turned out that this task was far from easy. In order to ensure that single-reference methods are able to calculate a reliable reaction path, only reactions with theoretical papers where, e.g., a TS-optimization was done (and reported with some detail) could be considered.

Therefore, reactions for which experimental and theoretical (containing detailed descriptions of QM-reference calculations) studies are available were chosen. Ideally, more than one experimental study should be available as well since their results tend to differ significantly in some cases (see below). These prerequisites excluded approximately 95-98 % of the reactions listed in the database. From the remaining ones, fifteen reactions were finally chosen, still offering a large variety both in the involved elements and in the reaction mechanisms. Unfortunately, the vast majority of reactions listed in NIST with enough references available are simple bimolecular exchanges.

Table 6.1: List of chosen reactions for the benchmark of the `evb_kt_driver.x` program. They are ordered according to (ascending) atom numbers in the system, references to pages where the results are shown are listed as well.

Reaction	No. atoms	On page
$I_2 + H \rightarrow HI + I$	3	103
$CN + H_2 \rightarrow HCN + H$	4	108
$PH_3 + H \rightarrow PH_2 + H_2$	5	105
$CH_3NC \rightarrow CH_3CN$	6	108
$CH_3Cl + Cl \rightarrow CH_2Cl + HCl$	6	108
$CH_2Cl_2 + Cl \rightarrow CHCl_2 + HCl$	6	112
$SiH_4 + Cl \rightarrow SiH_3 + HCl$	6	113
$GeH_4 + H \rightarrow GeH_3 + H_2$	6	113
$C_2H_4 + H \rightarrow C_2H_5$	7	113
$CH_3OH + Cl \rightarrow CH_2OH + HCl$	7	116
$C_2H_6 \rightarrow C_2H_4 + H_2$	8	117
$CH_4OH + CH_3 \rightarrow CH_3 + CH_4$	9	118
$C_2H_6 + NH \rightarrow C_2H_5 + H_2N$	10	120
$CF_3O + CH_4 \rightarrow CF_3OH + CH_3$	10	121
Norbornene $\rightarrow C_2H_4 +$ Cyclopentadiene	17	122

It should be noted that the experimental approaches that were used to measure the listed rate constants and Arrhenius parameters in the reference publications will not be mentioned nor discussed within this thesis. Error bars, systematic errors and other aspects that might be helpful for estimation of their degree of reliability are not discussed either, only the final resulting rate constants at the different temperatures as also listed within the NIST database are taken into consideration for the benchmark. For further studies of the different experiments the reader is referred to the given citations.

The final collection of reactions is listed in table 6.1. Most of them are basically exchanges of hydrogen atoms, since (covalent) forming and breaking of heavy atom bonds mostly involves multi-reference character. Two exceptions are the CH_3NC-rearrangement and the cycloreversion of norbornene.

In total four different mechanisms are included: mostly bimolecular exchanges, but also a rearrangement, an eliminiation and a cycloreversion. Further, ten different elements are part of at least one system treated, which illustrates the strength of QMDFF to provide reasonable (diabatic surface) descriptions for molecules including all 92 stable elements.

For all reactions but the last (cycloreversion of norbornene) theory papers exist which describe their parametrization with certain QM methods. In contrast to the cited theoretical references it was *not* the aim of this chapter to reproduce the experimental rate constants *as good as possible* but instead to benchmark how good the *black-box* approach can reproduce these rates. This includes that no trial-and-error approach for finding the best possible level of theory was applied but instead global settings or those from the reference papers were chosen. It is certainly possible to improve the shown results by means of the TREQ-RPMD method if, e.g., a large variety of QM-references or other settings within the TREQ method would be tested and gradually optimized towards the experimental reference.

The QM methods and respective basis sets from the theoretical references were sometimes adopted for the *black-box* studies as well. If the respective theory papers are quite old, thus

containing rather cheap QM methods (e.g., HF with a small basis set), superior methods were chosen. In addition, a higher QM level was adapted for the calculation of IRC energies as needed for the *dual-level* approach (see section 3.3.8). This level is in all cases DLPNO-CCSD(T) [154,155] in order to reduce the amount of calculation effort in comparison to, e.g., CCSD(T), especially for larger systems. In practice, the TS structure of the system was optimized first; if its imaginary eigenmode seemed to describe the reaction properly, the IRC optimization was started from the TS structure[1].

For the RPMD calculations, the same settings were used for all 15 examples. Since Arrhenius parameters should be calculated and compared to values obtained from literature references to get a distinct comparison between single numbers, k(T) calculations at several temperatures were done for all reported systems. The actual calculated temperatures depend on the ones at which experimental measurements were made. In total, a span between 200 and 2000 K is bridged by these calculations, showing the ability of the TREQ-RPMD approach to handle wide ranges of chemical reality (at least with respect to the temperature).

Two settings must be determined individually for each reaction. The first one is the *symmetry* of the reaction, i.e., if more than one path can be taken to get to the result. One example is a molecule with several identical hydrogen atoms undergoing a hydrogen abstraction reaction. The second setting is the required *number of beads* for sufficient consideration of quantum effects[2].

In order to get a balance between low costs and satisfying quality, a compromise was made: Instead of running one expensive k(T) calculation for one single temperature and hoping that it will be sufficiently well converged, five rather cheap k(T) calculations are done at each temperature with final averaging of their results. The single calculated values are plotted together with their averages and variances in the next section to enable a visual evaluation of the degree of convergence in the RPMD calculations. Finally, the Arrhenius parameters are determined by doing a fit through the averaged rate constant results of each temperature.

The used RPMD calculation settings are listed in table 6.3.

6.2 Example Reactions

6.2.1 The $I_2 + H \rightarrow HI + I$ Reaction

This reaction plays an important role for the translation of iodine in the gaseous phase. A theoretical study of it was done by CANNEUX and CANTREL as part of a larger study that should reveal the dynamics of bringing radioactive iodine into the environment in the case of a Pressured Water Reactor incident [157].

---

1 Initially, an even larger set of reactions was gathered (around 30 systems). However, TS and IRC calculations only worked for approximately one half of them, in the other cases convergence problems arose mostly in the IRC calculations, even if the same level of theory was used already in a reference paper. Since elaborate workarounds to solve these problems would have seriously harmed the desired *black-box* character, those systems were discarded. All systems for which TS and IRC calculations were successful are presented in this chapter.

2 Theoretically, both settings could also be determined in an automated manner: The reaction symmetry σ could be obtained by topological analysis of the reactants in comparison to the reaction path. If, e.g., a hydrogen abstraction reaction is handled, determine the initial bonding pattern of the hydrogen to be abstracted and search for hydrogens with identical patterns in the same reactant molecule, e.g., all hydrogens in ethane. The number of beads might be determined by doing a simple Wigner calculation of the transmission coefficient (eq. 2.16) for all temperatures. The needed imaginary frequency at the TS can, e.g., be obtained from the given data for the RP-EVB reference points. Depending on the magnitude of the tunneling correction the required number of beads could be estimated, e.g., by running a set of benchmarks with systems like the ones listed here and determine a correlation between the Wigner tunneling correction and the "asymptotic" number of RPMD beads above which no relevant change of the calculated reaction rate appears. However, since the choice of both settings can easily be made in a few seconds for most cases, the manual method was preserved so far.

Table 6.3: Input parameters for the RPMD k(T) calculations done within the black-box simulations of the 15 example reactions listed in table 6.1, similar to the format given in the papers by SULEYMANOV *et al.* [13, 156].

Parameter	value	explanation
Command Line Parameters		
temp	different	Temperature (K)
N_{beads}	1 or 8 or 16	Number of beads
Dividing Surface Parameters		
R_{∞}	30	dividing surface ξ_1 parameter (a_0) (only bimolecular)
N_{form}	(different)	number of forming bonds
N_{break}	(different)	number of breaking bonds
$\sigma_{E1}\sigma_{E2}$	(different)	symmetry factor of the reaction
Thermostat		
thermostat	"Andersen"	the chosen thermostat option
Biased Sampling Parameters		
N_{windows}	111	number of windows
ξ_1	-0.05	center of the first window
$d\xi$	0.01	window spacing step
ξ_N	1.05	center of the last window
dt	0.0002	time step (ps)
k_i	0.15	umbrella force constant ((T/K) a.u.)
$N_{\text{trajectory}}$	10	number of sampling trajectories per point
$N_{\text{trajectory}}$	15	duration of a sampling trajectory (ps)
Potential of Mean Force Calculation		
ξ_0	-0.04	start of umbrella integration
$\xi_{\#}$	1.04	end of umbrella integration
N_{bins}	5000	number of bins
Recrossing Factor Calculation		
dt	0.0002	time step (ps)
$t_{\text{equilibration}}$	10	equilibration period (ps) of the constrained (parent) trajectory
$N_{\text{total child}}$	10000	number of unconstrained (child) trajectories
$t_{\text{child sampling}}$	5	sampling increment along the parent trajectory (ps)
N_{child}	100	number of child trajectories per one initially constrained configuration
t_{child}	0.2	length of child trajectories (ps)

In the cited study, the IRC of the reaction was optimized with several different *ab-initio* and DFT methods. Frequencies of reactants and the TS were also calculated in order to perform TST rate constant calculations with the simple Wigner tunneling correction. Energies of the stationary points were calculated with CCSD(T) using several different basis sets. Since the combination of MP2/cc-pVTZ [158] IRC and CCSD(T)/cc-pVTZ energies of stationary points (CCSD(T)/cc-pVTZ//MP2/cc-pVTZ) led to (in the eyes of the authors) reasonable TST results, similar settings were used for the black-box method presented here: Because the cc-pVTZ basis set is not available for iodine in Gaussian16, the def2-TZVPP basis set which also has triple-zeta quality was chosen instead. For the energy corrections, the DLPNO-CCSD(T) method was used in place of "usual" CCSD(T).

The obtained structures of stationary points along the reaction path are shown in fig. 6.1 (a), the IRC itself in part (b)[3]. Starting from the IRC, the *black-box* calculations were done without complications. Their results are shown in fig. 6.1, (c). It can be seen that the experimental reference (LZ1979) obtained a (nearly) temperature-independent rate constant, corresponding to an Arrhenius activation energy of only 0.17 kJ mol^{-1} (table 6.4), whereas inverse temperature dependencies corresponding to negative activation energies of roughly -4 kJ mol^{-1} were obtained both from the *black-box* procedure and the theoretical reference (CC2010). Overall, the RPMD rates coincide well with both experimental and theoretical values in the investigated temperature range.
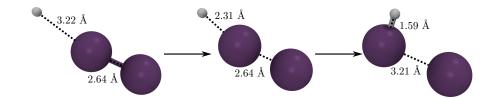
6.2.2 The CN + H$_2$ → HCN + H Reaction

This process has been well studied in theoretical kinetics over many decades [160,161], the stationary points along the RP are shown in fig. 6.2 (a). In the first theory paper at hand (TER HORST, SCHATZ, 1996 (HS1996) [160]), the authors used the CASSCF method for optimization of the reaction path and further scans of the available PES of the system. The GVB method [94] was used in the second paper by WAGNER and BAIR [161]. Since the deviations of barrier heights between the CAS and usual Restricted HF (RHF) calculations in HS1996 were smaller than for different basis sets, it was assumed that usual MP2 is able to handle this calculation as well. A look at the IRC optimized with MP2/aug-cc-pVTZ (fig. 6.2 (a)) fortifies this assumption because a smooth curve could been obtained. The IRC energies were recalculated with DLPNO-CCSD(T) as usual.
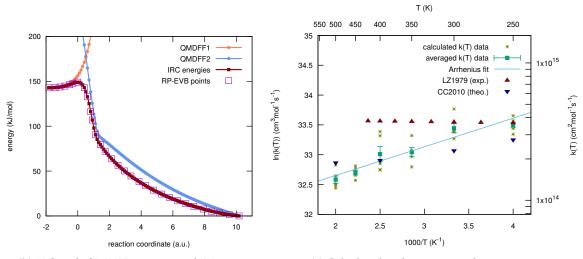
The symmetry factor of the reaction is $\sigma_{E1}\sigma_{E2} = 2$; since the temperatures between 300 and 700 K were calculated, a number of 16 RPMD bead was considered to be suitable.

The resulting k(T) values of the TREQ-RPMD samplings are plotted in part (c), together with experimental results of three authors and the TST rate constants with Wigner tunneling correction of the second mentioned theory paper (WB1986). It becomes obvious that the rate constants of the rather old theory paper deviate more than one order of magnitude from all experiments that are at close quarters to each other. The TREQ-RPMD values are close to the experimental ones especially at higher temperatures but have a too large slope. This corresponds to an Arrhenius activation energy *Ea* which is 4.5 kJ mol^{-1} larger than that of BM1981 and even more than 15 kJ mol^{-1} larger than that of SS1988 (table 6.4). It becomes clear that the activation energies (and prefactors) of the different experimental works differ from each other quite significantly, in spite of their similar rate constants in the investigated area. The theory paper WB1986 underestimates both activation energy and exponential prefactor.

---

3 It should be noted that the shown IRC energies in this and all following figures are the energies of the IRC optimization method (here: MP2) and not of the subsequent higher-level energy correction method, mainly in order to fairly show the quality of the QMDFFs which are themselves optimized from the lower level of theory.

(a) Mechanism of the reaction (reactants - TS - products)

(b) IRC with QMDFF energies and RP points

(c) Calculated and experimental rate constants

Figure 6.1: Summary of the *black-box* rate constant calculation for the I_2 + H $\rightarrow$ HI + I reaction. The reaction mechanism is illustrated by the structures of reactants, TS and products being part of the reference IRC in (a). The positions of the gradient and Hessian reference points along the reaction path that are calculated by `evb_kt_driver.x` are shown together with the energies of the IRC and both QMDFFs in (b). Finally, an Arrhenius plot of the resulting rate constants together with experimental and theoretical results from the literature is shown in (c). Here, LZ1979 stands for LORENZ, ZELLNER (1979) [159] and CC2010 means CANNEAUX, CANTREL (2010) [157].

(a) Mechanism of the reaction (reactants - TS - products)

(b) IRC with QMDFF energies and RP points

(c) Calculated and experimental rate constants

Figure 6.2: Summary of the *black-box* rate constant calculation for the CN + H$_2$ → HCN + H reaction. The reaction mechanism is illustrated by the structures of reactants, TS and products being part of the reference IRC in (a). The positions of the gradient and Hessian reference points along the reaction path that are calculated by `evb_kt_driver.x` are shown together with the energies of the IRC and both QMDFFs in (b). Finally, an Arrhenius plot of the resulting rate constants together with experimental and theoretical results from the literature is shown in (c). Here, BM1981 stands for Baulch, Montague (1981) [162], SS1988 means Sims, Smith (1988) [163], JS1989 refers to Jacobs, Smith (1989) [164] and WB1986 points at Wagner, Bair (1986) [161].

6.2.3   The $PH_3 + H \rightarrow PH_2 + H_2$ Reaction

This reaction plays an important role during the vapor deposition process in the production of P-doped Si-semiconductor materials [165]. Its (simple) mechanism is shown in fig. 6.3 (a).

In the theory paper of YU and SUN [165] (YS1999), the IRC of the reaction was optimized with the QCISD/6-311+G** level of theory. Based on this path, CVT/SCT calculations [25,37] of the rate constants were evaluated with the POLYRATE program by TRUHLAR *et al.* [10].

Due to the absence of analytical frequencies for QCISD, TS and IRC optimizations were redone with MP2/6-311+g(3df,3pd) [166,167] in this work. The energies of the path were again recalculated with the DLPNO-CCSD(T) method. The IRC is plotted together with the position of all RP-EVB points in part (b) of the figure.

The reaction has a symmetry factor of $\sigma_{E1}\sigma_{E2} = 3$ (due to the three hydrogens in the phosphine molecule). A temperature range of 200 to 500 K was calculated for optimal comparability to the experimental results. Due to the relatively low temperatures and the fact that a hydrogen is transferred in the reaction, all RPMD samplings were done with 16 beads.

If we look at the rate constant plot in fig. 6.3 (c), quite a good quality of the TREQ-RPMD rates can be seen. Their deviation to the experimental values (AC1997, LS1976) amounts to a factor of two to four, which is acceptable for reaction rates. The RPMD rates further seem of better quality than the theoretical ones of YS1999. In terms of Arrhenius parameters, the agreement is good as well (table 6.4), the values almost coincide exactly with the experimental ones of AC1997!

6.2.4   The $CH_3NC \rightarrow CH_3CN$ Reaction

This reaction is the first *unimolecular* process to be studied. It therefore served as a benchmark of the unimolecular rate calculation (eq. 3.21) implemented independently from the original RPMDrate code. It is one of the best known rearrangement processes in the literature and was studied theoretically already in the 1980s [170]. There, the reaction path was optimized with simple HF and a rather small basis.

Here, the IRC of the reaction was optimized with MP2/aug-cc-pVTZ, the results are shown in fig. 6.3 (a) and (b). If we look at the IRC energies, it can be seen that the potential energy barrier is much higher (180 kJ mol^{-1}) than of the bimolecular exchanges shown so far. The rate constant calculations were done for temperatures between 400 and 600 K, since no hydrogens are involved in the reaction, one RPMD bead (i.e., classical sampling) has been considered as sufficient for the samplings.

The resulting rate constants are plotted in part (c) of the figure. Both experimental and theoretical references are located quite exactly on the same line, the Arrhenius fit of the RPMD results is shifted roughly by a factor of five and is almost perfectly parallel. The Arrhenius parameters shown in table 6.4 confirm the visual impression: The activation energies are 160 kJ mol^{-1}. The exponential prefactor for the RPMD results is roughly a factor of three larger than the literature ones. Thus, the ability of EVB-QMDFF to calculate reasonable unimolecular rate constants has been proven.

6.2.5   The $CH_3Cl + Cl \rightarrow CH_2Cl + HCl$ Reaction

Chloromethanes are thought to play an important role in atmospheric chemistry [173]. In this section and the following, two variants of the same reaction are presented: The hydrogen abstraction of a chloride radical from a choloromethane molecule. Here, the chloromethane is CH_3Cl and in the next section it is CH_2Cl_2.

Both reactions were studied theoretically in the paper by XIAO and SUN (XS2002) [173]. They optimized reaction paths for different halomethanes with the BH&H-LYP-functional [174] and

(a) Mechanism of the reaction (reactants - TS - products)

(b) IRC with QMDFF energies and RP points

(c) Calculated and experimental rate constants
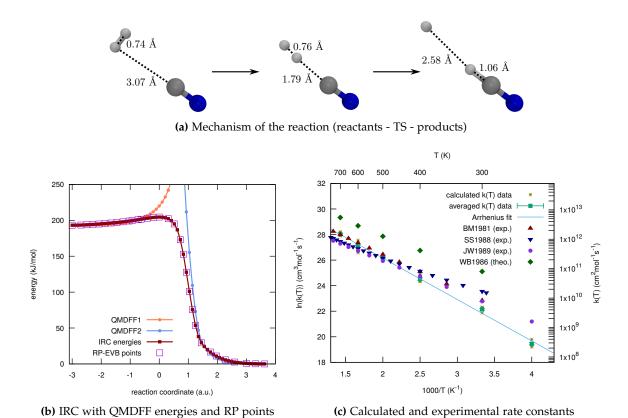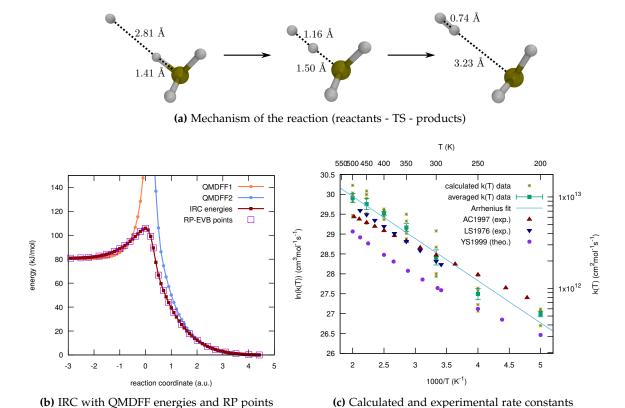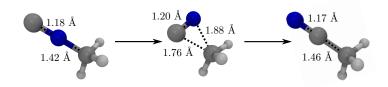
Figure 6.3: Summary of the *black-box* rate constant calculation for the $PH_3 + H \rightarrow PH_2 + H_2$ reaction. The reaction mechanism is illustrated by the structures of reactants, TS and products being part of the reference IRC in (a). The positions of the gradient and Hessian reference points along the reaction path that are calculated by `evb_kt_driver.x` are shown together with the energies of the IRC and both QMDFFs in (b). Finally, an Arrhenius plot of the resulting rate constants together with experimental and theoretical results from the literature is shown in (c). Here, LS stands for LEE, STIEF (1976) [168] and AC1997 means ARTHUR, COOPER (1997) [169].

(a) Mechanism of the reaction (reactants - TS - products)

(b) IRC with QMDFF energies and RP points

(c) Calculated and experimental rate constants
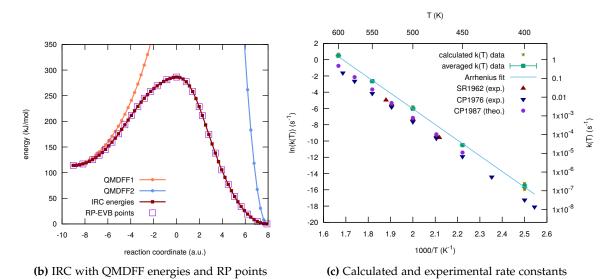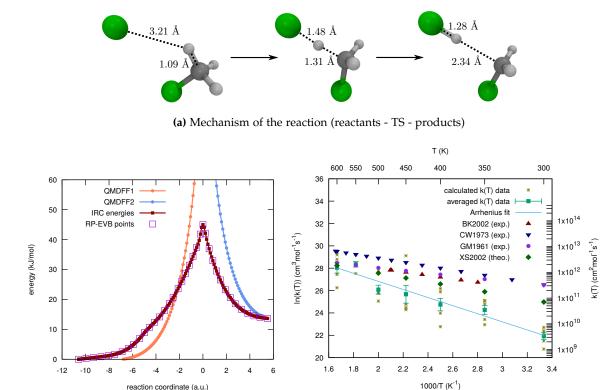
Figure 6.4: Summary of the *black-box* rate constant calculation for the $CH_3NC \rightarrow CH_3CN$ reaction. The reaction mechanism is illustrated by the structures of reactants, TS and products being part of the reference IRC in (a). The positions of the gradient and Hessian reference points along the reaction path that are calculated by `evb_kt_driver.x` are shown together with the energies of the IRC and both QMDFFs in (b). Finally, an Arrhenius plot of the resulting rate constants together with experimental and theoretical results from the literature is shown in (c). Here, SR1962 stands for SCHNEIDER, RABINOVITCH (1962) [171], CP1976 means COLLISTER, PRITCHARD (1976) [172] and CP1987 refers to CLARKSON, PRITCHARD (1987) [170].

(a) Mechanism of the reaction (reactants - TS - products)

(b) IRC with QMDFF energies and RP points

(c) Calculated and experimental rate constants

Figure 6.5: Summary of the *black-box* rate constant calculation for the $CH_3Cl + Cl \rightarrow CH_2Cl + HCl$ reaction. The reaction mechanism is illustrated by the structures of reactants, TS and products being part of the reference IRC in (a). The positions of the gradient and Hessian reference points along the reaction path that are calculated by `evb_kt_driver.x` are shown together with the energies of the IRC and both QMDFFs in (b). Finally, an Arrhenius plot of the resulting rate constants together with experimental and theoretical results from the literature is shown in (c). Here, GM1961 stands for GOLDFINGER, MARTENS (1961) [175], CW1973 means CLYNE, WALKER (1973) [176], BK2002 refers to BRYAKOV, KNYAZEV (2002) [177] and XS2002 means XU, SUN (2002) [173] .

calculated its energies with the QCISD(T) method. The rate constants of the different processes were calculated with the usual static CVT/SCT-method using POLYRATE. For the *black-box* calculations, the IRC was again optimized with MP2, now with the same basis set as used in the reference paper (6-311g(d,p)). The energies of the path were again recalculated with the DLPNO-CCSD(T) method. Structures and energies of the IRC are presented in fig. 6.5.

The rate constant calculations were done at temperatures from 300 to 600 K, 16 beads were used since significant quantum effects can be expected if a hydrogen atom is transferred; the reaction has a symmetry factor of three.

In part (c) of the figure the resulting rate constants are compared with two experimental papers and the CVT/SCT results of XS2002. The RPMD values are near the experimental ones for higher temperatures but show larger deviations from them for lower temperatures. Corresponding to this overestimated slope of the Arrhenius curve, the RPMD activation energy (30.1 kJ mol^{-1}, table 6.4) is much too high in comparison to that of experiments, which are between 6.6 and 14.9 kJ mol^{-1}. The same trend can be seen for the exponential prefactors. A possible reason for the deviations might be, e.g., an insufficient performance of the DLPNO-CCSD(T) energy correction method in reproducing the reaction barrier.
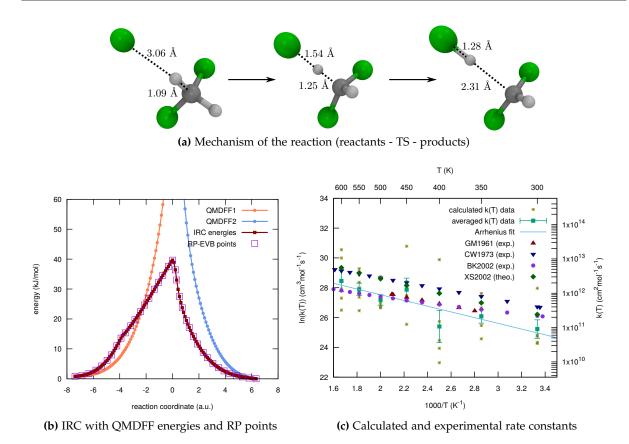
(a) Mechanism of the reaction (reactants - TS - products)

(b) IRC with QMDFF energies and RP points

(c) Calculated and experimental rate constants

Figure 6.6: Summary of the *black-box* rate constant calculation for the $CH_2Cl_2 + Cl \rightarrow CHCl_2 + HCl$ reaction. The reaction mechanism is illustrated by the structures of reactants, TS and products being part of the reference IRC in (a). The positions of the gradient and Hessian reference points along the reaction path that are calculated by `evb_kt_driver.x` are shown together with the energies of the IRC and both QMDFFs in (b). Finally, an Arrhenius plot of the resulting rate constants together with experimental and theoretical results from the literature is shown in (c). Here, GM1961 stands for GOLDFINGER, MARTENS (1961) [175], CW1973 means CLYNE, WALKER (1973) [176], BK2002 refers to BRYAKOV, KNYAZEV (2002) [177] and XS2002 links to XU, SUN (2002) [173].

6.2.6 The $CH_2Cl_2 + Cl \rightarrow CHCl_2 + HCl$ Reaction

This reaction is a small variation of the last one: one hydrogen in the chloromethane has been replaced by another chlorine atom. All calculation settings of reference and RPMD were the same as for the previous reaction. The symmetry factor is now two instead of three.

By looking at the results presented in fig. 6.6 an improvement of the RPMD quality with respect to the experiments in comparison to the $CH_3Cl + Cl$ system can be seen: The determined Arrhenius fit of the TREQ-RPMD rate constants coincides almost exactly with the rates of GM1961. The deviations to CW1972 and BK2002 are smaller than one order of magnitude for the whole investigated temperature range. The Arrhenius parameters show a similar trend (table 6.4): The RPMD ones are very similar to GM1961 and CW1973 (there with a larger deviation of preexponential factors). The BK2002 value of the activation energy again deviates substantially from the others.

If we do now the final comparison between the $CH_3Cl + Cl$ and $CH_2Cl_2 + Cl$ reactions, the general trend is reproduced correctly: The potential energy barrier expressed in part (b) of figs. 6.5-6.6 is higher for the $CH_3Cl + Cl$ reaction, which results in smaller rate constants and Arrhenius parameters for it. TREQ-RPMD is able to reproduce this trend, nevertheless its results deviate quite significantly for the $CH_3Cl + Cl$ reaction.

6.2.7   The SiH$_4$ + Cl → SiH$_3$ + HCl Reaction

Silanes are common precursors for the production of semiconductor devices [178]. Their reaction with radicals such as the chlorine radical are therefore of both theoretical and experimental interest.

PEI and LI (PL2004) have done parametric rate constant calculation for this reaction with the CVT/SCT method in POLYRATE. The reaction path was optimized with MP2/6-311+G(d), its energies were calculated with QCISD(T)//6-311+G(d,p) for the *dual-level* k(T) calculation approach. For the *black-box* calculation in this thesis, a slightly improved basis set was used for the IRC optimization (6.311+G(d,p)), its energies were calculated as usual with DLPNO-CCSD(T).

The results are shown in fig. 6.7 (a,b), a very low potential energy barrier (3.5 kJ mol^{-1}) can be seen, which is similar for the improved theory level. For the RPMD calculations between 300 and 600 K, 16 beads were used, the reaction has a symmetry factor of four. By looking at the calculated rate constants in part (c) it can be seen that the negative activation energy measured by experiment (DM1992) is reproduced by the RPMD calculation(-2.53 vs. -2.00 kJ mol^{-1} (table 6.4)), whereas the PL2004-theory erroneously predicts a small positive activation energy (0.93 kJ mol^{-1}). The absolute values of the RPMD rates deviate less than a factor of two from the experimental ones! Further, PL2004 reported non-Arrhenius behavior, whereas both RPMD and experimental rate constants are located on a straight line, thus indicating Arrhenius behavior, at least in the considered temperature range.

6.2.8   The GeH$_4$ + H → GeH$_3$ + H$_2$ Reaction

This reaction shows some similarity to the previous one and is also relevant in the context of semiconductor materials production. ZHANG and GU (ZG2002) [180] calculated rate constants as usual with the CVT/SCT method in POLYRATE based on a reaction path optimized with MP2/6-311G(2df,p) and energies corrected with the G2MP2 composite method [12].

For this thesis, the identical procedure as for the previous reaction was undergone: MP2/6-311+G(d,p) for the IRC optimization and DLPNO-CCSD(T) for the subsequent energy calculation. The results are shown in fig. 6.8.

The RPMD calculations were started with identical settings as well: 16 beads for the temperature range between 300 and 600 K and a symmetry factor of 4. By looking at the resulting RPMD rate constants in part (c), their quality is worse than for the SiH$_4$ + Cl reaction. They deviate approximately one order of magnitude from both experimental studies (NS1993 and AM1997), the rates of ZG2002 are located in between RPMD and experiment. The Arrhenius parameters in table 6.4 reveal that the activation energy obtained from RPMD is approximately twice as high as for the experiments, whereas the ZG2002 theory obtains a value which is much too small.

6.2.9   The C$_2$H$_4$ + H → C$_2$H$_5$ Reaction

This attachment reaction plays an important role, e.g., in the production of acetylene from methane [183]. It was studied theoretically quite thoroughly [183–187], however, no rate constants were calculated so far in the temperature range for which enough experimental data is available (300-600 K). Therefore, only comparisons to experiments are made here.

Early theory calculations of the reaction path (e.g., SOSA and SCHLEGEL in 1986 [187]) suggest that simple HF is sufficient to get at least a qualitatively correct reproduction. For the *black-box* calculation, the usual combination DLPNO-CCSD(T)/cc-pVTZ//MP2/6-311g(d,p) was used. The results are shown in fig. 6.9.

For the RPMD calculations, the newly implemented reaction type `merging` was needed (and detected automatically by `evb_kt_driver.x`), since only one bond is built but none is broken during the process. 16 RPMD beads were used for the calculated temperature range of 300-600 K, the

(a) Mechanism of the reaction (reactants - TS - products)

(b) IRC with QMDFF energies and RP points

(c) Calculated and experimental rate constants

Figure 6.7: Summary of the *black-box* rate constant calculation for the SiH$_4$ + Cl → SiH$_3$ + HCl reaction. The reaction mechanism is illustrated by the structures of reactants, TS and products being part of the reference IRC in (a). The positions of the gradient and Hessian reference points along the reaction path that are calculated by `evb_kt_driver.x` are shown together with the energies of the IRC and both QMDFFs in (b). Finally, an Arrhenius plot of the resulting rate constants together with experimental and theoretical results from the literature is shown in (c). Here, DM1992 stands for DING, MARSHALL (1992) [179] and PL2004 refers to PEI, LI (2004) [178].

(a) Mechanism of the reaction (reactants - TS - products)

(b) IRC with QMDFF energies and RP points

(c) Calculated and experimental rate constants

Figure 6.8: Summary of the *black-box* rate constant calculation for the $GeH_4 + H \rightarrow GeH_3 + H_2$ reaction. The reaction mechanism is illustrated by the structures of reactants, TS and products being part of the reference IRC in (a). The positions of the gradient and Hessian reference points along the reaction path that are calculated by `evb_kt_driver.x` are shown together with the energies of the IRC and both QMDFFs in (b). Finally, an Arrhenius plot of the resulting rate constants together with experimental and theoretical results from the literature is shown in (c). Here, NS1993 stands for Nava, Stief (1993) [181], AM1997 means Arthur, Miles (1997) [182] and ZG2002 refers to Zhang, Gu (2002) [180].

(a) Mechanism of the reaction (reactants - TS - products)

(b) IRC with QMDFF energies and RP points
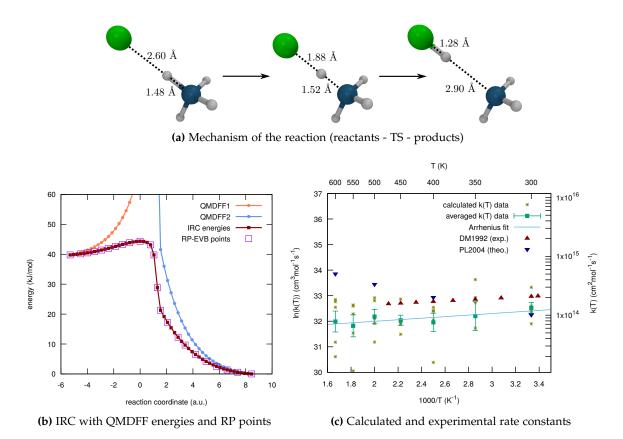

(c) Calculated and experimental rate constants
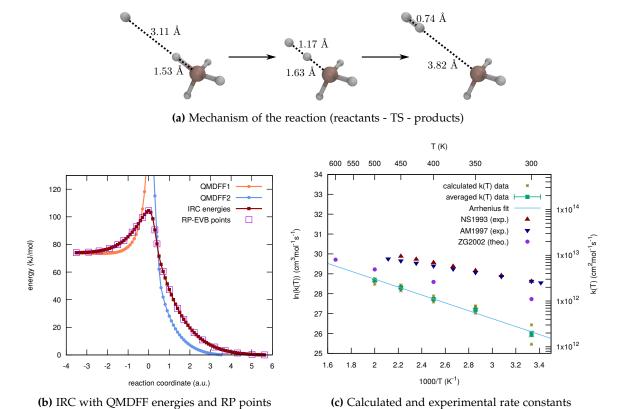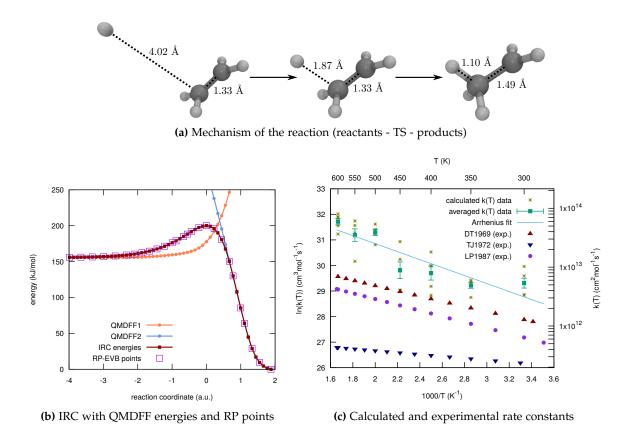
Figure 6.9: Summary of the *black-box* rate constant calculation for the $C_2H_4 + H \rightarrow C_2H_5$ reaction. The reaction mechanism is illustrated by the structures of reactants, TS and products being part of the reference IRC in (a). The positions of the gradient and Hessian reference points along the reaction path that are calculated by `evb_kt_driver.x` are shown together with the energies of the IRC and both QMDFFs in (b). Finally, an Arrhenius plot of the resulting rate constants together with experimental and theoretical results from the literature is shown in (c). Here, DT1969 stands for DODONOV, TALROZE (1969) [188], TJ1972 means TENG, JONES (1972) [189] and LP1987 refers to LIGHTFOOD, PILING 1987 [190].

symmetry factor of the reaction is two (both carbon atoms). With this, bimolecular rate constants were calculated and fitted to get the Arrhenius parameters, the results are shown in part (c) of the figure. The three experimental studies differ quite largely from each other, TJ1972 obtained much lower rates than the other two. The RPMD rates are estimated too large. By looking at the Arrhenius parameters (table 6.4), we can see that LP1987 coincides quite well with RPMD at least for the Ea-values. Both parameters of TJ1972 are much smaller than of the others.

6.2.10 The $CH_3OH + Cl \rightarrow CH_2OH + HCl$ Reaction

This reaction of methanol with a chlorine radical is believed to play an important role during the combustion of methanol [191]. It is one of two possible reaction pathways (in the other, the hydroxyl hydrogen is abstracted). JODKOWSKI and RAYES (JR1998) [191] optimized the IRC of the reaction with different theory levels (HF, MP2, MP4) and calculated the rate constants of the process with a method based on state sums for different possible reaction channels developed by themselves [191].

For the *black-box* method, the DLPNO-CCSD(T)/cc-pVTZ//MP2/6-311g(d,p) combination of methods was again used to get the needed QM reference information (fig. 6.10).
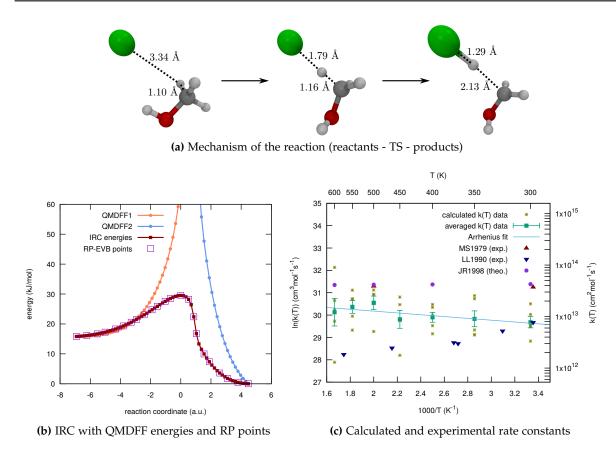
(a) Mechanism of the reaction (reactants - TS - products)

(b) IRC with QMDFF energies and RP points

(c) Calculated and experimental rate constants

Figure 6.10: Summary of the *black-box* rate constant calculation for the $CH_3OH + Cl \rightarrow CH_2OH + HCl$ reaction. The reaction mechanism is illustrated by the structures of reactants, TS and products being part of the reference IRC in (a). The positions of the gradient and Hessian reference points along the reaction path that are calculated by `evb_kt_driver.x` are shown together with the energies of the IRC and both QMDFFs in (b). Finally, an Arrhenius plot of the resulting rate constants together with experimental and theoretical results from the literature is shown in (c). Here, MS1979 stands for MICHAEL, STIEF (1979) [192], LL1990 means LIGHTFOOD, LESCLEAUX (1990) [193] and JR1998 refers to JODKOWSKI, RAYEZ (1998) [191].

The process is a usual bimolecular exchange of hydrogen, therefore the rate constants were calculated with 16 beads at all temperatures between 300 and 600 K, with a symmetry factor of three. When we look at the results in part (c) of the figure, we see that the absolute values of the RPMD rates are located between both experimental studies (MS1979, LL1990), however, the temperature dependence is wrong: The RPMD rate constants raise with temperature, whereas the experimental ones suggest an inverted behavior, corresponding to a negative activation energy. This is confirmed from the obtained Arrhenius parameters (table 6.4). The absolute deviations of activation energies between RPMD and LL1990 and JR1998 (theory) are nevertheless within chemical accuracy, the exponential prefactors are very similar for all processes, therefore a satisfying quality of TREQ-RPMD can be stated for this example.

6.2.11 The $C_2H_6 \rightarrow C_2H_4 + H_2$ Reaction

The *elimination* of hydrogen from ethane leading to ethylene is well known to each chemist. Since this is a *unimolecular* process, the example provides a second benchmark for the newly implemented unimolecular option in the `rpmd.x` program. Interestingly, only a few experimental studies exist for this reaction. I was not able to extract useful rate data from them at all (they differ many

orders of magnitude from the RPMD and the theoretical reference). It is assumed that the gaseous environment plays a huge role for this process which takes place at temperatures well beyond 1000 K.

GE and FOX (GF2010) studied this process as part of a larger investigation of the pyrolysis of methyltrichlorosilane in the gas phase [186] with CVT and neglection of tunneling effects. They optimized all reaction paths with MP2/aug-cc-pVDZ [158] and calculated CCSD(T)/aug-cc-pVDZ energies on them. For the *black-box* calculations, the DLPNO-CCSD(T)/aug-cc-pVTZ//MP2/aug-cc-pVDZ combination of methods was used, the resulting path is shown in fig. 6.11. The barrier of 550 kJ mol^{-1} is the largest of all examples presented here, indicating that high temperatures are needed to obtain measurable reaction progress. This conforms to our intuition that eliminiations are only taking place at very high temperatures.

GF2010 calculated all their rate constants at temperatures between 1000 and 2000 K. Therefore, the RPMD samplings were done between 800 and 2000 K. These are the highest temperatures for which the `rpmd.x` program was used so far. In order to avoid complications with the dynamics, the time step was reduced to 0.1 fs. Since tunneling plays no role at these temperatures, one RPMD bead was used, the symmetry factor is nine[4]. The resulting RPMD rates are plotted together with GF2010 in part (c) of the figure. More than 20 orders of magnitudes are spanned by the resulting rates between 800 and 2000 K, which is due to the large activation barrier. The five single RPMD k(T) values are almost merged together at the average value, since their variance is much lower than the average change with temperature. The RPMD rates are approximately one order of magnitude larger than the values of GF2010. If we compare the Arrhenius parameters, activation energies of 464.7 and 517.1 kJ mol^{-1} were obtained. The deviation is quite high in absolute numbers, but seems to be acceptable if we see it in relation.

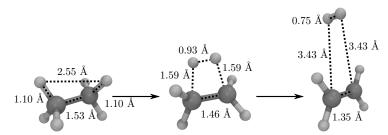### 6.2.12   The CH_4 + CH_3 → CH_3 + CH_4 Reaction

This symmetric exchange of hydrogen between methane and methylene plays an important role during the combustion process of hydrocarbons [194]. KUNGWAN and TRONG (KT2005) studied it theoretically as part of a larger investigation on similar hydrogen exchange reactions between hydrocarbons [194]. They optimized the reaction path with the BH&H-LYP DFT functional [174] and calculated CCSD(T) energies on it. The rate constants were determined with the CVT/SCT method.

For the *black-box* calculations, the QM reference was again DLPNO-CCSD(T)/aug-cc-pVTZ// MP2/aug-cc-pVDZ. The resulting IRC is shown in fig. 6.12. 16 RPMD beads were used for the rate constant calculations between 300 and 600 K, the symmetry factor of the reaction is four (each of the CH_4 hydrogens could be abstracted by the CH_3 radical.
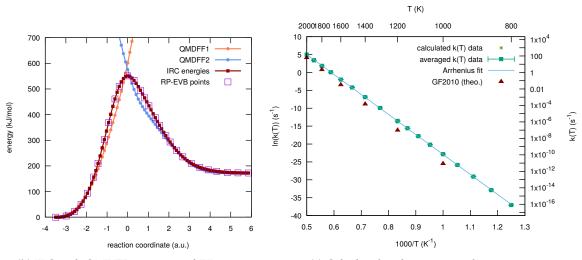
If we look at the resulting rate constants in part (c) of the figure, a huge shift of our RPMD values towards both theoretical and experimental reference becomes obvious. The RPMD rate constants are more than five orders of magnitude too large! The slope of the resulting Arrhenius plot fits the references quite well (54 against 60-61 kJ mol^{-1}) but the exponential prefactor (i.e., the y-intercept of the plot) is three orders of magnitude larger than of the references.

This example reaction gave the worst results of all, at least with respect to the absolute derivation of single RPMD rate constants from the reference. Since RPMD worked well for almost all other reactions it is assumed that the QM reference is somewhat improper for this example. We could redo the calculations with, e.g., another energy correction method but this chapter shall serve as a realistic benchmark of the *black-box* k(T) calculation procedure such that only one try was taken for

---

4 Each carbon atom has three hydrogens attached, the possible eliminiations are: $H_{1,1}$-$H_{2,1}$, $H_{1,1}$-$H_{2,2}$, $H_{1,1}$-$H_{2,3}$, $H_{1,2}$-$H_{2,1}$, $H_{1,2}$-$H_{2,2}$, $H_{1,2}$-$H_{2,3}$, $H_{1,3}$-$H_{2,1}$, $H_{1,3}$-$H_{2,2}$ $H_{1,3}$-$H_{2,3}$. These are nine possible equivalent eliminiation reactions, leading to a symmetry factor of nine for the total reaction.

(a) Mechanism of the reaction (reactants - TS - products)

(b) IRC with QMDFF energies and RP points

(c) Calculated and experimental rate constants

Figure 6.11: Summary of the *black-box* rate constant calculation for the $C_2H_6 \rightarrow C_2H_4 + H_2$ reaction. The reaction mechanism is illustrated by the structures of reactants, TS and products being part of the reference IRC in (a). The positions of the gradient and Hessian reference points along the reaction path that are calculated by `evb_kt_driver.x` are shown together with the energies of the IRC and both QMDFFs in (b). Finally, an Arrhenius plot of the resulting rate constants together with experimental and theoretical results from the literature is shown in (c). Here, GF2010 refers to GE, FOX (2010) [186].
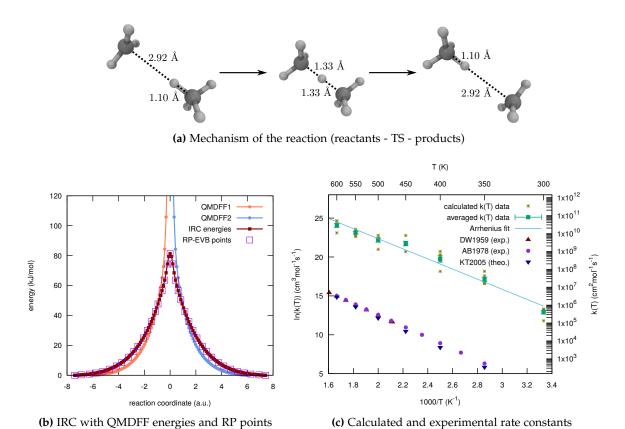
(a) Mechanism of the reaction (reactants - TS - products)

(b) IRC with QMDFF energies and RP points

(c) Calculated and experimental rate constants

Figure 6.12: Summary of the *black-box* rate constant calculation for the $CH_4OH + CH_3 \rightarrow CH_3 + CH_4$ reaction. The reaction mechanism is illustrated by the structures of reactants, TS and products being part of the reference IRC in (a). The positions of the gradient and Hessian reference points along the reaction path that are calculated by `evb_kt_driver.x` are shown together with the energies of the IRC and both QMDFFs in (b). Finally, an Arrhenius plot of the resulting rate constants together with experimental and theoretical results from the literature is shown in (c). Here, DW1959 stands for DAINTON, WILKINSON (1959) [195], AB1978 refers to ARTHUR, BELL (1978) [196] and KT2005 refers to KUNGWAN, TRONG (2005) [194].

each system and no variation of the reference or other settings was done until we would "move towards" the experiment.

6.2.13   The $C_2H_6 + NH \rightarrow C_2H_5 + H_2N$ Reaction

This process is relevant in the combustion mechanism of energetic materials [197]. XU and SUN (XS2002) [197] have studied it with the CVT/SCT method as implemented in POLYRATE. They optimized the reaction path at different levels of theory and basis set sizes (HF, MP2, Pople basis sets [166, 167]).

For the *black-box* procedure the popular *dual-level* approach with DLPNO-CCSD(T)/cc-pVTZ// MP2/6-311g(d,p) was used again. The resulting reaction path is plotted in fig. 6.13. On the related TREQ PES, RPMD samplings were done with 16 beads for temperatures between 300 and 600 K, whereas the symmetry factor was chosen to be six (each hydrogen of the ethane).

The results are shown in part (c) of the figure together with the theoretical results of XS2002. It can be seen that both sets are located quite exactly on the same linear curve, indicating a very good agreement between both. This impression is confirmed if we look at the Arrhenius parameters (table 6.4). The activation energies of RPMD calculations and theoretical reference are almost identical; the preexponential factors deviate by roughly one order of magnitude. In
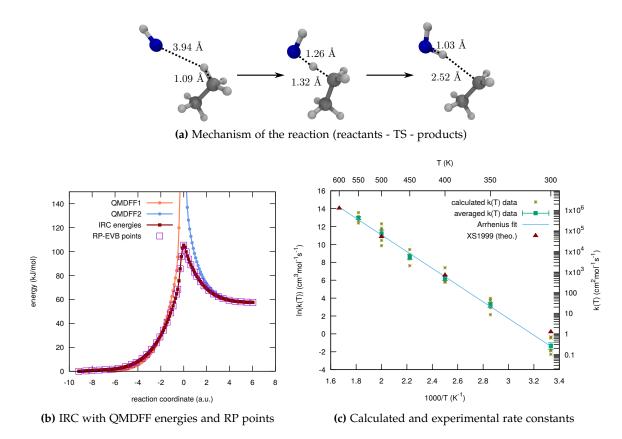
(a) Mechanism of the reaction (reactants - TS - products)

(b) IRC with QMDFF energies and RP points

(c) Calculated and experimental rate constants

Figure 6.13: Summary of the *black-box* rate constant calculation for the $C_2H_6 + NH \rightarrow C_2H_5 + H_2N$ reaction. The reaction mechanism is illustrated by the structures of reactants, TS and products being part of the reference IRC in (a). The positions of the gradient and Hessian reference points along the reaction path that are calculated by `evb_kt_driver.x` are shown together with the energies of the IRC and both QMDFFs in (b). Finally, an Arrhenius plot of the resulting rate constants together with experimental and theoretical results from the literature is shown in (c). Here, XS1999 refers to XU, SUN (1999) [197].

the table an experimental reference (ROHRIG, WAGNER 1994 [198]) is added. They measured rates between 1010 and 1170 K, nevertheless the activation barrier fits both theoretical ones quite well. The preexponential factor of the experiment is one order of magnitude smaller than the RPMD one and two orders smaller than XS1999, indicating that RPMD performs better with respect to the experiment (if we assume that near-ideal Arrhenius behavior is preserved along the whole temperature range).

6.2.14 The $CF_3O + CH_4 \rightarrow CF_3OH + CH_3$ Reaction

The CF_3O-molecule has been proposed as eco-friendlier alternative to cholorocarbons since it seems to have less impact on ozone layer destruction and the greenhouse effect [199]. JING and SUN (JS2005) [199] have studied the kinetics of this reaction with CVT/SCT. They optimized the reaction path with both B3LYP [200, 201] and MP2; energies were then calculated with the QCISD method.

Due to the larger number of heavy atoms in this system, DLPNO-CCSD(T)/cc-pVTZ//B3LYP/6-311g(d,p) was used as black-box QM method (i.e., DFT instead of MP2 for the IRC optimization and frequencies). The optimized reaction path is shown in fig. 6.14.

RPMD rate constant calculations were done at 300-600 K with 16 RPMD beads each, the symmetry factor is four. The results are plotted together with the CVT/SCT values of JS2005 and
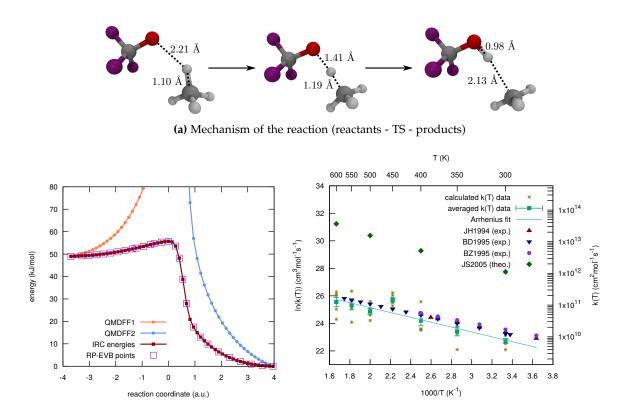
(a) Mechanism of the reaction (reactants - TS - products)

(b) IRC with QMDFF energies and RP points

(c) Calculated and experimental rate constants

Figure 6.14: Summary of the *black-box* rate constant calculation for the $CF_3O + CH_4 \rightarrow CF_3OH + CH_3$ reaction. The reaction mechanism is illustrated by the structures of reactants, TS and products being part of the reference IRC in (a). The positions of the gradient and Hessian reference points along the reaction path that are calculated by `evb_kt_driver.x` are shown together with the energies of the IRC and both QMDFFs in (b). Finally, an Arrhenius plot of the resulting rate constants together with experimental and theoretical results from the literature is shown in (c). Here, JH1994 stands for JENSEN, HOWARD (1994) [202], BD1995 means BOURBON, DEVOLDER (1995) [203] and BZ1995 refers to BEDNAREK, ZELLNER (1995) [204].

three experimental studies in part (c) of the figure. We can see that the rate constants calculated by JS2005 deviate heavily from the experiments, whereas our RPMD results match the experiments quite nicely, the deviations are less than half an order of magnitude. The Arrhenius parameters affirm these findings (table 6.4): The RPMD parameters barely deviate from the three experiments, whereas both activation barrier and preexponential factor of JS2005 are much too low.

6.2.15   The Bicyclo[2.2.1]hept-2-ene $\rightarrow$ C_2H_4 + Cyclopentadiene Reaction

The final example reaction is the *cycloreversion* of Norbornene (Bicyclo[2.2.1]hept-2-ene) to C_2H_4 and Cyclopentadiene. This reaction was one of the examples presented in the first EVB-QMDFF paper by HARTKE and *Grimme* [16]. There it was shown that the simple energy-gap coupling term is able to reproduce the reference energies along the reaction path with good quality. I had deepened the investigation by performing two-dimensional scans in order to look at the quality of dE-EVB offside the reaction path (see supporting information, section 11.6.1).

We now want to go "back to the roots" and calculate the rate constant for the cycloreversion. Since the *black-box* approach uses TREQ as default PES description, it is used instead of energy-gap coupling. The IRC was optimized and corrected with the DLPNO-CCSD(T)/cc-pVTZ//PBE0/def2-
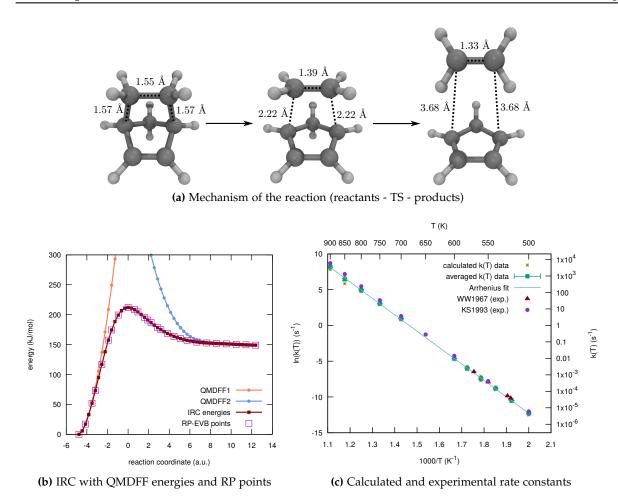
(a) Mechanism of the reaction (reactants - TS - products)

(b) IRC with QMDFF energies and RP points

(c) Calculated and experimental rate constants

Figure 6.15: Summary of the *black box* rate constant calculation for the Bicyclo[2.2.1]hept-2-ene (Norbornene) $\rightarrow$ C_2H_4 + Cyclopentadiene reaction. The reaction mechanism is illustrated by the structures of reactants, TS and products being part of the reference IRC in (a). The positions of the gradient and Hessian reference points along the reaction path that are calculated by `evb_kt_driver.x` are shown together with the energies of the IRC and both QMDFFs in (b). Finally, an Arrhenius plot of the resulting rate constants together with experimental and theoretical results from the literature is shown in (c). Here, WW1976 means WALSH, WELLS (1976) [208] and KS1978 stands for KIEFER, SUNDERAM (1978) [209].

SVP(D3 empirical dispersion) [205–207] combination of methods, DFT was used due to the large size of the system. The resulting path is shown in fig. 6.15.

For the RPMD calculations, the unimolecular `cycloreversion` mechanism was determined automatically by the `evb_kt_driver.x` program. Due to the size of the system, the automated determination of internal coordinates consisting of bond lengths and angles needed a slight manual correction, where a handful of dihedrals located in the aromatic ring were added. The rates were calculated between 500 and 900 K, with one RPMD bead and a symmetry factor of one. When we look at the results presented in part (c) of the figure, TREQ-RPMD performs quite well. The deviation between experimental and calculated rate constants is less than a factor of 3 to 4 for the whole temperature range, in spite of the heavy temperature dependence of the rates. The Arrhenius parameters plotted in table 6.4 are also quite encouraging. The RPMD activation energy and the preexponential factor are almost exactly in the middle of both experimental results. Unfortunately, no other theoretical rate constant calculation has been published so far for this system.

6.3   Evaluation and Summary

We have gone through fifteen different examples arbitrarily chosen from the literature in quite large detail. This was tedious but thoroughly revealed the strengths and weaknesses of the TREQ-RPMD *black-box* method. In order to make a final overview, the Arrhenius parameters of all fifteen reactions are listed together with the literature values for comparison in table 6.4.

At first it can be noticed that the Arrhenius parameters of different literature studies often deviate quite significantly from each other (e.g., for the $CH_3Cl + Cl$ reaction) which makes it hard to judge what the "true" parameters are that we want to reproduce. With this uncertainty in mind, our method is competitive in almost all cases (apart from the $CH_3Cl + Cl$ and $CH_4 + CH_3$ reactions) where its deviation from the average experimental values it not larger than the deviations between the single experimental references. In other cases where all experiments coincide quite well TREQ-RPMD performs very well ($PH_3 + H$, CH_3NC, $CF_3O + CH_4$) and easily within chemical accuracy.

This first benchmark showed that the TREQ-RPMD *black-box* method as implemented in the `evb_kt_driver.x` program is promising but might need further tests and, e.g., applications to larger reaction networks in order to show its full capability (and possible weaknesses that we might need to eliminate, either in the TREQ construction or the *black-box* algorithm).

Table 6.4: Comparison of Arrhenius parameters resulting from TREQ-RPMD calculations as well as experimental and theoretical references from the literature for the 15 reactions presented in section 6.2. For each Arrhenius plot, activation energies (*Ea*) and exponential prefactors *A* are listed. 1(-14) means $1 \cdot 10^{-14}$. The literature values are referenced with the names of first and last authors and the year of publication, respectively.

Reference	*Ea* (kJ mol^{-1})	*A*
$I_2 + H \rightarrow HI + I$		
TREQ-RPMD	-4.00	9.64(-11)
Lorenz, Zellner 1979 [159]	0.17	6.59(-10)
Canneaux, Cantrel 2010[a] [157]	-4.80	5.52(-11)
$PH_3 + H \rightarrow PH_2 + H_2$		
TREQ-RPMD	8.81	1.40(-10)
Lee, Stief 1976 [168]	6.14	4.52(-11)
Arthur, Cooper 1997 [169]	8.73	1.09(-10)
Yu, Sun 1999[a] [165]	7.31	1.18(-11)
$CN + H_2 \rightarrow HCN + H$		
TREQ-RPMD	26.95	2.48(-10)
Baulch, Montague 1981 [162]	22.45	1.13(-10)
Sims, Smith 1988 [163]	11.14	2.41(-12)
Jacobs, Smith 1989 [164]	19.71	3.49(-11)
Wagner, Bair 1986[a] [161]	9.40	5.65(-12)
$CH_3NC \rightarrow CH_3CN$		
TREQ-RPMD	160.18	2.13(-10)
Schneider, Rabinovitch 1962 [171]	160.00	6.61(-11)
Collister, Pritchard 1976 [172]	160.00	3.72(-11)
Clarkson, Pritchard 1987[a] [170]	160.00	6.16(-11)
$CH_3Cl + Cl \rightarrow CH_2Cl + HCl$		
TREQ-RPMD	30.10	1.03(-09)
Goldfinger, Martens 1961 [175]	12.89	5.52(-11)
Clyne, Walker 1973 [176]	14.88	2.13(-10)
Bryakov, Knyazev 2002 [177]	6.61	7.56(-12)

Xu, Sun 2002[a] [173]	16.21	7.71(-11)
$CH_2Cl_2 + Cl \rightarrow CHCl_2 + HCl$		
TREQ-RPMD	15.95	6.96(-11)
Goldfinger, Martens 1961 [175]	13.05	4.17(-11)
Clyne, Walker 1973 [176]	12.06	6.45(-13)
Bryakov, Knyazev 2002 [177]	2.99	1.20(-12)
Xu, Sun 2002[a] [173]	6.79	5.96(-12)
$SiH_4 + Cl \rightarrow SiH_3 + HCl$		
TREQ-RPMD	-2.53	7.11(-11)
Ding, Marshall 1992 [179]	-2.00	1.56(-10)
Pei, Li 2004[a] [178]	0.93	2.41(-10)
$GeH_4 + H \rightarrow GeH_3 + H_2$		
TREQ-RPMD	16.51	2.64(-10)
Nava, Stief 1993 [181]	9.40	4.38(-12)
Arthur, Miles 1997 [182]	7.31	8.90(-11)
Zhang, Gu 2002[a] [180]	2.44	4.79(-12)
$C_2H_4 + H \rightarrow C_2H_5$		
TREQ-RPMD	12.99	9.47(-10)
Dodonov, Talroze 1969 [188]	6.69	3.11(-11)
Teng, Jones 1972 [189]	3.05	1.31(-12)
Lightfood, Piling 1987 [190]	9.40	4.57(-11)
$CH_3OH + Cl \rightarrow CH_2OH + HCl$		
TREQ-RPMD	3.37	4.77(-11)
Michael, Stief 1979 [192]	-7.38	6.33(-11)
Lightfood, Lescleaux 1990 [193]	0.27	6.93(-11)
Jodkowski, Rayez 1998[a] [191]	-0.19	6.60(-11)
$C_2H_6 \rightarrow C_2H_4 + H_2$		
TREQ-RPMD	464.67	3.46(-10)
Ge, Fox 2010[a] [186]	517.14	7.71(-09)
$CH_4 + CH_3 \rightarrow CH_3 + CH_4$		
TREQ-RPMD	54.09	3.78(-09)
Dainton, Wilkinson 1959 [195]	61.28	1.12(-12)
Arthur, Bell 1978 [196]	60.70	1.05(-12)
Kungwan, Trong 2005[a] [194]	61.10	7.95(-13)
$C_2H_6 + NH \rightarrow C_2H_5 + H_2N$		
TREQ-RPMD	77.65	1.36(-11)
Rohrig, Wagner 1994 [198]	70.01	1.16(-10)
Xu, Sun 1999[a] [197]	79.00	1.47(-12)
$CF_3O + CH_4 \rightarrow CF_3OH + CH_3$		
TREQ-RPMD	14.70	4.73(-12)
Jensen, Howard 1994 [202]	12.22	3.11(-12)
Bourbon, Devolder 1995 [203]	13.39	4.48(-12)
Bednarek, Zellner 1995 [204]	11.89	3.30(-12)
Jing, Sun[a] 2008 [199]	5.12	1.41(-11)
Bicyclo[2.2.1]hept-2-ene $\rightarrow C_2H_4$ + Cyclopentadiene		
TREQ-RPMD	190.75	6.50(-10)
Walsh, Wells 1976 [208]	186.00	3.02(-10)
Kiefer, Sunderam 1978 [209]	194.00	1.74(-09)

[a]: The Arrhenius parameters were calculated with theoretical methods (TST and/or its improvements).

CHAPTER

7

Covalent Mechanochemistry

This chapter constitutes a little excursion beyond the calculation of rate constants discussed so far. It is well known that chemical reactions can be initiated by several forms of energy, e.g., thermal, electric or photonic. Another source is *mechanical force* applied to the molecule, treated within the field of *mechanochemistry*. Its theoretical description is one of the research topics of our workgroup. The PhD thesis of MÜLLER [210] examined, e.g., mechanochemical simulations on disulfides, which were described by the ReaxFF force field.

Since many mechanochemical processes involve the breaking of single covalent bonds constituting the weakest point within a molecule, they can be described well with a *single QMDFF*. We have learned (section 2.3) that QMDFF is a *semireactive* force field that is able to describe bond dissociations with reasonable quality yet is unable to describe the formation of new bonds. In contrast to thermal reaction processes presented so far mechanochemical reactions usually do not involve formation of new bonds (at least not directly after the *rupture event*). A molecule (called *mechanophore*) is torn in two parts, either by ultrasound or by an *atomic force microscope* (AFM). After the breaking event, the parts are usually pulled away from each other, unable to perform possible rebindings.

Therefore, a large part of covalent mechanochemistry can be described well with QMDFF. However, there are exceptions: QMDFF is parametrized to model the dissociation of single isolated bonds correctly but it is unable to describe, e.g., cycloreversions, where two or more electronically dependent bonds are broken simultaneously. For such processes, EVB-QMDFF is needed. This chapter constitutes a small but nevertheless noticeable novelty in computational chemistry: to my knowledge, no mechanochemical processes were studied with RPMD, i.e., with real-time dynamical inclusion of quantum chemical effects, so far. It will be shown below that quantum effects modeled by RPMD have a noticeable effect on rupture forces at least for very low temperatures.

In section 7.1 a short summary of mechanochemical theory is given in order to understand its peculiarities. The simulation of mechanochemical processes was possible due to some minor modifications in the EVB-QMDFF program code, these are described in section 7.2. A first benchmark of mechanochemical simulations based on QMDFF is given in section 7.3, where rupture forces of different covalent bonds are determined and compared to literature values. A broader view on more realistic applications of the methodology was tried in section 7.4, where three examples are investigated with some detail. Finally, a connection between mechanical and thermal activation is made in section 7.5: There, rate constants for bond dissociation processes are calculated with the usual TREQ-RPMD *black-box* method but with addition of mechanochemical bias potentials. Their influence on free energy surfaces, rates and Arrhenius parameters is revealed.
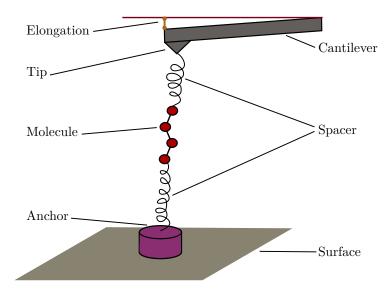
Figure 7.1: Illustration of an AFM experiment. A molecule to be studied is clipped between a pair of suitable spacer molecules. One is attached to a surface across an anchor molecule, the other is bonded to a tip belonging to the cantilever of the measurement apparatus. The cantilever behaves like a spring and gets elongated from the molecule-string below it. The force acting on the molecule can be calculated from the measured elongation of the cantilever.

7.1 Theoretical Background

Since mechanochemistry is not the central topic of this thesis but rather another example for the application of (EVB-)QMDFF-RPMD, only parts of its theory needed for the understanding of the shown studies are summarized here. A much more detailed discussion of it can be found in the PhD thesis by MÜLLER [210] or reviews of the topic [211, 212].

A mechanochemical trajectory describes the time-evolution of a system under influence of an external force attached to it. The possible origins of this force are manifold: They might be a result of milling, compactifying or drawing of a bulk material, or – to be less rough – of applying ultrasound. All those methods are quite hard to study experimentally in molecular detail, since we cannot look at single molecules of a bulk that is milled or compactified.

The origin of theoretical mechanochemistry was essentially the introduction of the AFM in 1986, which made it possible to stretch single molecules and detect what happens in them [213]. This experiment is shown schematically in fig. 7.1.

The molecule of interest is attached in a complicated sequence of elements, however, the underlying concept is quite easy. A force is applied via a *cantilever* that is gradually moved up. The applied force can be measured similar to traditional force measurements of "macroscopic" setups: The elongation of the cantilever from its ideal position is measured with laser optics; by knowing its force constant the acting force is obtained via *Hooke's law*.

All theoretical models presented in this chapter are based on the AFM experiment. Basically, two force vectors with identical lengths are attached on atoms located in opposite parts of the molecule. What happens is a modification of the molecule's Hamiltonian:

$$H(\mathbf{x}, t, \mathbf{F}) = H(\mathbf{x}, t) + V(\mathbf{x}, t, \mathbf{F}), \tag{7.1}$$

where $\mathbf{x}$ are the cartesian coordinates of the system, t the time and $\mathbf{F}$ a vector of force constants on which the additional potential depends[1]. Another example of such modifications of the

---

1 In the examples presented below, both time-independent and time-dependent forces are applied to molecules.

(a) Morse potential and force   **(b)** Force applied to Morse potential
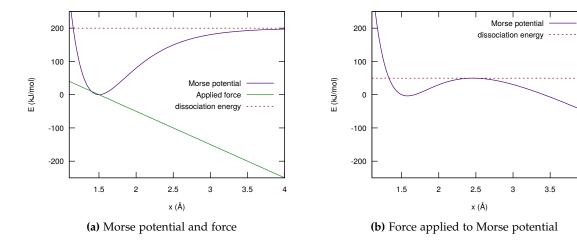
Figure 7.2: Illustration of the effect of an applied force to a chemical bond, represented by a Morse potential. The parameters of eq. 7.2 used for the plots are: D_e=200 kJ mol^{-1}, x_0=1.5 Å, ζ=2 Å^{-1}, F=100 kJ mol^{-1} Å^{-1}). The usual shape of the Morse potential is plotted together with the linear decaying potential resulting from the $F(x - x_0)$ term in (a). If the potential arising from the attached force is added to the Morse potential, its shape alters. Instead of an asymptotic dissociation limit a local potential energy maximum at $x \approx 2.5$ appears and the dissociation energy goes down to less than 50 kJ mol^{-1}, the bond becomes weaker (b).

Hamiltonian is the umbrella sampling method being base for the k(T) calculation method used throughout this thesis (section 2.1.3).

With this it can be said that all what mechanochemical experiments do is to alter the Hamiltonian (or: the potential energy surface) of the mechanophore, leading to different behaviors of it. If we look at the *free energy* surface of a system instead, the analogy of activation between mechanochemistry and usual thermochemical processes becomes apparent: In the case of mechanochemistry the *potential energy*, i.e., the inner energy contribution for the molecule is changed, whereas the *entropy* contribution of the inner energy is changed in the case of thermochemical processes by means of heating.

If we look at AFM experiments, the applied force usually leads to breaking of single bonds within a clamped molecular chain. Chemical bonds can be modeled with Morse potentials. With this, a simple model can be derived from eq. 7.1, with the applied force acting on a single bond:

$$V(x, F) = D_e \left[1 - \exp(-\zeta(x - x_0))^2 \right] - F(x - x_0), \tag{7.2}$$

where D_e is the *dissociation energy* of the bond, ζ describes its *stiffness*, x_0 is the *equilibrium length* of the bond and F is the *force constant* of the applied force. This general situation is shown in fig. 7.2.

If an external force is applied on the Morse potential, the asymptotic shape disappears and a local maximum appears as the barrier to overcome for dissociation. The stronger the applied force is (i.e., the larger F), the more this local maximum moves leftwards toward the equilibrium bond length, with decreasing barrier height. The global minimum at the equilibrium bond length simultaneously moves gradually to the right, corresponding to a slight elongation of the bond. If F reaches a certain value, the local barrier vanishes and the whole potential becomes dissociative. In terms of chemical dynamics it follows that the lifetime of a chemical bond decays if a force is applied to it. It will dissociate earlier the stronger that force is. After a certain threshold, the bond will dissociate within one molecular vibration.
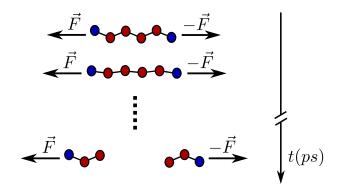
Figure 7.3: Illustration of a constant force mechanochemistry simulation to be done with `dynamic.x`. Two atoms of the molecule are chosen to be anchors for the attached force (blue circles). Force vectors of opposite direction and identical absolute value are added to their gradients throughout the simulation. At some time a bond-breaking event might happen, resulting in two separated fragments (last picture).

7.2   Implementations

Within this thesis, mechanochemical processes were studied with three different types of simulation setups. All three are implemented into EVB-QMDFF and can be called with their respective keywords that are noted here as well.

7.2.1   The Constant Force Experiment

This is the simplest possible way of attaching an external force to a molecule: A constant force vector is added to two atoms. In order to avoid movements of the whole system towards infinity equally strong forces need to be applied in opposite directions, such that the total force applied is twice the force applied per side and no overall translation of the system is caused.

Such an experiment can be invoked for the `dynamic.x` program if the following program lines are added to the `qmdff.key` file[2]:

```
add_force
force1 [atom] [strength (N)] [vector (x, y, z)]
force1 [atom] [strength (N)] [vector (x, y, z)]
```

Now a dynamics trajectory with the ordered number of time steps is started, with a constant force of the specified directions and strengths added to the chosen atoms. This experiment essentially tests the lifetime of a bond since only two events can happen: (1) nothing (besides some stretching) and (2) a bond breaks. If the second event happens, both fragments begin to move apart in the directions of the opposite force vectors. This behavior is illustrated in fig. 7.3.

For most forces attached either nothing happens or the bond breaks always after some time steps. There exists, however, a narrow transition region between both cases: There, for an ensemble of, e.g., 10 simulation trajectories started from the same initial structures, e.g., only six bond breaks happen, with the other four remaining intact.

With this in mind, we can estimate the critical force that is needed at least to break the bond after a desired time: We must do a *force strength scan*. We could, for instance, scan the range between 0 and 10 nN with an increment of 0.1 nN and run 100 trajectories for each force strength. For most

---

2 Indeed it is possible with the current setup to pull both atoms in arbitrary directions, causing overall translations. Therefore, it might be useful for future program versions to, e.g., only choose the atom numbers and the strength of the force and then to calculate the vectors automatically from the cartesian difference vector of both atoms' positions.

forces, either 0 or 100 trajectories will be reactive, i.e., the molecule will be ripped apart. For a small transition region, however, the number will raise smoothly from 0 to 100. The center of this transition region depicts the critical force (the maximum of the reactivity-change)

For small numbers of trajectories the manual estimation of their reactivity is quite easy to manage: We simply look at the last structure. If the molecule is disrupted, the trajectory was reactive. This inspection of course becomes tedious and almost unmanageable for thousands of trajectories. Therefore, a simple reactivity estimation method was implemented in a two-layer process. In the first layer, the `dynamic.x` program notes the initial and final separations of both atoms to which the force vectors were added after the calculation is finished. In the second layer, an external script named `vary_force_mecha.pl` starts a number of single `dynamic.x` calculations for various strengths of the applied forces and reads in both initial and final distances for each run. Then, based on a reactivity criterion given by the user, each trajectory is classified reactive or non-reactive. This criterion is the proportion of initial and final lengths of the molecule. If the criterion is 2, a trajectory is rated as reactive whenever its final length is more than twice the initial[3].

As will be seen in section 7.5, this method only has expressiveness with respect to the simulated time interval per trajectory. Since forces attached to atoms shorten the lifetimes of the bonds we can expect that the critical force becomes smaller the longer the calculated trajectories are, since now also rarer events might happen more frequently. Secondly, if we would simulate billions or trillions of trajectories, the transition region will become broad since now also very rare events will happen in one of the many trajectories. These features are further investigated in section 7.5.

7.2.2   The AFM Simulation Experiment

If an AFM experiment is conducted in the laboratory, the attached force is not constant. Instead, the cantilever is slowly moved up and the attached force is measured indirectly by the cantilever's elongation from the equilibrium position. With this, the force usually increases gradually until it suddenly jumps down, namely at the point when the mechanophore (or something in the spacer molecules) was ripped apart.

The movement of the cantilever happens very slowly on the time scale usually considered for molecular dynamics calculations. If the whole process would take, e.g., 10 seconds, the cantilever stays several nano- to milliseconds at almost exactly the same position, exercising almost the same force on the molecule. It therefore is a reliable approximation to do the constant force experiment described above for several magnitudes of the external force and to do a mosaic-like assembling of their results to get the full picture.

However, as we have stated, thousands to millions of single constant force trajectories are needed to get a reliable force-reactivity plot of the mechanochemical process, causing this to be a quite expensive calculation method.

What if we simply translate the full AFM experiment to the realm of trajectory sampling? The AFM experiment basically does the following (see also figure 7.1): Instead of moving two atoms of the molecule with antiparallel force vectors in opposite directions, one of these atoms is (essentially) fixed, since it is connected via anchor and spacer to the underlying surface. The second of these atoms is linearly moved away from the surface since it is attached to the tip. Measurement of the acting force is done via determination of the cantilevers' elongation. This very procedure was implemented into EVB-QMDFF.

All what is needed to start an AFM simulation is to add the following keywords to the `qmdff.key` file:

    afm_run

---

3 In practice a rather generous reactivity criterion (i.e., a factor of two or three for the length increment) can be applied without problems since the fragments are quickly moving apart several hundreds of Ångstroms after a bond breaking happened.
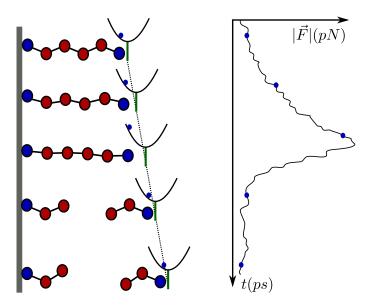
Figure 7.4: Illustration of an AFM mechanochemistry simulation as implemented in `dynamic.x`. The left anchor atom (blue circle) is fixed throughout the simulation, whereas a virtual ghost atom marked as a bold green line which has initially the same position as the right anchor atom is moved linearly to the right with a direction vector determined by the user. In each dynamics step, the position-difference vector between the right anchor and the ghost atom is determined and a force is added to the gradient of the anchor atom according to Hooke's law which compels the anchor to move towards the ghost. Simultaneously the distance between anchor and ghost atoms is used to calculate the force acting on the anchor atom. This force is monitored throughout the simulation analogously to the measurement of the elongated cantilever in the experiment (plot to the right).

```
afm_fix [atom]
afm_move [atom] [maximum elongation (A)] [vector (x, y, z)]
```

The atom specified with the `afm_fix` command is frozen throughout the trajectory, i.e., its gradient components are set to zero for the Verlet-iterations. The atom specified with `afm_move` is thought to be connected to the AFM tip. At the first dynamics step, a virtual atom is generated at the position of the `afm_move` atom and then starts to move along the specified vector linearly throughout the trajectory until the maximum elongation is reached. The moved atom itself is linked to the ghost atom *via* a harmonic spring force such that an additional gradient is added that tries to move the `afm_move` atom towards the position of the ghost atom. This whole process is illustrated in fig. 7.4.

Assuming the molecule of interest is an alkane chain, its natural alignment will be partially folded such that its length can be somewhat increased nearly without steric resistance, resulting in a small distance between moved and ghost atoms. Hence, a small AFM force is detected (first sketch in the figure). After some comfortable extension the whole chain will become almost linear and the moved atom cannot follow the ghost atom almost instantaneously; the acting force increases. Shortly later the tension reaches its peak and the added force causes the molecule to be torn in two parts (third to fourth sketch). Now, both fragments do not fly away in opposite directions as in the constant force experiment, instead the left fragment remains plugged to the fictional anchor and the right fragment follows the ghost atom which still moves to the right with constant velocity. The force between ghost and moved atom almost falls to zero since no counterforce from the fixed part remains but only random noise introduced by the thermostat.

After the simulation is finished, a force-time profile similar to that in the right part of fig. 7.4 is written to file. The effective strength of the ruptured bond corresponds to the maximum force recorded throughout the simulation. In contrast to the constant force experiment only one simulation run is needed to calculate the bond strength. However, it is recommended to simulate an ensemble of trajectories instead since thermal and configurational fluctuations influence this result. Further, these trajectories should of course be much longer in order to get at least somewhat nearer to the experimental time scales (see below).

In order to avoid manual calculation of the maximum force for each run, its respective value and corresponding elongation of the molecule are written to the logfile of the calculation from where they can be analyzed by an external script named `sample_afm.pl`.

7.2.3 Calculation of Rate Constants

This experiment closely resembles the first one but is able to produce more quantitative and general results. The rate constant of a reaction (usually a bond breaking or cycloreversion) is calculated as usual by means of the `rpmd.x` program, with one minor change: A constant force is applied to two atoms in the system, in the same way (and with the same keywords) as for the first experiment. Therefore, the whole k(T) calculation process, i.e., umbrella sampling, PMF-profile calculation, recrossing, is done with the constant force attached.

With this, we can quantify how an attached force alters the lifetime of a bond: The unimolecular rate constant of a bond cleavage essentially tells how often the reaction is expected to happen in one second (frequency). Its inverse therefore is the average lifetime in seconds. With this, we can not only predict what forces are needed to break a bond after some ps of simulation time but also how many seconds, hours, years it would take to break it if a much smaller force is attached! This further illustrates the predictive power of rare-event samplings.
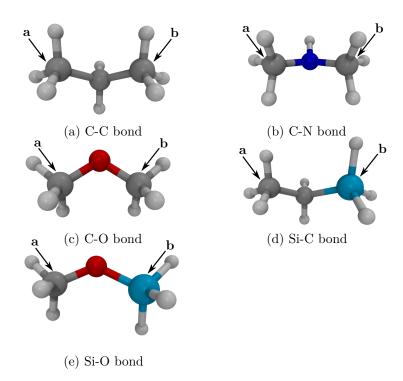
(a) C-C bond

(b) C-N bond

(c) C-O bond

(d) Si-C bond

(e) Si-O bond

Figure 7.5: Screenshots of the five different molecules used for the measurements of bond strengths according to the GAUB paper. The atoms at which forces are attached during simulations are marked with arrows. **a** indicates that the atom is kept fix during an AFM simulation, **b** indicates that the ghost atom is linked to it via a harmonic potential. The arrows do not indicate the actual force vectors but only which atoms are marked with the respective letters.

7.3 Basic Mechanochemical Processes

7.3.1 Choice of Systems

A pivotal point in the history of mechanochemistry was the publication by GAUB *et al.* [214]. Here, the strengths of different covalent bonds were measured by AFM experiments and calculated theoretically by means of relaxed surface potential energy scans. The results of such scans were fitted to a Morse potential; then, a constant force term was substracted from it resulting in shapes of the type shown in fig. 7.2 and rupture probabilities were calculated by application of the simple Arrhenius law (eq: 2.1) to barrier heights for different linear force terms.

Conveniently, the example cases of this early study were taken as first benchmarks for the newly implemented mechanochemical features of EVB-QMDFF. In the study, five bond types were investigated, with the respective molecules used for the theoretical studies in brackets: (a) the C-C bond ($H_3CCH_2CH_3$), (b) the C-N bond (H_3CNHCH_3), (c) the C-O bond (H_3COCH_3), (d) the Si-C bond ($H_3SiCH_2CH_3$) and (e) the Si-O bond (H_3SiOCH_3). The respective mechanophores are shown in fig. 7.5.

Since the AFM experiments in the paper gave rather unspecific results, with recorded rupture forces assigned to Si-C bonds which are the weakest, all calculated rupture forces within this section will be compared to the recorded theoretical values[4].

---

4 For the relaxed surface scans the distance between two hydrogens attached to the outer heavy atoms was varied. Initially, the force was applied between those hydrogens for the shown simulations as well, however, it turned out that Si-H bonds broke before the Si-C or Si-O bonds. Therefore, forces were applied directly at the outer heavy atoms for all systems.
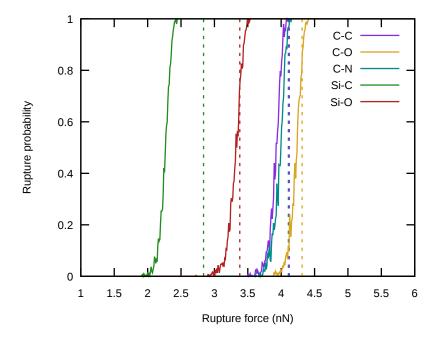
Figure 7.6: Reactivity of five different bond types for various rupture forces in the range of 0 to 6 nN plotted together with the calculated rupture forces by GAUB *et al.* (dotted lines). Note that the dotted lines for C-C and C-N coincide almost exactly, with C-C being located at a slighly larger rupture force.

All five reactions are simple bond dissociations that can be described well using a single QMDFF. Therefore, QMDFFs were parametrized for the structures in fig. 7.5 whose geometries were optimized with MP2/aug-cc-pVTZ [158]. The QMDFF reference calculations were done with the same level of theory.

7.3.2 Constant Force Simulations

The five mechanophores shown in fig. 7.5 were investigated first by means of constant force simulations. The attached forces on both sides were varied between 0 and 6 nN in 500 steps. 300 trajectories were sampled at 300 K for 100 ps with time steps of 0.5 fs for each force strength, resulting in a total number of 150000 trajectories (or 15 μs of simulation time) per molecule. The reactivity criterion was that the distance between both outer atoms should be twice the initial distance of the equilibrium structures.

In fig. 7.6 the resulting force-reactivity profiles are plotted together for all five systems. In addition, the rupture forces calculated by GAUB *et al.* are indicated there as dotted lines of the same color for each system. We see first that the bond strength increases in the succession Si-C, Si-O, C-C, C-N, C-O, where C-C and C-N are very similar. Both the results by GAUB *et al.* and the `dynamics.x` calculations give the same succession of stability.

Further, the deviations between our calculations and the reference are quite modest for all but the Si-C bond, where the values deviate by almost 1 nN.

In the next step, the temperature-dependence of the calculated rupture forces was investigated. The same ensemble of constant force trajectories as described above was sampled for 50 K, 100 K, 200 K, 400 K and 500 K. The results are shown in fig. 7.7.

In part (a) of the figure the obtained force-reactivity profiles similar to fig. 7.9 are shown. The picture looks quite crowded, however, we can see that the width of the transition regions between solely nonreactive and solely reactive ensembles of trajectories grows with raising temperature. If
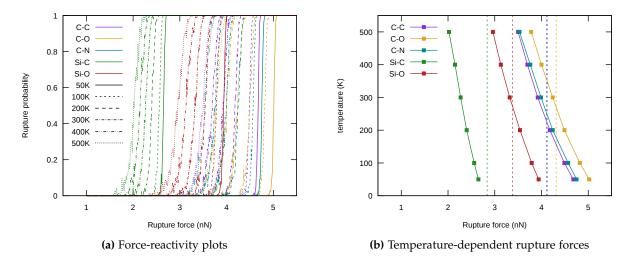
(a) Force-reactivity plots

(b) Temperature-dependent rupture forces

Figure 7.7: Temperature-dependence of the constant-force simulations for the five different systems by GAUB
et al.. Shown are all force-reactivity plots as well as the resulting rupture forces (here: the force at
which the reactivity is 0.5). Note that the dotted lines for C-C and C-N coincide almost exactly,
with C-C being located at a slighly larger rupture force.

we look, e.g., at the Si-C bond the transition region has a width of 0.17 nN for 50 K, in contrast to
0.73 nN at 500 K. This is probably due to thermal activation that leads to an increased number of
reactions for situations where the barrier is lowered by the attached force but still existent.

In part (b) of the figure the forces at which 50 % of the sampled trajectories were reactive are
plotted for the different temperatures. We see that the rupture force decreases with temperature
for all systems, which is quite understandable since the rate constants of the bond ruptures will be
accelerated for higher temperatures, leading to reactive trajectories already at smaller forces. If we
would heat up the systems even more (2000 to 3000 K), the curves will eventually cut the y-axis,
corresponding to zero force needed for rupture. Then, thermal decomposition of the bonds has
begun at short time scales. The change of rupture force with temperature is larger for the more
stable bonds (C-O) than for the weaker ones (Si-C). This is similar to usual Arrhenius behavior
of reaction rates: The larger the reaction barrier, the stronger the temperature-dependence of
reactivity.

Finally, the reference values as calculated by GAUB *et al.* are shown as vertical dotted lines for
comparison in part (b). For all systems but the Si-C bond those lines cross our rupture-force-
temperature plots at approximately 250 K. The Si-C system seems to be a special case, probably
due to different dissociation energy parameters in the global QMDFF-arrays for this element
combination.

7.3.3   AFM Simulations

Now, the same five systems were investigated with the AFM simulation protocol explained above.
For each system, 500 independent AFM simulation trajectories were sampled for 100 ps with a time
step of 0.5 fs at 300 K. The maximum elongation was chosen to be 5 Å in all cases, corresponding
to movements of the ghost atom of 2 to 2.5 Å to the right during the simulation, dependent on the
initial distance between the pulled atoms. This corresponds to a moving velocity or *pulling speed* of
the ghost atom of 0.02 to 0.025 Å ps^{-1}[5].

---

5   The far too short timescales used within the AFM simulations can be illustrated by converting the ghost atom velocities
into day-to-day units. Then, it moves at 2 to 2.5 m s^{-1}. An AFM experiment, however, is usually conducted within
some seconds, where the tip is moved only some *hundreds of nm* at all [214]!

(a) Snapshots of trajectory keyframes

(b) Calculated forces for each MD step

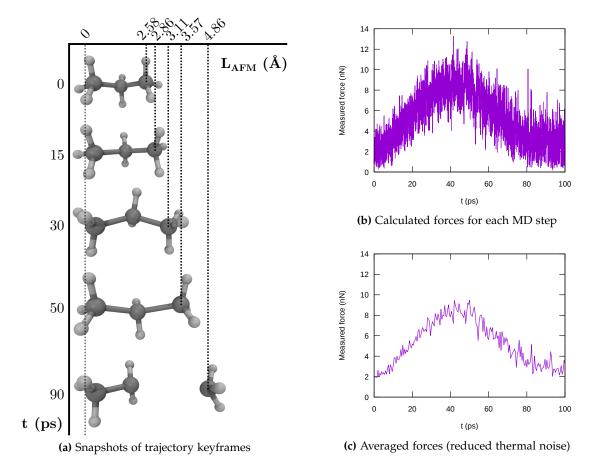**(c)** Averaged forces (reduced thermal noise)

Figure 7.8: Example trajectory of the C-C bond AFM experiment. Shown are some screenshots with the respective times and distances between the anchor atoms (a). The force-time plot of the same trajectory is shown in (b). Since this is quite noisy, slices of 50 neighbored points were averaged, resulting in the plot shown in (c).

The maximum force throughout the simulation was recorded by the `dynamic.x` program and written out for each simulation. Since thermal fluctuations lead to short high peaks of the recorded force-time profile, they were filtered out by averaging slices of 50 neighbored force values. Forces and distances are written out every 10 fs, after removal of thermal fluctuations a value is thus written out every 0.5 ps, resulting into 200 values in total. This is shown for a C-C bond example trajectory in fig. 7.8.

The results of the AFM simulations are shown in fig. 7.9. The calculated rupture forces together with the molecule length (also called AFM elongations) in the moment of rupture are illustrated as scattering plots containing 500 points, the averaged rupture forces are plotted as straight vertical lines. We see that the AFM elongations are different for the systems, since the included bond lengths are different for all combinations. Further, the same ordering of bond strengths as in the constant force experiments can be found, with increasing bond lengths in the succession Si-C, Si-O, C-C, C-N, C-O. It should be noted that the resulting forces (e.g., plotted in fig. 7.8) of the AFM experiments are halved for this plot in order to establish comparability: In the constant force experiments, force vectors of the depicted strengths are added to both sides of the molecule, resulting in a total force twice as large, whereas in the AFM experiment the whole (doubled) force is applied to the moved atom.

The theoretical values of GAUB *et al.* were added again as comparison. We see that these are smaller than the averaged AFM forces for all five systems, where the Si-C bond now has the best accordance (0.15 nN difference). The other systems show slightly larger differences of 0.3 to 0.5 nN.
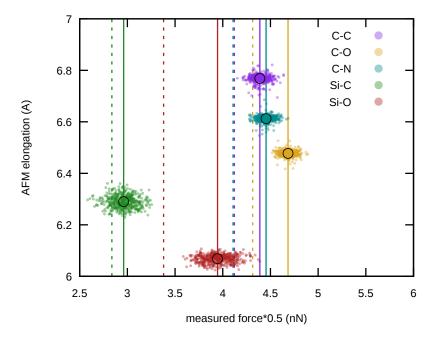
Figure 7.9: Scatter-plots of AFM rupture events for the five different investigated systems, shown within one coordinate system. Both the averages of calculated rupture forces and the rupture forces calculated by GAUB *et al.* are shown as vertical lines (solid and dotted, respectively). Note that the dotted lines for C-C and C-N coincide almost exactly, with C-C being located at a slighly larger rupture force.

If we compare these AFM results to the constant force experiments done above, we see that the AFM rupture forces are larger. This is probably due to the shorter time a certain force is exerted on the mechanophores. In the constant force experiment, each force is applied 100 ps on the molecule. In the AFM experiment, the force fluctuates throughout the simulation (fig. 7.8), therefore adding a certain force only a few ps or less on the system. As already stated, the lifetime of a bond is decreased by application of a certain force to it. For slightly larger forces, thus even shorter lifetimes are needed (or even almost no time due to total removance of the remaining potential energy barrier) if they are only applied shorter times on the system. Further, the rupture forces in the constant force experiments were defined to be the values where *one half* of the trajectories are reactive (due to the easier and more robust determination). In the AFM experiment, each trajectory is reactive, which rather corresponds to the minimum force in the constant force experiments where *all* trajectories are reactive. This is of course located at slightly larger forces as well.

In the next step, the temperature-dependence of the AFM rupture forces was investigated. The same calculations as above were repeated for temperatures between 100 and 1000 K, the averaged rupture forces for the five systems are shown in fig. 7.10, together with the theoretical reference by GAUB *et al.*.

A quite astonishing result can be seen! In contrast to the constant force experiment (fig. 7.7) where the rupture forces decreased with temperature they are increasing in the AFM experiment! A probable explanation might be that thermal activation leading to decreased rupture forces can be neglected in the case of AFM since the system has barely time to climb the remaining potential energy barrier by itself. A rupture will happen only if the barrier has (almost) entirely vanished. The location of this event is approximately temperature-independent because no intermolecular (thermal) vibrations are needed to move the system above a barrier. Then, another aspect of the simulation comes into play. The rupture force is determined by the distance between moved atom and ghost atom. In the case of high temperatures, thermal fluctuations might enhance the
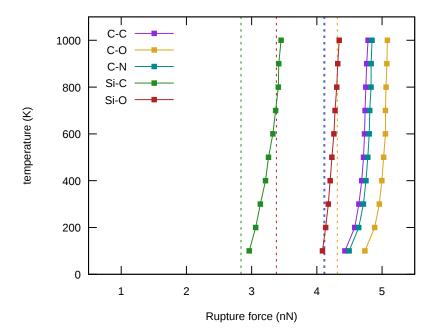
Figure 7.10: Temperature-dependence of the average AFM rupture forces for the five different bond types under investigation, plotted together with the theoretical results by Gaub *et al.* (dotted lines). Note that the dotted lines for C-C and C-N coincide almost exactly, with C-C being located at a slighly larger rupture force.

random motion of the moved atom, bringing it slightly more apart from the ghost than in a nearly frozen case. Therefore, the different temperature-dependencies are an artifact of the measuring conditions modeled by both simulations. If we would, on the other hand, run AFM simulation trajectories with realistic timescales (i.e., some seconds long, resulting in 10^{15} MD steps or more) the temperature-dependence should revert that of the constant-force experiments, since then thermal activation again plays a crucial role.

Next, the influence of *quantum effects* on mechanochemistry is investigated. So far, all calculations were done with one single RPMD bead, which is justified due to the fact that covalent bonds between heavy atoms are broken, for which the influence of tunneling should be negligible. However, if we come to very low temperatures, tunneling might indeed become important. This is shown in fig. 7.11. Here, AFM rupture forces averages were calculated for temperatures between 20 and 100 K for 1 to 64 beads.

The rupture forces are *decreasing* for all systems and temperatures if more beads are used, since the ability of the system to tunnel through the remaining potential barrier according to fig. 7.2 is increased. If we take a closer look we can see that the rupture forces still decrease between 32 and 64 beads for 20 K, whereas they remain (nearly) constant for 8 beads and more at 100 K, indicating that convergence is reached for smaller number of beads if higher temperatures are used (similar to usual k(T) calculations).

Further, the influence of quantum effects seems to depend on the actual system: the C-O bond rupture forces are changing more than the Si-C bond rupture forces. This is due to the atomic masses bonded together. The heavier the bonding partners, the lower the amount of tunneling in the bond rupture. All bonds with heavy Si-atoms involved are therefore less affected by tunneling.

(a) 20 K

(b) 40 K
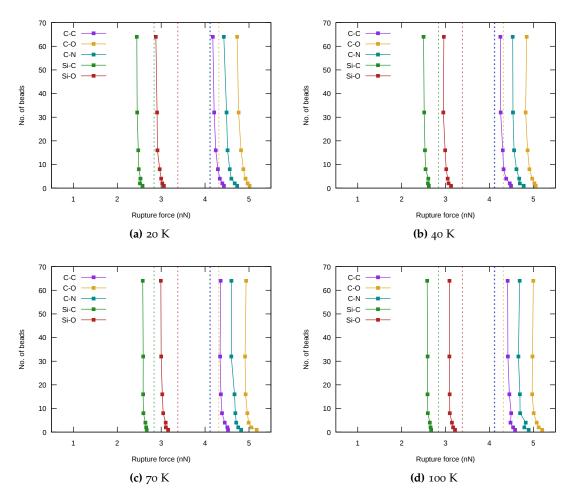
(c) 70 K

(d) 100 K

Figure 7.11: Influence of quantum effects on the results of AFM simulation trajectories. Shown are the RPMD bead-dependent averaged rupture forces for the five systems studied so far at four different temperatures between 20 and 100 K. Note that the dotted lines for C-C and C-N coincide almost exactly, with C-C being located at a slightly larger rupture force.

(a) Disulfide

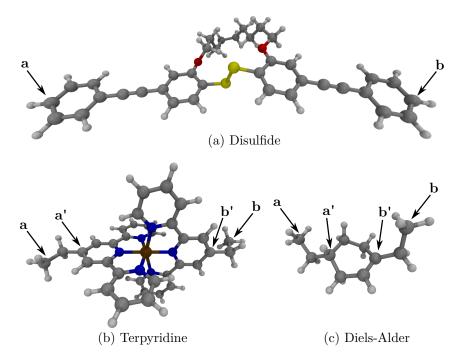(b) Terpyridine   (c) Diels-Alder

Figure 7.12: Optimized reactant minimum structures of the three mechanophores to be investigated with (EVB-)QMDFF mechanochemistry. Noted are the atoms on which the forces are applied (**a** and **b**) as well as those on which forces are applied due to unexpected bond ruptures (**a'** and **b'**). The arrows do not indicate the actual force vectors but only which atoms are marked with the respective letters.

7.4 Other Examples

We have seen so far that the implemented mechanochemical methods are able to reproduce the theoretical results by GAUB *et al.* quite well. In the next step three more realistic cases were chosen from the literature. The respective molecules are presented in fig. 7.12.

Molecule (a) is a bridged disulfide system with aromatic anchor. It was studied both experimentally and theoretically within the University of Kiel, with the theoretical studies done by MÜLLER [215, 216]. Structure (b) contains a Ru^{2+}-ion coordinated by two terpyridine molecules. The force needed to rip both terpyridines apart was measured by GAUB *et al.* in 2003 [217]. System (c) has no experimental example; it was chosen in order to study a Diels-Alder reaction by means of mechanochemistry.

Both geometry optimizations and QMDFF reference calculations were done with the B3LYP(D3 empirical dispersion)/cc-pVDZ level of theory [158, 201, 207].

7.4.1 The Bridged Disulfide Molecule

This system was designed to be a *two-stage* mechanophore: If a force is applied on both anchor atoms shown in fig. 7.12, the shorter chain with the disulfide bond in the middle will be stretched first. Since the S-S bond is much weaker than all other bonds in the line, it will break at some force value during the AFM experiment. But the story is not over yet: Both fragments are still connected *via* the longer ether bridge in the background. The anchor atoms will be moved much
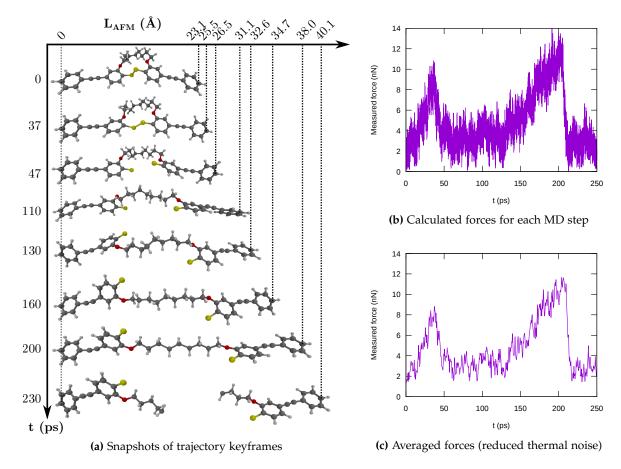
(a) Snapshots of trajectory keyframes

(b) Calculated forces for each MD step

(c) Averaged forces (reduced thermal noise)

Figure 7.13: Illustration of the disulfide AFM experiment. A 250 ps trajectory was calculated with 500.000 single Verlet steps, whereas the outermost left carbon atom was hold during the dynamics (acting as the anchor atom) and the outermost right carbon atom was linearly moved to the right.

further, until the ether bridge is stretched as well. It will break at some time, causing the second mechanochemical reaction[6].

In order to further illustrate this two-step reaction, AFM experiments were conducted first where both steps can be seen within one trajectory. This is shown in fig. 7.13. Two force-peaks appear within the MD. The first lower maximum can be assigned to the rupture of the rather weak S-S bond, whereas the second shows the rupture of a C-C bond in the ether bridge.

These findings were further quantified with constant force experiments. Since two reactive events occur in the bridged disulfide system, the original setup needs to be slightly modified. It was told in the program section that the `dynamics.x` program ejects both initial and final lengths of the mechanophore and that an additional Perl script investigates the reactivity based on a predefined length-change criterion. All what was needed to be changed was the external script: Two reactivity criteria (i.e., two length changes) are now given, where the first describes the S-S bond rupture and the second the final C-C bond rupture. It turned out that length change criteria of 1.35 and 2.5 for both reactions were optimal choices for the case of the bridged disulfide, such that a S-S bond rupture is signalized if the distance between both anchor atoms is at least 1.35 times larger than at the beginning and that the C-C bridge rupture is signalized if the distance becomes at least 2.5 times the initial.

---

6 We have seen in the previous section that C-O bonds are stronger than C-C bonds; aromatic systems and triple bonds are even more stable, resulting in the expected breaking-point located in the ether bridge.
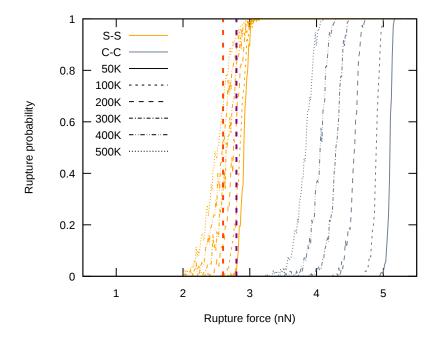
Figure 7.14: Reactivities of the S-S bond and the ether bridge of the bridged disulfide molecule as shown in fig. 7.12. The calculated reference values (50 % reactivity) of Müller *et al.* [216] are noted as vertical dotted lines: S-S (red) and C-C (purple).

With these modifications, force-reactivity plots could be obtained for both the S-S and C-C bonds. Separate from the reactivity criteria identical settings as for the simple mechanophores in section 7.3 were used for temperatures between 50 and 500 K. The results are shown in fig. 7.14.

We see the usual behavior already revealed for the small mechanophores in fig. 7.3. The rupture forces for both events are decreasing with temperature, with the widths of the transition regions being increased. The much weaker S-S bond shows less temperature-dependence than the C-C bonds in the bridge, in accordance with the Arrhenius law. Thus, if we would further heat up the system, both rupture forces are converging to each other and, in combination with the broader transition regions, there will be rupture forces where some trajectories are nonreactive, some only show the S-S rupture and some show both reactions happening, thus limiting the ability of the system to perform two independent reactions.

In addition, the simulated rupture forces of Müller *et al.* [216] are shown in the figure as well. They were calculated with the constant force setup, with a reparametrized ReaxFF force field delivering the description of the bridged disulfide molecule. A force range of 2.4 to 2.75 nN was sampled with 15 different forces and 100 trajectories of 50 ps each. These simulations were conducted at 300 K in a toluene solvent box described by a traditional nonreactive force field.

The calculated rupture force for the S-S bond (2.6 nN) almost perfectly matches our 50 % value at 300 K, however, the rupture force for the C-C bond (2.8 nN) deviates significantly. Since the simulations of single C-C bonds (section 7.3) revealed good agreement with the theoretical values by Gaub *et al.*, the deviations to this study might originate in the addition of solvent in the reference or slightly lower C-C bond dissociation energies in the ReaxFF force field used there in comparison to QMDFF.

If our results are meaningful the two rupture events happen at quite different forces, such that two clearly distinct force regions for the ruptures should also be recorded in AFM experiments, at least if these are conducted at, e.g., room temperature.

Finally, bunches of AFM simulation trajectories were sampled to calculate rupture forces of both S-S and C-C bonds in the bridged disulfide. As in the simple mechanophores from section 7.3, 400
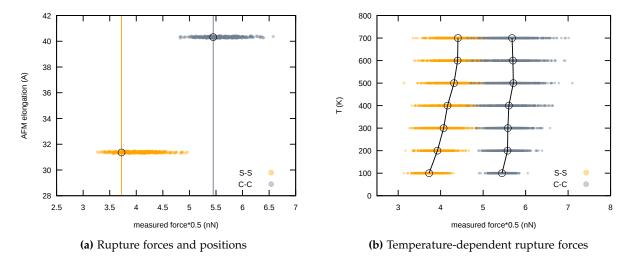
(a) Rupture forces and positions

(b) Temperature-dependent rupture forces

Figure 7.15: AFM simulation experiments for the bridged disulfide molecule. The rupture forces and anchor atom distances (S-S and C-C bonds) for simulations at 300 K are shown in (a), whereas the temperature dependence of the rupture forces is illustrated in (b).

single AFM trajectories were started at different temperatures (100 to 700 K). The ghost atom was moved a distance of approximately 23 Å during the simulation, resulting in a velocity of 0.092 Å ps^{-1}, thus roughly four times faster than in the case of the small systems presented in section 7.3. In order to monitor both reactive events (S-S and bridge ruptures), a special setting was added for dynamic.x. If the keyword

```
afm_second [number of MD steps]
```

is added, the final evaluation of the force-time curve will divide it into two parts at the given number of MD steps. Since all disulfide AFM trajectories were 500.000 steps (250 ps) long, the division was made at 250.000 steps (125 ps). For each part, its local maximum will be determined and written out. When we look back at fig. 7.13, we see that the S-S rupture happens roughly at 40 ps and the final bridge rupture at 200 ps, thus justifying the division between both events at 125 ps.

The AFM results are shown in fig. 7.15.

The rupture forces and anchor atom distances for both reactive events at 300 K are shown in part (a). We see that the anchor atom distances (a.k.a. AFM elongations) show very modest variation, whereas the rupture forces fluctuate much more. This impression is fortified if we look at part (b), where the temperature-dependent rupture forces for all trajectories are plotted. The variation of this force becomes so significant at 300 K and above that both S-S-bond and ether-bridge are breaking at similar or reversed forces at a number of runs.

By looking at the average forces a similar picture as in fig. 7.10 is received: They are growing for higher temperatures, in contrast to the constant force simulations.

7.4.2 The Ruthenium-Terpyridine Complex

In the reference paper of Gaub *et al.* [217] molecule (b) of fig. 7.12 was put between two long poly(ethylene oxide) spacers. Several AFM runs with force loading rates of 1 nN s^{-1} were done, with recorded rupture forces of ca. 0.1 nN. Since these are much smaller than those needed to rupture covalent bonds it was supposed that the recorded events were caused by openings of the metallo-supramolecular complex, i.e., separations of both terpyridines, where the Ru^{2+}-ion is taken by one of them.

This experimental setting was reconstructed by means of the AFM simulation method in `dynamics.x`. The outer carbon atom termed **a** was frozen and its counterpart **b** coupled to the moved ghost atom. An ensemble of AFM trajectories was sampled at 300 K with each trajectory being 250 ps long. Unfortunately all of them showed another reaction than expected: The methyl or ethyl group containing atom **b** was torn apart, with the main ruthenium complex remaining intact (fig. 7.16). The observed rupture forces were around 4-4.5 nN, thus similar to our results for the C-C model system.

The Ru-N bonds in the complex are apparently much stronger than they should be if QMDFF is used to model them. The situation within this complex is of course much more complicated than for single covalent bonds described so far, it seems that the global fitting approach within QMDFF is not sufficient for this reaction. Another possible reason is that two of the three bonds from each terpyridine molecule are almost *perpendicular* towards the applied force vector. Only a small fraction of the rupture force is effective on them. A similar discussion is made for the Diels-Alder system in the next section.

Nevertheless the force needed to break this complex was calculated: Instead of using peripheral carbon atoms as anchors aromatic carbons in the terpyridines were chosen (**a′** and **b′** in fig. 7.16). Now, the desired reaction happens: The Ruthenium complex gets cracked, the Ru^{2+}-ion remains bonded to one ruthenium, with the other one moving away alone. More than 8 nN was needed to trigger this event, i.e., twice the C-C rupture force and almost 100 times the experimental value by Gaub *et al.* (actually almost 200 times since the total force exerted by the "AFM" moving atom is actually twice as large (see above)).

In spite of this wrong mechanistic prediction, series of AFM trajectories were started for the **a′-b′** anchor atoms at temperatures between 100 and 700 K (250 ps each, with the ghost atom moved approx. 5 Å, resulting in a velocity of 0.02 Å ps^{-1}). The results are presented in fig. 7.18 (a). A similar behavior to the model systems in fig. 7.9 can be seen, with both variances and expectation values of the rupture forces increasing with temperature.

If theory and experiment should be compared directly, an EVB-QMFFF (probably TREQ) of the reaction should be parametrized, which is quite tricky due to the presumptive multireference character of the Ru-N bond breakings requiring demanding QM reference calculations and the very size of the system making both an accurate choice of TREQ internal coordinates and the calculation of reference frequencies etc. very demanding.

7.4.3 The Diels-Alder Reaction

We have seen that the mechanochemistry of the ruthenium terpyridine complex cannot be described properly with one single QMDFF. A similar case is a cycloreversion. QMDFF is parametrized for single covalent bond ruptures but not for cycloreversions involving electronic influence of the whole aromatic system. Therefore, EVB-QMDFF should be used here as well. A simple example is the basic Diels-Alder reaction (1,3-butadiene and ethylene), with ethyl substituents for application of the rupture forces. The reaction path of this system was calculated starting from the TS. Then, a *black-box* rate constant calculation with `evb_kt_driver.x` was done. In fig. 7.17 the reaction path is shown together with the positions of the RP-EVB reference points and the energies of both QMDFFs. Structure inlets show the actual mechanism of the reaction.

After the *black-box* setup was finished, the resulting TREQ force field can be used equally well for other tasks such as AFM simulation trajectories. Atoms **a** and **b** shown in fig. 7.12 were used in the same way as for the terpyridine system. Again one of the outer C-C bonds was ruptured first, as can be seen in fig. 7.16.

This behavior is quite interesting since we now know the potential energy barriers of both C-C bond rupture (ca. 500 kJ mol^{-1}) and cycloreversion (ca. 250 kJ mol^{-1}). From this simple comparison we should assume that cycloreversions are largely preferred in this case. However, if the
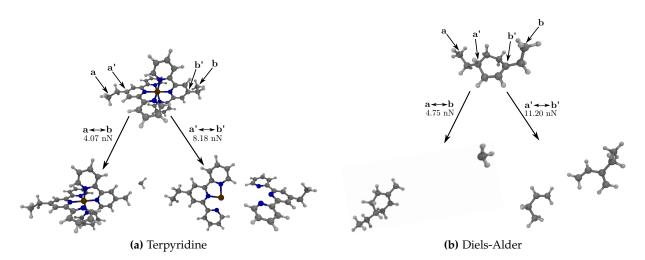
Figure 7.16: Observed reaction events in the Terpyridine and Diels-Alder systems depending on the atoms that were chosen to be anchor and moved atoms. Alkyl chain ruptures happen in both cases if the outer carbon atoms are torn apart (**a**, **b**), whereas the desired reaction only occurs at much larger forces if carbon atoms being part of the reactive subunit were chosen (**a′**,**b′**).
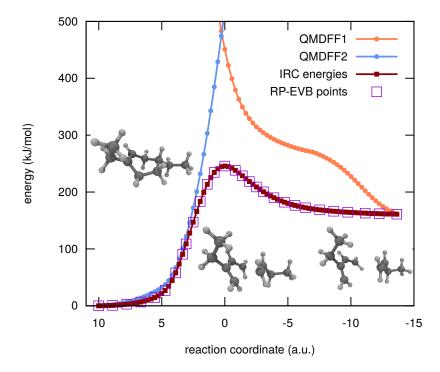
Figure 7.17: DFT reaction path of the Diels-Alder reaction together with the energies of both QMDFFs and the positions of TREQ gradient and Hessian reference points chosen by the `evb_kt_driver.x` black-box program.).

Figure 7.18: Temperature-dependent calculated AFM rupture forces for the Terpyridine and the Diels-Alder systems. Shown are scattering plots of all events and their respective averages.

atoms **a'** and **b'** within the aromatic system are chosen for the AFM simulation, the cycloreversion happens at 11-12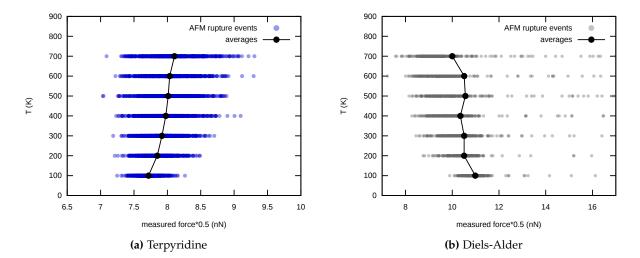 nN, thus at almost three times the force for a simple C-C rupture (ca. 4.5 nN). An insufficient PES-description of the process should be now rather unlikely since at least the direct vicinity of the reaction path is described well by construction. One possibility could be that the mechanochemical trajectories follow paths far offside the equilibrium RP, where the quadratic Taylor series approximation included into TREQ performs quite badly. Another possibility is offered by studying the literature.

Müller has shown in his PhD thesis [210] that the *retro-click* reaction of triazole, which is essentially a cycloreversion, needs a larger force for activation than the simple C-C bond rupture between the triazole ring and the adjacent alkyl chain, even though the reaction path for the C-C dissociation has a higher barrier than for the retro-click. The explanation for this behavior was that the force is not applied parallel to the retro-click reaction path but with an angle of 50°, with thus only a fraction of the applied force available to pull the system above the PES barrier. Our case is quite similar: The ethyl substituents on diene and dienophile are inclined with respect to the cycloreversion coordinate. They cannot be located parallel to the reaction path since both reactants have an equal number of carbon atoms and thus no central point to attach at.

Nevertheless, AFM simulation trajectories were ran with forces acting on atoms **a'** and **b'** (fig. 7.18 (b)). The temperature-dependence is different than for the dissociations seen before: The averaged rupture force *decreases* with temperature, as we would have usually expected it. No clear explanation for the different temperature-dependencies of AFM simulations for single bond ruptures and the cycloreversion could be found so far, a reason might be the altered PES shape (no asymptote but instead an additional product minimum). Further, a large number of "outliers" located at much higher forces are visible, which probably are artifacts due to trajectories running over areas far away from the TREQ reference path were the PES construction gets unstable.

7.5 Calculating Rate Constants

We have seen so far that the *time scale* of a mechanochemistry calculation significantly affects the resulting rupture force for an event, such that the forces calculated by the constant force method are much smaller than the ones calculated by AFM simulations, since a certain force acts on the system much longer in case of the former method, giving the system more chances to climb the remaining

barrier by itself. This final section will show this influence of time scales more quantitatively, by calculations of rate constants.

The `rpmd.x` program is able to calculate rate constants of dissociation and cycloreversion reactions (table 3.4) and thus of all mechanochemical processes studied in this chapter.

In the first step, RPMD-k(T) calculations were done for four of the five dissociation reactions of section 7.3 for several temperatures and rupture forces; then, these calculations were repeated with the Diels-Alder system.

7.5.1 Free Energy Profiles

The `rpmd.x` setup requires the definition of transition states, where the ζ_1-dividing surface is located. Dissociations of covalent bonds usually have *asymptotic* potential curves, without a transition state on it. For all systems the lengths of the dissociated bonds were therefore set to 6 Å, where a sufficient degree of asymptotic character was assumed. With this, usual "semi *black-box*" k(T) calculations similar to those reported in the previous chapter were initiated. During all steps of the RPMD calculations, i.e., structure generations, umbrella generations and samplings as well as recrossings, constant forces of preset values were applied to the **a** and **b** atoms of fig. 7.5. The syntax for applying them is identical to this for the constant force simulation with `dynamic.x` as it was reported in section 7.2.

For all systems, forces between 0 and 5 nN on both anchor atoms were applied in steps of 0.5 nN. Each of these force settings was calculated at temperatures between 300 and 700 K, with 5 single k(T) calculation runs per temperature for subsequent Arrhenius fits. One RPMD bead was used, i.e., classical trajectories were sampled.

The resulting free energy surfaces that are calculated from the umbrella samplings for the C-C, C-N, Si-C and Si-O systems are shown in fig. 7.20, where one of the RPMD samplings at 300 K were chosen, respectively.

The influence of the applied forces on these surfaces can be seen quite nicely, at least for C-C and C-N. If we compare their shape to the mathematical example of a Morse potential in fig. 7.2, a close relationship is obvious. The Morse-like shapes of the bond potentials[7] are being pressed down by a linear addition term, whose slope is described by the strength of the attached force. Free energies are of course different from potential energies, since they include entropic contributions, however, their total shape is similar since the entropic contribution will change less significantly throughout the bond-breaking process (maybe with larger changes for the Si-C and Si-O bonds).

As it can be expected, less strong forces are needed to lower the dissociation barriers of rather weak Si-C and Si-O bonds to certain levels than the C-C and C-N bonds. Only free energy curves up to 3, 2.5 or 1.5 nN are shown for the different systems since the k(T) calculations failed to converge for the stronger forces. This probably has the origin in the fact that only one of the two bonds that are pulled by the forces are hold by the umbrella sampling bias at the position of the respective sampling window; the other is still free to dissociate at any point, then changing the physics of the system significantly and thus violating one of the requirements for useful free energy samplings. Therefore k(T) calculations failed for less strong forces in the case of weaker bonds: Accidental bond breakings happen much easier.

7.5.2 Force-Dependent Lifetimes

Other useful insights can be gained by looking at the *rate constants*, which are essentially obtained from the free energy barriers and a recrossing correction. Bond breakings are unimolecular reactions, their rate constants with units of s^{-1} therefore have quite a graphic meaning: They

---

7 If we recollect our findings from the theory chapter, we know that QMDFF actually uses polynomial potentials, which are similar to Morse potentials in shape (eq. 2.109).

(a) C-C

(b) C-N

(c) Si-C

(d) Si-O
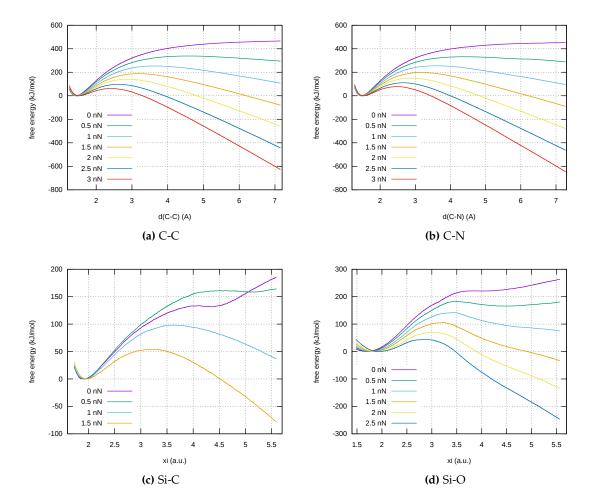
Figure 7.19: Calculated free energy profiles for the C-C, C-N, Si-C and Si-O bond dissociation reactions under influence of external forces. All shown profiles were calculated at 300 K, the values of the reaction coordinate ξ were converted to bond lengths. The 0 and 0.5 nN curves for the Si-C and Si-O systems are quite exceptional: Unlike all others they show no initial asymptotic behavior which is successively pulled down by the added force, instead the unbiased curves show *inflection points* at 4-4.5 Å. The 0.5 nN curve of Si-C is even *below* the 0 nN curve, which seems to show a partially *inversed* force-dependence! A satisfying explanation for these unexpected shapes could not been found so far, however, we should remember that these are free energy curves which result from millions of different sampled structures. Maybe some local long-range stabilization might take place between both fragments at a bond length of 4 to 4.5 Å, with the Si atom playing a central role in it (since the inflection points are absent for the C-C and C-N systems).

describe the inverse of the average lifetime a bond has before it dissociates. If we therefore calculate rate constants of bond dissociations, we know the bond's expected lifetime after taking the inverse of the rate.

We now want to investigate how attached forces change the lifetime of covalent bonds. This is shown in fig. 7.20. Here, averaged rate constants at 300 K are plotted against the attached forces in a logarithmic scale. Next, a fit of these force-dependent rates was tried. It can be seen that no easy exponential dependence resulting in a linear plot on the logarithmic scale exists. The solution is to apply a slightly altered exponential fit:

$$k(F) = a \exp \left(aF + b \ln(F) \right),$$ (7.3)

where the logarithmic correction is needed to bend the plot at large forces (or to make the progress more steep for low forces). This slightly more complicated exponential dependence of reaction rates on forces can be evaluated theoretically for Morse potentials (eq. 7.2) [210]:

$$k(F, T) = k_0(T) \exp \left[\frac{F}{\beta} \left(\sqrt{\frac{\beta D_e}{F} \left(\frac{\beta D_e}{F} - 2 \right)} - \ln \left(\frac{\beta D_e}{F} + \sqrt{\frac{\beta D_e}{F} \left(\frac{\beta D_e}{F} - 2 \right)} - 1 \right) \right) \right],$$ (7.4)

where we essentially have a constant and a logarithmic term in the exponential. This confirms the similarity of the QMDFF's polynomial potentials to Morse potentials.

What do those rate constants reveal? Some interesting insight can be gained if we use the inverse correspondence to bond lifetimes. A couple of horizontal dotted lines is added to the plots in fig. 7.20. They shall give a descriptive view on the covered timescales and are placed where the inverse of the actual rates correspond to the measured times. The shortest useful time period in MD is a *single molecular vibration*. If the potential of a bond is repulsive it will dissociate within this time and not earlier. A typical value is 10 fs. An attached force that results in a lifetime of 10 fs therefore instantly breaks the bond. The forces that correspond to the different lifetimes are listed in table 7.1.

We see that instant bond ruptures are caused between 2.15 nN (Si-C) and 4.16 nN (C-N). The ranking of the different bonds coincide with that done, for instance, in fig. 7.9. The actual values, however, are much larger in the AFM simulations, where we could expect that instant bond ruptures are caused by the actual forces. This might be assigned to instantaneous thermal peaks of the displacement (in spite of the partly averaging), an effect which is totally averaged out in the free energy profiles. The next time span is 100 ps, corresponding to the lengths of *constant force trajectories* in section 7.3. This slightly longer time scale has a noticeable effect on the forces needed to rupture a bond: they decrease by approx. 0.3 nN. Compared to fig. 7.7 the values of the rupture forces calculated from the constant force trajectories are shifted by approx. 0.4 nN to higher values but nevertheless fit quite well. If we compare the rupture forces calculated by AFM and constant force simulations the AFM rupture forces are indeed larger, in agreement with tab. 7.1.

Another important change in timescale is the step towards *experimental AFM simulations*. If we assume that the force remains constant (i.e., varies less than 1 pN) for 1 ms, this time interval is seven orders of magnitudes larger than that of constant force simulations! The attached forces needed for bond rupture therefore decrease quite considerably, by approximately 0.6 nN. This fits well to the much weaker rupture forces reported in AFM experiments in comparison to the respective calculations [214, 217]. It would be almost impossible to sample an ensemble of constant force or even AFM simulation trajectories for the required timescales, since 10^{12} and more MD steps would be needed per simulation. The k(T) calculations offer an elegant method to circumvent this problem, even if we do not directly see any reactive event. By looking back at the theory chapter and forward to the KMC chapter, the *rare event* problem and its elegant solution provided by free energy samplings becomes clearly apparent.

(a) C-C

(b) C-N

(c) Si-C

(d) Si-O
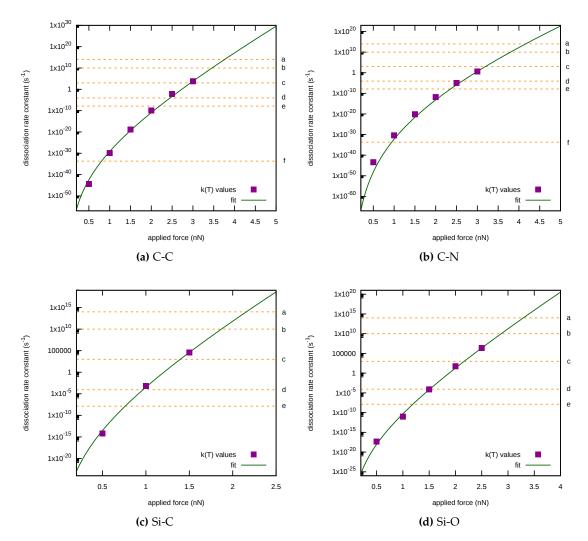
Figure 7.20: Force-dependent logarithmic plot of calculated rate constants for the C-C, C-N, Si-C and Si-O bond dissociation reactions at 300 K. Besides the single rates, fits made with eq. 7.3 are plotted for their inter- and extrapolation. The dotted horizontal lines mark some descriptive time spans linked with the inverse of the rate constants:

a: A molecular vibration (ca. 10 fs)

b: the elapsed time during a constant force trajectory calculated in sec. 7.3 (100 ps)

c: a nearly constant force (1 pN change) acting on a molecule during a real-life AFM experiment (1 ms) [210]

d: One day (86400 s)

e: Time the author of this thesis has needed to complete it (ca. 4.25 years)

f: Age of the earth (ca. 4.5 billion years)

Table 7.1: Resulting bond lifetimes (expressed in well known quantities) depending on the attached force in nN.

Bond lifetime	attached force (nN)			
	C-C	C-N	Si-C	Si-O
molecular vibration	3.76	4.16	2.15	3.29
constant force simulation	3.45	3.79	1.87	2.86
AFM experiment	2.94	3.19	1.39	2.16
one day	2.45	2.64	0.96	1.51
duration of PhD	2.19	2.35	0.75	1.19
age of earth	0.80	0.95	-	-

Besides these "scientific timescales" some rather pointless times are added as a small canapé of amusement. If a constant force would be exerted a whole day long, the rupture forces would decrease another 0.5 nN, if the experiment would have been continued throughout my PhD time (ca. 4.25 years) the resulting further decrease with respect to the one day experiment is only about 0.3 nN. Waiting 5 billion years (the approximated age of earth) decreases the needed forces to below 1 nN even for the C-C and C-N bonds. This contemplation is of course only of mathematical interest: No one could execute an AFM simulation for longer than a few seconds, since possible sources of errors or irritations are becoming too dominant. The rupture will happen much earlier even for very weak forces, due to vibrations of the apparatus or collisions with solvent/gas molecules. Further, spontaneous forces due to collisions are existent also in the natural environment, which will lead to accidental ruptures of C-C bonds in molecules even without any systematic forces attached to them.

If we look at the temperature-dependence of rate constants, the usual Arrhenius behavior is retained throughout all attached forces. The resulting parameters are shown in table 7.2. The activation energies coincide quite well with the barrier heights along the free energy plots in fig. 7.20: they decrease with the attached force, where the decrease gets slower for larger force constants, E_a seems to have an asymptotic behavior. The activation energies at 3 nN for both C-C and C-N seem to be quite low if we compare them to the free energy profiles. Since the deviation between single k(T) values also gets larger for this force, beginning complications of the samplings, that fail at the next stronger force, are assumed.

7.5.3   The Diels-Alder Reaction

Finally, we should again take a look at the Diels-Alder reaction. It has a substantial difference to the single bond breakings shown above: Its potential energy curve has no asymptotic progression. *Black-box* k(T) calculations were done for this system as well, where the cycloreversion reaction type was used. The resulting free energy curves for different attached forces are shown in fig. 7.21 (a).

The unbiased profile shows the maximum at the TS and a part of the decrease towards the products. Now, an interesting fact becomes apparent: We already knew from section 7.4 that the force needed to induce the Diels-Alder reaction is much larger than that to break a single C-C bond. Here we see the reason why. Forces up to 9 nN could be added without problems if atoms **a'** and **b'** were chosen (fig. 7.18). However, the effect of the forces to the free energy curves is quite small. In contrast to the single bonds, where, e.g., a force of 3nN is sufficient to pull the free energy to -600 kJ mol^{-1} at the TS (fig. 7.20 (a)), here a force of 8 nN, thus more than twice as large, only lowers the free energy at the TS by around 200 kJ mol^{-1}.

Table 7.2: Calculated Arrhenius parameters for the four different bond dissociation processes, resulting from Arrhenius plots done at the several attached constant forces throughout the RPMD samplings. 1(-14) means $1 \cdot 10^{-14}$.

System	attached force (nN)	E_a(kJ mol^{-1})	A
C-C	0	503.6	2.95(-03)
	0.5	357.1	5.44(-07)
	1	264.5	7.56(-09)
	1.5	195.1	4.73(-10)
	2	142.7	2.83(-19)
	2.5	77.0	5.41(-14)
	3	11.6	1.30(-18)
C-N	0	482.3	9.79(-05)
	0.5	350.6	7.34(-07)
	1	272.9	2.28(-07)
	1.5	209.8	4.01(-08)
	2	158.9	9.95(-09)
	2.5	117.7	5.39(-09)
	3	11.7	4.89(-19)
Si-C	0	258.6	2.00(+03)
	0.5	250.4	6.14(+03)
	1	134.0	4.03(-04)
	1.5	70.6	4.58(-07)
Si-C	0	280.2	5.63(-07)
	0.5	195.5	2.38(-08)
	1	154.2	1.14(-08)
	1.5	112.2	4.04(-09)
	2	73.7	5.86(-10)
	2.5	46.9	5.80(-10)

(a) Force-dependent free energy plots

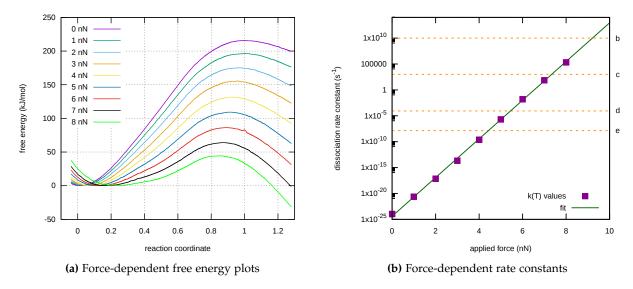**(b)** Force-dependent rate constants

Figure 7.21: Results of force-dependent rate constant calculations for the Diels-Alder example system. Shown are free energy plots (a) as well as force-dependent rate constants being fitted with an exponential function (b).

What is the reason for this behavior? It seems that only a fraction of the totally applied force effectively acts along the reaction coordinate and lowers its free energy. The largest part gets redistributed into other internal coordinates, due to the oblique placement of the force vector with respect to the reaction coordinate and probably also due to the larger number of coordinates directly taking part on the reaction. In the case of a C-C bond break, essentially all attached force will act at some point at this single bond coordinate, whereas a large number of other bonds, angles and dihedrals can absorb significant parts of it in the Diels-Alder system and transform it to thermal vibrations. Similar conclusion were made in theoretical studies of cyclopropane and cyclobutane ring-openings, where higher-than-expected activation forces were explained with couplings between the reaction coordinates and other vibrations within the molecules [218,219].

If we look next at the force-dependent cycloreversion rate, we see that the rate at zero force attached is almost 30 orders of magnitudes *larger* than for the C-C bond rupture (10^{-30} vs. 10^{-60} s^{-1}). However, the rate increases much slower with the force than for the single bonds, in accordance with the free energy profiles. For this reaction, the force-dependence of the rate shows indeed a simple exponential behavior, presumably due to the absent asymptote of the energy.

CHAPTER

8

Urethane Synthesis

A significant part of my work during the last years was spent on a cooperation with Covestro AG, which is still active at the time this thesis was finished. Since one of Covestro's main occupation fields is the production of polyurethane materials, their theoretical chemistry section has built a significant expertise on this field. Soon after publication of the second EVB-QMDFF paper in 2017 [17], we were contacted by the Covestro researchers and a cooperation was initiated.

The aim was to do rate constant calculations for (poly-)urethane synthesis reactions with EVB-QMDFF-RPMD in order to enable large-scale modeling of its synthesis with methods like KMC. In a first step, rate constants of different autocatalytic mechanisms were calculated to benchmark the ability of the method to simulate this kind of reactions. So far, only parametric k(T) calculations based on TST with tunneling corrections had been done. This study therefore constitutes to the best of my knowledge the first ever RPMD study of urethane synthesis. In order to make the calculations possible, the initial approach of connecting the RPMDrate program by SULEYMANOV with an EVB-QMDFF PES function was revised with a global *black-box* approach uniting PES description and flexible RPMD rate constant calculation within one program package (see section 3.1).

Publication of the results presented in this chapter is under preparation at the time this thesis was completed [220]. Due to privacy concerns regarding the theoretical and experimental results produced by Covestro, these will not be revealed before our cooperation paper has been published. In the actual publication, only results for suitable model reactions will be revealed, whereas applications to actual industrial synthesis done by Covestro will not be disclosed at all. In order to nevertheless give a rough estimation of the EVB-QMDFF result's quality, they will be compared to other theoretical papers that handle the topic of urethane autocatalysis.

In section 8.1 a short review of the urethane chemistry will be given such that the importance of our results for this topic can be better understood. In section 8.2 a benchmark study with selected DFT functionals is presented from which a method of high quality and modest scaling for future calculations of larger systems can be proposed. This is followed by the actual RPMD calculations, both settings and results, that are presented in section 8.3. A short excursion on the topic of *subsequent urethanation* is presented in section 8.4.

8.1 Synthesis of Urethanes - a Long Story Short

Polyurethanes are one of the most important synthetic materials [221]. In contrast to most other plastics like polyethylene or polystyrene, the properties of polyurethanes can be widely varied. This is due to the mechanism from which they are formed. They are not built by adding the same monomer to growing monotonous chains but instead by combining isocyanates and alcohols that react to the urethane group. Whereas *toluene diisocynaate* (TDI) and *methylene diphenyl isocyanate*

(MDI) are widely used as diisocyanates in practice (the first for flexible, the second for rigid polyurethane products), the structures of used di-(or poly-)ols enable a wide variability and thus individual fine-tuning of the desired polymer properties.

We can, e.g., choose if diols (resulting in long chains) or polyols (leading to polymer networks) are used. The overall size of polyol molecules might also vary and with it noncovalent interactions between them. Besides this, different degrees of foaminess can be achieved by adding variable amounts of water to the reaction mixture, which produces CO_2 by reaction with isocyanates.

A huge number of different side reactions from isocyanates make the field of urethane chemistry very complex in practice [221–223]. Here, we ignore such intricacies and restrict ourselves on the description of the basic mechanism and possible autocatalytic pathways.

8.1.1 Basic Mechanism

In general, polyurethanes result from an addition reaction of an isocyanate and an alcohol[1]:

$$R^1-N=C=O \ + \ R^2-OH \ \rightleftharpoons \ R^1\underset{H}{\overset{O}{\underset{|}{N}}}\!\!\!\!\!\!\!\!\!\overset{\displaystyle\|}{C}\!\!\!\!O-R^2. \tag{8.1}$$

The reaction proceeds by a nucleophilic attack of the alcohol oxygen at the carbon of the isocyanate. After establishing the first bond, both the oxygen and nitrogen of the former isocyanate have (partial) negative charges, what leads to a subsequent abstraction of the alcohol hydrogen by the adjacent nitrogen, concluding in the final urethane group [221]:

$$R^1-N=C=O \ + \ R^2-OH \ \rightleftharpoons \ \left[\begin{array}{c} R-N=C-\overset{\ominus}{O} \\ | \quad\;\; | \\ H-\underset{\oplus}{O}-R^2 \end{array} \longleftrightarrow \begin{array}{c} R-\overset{\ominus}{N}-C=O \\ | \quad\;\; | \\ H-\underset{\oplus}{O}-R^2 \end{array} \right]$$

$$\longrightarrow R^1\underset{\underset{H}{|}}{\overset{O}{\overset{\|}{N}}}\!\!\!\!\!\overset{}{C}O-R^2 \qquad . \tag{8.2}$$

A lot of research has been undergone in order to rank substituents of both alcohols and isocyanates regarding to their reactivity. It has been found that *electron withdrawing* groups attached to the isyocanate group *enhance* its reactivity by increasing the positive partial charge on the carbon atom to be attacked. Since aryl residues impose a stronger electron withdrawing effect than alkyls, they are commonly used as isocyanate backbone. Due to the proposed quadrangular reactive complex (and larger cyclic ones presented below), *steric effects* play a role as well. It has been found that the reaction velocity depends on the R^2-residue of the alcohol R^2-OH as: Me < Et > 2-Pr > tBu, mainly due to the steric hindrance of the larger alkyl substituents, compensating their accelerating +I effect [224].

8.1.2 Catalysis

In reality, the simple picture of both reactants merging directly to the urethane becomes at least questionable. Kinetic studies of the urethane reaction revealed that if a catalyst is added the reaction follows second order kinetics (as it would be expected from the simple mechanism shown in eq. 8.2). Since uncatalyzed urethane synthesis proceeds quite slowly, a large collection of catalysts has been developed throughout the decades [225, 226].

---

1 Isocyanates reacting with thiols result in thiourethanes, reactions with amines result in urea bonds and reactions with water result in amine and CO_2.

However, several studies revealed that especially if alkyl alcohols and no catalysts are used the kinetics becomes *third order* [224, 227, 228]. The usual explanation for this behavior is *autocatalysis*, either from the reactants or the urethane itself, which stabilizes an intermediate that finally reacts with either the alcohol or the isocyanate to the urethane. Since most metal-organic catalysts are highly toxic[2], a deeper knowledge of autocatalysis which could lead to strategies for utilizing it in practice is very important.

There are some different ways in which autocatalysis can proceed. First, the reaction can be second order with respect to the alcohol molecule: A first alcohol molecule R^2-OH attacks the isocyanate group and destabilizes the isocyanate group. Then, a second alcohol molecule R^3-OH attacks the reactive complex and finally forms the product [222, 224, 229–231]:

$$R^1-N=C=O \; + \; R^2-OH \; \rightleftharpoons \; \left[\begin{array}{c} R-N=C-\overset{\ominus}{O} \\ | \\ H-\overset{\oplus}{O}-R^2 \end{array} \right] \xrightarrow{R^3-OH} R^1 \underset{H}{\overset{O}{\underset{N}{\bigwedge}}} O-R^3 \; + \; R^2-OH. \quad (8.3)$$

The second possibility is that already built urethane groups act as catalyst [221, 223, 232]. Their nitrogen performs a nucleophilic attack on the isocyanate and destabilizes the group, whereas the secondary amine acts similarly as the the alcohol during the first autocatalysis in eq. 8.3.

$$R^1-N=C=O \; + \; R^2\underset{H}{\overset{O}{\underset{N}{\bigwedge}}}O-R^3 \; \rightleftharpoons \; \left[\begin{array}{c} R-N=C-\overset{\ominus}{O} \\ | \\ R^2-N-C=O \\ | \quad | \\ H \quad O-R^3 \end{array} \right] \xrightarrow{R^4-OH} R^2\underset{H}{\overset{O}{\underset{N}{\bigwedge}}}O-R^3$$
$$+ \; R^1\underset{H}{\overset{O}{\underset{N}{\bigwedge}}}O-R^4 \qquad (8.4)$$

In our cooperation, however, another important autocatalytic pathway has been studied: *Hydrogen bond networks* that connect two or three R^2-OH molecules and the isocyanate together such that the actual reaction takes place over a cyclic rearrangement of the whole involved network [230–233]. If two R^2-OH form a dimer, the reaction proceeds as follows:

$$R^1-N=C=O \; + \; 2R^2-OH \; \rightleftharpoons \; \left[\begin{array}{c} R^1-N=C=O \\ | \\ H\cdots O-R^2 \\ | \quad | \\ R^2-O\cdots H \end{array} \right] \; \rightleftharpoons \; \left[\begin{array}{c} R^1 \quad O \\ \diagdown N-C\diagup \\ H \qquad O \\ \diagdown O\cdots H \diagup R^1 \\ R^2 \end{array} \right].$$
$$\xrightarrow{\quad} R^1\underset{H}{\overset{O}{\underset{N}{\bigwedge}}}O-R^2 \; + \; R^2-OH \qquad (8.5)$$

In the first step, the involved R^2-OH molecules build the *dimer* (or, what is more probable: they exist already mainly as dimers or *n*-mers in solution). Then, the isocyanate approaches it and a six-membered ring (*6-ring*) stabilized by hydrogen bonds is built. The actual reaction to the urethane now takes place as a rearrangement of the whole ring system, where both hydrogens are transferred simultaneously. As we will see in the next section, this dimer-process has a much lower activation barrier than the generic bimolecular process depicted in eq. 8.2.

If we think further, the next step is to include alcohol *trimers* that might exist in solution. They build 6-ring structures, which are, if we consider the intrinsic sixfold symmetry of hydrogen bonds

---

2 Indeed, isocyanates are toxic as well, leading to developments of slightly altered urethanes without isocyanates [221].

that comes into play if ice crystals are built, especially favorable. Further, the trimer is believed to be three orders more reactive than a single R^2-OH molecule [223]. In connection with the favorable six-ring structure we therefore could assume that most of the additions leading to formation of urethane actually proceed over an *8-ring* intermediate:

$$
R^1-N=C=O \; + \; 3R^2-OH \; \rightleftharpoons \;
\left[
\begin{array}{c}
R^1-N=C=O \\
+ \quad R^2 \\
H \cdots O \\
R^2-O \qquad H \\
H-O \\
R^2
\end{array}
\right]
\; \rightleftharpoons \;
\left[
\begin{array}{c}
R^1 \qquad O \\
N-C \\
H \qquad O-R^2 \\
O \qquad H \\
R^2 \quad H-O \\
R^2
\end{array}
\right] . \tag{8.6}
$$

$$
\longrightarrow \quad R^1{\underset{H}{\overset{O}{\underset{N}{\big|\big|}}}}O-R^2 \; + \; 2R^2-OH
$$

Further indications that these intermediary complexes might be the dominant ones in practice is that the reaction rate constant rises with large concentration of R^2-OH and falls if protic solvents are used that hinder the alcohols to form their four- or six-membered ring structures by connecting them with their own hydrogen bond networks.

8.1.3 Sequenctial Reactivity

Besides the investigation of autocatalysis with cylic transition states, the influence of already built urethane groups on the reactivity of the diisocyanate shall be investigated. It is known from literature [234] that this influence appears to be negligible in practice, i.e., that the first urethane reaction on a diisocynate happens equally fast as the second. However, a theoretical proof of this independence would of course be desirable.

1,5-naphtyl-diisocynaate (NDI) is frequently used for monitoring the forthcoming of urethane reactions. The two connected benzene rings build a conjugated aromatic system that absorbs UV-radiation. Depending on the number of already happened reactions, i.e., if the diisocynaate, its *monourethane* or its *diurethane* is present, the UV absorption band gets a red shift.

With this, the fractions of NDI, monourethane and diurethane can be determined time-dependently by integrating their respective peaks in the UV-spectrum. The sequential reactions are shown in eq. 8.7. In practice, a small amount of NDI is added to the reaction mixture that mainly contains MDI or others, which themselves impose better properties of the polyurethane matrix.

$$(8.7)$$

8.2   Benchmark of QM Reference Methods

As usual, the calculation of QM reference data was the first step of the EVB-QMDFF setup in this study. In contrast to the other examples presented so far in this thesis, a wise choice of the QM reference is essential, since we want to be able to calculate the urethane reaction rate constants with high quality. Further, we want to have a method that imposes modest scaling since applications to k(T) calculations of even larger systems (i.e., larger substituents of both alcohol and isocyanate molecules) are scheduled for the future.

8.2.1   Settings and Strategy

The present study covers six different systems: The basic bimolecular urethane reaction (eq. 8.2) as well as the autocatalytic cyclic rearrangement pathways (eqs. 8.5-8.6) were studied with two different alcohol molecules each: The simplest possible methanol (MeOH) as well as the 2-methoxyethanol (MeOCH$_2$CH$_2$OH) constituting a more realistic sidechain for real synthesis [3].

Even if the chosen systems are still quite small model cases, their size (up to 46 atoms) is nevertheless much larger than anything treated before with EVB-QMDFF (exceptions are the KMC calculations presented in the next chapter, where most atoms are located in the passive metal bulk). Therefore it became clear in advance that very expensive QM methods like CCSD(T) were out of reach even for calculations of energy corrections. Another strategy was pursued: MP2 will usually be a reliable method for the cases presented here, however it becomes much too expensive for even larger systems than the ones presented here. Alternatively, DFT-based methods impose modest scaling with system size by simultaneously being able to permit high-quality descriptions. However, the actual quality strongly depends on the chosen DFT functional. A whole bunch of them has been emerged since the 90s, and for one specific type of reaction DFT performance may differ from the average performance determined in huge, general benchmarks [235, 236]. Therefore, a benchmark for this particular purpose was performed. MP2 calculations of all six systems were performed (with the cc-pVTZ basis set [237] for the MeOH-substituents and the cc-pVDZ basis set for the MeOCH$_2$CH$_2$OH-substituents), which serves as reference. Since the TREQ method shall be used for PES setup it is useful to calculate the energies of the reaction path with a separate QM method of higher quality (*dual-level* approach, see chapter 5). Therefore, the energies of the MP2 RP were calculated with DLPNO-CCSD(T)[4] [154, 155] and the def2-TZVP basis set [158] using Orca [130, 131]. Then, these calculations were done with 17 different popular functionals as well, using the cc-pVDZ basis set for all of them. The D3 empirical dispersion correction by GRIMME [91] was applied. In addition, three different semiempirical methods, constituting an even cheaper alternative, were investigated as well.

For all methods, TS and IRC optimizations were done with Gaussian 16 [99], the frequencies of the imaginary TS modes that describe the shape of the reaction path at the transition state as well as the total potential energy barrier heights obtained from the IRCs were taken as quality criteria. A DFT method is assumed to perform well in this case if its TS imaginary frequency is similar to that of MP2, the barrier heights are compared with the DLPNO-CCSD(T) energies, calculated on IRC paths optimized with MP2. The TS structures of the six systems optimized with MP2 are shown in fig. 8.1.

---

3 In reality, much longer chains with at least two hydroxyl groups are of course in usage. The pattern of ether groups connecting a sequence of rather small alkyl fragments is quite common, though, therefore making these calculations comparable to real world systems at least in the first place. Calculations of longer chains are the logical next step (see chapter 10).

4 The DLPNO-CCSD(T)-method claims to provide similar quality as "real" CCSD(T) calculations by simultaneously impose much more favorable scaling.
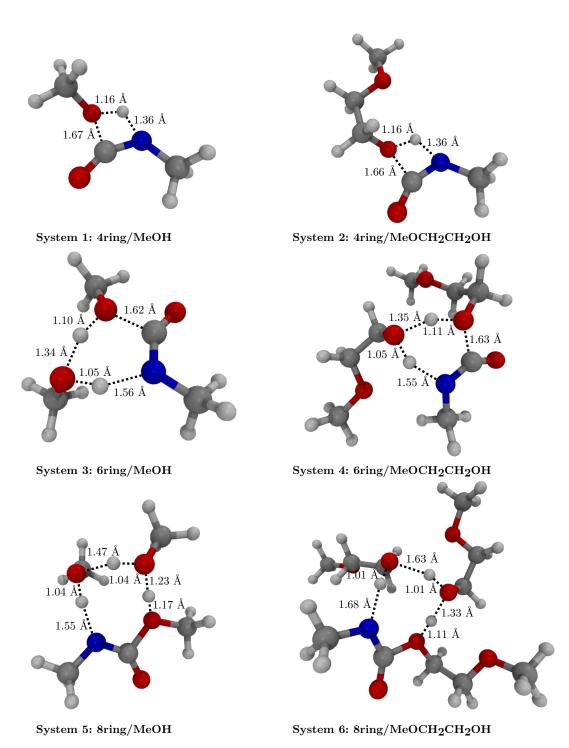
System 1: 4ring/MeOH

System 2: 4ring/MeOCH2CH2OH

System 3: 6ring/MeOH

System 4: 6ring/MeOCH2CH2OH

System 5: 8ring/MeOH

System 6: 8ring/MeOCH2CH2OH

Figure 8.1: Snapshots of TS structures for all six investigated urethane reactive complexes, as optimized with MP2/cc-pVTZ for 1, 3, 5 and with MP2/cc-pVDZ for 2, 4, 6. The bonds involved in the synchronous reaction process are marked, as well as their lengths at the TS.

8.2.2 Computational Details

Depending on the systems and the reference methods, some special care was needed in order to obtain reasonable results for TS and IRC structures.

In order to accelerate the TS optimization, the option `TS=(calcfc)` was used. With this, the Hessian matrix is only calculated once at the beginning of the calculation. In some cases, the TS optimization failed to converge for this setup. Then the maximal number of steps was increased with the options `maxcycles=500` as well as `iop(1/152=500)`. To further promote convergence, the geometry convergence criterion was decreased from `verytight` to `tight` in some cases (usually larger systems).

Starting from the optimized transition states with the correct transition mode IRC calculations were initiated. To decrease the number of Hessians to be calculated, the option `IRC=(calcfc)` was added here again. However if only this option is used, most calculations aborted with corrector step errors. Therefore the option `IRC=(recalc=N)` was added, where `N` was varied between 20 and 5 until the errors vanished. This option requires additional calculations of the hessian at every `N`'th point. For the largest systems this would have been too expensive. For them (4 as well as 6), another IRC algorithm was used instead: *local quadratic approximation* (LQA) for the corrector step. This needs no additional Hessian calculations after the first one, however the obtained IRC path has some "background noise" instead of monotonically decreasing to the minima. This seems to be no huge drawback since in the areas near the minima the QMDFFs are becoming dominant.

8.2.3 Results

In table 8.1 the transition state frequencies for the six systems calculated with the 20 different chosen levels of theory are shown. As indicated above, MP2/cc-pVTZ calculations were only performed for systems 1, 3 and 5 (fig. 8.1), whereas the double zeta basis was used for the larger substituents.

The semiempirical frequencies deviate significantly from the MP2 ones, where AM1 and AM3 overestimate and PM6 underestimates them. The DFT methods show much lower deviations at least for systems 1 and 2. For systems 3 to 6 some of the functionals (e.g., PBE0 or PBEPBE) underestimate the frequencies significantly, where some other functionals did not converge for all systems or revealed other difficulties.

The results of the IRC optimizations are listed in table 8.3. We see similar trends. The semiempirical methods perform worst, AM1 and AM3 overestimate the barrier whereas PM6 underestimates it.

They are further compared with the calculations done in the paper by RASPOET *et al.*. There, the three different reaction mechanisms were evaluated theoretically by optimizing TS as well as reactants and products structures. They used methanol and isocyanic acid (HNCO) as reactants and the MP2/6-31G(d,p) [166, 167] level of theory. We have methanol molecules in systems 1, 3 and 5 as well, but methylisocyanate instead of isocyanic acid, which makes the calculations not fully comparable. Nevertheless, the comparison was made in the table, since the systems are similar.

We see that the TS imaginary frequencies of RASPOET *et al.* are much higher than ours. Since the QM method is basically the same, the reason is probably the different substituent of the isocyanate group. The barrier heights are in turn very similar to our MP2 results, showing that both systems can be well compared in barrier height but not in barrier width (which can be determined from the TS imaginary frequency).

Table 8.1: Transition state optimizations for the six different reactions at several semiempirical and DFT/cc-pVDZ (with D3 dispersion correction) levels, all compared to MP2 results. The absolute of the imaginary mode is given in cm^{-1} in all cases. The default settings were `verytight` TS optimizations with Gaussian16 using an `ultrafine grid` for the DFT methods. In some cases the TS did not converge for this settings, then the `tight` criterion was used.

Method	4ring		6ring		8ring	
	small[a]	large	small	large	small	large
MP2/cc-pVDZ	1416.7	1439.1	623.3	615.1	560.5	318.7
MP2/cc-pVTZ	1426.3	-[b]	519.1	-[b]	441.2	-[b]
AM1 [238]	1820.5	1833.2	1312.4	1187.3	1199.4	-[c]
PM3 [239]	1918.4	1963.1	1674.6	1618.5	1595.1	1522.3
PM6 [240]	1282.4	1061.0	299.8	295.4	185.0	113.0
B2PLYP [241]	1494.2	1519.3	718.4	719.1	616.4	-[d]
B97 [242, 243]	1397.4	1410.5	713.8	737.7	551.8	383.0
B3LYP [200, 201]	1481.5	1511.0	655.6	653.9	539.7	309.8
BLYP [174, 244]	1384.9	1405.8	773.2	809.5	626.6	446.8
PBE0 [205, 206]	1343.7	1382.8	239.0	240.7	78.9	137.4
PBEPBE [245]	1222.0	1258.2	277.8	303.4	108.7	105.4
BP86 [246]	1254.8	1289.4	327.2	360.4	123.0	108.5
BPBE [247]	1252.8	1285.5	362.1	386.3	163.5	124.2
B3PW91 [200]	1371.5	1408.2	356.4	345.5	168.3	132.7
BMK [248]	1314.7	1458.4	594.2	588.9	467.3	162.4
CAM-B3LYP [249]	1446.1	1481.9	360.1	344.8	231.0	124.5
LC-wPBE [250]	1305.9	1351.9	149.1	172.0	-[d]	-[d]
M05 [251]	1087.7	1104.6	642.8	615.0	455.3	213.0
M052X [252]	1391.5	1444.3	134.9	-[d]	71.5	167.7
M06 [253]	1205.5	1226.3	642.0	713.4	287.1	310.0
M062X [253]	1379.2	1424.7	180.1	200.1	137.9	149.5
Raspoet [231]	1963[e]	-	1297[e]	-	1013[e]	-

[a]: *Small* means that MeOH molecules are used as alcohol, *large* means that MeOCH$_2$CH$_2$OH are used instead.
[b]: The systems with the larger alcohol side chains were not calculated with MP2/cc-pVTZ due to the unfavorable scaling with the larger basis set.
[c]: No frequency given because the TS optimization converged to a structure with wrong imaginary mode that belongs to a different kind of reaction.
[d]: The TS optimization did not converge.
[e]: The isocyanate was HNCO instead of CH$_3$NCO, the reference method was MP2/6-31G(d,p).

Table 8.3: IRC optimizations for the six different reactions and levels of theory already noted in table 8.1. All IRCs were optimized with Gaussian16, using the TS structures from table 8.1 as starting points. The basis sets used are the same as for the TS optimizations. The barrier heights stated in this table are given in kJ/mol and were measured by calculating the difference between the TS energy and the energy of the reactants asymptotic regime.

Method	4ring		6ring		8ring	
	small[a]	large	small	large	small	large
MP2	127.73	131.74	58.10	64.36	57.22	50.73
*/DLPNO-CCSD(T)[b]	134.39	139.67	62.94	71.51	61.42	55.50
AM1	237.78	232.54	215.85	206.83	-[c]	-[d]
PM3	171.12	164.72	184.14	-[c]	170.82	240.34
PM6	96.32	82.34	27.37	34.90	28.88	20.59
B2PLYP	149.10	154.94	77.12	83.79	78.69	-[d]
B97	111.30	124.27	42.52	50.59	39.32	38.26
B3LYP	116.85	128.45	45.92	55.66	44.71	41.57
BLYP	103.57	120.90	39.16	48.47	36.83	36.24
PBE0	102.85	112.01	28.57	39.11	78.90	27.78
PBEPBE	85.20	99.22	17.48	29.07	39.10	17.28
BP86	86.49	101.79	16.33	25.28	-[e]	13.11
BPBE	90.88	104.12	22.32	29.94	16.98	16.27
B3PW91	106.89	116.32	33.34	42.26	29.34	28.11
BMK	111.31	120.55	46.14	58.63	42.37	43.19
CAM-B3LYP	109.65	119.94	32.75	44.78	32.21	31.68
LC-wPBE	102.93	112.35	27.76	37.81	-[d]	-[d]
M05	129.10	133.98	49.43	83.12	75.86	71.48
M052X	107.09	113.60	26.90	-[d]	-[c]	30.38
M06	123.45	126.57	50.38	64.47	62.53	55.31
*/DLPNO-CCSD(T)[b]	133.47	135.55	61.57	66.23	59.83	51.23
M062X	113.09	119.16	33.37	43.95	137.90	33.29
Raspoet [231]	135[f]	-	69[f]	-	53[g]	-

[a]: *Small* means that MeOH molecules are used as alcohol, *large* means that $MeOCH_2CH_2OH$ are used instead.

[b]: */DLPNO-CCSD(T) means that the path geometries of the method in the line above (here MP2 or M06) were taken and DLPNO-CCSD(T)/def-TZVP energies were calculated on them. The barrier height was then calculated in the usual way.

[c]: No barrier height given because the IRC did not converged/ended with error messages.

[d]: The TS optimization did not converge, therefore no IRC calculation was possible.

[e]: The LQA method was used for the IRC calculation and did not converge to a minimum but reached even higher energies.

[f]: The isocyanate was HNCO instead of CH_3NCO, the reference method was MP2/6-311++G** based on MP2/6-31G(d,p) geometries.

[g]: The isocyanate was HNCO instead of CH_3NCO, the reference method was MP2/6-31G** based on MP2/6-31G(d,p) geometries.

In table 8.5 averaged results of the benchmark are shown. They were determined by summing up the differences between MP2/cc-pVTZ (systems 1,3 and 5) or MP2/cc-pVDZ (systems 2,4 and 6) and all other methods to be investigated. This was done for TS frequencies and IRC barrier heights as well. Based on these differences a quantitative ranking of all involved methods could finally been done. The three best-performing methods for reproduction of imaginary TS frequencies and IRC barrier heights are marked in the table.

As already seen above, the empirical methods are of insufficient quality for both tasks, many DFT functionals either did not converge for some systems or introduced large errors for one or both values. Based on the ranking, the *M06 functional* was finally chosen. It performs best for barrier heights and is satisfactory for frequencies, at least much better than other methods with similar performance for the barrier heights.

Similar to the MP2 reference, an additional DLPNO-CCSD(T) energy correction was imposed as well for the chosen M06 method. The resulting average difference to the corrected MP2 barriers is also listed in the table. We can see that DLPNO-CCSD(T)//M06 is able to reproduce the DLPNO-CCSD(T)//MP2 barriers with chemical accuracy on average.

The TREQ reference gradients and frequencies for the next section were therefore calculated with M06/cc-pVDZ.

8.3   RPMD Rate Constant Calculations

8.3.1   TREQ Setup

Following QM reference method benchmarks, *black-box* k(T) calculations were started, where the PES shall be described with the TREQ method[5]. As described in section 3.3.8, the program `evb_kt_driver.x` is able to calculate rate constants and Arrhenius parameters if an IRC and a generic input file with some general input parameters is given by the user.

For all six systems, the actual approach was similar. Since MO06/cc-pVDZ with DLPNO-CCSD(T) energy corrections has been shown to be the best performing DFT method, the optimized M06 IRCs were taken as input. A number of gradients and Hessians along the reaction paths was calculated with M06 as well. The number and positions of those points are also determined automatically, where the total number of those points raises with system size.

The positions of the picked gradient/Hessian reference points are plotted in fig. 8.5. Due to the large size and dimensionality of the investigated systems, a rather dense grid of gradient/Hessian points was chosen. In the TS region where the slopes are high, almost each IRC energy point is also a gradient/Hessian point, whereas this proportion shrinks to about 3:1 at the reactants/products asymptotes.

8.3.2   Special Settings for RPMD

In contrast to the smaller systems presented in chapters 5 and 6, the k(T) calculations for the urethane systems were no "true" *black-box* ones, which is due to the set of internal coordinates. The algorithm for their automated determination in `evb_kt_driver.x` is only able to pick bond lengths and bond angles according to the bonding configuration of the system. This works well for small systems (up to approximately 10-15 atoms) but is insufficient for the urethane systems investigated here. Besides their larger size, the planarity of the transition states might impose other problems (incompleteness of the internal coordinate set), which causes the systems to explode during MD trajectories.

---

5 The k(T) calculations were done on DG-EVB-QMDFF surfaces in the first place, resulting in rugged free energy surfaces and poorly converged reaction rate constants, probably due to insufficient validity of the underlying damped Taylor expansions in the transition region (see chapter 5 as well).

Table 8.5: Quality of the different levels of theory used in comparison to the method viewed as reference with the best quality. In the case of the TS imaginary frequencies, MP2/cc-pVTZ frequencies were used as reference where calculated, else MP2/cc-PVDZ. In the case of the barrier heights, the DLPNO-CCSD(T) energies calculated on the MP2/cc-pVDZ path structures were used as reference. Deviations of all methods to these were calculated by adding the absolute values of differences between method and reference. The given deviations are the sum of all six systems, divided through the number of available data for this method. Methods which did not converge in all systems (either at TS or IRC calculations, respectively) are printed in italics, the three best performing methods for both topics are printed in bold.

Method	imag. TS freq.	barrier height
MP2/cc-pVDZ	77.70[a]	**5.924**
*/DLPNO-CCSD(T)	-[b]	0.00
MP2/cc-PVTZ	0.00	-[c]
AM1	*582.4*	*121.1*
PM3	922.08	*95.44*
PM6	253.81	39.17
B2PLYP	*125.32*	*14.74*
B97	91.616	19.86
B3LYP	**68.3**	15.37
BLYP	139.45	23.37
PBE0	222.83	28.69
PBEPBE	247.33	39.68
BP86	216.03	*44.20*
BPBE	197.51	40.82
B3PW91	162.81	28.19
BMK	**69.1**	17.20
CAM-B3LYP	149.38	25.73
LC-wPBE	*255.17*	*31.91*
M05	152.78	11.08
M052X	*188.98*	*28.63*
M06	136.26	**7.49**
*/DLPNO-CCSD(T)	-[b]	**2.924**
M062X	214.66	32.93

[a]: The difference was only calculated for the three small systems, in relation to the MP2/TZ reference values.
[b]: Due to the lack of analytic gradients, only energies were calculated with DLPNO-CCSD(T), therefore no frequency deviations could be measured.
[c]: Only two of three MP2/cc-PVTZ IRC-calculations for the small systems finished in time, therefore no barrier heights were calculated with them.

(a) 4ring/MeOH

(b) 4ring/MeOCH$_2$CH$_2$OH

(c) 6ring/MeOH

(d) 6ring/MeOCH$_2$CH$_2$OH

(e) 8ring/MeOH

(f) 8ring/MeOCH$_2$CH$_2$OH
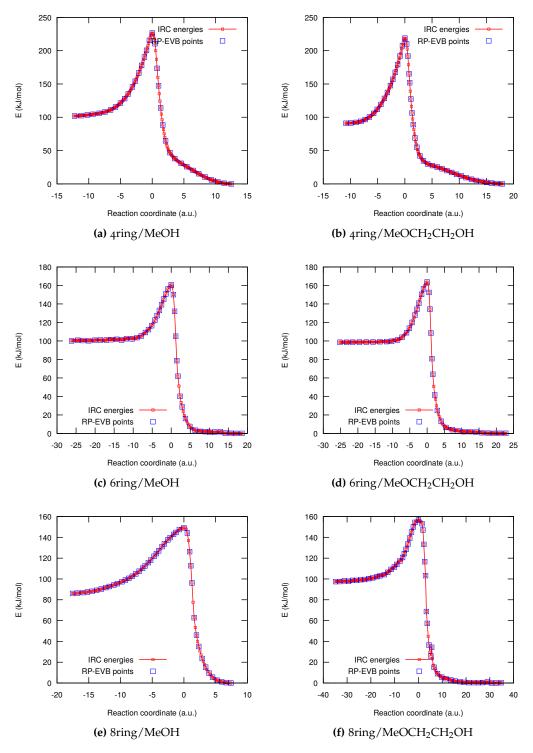
Figure 8.2: Location of the RP-EVB gradient and Hessian reference points on the M06 IRC curves used as interpolation for the TREQ method.

This problem was solved by introduction of *dihedral* and *out-of-plane* angle coordinates. If we add some of these coordinates to the atoms that become part of the cyclic TS during the reaction the bad behavior can be avoided. So far, no clever algorithm for the right choice of additional dihedral and out-of-plane coordinates was developed, therefore they were chosen manually.

Two changes concerning the RPMD k(T) calculations shall be mentioned as well. In the simplest case (systems 1 and 2), the urethane is built by an addition reaction, where one bond is broken and two are built. Since the RPMDrate program by SULEYMANOV is unable to calculate k(T) values for such reactions, the `rpmd.x` program with a more general definition of the dividing surface has been developed (section 3.3.7). With this, the simple urethane reaction mechanism can be treated as a simple bimolecular addition reaction. However, things get more complicated when we look at the autocatalytic reaction mechanisms expressed by systems 3 to 6. Here, three or four reactant molecules come together and react simultaneously at the TS. We might expect that these are tri- or tetramolecular reactions, respectively, due to the number of reactants that come together simultaneously. This is shown in fig. 8.3, (a).

In reality, reaction orders of three or four are almost unknown since synchronous hits of three or four molecules coming from different directions are extremely unlikely. Therefore, another mechanism is calculated in the examples. As already shown above (eqs. 8.5-8.6) it is assumed in the literature that the alcohol molecules build dimers or trimers if no protic solvent is used. Urethane reactions with autocatalysis now start if the isocyanate molecule and an alcohol cluster approach each other such that they can build the cyclic TS complex (fig. 8.1). This reaction then is a bimolecular one where the alcohol cluster can be treated as a single molecule at least in the asymptote of distant approach.

In order to teach `rpmd.x` to calculate such a reaction, the definitions of reactants and TS dividing surfaces must be set independently. The reactant dividing surface (eq. 3.10) is that of a bimolecular reaction ($N_{ed} = 2$), since the alcohol cluster can be seen as a single molecule from afar. The umbrella bias is therefore applied on the center of mass of all two or three alcohol molecules, letting them build a hydrogen bond network freely. If the molecules stick together and build the reactive complex, the simplified picture of two molecules must be broken at least partly. Depending on the number of molecules involved we have a larger number of built and broken bonds (according to the reformed hydrogen bond network) than in the simplest case. Near the TS, the bias is applied on all those bonds (eq. 3.11), thus treating all involved molecules as separate entities. Therefore, the TS dividing surface is rather that of a tetramolecular reaction than that of a bimolecular one. This composite reaction type has been introduced into `rpmd.x` with the descriptors *3 educt cyclic addition (SC)* and *4 educt cyclic addition (SC)*, where SC stands for solvent complex (table 3.4).

Experimental works obtained indications that the actual autocatalytic reaction has a reaction order between two and three, according to a mixture of solvent complex reaction and "real" tri- or maybe even tetramolecular reactions with separate approaching of the alcohol molecules. Here we assume that the reactions are fully bimolecular at least in the asymptotic limit, such that the usual bimolecular RPMD k(T) formula can be applied. This assumption seems to be legitimate, as will be shown when the RPMD results are compared with experimental results from Covestro in the prepared publication.

The second change that needs to be applied on `rpmd.x` is the way in which the free energy surface is postprocessed for the final k(T) calculation (eq. 2.103). Usually, the free energy of the reactants is evaluated at the reactants asymptote ($\xi = 0$). This scheme might be called the *asymptote barrier* approach (see fig. 8.4). For the urethane reactions it turned out that the resulting Arrhenius parameters agree much better with the experimental ones if a slight change is made: Instead of taking the free energy value at $\xi = 0$ for the reactants, the global minimum of the calculated free energy curve is determined and the free energy of the reactants is calculated at this point, resulting in a larger barrier and a lower rate constant.

The reason why this modification leads to better agreement with experiment might be that the measurements were done in solution and not in the gas phase as our calculations. In solution, the
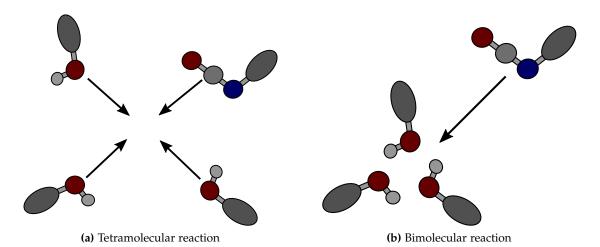
(a) Tetramolecular reaction   **(b)** Bimolecular reaction

Figure 8.3: Schematic illustration of the difference between a "true" tetramolecular reaction (all four reactants approach simultaneously from different directions in space) (a) and a solvent-complex bimolecular reaction, where the fourth reactant approaches to an aggregate of all three other reactants, acting as a single reactant from afar (b).

concentration of reactants is of course much higher, such that most reactive processes will happen not by collisions from two entities approaching from apart but instead will start from closely aggregated reactants that might, e.g., already be stabilized by the surrounding hydrogen bond network. The actually calculated reaction now starts from the local minimum of both reactants (isocyanate and diol to triol) already experiencing some stabilizing noncovalent interactions. In the dimension of the reaction path this can be expressed by locating the reactants dividing surface at the free energy minimum before the TS. This approach shall be termed *aggregation barrier* in the scope of this thesis. A special switch was introduced into the `rpmd.x` handling (`pmf_minloc`) that allows to vary between both reactants definitions.

8.3.3 Rate Constant Calculations

All subsequent steps, TREQ parametrization as well as running the RPMD calculations, were then done in true *black-box* fashion. For optimal comparison with experimental results from Covestro (not shown here), temperatures between 300 and 500 K were calculated. In order to estimate the degree of convergence of the RPMD calculations, five single k(T) calculations with `rpmd.x` were invoked by `evb_kt_driver.x` for each temperature, the resulting rate constants were then averaged in order to determine Arrhenius and Eyring parameters for later comparison with data from Covestro.

Initially, RPMD calculations with one bead, i.e., classical trajectory samplings, were done with all six reactions. For the first five systems, reasonable k(T) values were obtained (with low variances of the five single runs), whereas it was not possible to converge the rate constants for system six. For this system, the five single RPMD calculations gave wide-spread values, such that no reasonable fit for Eyring parameters was possible. We were not able to decrease the variance significantly by improvement of the settings such as longer sampling trajectories or other internal coordinate sets for TREQ. As mentioned above, this problem might originate in the huge coordinate space or improper sets of internal coordinates. The calculated reaction rates for the first five systems at different bead numbers, averaged over five single calculations, are shown in table 8.7.

It becomes obvious that quantum effects play a significant role for the 4-ring systems as, e.g., the k(T) values of system 1 at 300 K are accelerated by four orders of magnitudes going from one to 16 beads. This is due to the narrow IRC barriers (fig. 8.5), which allow for significant tunneling. For
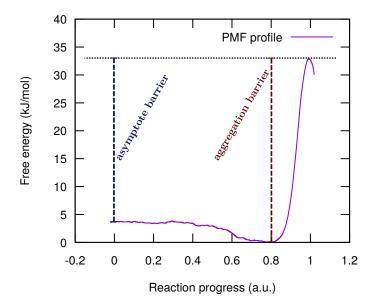
Figure 8.4: Illustration of the slightly changed dividing surface definition used for the final k(T) calculations. Instead of using the asymptotic free energy value as reactants free energy value, the global minimum of the curve is chosen, corresponding to the assumption that the reaction will actually start from an aggregated complex. The shown free energy surface is of system 1 at 300 K, calculated with 16 beads.

the larger rings, the barriers become broader and thus the effect of tunneling decreases. For system 5, tunneling accounts only for a factor of 30 k(T)-increment at 300K. RPMD calculations of system 5 with 8 or more beads show similar problems as the one-bead calculations of system 6, probably due to the enlarged coordinate space of the ring polymers, leading to insufficient samplings even for more expensive calculations.

8.3.4 Arrhenius and Eyring Fits

In table 8.9 results for Arrhenius as well as Eyring fits of the averaged rate constants for the first five systems are listed for all calculated RPMD bead numbers. Besides this, the results of TST calculations done by Covestro [254] are listed for comparison.

The *linear correlation coefficient R^2* indicates how well the linear Arrhenius behavior is reproduced (if we assume that exact calculations would indeed obey Arrhenius law). This quality seems to deteriorate slightly with system size. Where for system 1 the averaged rate constant are almost exactly linear ($R^2 > 0.999$), it becomes approximate 0.995 for systems 4 and 5.

With respect to the Eyring-parameters, similar behaviors can be seen for systems 1 and 2. The RPMD activation enthalpy is much larger than the TST one, whereas the absolute value of the activation entropy is larger for TST than for RPMD. Since the RPMD calculations are well converged for them, the TST values are probably of lower quality. The large values of the TST activation enthalpies signalize that the tunneling effects might be treated insufficiently. Both methods coincide well for the 6-ring systems 3 and 4. For system 5, the differences are again much larger, probably due to incomplete RPMD sampling of the more complex coordinate space or deficiencies in the proposed reaction model of the isocyanate approaching the aggregated alcohol molecules, which is not considered in the TST calculations.

In fig. 4, Eyring plots for the first five reactions are shown. In all cases, the calculations with the largest bead number are presented, i.e., 16 beads for the 4-ring systems, 8 beads for the 6-ring systems and 4 beads for the 8-ring system.

Table 8.7: Calculated RPMD reaction rate constants for the first five urethane reaction systems. Shown are the average values of five k(T) values per setting, for different temperatures as well as bead numbers. Units are cm^3 molecule^{-1} s^{-1}, 1(-14) means $1 \cdot 10^{-14}$.

RPMD beads	T(K)				
	300	350	400	450	500
		System 1			
1	6.39(-32)	5.50(-29)	8.08(-27)	3.89(-25)	9.31(-24)
2	4.68(-29)	8.33(-27)	4.75(-25)	1.01(-23)	1.15(-22)
4	3.97(-28)	3.16(-26)	1.24(-24)	2.67(-23)	2.70(-22)
8	3.85(-28)	4.70(-26)	2.24(-24)	3.83(-23)	4.50(-22)
16	6.42(-28)	8.84(-26)	3.83(-24)	6.76(-23)	6.51(-22)
		System 2			
1	9.54(-35)	2.51(-31)	4.27(-29)	3.62(-27)	1.12(-25)
2	7.03(-32)	1.17(-29)	1.11(-27)	8.94(-26)	7.90(-25)
4	1.85(-32)	2.20(-30)	1.49(-28)	8.96(-27)	3.77(-25)
8	8.43(-33)	1.66(-30)	3.57(-28)	1.90(-26)	3.93(-25)
16	2.31(-32)	3.13(-30)	4.11(-28)	1.47(-26)	2.86(-25)
		System 3			
1	3.49(-32)	2.12(-30)	7.70(-29)	9.50(-28)	4.89(-27)
2	2.93(-30)	2.07(-28)	2.15(-27)	7.22(-26)	1.52(-25)
4	1.63(-29)	3.38(-28)	1.04(-26)	5.01(-26)	3.97(-25)
8	3.92(-29)	1.85(-27)	2.24(-26)	1.90(-25)	9.40(-25)
		System 4			
1	2.05(-28)	2.80(-27)	9.44(-26)	2.62(-25)	1.93(-24)
2	7.46(-28)	1.18(-26)	1.17(-25)	1.56(-24)	4.94(-24)
4	2.62(-27)	4.08(-26)	5.26(-25)	3.68(-24)	6.66(-24)
8	2.85(-27)	2.70(-25)	1.37(-24)	8.93(-24)	2.06(-23)
		System 5			
1	9.13(-31)	8.88(-30)	1.10(-28)	2.16(-28)	3.00(-28)
2	6.01(-30)	1.06(-28)	5.34(-28)	4.67(-27)	1.42(-26)
4	2.79(-29)	3.95(-28)	1.27(-27)	7.17(-27)	2.01(-26)

8.4 Influence of Prior Reactions

As explained in section 8.1, one objective of our cooperation is to investigate the influence of prior urethane reactions on the rate constant of the actual one. In eq. 8.7, two rate constants k_1 and k_2 are shown. The first rate describes the process of an alcohol molecule reacting with the NDI to its monourethane. The second rate then describes the reaction of monourethane with a second alcohol to the final diurethane molecule. In order to benchmark the ability of RPMD to reproduce experimental trends in urethane chemistry, we wanted to calculate rate constants for both processes and compare them which each other.

Table 8.9: Arrhenius and Eyring parameters obtained from fitting of their respective plots for all investigated systems and bead numbers. For comparison, TST results from Covestro are listed as well. The units for the activation energies (E_a), activation enthalpies ($\Delta H^\ddagger$) as well as activation entropies ($\Delta S^\ddagger$) are kJ mol^{-1}. 1(-14) means $1 \cdot 10^{-14}$.

beads	Arrhenius plot			Eyring plot			
	E_a	A	R^2	E_a	A	$\Delta H^\ddagger$	$\Delta S^\ddagger$
system 1							
1	116.94	1.48(-11)	0.999998	116.27	1.15(+08)	113.77	-91.64
2	92.17	4.92(-13)	0.999986	91.49	3.82(+06)	89.00	-119.95
4	84.15	1.44(-13)	0.999289	83.48	1.12(+06)	80.98	-130.14
8	86.99	5.00(-13)	0.999895	86.31	3.89(+06)	83.82	-119.82
16	86.50	7.27(-13)	0.999998	85.83	5.62(+06)	83.33	-116.71
TST	-	-	-	131	7.01(+04)	129	-180
system 2							
1	127.90	1.90(-12)	0.999427	127.22	1.48(+07)	124.73	-108.71
2	103.31	4.27(-14)	0.998504	102.64	3.32(+05)	100.14	-140.27
4	106.76	2.34(-14)	0.994085	106.08	1.82(+05)	103.59	-145.26
8	111.79	1.34(-13)	0.998718	111.11	1.04(+06)	108.62	-130.74
16	104.08	1.58(-14)	0.997967	103.41	1.23(+05)	100.91	-148.55
TST	-	-	-	140	4.11(+04)	138	-184
system 3							
1	73.05	1.88(-19)	0.998277	72.38	1.46(+00)	69.88	-242.84
2	69.38	3.52(-18)	0.995857	66.21	2.74(+01)	66.21	-218.45
4	63.35	1.34(-18)	0.997680	60.18	1.04(+01)	60.18	-226.47
8	63.46	3.66(-18)	0.998995	62.89	2.84(+01)	60.29	-218.14
TST	-	-	-	63	2.34(+03)	60	-208
system 4							
1	57.57	1.68(-18)	0.993768	56.90	1.31(+01)	54.40	-224.60
2	55.91	3.06(-18)	0.995913	55.23	2.38(+01)	52.74	-219.63
4	51.66	2.33(-18)	0.995730	50.98	1.81(+01)	48.49	-221.88
8	54.34	1.32(-17)	0.988085	53.67	1.03(+02)	51.17	-207.47
TST	-	-	-	70	1.91(+03)	68	-210
system 5							
1	32.11	5.14(-25)	0.923282	31.44	4.00(-06)	28.94	-349.32
2	48.44	1.27(-21)	0.998808	47.76	9.88(-03)	45.27	-284.37
4	41.66	4.10(-22)	0.997319	40.99	3.19(-03)	38.50	-293.77
TST	-	-	-	51	3.36(+04)	49	-186

(a) 4ring/MeOH

(b) 4ring/MeOCH$_2$CH$_2$OH

(c) 6ring/MeOH

(d) 6ring/MeOCH$_2$CH$_2$OH

(e) 8ring/MeOH
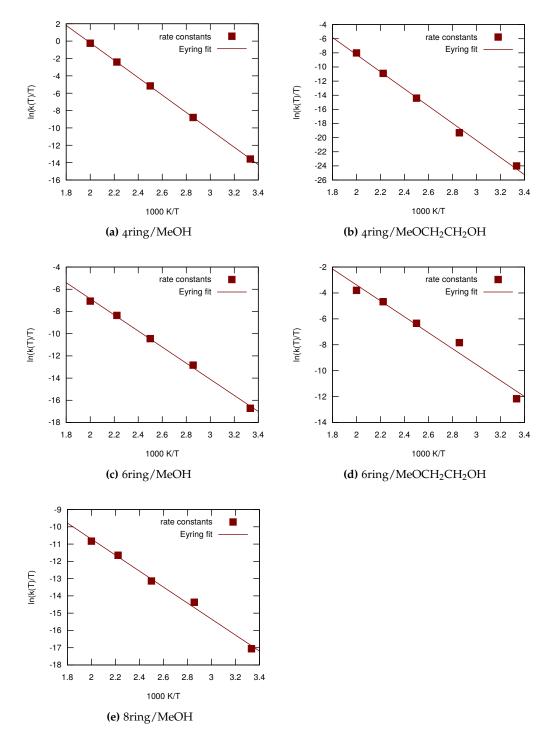
Figure 8.5: Eyring plots for the first five urethane systems shown in fig. 8.1. Each data point was obtained by averaging of five single reaction rate constant calculations.

System 7: 4ring/MeOH

System 8: 4ring/MeOCH$_2$CH$_2$OH

System 9: 6ring/MeOH

System 10: 6ring/MeOCH$_2$CH$_2$OH
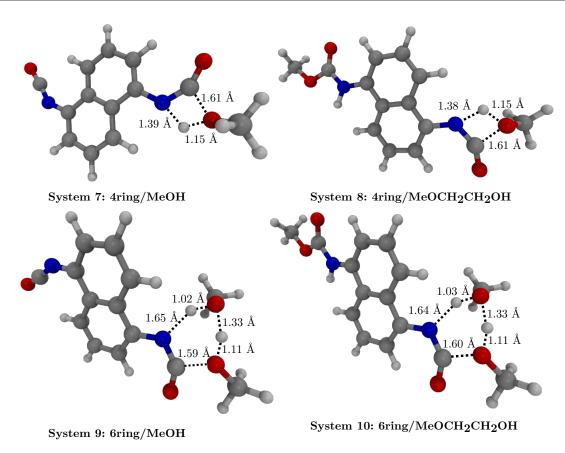
Figure 8.6: Optimized TS structures for the four different reactions possible with the two-step urethanation of NDI. The structures were optimized with MP2/cc-pVDZ.

The first step is of course again to find a reliable QM method for the calculation of TREQ reference data. As depicted above, the DFT benchmark done in section 8.2 has the claim that the best method found there can be used for all urethane reactions.

Therefore, the M06/cc-pVDZ level of theory with D3 empirical dispersion correction was used to calculate the reaction paths of first and second urethanations. These reactions can of course also be accelerated by autocatalysis. Interestingly we found out that the 8-ring cyclic process present in reactions 5 and 6 could not happen if NDI is the isocyanate, since the aromatic system is too bulky for the formation of a hydrogen bond system with three alcohols in its direct vicinity. With this, only four reactions could be studied in total: First and second urethanation with the 4-ring and 6-ring mechanisms, respectively. Transition states of those reactions optimized with MP2/cc-pVDZ are presented in fig. 8.6.

In order to check if the M06 method performs also well for the NDI reactions (i.e., gives similar results to MP2), IRC optimizations were done with both methods for all four reactions. Finally, DLPNO-CCSD(T) energies for all IRC structures were calculated as well in order to use them for the TREQ *two-level* approach. The results of these calculations are shown in table 8.10. If we compare the MP2 activation barriers with the M06 ones, we see that they differ by less than 3 kJ/mol for all four systems. If the DLPNO-CCSD(T) calculations on the MP2 and M06 paths are compared, the differences slightly shrink for the 4-ring reactions and grow for the 6-ring reactions. For all combinations, the differences are within chemical accuracy, thus indicating that M06 works well also for this kind of urethane reactions.

By further comparing the activation barriers of the first and second reactions, the differences are even smaller. For the 4-ring reactions, they are less than 1.5 kJ/mol, for the 6-ring reactions, they

Table 8.10: Barrier heights for the urethane reactions with NDI as isocyanate. 4- and 6-ring transition states are considered, calculations are done with MP2 and M06, which was the best performing DFT method from the investigation above. The barrier heights were also calculated with DLPNO-CCSD(T).

Method	4-ring		6-ring	
	first	second	first	second
MP2	120.26	119.70	51.09	52.80
*/DLPNO-CCSD(T)^a	126.53	126.95	55.41	57.13
M06	117.52	117.96	51.88	52.14
*/DLPNO-CCSD(T)^a	124.49	125.68	51.69	53.58

^{a}: */DLPNO-CCSD(T) means that the path geometries of the method in the line above (here MP2 or M06) were taken and DLPNO-CCSD(T)/def-TZVP energies were calculated on them. The barrier height was then calculated in the usual way.

are slightly larger, but still below 2 kJ/mol. This undermines the proposed independence of the reaction rate constant on the first urethane reaction at a NDI molecule.

Unfortunately, it was so far not possible to obtain reasonably converged rate constants for all four systems based on the TREQ surface. The reason appears to be similar to system 6 in the previous section, i.e., the huge coordinate space or an improper set of internal coordinates.

Kinetic Monte Carlo

So far we have seen how the EVB-QMDFF methodology can be used to calculate k(T) values of several reactive systems. By using the *black-box* procedure developed in this thesis the user-sided effort for setup and performing such calculations is almost set to zero, at least if the systems are not too large or otherwise pathological.

However, in real chemical systems, several different reactions are usually taking place in parallel. Calculations of rates for single elementary reactions are of great importance for their understanding as well as benchmark of accurate theoretical methods, but of course it should be our demand as well to study everyday chemical systems. For them, the aseptic picture of single independent gas-phase reactions becomes cracky: even for relatively simple systems (with respect to the number of different elements involved) like the combustion of hydrogen, alkanes or alcohols, a whole zoo of dozens to hundreds of different elementary reactions can take place [255, 256]. If we found out which of them are important, we can calculate all their k(T) values. But still it is not clear how we can set them together in order to get the overall large-scale dynamics. When does which reaction occur? There are many different *continuum kinetic* models for, e.g., certain combustion processes, such as of H_2 [257], Kerosene [258] and CO [259]. As it was mentioned in the introduction, continuum and particle kinetics are two different concepts of modeling chemical reality: in continuum kinetics we are unable by definition to look at the processes of interest with molecular resolution. We can simulate systems of real-world size, but with no real existence of it in space. It is silently assumed that, for instance, reactants are distributed equally. In reality, we might be interested in spatially varying reactant concentrations or in the fate of single molecules during the process, which can only be handled by particle kinetics. Therefore, continuum kinetic approaches are improper for our desires.

One alternative is to return to a real-time simulation of the whole system: Instead of calculating k(T) values for a bunch of model reactions we could simply run reactive dynamics of a large vessel of, e.g., carbohydrate molecules and look what happens. Since most reactions are rare events even at high temperatures, millions to trillions of time steps will be needed to consider the large-scale low-frequency coupled reactive processes which might take milliseconds or even seconds. Further, several local reactions might be influenced by their neighborhood, e.g., if a needed reactant for reaction B is the product of reaction A, such that B can only occur if A has been completed some Ångstroms away. In order to model such interactions realistically and quantitatively, thousands to millions of atoms must be propagated simultaneously. Such timescales are accessible if we use simple MM methods specialized for biochemical systems, e.g., in order to study protein folding [260, 261].

Unfortunately we need a PES description that is able to describe bond fissions and other reactive processes with high quality, which requires the usage of *ab-initio* MD. This is of course unfeasible even if semiempirical models are used[1].

One quite popular alternative is the ReaxFF force field (section 2.2.2) since it can describe all relevant reactive processes and imposes a relatively moderate scaling located between traditional nonreactive FFs and semiempirical methods. Large scale ReaxFF calculations were conducted, e.g., for the simulation of hydrogen combustion [263], ignition front propagation [264] and combustions of different coal brands [265, 266][2].

Unfortunately, the ReaxFF parametrization might become quite complicated, especially if complex catalytic processes with hundreds to thousands of possible reactive pathways shall be treated. We need to choose a useful set of *ab-initio* information, further, the user must monitor the whole parametrization process of the interdependent parameters thoroughly in order to avoid artifacts (like unphysical side reactions) that might diminish the quality of the FF [79].

It is almost impossible to parametrize a ReaxFF force field that is able to describe the PES sections of all relevant reactive processes with *chemical accuracy*, which is needed due to the heavy dependence of k(T) values to the barrier heights and shapes (eq. 2.10)[3].

An alternative is the *Kinetic Monte Carlo* method [267, 268], that is able to combine high-quality k(T) values of several elementary reactions to a realistic simulation of the whole reactive system.

In section 9.1 the general idea and mathematical foundation of the method is presented, in section 9.2 a generic application of the method to a mathematical example system is shown. This general procedure is translated to realistic chemical situations in the last two sections: The diffusion of hydrogen atoms on a Cu(001) surface (section 9.3), named *H@Cu(001)* and the diffusion and aggregation of copper atoms on the same surface (section 9.4), named *Cu@Cu(001)*. Compared to the combustion examples shown above the KMC applications presented here look quite primitive, however, they shall serve as a first proof-of-principle that it is possible to connect the EVB-QMDFF-RPMD k(T) calculation machinery to large scale chemical simulations.

9.1   Foundations

Since chemical reactions are rare events, the system's trajectory will usually be trapped some amount of time in a potential energy minimum, corresponding to a certain molecular configuration, until it is finally able to cross the barrier to a neighbored minimum. The vibrational movement inside these local minima takes place in the range of femtoseconds, such that small MD time steps are needed to describe them properly. However, if we are interested in chemical reactions, vibrations around local minima are of no importance at all, only transitions between neighbored minima are relevant for us. Good insights on the separated timescales of molecular vibrations and reactive events can be gained by reviewing the k(T) calculations in the covalent mechanochemistry chapter (section 7.5).
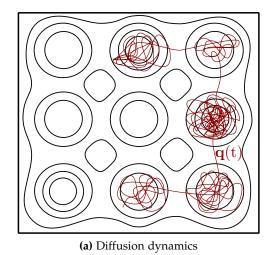
In KMC the coordinate space of the system is subdivided into different *sites* that contain the vicinity of a local minimum. The different sites border to each other at *transition state dividing surfaces* (section 2.1.1).

---

1 There exist some prominent studies of *ab-initio* nanoreactors, e.g., by MARTINEZ *et al.* [262], but these are very expensive and rather small in scale (e.g., around 40 initial molecules in use). Several tricks like high temperature and pressure as well as modified dynamics that push reactants out of their local PES minima need to be utilized for them. They reveal, however, that hundreds of chemical species and reactions become important even if we start from rather simple molecular species.

2 The last mentioned example of the combustion of Illinois no. 6 coal was simulated with 50000 atoms (728 molecules) over a evolved time of 250 ps, where a high temperature of 2000 K was used in order to accelerate the reactive processes.

3 If we rather want to simulate *qualitatively* what happens, for instance, which molecules can be built from an original set of structures, ReaxFF is of course still very useful, since it usually provides at least a qualitatively correct picture of the reactions and their relative velocities.

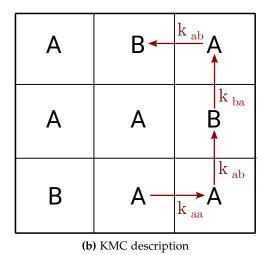**(a)** Diffusion dynamics   **(b)** KMC description

Figure 9.1: The general idea of KMC, illustrated for a simple gas-phase diffusion process. In reality, an atom noncovalently bonded onto the surface will usually be trapped into one of the local minima (here, minima of different depths are present), transitions between those minima are rare events (a). In KMC, the surface is represented by a discrete lattice, where each local minimum is seen as one site. All dynamics is reduced to randomized transitions between the lattice sites, with chemical reaction rates of the transition processes determining their incidence.

The detailed movement of the system in coordinate space is ignored, all what matters is in which site (i.e., in which local PES minimum) the system is located at a certain time. Hence the KMC dynamics of the system can be fully described if only crossings between different sites are calculated correctly. This model closely resembles TST (section 2.1.1), in which only trajectories crossing the TS dividing surface contribute to the total $k(T)$ value. All dynamics around the reactants minimum is considered by calculation of its partition sum.

Thanks to this formal agreement between TST and KMC it can be shown that the overall dynamics of a system is described properly if all relevant (i.e., sufficiently many) $k(T)$ values for transitions between its PES sites are known [267]. In principle, the dynamics of each chemical system could be properly described by KMC. After dividing the PES of the system into a number of sites, one for each local minimum that is sufficiently accessible, $k(T)$ calculations must be done for all relevant transitions between neighbored sites. Then a KMC simulation as explained in the next sections can be done by performing the reactions according to their relative rates as simple steps from one site to another (like in a game of chess). This is illustrated in fig. 9.1.

It should be noted that (at least so far) KMC is mostly applied to reactions on surfaces, such as catalytic processes[4]. The reason is that the number of accessible local minima as well as reactive transitions between pairs of them grows exponentially with the system size for most systems. If, e.g., reactions in enzymes are investigated, separate $k(T)$ values might be needed for each thermally accessible configuration of the side chains around the reactive core, since they could affect the reactivity. The number of those configurations can easily be of astronomic scale, such that the number of $k(T)$ values might be astronomic as well.

Surface reactions have the huge advantage that the PES is periodic and two-dimensional (if the internal structure of molecules on the surface is neglected at first). Hence the number of sites only grows quadratically with the size of the system instead of exponentially in the case of enzymes. Further, only transitions that are possible in the given unit cell must be treated. With this, we can

---

4 There also exist KMC studies of gas phase diffusion processes, where the same methodology is used as shown below, with the exception that reactive events are now *collisions*, whose rate and location is determined by chance [269]. Besides this, the more general *off-lattice* KMC can be used, where Monte Carlo dynamics in continuum space is used to guide the system between reactive events and no initial definition of lattice sites is needed [270].

simulate surfaces of millions of atoms by only knowing some dozens of relevant reaction rates. Therefore, only surface diffusions are shown here.

9.1.1   Integrating the Master Equation

The KMC formalism is based on the *Master equation* [267], which describes the time evolution of a state α by means of its interaction to all other states β:

$$\frac{dP_\alpha}{dt} = \sum_\beta \left[W_{\alpha\beta} P_\beta - W_{\beta\alpha} P_\alpha \right].$$ (9.1)

Here, the sum runs over all other states β of the system, and $W_{\alpha\beta}$ is the probability per unit time of the system to go from state α to β. As it can be shown [267], these transition probabilities are actual transition *rates*, such that our calculated k(T) values can be inserted for the $W_{\alpha\beta}$ values.

Since we want to have the actual time-dependent state occupations rather than their time derivatives, an *integral formulation* of the Master equation is needed. For this, it is instructive to introduce a *transition probability matrix* $\mathbf{W}_{\alpha\beta}$ which contains all transition rates $W_{\alpha\beta}$ between the states located in the rows and columns. We are only interested in transitions between different states, therefore the diagonal elements of the transition matrix need to be zero:

$$W_{\alpha\alpha} = 0.$$ (9.2)

Besides matrix $\mathbf{W}_{\alpha\beta}$, which describes the influx to state α from all states β, another diagonal matrix describing the drain from state α to all other states is needed:

$$\mathbf{R}_{\alpha\beta} \equiv \begin{cases} 0 & \Leftrightarrow \alpha \neq \beta, \\ \sum_\gamma W_{\gamma\beta} & \Leftrightarrow \alpha = \beta. \end{cases}$$ (9.3)

With these two matrices, the initial Master equation (eq. 9.1) can be rewritten as a vector equation[5], where the initial probabilities of all possible configurations are given by vector $\mathbf{P}$, which has the dimension of accessible configurations:

$$\frac{d\mathbf{P}}{dt} = -(\mathbf{R} - \mathbf{W})\mathbf{P}.$$ (9.4)

Since matrix $\mathbf{R}$ describes the decrease of probability for all states α, it can be used to model the exponential decrease of all states with time $\mathbf{Q}(t)$ in an integrated form:

$$\mathbf{Q}(t) \equiv \exp[-\mathbf{R}t].$$ (9.5)

Depending on the amount of drain from state α, the decrease of its probability can be calculated by applying this decrease function to the initial probability vector. Of course, each probability-decrease will lead to an increase of another state, such that the total probability to find the system in any state stays unity. As we have seen, matrix $\mathbf{W}_{\alpha\beta}$ describes those changes. The integrated Master equation can therefore be obtained by adding a time-integral of this matrix, working on the actual state vector $\mathbf{P}(t')$.

$$\mathbf{P}(t) = \mathbf{Q}(t)\mathbf{P}(0) + \int_0^t dt' \mathbf{Q}(t - t')\mathbf{W}\mathbf{P}(t')$$ (9.6)

This equation is still difficult to handle, because the unknown time-dependent state vector $\mathbf{P}(t')$ must be integrated over time. If we express the unknown $\mathbf{P}(t')$ term again by equation 9.6 (where t

---

5 The resulting equation can be seen as a time-dependent Schrödinger equation (eq. 11.24) in imaginary time, where $\mathbf{R} - \mathbf{W}$ is the Hamiltonian of the system and $\mathbf{P}$ the wave function, expressed in its eigenstates.

should be replaced by t' and t' by t''), we can build an infinite recursive equation, which finally will act on the starting point $\mathbf{P}(0)$:

$$
\mathbf{P}(t) = \Bigg[\mathbf{Q}(t) + \int_0^t \mathbf{Q}(t-t')\mathbf{W}\mathbf{Q}(t')dt'
$$
$$
+ \int_0^t \int_0^{t'} \mathbf{Q}(t-t')\mathbf{W}\mathbf{Q}(t'-t'')\mathbf{W}\mathbf{Q}(t'')dt'dt'' + ... \Bigg] \mathbf{P}(0)
\tag{9.7}
$$

It can be interpreted as follows: The first term on the right describes the probability that the state of the system does not change in the time interval under consideration. The second term gives the contribution to the probability change for the case that one reaction takes place until time t' and the third term describes the situation where two reactions take place at times t' and t''. Following terms describe contributions to the probability change that arise from three, four and more subsequent reactions.

9.1.2   KMC as a Probabilistic Approximation

Equation 9.7 is indeed a valid Master equation. If the transition matrices $\mathbf{R}$ and $\mathbf{P}$ are known, the time evolution of the system can be evaluated. Unfortunately, an *infinite series* of summands is needed to do this. In KMC, the analytic propagation of the complete distribution is replaced by a probabilistic propagation of a single state.

Consider an initial state α, which might be, e.g., a hydrogen atom located at a certain site of a metal surface (fig. 9.1). In eq. 9.7 the time before a reaction takes place was of central importance.

A KMC simulation starting at state α consists of repeating two alternating steps:

1. Calculate the time interval Δt in which no reaction takes place. According to eq. 9.5, the probability distribution for the length of that interval can be calculated as $\mathbf{Q}_{\alpha\alpha}(t) \equiv \exp[-\mathbf{R}_{\alpha\alpha}t]$. The actual time interval is now picked by choosing a value of the probability distribution by means of MC probability sampling. If p_1 is a random variable sampled on the unit interval, it can be set:

$$
\exp[-\mathbf{R}_{\alpha\alpha}t'] = p_1.
\tag{9.8}
$$

   To get Δt, the equation needs to be solved for the time:

$$
\Delta t = -\frac{1}{\sum_\beta W_{\beta\alpha}} \ln p_1.
\tag{9.9}
$$

   As can be seen, the time interval depends on the sum of all transition rates from the actual α to other states, i.e., the more and faster reactions are possible from the state, the shorter will the system will stay in it.

2. Once we know *when* the reaction shall take place, it is still not known *which* reaction shall be chosen. In the simple example of a hydrogen on a metal surface, the possible reactions are diffusion steps into different directions and a desorption into the gas phase (or a diffusion into the metal bulk, which would be identical to a desorption for two-dimensional KMC).

   This choice depends on the rates for the different processes. Of course a faster process will happen more likely than a slow one. Again a random variable is sampled on the unit interval, it is then assigned to one of the possible processes, with the probability

$$
P_{\alpha'\alpha} = \frac{W_{\alpha'\alpha}}{\sum_\beta W_{\beta\alpha}},
\tag{9.10}
$$

for the reaction of α to a new state α', such that the probability of the reaction is proportional to its rate[6]. When the chosen process was conducted, step one starts again for state α'.

9.1.3 Implementation

Instead of writing my own KMC code (which would be possible given the relative ease of the method at least for two-dimensional diffusion processes) I decided to use an existent KMC program from the literature, which should also be able to perform more complicated calculations than shown here (e.g., surface reactions, 3D diffusion in sublayers etc.), such that future applications based on EVB-QMDFF rate constants could as well be done with the setup presented here. There is a vast number of different KMC simulation programs. Some examples are the CARLOS program suite [271] (commercial), the MoCKa web interface [272] (no local installation possible), the Zacros program suite [273] (partly commercial), the Nascam package [274] (no consideration of surface reactions possible), the kmos program [275] (deprecated due to dependence on expired Python packages) and the SPPARKS program package [276, 277] (no inclusion of individual k(T) values possible). As noted, all those programs mentioned so far are unable to do what we want. Fortunately, I finally found a program package (or rather a Python library) that is able to do so: KMClib [278, 279].

Its structure allows the user to write a python input script that basically does itself the KMC propagation, by initializing objects and calling functions that are provided by KMCLib. We can individually design all possible reactive events, based on the local environment to be looked at. For each event, k(T) values calculated by the user (here of course with EVB-QMDFF) can be included. Arbitrary successions of propagations and analyses can be set up. With the general definition of reactive events, adsorptions, desorptions, diffusions as well as surface reactions (by introducing new site occupants) can be described. Further, one- as well as three-dimensional processes might be simulated, which opens promising perspectives for future applications, e.g., with polyurethane systems (chapter 8).

9.2 Abstract Model Systems

Before going to connect actual EVB-QMDFF rate constant calculations to KMC, some abstract calculations without any chemical relevance (but with close connection to real chemical situations) are presented in order to give an example of the capabilities of KMC.

9.2.1 Properties

The model system is quite simple: Assume we have a quadratic cut-out of a regular metal surface with a cubic lattice. On this surface, a number of adsorption sites is available: All its *hollow*-positions can be occupied (fig. 9.2). When a simulation is started, no adatoms are placed on the surface, i.e., the surface is clean. We now assume that an atomic gas (e.g., a noble gas) fills the space above the metal surface. Due to the randomized movements of the gas atoms, some of them will approach the metal irregularly in time and space. This is modeled by a separate KMC process: Add an atom in an empty surface site. All gas atoms hitting the surface are assumed to stay on them, unless they approach on a site that is already occupied by another gas atom: then it is flashed back and nothing happens to the model. Therefore, all empty positions, no matter how many absorbed atoms are present in their neighborhood, can be filled by the absorption process with an equal rate constant (which will depend on the gas pressure and temperature for real chemical situations).

---

6 Since the process is chosen without any knowledge of the previous evolution of the system, KMC generates *first order Markov chains*.
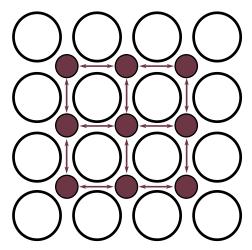
Figure 9.2: Model for the investigated surface diffusions in the rest of this chapter. A cubic surface lattice is assumed (empty cycles), with the absorption sites at the hollow-site positions above the lattice (red cycles). Absorbed atoms are able to diffuse only parallel to the lattice, i.e., no cross-steps are possible.

Gas atoms that approached the surface are trapped on it, i.e., no desorptions are possible. However, they are able to diffuse between neighbored absorption sites, if the destination is empty. Due to the expected much higher barrier of diagonal diffusion steps, only *vertical* and *horizontal* steps are considered. Depending on the chemical properties of the gas atoms, neighbored ones might interact *attractively* or *repulsively*. If the gas interactions are attractive, the rate of diffusion steps that increment the number of vertical and horizontal neighbors will be larger than those that do not change or even decrement this number. Alternatively, repulsive interactions will tempt the atoms to move away from each other. If (approximately) no interactions are present at all (besides Born repulsions if an already occupied site shall be visited), only one global diffusion rate will be enough.

The different diffusion reactions depending on the number of neighbors at the start and end site are presented in figure 9.3. If the chirality of the situation is neglected, six different configurations for both initial and final positions of the diffusion step are possible, resulting in a total amount of 36 individual diffusion reactions that all might possess different rate constants.

It should be noted that, with consideration of chirality, eight different neighborhoods for both initial and final positions exist, resulting in 64 different diffusion reactions at all. Further, the direction of the diffusion might play a role (left or right, up or down), for example due to an inhomogeneous electric field or a temperature gradient effective along the surface. Then, a total number of 256 different diffusions would exist, even in this seemingly simple system! In the KMCLib setup we must specify all 256 reactions explicitly, whereas only up to 36 will have different k(T) values.

For our model calculations, we choose a periodic surface slab of 40 times 40 adsorption sites, resulting in 1600 sites in total. In fig. 9.4 the chemical situation of gas atoms on a metal surface and the simplified histogram picture used in the following are compared with each other.

9.2.2 Diffusion Calculations

No Interactions

As discussed above, the simplest possible model is to make the diffusion rate independent of the local environment of the atom to be moved. Then, only two rate constants are needed for a complete description of the system: Adsorption rate and diffusion rate. In the current example,
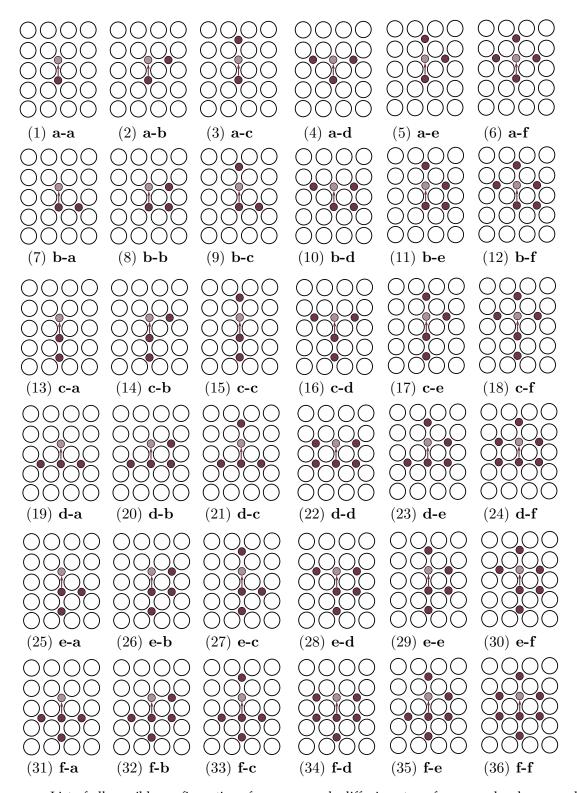
Figure 9.3: List of all possible configurations for an upwards diffusion step of a gas molecule on a cubic metal surface if any dependence on chirality is neglected (else, 64 combinations are possible). The labeling refers to the configurations of the neighbored sites at the initial and final positions of the diffusion step, a-a for example means that no neighbors are present initially and finally, whereas a-f means that three atoms are present finally.

(a) Atoms adsorbed on a surface

(b) Occupied and unoccupied sites
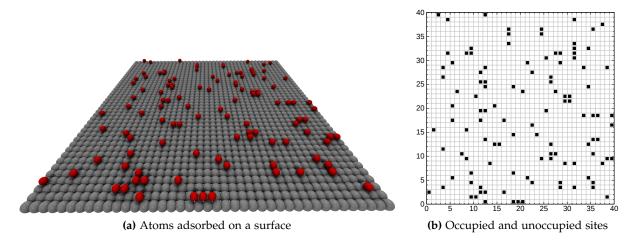
Figure 9.4: Illustration of the simplified KMC site plot used in the next sections. Originally, our model is a metal surface with a number of adsorbed gas atoms on it that are able to diffuse around (a). In the simplified picture, the underlying surface ceases to exist, instead, a grid of all adsorption sites is shown, with black squares for all occupied ones (b).

the adsorption rate was chosen to be 0.02 (arbitrary units), whereas the diffusion rate is 1.0[7]. We could think that now, with a diffusion rate 50 times larger than the adsorption, almost no new gas atoms will be adsorbed on a surface within a given number of KMC steps. But there are 1600 independent sites on which atoms might be adsorbed! For each of these sites, the respective rate that an atom will be trapped in it, is 0.02 per time unit, such that in total many adsorptions will happen especially at the beginning of the calculations.

For all three situations (attractive, repulsive and no interactions), a KMC run with 30000 steps was done. This means that 30000 single reactive events were calculated, according to the algorithm explained in section 9.1.2. In fig. 9.5, six snapshots of the resulting KMC trajectory for independent particles are presented. It is obvious that the total number of adsorbed particles increases with the number of KMC steps, however, there is no regular pattern, the gas atoms are distributed accidentally, resembling the image noise of ancient days tube TVs.

In the next step, interactions between the adsorbed gas molecules are considered. As mentioned above, attractive interactions will lead to larger rates for processes that bring atoms together, whereas repulsive interactions will result in the opposite. In table 9.1, diffusion rate constants for all three systems as being used in the KMC simulations are listed. Note that it was assumed that only the number of neighbors at the initial and final site but not their actual position influence the diffusion rate. Therefore, configurations b and c as well as d and e according to fig. 9.3 are seen as equal. Further, the rates for attractive and repulsive interactions are reciprocal with respect to the independent particle model, such that rates are accelerated and slowed by the same factor if the number of neighbors changes in a certain way.

Attractive Interactions

The resulting KMC dynamics for the *attractive interaction model* is shown in fig. 9.6. By comparing it with the independent particle dynamics, significant changes become obvious. Instead of random noise that becomes darker with advancing time, the adsorbed gas particles aggregate to a shrinking

---

7 In order to avoid confusion it should be noted that the magnitude of a single rate constant does not determine its actual probability to happen, i.e., a rate of 1 does not mean that the associated event happens always (i.e., having a probability of one). All what matters are the relative magnitudes of the rates, such that a rate of 1 is large if all others are 0.01 and is small if all others are 100. The absolute values only matters for the elapsed time during the dynamics (see below).

(a) 300 steps

(b) 4800 steps

(c) 9000 steps

(d) 13200 steps

(e) 17400 steps

(f) 21600 steps
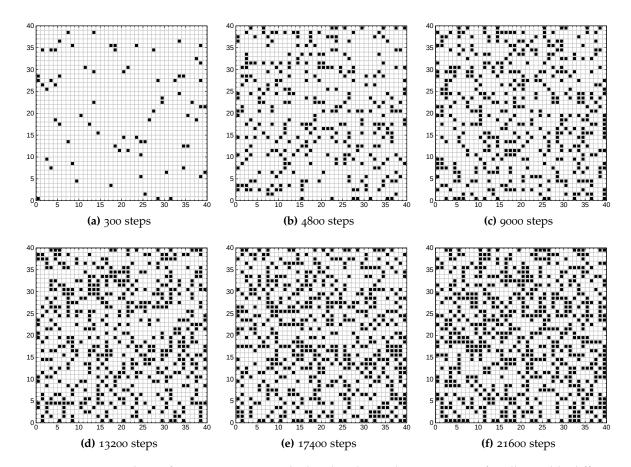
Figure 9.5: Six snapshots of a KMC trajectory calculated with equal rate constants for all possible diffusion processes. Besides the increasing number of adsorbed particles no clear pattern regarding their distribution can be seen. Since the simulation is entirely random with respect both to adsorption and diffusion processes this behavior has been expected.

Table 9.1: List of reactive processes and their chosen rate constants for the three different model system KMC simulation runs shown in figs. 9.5-9.7. All processes from fig. 9.3 with equal number of initial and final neighbors are merged to have one rate constant each. The list of included processes is shown in the third column. Further, the rates for attractive and repulsive interactions are inverse, such that the rate for the step from zero to three neighbors is 50 times larger than of a step without change of neighborhood for attractive but 50 times smaller for repulsive interactions.

NB start	NB end	processes	rate constants		
			independent	attractive	repulsive
0	0	a-a	1	1	1
0	1	a-b, a-c	1	5	0.2
0	2	a-d, a-e	1	20	0.05
0	3	a-f	1	50	0.02
1	0	b-a, c-a	1	0.2	5
1	1	b-b, b-c, c-b, c-c	1	1	1
1	2	b-d, b-e, c-d, c-e	1	5	0.2
1	3	b-f, c-f	1	20	0.05
2	0	d-a, e-a	1	20	0.05
2	1	d-b, d-c, e-b, e-c	1	0.2	5
2	2	d-d, d-e, e-d, e-e	1	1	1
2	3	d-f, e-f	1	5	0.2
3	0	f-a	1	0.02	50
3	1	f-b, f-c	1	0.05	20
3	2	f-d, f-e	1	0.2	5
3	3	f-f	1	1	1

number of gradually growing clusters. After 300 steps, most particles are scattered independently along the surface, but at 4800 and at the latest after 9000 steps the attractive interactions are becoming visible. Since all interactions only act on direct neighbors, a sufficiently dense packing of gas particles is needed for them to deploy.

Another interesting feature is that the positions of the main clusters are determined at quite early stages. The two parallel diagonal structures around x=15-20 and y=20-30 after 4800 steps as well as the diagonal band at x=25-35 and y=20-30 grow in subsequent stages, which is very noticeable especially at 13200 and 17400 steps, where the global distribution of gas particles can be reduced to a handful of broad diagonal bands. Therefore it can be stated that clusters of gas molecules formed at early stages of KMC dynamics act as *seed crystals* for subsequent growth, since it is highly unlikely that they will break into pieces, due to the low rate constants for decomposition processes.

Repulsive Interactions

The KMC dynamics of the *repulsive interactions model* is shown in fig. 9.7, again for the same number of elapsed KMC steps. As it might be expected, the resulting pattern is completely different to the attractive interactions. Instead of large band-like structures whose seed crystals are built at early stages of the dynamics, a regular chessboard-like pattern is developed after 9000 steps and later. The reason is that no diagonal interactions are considered. If a gas particle has only diagonal neighbors, as it would be the case in an ideal chessboard pattern, it experiences no repulsive interactions at all. Therefore, in spite of the randomness of single processes, the system globally moves to a shape that minimizes the number of repulsions, thus minimizing its energy.

(a) 300 steps

(b) 4800 steps

(c) 9000 steps

(d) 13200 steps

(e) 17400 steps

(f) 21600 steps
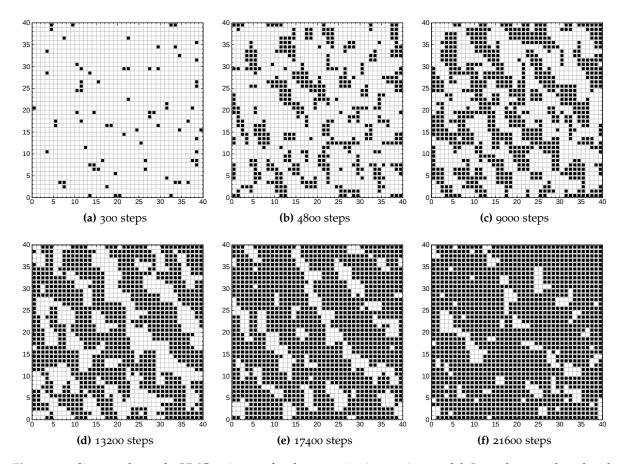
Figure 9.6: Six snapshots of a KMC trajectory for the attractive interaction model. It can be seen that already at early stages (4800 and 9000 steps) first clustered structures are build which act as seed crystals for subsequent adsorptions. The early fragmented clusters grow together to continuous bands at 9000 steps. In later stages, those bands grow in size, before they merge to a large bulk with single holes in it after 21600 steps.

(a) 300 steps   **(b)** 4800 steps   **(c)** 9000 steps

(d) 13200 steps   **(e)** 17400 steps   **(f)** 21600 steps
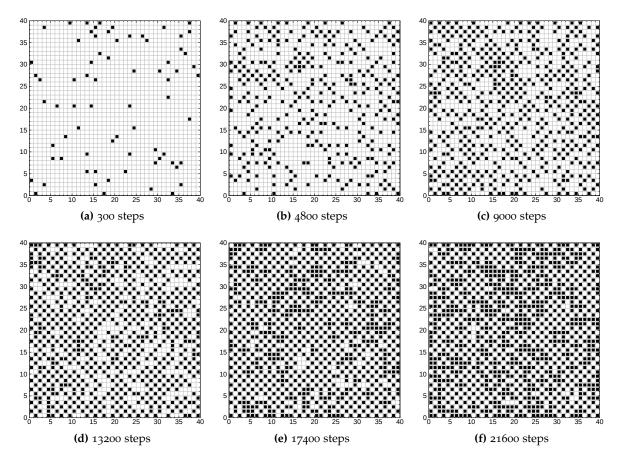
Figure 9.7: Six snapshots of a KMC trajectory for the repulsive interaction model. In accordance with the prerequisites that particles tend to move away from places with more neighbors around it, a chessboard-like pattern is gradually developed, particularly well visible at 13200 and 17400 steps. Before the number of adsorbed particles gets larger than the half of all available adsorption sites the system seems to be able to place almost each of them at a place with no direct neighbors. In reality, also diagonal as well as straight interactions to the next but once particles will play some role, such that the ideal chessboard pattern is rather artificial.

Time Evolution

Besides the detailed surface structures presented above, the quantitative development of the *occupation number* is a statistic quantity of great importance. In fig. 9.8 the number of adsorbed particles during the three simulations is plotted dependent on the number of calculated KMC steps as well as the elapsed time (summed up from all calculated time intervals Δ*t*).

The number of adsorbed particles after the given amount of KMC steps strongly depends on the chosen model. At the end, approx. 800 particles were adsorbed in the independent particles model, whereas for the attractive interactions this number is almost twice as large, with nearly all available sites populated. If the same results are plotted with respect to the *elapsed time*, it becomes clear that there is no fixed relation between a certain number of KMC steps and the actual time! Whereas almost 200 a.u. were simulated for the attractive interaction model, only less than 40 were simulated for the independent particle model. Since all three curves coincide quite well at the beginning it seems that their differences in the KMC-step dependent plot arise solely due to different rates of progress.

But why one model evolves much faster than the other with respect to real time? This becomes clear if we consider what *time* actually means in KMC. In contrast to MD, where the time evolves monotonously and the total amount of elapsed time is determined by the number of MD steps, the elapsed time in KMC depends on the possible reactions (eq. 9.9). The equation is evaluated for each KMC step. The more reactions with larger k(T) values are possible, the shorter the time interval until the next event happens will be, since it is very unlikely that none of the many probable events will happen during a longer period.

In our calculations, the largest interval of time was spanned in the attractive interactions model. As we have seen in fig. 9.6, large clusters of adsorbed gas atoms are built. Inside these clusters, no diffusions are possible, since only gas atoms with three or less neighbors are able to take a diffusion step. Therefore, the number of possible reactions is reduced, with the remaining diffusions (starting from the cluster edges) being slow since they will reduce the number of neighbors. The total number of possible adsorption events only depends on the free sites, no matter what their environment might be. However, the rate for adsorptions is low (0.02), therefore the probability of a reactive event in a certain time span is greatly reduced in the attractive interactions model, which leads to a faster passage of time during a given number of KMC steps.

9.3   Hydrogen Diffusion on a Cu(001) Surface

We have seen how KMC works in principle for an artificial model system. However, our true desire is of course to simulate real chemical systems. Before going to a system similar to the abstract one of several gas atoms diffusing on a metal surface, a much simpler model will be looked at: A single hydrogen atom moving on a Cu(001) surface (*H@Cu(001)*). The reason why this system was chosen is that both theoretical and experimental studies were performed based on it, mainly in order to investigate tunneling effects which impose corrections to the standard Arrhenius behavior of chemical reactions [280–283].

Further, a similar study (hydrogen on a Ni(100) surface) was done by SULEYMANOV, imposing the RPMD methodology [152]. That study was done with a separate RPMD program, which is not freely available (since RPMDrate is only able to handle bimolecular gas phase reactions), however, the `rpmd.x` program developed in this thesis is able to calculate k(T) values for this kind of reactions as well (section 3.3.7).

The original intention was indeed to simulate several hydrogen atoms on a Cu(001) surface moving simultaneously on it. Unfortunately it turned out that the standard pattern of hydrogens occupying the hollow positions on the surface was only valid for low occupancies (at least for the used reference calculation, see below). If many neighbored lattice positions are occupied with
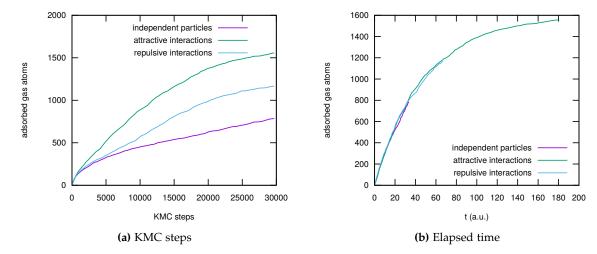
(a) KMC steps

(b) Elapsed time

Figure 9.8: Number of adsorbed gas molecules for the three investigated models, depending on KMC steps as well as elapsed time. We can see that after 30000 KMC steps different numbers of particles were adsorbed for each model (a). The number for the attractive interactions model is almost twice as large as for the independent particles model. If the look at the elapsed time (b), we see that all three cases show similar time-dependent curves, only depending on how much of the curve could already be calculated.

hydrogen atoms (e.g., in the case of the (f-d or f-e reactions in fig. 9.3), only a single local minimum exists on the diffusion path *between* two sites: on the central *bridge* position. Of course it would be possible to build up a slightly altered KMC model with explicit consideration of bridge and (if needed) also top positions on the surface, but this would in turn lead to an explosion of the possible single KMC diffusion steps, since now the environment must be classified not only based on the number of hydrogen neighbors on initial and final positions, but as well on the number of neighbors on hollow, side, and top positions. Therefore, only one single hydrogen atom on the surface will be looked at.

9.3.1 Quantum Chemical Reference

In order to study diffusions on metal surfaces, a different kind of quantum chemical reference than used so far in this thesis is needed. Instead of usual *ab-initio* or DFT calculations based on Gaussian type basis sets as done for gas phase systems, we need to include the *periodicity* of the metal surface in order to describe it properly. The CP2K program package [133, 134] was chosen to do these calculations. CP2K is open source and able to perform usual gas phase *ab-initio* calculations as well as 1-, 2- and 3-dimensional *periodic* calculations based on *pseudopotentials* with the Gaussian and plane wave schemes.

If we look at fig. 9.3 it is obvious that the minimum cutout used for reference calculations should be five copper atoms long and four atoms wide[8]. Further, the metal unit cell should be deep enough such that it reliably resembles the metal bulk. Therefore, it was chosen to be four layers deep. The resulting system is shown in fig. 9.9.

---

8 Since only isolated diffusion steps on a clear surface are considered for the hydrogen on Cu(001) system, we could think about taking only a 3 times 2 atoms large unit cell that includes both the initial and final location of the hydrogen. However, in this case the hydrogen could "see" itself in the neighbored cell of the periodic treatment. This can be avoided by calculating a larger system with free surface around the central diffusion region, as it is done here,
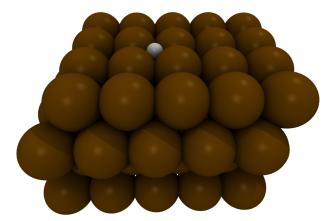
Figure 9.9: The surface section used as unit cell in the periodic DFT reference calculation for the H@Cu001 system. It consists of in total 81 atoms, where the surface is four layers deep and a space of 30 Ångstrom was added for duplications along the z-axis.

Since CP2K offers no possibility of doing an IRC calculation, the *nudged elastic band* (NEB) formalism was applied[9]. Starting from preoptimized structures of both reactant and product, thus with the hydrogen atom located at both sides of the barrier, 29 NEB segments were generated for with the usual NEB algorithm was applied to get a minimum energy path of the reaction. Thereupon, QMDFF reference data was calculated for both minima. For all reference calculations, the spin-polarized PBE DFT functional [284] was used in combination with the D3 correction scheme by GRIMME [91].

The *Goedecker-Teter-Hutter* (GTH) pseudopotential [285–287] was utilized for the description of the atoms core regions and the relativistic effects for heavy atoms like copper. The MOLOPT basis set [288] specialized for GTH calculations was taken. For copper atoms, the GTH-PBE-q11 potential with a SZV-MOLOPT-SR-GTH basis was used, whereas for the hydrogen atom, the GTH-PBE-q1 with a TZV2PX-MOLOPT-GTH-q1 basis set was used. Due to the rather cheap basis set for copper, in order to make the Cu@Cu(001) model presented in the next section computationally feasible as well, no quantitative agreement with experimental data can be expected. This chapter therefore mainly works in a proof-of-principle manner.

In fig. 9.10 all 31 structures of the optimized NEB are shown as overlay. It becomes clear that the copper atoms of the surface are almost immobile during the reaction, only the two copper atoms forming the central barrier are marginally pushed down as the hydrogen climbs the barrier.

9.3.2 EVB-QMDFF Setup

After setting up a working QM reference model for the reactions of interest, the next step was of course to express the relevant areas of the QM PES with a suitable EVB-QMDFF coupling term. First it should be noted that QMDFF is unable to describe periodic systems directly. Therefore, the chosen cell in fig. 9.9 which sees its replica for the QM calculations is instead treated as an *isolated cluster* in EVB-QMDFF. At first we might suspect that therefore the whole EVB-QMDFF approach must fail since it makes a huge difference if an isolated cluster or an infinite metal surface is looked at.

Fortunately the periodicity is translated into QMDFF by the QM reference data used for its setup. That is, the force constants for the atoms positioned at the edges of the unit cell are designed such that those atoms will stay at their positions during a MD trajectory as if the neighbored replica are

---

9 For this simple case of a single atom moving in one direction a single relaxed position scan of this atom would have been enough. The NEB method was used nevertheless in order to develop a method that is universal.
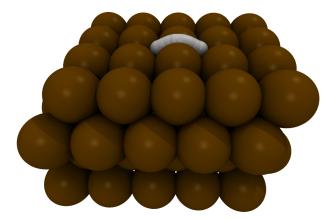
Figure 9.10: Overlay image of all RP structures for the H@Cu(001) reaction. Whereas the hydrogen atoms are nicely arranged as a rope of beads, no visible change in the position of the copper atoms can be seen.

still present (which is due to the reference Hessian used for the parametrization). Therefore, the structure of the chosen cell remains intact during a MD trajectory.

Concerning the choice of the EVB coupling term the best one would of course be the TREQ approach. Unfortunately, we need a complete description of the whole unit cell in terms of internal coordinates to avoid atom mergings at the direct interpolation section (chapter 5). Since the H@Cu(001) model structure consists of 81 atoms, the dimensionality of the system in terms of internal coordinates is huge (considering that the number of Hessian elements depends on the square of the number of internal coordinates), leading to expensive RPMD samplings.

It turned out that the simple energy-gap coupling term works quite well for the H@Cu(001) system. In fig. 9.11, reference as well as QMDFF and EVB-QMDFF energies are plotted together for the H@Cu(001) reaction path. The agreement between EVB-QMDFF and reference appears to be rather poor, however, if we consider that the barrier is only 9 kJ/mol high these deviations are in turn well below 1-2 kJ/mol and thus confirming a fair quality of the PES.

In order to find out if the PES behaves equally well *offside* the reaction path, the whole accessible PES can be scanned in this particular example. If we assume that the copper atoms stay approximately on the same position during the MD calculations the effective PES of the reaction shrinks to the section of cartesian space above the metal surface in which the hydrogen is expected to move during the whole RPMD samplings.

In fig. 9.12 the QM reference energies for this cartesian subspace surrounded by six copper atoms are plotted for 12 layers parallel to the metal surface with different heights in z-direction. It can be seen that large areas of low energy exists on both hollow positions, with the minima being located at z≈7.9, whereas the transition path between both minima at the central bridge position is most favorable at z≈8.3, thus indicating a slight upward movement of the hydrogen near the TS, which can as well be seen in fig. 9.10. Interestingly, for even higher positions above the surface the sole minimum exists at the bridge position in the middle, with PES maxima located at the hollow positions.

In fig. 9.13 the EVB-QMDFF quality for the same sections of cartesian space is shown, whereas the contour lines indicate the shape of the reference PES. The best agreements can be seen for the area between both minima at heights from z≈7.7 to z≈8.3. Outside the hollow positions to the left (y≤4) and to the right (y≥ 6.5) the agreement is much worse, which is no surprise since only the RP between both hollow minima was used for the EVB parametrization. By taking a closer look at fig. 9.11 we see that both QMDFF energies are rising much too fast, thus leading to a rather bad description of the PES if no EVB coupling is present, which is the case at the outer regions left and
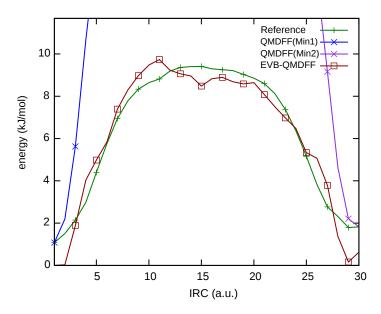
Figure 9.11: EVB-QMDFF quality along the reference NEB reaction path of the H@Cu(001) system. Note the low barrier of the reaction.

right. All other sections relevant for the actual reaction path are indeed reproduced well, mostly with chemical accuracy, indicated by dark blue color coding.

9.3.3 RPMD Calculations

With the knowledge that the EVB-QMDFF PES is reliable, the actual RPMD calculations on it can be performed. As noted in the program chapter (section 3.3.7), the `rpmd.x` program is able to calculate rate constants of unimolecular reactions as well. The diffusion of hydrogen on a metal surface is of course a unimolecular reaction since to segmentations of the whole structure are taking place during it.

Settings and Algorithm

For the purpose of simulating diffusion steps on surfaces a specialized reaction type was introduced within `rpmd.x`: The `atom_shift` reaction. Here, both reactants and TS dividing surfaces are solely defined with respect to the coordinate along which the shift occurs [152]. By looking at fig. 9.12 we see that the reaction proceeds parallel to the cartesian y-axis. As noted in table 11.2 of the appendix, only three pieces of information are needed to setup the bias potential for the diffusion reaction:

1. Which atom shall be moved? (The hydrogen atom)

2. In which direction the atom shall be moved? (Along the y-axis)

3. Within which interval the movement shall be described (between $y_1 \approx 6.5$ (reactant) and $y_0 \approx 5.1$ (TS), where the direction is from right to left with respect to fig. 9.12)

The dividing surfaces are then defined as:

$$\xi_0(\bar{\mathbf{q}}) = H_y(\bar{\mathbf{q}}) - y_0$$
$$\xi_1(\bar{\mathbf{q}}) = H_y(\bar{\mathbf{q}}) - y_1. \tag{9.11}$$
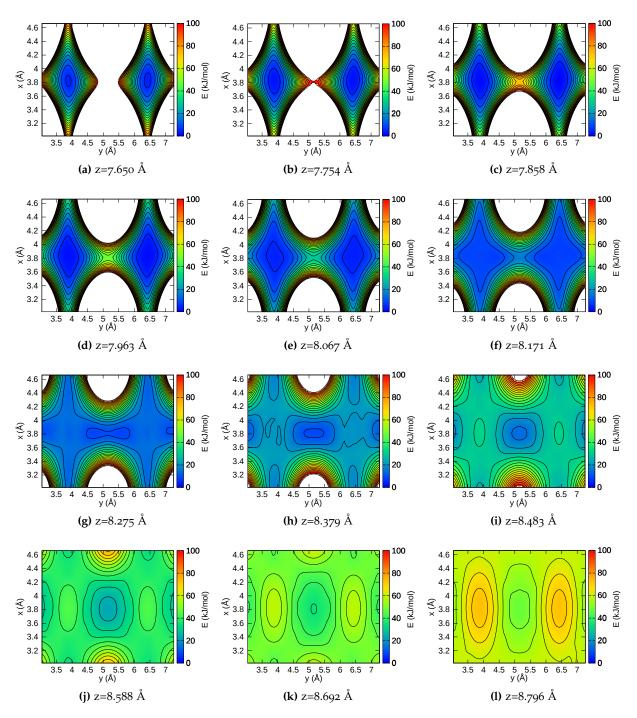
Figure 9.12: Three-dimensional scan of QM reference energies for the H@Cu(001) reaction, where the adjacent hydrogen was moved on a fixed copper surface.

(a) z=7.650 Å

(b) z=7.754 Å

(c) z=7.858 Å

(d) z=7.963 Å

(e) z=8.067 Å

(f) z=8.171 Å

(g) z=8.275 Å

(h) z=8.379 Å

(i) z=8.483 Å

(j) z=8.588 Å

(k) z=8.692 Å

(l) z=8.796 Å
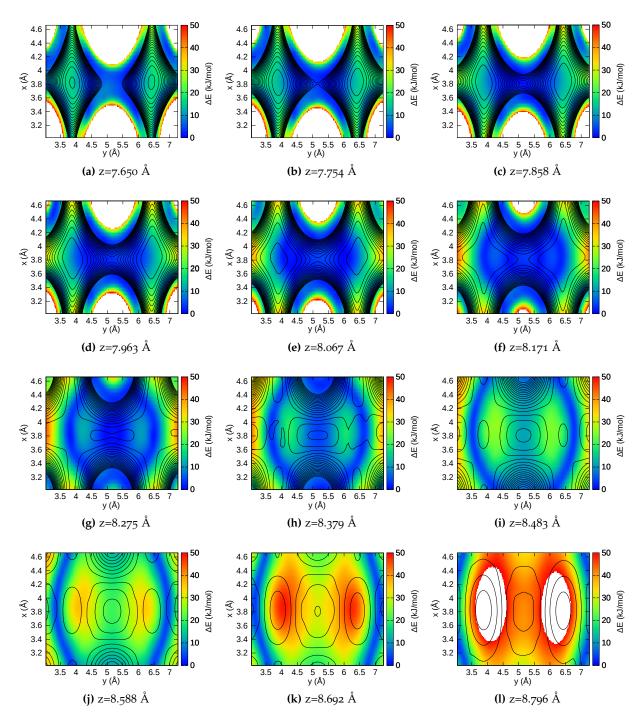
Figure 9.13: Quality of the energy-gap EVB coupling term used for parametrization of the EVB-QMDFF PES for the H@Cu(001) reaction. Shown are the differences of reference and EVB-QMDFF energies for the same coordinate space as in fig. 9.12.

After performing the sampling as well as umbrella integration and recrossing the unimolecular rate constant can be calculated with eq. 3.21.

Only one fix needs to be made for the samplings: If a bias potential is applied solely on the adjacent hydrogen atom during the RPMD k(T) calculations, it turns out that the whole unit cell structure is gradually moved in this direction. If the hydrogen atom shall be moved from the right minimum over the TS to the left minimum during the umbrella structure generation phase, the bias is applied on the *absolute* position of the atom in cartesian space, i.e., along the y-axis in our case. Then, the whole metal cluster can be moved together with the hydrogen to the left, leaving the hydrogen into its reactant minimum, since this overall translation (obviously) has a lower energy barrier than the local translation of the hydrogen over the fixed surface. This behavior can be prevented by artificial freezing of the *lowest layer* of copper atoms by setting its momentum to zero during the sampling trajectories. Since three additional layers exist between the frozen one and the hydrogen atom the introduced error will be small, by simultaneously solving the problem of global translation.

In order to thoroughly investigate quantum effects at low temperatures, the samplings were conducted between 20 and 120 K. Further, the calculations were repeated for the *D@Cu(001)* system, where the hydrogen is replaced by *deuterium*. For this case, the QM reference as well as the EVB-QMDFF stay the same but the rate constants change significantly (see below). The used RPMD settings are summarized into table 9.2. Since the total internal coordinate space to be sampled is quite small in comparison to usual gas phase reactions, the chosen settings are rather cheap. The number as well as the durations of the umbrella trajectories is rather short, nevertheless resulting in RPMD rates of good convergence.

The calculations were made with the objective to compare their results with those of Kua and Lauhon [281] who calculated diffusion (or *direct hopping*) rates of H@Cu(001) and D@Cu(001)[10] and compared them with experimental *scanning tunneling microscope* (STM) measurements, where the actual hopping rates were determined from diffusion coefficients of single tracked hydrogen and deuterium atoms. To make a direct comparison possible, RPMD calculations were performed for very low temperatures between 10 and 120 K for both H@Cu(001) and D@Cu(001).

Illustration of RPMD

In order to illustrate the actual behavior of RPMD for very low temperatures where quantum effects become important, trajectory snapshots are presented in fig. 9.14. There, structures of umbrella sampling trajectories at 10 K with the bias potential located at the transition state are compared with another for one to 256 beads. The positions of the copper atoms remain almost constant; although they all are expressed as well with the respective number of RPMD beads, their separation seems to negligible.

Interestingly all hydrogen replicas are located in one of the minima for 2 to 16 beads in total even though the bias potential is located at the TS between them! This is due to the RPMD centroid assumption (eq. 2.102), where the bias potential is not applied on each bead directly but only indirectly over the centroid, i.e., the center of mass for all beads. If one half of the beads is located left and the other half is located right, their center of mass is consequently located directly at the TS as it should be. For 32 and more beads, the single replicas are scattered more regularly along the whole reaction path, such that basically all cartesian space with sufficiently low energy is filled with hydrogen replicas at 256 beads; in narrow correspondence to a wave function of the hydrogen calculated for real quantum dynamics, where the density of replicas per space segment is related to the square of the wave function, i.e., the probability to find the particle there. The actual

---

10 The theoretical k(T) calculations of Kua and Lauhon basically consist of two parts: For the thermally activated regime (see below) simple TST was used, where for the quantum tunneling regime the *Wentzel-Kramers-Brillouin* (WKB) approximation was used in order to calculate a sole tunneling rate. Thus, tunneling was neglected in the first part and the thermal rate in the second, resulting in a sharp transition between both parts, visible in fig. 9.17.

Table 9.2: Input parameters for the RPMD k(T) calculations of the H@Cu(001) and D@Cu(001) reactions with rpmd.x, similar to the format given in the papers by SULEYMANOV *et al.* [13, 156].

Parameter	value	explanation
Command Line Parameters		
temp	20-120	Temperature (K)
N_{beads}	1, 2, 4, 8, 16, 32, 64	Number of beads
Dividing Surface Parameters		
direction	y	along which cartesian axis the reaction proceeds
y_0	5.07	dividing surface ξ_0 position of the H/D atom
y_1	6.435	dividing surface ξ_1 position of the H/D atom
Thermostat		
thermostat	"Andersen"	the chosen thermostat option
Biased Sampling Parameters		
$N_{windows}$	71	number of windows
ξ_1	-0.1	center of the first window
$d\xi$	0.02	window spacing step
ξ_N	1.3	center of the last window
dt	0.0002	time step (ps)
k_i	0.04	umbrella force constant ((T/K) a.u.)
$N_{trajectory}$	10	number of sampling trajectories per point
$N_{trajectory}$	15	duration of a sampling trajectory (ps)
Potential of Mean Force Calculation		
ξ_0	-0.05	start of umbrella integration
$\xi_{\#}$	1.2	end of umbrella integration
N_{bins}	5000	number of bins
Recrossing Factor Calculation		
dt	0.0002	time step (ps)
$t_{equilibration}$	10	equilibration period (ps) of the constrained (parent) trajectory
$N_{total child}$	10000	number of unconstrained (child) trajectories
$t_{child sampling}$	5	sampling increment along the parent trajectory (ps)
N_{child}	100	number of child trajectories per one initially constrained configuration
t_{child}	0.2	length of child trajectories (ps)

(a) 1 bead **(b)** 2 beads **(c)** 4 beads

(d) 8 beads **(e)** 16 beads **(f)** 32 beads

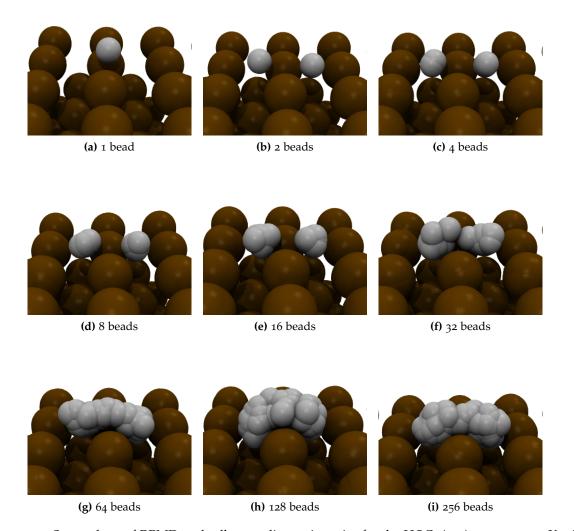**(g)** 64 beads **(h)** 128 beads **(i)** 256 beads

Figure 9.14: Screenshots of RPMD umbrella sampling trajectories for the H@Cu(001) system at 10 K with different numbers of beads. The screenshots are taken from samplings with the umbrella bias located at the transition state of the system. In the classical case of 1 bead, the hydrogen is indeed positioned at the TS region. For 2 to 16 beads, the hydrogens are located in one of the potential minima (reactants or products), for 32 beads and more both separated "clouds" are slowly growing together, expressing a hydrogen atom that is basically spread over the whole coordinate space relevant for describing the diffusion reaction, indicating the dominance of tunneling for this temperature. Note that the copper atoms experience almost no delocalization at all, the small spaces between their beads are only visible from "grooves" in the atom surfaces, e.g., in the 32 beads picture. This indicates that the heavy copper atoms could be treated classically even at 10 K.

k(T)-calculations were performed with 1 to 64 beads, since even larger numbers, being expensive to calculate, had nearly no effect on the calculated rates.

Transmission Coefficients

Before going to the final results of reaction rate calculations, it is interesting to investigate the recrossing calculations in more detail. In fig. 9.15 the time-dependent transmission coefficients $\kappa(t)$ for the investigated temperatures of both H@Cu(001) and D@Cu(001) are plotted (see fig. 2.5 in the theory part for better understanding of how $\kappa(t)$ is calculated).

In both figures, the overall shape of the $\kappa(t)$-curves strongly depends on the calculated temperature. For H@Cu(001) the time-profile for 20 K shows a very flat shape near unity. Since this is completely different to all other temperatures, problems of RPMD with the low temperature are assumed (calculations for 10 K gave no useful results at all, see below). Further, the 20 K time-profile for D@Cu(001) shows no such peculiarity, probably due to the doubled masses that lead to stiffer forces between the beads[11]. For 30 to 60 K, similar shapes can be seen. The final value of $\kappa(t)$ rises with temperature, further, quite eye-catching *oscillations* of $\kappa(t)$ exist, whose strength decreases with increasing temperature. If we compare these oscillations of hydrogen and deuterium, we can further see that the "wavelength" of the first oscillation at 30 K is for deuterium roughly one and a half times larger than for hydrogen, corresponding to the well known *isotope effect* in hydrogen/deuterium vibrations in molecules, where the exact proportion is $\sqrt{2}$.

These oscillations exist also in similar low-temperature RPMD studies of hydrogen (or deuterium) transfers and can be attributed to vibrational motions of the ring polymer beads in the reactant and product minima as the centroid crosses the transition state in the recrossing calculations (see fig. 9.14) [152, 289]. Those vibrations lead to artificial back-and-forth movements of the centroid through the TS dividing surface, causing back-and-forth recrossings as well. Here we see indeed one of the deficiencies of the RPMD centroid approximation introduced in eq. 2.102.

For higher temperatures, the oscillations gradually disappear, presumably due to the stronger inter-bead forces that keep single beads from oscillating in the reactants or product basins when the centroid is located in the transition region. If we look at H@Cu(001) a substantial change can be seen between 60 and 80 K. For low temperatures, the oscillations declined with time, leading to quite well converged values of $\kappa(t)$. For 80 K and above, however, a number of *decreasing steps* can be seen in the $\kappa(t)$ profile, for instance, at approximately 120, 200, 270 and 390 fs for 100 K. They were observed as well in the publication of SULEYMANOV where rates for the diffusion of hydrogen on a Ni(001) surface were calculated [152]. The steps can be explained with recrossings of trajectories that already reached the product basin, vibrate there and then climb the activation barrier again from the other direction. The higher the temperature the earlier those steps appear, matching the fact that the vibrations in the minimum will have larger amplitudes if the temperature is higher, such that the chance of leaving reactants or products basins increases. If we would run much longer recrossing child trajectories, we should see that the steps are becoming smaller and shorter at later times, since the trajectories are becoming less and less correlated, ultimately resulting in a smoothly decaying curve. This decay should continue until $\kappa(t) \approx 0.5$ is approached, at least if no complete vibrational redistribution to the underlying copper surface takes place in the investigated time scales. Then, due to the symmetric PES, half of the trajectories should be located in the reactants and the other in the products basin, with equal probability for both sides to react, thus holding up an equilibrium[12].

---

11 An interesting feature of RPMD is that the masses of atoms have a direct influence on the force acting on them *via* the harmonic spring forces attached between the beads (see eq. 2.99). For classical MD simulations, the masses have no influence on the gradient and come only into play *via* the thermostat and the Verlet algorithm itself [40].

12 This stepwise decrease of $\kappa(t)$ cannot be seen for usual gas-phase reactions studied so far, since there the energy present in the reactive mode is quickly redistributed to all other vibrational modes of the product structure, thus preventing it from coming back in almost all cases (even if a slow decrease of $\kappa(t)$ for extremely long time intervals will also be seen there, which can be accelerated by calculating much higher temperatures). For the H@Cu(001) model,
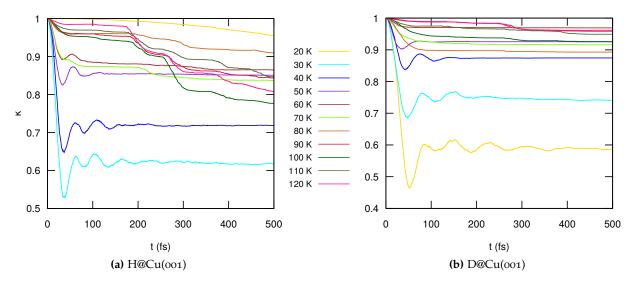
Figure 9.15: Plot of time-dependent RPMD transmission coefficients for the H@Cu(001) and D@Cu(001) diffusion reactions at temperatures between 20 and 120 K.

For D@Cu(001) the step structure of $\kappa(t)$ can be seen as well, but now much later and much smaller. This is due to the larger mass of deuterium, which decreases the probability of tunneling back especially for low temperatures (see next section).

Rate Constants and Crossover

In fig. 9.16 the calculated RPMD k(T) values for 1 to 64 beads at temperatures between 20 and 120 K are shown. Interestingly the RPMD calculations failed to converge to useful k(T) values at 10 K. Whereas the rates hardly change for temperatures below 50 K if the number of beads is sufficiently large, the values for 10 K were several magnitudes smaller even if a larger number of beads is used. Although the trajectory snapshots for 20 K looked very similar to those for 10 K shown in fig. 9.14, with the difference that single replicas are located near the barrier already at 16 K and general slightly smaller distances between them are seen, it seems that the underlying RPMD centroid assumption breaks down if the temperatures are too low (the oscillations in the transmission-time profiles shown in the last section are first indications of this behavior). Indeed no examples could be found in the literature where RPMD rate constants were calculated below 20 K, in contrast to some examples for 20-50 K [152, 290, 291].

The rate constants calculated with one bead (i.e., fully classical) show usual Arrhenius behavior with a linear progress in the plot. The rate constants become tremendously small ($1.04 \cdot 10^{-23}\text{s}^{-1}$ for 20 K). For two beads, a significant shift of all rates to larger values can be seen, e.g., of almost 18 orders of magnitude at 20 K, however, they still show Arrhenius behavior. For 4 to 64 beads, the changes are much smaller. The rates decrease up to approx. 70 K, for even lower temperatures they reach an asymptotic value of about $2 \cdot 10^5\text{s}^{-1}$. The usage of large bead numbers (32 to 64) is nevertheless useful, since differences between 4, 8 and 16 beads can be clearly seen at 30 or 50 K, despite the large span of the y-axis.

In fig. 9.17 the calculated RPMD rate constants for H@Cu(001) and D@Cu(001) are plotted as well as the calculated and experimental results by Kua and Lauhon [281] in order to serve as "real-life comparison". By looking at the RPMD results a clear *two-stage behavior* can be identified for both reactions. For large temperatures the k(T) values obey Arrhenius law, i.e., grow linearly with

---

this vibrational redistribution happens much slower, presumably due to the almost fixed copper atoms, such that a significant part of the reaction energy stays in the reaction coordinate much longer.
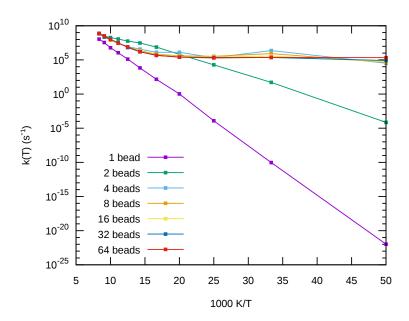
Figure 9.16: Calculated diffusion rate constants for the H@Cu(001) reaction for temperatures between 20 and 120 K for 1 to 64 beads. A logarithmic plot is shown in order to reveal Arrhenius behavior, then resulting in linear progress with temperature.

inverse temperature in the logarithmic scale. Below a certain temperature the Arrhenius behavior fades and the growth declines until the rates remain constant for very low temperatures. Both H@Cu(001) and D@Cu(001) show the same pattern, only deviating in the temperature where the *crossover* between Arrhenius and constant k(T) happens and the actual value of the basement rate.

This can be explained as follows: The actual reaction rate consists of two contributions, a thermal (classical) contribution that shows Arrhenius behavior i.e., grows exponentially with temperature and a quantum tunneling contribution originating from tunneling through the barrier that is temperature-independent and thus constant. For room temperatures down to 100 K the thermal contribution is several orders of magnitudes larger than the quantum contribution, resulting in usual Arrhenius behavior of the total rate. Since the thermal contribution decreases exponentially with decreasing temperature, it will be so low at some point that the addition of the quantum contribution leads to a visible correction of the whole rate, gaining influence for lower temperatures. For H@Cu(001) this *mixed region* is located at about 55-70 K. If we go even lower, the thermal contribution becomes several orders of magnitudes smaller than the constant quantum contribution, resulting in a constant overall rate (below 55K for H@Cu(001).

Since deuterium is twice as heavy as hydrogen, the tunneling contribution is almost five orders of magnitudes lower than for hydrogen. This leads to a lower temperature below which no relevant thermal contribution remains. In order to quantify this switching between two regimes (thermally activated and quantum tunneling), a *crossover temperature* T_C can be introduced. It has been determined as the x-value of the intersection between the extrapolated Arrhenius curve and the extrapolated curve of the basement rate. For H@Cu(001), T_C is 62 K, for D@Cu(001) T_C is 48 K.

Experimental Reference

If we now compare our RPMD results with the paper of Kua and Lauhon shown in the right, we see at first a similar overall shape of the k(T) curves. They also show Arrhenius behavior for larger temperatures and become constant for smaller temperatures, the relation of hydrogen and deuterium curves is similar as well. Unfortunately, the apparent similarity gets destroyed if we look at the *absolute values* of the reaction rates: The RPMD rates are almost eight orders of magnitude
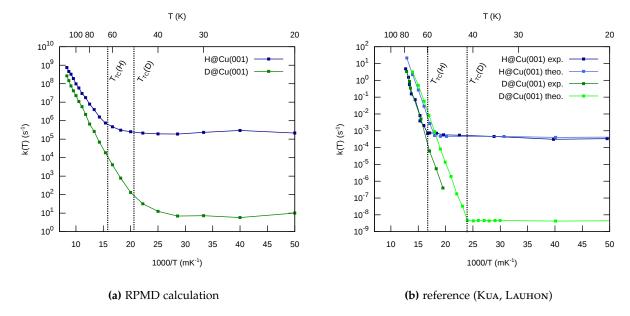
(a) RPMD calculation

(b) reference (Kua, Lauhon)

Figure 9.17: Calculated rate constants for the diffusion of hydrogen and deuterium on a Cu(001) surface. The values calculated with our rpmd.x program are shown left, reference values (experimental as well as parametric TST calculations) from Kua and Lauhon [281] are shown right. The temperatures T_C where the barrier-dominated Arrhenius behavior turns into a barrierless tunneling control are depicted with dotted lines for all cases. The values are: H(RPMD): 62 K, H(ref): 60 K, D(RPMD): 48 K, D(ref): 42 K.

larger than the reference ones! The reason for this huge discrepancy is the used reference method. In their paper, Kua and Lauhon described that they calculated a diffusion barrier of approximately 4.5 kcal/mol (18.8 kJ/mol), which is more than twice the barrier height calculated with the CP2K reference (9 kJ/mol)! The much larger barrier leads of course to much lower k(T) values. Therefore it can be assumed that the quite cheap SZV-MOLOPT-SR-GTH basis set for Cu is insufficient for a quantitative description of the system.

Fortunately nearly all other aspects of the reaction rate profiles are similar for both reference and EVB-QMDFF. The crossover temperatures for Kua and Lauhon are 60 K for H@Cu(001) and 42 K for D@Cu(001). Since the last value was obtained from their calculations which are apparently shifted with respect to the measurements, we can estimate a T_C value of roughly 50 K by extrapolating the D@Cu(001) exp. curve. With this, the crossover temperatures are almost exactly the same for our calculations and the experimental reference, which indicates that RPMD is well capable of calculating the quantum regime reliably. Further, the relative basement rates of hydrogen and deuterium deviate roughly five orders of magnitude, both for RPMD and the Kua-Lauhon reference.

9.3.4 Diffusion Coefficients

For particles moving on surfaces, the single diffusion steps are hard to monitor (especially if the movement is fast) yet their rate constants are of little interest for the average chemist. Fortunately, it is possible to connect these rate constants with the *diffusion coefficient* which itself is much easier to measure. In general, the diffusion coefficient originating from the *Einstein relation* is defined via the mean squared distance per time interval the particle under consideration has moved [292]:

$$D = \frac{\langle |\Delta \mathbf{x}|^2 \rangle}{2t}.$$ (9.12)

For the simple case of particles moving on a two dimensional regular grid, an *analytical solution* exists that connects the diffusion coefficient with the length of a single diffusion hop l, its rate k(T) and the symmetry factor of the reaction σ [152]:

$$D(T) = \frac{\sigma}{2}k(T)l^2. \tag{9.13}$$

In our case, the distance l covered by a proton during a single diffusion step is 2.564 Å, the relevant temperature-dependent rate constants are plotted into fig. 9.17 and the symmetry factor σ is four since four equivalent ways exist for a proton to reach a neighbored hollow site if no vertical movements over copper atoms are considered. Therefore, we are able to get the diffusion coefficients directly from our RPMD rates in this particular example by simply multiplying a constant geometry-dependent prefactor.

However, in order to show that KMC is able to obtain the analytical result through probabilistic samplings (and in order to give a simple but detailed example of its machinery), KMC runs were calculated for a single hydrogen atom on the surface, where the aim is to calculate the covered distance $\Delta \mathbf{x}$ and the elapsed time t needed for determination of $D(T)$, which in turn will be compared to the analytical results. Now, instead of 256 different reactions (or 36 per direction if chirality is neglected, fig. 9.3) only four need to be considered: diffusions in in +x,-x,+y and -y, each having identical rate constants (fig. 9.2).

Therefore, the KMC runs are actually independent of the rate since all results simply need to be multiplied by its actual value (the diffusion coefficient will be four times larger if the rate of a single diffusion step is four times larger). In general, where different processes are considered (as in the previous section), this is of course not the case since the relative values of those rates will vary with temperature (see Cu@Cu(001) in the next section).

Due to this independence, the KMC runs were done with a generic diffusion rate of 1 and with a diffusion step length of 2. The particle was started at the origin and then propagated 10000 KMC steps. According to eq. 9.9, the elapsed time is basically a random variable divided through the sum of all possible rates (here: $4 \cdot 1 = 4$). In the long time average, a reaction will therefore occur each quarter time unit. Which of the four possible processes occurs (i.e., in which direction the particle will move) is of course determined by chance as well (eq. 9.10). The whole movement therefore reduces to a simple two-dimensional random walker model[13].

In fig. 9.18, four example KMC trajectories of the hydrogen on the abstract copper surface are shown, whereas the actual covered distance is indicated by a dotted line connecting initial and final positions.

As we see, it is clearly insufficient to simply calculate a dozen trajectories and determine the average value of $\Delta \mathbf{x}$, since the single runs deviate heavily. In fact, it became obvious that a significantly higher number of trajectories was needed. Therefore, 10000 trajectories with 10000 KMC steps each were calculated; the covered distances as well as the elapsed times for all of them are shown in histograms (fig. 9.19), the calculated global average values are indicated there as vertical lines. The average covered distance (with a single diffusion step being 2 a.u. long) was 176.819, the average elapsed time was 2499.994. Since the average time needed for a single diffusion step is 0.25, after 10000 diffusion steps 2500 time units should be elapsed at average, which is almost exactly the case here. We further see that single outliers tend to be 100 units shorter or longer, corresponding to 2.5% of the total interval.

If the squared mean of covered distances $\langle|\Delta\mathbf{x}|^2\rangle$ is determined by averaging over all 10000 runs, the value is 39956.177, near to 40000, which would be obtained by adding all squared 10000 step lengths.

Now we know both t and $\langle|\Delta\mathbf{x}|^2\rangle$. In order to introduce actual physics, the abstract model dimensions of transition times and diffusion step lengths need to be converted into the values

---

13 Since the KMClib program is rather slow, a separate Fortran program for the simple diffusion calculations of a single particle on a surface was written and used to produce the following results in this section.
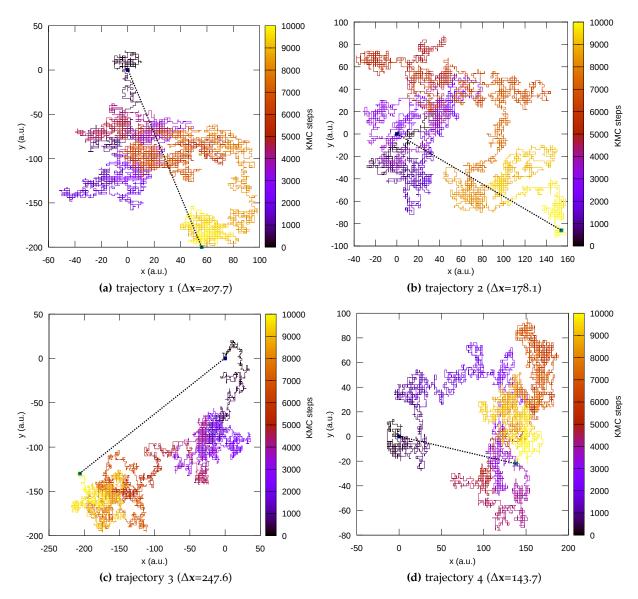
(a) trajectory 1 (Δx=207.7)

(b) trajectory 2 (Δx=178.1)

(c) trajectory 3 (Δx=247.6)

(d) trajectory 4 (Δx=143.7)

Figure 9.18: Four example trajectories for the random movement of a particle on a regular surface (two dimensional random walker model), which can be used to calculate diffusion coefficients for the H@Cu(001) system. It can be seen that the covered distances needed for calculation of diffusion coefficients vary strongly between the single runs.

(a) covered distances

(b) evolved times
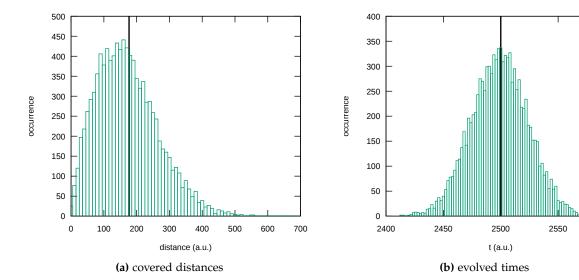
Figure 9.19: Histograms generated by evaluation of 10000 single KMC simulations of the generic particle on a two-dimensional surface model (fig. 9.18).

representing the systems of interest. If we look for example at the H@Cu(001) system at 100 K, we see that the step length is 2.564 Å (equal for all calculations) and the reaction rate constant is $9.83 \cdot 10^7$ s^{-1}. This results in a prefactor of $1.02 \cdot 10^{-8}$ s for the evolved time (the inverse rate, since less time will evolve the faster a single reaction takes place). The prefactor for the mean squared distance $\langle |\Delta\mathbf{x}|^2 \rangle$ is $1.64 \cdot 10^{-20}$ m, resulting from the squared step length and the one quarter correction for the model step length of 2.

With this and eqs. 9.12-9.13, both KMC and analytical diffusion coefficients can be calculated. The results are shown in table 9.3. By looking at them, it becomes obvious that KMC is able to reproduce the analytic diffusion coefficients with high quality.

Last but not least it shall be investigated if the underlying KMC assumption of independent single diffusion steps (i.e., a first order Markov chain of events) is valid for our model system and the calculated rate constants. Two following reactions (or diffusion steps) will only be independent of each other if the system has enough time in between to loose any correlation to the previous event, such that both steps are entirely uncorrelated.

In practice, the system should be able to perform a sufficient number of vibrations before the next reactive event happens. In table 9.3, the average time the system will be trapped in the actual site (t_{site}) and the time for a single vibration of the hydrogen atom in this site (t_{vib}) as obtained from the QM reference calculations of the reactant minimum are compared. We see that for all investigated temperatures at least seventy thousand vibrations happen in average between two reactions, therefore suggesting that KMC can be readily applied to the systems[14]. If we go to much higher temperatures, however, successive diffusions might get strongly correlated, requiring explicit simulations of the whole movement on the surface in order to define the diffusion coefficient independently of single isolated diffusion steps [152].

---

14 Interestingly, we saw above that especially in the H@Cu(001) system recrossings from the products minimum readily occur after some hundred fs, which can be seen as subsequent diffusion steps. This might indicate that the time between two diffusion steps is much smaller than it appears from the rate constant. The time interval calculated from the inverse rate constant is only valid if the energy of the system is completely redistributed in all bound vibrational modes.

Table 9.3: Reaction rates, diffusion coefficients (both KMC (D_{KMC}) and analytically (D_{an})) and periods of hydrogen-on-surface vibrations (t_{vib}) as well as lattice stays (t_{site}) for the H@Cu(001) as well as D@Cu(001) systems at different temperatures. The relation between t_{site} and t_{vib} reveals that the single diffusion moves can be seen as uncorrelated, justifying the application of KMC. 1(-10) means $1 \cdot 10^{-10}$.

		T(K)					
	property	20	40	60	80	100	120
H@Cu(001)	k(T) (s^{-1})	2.15(+05)	1.94(+05)	4.66(+05)	7.87(+06)	9.83(+07)	7.51(+08)
	D_{KMC}(T) (s^{-1}cm^2)	2.82(-10)	2.55(-10)	6.12(-10)	1.03(-08)	1.29(-07)	9.86(-07)
	D_{an}(T) (s^{-1}cm^2)	2.83(-10)	2.55(-10)	6.13(-10)	1.03(-08)	1.29(-07)	9.87(-07)
	t_{site} (s)	1.16(-06)	1.29(-06)	5.36(-07)	3.18(-08)	2.54(-09)	3.33(-10)
	t_{vib} (s)^a	4.77(-16)	4.77(-16)	4.77(-16)	4.77(-16)	4.77(-16)	4.77(-16)
	$\frac{t_{site}}{t_{vib}}$	2.43(+09)	2.70(+09)	1.12(+09)	6.67(+07)	5.32(+06)	6.98(+05)
D@Cu(001)	k(T) (s^{-1})	1.01(+01)	1.25(+01)	4.11(+03)	6.56(+05)	2.27(+07)	2.66(+08)
	D_{KMC}(T) (s^{-1}cm^2)	1.33(-14)	1.64(-14)	5.40(-12)	8.62(-10)	2.98(-08)	3.49(-07)
	D_{an}(T) (s^{-1}cm^2)	1.33(-14)	1.64(-14)	5.40(-12)	8.63(-10)	2.98(-08)	3.50(-07)
	t_{site} (s)	2.48(-02)	2.00(-02)	6.08(-05)	3.81(-07)	1.10(-08)	9.40(-10)
	t_{vib} (s)^b	6.75(-16)	6.75(-16)	6.75(-16)	6.75(-16)	6.75(-16)	6.75(-16)
	$\frac{t_{site}}{t_{vib}}$	5.20(+13)	4.19(+13)	1.27(+11)	7.99(+08)	2.31(+07)	1.97(+06)

^{a}: Duration calculated from frequency of hydrogen vibrating in the site (702 cm^{-1} from the reference calculation for QMDFF1 (see above)). ^{b}: Calculated from kinetic isotope effect $\left(\frac{\nu_H}{\nu_D} = \sqrt{2} \right)$.

9.4 Copper Diffusion on a Cu(001) Surface

So far, we have handled a single hydrogen atom moving isolated on a Cu(001) surface. The next step is to propagate several particles *together* on a surface as it was done in section 9.2 for the abstract test system. As explained below it was impossible to propagate several hydrogen atoms on Cu(001) by simultaneously preserving the assumption that only hollow sites shall be populated.

Therefore, a slightly altered model was chosen: copper atoms moving on a Cu(001) surface, in short Cu@Cu(001). Here, it was indeed possible to optimize the reaction path for all 36 different reactions listed in fig. 9.3 and thus to fill the abstract model with life.

9.4.1 Reference and EVB Setup

The QM reference calculations for the Cu@Cu(001) system were done with nearly identical settings as the H@Cu(001) system described above. Therefore, only a short summary of specific features will be given.

First, now several different reaction paths need to be calculated instead of one single path. For each path, the pattern of neighboring atoms varies according to fig. 9.3. Further, it turned out that the CP2K NEB calculations struggled to converge for an uneven number of copper atoms in the system, requiring open-shell unrestricted DFT calculations. In order to avoid unrestricted calculations with struggling convergence behavior a trick was applied: To make the number of atoms even, an additional "spectator atom" located on one of the corners of the surface (i.e., being a surface-adatom) was added. Due to the diagonal location it was assumed that the interaction between the spectator and the transmitted copper can be neglected at least in the first place.

In fig. 9.20 two examples of calculated reaction paths for the e-e and the b-d diffusion steps are shown. Note the spectator atom in the e-e model. The total number of such paths is smaller than 36 since all asymmetric paths describe two elementary processes (forward and back reaction). The

(a) b-d and d-b reactions   **(b)** e-e reaction
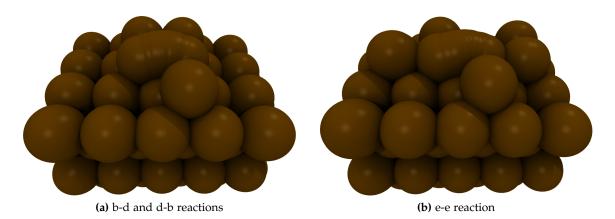
Figure 9.20: Overlay plots of optimized NEB reaction path structures for two exemplary Cu@Cu(001) elementary diffusion reactions. The path shown in (a) can be used to parametrize an EVB-QMDFF for both the b-d and the d-b reactions, whereas the path in (b) is used for the e-e reaction. In order to get an even total number of copper atoms in the system, a spectator atom was added for the e-e model, shown in the upper right.

first reaction path of fig. 9.20 is therefore valid for the b-d but as well the d-b reaction. With this, a total number of 21 reaction paths needs to be calculated.

In fig. 9.21 the optimized NEB reaction paths for all reactions starting from the a site (i.e., without direct neighbors) are plotted together[15]. If we compare the relative energies of reactant and product sites for all those paths it becomes clear that the product site gets more stabilized if more neighbors surround it, indicating *attractive interactions* between adjacent copper atoms on the surface. Further, if two configurations have the same number of neighbors (a-b, a-c and a-d, a-e), the one with a copper atom located *rearward* of the product site (viewed from the reactant site) stabilizes the product more than the atom located *sidewards* of the product site. The position of the TS on the reaction path also depends on the number of neighbors at the product site. It seems that the TS moves nearer to the reactant site if more neighbors surround the product, such that the whole product site grows, with the a-f TS located at RP structure 10 and the a-d and a-e TSs located at RP structure 12, whereas the TS of the symmetric a-a reaction is located at structure 14.

In the next step, EVB-QMDFF potential functions can be set up for all 21 different reactive systems. Similar to H@Cu(001), the QMDFFs were parametrized based on the optimized geometries of reactants and products potential energy minima, originating at the first/last RP structures. Due to the large number of atoms in the system, TREQ cannot be used, restricting the choice to DG-EVB and the simple energy gap dE-EVB. For all systems, dE-EVB was tried first in analogy to the H@Cu(001) system, if the path reproduction was too bad a DG-EVB coupling term was optimized. In most cases, DG-EVB (mode 1 or 2) gave better results than dE-EVB[16]. EVB-QMDFF energies for four chosen reaction paths are presented in fig. 9.22. It can be seen that the EVB quality is rather different, a-a is reproduced very well whereas b-e and b-f show quite large wiggles along the path.

---

15 In order to hold the amount of figures in this chapter manageable, only some of the 21 different possible plots are shown for the next investigations (reaction paths and EVB-QMDFF qualities). In table 9.4 barrier heights for all reactions are shown, thus completing the set of information for the different paths.

16 In contrast to many small to medium-sized gas-phase systems where the DG-EVB method fails to produce a reliable PES offside the RP those problems were absent for the copper diffusions, presumably due to the rather small coordinate space above the surface that was visited during the samplings.
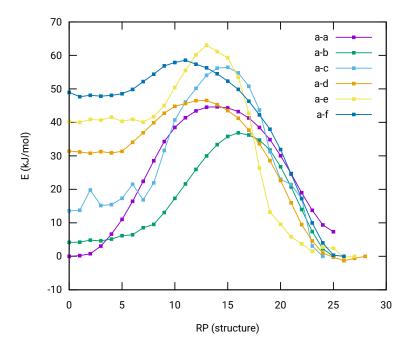
Figure 9.21: Optimized NEB reaction paths for the different a-x reactions, with x=a,b,c,d,e,f (according to fig. 9.3). We can see that the energy of the product site gets lower with respect to the reactant site if more neighbors surround it, indicating attractive interactions between neighbored copper atoms. The different number of NEB frames originates at convergence problems of the NEB calculation for the last 2-4 structures, leading to very high energies of them. All unreliable NEB frames were therefore discarded for the plot and the actual EVB-setup.

9.4.2 Rate Constant Calculations

Based on the constructed EVB-QMDFF surfaces, RPMD reaction rates can be calculated. The initial question was for which temperatures the whole KMC simulation should be done. For the H@Cu(001) system the investigation of tunneling crossover at low temperatures was an important motivation to chose the interval 20 to 120 K. In contrast, tunneling can be neglected for the Cu@Cu(001) system, since the copper atom is 63 times heavier than hydrogen. As we had seen, e.g., in fig. 9.14 all beads of the surface copper atoms remained at nearly identical positions even at 10 K where the adjacent hydrogen is significantly smeared out. Further, the reaction barriers are much higher for the Cu@Cu(001) diffusion processes than for H@Cu(001), as will be shown below.

Considering these arguments, the decision was made to investigate dynamical behavior at 200 to 1500 K, thus doing a high-temperature stress test of the RPMD program. Since tunneling is negligible all calculations were done with one bead per atom, i.e., in a purely classical manner. The question now was how randomly spread copper atoms on a Cu(001) surface behave at different temperatures. Will they move together or rather stay apart, what patterns will they form?

In order to investigate this, rate constants for all 36 different elementary processes listed in fig. 9.3 were calculated at 200, 300, 500, 1000 and 1500 K. The settings for the RPMD calculations were basically the same as for H@Cu(001) (table 9.2), with the exception that only one bead was calculated. Rate constant calculations for asymmetric reaction paths (e.g., a-b and b-a) were calculated on the same EVB-QMDFF surface, respectively, only the values of y_0 and y_1 must be changed in order to calculate the opposite direction.

The results of these calculations are 180 rate constants, listed in table 9.4, together with barrier heights obtained from the QM reference reaction paths. The general trend is that at 200 K the rate constants deviate much more from another than at 1500 K. The largest rate at 200 K (d-f) is

(a) a-a (DG-EVB, mode2)

(b) b-e (DG-EVB, mode1)

(c) b-f (DG-EVB, mode1)
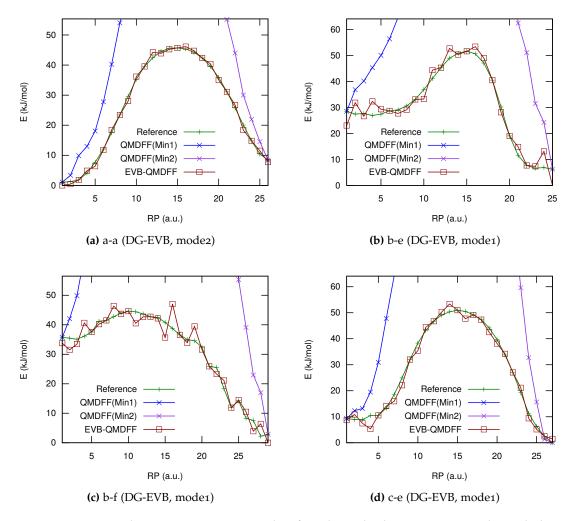
(d) c-e (DG-EVB, mode1)

Figure 9.22: Four example EVB-QMDFF energy plots for arbitrarily chosen reaction paths, including notes which EVB coupling term was used.

13 orders of magnitude larger than the smallest one (e-a), whereas this difference shrinks down to less than two orders of magnitude at 1500 K. This means that the *relative importance* of the site environment grows for lower temperatures, thus favoring more ordered structures than for higher temperatures.

9.4.3 KMC Simulations

After determination of diffusion rate constants for all 36 different processes existing in our model, we are able to do KMC simulations similar to those of section 9.2. The abstract gas atoms mentioned there are now of course copper atoms distributed on a regular Cu(001) surface. Since gas phase adsorption of copper seems to be rather implausible, a slightly different model was used: Instead of starting with a clean surface that is successively populated with suddenly appearing copper atoms, the starting condition is a surface with randomly distributed atoms on it. The periodic surface of 40 times 40 hollow sites, i.e., consisting of 1600 sites in total, is randomly populated with 400 copper atoms at the beginning.

After starting the KMC simulation, no further adsorption or desorption is possible, only diffusion of the 400 present copper atoms until a clearly identifiable pattern is generated or no significant changes happen after a certain stage of simulation.

In fig. 9.23 an example KMC trajectory of 450000 steps for the model at 300 K is shown. Shortly after the beginning the copper atoms are still distributed by chance (a). After 30000 steps a clear pattern can be seen, a number of small crystals has grown (b), clearly indicating attractive interactions, as already seen in fig. 9.21. In the following, these initial clusters merge, such that a smaller number of larger clusters dominates the surface. After 90000 steps only one cluster remains (with consideration of periodic boundaries). For the rest of the propagation, a *steady state* between the large cluster and 10-30 single Copper atoms seems to be established.

The overall résumé is therefore that arbitrary distributed copper atoms on a Cu(001) surface will grow together to a large cluster behaving like an additional surface layer (if we would go to even larger systems). This of course is no surprise since copper is solid at the temperatures and therefore expected to build ordered and compact structures rather than single distributed atoms.

The next question is if and how this behavior changes for higher temperatures. In fig. 9.24 the results of 400 randomly distributed copper atoms propagated for 450000 KMC steps at 200 to 1500 K are shown. The resulting patterns are almost identical between 200 and 500 K: one large cluster is built, with almost all surface atoms united in it[17]. A significant change takes place at 1000 K: Here, a rather pitted structure is built, with many atoms staying isolated around it. For 1500 K, the pattern is completely burst. Here, some smaller, irregular clusters seem to be build but they are not larger than 30-40 atoms in total. We could think that perhaps more steps are needed since the cluster growth is slower than for lower temperatures. But even for twofold or threefold step numbers no significant change of this structure can be seen, indicating that this is indeed the "final" pattern the system aspires to build[18].

Reviewing our insights concerning the reaction rate (table 9.4) this is of course no surprise since the rates for different steps resulting in cluster growth or shrinkage are becoming more and more similar the higher the systems temperature is. Ergo it is much less probable that all particles end in one large cluster for those higher temperatures since steps that move particles away from it will happen much more frequent.

---

17 The pattern of cluster (a) in fig. 9.24 looks slightly irritating, since the right and upper boundaries are completely straight, with irregular lower and left boundaries. Usually we would assume that no direction-specific changes in the shape should occur, because all KMC processes have the same rates for all space directions. The regular pattern in (a) might either origin in a kind of accidental seed crystal for a straight boundary, that has enlarged during the start, or in a bug of the KMC program.

18 Of course particles are still moving after a large number of steps, but now the built cluster structures are slowly moving and changing its shape, by simultaneously maintaining their characteristics, see fig. 9.23.

Table 9.4: Reaction path barriers as well as calculated rate constants for the 36 different diffusion steps needed for the KMC description of the Cu@Cu(001) system. Units are cm^3 molecule^{-1} s^{-1} for the rate constants, 1(-14) means $1 \cdot 10^{-14}$.

| process	barrier (kJ mol^{-1})	rate constants				
		200K	300K	500K	1000K	1500K
a-a	44.59	8.69(+01)	6.97(+05)	1.39(+09)	5.10(+11)	5.37(+12)
a-b	32.66	1.20(+05)	8.59(+07)	2.78(+10)	2.89(+12)	1.51(+13)
a-c	42.95	3.41(+02)	2.41(+06)	3.22(+09)	1.06(+12)	8.26(+12)
a-d	15.47	8.59(+09)	2.63(+11)	4.62(+12)	5.97(+13)	2.28(+14)
a-e	22.66	5.91(+07)	5.17(+09)	2.91(+11)	1.15(+13)	3.86(+13)
a-f	10.88	7.98(+10)	9.57(+11)	1.09(+13)	1.14(+14)	2.22(+14)
b-a	36.79	2.89(+04)	6.12(+07)	4.35(+10)	7.04(+12)	3.63(+13)
b-b	32.83	9.48(+04)	9.28(+07)	3.58(+10)	4.01(+12)	2.84(+13)
b-c	31.25	3.90(+05)	3.43(+08)	8.05(+10)	6.18(+12)	4.16(+13)
b-d	18.26	1.23(+09)	7.09(+10)	1.77(+12)	3.65(+13)	1.21(+14)
b-e	24.60	2.40(+07)	5.81(+09)	4.62(+11)	1.35(+13)	6.27(+13)
b-f	9.611	4.75(+11)	3.51(+12)	2.88(+13)	1.51(+14)	3.11(+14)
c-a	56.57	1.01(-01)	1.21(+04)	1.96(+08)	3.75(+11)	6.70(+12)
c-b	53.13	9.78(-01)	4.92(+04)	2.71(+08)	3.51(+11)	3.80(+12)
c-c	57.49	4.30(-02)	7.01(+03)	1.12(+08)	2.13(+11)	3.54(+12)
c-d	35.19	2.05(+04)	5.09(+07)	2.67(+10)	4.24(+12)	2.86(+13)
c-e	41.98	7.10(+02)	5.18(+06)	6.88(+09)	2.86(+12)	2.34(+13)
c-f	24.21	4.31(+07)	7.70(+09)	5.66(+11)	1.50(+13)	6.10(+13)
d-a	47.82	1.27(+01)	3.43(+05)	1.20(+09)	8.21(+11)	7.94(+12)
d-b	33.21	1.89(+05)	2.40(+08)	8.04(+10)	8.66(+12)	5.33(+13)
d-c	36.25	3.05(+04)	6.71(+07)	4.42(+10)	6.33(+12)	3.08(+13)
d-d	18.71	5.88(+08)	4.05(+10)	1.36(+12)	2.80(+13)	7.74(+13)
d-e	25.23	6.65(+06)	1.41(+09)	1.48(+11)	8.97(+12)	3.92(+13)
d-f	9.511	9.96(+10)	1.10(+12)	8.58(+12)	5.09(+13)	1.27(+14)
e-a	63.12	4.67(-03)	1.98(+03)	7.98(+07)	2.02(+11)	3.68(+12)
e-b	45.31	3.32(+01)	4.65(+05)	1.36(+09)	6.25(+11)	5.66(+12)
e-c	51.06	4.36(+00)	1.71(+05)	9.21(+08)	8.09(+11)	1.04(+13)
e-d	29.08	1.61(+06)	1.03(+09)	1.97(+11)	1.45(+13)	5.12(+13)
e-e	30.54	3.94(+05)	3.84(+08)	7.75(+10)	8.04(+12)	3.72(+13)
e-f	22.76	1.50(+08)	1.40(+10)	1.18(+12)	3.30(+13)	1.22(+14)
f-a	58.50	3.58(-02)	4.75(+03)	9.28(+07)	2.41(+11)	3.25(+12)
f-b	42.43	2.14(+02)	1.99(+06)	3.91(+09)	1.42(+12)	1.18(+13)
f-c	45.88	1.62(+01)	3.36(+05)	9.31(+08)	4.77(+11)	4.32(+12)
f-d	19.92	3.33(+08)	3.08(+10)	1.28(+12)	3.08(+13)	1.25(+14)
f-e	33.03	3.26(+05)	3.77(+08)	9.70(+10)	8.16(+12)	4.17(+13)
f-f	21.22	3.37(+08)	3.29(+10)	1.13(+12)	2.70(+13)	1.12(+14)
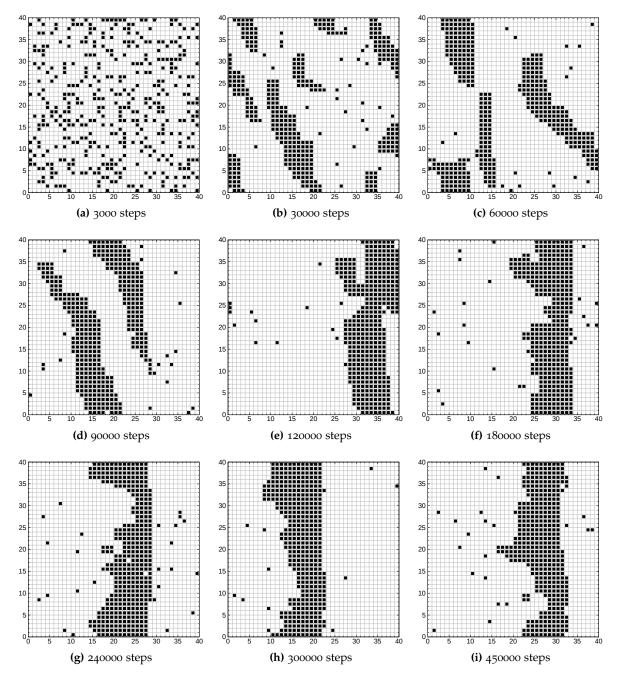
Figure 9.23: Eight snapshots of a KMC trajectory for the diffusion of copper atoms on a Cu(001) surface at 300 K, based on the calculated k(T) values listed in table 9.4. Similar to the attractive interaction model in fig. 9.6, seed-crystal-like structures are built already at 30000 steps.
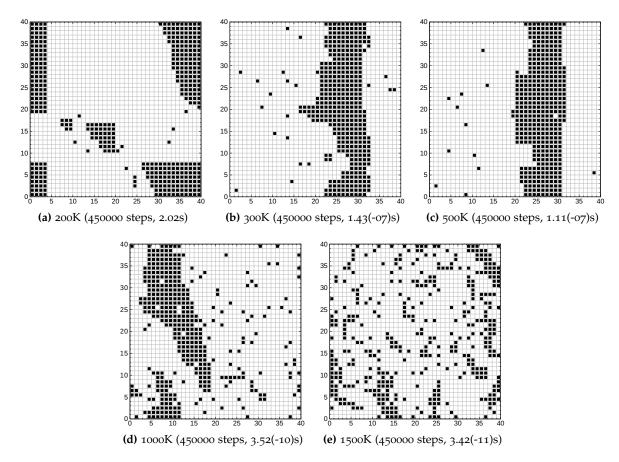
(a) 200K (450000 steps, 2.02s)   **(b)** 300K (450000 steps, 1.43(-07)s)   **(c)** 500K (450000 steps, 1.11(-07)s)

(d) 1000K (450000 steps, 3.52(-10)s)   **(e)** 1500K (450000 steps, 3.42(-11)s)

Figure 9.24: Final configurations of KMC runs for copper diffusion on a Cu(001)-surface for different temperatures (using the k(T)-values depicted in table 9.4). 1(-11) means $1 \cdot 10^{-11}$. The higher the temperature, the more equally spread are the adherent copper atoms. Further, the simulated timescales get shorter for higher temperatures, since all processes happen much faster.

If we compare this to the *melting point* of copper being 1357 K, this failure to build one large cluster at 1500 K could be connected to the disintegration of the whole crystal at those temperatures (i.e., the melting process), that might happen here as well if we had not fixed the underlying surface and would do instead a three dimensional KMC simulation. Of course the presented results have no claim of quantitatively representing the chemical reality since the QM reference calculations were rather cheap and some approximations were made (no cross-steps possible, no building of three dimensional structures possible, no interactions with more distant atoms on the surface). However, they give insight into the possibilities of KMC to simulate large-scale (both spacial and temporal) chemical processes and are at least of qualitative plausibility with respect to the melting point of copper.

Future Challenges

> One of the basic rules of the universe is that nothing is perfect. Perfection simply doesn't exist. Without imperfection, neither you nor I would exist.
>
> (*Stephen Hawking*)

Instead of a summarized outlook, some of the obvious and less obvious challenges to be tackled in the future will be formulated in a handful of questions which the author (and hopefully the interested reader too) might ask him or herself during a calm hour of intense EVB-QMDFF regarded soul-searching.

Can we move to a true black-box method?

Looking back at chapter 6 we have seen that calculations with `evb_kt_driver.x` already are quite good realizations of that what we call *black-box*: Once a reaction path and suitable QM methods for calculation of additional reference data are given, the program does the rest by itself and finally ejects rate constants and Arrhenius parameters. But what about those first steps, namely the calculations of reaction path and choice of suitable QM methods? By far the largest amount of work done for chapter 6 was invested to optimize TSs and IRCs, which often suffered from either wrong results (e.g., IRCs leading to other products than desired) or convergence problems.

Unfortunately, there is no way of avoiding those difficulties, since quantum chemical modeling of a new reactive system always needs some manual intervention and intellectual reflection: Are parts of the reaction path of multireference character? Should diffuse basis functions be added to correctly describe some dispersion interactions crucial for the mechanism? Many of those questions need to be answered before we can really be sure that the optimized reaction path offers a good foundation for a high-quality *black-box* calculation. Doing all this in *black-box* fashion seems to be impossible, since such a *black-box* program should basically know everything what a good computational chemist knows.

But is this really that bad? Even if the correct approach of multireference methods is far from easy, there are many easy to handle *graphical user interface* (GUI) based programs such as GaussView available that try to make the correct application of QM methods possible for the average user. These utilities of course do not prevent the user from making popular mistakes like using B3LYP/6-31G(d,p) for each and every chemical system as a quasi *black-box* method, whose correction is

certainly out of scope for the present project. The rather nasty part of setting up a rate constant calculation, however, is now fully automated, therefore removing a large part of work.

Is TREQ really the final answer?

The TREQ method has indeed proven to be quite successful for *black-box* k(T) calculations at least for small and medium-sized systems. On the other hand we have seen that the description of the larger urethane systems in chapter 8 was problematic. Either manual improvement of the internal coordinate system was needed to stabilize the MD trajectories or the method was unable to describe them at all[1].

Even though the definite reason for that failure is unclear so far, it can be assumed that the orthogonal projection of the actual point in coordinate space on the MEP needed for the following Taylor series evaluation from there plays a central role. For small to medium-sized systems this projection should usually be clear, especially if the space of interest can be fully described in terms of bond lengths and angles. If we, however, go to very large systems with high-dimensional coordinate space (remember the $3N - 6$ scaling if N is the number of atoms!), the projection almost certainly will become ambiguous or unstable. This might lead to sudden jumps of the projected positions on the MEP if the system itself moves only gradually within one time step. This jump will cause large changes in the gradient, potentially leading to explosions within the dynamics.

How can this deficiency be solved? If we do not want to change the mathematical foundations of TREQ itself there seems to be little room to escape. One possibility could be to remember that the size of the reactive center itself usually stays rather small. If we look back again to the urethane reactions in chapter 8 we have seen that the large systems still have the same reaction mechanism but larger substituents around it. Long alkyl chains or benzene rings, however, usually do not have much influence on the reaction itself (some sterics and small electronic effects), but in usual TREQ their whole coordinate space is included and complicates the projection algorithm on the MEP.

A possible solution therefore might be to *subdivide* the system into a reactive part which must be described by direct interpolation in the transition region and the remaining part (similar to QM/MM methods [294]), that could be described by either RP-EVB or the QMDFFs alone. Since the description of outer alkyl chains will stay identical for both reactants and products QMDFFs (i.e., same connectivity and almost the same force constants), we also could assume that no high-level description is needed for a reasonable modeling of the transition between them. The practical implementation might look like this: We define a subspace of internal coordinates which are located in the reactive part of the system. Then we project the reference gradients and Hessians on those as it is done for usual TREQ so far. Energy and gradient for the atoms in this part are fully defined by the direct interpolation. The neighbored atoms, however, are described by, e.g., RP-EVB, where a small set of coordinates is enough since the QMDFFs act as a stable foundation of the surface. Possibly a smooth switching will be needed between the reactive part and the outer alkyl chains of the substituents.

Such a partitioning certainly will become quite complicated, we should, for instance, investigate for each atom how much its gradient components change during the reaction in order to allocate it to a reactive or less reactive part of the system, however, we should remember that TREQ was not designed to be mathematically elegant or nice to look at. It was designed to avoid any manual intervention in its setup! Therefore, if we are able to automate a very complicated setup such that it will work for (almost) any system, we do not need to worry about it.

If those problems are solved someday, another issue might be that of *very high quality* descriptions. So far, only a second order Taylor series is used to describe regions offside the reaction path. It is

---

1 Another possibility for those problems could be that the RPMD algorithm itself is proven to be unstable as well, a problem that might get worse for large systems [293]. We will not discuss this point here in more detail, since there is no easy way to solve it.

not possible to improve this description so far, thus no convergence to exactness (with respect to the QM reference method) can be achieved even if large amounts of computational power are available. To enable such convergence the Taylor expansion perpendicular to the MEP could be *expanded*. The straightforward method would be to simply add the cubic term of the Taylor expansion. This term, however, needs the *third* derivatives of the QM method, which are very expensive to calculate even for rather small systems. The only reasonable way would be to avoid their full calculation but instead to construct an approximated correction, e.g., by randomly calculating energies of points farther offside the MEP and to optimize some internal coordinate specific correction terms to them.

Can we describe polymerization processes?

This question looks rather specific. It becomes relevant, however, if our cooperation with Covestro for the theoretical description of urethane reactions is reconsidered (chapter 8). There we have calculated rate constants for rather small urethane systems, i.e., of single monomers coming together and starting a new polymer chain. In reality those reactions will mainly occur at the ends of already growing chains or even by merging of two large chains. One central question therefore is how the reaction rate constants are affected by the growing polymer chain. Does the polymerization proceed with equal speed if the attached chain grows or is it accelerated or is it slowed down?

This problem reveals quite a broad field to be investigated: We have seen in the last section of the chapter that no 8-ring autocatalysis is possible for the reaction of NDI with methanol. If the substituents of the alcohols grow, will the 6-ring reaction still be possible or could the steric hindrance of long polymer substituents become too large even for this mechanism? Besides this steric problem at the reaction site, stabilizations via hydrogen bonds between urethane, isocyanate and alcohol groups of the substituents might as well play an important role. Further, electronic effects (+I,-I) of the side chains might also influence the reaction by raising/lowering the reaction barrier. If we consider in the first place a study of rate constants depending on growing side chains of one involved alcohol molecule, we could repeat rate constants calculations for one monomer (e.g., butandiol), the monomer reacted with an diisocyanate (A-I), with the diisocyanate reacted with another alcohol (A-I-A) and so forth. These calculations could be done from scratch, i.e., optimizing TS and IRC for the different chains, parametrizing TREQ and do the k(T) calculations with RPMD.

Considering the unfavorable scaling of QM methods with system size, it becomes clear that "direct" calculations of very long chains containing hundreds of atoms are essentially out of reach even if DFT methods are used as reference. A possible loophole is to make the central property of a polymer chain (e.g., being a succession of identical subunits) part of the PES construction. Instead of calculating the whole system and generate QMDFFs as well as EVB from its reference data, we might think of a *modular approach*. We then would calculate, for instance, the full set of QM reference data for the 6-ring reaction of an isocyanate with a diol molecule that itself already has formed another urethane bond with an additional isocyanate. After calculation of QM reference data and generation of QMDFF files, we take a further look at the QMDFFs.

As explained in section 2.3, the QM reference information from Hessian, bond orders, charges and equilibrium geometry is transformed into a bunch of covalent force field terms, each consisting of involved atom indices, equilibrium values and force constants and some noncovalent ones, depending on distances, charges and global parameters. If we now pick the atoms of the alcohol-isocyanate side chain that shall be polymerized, we could build a polymer structure from them, e.g., by simply plugging the same unit many times together, with adequate cartesian translation of the single unit's atoms. All partial charges stay identical for the units, as well as the force constants of their internal coordinates. We then must consider *inter-unit* interactions. These are first noncovalent interactions like dispersions. Their parameters are set by the QMDFF program

itself such that we only need to specify all possible interaction pairs. Slightly more complicated are covalent interactions in the transition regions between neighbored units. Here we could adopt force constants from other regions of the initial molecule. If, e.g., an urethane unit builds the transition region, we could take the force constants from the central urethane unit present in the products QMDFF. It should be possible to automate this "QMDFF polymerization" with a separate script or as part of an EVB-QMDFF subroutine especially designed for description of polymer chains.

Besides the QMDFFs, the EVB coupling term itself should as well be polymerized. If we would take the simple energy-gap coupling term, this would be trivial, since all needed changes were already made in the QMDFFs on which the EVB term depends. Unfortunately the quality of dE coupling has proven to be insufficient for reliable description of urethane reactions, therefore we must use either DG-EVB or TREQ. For their treatment it is important to note that the *spatial distribution* of the needed coupling strength is closely restricted to the sections of the molecule that are taking part in the reaction. Therefore the polymerized side chains are negligible for the coupling term. If we would use DG-EVB or RP-EVB without TS correction (or TREQ with QM-MM, see above) we usually operate in a reduced space of internal coordinates (see chapter 4), where, e.g., only built and broken bonds are included. Since all gradient and Hessian reference data is projected onto this reduced set of internal coordinates before being used for the coupling setup, we readily could use the QM reference data of the original system *without* polymerized sidechains, since all reactive coordinates will be located in it. Thus, the projection *cartesian to internal* operates from a reduced set of cartesian information to an even further reduced set of internals. We now could argue that this treatment makes the whole experiment unnecessary, since the transition region (almost) solely depends on the coupling and this coupling is constructed to be *independent* of the added side chains. Since the rate constant largely depends on this transition region, no influence of the degree of polymerization in the side chain could be seen by construction.

Here, one central property of EVB proves to be quite helpful: The independence of the coupling term from the molecular environment [101] (see section 2.4.2). If we parametrize an EVB-QMDFF for a system in vacuum and now want to simulate it in a solvent, we only need to calculate the influence of the solvent on the *diabatic surfaces*, i.e., on the QMDFFs, whereas the coupling term can stay the same. If we assume that the polymer chains have similar (indirect) influence on the reactive center as a solvent, we therefore can indeed use reference data from the original unpolymerized system for the parametrization of the coupling.

Is an online black-box k(T) portal possible?

As pointed out already in the introduction, the main objective of this thesis was to develop a method suitable for the average chemist. Since popular quantum chemistry programs like Gaussian [99] that should be known to almost every chemist in our days usually have nice GUIs (here: GaussView), the question seems to be legitimate if EVB-QMDFF itself should get a modern GUI to become more attractive for everyone.

If we assume that most average chemists simply want to calculate rate constants and/or Arrhenius parameters for the system of interest, we can restrict that discussion to the `evb_kt_driver.x` program. Looking back at its description in section 3.3.8 we saw that all needed settings can be defined in a single `qmdff.key` input file. This type of handling certainly was the standard throughout the last decades. However, it might be rather challenging to convince the average user that obeying certain syntax for keywords or absolute paths to called programs is really up to date, especially if we look at the general development of, for instance, smartphones that try to hide as much "nerdy" details as possible from the user.

Therefore, it is certainly desirable to develop a program similar to GaussView where some clicks and entries in well-placed question boxes are sufficient to initiate a rate constant calculation. Similar to GaussView, which is a separate interface to the Gaussian program itself that can as well

be controlled in the classical way, i.e., by editing input files with text viewers, the GUI should be a separate program, taking the role of `evb_kt_driver.x`, that calls the other single programs of the EVB-QMDFF program package when they are needed.

A possible design of a *black-box* k(T) GUI would be like that: After the user has opened it, the program asks for a calculated reaction path to be imported. Alternatively, it could be extended such that also the TS and IRC optimization are managed with it. In this case, a molecule builder gets opened where a TS guess structure must be clicked together. Then, suitable QM program packages are called to do the optimizations.

No matter if TS and IRC shall be calculated within the program package or not, it should search the system for existent QM program packages like Gaussian, Orca or Turbomole [99, 130, 132]. After the IRC has been calculated or loaded, the user is asked for which direction of the path the k(T) values shall be determined. This decision is eased by animated visualizations of the reaction proceding in the chosen way. Then, the QM method for further TREQ reference calculations must be determined. Ideally, the program automatically reads in the level of theory used for the calculation of the given IRC or, if the user does also the TS and IRC calculation with our program, he or she might get a drop-down menu similar to GaussView where usual methods (depending on the availability in the located QM program packages) can be found. Such a menu is needed as well for higher-level energy corrections of the path.

After those settings are determined, the QM reference calculations (QMDFF minima as well as TREQ gradient/Hessian reference) can be started. Since those might take many hours or days, a progress-update indicating the quality of the single calculations might be very desirable. A schematic picture of the reaction path might exist with little boxes on it representing the single reference points. Their color might change from red to green if the reference calculation for one of them is finished, then offering to click on it, where, e.g., normal modes of the calculated Hessian can be inspected in order to control if everything is alright. Similarly, the QMDFF optimizations can be monitored, e.g., by automated evaluation of the QMDFF force constant fit (how large the deviations between QMDFF and QM reference frequencies are). Settings for the RPMD calculations are determined in a fully automated fashion, such that the user must not care about it. Of course, they can be altered as well, either during the QM reference calculations or after the RPMD calculations when, e.g., a too large variance of single k(T) values is monitored.

Moving further to the future, where cloud-computing gets more and more important, a webbrowser-based application (or an app on the smartphone) to start and manage the *black-box* k(T) calculations would be preferable to the local GUI, especially if probably very expensive QM reference calculations are run that might take days on usual desktop computers. Locating the calculations on high-performing computing centers allows the user to turn off his or her desktop PC and look on the progress via the webpage. Depending on the field of application (research or industry) suitable models for accessing those central computing facilities should of course be developed as well. To finally answer the question: Yes, online black-box k(T) calculations are certainly possible.

What if we want to describe reactions in solution?

All reactions calculated in this thesis are thermal gas phase reactions on the electronic ground state. In chemical reality, however, most reactions of interest are taking place in solution. Therefore it would be preferable to include the influence of solvents into our *black-box* protocol. There are two ways of doing this.

First, implicit solvation could be used [295]. Here, the surrounding solvent molecules are approximated by modeling their electrostatic effects on the reaction of interest. Implicit solvation should be included into the QM reference calculation by, e.g., using COSMO [296].

Second, the solvent might be added explicitly by simulating the reaction in a *solvent box*. This leads to a *multi scale* model, where the reactive system itself (or maybe only its reactive center, see above) is described with TREQ and the solvent molecules around it with a traditional nonreactive force field. Further, we should restrict the *RPMD description* to the reactive system, such that this would be described by, e.g., 8 or 16 beads, whereas all solvent molecules are still described by one bead. Interactions between the RPMD beads and the solvent molecules are then simply summed up over all replicas, divided through the number of beads, i.e., the solvent sees, e.g., one eighth of each replica. Such RPMD-classical hybrid simulations, mostly for single particles like protons or electrons in classical environments, were already done by several authors [152, 297, 298].

The main issue is how good TREQ can be combined with a solvent environment. We have learned that EVB is able to include solvent interactions by modifying the diabatic surfaces (section 2.4.2). Further studies should now made how the *direct interpolation part* in TREQ is affected by interactions with solvent molecules.

How can we get to large-scale chemical systems?

The *black-box* rate constant methodology was applied to single elementary reactions so far. In chapter 9, though, we have seen that the KMC method is able to describe a whole ensemble of reactive sites by reducing single reactive events to state changes whose incidence is determined by the pre-calculated rate constants.

There, only very simple diffusions of gas or metal atoms on metal surfaces were treated, with very little relevance for most kinetical descriptions. If we look on the field of heterogeneous catalysis, though, we see that reactions happening on metal surfaces can be indeed of great importance. The KMC algorithm presented in chapter 9 is able to include those more complex events as well.

If we consider a metal surface which acts as a catalyst for the subsequent assembling of small gas-phase molecules to the desired products, all reactions will still happen on the various sites of the metal surface. Depending on the partial pressure of the components (e.g., A, B and C), they will randomly spawn on the surface with different probabilities. If two possible reactants (A and B) are located on neighbored sites, a reaction event will happen with a certain rate that merges both to a new molecule (A+B $\longrightarrow$ D) that will either occupy one of the sites or leave to the gas phase, changing its respective partial pressure and thus its probability to spawn on another free site. This simple model can of course be made much more complicated, for instance, by introducing more kinds of reactants and intermediates, different ways to react (depending on the relative locations of the occupied sites on the surface) and so forth. Rate constants for all possible processes can then be calculated with EVB-QMDFF-RPMD and subsequently added to the growing KMC model.

If we move to other kinds of reactions, e.g., polyurethane synthesis, the system is much more complicated: It is three-dimensional and has no discrete sites located in cartesian space between which the system can move or distinct reactions can happen. Instead, reactions might happen everywhere where the reactive groups approach each other in space.

Fortunately, there also exist *off-lattice* KMC methods [270]. Here, the system is propagated in cartesian space with usual Monte Carlo sampling until two molecular groups approach each other. Then, it is evaluated if a reaction takes place or not, depending on the calculated reaction rate. If the detected possible reaction is not listed in our global arrays so far, its rate constant might be calculated *on the fly* by the *black-box* program and added to the table. In the case of urethane reactions, only a limited number of reactions are interesting for us. Therefore we can calculate their rates in advance and propagate the system with *off-lattice* KMC, where this method should be optimized for the usage with polymer chains in solution. *Off-lattice* KMC will of course also work for several other kinds of reactive systems either in the gas phase or in solution.

Appendix

11.1 Supervised Projects

In line with this thesis, four lab courses were supervised by me: two advanced lab courses in theoretical chemistry ("F3"), one lab course being part of the theoretical chemistry compulsory elective core subject ("F2") and one voluntary short-term course. Depending on the status my work had at these points in time, different tasks were offered to the four participants, from which two of them wrote a protocol as well. The most important parts of their results, especially if they had an impact on the further development of my whole work, shall be described here briefly.

11.1.1 Jan-Moritz Adam

Jan-Moritz Adam did an advanced lab course between March and May 2016, i.e., quite shortly after I began my PhD. At this time, the EVB-QMDFF program was in the early stages of version 3 (section 3.1); the coupling to RPMDrate was not done yet and only DG-EVB version 1 (i.e., energies as reference) was implemented. He tried to setup EVB-QMDFF for some small reactions which he chose from the NIST Chemical Kinetics Database [153].

Two of these reactions were $NH_3+OH \longrightarrow NH_2+H_2O$ and $CH_3F+CH2Cl \longrightarrow CH_2F+CH_3Cl$. Besides the manual calculation of reference data for both QMDFF and DG-EVB, he wrote a first script that automated the choice of structures and energies along the reaction path to be used for the DG-EVB setup. With different sets of internal coordinates he tried to reproduce the reference energies along the reaction paths as well as possible.

Unfortunately he aborted the lab course before final results were obtained. His automated DG-EVB reference energy script however was indeed one of the first small early steps for that what is now known as the *black-box* TREQ setup.

11.1.2 Jennifer Müller

Jennifer Müller did her advanced lab course between August and September 2017. At this time, program version 3 was completed and, after publication of the second EVB-QMDFF paper, I applied the DG-EVB-k(T) calculation method to as many example reactions as possible in order to research its abilities and limitations (of which, sadly, many existed).

Jennifer assisted me in this task and chose a number of reactions for which experimental data was available. She did the QM reference calculations and optimized the respective DG-EVB coupling terms, where the number of DG-EVB reference points, the set of internal coordinates for the coupling and the DG-EVB mode were varied until the reference path was reproduced as well as possible.

The first set of reactions were radical hydrogen abstractions of hydroxyl from primary, secondary and tertiary carbon atoms:

$$CH_3CH_3 + OH \longrightarrow CH_3CH_2 + H_2O, \tag{11.1}$$

$$(CH_3)_2CH_3 + OH \longrightarrow (CH_3)_2CH_2 + H_2O, \tag{11.2}$$

$$(CH_3)_3CH_3 + OH \longrightarrow (CH_3)_3CH_2 + H_2O. \tag{11.3}$$

QM references for all three reactions were calculated with MP2/cc-pVTZ. For reaction 11.1 DG-EVB mode 2 with 9 reference points along the path was used, the forming O-H and breaking C-H bonds as well as two other distances in the reactive area were chosen as internal coupling coordinates. In the case of reaction 11.2, DG-EVB mode 3 with 6 DG-EVB points and the forming O-H and breaking C-H bonds as internal coordinates gave good results. For all following reactions, the smallest possible internal coordinate set of breaking and forming bond was sufficient. Reaction 11.3 was calculated with the same settings as 11.2. The resulting DG-EVB energies are plotted together with both QMDFF- and QM reference energies in fig. 11.1. We can see that DG-EVB is able to reproduce the reference path with high quality in all cases.

The second set of reactions were bimolecular nucleophilic substitutions of monocholormethane with fluoride, cyanide and isocyanide anions:

$$CH_3Cl + F^- \longrightarrow CH_3F + Cl^-, \tag{11.4}$$

$$CH_3Cl + CN^- \longrightarrow CH_3CN + Cl^-, \tag{11.5}$$

$$CH_3Cl + NC^- \longrightarrow CH_3NC + Cl^-. \tag{11.6}$$

Here, the calculation of QM reference data was slightly more demanding, both MP2/cc-pVTZ and PBE0/aug-cc-pVTZ were used as methods of choice. For reaction 11.4 the IRC calculations did not converge, the reaction path was therefore parametrized with two bond length scans (of both breaking and forming bonds). DG-EVB mode 3 with 8 reference points gave the best results. The reactions 11.5 and 11.6 are very similar. IRC calculations failed for both of them, and were therefore replaced with bond length scans. Parametrization of DG-EVB was done again with mode 3, 8 reference points and the minimal set of internal coordinates. The resulting energies are shown in fig. 11.1, where for reaction 11.4 the parametrization with respect to the PBE0 path is taken, in contrast to the MP2 paths of both 11.5 and 11.6. Very good agreements between DG-EVB and reference can be seen again.

Based on these DG-EVB PESs, Jennifer did rate constant calculations with the RPMDrate program for 300 K and 16 (reactions 11.1-11.3) or 8 (reactions 11.4-11.6) beads, depending on the amount of tunneling to be expected. The results are shown in table 11.1. Unfortunately the method only gave useful results for three of six systems. For the others, severe complications in the umbrella samplings, resulting in damaged free energy curves and thus useless rate constants, occurred. Presumable reasons were the difficulties of DG-EVB to guarantee a smooth description of the whole accessible PES offside the reaction path.

Jennifer's work gave important insights into the apparent problems of DG-EVB: Even if reaction paths are reproduced with very good quality, the whole PES accessible during RPMD umbrella samplings might be insufficient. It constituted one of the motivations that led to the development of TREQ.
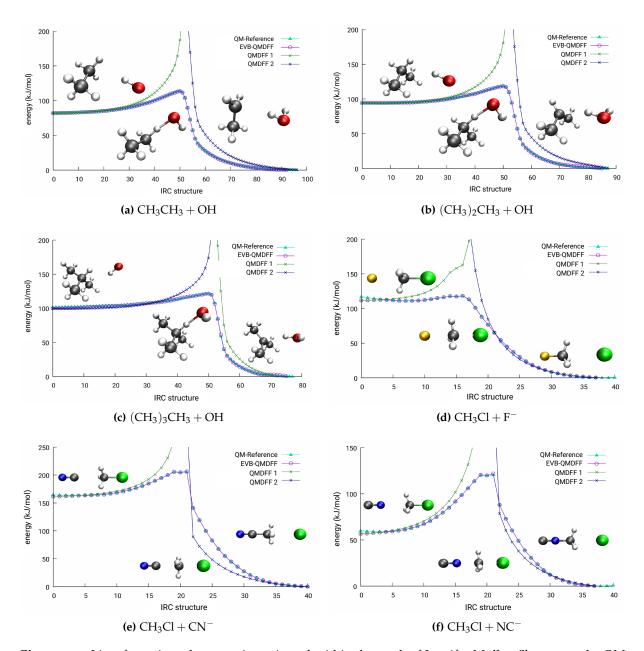
(a) CH$_3$CH$_3$ + OH

(b) (CH$_3$)$_2$CH$_3$ + OH

(c) (CH$_3$)$_3$CH$_3$ + OH

(d) CH$_3$Cl + F$^-$

(e) CH$_3$Cl + CN$^-$

(f) CH$_3$Cl + NC$^-$

Figure 11.1: List of reactions that were investigated within the work of Jennifer Müller. Shown are the QM reference reaction paths together with the QMDFF- and (DG-)EVB-QMFFF energies. Almost no difference between reference and EVB-QMDFF can be seen, showing good qualities of DG-EVB at least along the paths themselves.

Table 11.1: DG-EVB-QMDFF rate constants calculated by Jennifer Müller in her advanced lab course. Units are cm^3 molecule^{-1} s^{-1}, 1(-14) means $1 \cdot 10^{-14}$.

System	k(T) values	
	DG-EVB-QMDFF	reference
$CH_3CH_3 + OH$	-^{a}	-
$(CH_3)_2CH_3 + OH$	2.40(-13)	8.38(-13) [299]
$(CH_3)_3CH_3 + OH$	1.03(-14)	1.83(-12) [299]
$CH_3Cl + F^-$	4.19(-13)^b	8.00(-10) [300]
$CH_3Cl + CN^-$	-^{a}	-
$CH_3Cl + NC^-$	-^{a}	-

^{a}: No useful EVB-QMDFF rate constant could be calculated for this system.
^{b}: The EVB-QMDFF based on PBE0 reference gave 4.19(-13), the MP2-based EVB-QMDFF gave 1.57(-14).

11.1.3 Michael Schulz

Michael Schulz did his voluntary two-week course in August 2018. The TREQ method was under construction, therefore he used the DG-EVB method in connection with the newly developed `rpmd.x` program for his calculations. After a detailed introduction of the topic by myself we decided to try the calculation of bimolecular reactions with one product, i.e., additions and mergings, which was already possible due to the generalized definition of dividing surfaces introduced for the urethane reactions (chapter 8). He calculated rate constants of, e.g., the $SiH_2+H_2 \longrightarrow SiH_4$ and the $CH_2O+H_2 \longrightarrow CH_3OH$ reaction.

Since it was no formal lab course, no protocol was written. Nevertheless, we did some important advances in the handling and debugging of the `rpmd.x` program, further, Michael wrote a Python script for the calculation of Arrhenius parameters and their comparison to experimental references, which was a base point for the subsequent *black-box* calculations.

11.1.4 Sven Schultzke

Sven Schultzke did his advanced lab course between November and December 2018. At this point, the TREQ method was fully implemented, an early version of the `evb_kt_driver.x` program was available as well.

Main objective was a benchmark of TREQ, particularly for rather challenging cases, i.e., large or unusual systems. Some of them were:

$$CH_2BrCH_2CH_3 \longrightarrow CH_3CH_2CH_2Br, \tag{11.7}$$

$$C_2H_4 + OH \longrightarrow CH_2OHCH_3, \tag{11.8}$$

$$CH_2Ph + HO_2 \longrightarrow CH_2OPh + OH. \tag{11.9}$$

Reaction 11.7 is a rearrangement and thus an unimolecular process, for which no rate constants could be calculated at the point of Sven's work (therefore, we investigated if the free energy surface was reasonable). The addition reaction 11.8 could be parametrized and calculated with the `evb_kt_driver.x` program. Some problems regarding the choice of internal coordinates for TREQ and thus the stability of the samplings occurred. The resulting rate constants were very poor, deviating some orders of magnitude from the experiment. Reaction 11.9 was the most interesting

one: Initially the RPMD dynamics exploded almost instantly and the reason was not clear. Later we found out that the standard choice of internal coordinates consisting of bond lengths and angles was insufficient to describe the benzene ring. Addition of newly implemented dihedrals and out-of-plane angles finally made it possible to do the samplings, the resulting rate constant at 300 K ($4.0 \cdot 10^{11}$ cm^3 mol^{-1} s^{-1}) was close to the experimental value ($1.2 \cdot 10^{11}$ cm^3 mol^{-1} s^{-1}). Samplings at higher temperatures still suffered from instability.

This most recent lab course was important for the improvement of the TREQ method as well as for the final implementation steps of `evb_kt_driver.x`. Further, the elaborate error-handling features of `rpmd.x` could be improved based on Sven's findings concerning PES instabilities.

11.2 Theoretical Details and Derivations

11.2.1 Schrödinger Equation from Path Integrals

In order to clarify the correspondence between the path integral and the Schrödinger picture of quantum mechanics, a short proof shall be given that the popular differential formulation of QM is indeed identical to the path PI introduced in section 2.1.5, by obtaining the time dependent Schrödinger equation from the PI propagator [50]. In order to get to the differential formulation, it is useful to introduce *wave functions*.

As noted in section 2.1.5, a *kernel* describes the probability of going from location *a* to *b*. If we include the time as parameter, the kernel for one dimension can be defined as: $K(x_b, t_b, x_a, t_a)$. Thus, it describes the probability for a particle being at x_b at time t_b under the condition that it was at x_a at time t_a. The wave function $\psi(x_b, t_b)$ describes also a quantum mechanical amplitude of being at x_b at time t_b, but no matter from which position the particle has actually started.

Both kernel and wave function are adequate for a complete description of a quantum mechanical system, i.e., we can calculate its state for all future time if $K(x_b, t_b, x_a, t_a)$ or $\psi(x_b, t_b)$ are known. The kernel can also be used to propagate a wave function in time: The probability of arriving at x_b at time t_b can be calculated from the wave function $\psi(x_c, t_c)$ (arriving at x_c at time t_c), multiplied by the amplitude to go from *c* to *b*, integrated over all possible values of x_c:

$$\psi(x_b, t_b) = \int_{-\infty}^{\infty} K(x_b, t_b, x_c, t_c)\psi(x_c, t_c)dx_c. \tag{11.10}$$

In order to get to the Schrödinger equation, which shall also describe the time evolution of a wave function, but not by integrals, a *differential description* is needed. Our task is to transform an integral equation into a differential equation. Therefore, an *infinitesimal time step* is considered, i.e., $t_b = t_c + \epsilon$.

Now, eq. 11.10 can be specified for this situation, where the particle shall be at *y* before the propagation and at *x* after the propagation, when ϵ was added to the actual time:

$$\psi(x, t + \epsilon) = \frac{1}{A} \int_{-\infty}^{\infty} \exp\left[\frac{i}{\hbar}\epsilon L\left(\frac{x-y}{\epsilon}, \frac{x+y}{2}\right)\right]\psi(y, t)dy. \tag{11.11}$$

Here, the general expression for the kernel (eq. 2.70) was used and simplified: Since we only look at an infinitesimal step, only one single intersection is evaluated for all paths, resulting in one single integral over all *y*. For the infinitesimal step, the action (i.e., the time integral of the Lagrangian) can be approximated by a single box of height $L(\dot{x}, x)$ and width ϵ: $S[a, b] = \int_{t_a}^{t_b} L(\dot{x}, x, t)dt \approx \epsilon L(\dot{x}, x)$.

Further, actual position $\frac{x+y}{2}$ and velocity $\frac{x-y}{\epsilon}$ are approximated linearly in terms of start and end points.

Next, the Lagrangian should be evaluated. In the case of a particle moving in one dimension under influence of a potential energy $V(x,t)$, the expression is:

$$L(\dot{x}, x, t) = \frac{m}{2}\dot{x}^2 - V(x,t). \tag{11.12}$$

After inserting this Lagrangian into eq. 11.11 and evaluating the exponentials, the result is:

$$\psi(x, t+\epsilon) = \frac{1}{A}\int_{-\infty}^{\infty} \exp\left[\frac{i}{\hbar}\frac{m(x-y)^2}{2\epsilon}\right]\exp\left[-\frac{i}{\hbar}\epsilon V\left(\frac{x+y}{2}, t\right)\right]\psi(y,t)dy. \tag{11.13}$$

For large differences of x and y (i.e., large movements in the time interval ϵ) the quantity $\frac{(x-y)^2}{2\epsilon}$ will get very large and huge oscillations of the whole exponential will occur, canceling out the integral for these regions[1]. Therefore, only areas with small $x-y$-difference will contribute significantly to the whole propagator. The approximation $y = x + \eta$ can be made, whereas η shall be a small (but usually not infinitesimal) step in x. Then, the whole expression gets much simpler:

$$\psi(x, t+\epsilon) = \frac{1}{A}\int_{-\infty}^{\infty} \exp\left[\frac{im\eta^2}{2\hbar\epsilon}\right]\exp\left[-\frac{i}{\hbar}\epsilon V\left(x + \frac{\eta}{2}, t\right)\right]\psi(x+\eta, t)d\eta. \tag{11.14}$$

Now, the initial and final wave functions are expanded as Taylor series, up to first order in time (due to the infinitesimal change) and up to second order in position. We get:

$$\psi(x, t+\epsilon) \approx \psi(x, t) + \epsilon\frac{\partial\psi}{\partial t},$$
$$\psi(x+\eta, t) \approx \psi(x, t) + \eta\frac{\partial\psi}{\partial x} + \frac{1}{\eta}\frac{\partial^2\psi}{\partial x^2}. \tag{11.15}$$

The potential energy exponential may also be developed, but only to first order due to the ϵ-prefactor and neglection of $\frac{\eta}{2}$: $\exp\left[-\frac{i}{\hbar}\epsilon V\left(x+\frac{\eta}{2}, t\right)\right] \approx 1 - \frac{i}{\hbar}\epsilon V(x,t)$. With this, we obtain:

$$\psi(x,t) + \epsilon\frac{\partial\psi}{\partial t} = \frac{1}{A}\int_{-\infty}^{\infty} \exp\left[\frac{im\eta^2}{2\hbar\epsilon}\right]\left[1 - \frac{i}{\hbar}\epsilon V(x,t)\right]\left[\psi(x,t) + \eta\frac{\partial\psi}{\partial x} + \frac{1}{\eta}\frac{\partial^2\psi}{\partial x^2}\right]d\eta. \tag{11.16}$$

Two tasks remain to be done: The normalization factor A should be quantified and the integral in η must be solved such that only differentials remain and we get the desired differential equation. In order to make actual integrations possible, eq. 11.16 can be factorized, all terms that do not depend on η are dragged before the integrals:

$$\psi(x,t) + \epsilon\frac{\partial\psi}{\partial t} = \frac{1}{A}\left[1 - \frac{i}{\hbar}\epsilon V(x,t)\right]\left\{\psi(x,t)\int_{-\infty}^{\infty}\exp\left[\frac{im\eta^2}{2\hbar\epsilon}\right]d\eta + \right.$$
$$\left.\frac{\partial\psi}{\partial x}\int_{-\infty}^{\infty}\eta\exp\left[\frac{im\eta^2}{2\hbar\epsilon}\right]d\eta + \frac{1}{2}\frac{\partial^2\psi}{\partial x^2}\int_{-\infty}^{\infty}\eta^2\exp\left[\frac{im\eta^2}{2\hbar\epsilon}\right]d\eta\right\}. \tag{11.17}$$

These three Gaussian integrals are standard textbook examples and thus possess analytical solutions. The first one gives:

$$\int_{-\infty}^{\infty}\exp\left[\frac{im\eta^2}{2\hbar\epsilon}\right]d\eta = \sqrt{\frac{2\pi i\hbar\epsilon}{m}}. \tag{11.18}$$

---

1 This is similar to the classical correspondence discussed in section 2.1.5. If the action (here approximated by the Lagrangian itself) becomes huge for certain paths, these are negligible in practice. This is also the reason why extreme motions rarely occur even in the quantum mechanical regime, e.g., tunneling over more than one or two Ångstroms. Here, it means that it is very unlikely that the particle will move a large distance in an infinitesimal time step.

Now, the normalization factor A can already be determined. Consider the case that the infinitesimal time interval ϵ becomes zero. Then, eq. 11.17 must still be valid. On the left, only $\psi(x,t)$ remains. On the right, $\psi(x,t)$ has the prefactor $\frac{1}{A}\sqrt{\frac{2\pi i \hbar \epsilon}{m}}$. With this, it becomes clear that

$$A = \sqrt{\frac{2\pi i \hbar \epsilon}{m}}. \tag{11.19}$$

Two integrals remain. The second integral, $\int_{-\infty}^{\infty} \eta \exp\left[\frac{i m \eta^2}{2\hbar\epsilon}\right] d\eta$ is zero, since an uneven function is integrated over a symmetric interval. The last integral becomes, with consideration of the normalization factor:

$$\frac{1}{A}\int_{-\infty}^{\infty} \eta^2 \exp\left[\frac{i m \eta^2}{2\hbar\epsilon}\right] d\eta = \frac{i\hbar\epsilon}{m}. \tag{11.20}$$

Inserting all this into eq. 11.17 results in:

$$\psi(x,t) + \epsilon\frac{\partial\psi}{\partial t} = \left[1 - \frac{i}{\hbar}\epsilon V(x,t)\right]\left\{\psi(x,t) + \frac{i\hbar\epsilon}{2m}\frac{\partial^2\psi}{\partial x^2}\right\} =$$
$$\psi(x,t) - \frac{i}{\hbar}\epsilon V(x,t)\psi(x,t) + \frac{i\hbar\epsilon}{2m}\frac{\partial^2\psi}{\partial x^2} + \frac{\epsilon^2}{2m}V(x,t)\frac{\partial^2\psi}{\partial x^2}. \tag{11.21}$$

Since we only developed to first order in ϵ, the term containing ϵ^2 can be neglected, such that we get as the final expression for the time development:

$$\psi + \epsilon\frac{\partial\psi}{\partial t} = \psi + \frac{i}{\hbar}\epsilon V\psi + \frac{i\hbar\epsilon}{2m}\frac{\partial^2\psi}{\partial x^2}. \tag{11.22}$$

Solving for the time derivative of ψ results in the following equation, valid to order ϵ:

$$\frac{\partial\psi}{\partial t} = -\frac{i}{\hbar}\left[-\frac{\hbar}{2m}\frac{\partial^2\psi}{\partial x^2} + V\psi\right]. \tag{11.23}$$

This is finally the time dependent Schrödinger equation (TDSE). Perhaps more popular is its slightly altered version:

$$i\hbar\frac{\partial\psi}{\partial t} = \left[-\frac{\hbar}{2m}\frac{\partial^2}{\partial x^2} + V\right]\psi, \tag{11.24}$$

where $\mathfrak{H} = -\frac{\hbar}{2m}\frac{\partial^2}{\partial x^2} + V$ is the *Hamiltonian* for the one dimensional particle in the potential $V(x,t)$. Thus we have shown that the path integral propagator $K(x_b, t_b, x_c, t_c)$ operating on a wave function can indeed be represented by the TDSE in the case of infinitesimal time differences[2].

11.2.2 The RPMD Reaction Rate

In this section we want to explore how the expression for the RPMD reaction rate constant (eq. 2.103) can be obtained from the reactive-flux formulation of QTST in connection with two dividing surfaces constructed in the system's coordinate space [301, 302].

---

2 Interestingly, we can also define a TDSE of the path integral, which as we have seen is very similar to a wave function. This TSDE is: $\frac{\partial}{\partial t_b}K(b,a) = -\frac{i}{\hbar}H_b K(b,a)$, where H_b is a Hamiltonian only working on variable b (the endpoint of the particle).

(a) Classical TST (nonzero $t \to 0_+$)   (b) Quantum TST (zero $t \to 0_+$)
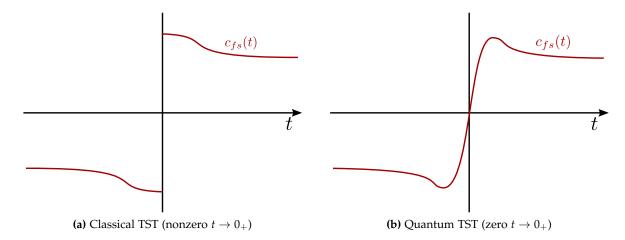
Figure 11.2: Flux-side correlation time profiles of a typical reaction for classical (a) as well as quantum (b) treatment [9]. For classical calculations, a nonzero $t \to 0_+$ limit exists, whereas the subsequent drop can be accounted for by a separate recrossing calculation. For true quantum TST, the zero time limit is zero, such that a longer calculation will be needed. Since the centroid coordinates of RPMD are considered for the correlation function, the RPMD c_{fs} time profile has a similar shape as the classical one, i.e., with a finite value for $t \to 0_+$, which leads to the recipe to take its short time limit for RPMD-k(T) calculations and do a separate recrossing calculation.

Originating from the exact quantum mechanical reactive-flux rate expression in eq. 2.100, we can formulate an equivalent RPMD reactive-flux rate:

$$k(T) = \frac{1}{Q_r^{(n)}(T)} \lim_{t \to \infty} \tilde{c}_{fs}^{(n)}(t),$$ (11.25)

where $Q_r^{(n)}(T)$ is the quantum mechanical partition function of the reactants per unit volume, approximated by the n-bead path integral and $\tilde{c}_{fs}^{(n)}(t)$ is the RPMD flux-side correlation function of a ring-polymer with n beads (similar to eq. 2.101):

$$\tilde{c}_{fs}(t) = \frac{1}{(2\pi\hbar)^n} \int \int e^{-\beta H_n(\mathbf{p}_0, \mathbf{q}_0)} \delta[\bar{s}(\mathbf{q})] \bar{v}_s(\mathbf{p}, \mathbf{q}) \Theta[\bar{s}(\mathbf{q}_t)] d^N \mathbf{p}_0 d^N \mathbf{q}_0.$$ (11.26)

Similar to the flux-flux autocorrelation explained in section 2.1.4, where the initial flux at $t = 0$ is compared to its value at later times, the flux-side correlation connects the initial flux through the transition state dividing surface at $t = 0$ to the *population of the products side* of the dividing surface at later times t.

The numerical evaluation of flux-side correlations in the long time limit is complicated, due to the rare-event character of the investigated reactions. Fortunately, it can be shown that in the classical and semiclassical case, the short time limit (i.e., $\lim_{t \to 0_+} \tilde{c}_{fs}(t)$) is equal to the long time asymptote, if recrossing is considered separately, such that the recrossing correction is the relation between exact long time asymptote and short time limit:

$$\kappa^{(n)}(\xi_1) = \frac{c_{fs}^{(n)}(t \to \infty; \xi_1)}{c_{fs}^{(n)}(t \to 0_+; \xi_1)}.$$ (11.27)

With this, we can evaluate the short time limit of the flux-side correlation and later correct it with a separate recrossing calculation. The typical shape of flux-side correlation time profiles for classical as well as quantum calculations is shown in fig. 11.2.

The short time limit can be calculated as:

$$\lim_{t \to 0_+} \tilde{c}_{fs}(t) = \prod_{i=1}^{f} \left(\frac{\mu_i}{2\pi\beta_n\hbar^2} \right)^{\frac{n}{2}} \int e^{\beta_n V_n(\mathbf{q})} \delta[\bar{\xi}(\mathbf{q})] \bar{f}_\xi(\mathbf{q}) d^{fn}\mathbf{q}, \tag{11.28}$$

where f is the number of degrees of freedom in the system and

$$\bar{f}_\xi(\mathbf{q}) = \sqrt{\sum_{i=1}^{f} \frac{1}{2\pi\beta_n\mu_i} \left[\frac{\partial\bar{\xi}(\mathbf{q})}{\partial\bar{q}_i} \right]^2}. \tag{11.29}$$

The evaluation of this integral is still very complicated. It can be simplified significantly if *another dividing surface* besides the first at the transition state is introduced. We choose a dividing surface located at the asymptotic reactants valley (eq. 3.10):

$$\xi_0(\mathbf{q}) = R_\infty - |\mathbf{R}| = 0, \tag{11.30}$$

where $|\mathbf{R}|$ is the cartesian distance between the reactants center of masses and R_∞ is a manually chosen asymptotic distance at which the interactions between the reactants are negligible. If we calculate the short-time flux-side correlation function (eq. 11.28) with respect to this dividing surface instead of the one located at the transition state, we get

$$f_{\xi_0}(\mathbf{q}) = \sqrt{\frac{1}{2\pi\beta\mu_R}} \tag{11.31}$$

and subsequently for the flux-side correlation:

$$\lim_{t \to 0_+} \tilde{c}_{fs}(t; \xi_0) = 4\pi R_\infty^2 \sqrt{\frac{1}{2\pi\beta\mu_R}} Q_r^n(T). \tag{11.32}$$

If we compare this with eq. 11.25, we see that the same partition function $Q_r^n(T)$ is located there in the denominator, such that they can be cut to get the rate constant expression:

$$k^{QTST}(\xi_0) = 4\pi R_\infty^2 \sqrt{\frac{1}{2\pi\beta\mu_R}}. \tag{11.33}$$

This expression is surprisingly simple, in fact, it depends only on a handful of predefined parameters, we no longer need to evaluate any partition functions [302]. Further, it is quite descriptive: The $4\pi R_\infty^2$-factor is the *surface area* of a sphere with radius R_∞ and $\sqrt{\frac{1}{2\pi\beta\mu_R}}$ is, according to the kinetic theory of gases, the averaged speed of reactant molecules entering this sphere. Thus, a reaction with respect to the ξ_0-dividing surface always happens if both reactants approach to R_∞ distance from infinity, or, if one molecule is the frame of reference, the second reactant enters the imaginary sphere with R_∞ radius around it. However, if we want to achieve a reasonable quantification of the whole reaction, we still need to include the transition state dividing surface, which was the basis of the whole reactive-flux formulation so far. Or, more descriptive, we must compute the probability that reactants approaching to R_∞ actually react to the products. For an arbitrary pair of dividing surfaces (here: ξ_0 and ξ_1), we can define the ratio of their respective flux-side correlation functions (i.e., the reaction rate at the first surface relative to the second) as:

$$p^{(n)}(\xi_1, \xi_0) = \frac{c_{fs}^{(n)}(t \to 0_+; \xi_1)}{c_{fs}^{(n)}(t \to 0_+; \xi_0)}. \tag{11.34}$$

This ratio can be expressed by means of *canonical probabilities* of the system to be at the respective dividing surfaces, i.e., at $\xi = 0$ or $\xi = 1$ [302]:

$$p^{(n)}(\xi_1, \xi_0) = \frac{P^{(n)}(1)}{P^{(n)}(0)}, \tag{11.35}$$

with

$$P^{(n)}(\xi) = \frac{\int e^{-\beta_n H_n^{\xi}(\mathbf{p},\mathbf{q})} \delta[\bar{\xi}(\mathbf{q}) - \xi] d^{fn}\mathbf{p} d^{fn}\mathbf{q}}{\int e^{-\beta_n H_n^{\xi}(\mathbf{p},\mathbf{q})} d^{fn}\mathbf{p} d^{fn}\mathbf{q}}. \tag{11.36}$$

We already learned something about these coordinate-dependent distributions in section 2.1.3, e.g., that they can be expressed by means of coordinate-dependent free energy curves. If we recall eq. 2.27 in connection with eq. 2.28, the free energy can be expressed as:

$$A^{(n)}(\xi) = -\frac{1}{\beta_n} \ln P^{(n)}(\xi). \tag{11.37}$$

Solving this equation for the probability distribution $P^{(n)}(\xi)$ gives:

$$P^{(n)}(\xi) = e^{-\beta_n A^{(n)}(\xi)}. \tag{11.38}$$

Now, the ratio between the flux-side correlation functions from eq. 11.34 can be expressed by means of free energies of the reaction coordinate at the dividing surfaces ξ_0 and ξ_1:

$$p^{(n)}(\xi_1, \xi_0) = \exp\left(-\beta_n \left[A^{(n)}(1) - A^{(n)}(0)\right]\right). \tag{11.39}$$

The bimolecular RPMD rate constant evaluated from the flux-side correlation at the transition state dividing surface can be obtained by connecting the rate at the reactants dividing surface (eq. 11.33) with the ratio of flux-side correlation functions at reactants and transition state (eq. 11.39) as well as with the recrossing factor introduced by taking the short-time limit for the flux-side correlation in eq. 11.27:

$$\begin{aligned}
k_{RPMD}(T) &= \kappa k^{QTST}(\xi_0) p^{(n)}(\xi_1, \xi_0) \\
&= \kappa 4\pi R_\infty^2 \sqrt{\frac{1}{2\pi\beta\mu_R}} \exp\left(-\beta_n \left[A^{(n)}(1) - A^{(n)}(0)\right]\right).
\end{aligned} \tag{11.40}$$

This finally is the bimolecular RPMD k(T) expression shown in eq. 2.103, with $\Delta A = A^{(n)}(1) - A^{(n)}(0)$.

11.3　Internal Coordinates

As briefly described in the theory part of this thesis, the more complex formulations of the EVB-coupling terms in the DG-EVB as well as the TREQ formulation rely on the usage of internal coordinate systems.

Both directions of coordinate transformations are needed in practice: First, for DG-EVB and TREQ setup, reference gradients and Hessians given in cartesian coordinates need to be transformed to internals for their actual application in the Taylor expansions. Second, calculated gradients of the surfaces need to be transformed back to cartesian space such that they can be introduced into the velocity Verlet algorithm.

During the development of the EVB-QMDFF program package, four different kinds of internals were adopted subsequently: bond lengths, bond angles, dihedral angles and out-of-plane angles. Whereas small systems (up to approximately 10-15 atoms) could be described well only using bond lengths and angles, larger systems, especially if they shall be described with TREQ, tend to need also some dihedral and out-of-plane coordinates for reliable calculations.

In the first subsection, the general coordinate transformation algorithm as adopted from PULAY and FOGARASI [303] is described, whereas in the second subsection all four coordinate types are described in more detail. Based on these introduced coordinates, in the last two subsections formulations for their transformation matrix elements are given.

11.3.1 General Formalism

A molecular system is given, containing N atoms whose location in space can be fully described via a set $\mathbf{x}$ of $3N$ cartesian coordinates. If the total orientation of the system with respect to the laboratory frame is neglected, it can also be fully described *via* a set $\mathbf{q}$ of internal coordinates. This set might as well be *nonredundant* (containing $3N - 6$ coordinates) or *redundant* (containing a larger set), depending on the actual requirements.

If a given set of cartesian coordinates shall be converted into a corresponding set of internals, the *Wilson transformation matrix* $B_{ij} = \frac{\partial q_i}{\partial x_j}$ is needed:

$$\mathbf{q} = \mathbf{B}^{-1}\mathbf{x}. \tag{11.41}$$

Similar to geometries, *gradients* can also be converted from cartesian to internal coordinates. This however, requires the transposed inverse of the Wilson transformation matrix:

$$\mathbf{g}_q = (\mathbf{B}^{-1})^t \mathbf{g}_x. \tag{11.42}$$

By taking the derivative of the whole transformation formula, the respective expression for the cartesian *Hessian* matrix can be found:

$$\mathbf{H}_q = \mathbf{B}^{-1}(\mathbf{H}_x - \mathbf{B}'^t \mathbf{g}_q)(\mathbf{B}^{-1})^t. \tag{11.43}$$

For this operation, the tensor with the second cartesian derivatives of the internal coordinates $B'_{ijk} = \frac{\partial q_i}{\partial x_j \partial x_k}$, that might be seen as the cartesian derivative of the Wilson matrix itself, is needed.

If the numbers of internal and cartesian coordinates are different, which they will be in most cases, the Wilson-matrix is no square matrix and an inverse cannot be build. Nevertheless, *singular value decomposition* (SVD) of the Wilson matrix

$$\mathbf{B} = \mathbf{U}\mathbf{\Sigma}\mathbf{V}^t \tag{11.44}$$

might be applied in order to calculate its *pseudoinverse* thereafter, which fulfills the same task as a classical inverse for the transformations. The pseudoinverse of a SVD is calculated by inverting the diagonal matrix $\mathbf{\Sigma}$ containing the singular values:

$$\mathbf{\Sigma} = \begin{pmatrix} \sigma_1 & & & & \vdots & \\ & \ddots & & & \cdots\ 0\ \cdots & \\ & & \sigma_{r-1} & & \vdots & \\ & & & \sigma_r & & \\ \hline \vdots & & \vdots & & \vdots & \\ \cdots\ 0\ \cdots & & & \cdots\ 0\ \cdots & \\ \vdots & & & \vdots & \end{pmatrix}. \tag{11.45}$$

Bond length (q_b)   **Dihedral Angle** (q_d)

Bond angle (q_a)   **Out-of-plane angle** (q_o)
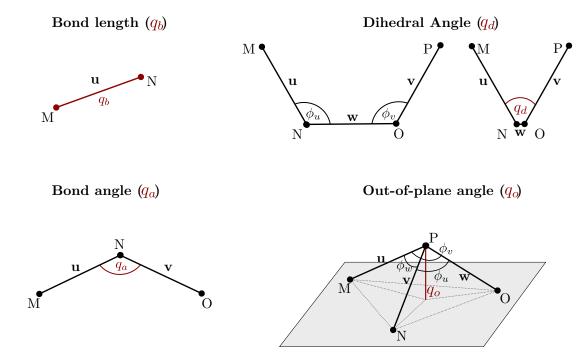
Figure 11.3: Schematic representation of internal coordinate types used in this thesis. Involved atoms are labeled with uppercase letters, bond vectors between atoms are labeled with bold lower case letters.

This inversion is done by simply taking the inverse of each *diagonal element*. However, this straightforward approach leads to numerical instabilities in many cases. If the set of internal coordinates is (approximately) redundant and some (near) linear dependencies exist between its members, some singular values might become zero (or almost zero). Building their inverse causes numerical explosions. To avoid that, all σ below a certain value (in the current implementation less than $1 \cdot 10^{-7}$) are set to zero:

$$\mathbf{\Sigma}^{-1} = \begin{pmatrix} \frac{1}{\sigma_1} & & & & \vdots \\ & \ddots & & & \cdots & 0 & \cdots \\ & & \frac{1}{\sigma_{r-1}} & & \vdots \\ & & & 0 & \\ \hline & \vdots & & & \vdots \\ \cdots & 0 & \cdots & & \cdots & 0 & \cdots \\ & \vdots & & & \vdots \end{pmatrix}. \tag{11.46}$$

11.3.2   Coordinate Types and Metric

In fig. 11.3, the four types of internal coordinates that are used in the scope of this thesis are listed schematically.

The simplest type of coordinates are *bond lengths*. They are defined as usual:

$$q_b = |\mathbf{x}_m - \mathbf{x}_n| = |\mathbf{u}|. \tag{11.47}$$

For the *bond angles*, a slightly different version than usual is used. A well known problem from the literature is that derivatives of linear angles are not defined, so that coordinate transformations might become erroneous for such configurations of the system [304].

An alternative formulation for a bond angle is to calculate the distance between the outside atoms (M and O in fig. 11.3) of the bonds by simultaneously normalize both involved bond lengths [304]:

$$q_a = \frac{1}{2}\left(\frac{\mathbf{u'}}{\lambda_u} - \frac{\mathbf{v'}}{\lambda_v}\right) = \frac{1}{2}(\mathbf{u} - \mathbf{v}) \tag{11.48}$$

where $\mathbf{u'} = \vec{x}_m - \vec{x}_n$, $\mathbf{v'} = \vec{x}_o - \vec{x}_n$, and λ_u, λ_v their respective bond lengths calculated with eq. 11.47. For the Wilson matrix elements shown below, normalized bond vectors are used almost exclusively, they are $\mathbf{u}$ and $\mathbf{v}$ in this case. Now, linear angles are no longer problematic.

Dihedral angles are defined as usual:

$$q_d = \arccos\left(\frac{(\mathbf{u} \times \mathbf{w}) \cdot (\mathbf{v} \times \mathbf{w})}{\sin(\phi_u)\sin(\phi_v)}\right), \tag{11.49}$$

where $\mathbf{u'} = \vec{x}_m - \vec{x}_n$, $\mathbf{w'} = \vec{x}_o - \vec{x}_n$, $\mathbf{v'} = \vec{x}_p - \vec{x}_o$ and $\mathbf{u}$, $\mathbf{w}$, $\mathbf{v}$ their normalized counterparts; further defined are $\sin(\phi_u) = \sqrt{1 - (\mathbf{u} \cdot \mathbf{w})^2}$ as well as $\sin(\phi_v) = \sqrt{1 - (\mathbf{v} \cdot \mathbf{w})^2}$. For this type of definition, care needs to be taken for invalid angle arguments: if the argument of the arccos function gets smaller than -1 or larger than $+1$, it is set to its limit values automatically.

The definition of the *out-of-plane coordinates* is shown in fig. 11.3. It was taken from the paper of KRIMM *et al.* [304] and has the advantage that in contrast to usual out-of-plane definitions no singularities can appear if involved angles get linear. The coordinate is basically a normalized triple product:

$$q_o = \frac{1}{\rho}\mathbf{u} \cdot (\mathbf{v} \times \mathbf{w}). \tag{11.50}$$

The normalization constant needed for calculation of the height is defined as:

$$\begin{aligned}
\rho^2 = 3 &- \cos^2\phi_u - \cos^2\phi_v - \cos^2\phi_w + 2[\cos\phi_u(\cos\phi_v - 1) \\
&+ \cos\phi_v(\cos\phi_w - 1) + \cos\phi_w(\cos\phi_u - 1)],
\end{aligned} \tag{11.51}$$

where the involved angles are defined as normalized dot products $\cos\phi_u = \mathbf{v} \cdot \mathbf{w}$, $\cos\phi_v = \mathbf{u} \cdot \mathbf{w}$, $\cos\phi_w = \mathbf{u} \cdot \mathbf{v}$.

11.3.3 Wilson Matrix Elements

As noted above, coordinate transformation matrices, mostly called Wilson matrices, are of integral importance for internal coordinate calculations. They consist of *partial derivatives* of internal coordinates with respect to cartesians:

$$B_{ij} = \frac{\partial q_i}{\partial x_j}. \tag{11.52}$$

The elements of this matrix can be calculated numerically by imposing finite differences. However, especially for dihedrals and out-of-planes this results in a large calculation overhead: four atoms need to be elongated in three cartesian directions with plus and minus, respectively, resulting in 24 coordinate calculations! During a MD calculation, a backwards coordinate transformation from internals to cartesians is needed in each step in order to calculate the EVB-QMDFF gradient, which makes the coordinate transformation a critical step for the scaling of the whole method. Therefore, analytical derivatives should be implemented to avoid such overhead. In this section, the analytical expressions for the elements of eq. 11.52 are listed and explained.

Similar work was done already before in a paper of HELGAKER [305], however, this was done there only for bonds, angles and torsions. Further, the torsional Wilson elements contain some errors which makes it problematic to implement (at least until all errors could be detected). Finally, the expression for the angle coordinate is different in my case.

To the best of my knowledge, the compilation of Wilson matrix elements shown in the following is the only one freely available for the collection of internal coordinates used in this paper. A new formalism was used in order to generalize the different expressions as much as possible. All derivatives are given as vector expressions, i.e., they constitute three entries in the Wilson matrix, the x-, y- and z- values.

The actual implementation of the coordinate transformation was made more effective by defining several intermediate vectors, dot- and cross-products in advance for each new Wilson matrix calculation.

Bond Lengths

For **bond lengths**, the following expression is valid[3]:

$$\frac{\partial q_b}{\partial x_{a,i}} = \zeta_{aMN} u_i \quad ; \quad a = M, N, \tag{11.53}$$

where a sign factor was introduced similar to the paper of HELGAKER:

$$\zeta_{amn} = \begin{cases} 1 & a = M \\ -1 & a = N \\ 0 & \text{else} \end{cases} . \tag{11.54}$$

Bond Angles

For the **bond angles**, cartesian derivatives of *normalized bonds* are needed. They can be defined as components of a derivative vector, where each entry is itself a vector.

$$\frac{\partial \mathbf{u}}{\partial \mathbf{x}} = \frac{1}{\lambda_u^3} \left(\begin{pmatrix} u_2^2 + u_3^2 \\ -u_1 u_2 \\ -u_1 u_3 \end{pmatrix} \begin{pmatrix} -u_2 u_1 \\ u_1^2 + u_3^2 \\ -u_2 u_3 \end{pmatrix} \begin{pmatrix} -u_3 u_1 \\ -u_3 u_2 \\ u_1^2 + u_2^2 \end{pmatrix} \right)^T . \tag{11.55}$$

With this abbreviation, Wilson matrix elements for a bond angle coordinate can be written in closed form:

$$\frac{\partial q_a}{\partial x_{a,i}} = -\frac{1}{4q_a} \zeta_{aMN} \zeta_{aNO} \left((1 - \delta_{aO}) \frac{\partial \mathbf{u}}{\partial x_i} \cdot \mathbf{v} + (1 - \delta_{aM}) \mathbf{u} \cdot \frac{\partial \mathbf{v}}{\partial x_i} \right) \quad ; \quad a = M, N, O. \tag{11.56}$$

Dihedral Angles

Dihedral angles result in much longer expressions, however these can still be expressed in terms of vectors and vector derivatives according to eq. 11.55.

With numerator $\theta = (\mathbf{u} \times \mathbf{w}) \cdot (\mathbf{v} \times \mathbf{w})$ and denominator $\kappa = \sin(\phi_u) \sin(\phi_v)$ the Wilson matrix elements for the dihedral angles are:

$$\frac{\partial q_d}{\partial x_{a,i}} = -\frac{\frac{\partial \theta}{\partial x_{a,i}} \kappa - \theta \frac{\partial \kappa}{\partial x_{a,i}}}{\sqrt{1 - \left(\frac{\theta}{\kappa}\right)^2 \kappa^2}}. \tag{11.57}$$

---

3 In the upcoming mathematical expressions, the following nomenclature is used (closely related to fig. 11.3): M, N, O, P are the up to four atoms for which the coordinate is calculated, $x_{a,i}$ depicts that the current derivative is built with respect to the i'th cartesian coordinate (x, y or z) of atom a (which can be M, N, O or P). Bold symbols $\mathbf{u}$, $\mathbf{v}$ and $\mathbf{w}$ describe the bond vectors included in the current coordinate description.

Now, the derivatives of the numerator and denominator of the dihedral expression are still missing. Although they might also be expressed in one closed formula (resulting in a long and nasty expression), I have decided to give them depending on the atom which coordinates are calculated. For the numerator the derivatives are:

$$
\frac{\partial \theta}{\partial x_{a,i}} = \begin{cases} \left(\frac{\partial \mathbf{u}}{\partial x_i} \times \mathbf{w}\right) \cdot (\mathbf{v} \times \mathbf{w}) & a = M \\ -\left[\left(\frac{\partial \mathbf{u}}{\partial x_i} \times \mathbf{w}\right) + \left(\mathbf{u} \times \frac{\partial \mathbf{w}}{\partial x_i}\right)\right] \cdot (\mathbf{v} \times \mathbf{w}) - (\mathbf{u} \times \mathbf{w}) \cdot \left(\mathbf{v} \times \frac{\partial \mathbf{w}}{\partial x_i}\right) & a = N \\ \left(\mathbf{u} \times \frac{\partial \mathbf{w}}{\partial x_i}\right) \cdot (\mathbf{v} \times \mathbf{w}) + (\mathbf{u} \times \mathbf{w}) \cdot \left[\left(\mathbf{v} \times \frac{\partial \mathbf{w}}{\partial x_i}\right) - \left(\frac{\partial \mathbf{v}}{\partial x_i} \times \mathbf{w}\right)\right] & a = O \\ (\mathbf{u} \times \mathbf{w}) \cdot \left(\frac{\partial \mathbf{v}}{\partial x_i} \times \mathbf{w}\right) & a = P \end{cases}.
\tag{11.58}
$$

The derivatives of the denominator are:

$$
\frac{\partial \kappa}{\partial x_{a,i}} = \begin{cases} -\left(\frac{\partial \mathbf{u}}{\partial x_i} \cdot \mathbf{w}\right)(\mathbf{u} \cdot \mathbf{w})\frac{\sin(\phi_v)}{\sin(\phi_u)} & a = m \\ \left[\left(\frac{\partial \mathbf{u}}{\partial x_i} \cdot \mathbf{w}\right) + \left(\mathbf{u} \cdot \frac{\partial \mathbf{w}}{\partial x_i}\right)\right](\mathbf{u} \cdot \mathbf{w})\frac{\sin(\phi_v)}{\sin(\phi_u)} \\ \quad + \frac{\sin(\phi_u)}{\sin(\phi_v)}\left(\mathbf{v} \cdot \frac{\partial \mathbf{w}}{\partial x_i}\right)(\mathbf{v} \cdot \mathbf{w}) & a = n \\ \quad - \left(\mathbf{u} \cdot \frac{\partial \mathbf{w}}{\partial x_i}\right)(\mathbf{u} \cdot \mathbf{w})\frac{\sin(\phi_v)}{\sin(\phi_u)} \\ -\left[\left(\frac{\partial \mathbf{v}}{\partial x_i} \cdot \mathbf{w}\right) + \left(\mathbf{v} \cdot \frac{\partial \mathbf{w}}{\partial x_i}\right)\right](\mathbf{v} \cdot \mathbf{w})\frac{\sin(\phi_u)}{\sin(\phi_v)} & a = o \\ -\left(\frac{\partial \mathbf{v}}{\partial x_i} \cdot \mathbf{w}\right)(\mathbf{v} \cdot \mathbf{w})\frac{\sin(\phi_v)}{\sin(\phi_u)} & a = p \end{cases}.
\tag{11.59}
$$

Out-of-Plane Angles

For the **out-of-plane-angles**, the Wilson matrix elements can be given again in one closed formula:

$$
\frac{\partial q_o}{\partial x_{a,i}} = \begin{cases} \frac{v}{\rho}\left(\frac{\partial \rho}{\partial x_{a,i}}\frac{v}{\rho} + \frac{\partial v}{\partial x_{a,i}}\right) & a = M, N, O \\ -\left(\frac{\partial q_o}{\partial x_{M,i}} + \frac{\partial q_o}{\partial x_{N,i}} + \frac{\partial q_o}{\partial x_{O,i}}\right) & a = P \end{cases}
\tag{11.60}
$$

where $v = \mathbf{u} \cdot (\mathbf{v} \times \mathbf{w})$.

The derivatives of the normalization factor with respect to the involved bond vectors can be expressed as:

$$
\frac{\partial \rho}{\partial x_{a,i}} = \begin{cases} \frac{2}{\rho}\frac{\partial \mathbf{u}}{\partial x_i} \cdot \Big[\mathbf{w}\left(-\cos(\phi_2) - 1 + \cos(\phi_1) + \cos(\phi_3)\right) + \\ \qquad \mathbf{v}\left(-\cos(\phi_3) - 1 + \cos(\phi_1) + \cos(\phi_2)\right)\Big] & a = M \\ \frac{2}{\rho}\frac{\partial \mathbf{v}}{\partial x_i} \cdot \Big[\mathbf{w}\left(-\cos(\phi_1) - 1 + \cos(\phi_2) + \cos(\phi_3)\right) + \\ \qquad \mathbf{u}\left(-\cos(\phi_3) - 1 + \cos(\phi_1) + \cos(\phi_2)\right)\Big] & a = N \\ \frac{2}{\rho}\frac{\partial \mathbf{w}}{\partial x_i} \cdot \Big[\mathbf{v}\left(-\cos(\phi_1) - 1 + \cos(\phi_2) + \cos(\phi_3)\right) + \\ \qquad \mathbf{u}\left(-\cos(\phi_2) - 1 + \cos(\phi_1) + \cos(\phi_3)\right)\Big] & a = O \end{cases},
\tag{11.61}
$$

where the angles ϕ_1 to ϕ_3 are shown in fig. 11.3.

The derivatives of the triple product in eq. 11.50 ($v = \mathbf{u} \cdot (\mathbf{v} \times \mathbf{w})$) are quite simple:

$$\frac{\partial v}{\partial x_{a,i}} = \begin{cases} \frac{\partial \mathbf{u}}{\partial x_i} \cdot (\mathbf{v} \times \mathbf{w}) & a = M \\ \mathbf{u} \cdot \left(\frac{\partial \mathbf{v}}{\partial x_i} \times \mathbf{w} \right) & a = N \\ \mathbf{u} \cdot \left(\mathbf{v} \times \frac{\partial \mathbf{w}}{\partial x_i} \right) & a = O \end{cases} . \tag{11.62}$$

Evaluating the symmetry of eq. 11.60, it is obvious that the Wilson matrix elements for atom P are basically the negative sum of the elements for all other atoms, due to the fact that P constitutes the peak of a tripod, with M,N and O building its base.

11.3.4 Wilson Matrix Derivatives

Similar to the Wilson matrix elements (i.e., the first derivatives of the internal coordinates with respect to cartesians) the Wilson matrix derivatives (i.e., the second derivatives of internal coordinates with respect to cartesians) can be simplified significantly if the expressions for bond-, dihedral- and out-of-plane angles are constructed in terms of bond derivatives.

Bond Lengths

The simplest case are again the **bond lengths**. Their Wilson matrix derivatives are given by HELGAKER, they are:

$$\frac{\partial^2 q_b}{\partial x_{a,i} \partial x_{b,j}} = (-1)^{\delta_{ab}} \frac{u_i u_j - \delta_{ij}}{\lambda_u}. \tag{11.63}$$

Similar to the expression for the first derivative of a normalized bond in dot- or cross-products in eq. 11.55, their second derivatives can be written as a symmetric second derivative matrix, with each entry being a vector itself (eq. 11.64).

$$\frac{\partial^2 \mathbf{u}}{\partial \mathbf{x} \partial \mathbf{x}} = \frac{1}{\lambda_u^5} \cdot$$
$$\begin{pmatrix} \begin{pmatrix} -3u_1(u_2^2 + u_3^2) \\ u_2(2u_1^2 - u_2^2 - u_3^2) \\ u_3(2u_1^2 - u_2^2 - u_3^2) \end{pmatrix} & \cdots & \cdots \\ \begin{pmatrix} -u_2(-2u_1^2 + u_2^2 + u_3^2) \\ -u_1(u_1^2 - 2u_2^2 + u_3^2) \\ 3u_1 u_2 u_3 \end{pmatrix} & \begin{pmatrix} u_1(-u_1^2 + 2u_2^2 - u_3^2) \\ -3u_2(u_1^2 + u_3^2) \\ u_3(-u_1^2 + 2u_2^2 - u_3^2) \end{pmatrix} & \cdots \\ \begin{pmatrix} -u_3(-2u_1^2 + u_2^2 + u_3^2) \\ 3u_1 u_2 u_3 \\ -u_1(u_1^2 - 2u_2^2 + u_3^2) \end{pmatrix} & \begin{pmatrix} 3u_1 u_2 u_3 \\ -u_3(u_1^2 - 2u_2^2 + u_3^2) \\ -u_2(u_1^2 + u_2^2 - 2u_3^2) \end{pmatrix} & \begin{pmatrix} u_1(-u_1^2 - u_2^2 + 2u_3^2) \\ u_2(-u_1^2 - u_2^2 + 2u_3^2) \\ -3u_3(u_1^2 + u_2^2) \end{pmatrix} \end{pmatrix} \tag{11.64}$$

Bond Angles

For the **bond angles**, the second derivatives can be written in one single expression if the first derivatives of eq. 11.56 are used:

$$\frac{\partial^2 q_a}{\partial x_{a,i} \partial x_{b,j}} = -\frac{1}{4q_a} \left(4 \frac{\partial q_a}{\partial x_{a,i}} \frac{\partial q_a}{\partial x_{b,j}} + \frac{\partial^2 (\mathbf{u} \cdot \mathbf{v})}{\partial x_{a,i} \partial x_{b,j}} \right). \tag{11.65}$$

In this formula, the general second derivatives of the dot product of the **u** and **v** bond vectors (fig. 11.3) are needed. They can be expressed depending on the vector derivatives in eq. 11.64:

$$\frac{\partial^2(\mathbf{u}\cdot\mathbf{v})}{\partial x_{a,i}\partial x_{b,j}} =$$

$$\begin{pmatrix} \dfrac{\partial^2\mathbf{u}}{\partial x_i\partial x_j}\cdot\mathbf{v} & -\dfrac{\partial^2\mathbf{u}}{\partial x_i\partial x_j}\cdot\mathbf{v}-\dfrac{\partial\mathbf{u}}{\partial x_i}\cdot\dfrac{\partial\mathbf{v}}{\partial x_j} & \dfrac{\partial\mathbf{u}}{\partial x_i}\cdot\dfrac{\partial\mathbf{v}}{\partial x_j} \\[2ex] -\dfrac{\partial^2\mathbf{u}}{\partial x_i\partial x_j}\cdot\mathbf{v}-\dfrac{\partial\mathbf{u}}{\partial x_j}\cdot\dfrac{\partial\mathbf{v}}{\partial x_i} & \dfrac{\partial^2\mathbf{u}}{\partial x_i\partial x_j}\cdot\mathbf{v}+\dfrac{\partial\mathbf{u}}{\partial x_i}\cdot\dfrac{\partial\mathbf{v}}{\partial x_j} & \dfrac{\partial\mathbf{u}}{\partial x_j}\cdot\dfrac{\partial\mathbf{v}}{\partial x_i}+\mathbf{u}\cdot\dfrac{\partial^2\mathbf{v}}{\partial x_i\partial x_j} \\ & \dfrac{\partial\mathbf{u}}{\partial x_j}\cdot\dfrac{\partial\mathbf{v}}{\partial x_i}+\mathbf{u}\cdot\dfrac{\partial^2\mathbf{v}}{\partial x_i\partial x_j} & \\[2ex] \dfrac{\partial\mathbf{u}}{\partial x_j}\cdot\dfrac{\partial\mathbf{v}}{\partial x_i} & -\dfrac{\partial\mathbf{u}}{\partial x_j}\cdot\dfrac{\partial\mathbf{v}}{\partial x_i}-\mathbf{u}\cdot\dfrac{\partial^2\mathbf{v}}{\partial x_j\partial x_i} & \mathbf{u}\cdot\dfrac{\partial^2\mathbf{v}}{\partial x_i\partial x_j} \end{pmatrix}, \tag{11.66}$$

where the dimensions of this matrix a and b run over the involved atoms M, N and O.

Dihedral Angles

For the **dihedral angles** the strategy for the first derivatives (eq. 11.57) is continued: In order to prevent one single extremely large expression, all is expressed depending on the numerator and denominator of the original dihedral formula (eq. 11.49), these two are again denoted as θ and κ.

Introducing these variables, the whole second derivative expression for dihedrals is quite manageable:

$$\frac{\partial^2 q_d}{\partial x_{a,i}\partial x_{b,j}} = \left[\theta^3\frac{\partial\kappa}{\partial x_{b,j}}\frac{\partial\kappa}{\partial x_{a,i}} - \kappa\theta^3\frac{\partial^2\kappa}{\partial x_{a,i}\partial x_{b,j}} + \kappa^3\left(\frac{\partial\theta}{\partial x_{b,j}}\frac{\partial\kappa}{\partial x_{a,i}} + \frac{\partial\kappa}{\partial x_{b,j}}\frac{\partial\theta}{\partial x_{a,i}} +\right.\right.$$

$$\left.\theta\frac{\partial^2\kappa}{\partial x_{a,i}\partial x_{b,j}}\right) - \kappa^4\frac{\partial^2\theta}{\partial x_{a,i}\partial x_{b,j}} + \kappa^2\theta\left(-2\frac{\partial\kappa}{\partial x_{a,i}}\frac{\partial\kappa}{\partial x_{b,j}} - \frac{\partial\theta}{\partial x_{a,i}}\frac{\partial\theta}{\partial x_{b,j}} +\right. \tag{11.67}$$

$$\left.\left.\theta\frac{\partial^2\theta}{\partial x_{a,i}\partial x_{b,j}}\right]\left[\kappa^3(\kappa^2-\theta^2)\sqrt{1-\frac{\theta^2}{\kappa^2}}\right]^{-1}$$

This equation contains first as well as second derivatives of both θ and κ. The first derivative expressions were already deduced for the first dihedral derivatives (eqs. 11.58, 11.59) and can be reused in perfect analogy. However, the second derivatives of both the numerator and denominator are also needed. Since four atoms are involved in the dihedral, in total 16 different second derivatives are possible. Similar to the bond angle expressions, the effective number of matrix elements reduces to 11 due to symmetry. In the following, all unique second derivatives of θ and κ with respect to the four involved atoms are listed.

These expressions become quite lengthy, therefore a shorthand notation is introduced for the partial derivatives: $\partial_{x_i}\mathbf{u}$ means $\frac{\partial\mathbf{u}}{\partial x_i}$ and $\partial_{x_i x_j}\mathbf{u}$ means $\frac{\partial^2\mathbf{u}}{\partial x_i\partial x_j}$.

The diagonal elements of the second derivatives of θ are:

$$\frac{\partial^2\theta}{\partial x_{M,i}\partial x_{M,j}} = (\partial_{x_i x_j}\mathbf{u})\cdot(\mathbf{v}\times\mathbf{w}), \tag{11.68}$$

$$
\begin{aligned}
\frac{\partial^2 \theta}{\partial x_{N,i} \partial x_{N,j}} = &[(\partial_{x_i x_j}\mathbf{u} \times \mathbf{w}) + (\partial_{x_i}\mathbf{u} \times \partial_{x_j}\mathbf{w}) + (\partial_{x_j}\mathbf{u} \times \partial_{x_i}\mathbf{w}) + \\
&(\mathbf{u} \times \partial_{x_i x_j}\mathbf{w})] \cdot (\mathbf{v} \times \mathbf{w}) + (\partial_{x_i}\mathbf{u} \times \mathbf{w}) \cdot (\mathbf{v} \times \partial_{x_j}\mathbf{w}) + \\
&(\mathbf{u} \times \partial_{x_i}\mathbf{w}) \cdot (\mathbf{v} \times \partial_{x_j}\mathbf{w}) + (\partial_{x_j}\mathbf{u} \times \mathbf{w}) \cdot (\mathbf{v} \times \partial_{x_i}\mathbf{w}) + \\
&(\partial_{x_j}\mathbf{u} \times \mathbf{w}) \cdot (\mathbf{v} \times \partial_{x_i}\mathbf{w}) + (\mathbf{u} \times \mathbf{w}) \cdot (\mathbf{v} \times \partial_{x_i x_j}\mathbf{w})
\end{aligned}
\tag{11.69}
$$

$$
\begin{aligned}
\frac{\partial^2 \theta}{\partial x_{O,i} \partial x_{O,j}} = &[(\mathbf{v} \times \partial_{x_i x_j}\mathbf{w}) - (\partial_{x_j}\mathbf{v} \times \partial_{x_i}\mathbf{w}) - (\partial_{x_i}\mathbf{v} \times \partial_{x_j}\mathbf{w}) + \\
&(\partial_{x_i x_j}\mathbf{v} \times \mathbf{w})] \cdot (\mathbf{v} \times \mathbf{w}) + (\mathbf{u} \times \partial_{x_i x_j}\mathbf{w}) \cdot (\mathbf{v} \times \mathbf{w}) + \\
&(\mathbf{u} \times \partial_{x_i}\mathbf{w}) \cdot (\mathbf{v} \times \partial_{x_j}\mathbf{w}) + (\mathbf{u} \times \partial_{x_i}\mathbf{w}) \cdot (\partial_{x_j}\mathbf{v} \times \mathbf{w}) + \\
&(\mathbf{u} \times \partial_{x_j}\mathbf{w}) \cdot (\mathbf{v} \times \partial_{x_i}\mathbf{w}) - (\mathbf{u} \times \partial_{x_j}\mathbf{w}) \cdot (\partial_{x_i}\mathbf{v} \times \mathbf{w})
\end{aligned}
\tag{11.70}
$$

$$
\frac{\partial^2 \theta}{\partial x_{P,i} \partial x_{P,j}} = \cdot(\mathbf{v} \times \mathbf{w}) \cdot (\partial_{x_i x_j}\mathbf{v} \times \mathbf{w}).
\tag{11.71}
$$

The off-diagonal elements of the second derivatives of θ are:

$$
\begin{aligned}
\frac{\partial^2 \theta}{\partial x_{M,i} \partial x_{N,j}} = &-[(\partial_{x_i x_j}\mathbf{u} \times \mathbf{w}) + (\partial_{x_i}\mathbf{u} \times \partial_{x_j}\mathbf{w})] \cdot (\mathbf{v} \times \mathbf{w}) \\
&-(\partial_{x_i}\mathbf{u} \times \mathbf{w}) \cdot (\mathbf{v} \times \partial_{x_j}\mathbf{w})
\end{aligned}
\tag{11.72}
$$

$$
\begin{aligned}
\frac{\partial^2 \theta}{\partial x_{M,i} \partial x_{O,j}} = &(\partial_{x_i}\mathbf{u} \times \mathbf{w}) \cdot [(\mathbf{v} \times \partial_{x_j}\mathbf{w}) - (\partial_{x_j}\mathbf{v} \times \mathbf{w})] + \\
&(\partial_{x_j}\mathbf{u} \times \partial_{x_j}\mathbf{w}) \cdot (\mathbf{v} \times \mathbf{w})
\end{aligned}
\tag{11.73}
$$

$$
\frac{\partial^2 \theta}{\partial x_{M,i} \partial x_{P,j}} = (\partial_{x_i}\mathbf{u} \times \mathbf{w}) \cdot (\partial_{x_j}\mathbf{v} \times \mathbf{w}),
\tag{11.74}
$$

$$
\begin{aligned}
\frac{\partial^2 \theta}{\partial x_{N,i} \partial x_{O,j}} = &-[(\partial_{x_i}\mathbf{u} \times \partial_{x_j}\mathbf{w}) + (\mathbf{u} \times \partial_{x_i x_j}\mathbf{w})] \cdot (\mathbf{v} \times \mathbf{w}) - \\
&[(\partial_{x_j}\mathbf{v} \times \partial_{x_i}\mathbf{w}) - (\mathbf{v} \times \partial_{x_i x_j}\mathbf{w})] \cdot (\mathbf{u} \times \mathbf{w}) - \\
&(\partial_{x_i}\mathbf{u} \times \mathbf{w}) \cdot (\mathbf{v} \times \partial_{x_j}\mathbf{w}) + (\partial_{x_i}\mathbf{u} \times \mathbf{w}) \cdot (\partial_{x_j}\mathbf{v} \times \mathbf{w}) - \\
&(\mathbf{u} \times \partial_{x_i}\mathbf{w}) \cdot (\mathbf{v} \times \partial_{x_j}]\mathbf{w}) + (\mathbf{u} \times \partial_{x_i}\mathbf{w}) \cdot (\partial_{x_j}\mathbf{v} \times \mathbf{w}) - \\
&(\mathbf{u} \times \partial_{x_j}\mathbf{w}) \cdot (\mathbf{v} \times \partial_{x_i}\mathbf{w})
\end{aligned}
\tag{11.75}
$$

$$
\begin{aligned}
\frac{\partial^2 \theta}{\partial x_{N,i} \partial x_{P,j}} = &-[(\partial_{x_i}\mathbf{u} \times \mathbf{w}) + (\mathbf{v} \times \partial_{x_i}\mathbf{w})] \cdot (\partial_{x_j}\mathbf{v} \times \mathbf{w}) - \\
&(\mathbf{u} \times \mathbf{w}) \cdot (\partial_{x_i x_j}\mathbf{v} \times \mathbf{w})
\end{aligned}
\tag{11.76}
$$

$$
\begin{aligned}
\frac{\partial^2 \theta}{\partial x_{P,i} \partial x_{P,j}} = &-[(\partial_{x_j}\mathbf{v} \times \partial_{x_i}\mathbf{w}) - (\partial_{x_i x_j}\mathbf{v} \times \mathbf{w})] \cdot (\mathbf{u} \times \mathbf{w}) + \\
&(\mathbf{u} \times \partial_{x_i}\mathbf{w}) \cdot (\partial_{x_j}\mathbf{v} \times \mathbf{w})
\end{aligned}
\tag{11.77}
$$

The second derivatives of the denominator κ are even more complicated than for θ. Their diagonal elements are:

$$
\begin{aligned}
\frac{\partial^2 \kappa}{\partial x_{M,i} \partial x_{M,j}} = {} & (\partial_{x_i x_k} \mathbf{u} \cdot \mathbf{w})(\mathbf{v} \cdot \mathbf{w}) + (\partial_{x_i} \mathbf{u} \cdot \mathbf{w})(\partial_{x_j} \mathbf{u} \cdot \mathbf{w}) \frac{\sin(\phi_v)}{\sin(\phi_u)} - \\
& (\partial_{x_i} \mathbf{u} \cdot \mathbf{w})(\partial_{x_j} \mathbf{u} \cdot \mathbf{w})(\mathbf{v} \cdot \mathbf{w})^2 \frac{\sin(\phi_v)}{\sin^3(\phi_u)}
\end{aligned}
\tag{11.78}
$$

$$
\begin{aligned}
\frac{\partial^2 \kappa}{\partial x_{N,i} \partial x_{N,j}} = {} & -\Big[(\mathbf{u} \cdot \mathbf{w}) \big([(\partial_{x_i x_j} \mathbf{u} \cdot \mathbf{w}) + (\partial_{x_i} \mathbf{u} \cdot \partial_{x_j} \mathbf{w}) + (\partial_{x_j} \mathbf{u} \cdot \partial_{x_i} \mathbf{w}) + \\
& (\mathbf{u} \cdot \partial_{x_i x_j} \mathbf{w})] + [(\partial_{x_i} \mathbf{u} \cdot \mathbf{w}) + (\mathbf{u} \cdot \partial_{x_i} \mathbf{w})][(\mathbf{u} \cdot \partial_{x_j} \mathbf{w}) + \\
& (\partial_{x_j} \mathbf{u} \cdot \mathbf{w})] \big) \frac{1}{\sin(\phi_u)} - [(\partial_{x_j} \mathbf{u} \cdot \mathbf{w}) + (\mathbf{u} \cdot \partial_{x_j} \mathbf{w})] \\
& [(\partial_{x_i} \mathbf{u} \cdot \mathbf{w}) + (\mathbf{u} \cdot \partial_{x_i} \mathbf{w})](\mathbf{u} \cdot \mathbf{w})^2 \frac{1}{\sin^3(\phi_u)} \Big] \sin(\phi_v) + \\
& \Big[[-(\mathbf{v} \cdot \partial_{x_i x_j} \mathbf{w})(\mathbf{v} \cdot \mathbf{w}) + (\mathbf{v} \cdot \partial_{x_i} \mathbf{w})(\mathbf{v} \cdot \partial_{x_j} \mathbf{w})] \frac{1}{\sin(\phi_v)} - \\
& (\mathbf{v} \cdot \partial_{x_i} \mathbf{w})(\mathbf{v} \cdot \partial_{x_j} \mathbf{w})(\mathbf{v} \cdot \mathbf{w})^2 \frac{1}{\sin^3(\phi_v)} \Big] \sin(\phi_u) + \\
& \Big[[(\partial_{x_i} \mathbf{u} \cdot \mathbf{w}) + (\mathbf{u} \cdot \partial_{x_i})](\mathbf{v} \cdot \partial_{x_j} \mathbf{w}) + [(\partial_{x_j} \mathbf{u} \cdot \mathbf{w}) + \\
& (\mathbf{u} \cdot \partial_{x_j} \mathbf{w})](\mathbf{v} \cdot \partial_{x_i} \mathbf{w}) \Big](\mathbf{u} \cdot \mathbf{w})(\mathbf{v} \cdot \mathbf{w}) \frac{1}{\sin(\phi_u) \sin(\phi_v)}
\end{aligned}
\tag{11.79}
$$

$$
\begin{aligned}
\frac{\partial^2 \kappa}{\partial x_{O,i} \partial x_{O,j}} = {} & -\Big[(\mathbf{v} \cdot \mathbf{w}) \big([(\partial_{x_i x_j} \mathbf{v} \cdot \mathbf{w}) - (\partial_{x_i} \mathbf{v} \cdot \partial_{x_j} \mathbf{w}) - (\partial_{x_j} \mathbf{v} \cdot \partial_{x_i} \mathbf{w}) + \\
& (\mathbf{v} \cdot \partial_{x_i x_j} \mathbf{w})] + [-(\partial_{x_i} \mathbf{v} \cdot \mathbf{w}) + (\mathbf{v} \cdot \partial_{x_i} \mathbf{w})][(\mathbf{v} \cdot \partial_{x_j} \mathbf{w}) - \\
& (\partial_{x_j} \mathbf{v} \cdot \mathbf{w})] \big) \frac{1}{\sin(\phi_v)} - [-(\partial_{x_j} \mathbf{v} \cdot \mathbf{w}) + (\mathbf{v} \cdot \partial_{x_j} \mathbf{w})] \\
& [-(\partial_{x_i} \mathbf{v} \cdot \mathbf{w}) + (\mathbf{v} \cdot \partial_{x_i} \mathbf{w})](\mathbf{v} \cdot \mathbf{w})^2 \frac{1}{\sin^3(\phi_v)} \Big] \sin(\phi_u) + \\
& \Big[[-(\mathbf{u} \cdot \partial_{x_i x_j} \mathbf{w})(\mathbf{u} \cdot \mathbf{w}) + (\mathbf{u} \cdot \partial_{x_i} \mathbf{w})(\mathbf{u} \cdot \partial_{x_j} \mathbf{w})] \frac{1}{\sin(\phi_u)} - \\
& (\mathbf{u} \cdot \partial_{x_i} \mathbf{w})(\mathbf{u} \cdot \partial_{x_j} \mathbf{w})(\mathbf{u} \cdot \mathbf{w})^2 \frac{1}{\sin^3(\phi_u)} \Big] \sin(\phi_v) + \\
& \Big[[-(\partial_{x_i} \mathbf{v} \cdot \mathbf{w}) + (\mathbf{v} \cdot \partial_{x_i})](\mathbf{u} \cdot \partial_{x_j} \mathbf{w}) + [-(\partial_{x_j} \mathbf{v} \cdot \mathbf{w}) + \\
& (\mathbf{v} \cdot \partial_{x_j} \mathbf{w})](\mathbf{u} \cdot \partial_{x_i} \mathbf{w}) \Big](\mathbf{v} \cdot \mathbf{w})(\mathbf{u} \cdot \mathbf{w}) \frac{1}{\sin(\phi_u) \sin(\phi_u)}
\end{aligned}
\tag{11.80}
$$

$$
\begin{aligned}
\frac{\partial^2 \kappa}{\partial x_{P,i} \partial x_{P,j}} = {} & (\partial_{x_i x_k} \mathbf{v} \cdot \mathbf{w})(\mathbf{u} \cdot \mathbf{w}) + (\partial_{x_i} \mathbf{v} \cdot \mathbf{w})(\partial_{x_j} \mathbf{v} \cdot \mathbf{w}) \frac{\sin(\phi_u)}{\sin(\phi_v)} - \\
& (\partial_{x_i} \mathbf{v} \cdot \mathbf{w})(\partial_{x_j} \mathbf{v} \cdot \mathbf{w})(\mathbf{u} \cdot \mathbf{w})^2 \frac{\sin(\phi_u)}{\sin^3(\phi_v)}
\end{aligned}
\tag{11.81}
$$

It can be seen that the second derivatives of κ are, similar to its first derivatives, somewhat symmetric with respect to the atoms, i.e., the second derivatives with respect to O can be obtained

from the ones respective to N by swapping all $\mathbf{u}$ and $\mathbf{v}$, additional a minus sign needs to be introduced for each derivative of $\mathbf{v}$ with respect to O. The derivatives with respect to M and P can be also interchanged by swapping of $\mathbf{u}$ and $\mathbf{v}$, here without any change of prefactors.

The off-diagonal elements of the denominator derivatives are:

$$
\frac{\partial^2 \kappa}{\partial x_{M,i} \partial x_{N,j}} = \Big[(\mathbf{u} \cdot \mathbf{w})[(\partial_{x_i x_j} \mathbf{u} \cdot \mathbf{w}) + (\partial_{x_i} \mathbf{u} \cdot \partial_{x_j} \mathbf{w})] + (\partial_{x_i} \mathbf{u} \cdot \mathbf{w})
$$
$$
[(\partial_{x_j} \mathbf{u} \cdot \mathbf{w}) + (\mathbf{u} + \partial_{x_j} \mathbf{w})] \Big] \frac{\sin(\phi_v)}{\sin(\phi_u)} + (\mathbf{u} \cdot \mathbf{w})^2 (\partial_{x_i} \mathbf{u} \cdot \mathbf{w}), \tag{11.82}
$$
$$
[(\partial_{x_j} \mathbf{u} \cdot \mathbf{w}) + (\mathbf{u} \cdot \partial_{x_j} \mathbf{w})] \frac{\sin(\phi_v)}{\sin^3(\phi_u)} - (\mathbf{v} \cdot \partial_{x_j} \mathbf{w})(\mathbf{v} \cdot \mathbf{w}) \frac{1}{\sin(\phi_u) \sin(\phi_v)}
$$

$$
\frac{\partial^2 \kappa}{\partial x_{M,i} \partial x_{O,j}} = -[(\partial_{x_i} \mathbf{u} \cdot \partial_{x_j} \mathbf{w})(\mathbf{u} \cdot \mathbf{w}) + (\partial_{x_i} \mathbf{u} \cdot \mathbf{w})(\mathbf{u} \cdot \partial_{x_j} \mathbf{w})]
$$
$$
\frac{\sin(\phi_v)}{\sin(\phi_u)} - (\partial_{x_i} \mathbf{u} \cdot \mathbf{w})(\mathbf{u} \cdot \partial_{x_j} \mathbf{w})(\mathbf{u} \cdot \mathbf{w})^2 \frac{\sin(\phi_v)}{\sin^3(\phi_u)} +, \tag{11.83}
$$
$$
[(\partial_{x_j} \mathbf{v} \cdot \mathbf{w}) - (\mathbf{v} \cdot \partial_{x_j} \mathbf{w})](\mathbf{v} \cdot \mathbf{w}) \frac{1}{\sin(\phi_u) \sin(\phi_v)}
$$

$$
\frac{\partial^2 \kappa}{\partial x_{M,i} \partial x_{P,j}} = (\partial_{x_i} \mathbf{u} \cdot \mathbf{w})(\partial_{x_j} \mathbf{v} \cdot \mathbf{w})(\mathbf{u} \cdot \mathbf{w})(\mathbf{v} \cdot \mathbf{w}) \frac{1}{\sin(\phi_u) \sin(\phi_v)}, \tag{11.84}
$$

$$
\frac{\partial^2 \kappa}{\partial x_{N,i} \partial x_{O,j}} = \Big[(\mathbf{u} \cdot \mathbf{w})[(\partial_{x_i} \mathbf{u} \cdot \partial_{x_j} \mathbf{w}) + (\mathbf{u} \cdot \partial_{x_i x_j} \mathbf{w}) + (\mathbf{u} \cdot \partial_{x_j} \mathbf{w})
$$
$$
(\partial_{x_i} \mathbf{u} \cdot \mathbf{w}) + (\mathbf{u} \cdot \partial_{x_i} \mathbf{w})] \frac{1}{\sin(\phi_u)} + [(\partial_{x_i} \mathbf{u} \cdot \mathbf{w}) + \mathbf{u} \cdot \partial_{x_i} \mathbf{w})]
$$
$$
(\mathbf{u} \cdot \partial_{x_j} \mathbf{w})(\mathbf{u} \cdot \mathbf{w})^2 \Big] \frac{\sin(\phi_v)}{\sin^3(\phi_u)} + \Big[(\mathbf{v} \cdot \mathbf{w})[-(\partial_{x_i} \mathbf{v} \cdot \partial_{x_j} \mathbf{w}) +
$$
$$
(\mathbf{v} \cdot \partial_{x_i x_j} \mathbf{w}) - (\mathbf{v} \cdot \partial_{x_j} \mathbf{w})(\partial_{x_i} \mathbf{v} \cdot \mathbf{w}) + (\mathbf{v} \cdot \partial_{x_i} \mathbf{w})] \frac{1}{\sin(\phi_v)} -, \tag{11.85}
$$
$$
[(\partial_{x_i} \mathbf{v} \cdot \mathbf{w}) + \mathbf{v} \cdot \partial_{x_i} \mathbf{w})](\mathbf{v} \cdot \partial_{x_j} \mathbf{w})(\mathbf{v} \cdot \mathbf{w})^2 \Big] \frac{\sin(\phi_u)}{\sin^3(\phi_v)} +
$$
$$
\Big[(\mathbf{u} \cdot \partial_{x_j} \mathbf{w})(\mathbf{v} \cdot \partial_{x_i} \mathbf{w}) + [-(\partial_{x_j} \mathbf{v} \cdot \mathbf{w}) + (\mathbf{v} \cdot \partial_{x_j} \mathbf{w})]
$$
$$
[-(\partial_{x_i} \mathbf{u} \cdot \mathbf{w}) + (\mathbf{u} \cdot \partial_{x_i} \mathbf{w})] \Big] (\mathbf{u} \cdot \mathbf{w})(\mathbf{v} \cdot \mathbf{w}) \frac{1}{\sin(\phi_u) \sin(\phi_v)}
$$

$$
\frac{\partial^2 \kappa}{\partial x_{N,i} \partial x_{P,j}} = [(\partial_{x_j} \mathbf{v} \cdot \partial_{x_i} \mathbf{w})(\mathbf{v} \cdot \mathbf{w}) + (\partial_{x_j} \mathbf{v} \cdot \mathbf{w})(\mathbf{v} \cdot \partial_{x_i} \mathbf{w})]
$$
$$
\frac{\sin(\phi_u)}{\sin(\phi_v)} + (\partial_{x_j} \mathbf{v} \cdot \mathbf{w})(\mathbf{v} \cdot \partial_{x_i} \mathbf{w})(\mathbf{v} \cdot \mathbf{w})^2 \frac{\sin(\phi_u)}{\sin^3(\phi_v)} -, \tag{11.86}
$$
$$
[(\partial_{x_i} \mathbf{u} \cdot \mathbf{w}) - (\mathbf{u} \cdot \partial_{x_i} \mathbf{w})](\mathbf{u} \cdot \mathbf{w}) \frac{1}{\sin(\phi_v) \sin(\phi_u)}
$$

$$\frac{\partial^2 \kappa}{\partial x_{N,i} \partial x_{P,j}} = -\Big[(\mathbf{v} \cdot \mathbf{w})[-(\partial_{x_i x_j}\mathbf{v} \cdot \mathbf{w}) + (\partial_{x_j}\mathbf{v} \cdot \partial_{x_i}\mathbf{w})] + (\partial_{x_j}\mathbf{v} \cdot \mathbf{w})$$

$$[-(\partial_{x_i}\mathbf{v} \cdot \mathbf{w}) + (\mathbf{v} + \partial_{x_i}\mathbf{w})]\Big]\frac{\sin(\phi_u)}{\sin(\phi_v)} - (\mathbf{v} \cdot \mathbf{w})^2(\partial_{x_j}\mathbf{v} \cdot \mathbf{w}). \tag{11.87}$$

$$[-(\partial_{x_i}\mathbf{v} \cdot \mathbf{w}) + (\mathbf{v} \cdot \partial_{x_i}\mathbf{w})]\frac{\sin(\phi_u)}{\sin^3(\phi_v)} - (\mathbf{u} \cdot \partial_{x_i}\mathbf{w})(\mathbf{u} \cdot \mathbf{w})\frac{1}{\sin(\phi_v)\sin(\phi_u)}$$

Out-of-Plane Angles

The Wilson matrix derivatives of the **out-of-plane angles** are surprisingly simple, mainly due to the inherent symmetry of the coordinate definition (derivatives to P are essential the sum of the derivatives to M, N and O). Similar to the Wilson matrix element expression in eq. 11.60, the Wilson derivatives expression can also be split up in four cases:

$$\frac{\partial^2 q_o}{\partial x_{a,i} \partial x_{b,j}} = \begin{cases} \dfrac{1}{\rho^2}\left(v\dfrac{\partial^2 \rho}{\partial x_{a,i}\partial x_{b,j}} + \dfrac{\partial \rho}{\partial x_{a,i}}\dfrac{\partial v}{\partial x_{b,j}} + \right. & \begin{array}{l} a = M, N, O\,, \\ b = M, N, O \end{array} \\ \left. \dfrac{\partial v}{\partial x_{a,i}}\dfrac{\partial \rho}{\partial x_{b,j}} + \rho\dfrac{\partial^2 v}{\partial x_{a,i}\partial x_{b,j}}\right) & \\ -\left(\dfrac{\partial^2 q_o}{\partial x_{M,i}\partial x_{b,j}} + \dfrac{\partial^2 q_o}{\partial x_{N,i}\partial x_{b,j}}\dfrac{\partial^2 q_o}{\partial x_{O,i}\partial x_{b,j}}\right) & \begin{array}{l} a = P\,, \\ b = M, N, O \end{array} \\ -\left(\dfrac{\partial^2 q_o}{\partial x_{a,i}\partial x_{M,j}} + \dfrac{\partial^2 q_o}{\partial x_{a,i}\partial x_{N,j}}\dfrac{\partial^2 q_o}{\partial x_{a,i}\partial x_{O,j}}\right) & \begin{array}{l} a = M, N, O\,, \\ b = P \end{array} \\ -\left(\dfrac{\partial^2 q_o}{\partial x_{M,i}\partial x_{P,j}} + \dfrac{\partial^2 q_o}{\partial x_{N,i}\partial x_{P,j}}\dfrac{\partial^2 q_o}{\partial x_{O,i}\partial x_{P,j}}\right) & a = P, b = P \end{cases} \tag{11.88}$$

The first derivatives appearing in eq. 11.88 are already listed in the Wilson matrix elements part (eqs. 11.61, 11.62). The second derivatives of the triple product v are quite obvious and trivial:

$$\frac{\partial^2 v}{\partial x_{a,i} \partial x_{b,j}} = \begin{cases} \partial_{x_i x_j}\mathbf{u} \cdot (\mathbf{v} \times \mathbf{w}) & a = M, b = M \\ \mathbf{u} \cdot (\partial_{x_i x_j}\mathbf{v} \times \mathbf{w}) & a = N, b = N \\ \mathbf{u} \cdot (\mathbf{v} \times \partial_{x_i x_j}\mathbf{w}) & a = O, b = O \\ \partial_{x_i}\mathbf{u} \cdot (\partial_{x_j}\mathbf{v} \times \mathbf{w}) & a = M, b = N \\ \partial_{x_i}\mathbf{u} \cdot (\mathbf{v} \times \partial_{x_j}\mathbf{w}) & a = M, b = O \\ \mathbf{u} \cdot (\partial_{x_i}\mathbf{v} \times \partial_{x_j}\mathbf{w}) & a = N, b = O \end{cases} \tag{11.89}$$

As in the case of bonds and dihedrals, Schwarz's theorem is fulfilled, i.e., all second derivatives are symmetric with respect to the order of taking partial derivatives. Due to the symmetry of the overall out-of-plane derivative, no derivative with respect to P needs to be specified here. The second derivatives of the normalization factor ρ are listed separately. First, the diagonal elements:

$$\frac{\partial^2 \rho}{\partial x_{M,i} \partial x_{M,j}} = -\frac{3}{\rho}\frac{\partial \rho}{\partial x_{M,i}}\frac{\partial \rho}{\partial x_{M,j}} - \frac{1}{\rho}\Big(\partial_{x_i x_j}\mathbf{u} \cdot [(\mathbf{w}(-\cos(\phi_2) - 1 + \cos(\phi_1) +$$

$$\cos(\phi_3)) + \mathbf{v}(-\cos(\phi_3) - 1 + \cos(\phi_1) + \cos(\phi_2))] +' \tag{11.90}$$

$$(\partial_{x_i}\mathbf{u} \cdot \mathbf{w} - \partial_{x_i}\mathbf{u} \cdot \mathbf{v})(-\partial_{x_j}\mathbf{u} \cdot \mathbf{w} + \partial_{x_j}\mathbf{u} \cdot \mathbf{v})\Big)$$

$$\frac{\partial^2 \rho}{\partial x_{N,i}\partial x_{N,j}} = -\frac{3}{\rho}\frac{\partial \rho}{\partial x_{N,i}}\frac{\partial \rho}{\partial x_{N,j}} - \frac{1}{\rho}\Big(\partial_{x_i x_j}\mathbf{v}\cdot[(\mathbf{w}(-\cos(\phi_1)-1+\cos(\phi_2)+$$
$$\cos(\phi_3)) + \mathbf{u}(-\cos(\phi_3)-1+\cos(\phi_1)+\cos(\phi_2))]+'$$
$$(\partial_{x_i}\mathbf{v}\cdot\mathbf{w}-\partial_{x_i}\mathbf{v}\cdot\mathbf{u})(-\partial_{x_j}\mathbf{v}\cdot\mathbf{w}+\partial_{x_j}\mathbf{v}\cdot\mathbf{u})\Big) \tag{11.91}$$

$$\frac{\partial^2 \rho}{\partial x_{O,i}\partial x_{O,j}} = -\frac{3}{\rho}\frac{\partial \rho}{\partial x_{O,i}}\frac{\partial \rho}{\partial x_{O,j}} - \frac{1}{\rho}\Big(\partial_{x_i x_j}\mathbf{w}\cdot[(\mathbf{v}(-\cos(\phi_1)-1+\cos(\phi_2)+$$
$$\cos(\phi_3)) + \mathbf{u}(-\cos(\phi_3)-1+\cos(\phi_1)+\cos(\phi_2))]+\cdot$$
$$(\partial_{x_i}\mathbf{w}\cdot\mathbf{v}-\partial_{x_i}\mathbf{w}\cdot\mathbf{u})(-\partial_{x_j}\mathbf{w}\cdot\mathbf{v}+\partial_{x_j}\mathbf{w}\cdot\mathbf{u})\Big) \tag{11.92}$$

The off-diagonal elements are:

$$\frac{\partial^2 \rho}{\partial x_{M,i}\partial x_{N,j}} = -\frac{3}{\rho}\frac{\partial \rho}{\partial x_{M,i}}\frac{\partial \rho}{\partial x_{N,j}} - \frac{1}{\rho}\Big(\partial_{x_i}\mathbf{u}\cdot\partial_{x_j}\mathbf{v}(-\cos(\phi_3)-1+\cos(\phi_1)+$$
$$\cos(\phi_2)) + \partial_{x_i}\mathbf{u}\cdot\mathbf{w}(\partial_{x_j}\mathbf{v}\cdot\mathbf{w}+\mathbf{u}\cdot\partial_{x_j}\mathbf{v})+'$$
$$\partial_{x_i}\mathbf{u}\cdot\mathbf{v}(-\mathbf{u}\cdot\partial_{x_j}\mathbf{v}+\partial_{x_j}\mathbf{v}\cdot\mathbf{w})\Big) \tag{11.93}$$

$$\frac{\partial^2 \rho}{\partial x_{M,i}\partial x_{O,j}} = -\frac{3}{\rho}\frac{\partial \rho}{\partial x_{M,i}}\frac{\partial \rho}{\partial x_{O,j}} - \frac{1}{\rho}\Big(\partial_{x_i}\mathbf{u}\cdot\partial_{x_j}\mathbf{w}(-\cos(\phi_2)-1+\cos(\phi_1)+$$
$$\cos(\phi_3)) + \partial_{x_i}\mathbf{u}\cdot\mathbf{w}(-\mathbf{u}\cdot\partial_{x_j}\mathbf{w}+\mathbf{v}\cdot\partial_{x_j}\mathbf{w})+'$$
$$\partial_{x_i}\mathbf{u}\cdot\mathbf{v}(\mathbf{u}\cdot\partial_{x_j}\mathbf{w}+\mathbf{v}\cdot\partial_{x_j}\mathbf{w})\Big) \tag{11.94}$$

$$\frac{\partial^2 \rho}{\partial x_{N,i}\partial x_{O,j}} = -\frac{3}{\rho}\frac{\partial \rho}{\partial x_{N,i}}\frac{\partial \rho}{\partial x_{O,j}} - \frac{1}{\rho}\Big(\partial_{x_i}\mathbf{v}\cdot\partial_{x_j}\mathbf{w}(-\cos(\phi_1)-1+\cos(\phi_2)+$$
$$\cos(\phi_3)) + \partial_{x_i}\mathbf{v}\cdot\mathbf{w}(-\mathbf{v}\cdot\partial_{x_j}\mathbf{w}+\mathbf{u}\cdot\partial_{x_j}\mathbf{w})+\cdot$$
$$\partial_{x_i}\mathbf{v}\cdot\mathbf{u}(\mathbf{v}\cdot\partial_{x_j}\mathbf{w}+\mathbf{u}\cdot\partial_{x_j}\mathbf{w})\Big) \tag{11.95}$$

11.4 DG-EVB Details

In chapter 2, the DG-EVB method is explained in a quite comprehensive matter, especially concerning the structure of the system of linear equations (eq. 2.158) which is presented in fig. 2.14. However, the actual mathematical details needed for filling both vector $\mathbf{f}$ and matrix $\mathbf{D}$ are still not shown. Since the implementation of this details was quite tedious I have decided to present them in this section, such that it is possible to reimplement DG-EVB based on the equations and cases listed below.

11.4.1 The f-Vector

Here, the actual coupling strengths at the different chosen DG-EVB-reference points and, depending on the used DG-EVB coupling mode, also its first and second derivatives are listed. Since both

DG-EVB and TREQ need coupling gradients and Hessians, the same equations are given in the TREQ publication in chapter 5 (but not with respect to vector entries).

The first M entries of the $\mathbf{f}$ vector can be calculated from the reference- and QMDFF-energies of the M different DG-EVB points:

$$f_i = [F_1(\mathbf{q}_i) - V(\mathbf{q}_i)][F_2(\mathbf{q}_i) - V(\mathbf{q}_i)], \tag{11.96}$$

where $\mathbf{q}_i$ is the structure of the respective i'th DG-EVB reference point.

If DG-EVB mode 1 is used, this would be the full $\mathbf{f}$-vector, for mode 2 and 3, the next MN entries consists of the coupling *gradients* on all M points, with N entries each, where N is the number of internal coordinates[4]:

$$f_{M+i(N-1)+j} = \left[\frac{\partial F_1(\mathbf{q}_i)}{\partial q_j} - \frac{\partial V(\mathbf{q}_i)}{\partial q_j}\right][F_2(\mathbf{q}_i) - V(\mathbf{q}_i)] +$$
$$[F_1(\mathbf{q}_i) - V(\mathbf{q}_i)]\left[\frac{\partial F_2(\mathbf{q}_i)}{\partial q_j} - \frac{\partial V(\mathbf{q}_i)}{\partial q_j}\right]. \tag{11.97}$$

For DG-EVB mode 3, the *second derivatives* of the coupling are filled into the bottom of the $\mathbf{f}$ vector according to eq. 11.98. Due to the symmetry of the Hessians, only the lower block diagonal elements of them are stored into $\mathbf{f}$.

$$f_{M(1+N)+i\left(\frac{N(N+1)}{2}\right)+j\left(N-\frac{i-1}{2}\right)+k} = \left[\frac{\partial^2 F_1(\mathbf{q})}{\partial q_j \partial q_k} - \frac{\partial^2 V(\mathbf{q})}{\partial q_j \partial q_k}\right][F_2(\mathbf{q}) - V(\mathbf{q})] +$$
$$[F_1(\mathbf{q}) - V(\mathbf{q})]\left[\frac{\partial^2 F_2(\mathbf{q})}{\partial q_j \partial q_k} - \frac{\partial^2 V(\mathbf{q})}{\partial q_j \partial q_k}\right] +$$
$$\left[\frac{\partial F_1(\mathbf{q})}{\partial q_j} - \frac{\partial V(\mathbf{q})}{\partial q_j}\right]\left[\frac{\partial F_2(\mathbf{q})}{\partial q_k} - \frac{\partial V(\mathbf{q})}{\partial q_k}\right] +$$
$$\left[\frac{\partial F_1(\mathbf{q})}{\partial q_k} - \frac{\partial V(\mathbf{q})}{\partial q_k}\right]\left[\frac{\partial F_2(\mathbf{q})}{\partial q_j} - \frac{\partial V(\mathbf{q})}{\partial q_j}\right]. \tag{11.98}$$

11.4.2 The D-Matrix

As explained in the main text, the $\mathbf{D}$-matrix is composed basically of three parts: distributed Gaussian basis functions (also termed in analogy to quantum chemistry as s-, p- and d-functions) as well as its first and second derivatives with respect to the chosen set of internal coordinates.

In order to prevent redundancies, the full set of equations for DG-EVB mode 3 is listed. For mode 2, only s- and p-functions up to first derivatives are needed and for mode 1, only s-function values are needed.

The structure of the matrix is shown schematically in fig. 11.4, which is identical to fig. 2.14 in the main text, except the detailed listing of run indices. During the listing of the single terms, their position in this example matrix of two DG-EVB points and two internal coordinate is explained.

All values of basis functions and their derivatives are calculated depending solely on the M different positions of the DG-EVB points and their respective basis functions. Therefore, $\Delta\mathbf{q}_{KL} = |\mathbf{q}_K - \mathbf{q}_L|$ means the distance between basis function at DG-EVB point K and another basis function at DG-EVB point L. The surface in between these basis functions is not considered

---

4 It should be noted in order to avoid confusion that the expressions for first and second coupling derivatives given in one of the original DG-EVB papers [122] (eqs. 18 and 19 there) are incorrect.
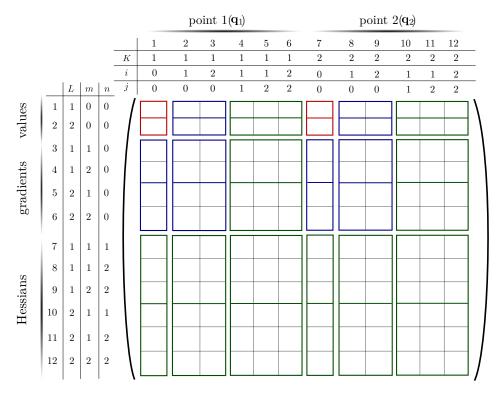
Figure 11.4: Detailed structure of the **D**-matrix in analogy to fig. 2.14 in the theory section. Shown are the entries for the different modes (1=red, 2=blue, 3=green), dependent of the up to six run-indices used also in the formulas presented below (eqs. 11.99 to 11.107).

explicitly in the parametrization, only indirectly by means of gradients and Hessians and the convergence radii of their respective imaginary Taylor series determined by the α_K-values. For all functions and derivatives, the exponential factors are identical, they will therefore be written in short form: $\mathrm{expo}(\mathbf{q}_{KL}) = \exp\left[\frac{1}{2}\alpha_K|\Delta\mathbf{q}_{KL}|^2\right]$.

Below all possible entries of the **D**-matrix are listed, depending on up to six indices: K and L describing the location of the DG-EVB points, m and n indicating the first and second partial derivatives as well as i and j the angular momentum numbers of the Gaussian basis functions. In comparison to fig. 11.4, all elements of the example matrix can be calculated by reading the needed indices and inserting them into the suited equations.

First, the expressions for the basis functions are shown:

$$g(\mathbf{q}_L, \mathbf{q}_K, 0, 0, \alpha_K) = \left[1 + \frac{1}{2}\alpha_K|\Delta\mathbf{q}_K|^2\right]\mathrm{expo}(\mathbf{q}_{KL}), \tag{11.99}$$

$$g(\mathbf{q}_L, \mathbf{q}_K, i, 0, \alpha_K) = (\Delta\mathbf{q}_K)_i\mathrm{expo}(\mathbf{q}_{KL}), \tag{11.100}$$

$$g(\mathbf{q}_L, \mathbf{q}_K, i, j, \alpha_K) = \left(1 - \frac{1}{2}\delta_{ij}\right)(\Delta\mathbf{q}_{KL})_i(\Delta\mathbf{q}_{KL})_j\mathrm{expo}(\mathbf{q}_{KL}). \tag{11.101}$$

In the actual code, first and second derivatives are implemented via many conditional branches. Here, these conditions were put together with Kronecker deltas ($\delta_{ij} = 1(i = j), 0(else)$), such that closed expressions could be obtained that might become quite lengthy, especially in the case of second derivatives:

$$\frac{\partial g(\mathbf{q}_L, \mathbf{q}_K, 0, 0, \alpha_K)}{\partial q_m} = -\frac{1}{2}\alpha_K^2|\Delta\mathbf{q}_{KL}|^2(\Delta\mathbf{q}_{KL})_m\mathrm{expo}(\mathbf{q}_{KL}), \tag{11.102}$$

$$\frac{\partial g(\mathbf{q}_L, \mathbf{q}_K, i, 0, \alpha_K)}{\partial q_m} = -\left[\alpha_K(\Delta\mathbf{q}_{KL})_i(\Delta\mathbf{q}_{KL})_m - \delta_{mi}\right]\text{expo}(\mathbf{q}_{KL}), \tag{11.103}$$

$$\frac{\partial g(\mathbf{q}_L, \mathbf{q}_K, i, j, \alpha_K)}{\partial q_m} = -\left(1 - \frac{1}{2}\delta_{ij}\right)\Big[\alpha_K(\Delta\mathbf{q}_{KL})_i(\Delta\mathbf{q}_{KL})_j(\Delta\mathbf{q}_{KL})_m -$$
$$\delta_{mi}(\Delta\mathbf{q}_{KL})_i - \delta_{mj}(\Delta\mathbf{q}_{KL})_j\Big]\text{expo}(\mathbf{q}_{KL}). \tag{11.104}$$

The second derivatives depend on up to six indices:

$$\frac{\partial^2 g(\mathbf{q}_L, \mathbf{q}_K, 0, 0, \alpha_K)}{\partial q_m \partial q_n} = -\frac{1}{2}\alpha_K^2\Big(\alpha_K|\Delta\mathbf{q}_{KL}|^2(\Delta\mathbf{q}_{KL})_m(\Delta\mathbf{q}_{KL})_n - 3\delta_{mn}|\Delta\mathbf{q}_{KL}|^2 -$$
$$2(1 - \delta_{mn})(\Delta\mathbf{q}_{KL})_m(\Delta\mathbf{q}_{KL})_n\Big)\text{expo}(\mathbf{q}_{KL}) \tag{11.105}$$

$$\frac{\partial^2 g(\mathbf{q}_L, \mathbf{q}_K, i, 0, \alpha_K)}{\partial q_m \partial q_n} = \alpha_K\Big[\alpha_K(\Delta\mathbf{q}_{KL})_i(\Delta\mathbf{q}_{KL})_m(\Delta\mathbf{q}_{KL})_n - \delta_{mn}(1 + 2\delta_{mi})(\Delta\mathbf{q}_{KL})_i -$$
$$(1 - \delta_{mn})(\delta_{ni}(\Delta\mathbf{q}_{KL})_n + \delta_{mi}(\Delta\mathbf{q}_{KL})_m)\Big]\text{expo}(\mathbf{q}_{KL}) \tag{11.106}$$

$$\frac{\partial^2 g(\mathbf{q}_L, \mathbf{q}_K, i, j, \alpha_K)}{\partial q_m \partial q_n} = \left(1 - \frac{1}{2}\delta_{ij}\right)\Bigg[\alpha_K^2(\Delta\mathbf{q}_{KL})_i(\Delta\mathbf{q}_{KL})_j(\Delta\mathbf{q}_{KL})_m(\Delta\mathbf{q}_{KL})_n -$$
$$\delta_{mn}\delta_{mi}\alpha_K(\Delta\mathbf{q}_{KL})_i(\Delta\mathbf{q}_{KL})_j - \delta_{ij}\Big\{2\alpha_K(1 - \delta_{mn})(\Delta\mathbf{q}_{KL})_i(\delta_{mi}(\Delta\mathbf{q}_{KL})_n +$$
$$\delta_{ni}(\Delta\mathbf{q}_{KL})_m) + \delta_{mn}(5\alpha_K(\Delta\mathbf{q}_{KL})_i(\Delta\mathbf{q}_{KL})_j - 2)\Big\} - (1 - \delta_{ij})$$
$$\Big\{\alpha_K(1 - \delta_{ni})(1 - \delta_{nj})[\delta_{mi}(\Delta\mathbf{q}_{KL})_j(\Delta\mathbf{q}_{KL})_n + \delta_{mj}(\Delta\mathbf{q}_{KL})_i(\Delta\mathbf{q}_{KL})_m] +$$
$$\alpha_K(1 - \delta_{mi})(1 - \delta_{mj})[\delta_{ni}(\Delta\mathbf{q}_{KL})_j(\Delta\mathbf{q}_{KL})_m + \delta_{nj}(\Delta\mathbf{q}_{KL})_i(\Delta\mathbf{q}_{KL})_n] +$$
$$\delta_{mi}\delta_{nj}(\alpha_K(\Delta\mathbf{q}_{KL})_i(\Delta\mathbf{q}_{KL})_m + \alpha_K(\Delta\mathbf{q}_{KL})_j(\Delta\mathbf{q}_{KL})_n - 1) +$$
$$\delta_{ni}\delta_{mj}(\alpha_K(\Delta\mathbf{q}_{KL})_j(\Delta\mathbf{q}_{KL})_m + \alpha_K(\Delta\mathbf{q}_{KL})_i(\Delta\mathbf{q}_{KL})_n - 1) +$$
$$3\alpha_K(\Delta\mathbf{q}_{KL})_i(\Delta\mathbf{q}_{KL})_j(\delta_{mi}\delta_{ni} + \delta_{mj}\delta_{nj})\Big\}\Bigg]\text{expo}(\mathbf{q}_{KL}) \tag{11.107}$$

11.4.3 Analytical Gradients

The methodology for calculating the DG-EVB gradient is similar to that for the TREQ gradient shown in chapter 5. Since only the *squared coupling* $C(\mathbf{q})^2$ is calculated from DG-EVB, the original EVB gradient formula resulting from building the derivative of eq. 2.130 needs to be slightly modified, as it is shown in the TREQ chapter.

The result is the following expression:

$$\frac{\partial V(\mathbf{q})}{\partial \mathbf{q}} = \frac{1}{2}\Bigg\{\left(\frac{\partial F_1(\mathbf{q})}{\partial \mathbf{q}}\right) + \left(\frac{\partial F_2(\mathbf{q})}{\partial \mathbf{q}}\right) -$$
$$\left[\frac{2\left(\frac{\partial C(\mathbf{q})^2}{\partial \mathbf{q}}\right) + [F_1(\mathbf{q}) - F_2(\mathbf{q})]\left[\left(\frac{\partial F_1(\mathbf{q})}{\partial \mathbf{q}}\right) - \left(\frac{\partial F_2(\mathbf{q})}{\partial \mathbf{q}}\right)\right]}{\sqrt{(F_1(\mathbf{q}) - F_2(\mathbf{q}))^2 + 4C(\mathbf{q})^2}}\right]\Bigg\}. \tag{11.108}$$

Almost all of this is known: the diabatic energies $F_1(\mathbf{q})$ and $F_2(\mathbf{q})$ as well as their gradients and the squared coupling. The remaining part is the gradient of the squared coupling $\frac{\partial C(\mathbf{q})^2}{\partial \mathbf{q}}$.

By looking at the original DG-EVB coupling expression (eq. 11.109), it becomes clear that the first derivatives of the single distributed Gaussian basis functions need to be built. The linear expansion prefactors b_{ijK} are coordinate-independent and thus remain identical, resulting in the following expression:

$$\frac{\partial C(\mathbf{q})^2}{\partial \mathbf{q}} = \sum_K^M \sum_{i \geq j \geq 0}^N b_{ijK} \frac{\partial g(\mathbf{q}, \mathbf{q}_K, i, j, \alpha_K)}{\partial \mathbf{q}}. \tag{11.109}$$

The first derivatives of the Gaussian basis functions with respect to the used set of internal coordinates ($\frac{\partial g(\mathbf{q}, \mathbf{q}_K, i, j, \alpha_K)}{\partial \mathbf{q}}$) are also needed for the setup of the **D**-matrix. Thus, the expressions of eqs. 11.102-11.104 can be reused for the purpose of calculating the coupling gradients, with the sole exception that the position $\mathbf{q}_L$ of the L'th reference point needs to be replaced by a generic position vector $\mathbf{q}$ of the current system's position in internal coordinate space.

11.5 Program Handling

In this section, some details concerning the application of the single programs contained into EVB-QMDFF are presented. All eight programs listed in section 3.3 are handled similarly. The needed keywords are listed in a `qmdff.key` file, the programs are started by, e.g.,

$$\texttt{rpmd.x qmdff.key.} \tag{11.110}$$

Other input files (e.g., DG-EVB reference data or the start structure for a calculation with `dynamic.x`) must be named with standard names. If the user wants to gather detailed information about the current program, he or she can execute the help command:

$$\texttt{rpmd.x -h.} \tag{11.111}$$

In the next section, a complete list of keywords is presented. They are divided into *general keywords* for EVB-QMDFF setup valid for (almost) all programs and *program specific keywords*. Finally, example input files for all programs but `qmdffgen.x` (where no input file is needed) are listed.

11.5.1 List of Keywords

Table 11.2: List of keywords currently (October 2019) in usage within the EVB-QMDFF program package. All used keywords need to be written in a `qmdff.key` file. Some of them are essential for the execution of the respective program, others can alter predefined values of several program parameters and are thus optional. The list begins with general EVB-QMDFF PES keywords that might be used for several application programs, following with sections for all individual programs. The parameter [value] indicates a real number parameter to be given, [number] an integer parameter and [word] or [filename] a character string. For the `evb_kt_driver.x` program, all keywords of `rpmd.x` can be added to the input as well in order to alter default values given for all RPMD sampling settings initiated with the driver.

keyword [parameters]	description
general keywords	
ffname [qmdff1/2/3]	Force field filenames for up to three QMDFFs.

`2evb [energies]`	Two QMDFFs with their energy shift calculated by `qmdffgen.x` shall be coupled.
`3evb [energies]`	Three QMDFFs shall be coupled.
`shift_manual`	Usually in the case of a 2×2-EVB, the QMDFF shift-energies are slightly corrected by the application-programs to exactly reproduce the first/last energy of the given reaction path. This keyword disables this automated change such that the values given with `2evb` or `3evb` are used.
`coupling [specifier]`	Used coupling function for dE- or dQ-EVB coupling terms as listed in tables 3.1 and 3.3 (default: 1g).
`evb_dq [TS xyz-file]`	The dQ-EVB coupling is activated, using the structure in the file as $\mathbf{q}_{TS}$ structure.
`dg_evb [number DG-points]`	Activates the DG-EVB coupling method, with the stated number of gradient/Hessian reference points to be used. The QM-reference for those points must be given in a `ref.input` file.
`dg_evb_mode [1/2/3]`	Which type of DG-EVB coupling term shall be used. 1: Only energies used as reference and only s-functions for the coupling term, 2: Energies and gradients as reference and s- and p-functions for the coupling term, 3: Energies, gradients and Hessians as reference and s-,p- and d-functions for the coupling term.
`double_alpha`	Separate α_K-parameters are used for the exponential prefactors of d-functions in DG-EVB. This results in a *doubled* number of α_K-parameters and might improve the overall DG-EVB performance. Note that enough reaction path energies need to be present in order to avoid overfitting!
`dg_mat_num`	The DG-EVB coefficients matrix $\mathbf{D}$ is calculated with numerical first and second derivatives instead of using the analytical expressions given in section 11.4.2. Should only be used for benchmarks or tests since the overall performance is affected significantly!
`gauss_threshold [value]`	Denotes the real number value for the Gaussian sheath of neighbored DG-EVB points under which their contributions to the coupling at point $\mathbf{q}$ is neglected. Raising this value will improve the performance but might deteriorate the quality if significant contributions are ignored.
`read_coord`	The internal coordinates to be used within the EVB coupling method (EVB-dQ, DG-EVB or TREQ). A file named `coord_def.inp` with one coordinate definition dependent on the numbers of the involved atoms of the type 1 2 3 4 per line needs to be present. Four types of coordinates can be defined: (1) bond lengths need two atoms numbers, (2) bond angles need three atom numbers, (3), torsional angles need a leading zero and four atom numbers, (4) out-of-plane angles need a leading one and four atom numbers.

`dist_matrix`	Enables the usage of a *distance matrix* as set of internal coordinates for EVB couplings. Only bond lengths will be used, one for each pair of atoms in the system. Since for this approach the number of internal coordinates scales quadratically with the system size, it should only be used if all other approaches to define internal internal coordinates have failed.
`path_dist_limit [value]`	Only used for pathological TREQ parametrizations. For complex systems the method of finding the nearest point along the RP to project on it might fail for structures far in the reactants or products valley. Then, a *s*-parameter value near the TS might be calculated and unreliably large energies result. To avoid this, the *s*-parameter is set automatically to one or zero if the minimal distance of the system to the RP is larger than the given value.
`pot_ana [name]`	One of the implemented analytical PES representations as listed in section 3.3.3 will be used.
`tradff`	A simple traditional-nonreactive force field will be used. The usual xyz-input file must be in the Tinker input format with atom types and connectivities. Only very basic compounds such as hydrocarbons can be simulated.
`treq [number refpoints]`	The TREQ coupling method is used with the given number of gradient/Hessian reference points. The QM-reference for those points must be given with a `ref.input` file.
`irc_struc [file name]`	File with the reaction path to be taken as reference for the TREQ method.
`irc_ens [file name]`	File with reaction path energies to be taken as reference for the TREQ method.
`interp_tol [value]`	The threshold value for the numerical calculation of the path parameter *s* in TREQ calculations. The value is the fraction of the total path length (1), which shall remain as uncertainty (default: 1E-8).
`par_eta [value]`	Inverse width of the interval along the parametrized path in TREQ over which the smooth switch-off of the QMDFFs in the reactants and products valleys (fig. 2.16) shall be applied (default: 20).
`rp_exp_coeff [value]`	Global α-damping parameter for the RP-EVB part in TREQ which determines the damping of the EVB coupling term with the distance from the parametrized reaction path (default: 4).
`s_borders_man [5 values]`	Borders of the different coupling regions along the parametrized reaction path in TREQ as given in eq. 2.164. The values are restrained between 0 and 1.
`rp_evb_mode [2/3]`	If the user wants to have only linear Taylor expansions offside the reaction path for TREQ. This tends to give problems in the direct interpolation region, therefore only used for benchmarks (default: 3).

irc_local [number]	For reaction path progress parameter calculations in TREQ, determine how many neighbored energy reference points of the RP shall be included for the initial localization of the nearest path segment (default: 10).
irc_grad_plot	If DG-EVB or TREQ are used for a calculation, the components of the internal EVB-QMDFF gradients are printed to file during each energy/gradient calculation.
int_coord_plot	Internal coupling coordinate values are plotted to file for each energy/gradient calculation.
num_grad	The EVB-QMDFF gradient is calculated numerically *via* finite differences. Should only be used for debug.
num_grad_step [value]	Cartesian elongation step size for numerical gradients (default: 1E-5).
gen_test [number]	For rpmd.x, only the initial umbrella structure generation part is performed, each N'th structure is printed to file, where N is the given parameter.

evbopt keywords	
start_points [number]	Number of single LM local optimizations during the MSLS algorithm for EVB parameter optimization (default: 100).
maxstep [number]	Number of local optimization steps per LM-run during the parameter optimization. If the LM is not converged after the given step number, the local search run is marked as failed (default: 200).
random_bonds [2 values]	Lower and upper bounds between the initial α_i-values (EVB coupling parameters) are generated in a randomized manner at the start of each local LM run during MSLS (default: 20-100).
lm_threshold [value]	Convergence criterion for the single LM-runs in terms of optimization step size in parameter space (1E-7).
more_info	Print additional output concerning every single LM-run during the optimization.

egrad keywords	
path_structure [filename]	Trajectory file in xyz-format with structures for which the energies and gradients shall be calculated.
debug	Print out each single QMDFF energy component (see section 2.3.2) for each structure in the energy/gradient calculation. Should only be used for detailed investigations of QMDFF properties.

evb_qmdff keywords	
xyzfile [filename]	xyz-file with structure whose properties shall be calculated.
opt_min	A geometry optimization of the initial structure is performed. If the keyword is not given, only gradient and frequencies of the structure will be calculated.
calc_frag	Only a part of the given molecular system will be considered for calculation. A file named fragment.inp with the numbers of the atoms to be considered must be present.

`opt_maxiter [number]`	Maximum steps for geometry optimizations (default: 500).
`opt_stepsize [value]`	Maximum length of a single geometry optimization step (default: 0.2).
`opt_ethr [value]`	Maximum energy change convergence criterion for geometry optimizations (default: 1E-7).
`opt_gthr [value]`	Gradient norm convergence criterion for geometry optimizations (default: 1E-7).
`opt_dthr [value]`	Geometry step norm convergence criterion for geometry optimizations (default: 1E-7).
`opt_gmaxthr [value]`	Largest component of gradient convergence criterion for geometry optimizations (default: 1E-7).
`opt_dmaxthr [value]`	Largest component of geometry step convergence criterion for geometry optimizations (default: 1E-7).

irc keywords

`xyzfile [filename]`	xyz-file with initial guess for TS optimization.
`read_coord`	Activate read-in of internal coordinates from provided file `coord_def.inp`.
`opt_maxiter [number]`	Maximum number of steps for TS geometry optimization (default: 200).
`opt_stepsize [value]`	Maximum length of a single TS optimization step (default: 0.05).
`opt_ethr [value]`	Maximum energy change convergence criterion for TS optimization (default: 1E-7).
`opt_gthr [value]`	Gradient norm convergence criterion for TS optimization (default: 1E-7).
`opt_dthr [value]`	Geometry step norm convergence criterion for TS optimization (default: 1E-7).
`opt_gmaxthr [value]`	Largest component of gradient convergence criterion for TS optimization (default: 1E-7).
`opt_dmaxthr [value]`	Largest component of geometry step convergence criterion for TS optimization (default: 1E-7).
`irc_maxstep [number]`	Maximum number of IRC steps in each direction (default: 200).
`irc_steplen [value]`	Desired length of an IRC step to be written out ($\text{amu}^{1/2}\text{bohr}$) (default: 0.1).
`irc_eulerlen [value]`	Desired length of an elementary Euler step for IRC optimization ($\text{amu}^{1/2}\text{bohr}$). Should be much smaller than the `irc_steplen` value (default: 0.005).
`irc_ethr [value]`	IRC energy change convergence criterion (default: 1E-7).
`irc_gthr [value]`	IRC gradient norm convergence criterion (default: 1E-7).

dynamic keywords

`xyzfile [filename]`	xyz-file with initial structure for MD calculation.
`steps [number]`	Number of single MD steps to be propagated.
`deltat [value]`	Length of a single Verlet-MD step in fs.
`temp [value]`	Temperature to be applied in the MD run.
`thermostat [name]`	The thermostat to be used during the MD (currently only Andersen).

andersen_step	After how many MD steps shall the velocities be reset by the Andersen thermostat according to a thermal random distribution (default: 100).
tdump [value]	Time, after which a new MD trajectory structure shall be written out, in fs.
bead_number [number]	Number of ring polymer beads in the system to be propagated with MD (default: 1).
add_force	Activates a constant force mechanochemistry simulation.
force1/2 [number] [4 values]	Must be added for constant mechanochemistry calculations for two atoms. The parameters are: index of the atom, applied force (N), cartesian direction vector.
afm_run	Activates an AFM simulation (mechanochemistry).
afm_fix [number]	Which atom shall be held fix during the AFM simulation.
afm_move [number] [4 values]	Which atom shall be linearly elongated by the imaginary AFM tip (parameters: atom index, maximum elongation (Å), cartesian direction vector).
e_con	If activated, the current total energy of the system will be written to file etot.log after each MD step.

rpmd keywords	
ts_struc [filename]	xyz-file with structure of the system's TS. The RPMD calculation will start from this structure.
deltat [value]	Length of a single MD time step for all MD calculations in the program.
temp [value]	Temperature for which the k(T) value shall be calculated (and thus all MD trajectories).
thermostat [name]	The thermostat to be used during the MD (currently only Andersen).
bead_number [number]	Number of ring polymer beads in the system to be propagated with MD during the umbrella samplings and recrossing calculations (default: 1).
generate_steps [number]	Number of MD steps per trajectory for initial generation of umbrella start structures.
equilibr_steps [number]	Number of MD steps for a single umbrella equilibration trajectory which will be calculated before each umbrella sampling trajectory.
umbrella_steps [number]	Number of MD steps for a single umbrella sampling trajectory.
umbrella_trajs [number]	Number of umbrella trajectories per umbrella-window that shall be calculated.
umbrella_bias [value]	Strength of the umbrella bias potential to be added for equilibrations and samplings, in a.u. .
umbrella_bonds [value1] [value2]	Range of ξ-coordinate in which umbrella samplings shall be done. The minimum range is 0 (reactants) to 1 (TS), however, usually a slightly larger range should be calculated.
umbrella_dist [value]	Step in ξ-coordinate between two neighbored umbrella windows (only equidistant windows possible so far).

umbrella_type [name]	Which type of reaction shall be calculated. The available types are listed in table 3.4, their keywords are (with same ordering as in the table): atom_shift, dissoc, cyclorever, rearr, elimination, merging, bimolec, addition, cycloadd, addition3, addition4, add3_solv and add4_solv.
educt(1-4) [list of numbers]	The atoms of each reactant molecule: one line per molecule (e.g., educt1 1 2 3, educt2 4 5) with the respective atom indices.
r_inf [value]	Distance between separated reactants where (almost) no interactions are present (eq. 2.103).
bond_form [list of bonds]	List of all bonds that are being formed during the reaction, written in the scheme a-b.
bond_break [list of bonds]	List of all bonds that are being broken during the reaction, same format as bond_form.
shift_atom [number]	If the atom_shift reaction type was chosen, the atom that is actually shifted must be defined here.
shift_coord [word]	We assume that the shift will happen parallel to a coordinate axis. Specify, which one it is (x, y or z).
shift_interv [value1] [value2]	Interval (in absolute cartesians), in which the shifted atom will be translated. The first number denotes the reactants-asymptotic, the second the TS-area.
fix_atoms [filename]	For surface reactions, it is wise to fix the lowest layer of surface atoms somehow in order to gain a pseudo-periodic behavior of the system. In the specified file, a list with all atoms that shall be fixed during the MD runs can be given.
pmf_xi_range [value1] [value2]	Interval in ξ in which the free energy surface of the reaction will be calculated. It should be slightly smaller than the range in umbrella_bonds.
pmf_bins [number]	Number of grid points along the interval for which the free energy surface shall be calculated.
pmf_method [name]	If the WHAM or the UI method shall be used for the free energy calculation (default: UI).
recross_equi [number]	Number of time steps for initial equilibration of the recrossing parent trajectory.
child_total [number]	Total number of child trajectories started during the recrossing calculation.
child_interval [number]	How many time steps of the parent trajectory shall be propagated between two started bunches of child trajectories.
child_perpoint [number]	How many child trajectories shall be started simultaneously for a certain bunch of them.
child_evol [number]	Number of time steps each child trajectory shall be sampled (usually quite short, e.g., 500-1000).
recross_mpi	If the recrossing calculation shall be parallelized with the available number of cores.
pmf_minloc [name]	If the minimum value of the free energy surface shall be located at $\xi = 0$ (zero) or at its global minimum (pmf_min).

print_polymer [value]	If the user wants to look at a RPMD sampling trajectory (and the RPMD beads), the first umbrella sampling at the specified ζ value will be written to file `rpmd_traj.xyz`.
tdump [number]	Time, after which a new structure shall be written to file if `print_polymer` is activated, in fs.
debug	All structures of the initial equilibration part are written to file `debug_traj.xyz`. Very huge file, only for test reasons!
no_check	Deactivates the RPMD error handling during the sampling. Should not be added for usual calculations.
max_error [number]	Total number of errors for which the whole RPMD-calculation will be canceled due to bad behavior.

evb_kt_driver keywords	
software [word]	Used QM-software-package for the IRC calculation (in order to read it in properly). Only Gaussian(g) supported so far.
irc_prefix [word]	File prefix for needed Gaussian IRC output files, `prefix.log` and `prefix.chk` need to be present.
irc_direction [word]	Which direction of the reaction path shall actually be sampled. Possible are `left2right` and `right2left`.
gf_method [string]	Used QM-reference-method for the calculation of gradients and frequencies at the TREQ reference points as well as the QMDFF-reference-calculations.
gf_basis [string]	Used QM basis set as well as other settings (e.g., empirical dispersion) for gradient and frequency calculations.
nprocs_total [number]	Number of available processors for the whole calculation (default: 1).
energy_extra [word]	If the energies of the IRC shall be recalculated with a higher-level QM method, generating a *dual-level* approach for the QM reference. The used software package must be specified; Gaussian or Orca are possible.
ens_nprocs [number]	Number of processors to be utilized for the energy calculations. Depending on the ratio of the total number of processors, the IRC is split up into pieces to be calculated in parallel (default: 1).
e_method [string]	Used QM reference method for the separate calculation of energies.
e_basis [string]	Used QM basis set (and other settings) for the separate calculation of energies.
min_rp_points [number]	Minimum number of gradient/Hessian reference points for TREQ, according to eq. 3.22 (default: 10).
rpmd_temps [list of values]	A list of temperatures for which k(T)-values shall be calculated. If two or more temperatures are specified, Arrhenius- and Eyring-fits will be done and their parameters will be written out.
kt_average [number]	Number of separate k(T) calculations that will be done for each specified temperature and averaged in the following (default: 1).

manual_int [filename]	All RPMD calculations will be done with a predefined set of internal coordinates, else, the set will be determined automatically (fig. 3.7).
min_procs [number]	Number of processors to be used for the optimization of QMDFF minima (default: 1).
rp_ref_nprocs [number]	Number of processors to be used for the calculation of gradient/Hessian reference points (default: 1).
ref_memory [value]	Size of memory (GB) to be used for each QM reference calculation (default: 4).
link_gaussian [path]	Absolute path to the Gaussian executable (default: g16).
link_orca [path]	Absolute path to the Orca executable (default: orca).
link_qmdffgen [path]	Absolute path to the qmdffgen.x executable (default: qmdffgen.x).
link_rpmd [path]	Absolute path to the rpmd.x executable (default: rpmd.x).
link_mpi [path]	Absolute path to the mpirun executable (default: mpirun).

11.5.2 Example Input Files

In this section input files (mostly qmdff.key but also others) that have been used for real calculations are shown for some of the EVB-QMDFF programs. There will be no explanation of the single keywords (this was done in the last section), instead, a short summary will be given what kind of calculation is ordered by the input file.

evbopt

Shown is the qmdff.key-input for the DG-EVB-parametrization of the CO_2H+CH_3-reaction. Energies, gradients and Hessians are used as reference for the DG-EVB points (DG mode 3), the used set of internal coordinates is read in from file coord_def.inp. The default range of α_i start values was slightly enlarged in order to get a better result.

```
ffname  min1.qmdff  min2.qmdff
2evb -154.10052506960473       -154.07454941338695
path_structure struc.xyz
path_energies ref.dat
dg_evb 7
dg_evb_mode 3
read_coord
start_points 100
random_bonds 10 300
```

The coord_def.inp-file defines a set of internal coordinates containing four bonds and one angle, that were manually chosen by the user:

```
1 2
2 6
5 7
4 8
1 2 6
```

The reference data for the DG-EVB energy-/gradient-/Hessian-reference points (as well as for gradient-/Hessian-points in a TREQ calculation) is stored into the `ref.input`-file:

```
NPOINTS 7

NATOM  8

*POINT 1

ENERGY    -154.093538

GEOMETRY
   0.3806243E+01  -0.1097917E+00   0.1123574E-04   0.1865978E+01   0.5001506E+00
   0.1465671E-04   0.4746086E+01   0.6119787E+00   0.1676215E+01   0.3875865E+01
  -0.2160839E+01  -0.3080984E-04   0.4746101E+01   0.6120479E+00  -0.1676154E+01
  -0.1868817E+01   0.9633374E+00   0.1178219E-04  -0.3015592E+01  -0.9470744E+00
  -0.2961372E-04  -0.2733848E+01   0.2891982E+01   0.5403210E-04
END

GRADIENT
  -0.1015742E-01   0.1779196E-02  -0.9013421E-09  -0.4602145E-03  -0.7348972E-03
  -0.1167703E-07  -0.1775501E-02  -0.1714216E-03  -0.1310762E-02  -0.3876552E-03
   0.1680861E-02   0.3201254E-07  -0.1775521E-02  -0.1714732E-03   0.1310737E-02
   0.1382985E-01  -0.2198107E-02   0.3606149E-07   0.3422417E-04   0.2034780E-03
  -0.8596180E-08   0.6922408E-03  -0.3876352E-03  -0.2174319E-07
END

HESSIAN
   0.5743987E+00  -0.7027415E-02   0.1763667E-07  -0.3095063E+00   0.8346702E-01
   0.2439431E-06  -0.1042063E+00  -0.4482100E-01  -0.1044270E+00  -0.4514272E-01
   ...
  -0.1934468E-02
END

*POINT 2

ENERGY    -154.086163

GEOMETRY
   0.3634502E+01  -0.1394213E+00   0.1120341E-04   0.1683308E+01   0.4116106E+00
   ...
```

egrad

With this `qmdff.key`-file, the TREQ-energies of a scanned 2D-surface for the collinear $H+H_2$-reaction are calculated. Since the TREQ-coupling term needs no optimization, this task can be started directly after initial QMDFF parametrizations and IRC optimization.

```
ffname  min1.qmdff  min2.qmdff
2evb  -1.6545070644440001      -1.6544511854286907
path_structure struc.xyz
rp_evb 9
```

```
irc_struc irc.xyz
irc_ens irc_ens.dat
read_coord
int_grad_plot
```

evb_qmdff

Here a `qmdff.key`-input file for a combined geometry optimization/frequency calculation task is shown. The used PES is the CH_4+H-surface (section 3.3.3). From the results of this calculation, combined with CM5 charges and Wiberg-Mayer bond orders from a QM calculation, a QMDFF was generated (see chapter 5).

```
xyzfile min1.xyz
pot_ana ch4h
read_coord
opt_min
newton_raphson
```

irc

For the same system as above, this `qmdff.key`-file facilitates the IRC optimization. An initial guess for the TS structure is submitted by the user in the file `ts.xyz`, after the TS was optimized, the IRC is evaluated and written to file `irc.xyz`.

```
xyzfile ts.xyz
pot_ana ch4h
read_coord
opt_min
irc_maxstep 100
newton_raphson
irc_steplen 0.05
```

In contrast to DG-EVB, a complete set of internal coordinates must be provided by the user in `coord_def.inp` for the TS optimization, which is done in internal coordinates:

```
1 2
2 5
2 3
2 4
4 6
1 2 5
3 2 4
2 4 6
1 2 4
```

dynamic

Here, all needed commands to start a MD of 50000 time steps for a cutout of a graphene surface are listed into `qmdff.key`. The simple energy-gap-EVB is applied (using the sp2d-coupling term, table 3.1), the MD is run at 298 K, each 20th dynamics step is written out.

```
ffname  min1.qmdff  min2.qmdff
2evb  -629.98510152277481      -629.86526221918541
```

```
coupling sp2d
xyzfile start.xyz
nbeads 1
steps 50000
deltat 0.5
tdump  10
thermostat andersen
temp 298
```

rpmd

The presented example for a RPMD-k(T) calculation with `rpmd.x` is the hydrogen diffusion on a copper(001)-surface. The results are shown in chapter 9. The hydrogen is moved along the x-axis starting from the TS position. A low temperature of 100 K is simulated with 16 beads, the PES is modeled by a simple Gaussian (1g) energy gap coupling term (table 3.1).

```
ts_struc ts.xyz
bead_number    16
npaths    1

ffname min1.qmdff min2.qmdff
2evb      -3850.13597864118219     -3850.13586849674994
coupling 1g
path_energies ref.dat
path_structure struc.xyz

deltat    0.5000000
temp      100
thermostat andersen
fix_atoms fix_atoms.dat

umbrella_type ATOM_SHIFT
shift_atom 81
shift_coord X
shift_interv 6.435 5.07

umbrella_bias     0.1000000
umbrella_bonds   -0.200000     1.400000
umbrella_dist     0.0200000
generate_steps    20000
equilibr_steps    10000
umbrella_steps    30000
umbrella_trajs       10

pmf_xi_range    -0.200000     1.300000
pmf_bins       5000
pmf_method integration
pmf_minloc ZERO

recross_equi    20000
child_total     10000
```

```
child_interval     5000
child_perpoint      100
child_evol     1000
recross_nocheck
recross_mpi


max_error     100
```

evb_kt_driver

Finally, a qmdff.key input file for the *black-box* k(T) calculation with the evb_kt_driver.x program is shown. Here, we are interested in the Arrhenius- and Eyring-parameters of the CF_3O+CH_4-reaction, where a temperature range of 300 to 600 K is considered (see section 6.2.14). The calculation was executed on a cluster at the university computing center. QMDFF optimizations as well as gradient/Hessian reference calculations were done with the B3LYP/6-311G(d,p)-level of theory [166, 167, 201] using the Gaussian16 program suite [99]. Additionally, IRC energies were corrected with the DLPNO-CCSD(T)/def2-TZVP-level of theory [154, 155, 158] using Orca [130].

```
software G
irc_prefix irc
irc_direction left2right
gf_method ub3lyp
gf_basis 6-311g(d,p) scf=MaxCycle=512 density=current
nprocs_total 32
min_nprocs 8
rp_ref_nprocs 4
ref_memory 4
min_rp_points 35
rpmd_temps 300 350 400 450 500 550 600

recross_nocheck
recross_mpi
max_error 10000
npaths 4
deltat 0.5
umbrella_bias 0.15
bead_number 16
kt_average 5
rp_exp_coeff     35.0000000

link_rpmd /sfs/fs5/home-sh/suphc213/bin/rpmd.x
link_qmdffgen /sfs/fs5/home-sh/suphc213/bin/qmdffgen.x
link_gaussian g16
link_orca /sfs/fs5/home-sh/suphc213/bin/orca_4_0_0_linux_x86-64/orca
link_mpi mpirun $NQSII_MPIOPTS

energy_extra 0
e_method dlpno-ccsd(t)
e_basis def2-TZVP def2-TZVP/C TightSCF
```

11.6 Supplementary Information

For both publications that are part of this thesis, supplementary information sheets were created that provide some additional insight into calculation setups, choices made by the author(s) and further results complementing the ones shown in the main publications.

Besides the papers in chapters 4 and 5 I wrote a part of the supplementary information of the first EVB-QMDFF paper of HARTKE and GRIMME [16]. This is therefore shown here as well.

11.6.1 First EVB-QMDFF Publication

The publication by HARTKE and GRIMME [16] introduced the EVB-QMDFF methodology. Reaction paths for three different systems were parametrized by using the simple 1g-energy-gap coupling term.

The supporting information presents an example of the even simpler constant coupling term (see table 3.1) in chapter 1. Further, it gives a first clue of how EVB-QMDFF is able to describe regions offside the reaction path in chapter 2, shown by two-dimensional sections of the potential energy surfaces for two example reactions. The results in chapter 2 were produced by myself.

11.6.2 RPMD Rate Constants with (DG-)EVB-QMDFF

This supplementary information shows further details for the second EVB-QMDFF publication reprinted in chapter 4. Since the overall quality of DG-EVB force fields depends on quite a few parameters, their influence on the force field is shown in chapter 1.

The tests were executed for both reactions that are calculated with DG-EVB in the main paper. Presented are different sets of internal coordinates as well as different numbers and positions of DG-EVB gradient and Hessian reference points. Two-dimensional scans of both parameter sets were done, resulting in the insight that the "correct" choice of internal coordinates is crucial for the overall force field quality and that the error sum converges to a minimum value if more than 8 or 9 DG-EVB reference points are used. In chapter 2, the number of energy reference points along the MEP is varied and its influence on the DG-EVB parameter optimization process can be seen.

The used RPMDrate settings are presented in chapter 3, whereas the influence of their variation on the calculated rate constants is shown in chapter 4. Convergence of the values with respect to bead number, lengths of MD time steps and the number of umbrella sampling trajectories exists.

Free energy curves and time-dependent transmission coefficients are presented in chapters 5 and 6.

11.6.3 TREQ - Development and Benchmark

The following sheet contains many details regarding the TREQ benchmarks that were done for 6 different reactions (see chapter 5).

Besides this, settings for the DG-EVB calculations used as a competitor are shown as well.

A more detailed overview of the shown results is presented on the first reprinted page.

CHAPTER 12

Bibliography

[1] B. Peters, *Reaction Rate Theory and Rare Events*, Elsevier, 1st ed., 2017.

[2] W. K. den Otter and W. J. Briels, *The Reactive Flux Method Applied to Complex Isomerization Reactions: Using the Unstable Normal Mode as a Reaction Coordinate*, J. Chem. Phys., 106 (1997), pp. 5494–5508, DOI: 10.1063/1.473573.

[3] K. J. Laidler and M. C. King, *Development of Transition-State Theory*, J. Phys. Chem., 87 (1983), pp. 2657–2664, DOI: 10.1021/j100238a002.

[4] H. Eyring, *Viscosity, Plasticity, and Diffusion as Examples of Absolute Reaction Rates*, J. Chem. Phys., 4 (1936), pp. 283–291, DOI: 10.1063/1.1749836.

[5] M. G. Evans and M. Polanyi, *Some Applications of the Transition State Method to the Calculation of Reaction Velocities, Especially in Solution*, Trans. Faraday Soc., 31 (1935), pp. 875–894, DOI: 10.1039/TF9353100875.

[6] J. A. Sansòn, M.-L. Sànchez, and J. C. Corchado, *Importance of Anharmonicity, Recrossing Effects, and Quantum Mechanical Tunneling in Transition State Theory with Semiclassical Tunneling. A Test Case: The H_2+Cl Hydrogen Abstraction Reaction*, J. Phys. Chem. A, 110 (2006), pp. 589–599, DOI: 10.1021/jp052849d.

[7] U. Manthe and W. H. Miller, *The Cumulative Reaction Probability as Eigenvalue Problem*, J. Chem. Phys., 99 (1993), pp. 3411–3419, DOI: 10.1063/1.465151.

[8] G. Nyman, *Computational Methods of Quantum Reaction Dynamics*, Int. J. Quantum Chem., 114 (2014), pp. 1183–1198, DOI: 10.1002/qua.24661.

[9] T. J. H. Hele, *Quantum Transition-State Theory*, PhD thesis, University of Cambridge, 2014.

[10] J. Zheng, J. L. Bao, R. Maena-Pañeda, S. Zhang, B. J. Lynch, J. C. Corchado, Y.-Y. Chuang, P. L. Fast, W.-P. Hu, Y.-P. Liu, G. C. Lynch, K. A. Nguyen, C. F. Jackels, A. F. Ramos, B. A. Ellington, V. S. Melissas, J. Villá, I. Rossi, E. L. Coitniño, J. Pu, T. V. Albu, A. Ratkiewicz, R. Steckler, B. C. Garrett, A. D. Isaacson, and D. G. Truhlar, *Polyrate-version 2017*, 2017.

[11] S. Habershon, D. E. Manolopoulos, T. E. Markland, and T. F. Miller III, *Ring-Polymer Molecular Dynamics: Quantum Effects in Chemical Dynamics from Classical Trajectories in an Extended Phase Space*, Annu. Rev. Phys. Chem., 64 (2013), pp. 387–413, DOI: 10.1146/annurev-physchem-040412-110122.

[12] F. Jensen, *Introduction to Computational Chemistry*, Wiley, 3rd ed., 2017.

[13] Y. V. Suleymanov, J. W. Allen, and W. H. Green, *RPMDrate: Bimolecular Chemical Reaction Rates from Ring Polymer Molecular Dynamics*, Comp. Phys. Comm., 184 (2013), pp. 833–840, DOI: 10.1016/j.cpc.2012.10.017.

[14] A. C. T. van Duin, S. Dasgupta, F. Lorant, and W. A. Goddard, III., *ReaxFF: A Reactive Force Field for Hydrocarbons*, J. Phys. Chem. A, 105 (2001), pp. 9396–9409, DOI: 10.1021/jp004368u.

[15] S. Grimme, *A General Quantum Mechanically Derived Force Field (QMDFF) for Molecules and Condensed Phase Simulations*, J. Chem. Theory Comput., 10 (2014), pp. 4497–4514, DOI: 10.1021/ct500573f.

[16] B. Hartke and S. Grimme, *Reactive Force Fields Made Simple*, Phys. Chem. Chem. Phys., 17 (2015), pp. 16715–16718, DOI: 10.1039/C5CP02580J.

[17] J. Steffen and B. Hartke, *Cheap but Accurate Calculation of Chemical Reaction Rate Constants from Ab Initio Data, via System-Specific, Black-Box Force Fields*, J. Chem. Phys., 147 (2017), p. 161701, DOI: 10.1063/1.4979712.

[18] J. Steffen, *A New Class of Reaction Path Based Potential Energy Surfaces Enabling Accurate Black Box Chemical Rate Constant Calculations*, J. Chem. Phys., 150 (2019), p. 154105, DOI: 10.1063/1.5092589.

[19] K. J. Laidler, *The Development of the Arrhenius Equation*, J. Chem. Educ., 61 (1984), pp. 494–498, DOI: 10.1021/ed061p494.

[20] P. L. Houston, *Chemical Kinetics and Reaction Dynamics*, vol. 1st, Dover Publications, 1st ed., 2006.

[21] W. Göpel and H.-D. Wiemhöfer, *Statistische Thermodynamik*, Spektrum Akademischer Verlag, 1st ed., 2000.

[22] A. Fernàndez-Ramos, J. A. Miller, S. J. Klippenstein, and D. G. Truhlar, *Modeling the Kinetics of Bimolecular Reactions*, Chem. Rev., 106 (2006), pp. 4518–4584, DOI: 10.1021/cr050205w.

[23] R. P. de Tudela, Y. V. Suleimanov, J. O. Richardson, V. S. Rábanos, W. H. Green, and F. J. Aoiz, *Stress Test for Quantum Dynamics Approximations: Deep Tunneling in the Muonium Exchange Reaction D+HMu $\longrightarrow$ DMu+H*, J. Phys. Chem., 5 (2014), pp. 4219–4224, DOI: 10.1021/jz502216g.

[24] Y. V. Suleimanov, R. Pérez de Tudela, P. G. Jambrina, J. F. Castillo, V. Sáez-Rábanos, D. E. Manolopoulos, and F. J. Aoiz, *A Ring Polymer Molecular Dynamics Study of the Isotopologues of the H+H$_2$ Reaction*, Phys. Chem. Chem. Phys., 15 (2013), pp. 3655–3665, DOI: 10.1039/c2cp44364c.

[25] D. G. Truhlar and B. C. Garrett, *Variational Transition-State Theory*, Acc. Chem. Res., 13 (1980), pp. 440–448, DOI: 10.1021/ar50156a002.

[26] D. G. Truhlar and B. C. Garrett, *Variational Transition State Theory*, Ann. Rev. Phys. Chem., 35 (1984), pp. 159–189, DOI: 10.1146/annurev.pc.35.100184.001111.

[27] B. C. Garrett and D. G. Truhlar, *Criterion of Minimum State Density in the Transition State Theory of Bimolecular Reactions*, J. Chem. Phys., 70 (1979), pp. 1593–1598, DOI: 10.1063/1.437698.

[28] S. C. Tucker and E. Pollack, *Microcanonical Variational Transition-State Theory for Reaction Rates in Dissipative Systems*, J. Stat. Phys., 66 (1992), pp. 975–990, DOI: 10.1007/BF01055711.

[29]   D. G. Truhlar, A. D. Isaacson, and B. C. Garrett, *Generalized Transition State Theory*, CRC Press, 1985, pp. 65–137.

[30]   W. H. Miller, *Unified Statistical Model for "Complex" and "Direct" Reaction Mechanisms*, J. Chem. Phys., 65 (1976), pp. 2216–2223, DOI: 10.1063/1.433379.

[31]   B. C. Garrett and D. G. Truhlar, *Canonical Unified Statistical Model. Classical Mechanical Theory and Applications to Collinear Reactions*, J. Chem. Phys., 76 (1982), pp. 1853–1858, DOI: 10.1063/1.443157.

[32]   J. Meisner and J. Kästner, *Atom Tunneling in Chemistry*, Angew. Chem. Int. Ed., 55 (2016), pp. 5400–5413, DOI: 10.1002/anie.201511028.

[33]   J. Pu, J. Gao, and D. G. Truhlar, *Multidimensional Tunneling, Recrossing, and the Transmission Coefficient for Enzymatic Reactions*, Chem. Rev., 106 (2006), pp. 3140–3169, DOI: 10.1021/cr050308e.

[34]   Y. V. Suleimanov and J. Espinosa-Garcìa, *Recrossing and tunnelling in the kinetics study of the OH+CH$_4$ $\longrightarrow$ H$_2$O+CH$_3$ reaction.*, J. Phys. Chem. B, 120 (2016), pp. 1418–1428, DOI: 10.1021/acs.jpcb.5b02103.

[35]   B. C. Garrett and D. G. Truhlar, *Accuracy of Tunneling Corrections to Transition State Theory for Thermal Rate Constants of Atom Transfer Reactions*, J. Phys. Chem., 83 (1979), pp. 200–203, DOI: 10.1021/j100464a026.

[36]   B. C. Garrett, D. G. Truhlar, R. S. Grev, and A. W. Magnuson, *Improved Treatment of Threshold Contributions in Variational Transition-State Theory*, J. Phys. Chem., 84 (1980), pp. 1730–1748, DOI: 10.1021/j100450a013.

[37]   R. T. Skodje and D. G. Truhlar, *A General Small-Curvature Approximation for Transition-State-Theory Transmission Coefficients*, J. Phys. Chem., 85 (1981), pp. 3019–3023, DOI: 10.1021/j150621a001.

[38]   D. G. Truhlar, B. C. Garrett, and S. J. Klippenstein, *Current Status of Transition-State Theory*, J. Phys. Chem., 100 (1996), pp. 12771–12800, DOI: 10.1021/jp953748q.

[39]   J. Kästner, *Umbrella Sampling*, WIREs Comput. Mol. Sci., 1 (2011), pp. 932–942, DOI: 10.1002/wcms.66.

[40]   A. R. Leach, *Molecular Modeling - Principles and Applications*, Pearson, 2nd ed., 2001.

[41]   G. M. Torrie and J. P. Valleau, *Nonphysical Sampling Distributions in Monte Carlo Free-Energy Estimation: Umbrella Sampling*, J. Comput. Phys., 23 (1977), pp. 187–199, DOI: 10.1016/0021-9991(77)90121-8.

[42]   S. Kumar, J. M. Rosenberg, D. Bouzida, R. H. Swendsen, and P. A. Kollman, *The Weighted Histogram Analysis Method for Free-Energy Calculations on Biomolecules. I. The Method*, J. Comput. Chem., 13 (1992), pp. 1011–1021, DOI: 10.1002/jcc.540130812.

[43]   J. Kästner and W. Thiel, *Bridging the Gap Between Thermodynamic Integration and Umbrella Sampling Provides a Novel Analysis Method: "Umbrella Integration"*, J. Chem. Phys., 123 (2005), p. 144104, DOI: 10.1063/1.2052648.

[44]   W. K. den Otter and W. J. Briels, *Solvent Effect on the Isomerization Rate of Calix[4]arene Studied by Molecular Dynamics Simulations*, J. Am. Chem. Soc., 120 (1998), pp. 13167–13175, DOI: 10.1021/ja9741739.

[45] D. Chandler, *Statistical Mechanics of Isomerization Dynamics in Liquids and the Transition State Approximation*, J. Chem. Phys., 68 (1978), pp. 2959–2970, DOI: 10.1063/1.436049.

[46] C. C. Marston, G. G. Balint-Kurti, and R. N. Dixon, *Time-Dependent Quantum Dynamics of Reactive Scattering and the Calculation of Product Quantum State Distributions - A Study of the Collinear F+H$_2$(v=0) $\longrightarrow$ HF(v')+H Reaction*, Theor. Chim. Acta, 79 (1991), pp. 313–322, DOI: 10.1007/BF01113699.

[47] W. H. Miller, *"Direct" and "Correct" Calculation of Canonical and Microcanonical Rate Constants for Chemical Reactions*, J. Phys. Chem. A, 105 (1992), pp. 793–806, DOI: 10.1021/jp9732080.

[48] T. Seidemann and W. H. Miller, *Calculation of the Cumulative Reaction Probability via a Discrete Variable Representation with Absorbing Boundary Conditions*, J. Chem. Phys., 96 (1992), pp. 4412–4422, DOI: 10.1063/1.462832.

[49] M. H. Beck, A. Jäckle, G. A. Worth, and H.-D. Meyer, *The Multiconfiguration Time-Dependent Hartree (MCTDH) Method: a Highly Efficient Algorithm for Propagating Wavepackets*, Phys. Rep., 324 (2000), pp. 1–105, DOI: 10.1016/S0370-1573(99)00047-2.

[50] R. P. Feynman and A. R. Hibbs, *Quantum Mechanics and Path Integrals*, Dover Publications, amended edition ed., 2005.

[51] A. Agarwal, *Path Integral Techniques in Molecular Dynamics Simulations of Open Boundary Systems*, PhD thesis, Freie Universität Berlin, 2016.

[52] C. Gorgulla, *Free Energy Methods Involving Quantum Physics, Path Integrals, and Virtual Screenings*, PhD thesis, Freie Universität Berlin, 2018.

[53] Y. V. Suleimanov, R. Collepardo-Guevara, and D. E. Manolopoulos, *Bimolecular Reaction Rates from Ring Polymer Molecular Dynamics: Application to H+CH$_4$ $\longrightarrow$ H$_2$+CH$_3$*, J. Chem. Phys., 134 (2011), p. 044131, DOI: 10.1063/1.3533275.

[54] I. N. Levine, *Quantum Chemistry*, Allyn and Bacon, 3rd ed., 1983.

[55] A. Szabo and N. S. Ostlund, *Modern Quantum Chemistry*, Dover, 2nd ed., 1989.

[56] S. Sato, *On a New Method of Drawing the Potential Energy Surface*, J. Chem. Phys., 23 (1955), pp. 592–593, DOI: 10.1063/1.1742043.

[57] S. Sato, *Potential Energy Surface of the System of Three Atoms*, J. Chem. Phys., 23 (1955), pp. 2465–2466, DOI: 10.1063/1.1741936.

[58] A. Persky and H. Kornweitz, *Oscillating Reactivity of the Light Atom Transfer Reaction Cl+HCl $\longrightarrow$ ClH+Cl: Dependence on the Nature of the Potential Energy Surface*, J. Phys. Chem., 91 (1987), pp. 5496–5503, DOI: 10.1021/j100305a023.

[59] L. Martin-Gondre, C. Crespos, P. Larrègaray, J. C. Rayez, D. Conte, and B. van Ootegem, *Detailed Description of the Flexible Periodic London–Eyring–Polanyi–Sato Potential Energy Function*, Chem. Phys., 367 (2010), pp. 136–147, DOI: 10.1016/j.chemphys.2009.11.012.

[60] G. C. Schatz, *The Analytical Representation of Electronic Potential-Energy Surfaces*, Rev. Mod. Phys., 61 (1989), pp. 205–264, DOI: 10.1103/RevModPhys.61.669.

[61] D. G. Truhlar and C. J. Horowitz, *Functional Representation of Liu and Siegbahn's Accurate Ab Initio Potential Energy Calculations for H+H$_2$*, J. Chem. Phys., 68 (1978), pp. 2466–2476, DOI: 10.1063/1.436019.

[62] J. M. Bowman, J. S. Bittman, and L. B. Harding, *Ab Initio Calculations of Electronic and Vibrational Energies of HCO and HOC*, J. Chem. Phys., 85 (1986), pp. 911–921, DOI: 10.1063/1.451246.

[63] K. A. White and G. C. Schatz, *Analytical Potential Energy Surfaces for Ethynyl, Acetylene, and Vinyl*, J. Phys. Chem., 88 (1984), pp. 2049–2057, DOI: 10.1021/j150654a023.

[64] P. M. Agrawal, D. L. Thompson, and L. M. Raff, *Trajectory Studies of Unimolecular Reactions of Si_2H_4 and SiH_2 on a Global Potential Surface Fitted to Ab Initio and Experimental Data*, J. Chem. Phys., 89 (1988), pp. 741–750, DOI: 10.1063/1.455197.

[65] C. M. Handly and J. Behler, *Next Generation Interatomic Potentials for Condensed Systems*, Eur. Phys. J. B, 87 (2014), p. 152, DOI: 10.1140/epjb/e2014-50070-0.

[66] M. A. Collins, *Molecular Potential-Energy Surfaces for Chemical Reaction Dynamics*, Theor. Chem. Acc., 108 (2002), pp. 313–324, DOI: 10.1007/s00214-002-0383-5.

[67] H. M. Netzloff, M. A. Collins, and M. S. Gordon, *Growing Multiconfigurational Potential Energy Surfaces with Applications to $X+H_2(X = C, N, O)$ Reactions*, J. Chem. Phys., 124 (2006), p. 154104, DOI: 10.1063/1.2185641.

[68] G. G. Maisuradze, D. L. Thompson, A. F. Wagner, and M. Minkoff, *Interpolating Moving Least-Squares Methods for Fitting Potential Energy Surfaces: Detailed Analysis of One-Dimensional Applications*, J. Chem. Phys., 119 (2003), pp. 10002–10014, DOI: 10.1063/1.1617271.

[69] B. Kolb, P. Marshall, B. Zhao, B. Jiang, and H. Guo, *Representing Global Reactive Potential Energy Surfaces Using Gaussian Processes*, J. Phys. Chem. A, 121 (2017), pp. 2552–2557, DOI: 10.1021/acs.jpca.7b01182.

[70] J. Behler, *Constructing High-Dimensional Neural Network Potentials: A Tutorial Review*, Int. J. Quantum Chem., 115 (2015), pp. 1032–1050, DOI: 10.1002/qua.24890.

[71] P. Dauber-Osguthorpe and A. T. Hagler, *Biomolecular Force Fields: Where Have We Been, Where Are We Now, Where Do We Need to Go and How Do We Get There?*, J. Comput.-Aided Mol. Des., 33 (2018), pp. 133–203, DOI: 10.1007/s10822-018-0111-4.

[72] A. T. Hagler, *Force Field Development Phase II: Relaxation of Physics-Based Criteria... or Inclusion of More Rigorous Physics into the Representation of Molecular Energetics*, J. Comput.-Aided Mol. Des., 33 (2018), pp. 205–264, DOI: 10.1007/s10822-018-0134-x.

[73] N. L. Allinger, Y. H. Yuh, and J. H. Lii, *Molecular Mechanics. The MM3 Force Field for Hydrocarbons. 1*, J. Am. Chem. Soc., 111 (1989), pp. 8551–8566, DOI: 10.1021/ja00205a001.

[74] A. K. Rappe, C. J. Casewit, K. S. Colwell, W. A. Goddard, III, and W. M. Skiff, *UFF, a Full Periodic Table Force Field for Molecular Mechanics and Molecular Dynamics Simulations*, J. Am. Chem. Soc., 114 (1992), pp. 10024–10035, DOI: 10.1021/ja00051a040.

[75] A. C. T. van Duin, S. Dasgupta, F. Lorant, and W. A. Goddard, III., *ReaxFF: A Reactive Force Field for Hydrocarbons*, J. Phys. Chem. A, 105 (2001), pp. 9396–9409, DOI: 10.1021/jp004368u.

[76] J. M. Dieterich and B. Hartke, *OGOLEM: Global Cluster Structure Optimisation for Arbitrary Mixtures of Flexible Molecules. A Multiscaling, Object-Oriented Approach*, Mol. Phys., 108 (2010), pp. 279–291, DOI: 10.1080/00268970903446756.

[77] H. R. Larsson, A. C. T. van Duin, and B. Hartke, *Global Optimization of Parameters in the Reactive Force Field ReaxFF for SiOH*, J. Comput. Chem., 34 (2013), pp. 2178–2189, DOI: 10.1002/jcc.23382.

[78] M. Dittner, J. Müller, H. M. Aktulga, and B. Hartke, *Efficient Global Optimization of Reactive Force–Field Parameters*, J. Comput. Chem., 36 (2015), pp. 1550–1561, DOI: 10.1002/jcc.23966.

[79] J. Müller and B. Hartke, *ReaxFF Reactive Force Field for Disulfide Mechanochemistry, Fitted to Multireference ab Initio Data*, J. Chem. Theory Comput., 12 (2016), pp. 3913–3925, DOI: 10.1021/acs.jctc.6b00461.

[80] S. Bureekaew, S. Amirjalayer, M. Tafipolsky, C. Spickermann, T. K. Roy, and R. Schmid, *MOF-FF – A Flexible First-Principles Derived Force Field for Metal-Organic Frameworks*, Phys. Status Solidi B, 250 (2013), pp. 1128–1141, DOI: 10.1002/pssb.201248460.

[81] L. Vanduyfhuys, S. Vandenbrande, T. Verstraelen, R. Schmid, M. Waroquier, and V. van Speybroeck, *QuickFF: A Program for a Quick and Easy Derivation of Force Fields for Metal-Organic Frameworks from Ab Initio Input*, J. Comput. Chem., 36 (2015), pp. 1015–1027, DOI: 10.1002/jcc.23877.

[82] P.-O. Norrby and T. Liljefors, *Automated Molecular Mechanics Parameterization with Simultaneous Utilization of Experimental and Quantum Mechanical Data*, J. Comput. Chem., 19 (1998), pp. 1146–1166, DOI: 10.1002/(SICI)1096-987X(19980730)19:10<1146::AID-JCC4>3.0.CO;2-M.

[83] E. Hansen, A. R. Rosales, B. Tutkowski, P.-O. Norrby, and O. Wiest, *Prediction of Stereochemistry Using Q2MM*, Acc. Chem. Res., 49 (2016), pp. 996–1005, DOI: 10.1021/acs.accounts.6b00037.

[84] I. Cacelli and G. Prampolini, *Parametrization and Validation of Intramolecular Force Fields Derived from DFT Calculations*, J. Chem. Theory Comput., 3 (2007), pp. 1803–1817, DOI: 10.1021/ct700113h.

[85] G. Prampolini, P. R. Livotto, and I. Cacelli, *Accuracy of Quantum Mechanically Derived Force-Fields Parameterized from Dispersion-Corrected DFT Data: The Benzene Dimer as a Prototype for Aromatic Interactions*, J. Chem. Theory Comput., 11 (2015), pp. 5182–5196, DOI: 10.1021/acs.jctc.5b00642.

[86] S. Grimme, *QMDFF - A General Quantum Mechanically Derived Force Field for Molecules and Condensed Phase Simulations*. `https://www.chemie.uni-bonn.de/pctc/mulliken-center/software/qmdff/qmdff`.

[87] K. B. Wiberg, *Application of the Pople-Santry-Segal CNDO Method to the Cyclopropylcarbinyl and Cyclobutyl Cation and to Bicyclobutane*, Tetrahedron, 24 (1968), pp. 1083–1096, DOI: 10.1016/0040-4020(68)88057-3.

[88] I. Mayer, *Charge, Bond Order and Valence in the Ab Initio SCF Theory*, Chem. Phys. Lett., 97 (1983), pp. 270–274, DOI: 10.1016/0009-2614(83)80005-0.

[89] A. V. Marenich, S. V. Jerome, C. J. Cramer, and D. G. Truhlar, *Charge Model 5: An Extension of Hirshfeld Population Analysis for the Accurate Description of Molecular Interactions in Gaseous and Condensed Phases*, J. Chem. Theory Comput., 8 (2012), pp. 527–541, DOI: 10.1021/ct200866d.

[90] W. Li, S. Grimme, H. Krieg, J. Möllmann, and J. Zhang, *Accurate Computation of Gas Uptake in Microporous Organic Molecular Crystals*, J. Phys. Chem. C, 116 (2012), pp. 8865–8871, DOI: 10.1021/jp2112632.

[91] S. Grimme, J. Antony, S. Ehrlich, and H. Krieg, *A Consistent and Accurate Ab Initio Parametrization of Density Functional Dispersion Correction (DFT-D) for the 94 Elements H-Pu*, J. Chem. Phys., 132 (2010), p. 154104, DOI: 10.1063/1.3382344.

[92]   A. Warshel and R. M. Weiss, *An Empirical Valence Bond Approach for Comparing Reactions in Solutions and in Enzymes*, J. Am. Chem. Soc., 102 (1980), pp. 6218–6226, DOI: 10.1021/ja00540a008.

[93]   S. Shaik and P. C. Hiberty, *Valence Bond Theory, Its History, Fundamentals, and Applications: A Primer*, in Reviews in Computational Chemistry, vol. 20, Wiley-VCH, 2004.

[94]   P. C. Hiberty and S. Shaik, *A Survey of Recent Developments in Ab Initio Valence Bond Theory*, J. Comp. Chem., 28 (2007), pp. 137–151, DOI: 10.1002/jcc.20478.

[95]   F. Duarte and S. C. L. Kamerlin, *Theory and Applications of the Empirical Valence Bond Approach*, Wiley, 1st ed., 2017.

[96]   W. Heitler and F. London, *Wechselwirkung neutraler Atome und homöopolare Bindung nach der Quantenmechanik*, Z. Physik, 44 (1927), pp. 455–472, DOI: 10.1007/BF01397394.

[97]   J. Gerratt, M. Raimondi, D. Cooper, and P. B. Karadakov, *Modern Valence Bond Theory*, Chem. Soc. Rev., 26 (1997), pp. 87–100, DOI: 10.1039/CS9972600087.

[98]   W. A. Goddard, III., J. Thom H. Dunning, W. J. Hunt, and P. J. Hay, *Generalized Valence Bond Description of Bonding in Low-Lying States of Molecules*, Acc. Chem. Res., 6 (1973), pp. 368–376, DOI: 10.1021/ar50071a002.

[99]   M. J. Frisch, G. W. Trucks, H. B. Schlegel, G. E. Scuseria, M. A. Robb, J. R. Cheeseman, G. Scalmani, V. Barone, G. A. Petersson, H. Nakatsuji, X. Li, M. Caricato, A. V. Marenich, J. Bloino, B. G. Janesko, R. Gomperts, B. Mennucci, H. P. Hratchian, J. V. Ortiz, A. F. Izmaylov, J. L. Sonnenberg, D. Williams-Young, F. Ding, F. Lipparini, F. Egidi, J. Goings, B. Peng, A. Petrone, T. Henderson, D. Ranasinghe, V. G. Zakrzewski, J. Gao, N. Rega, G. Zheng, W. Liang, M. Hada, M. Ehara, K. Toyota, R. Fukuda, J. Hasegawa, M. Ishida, T. Nakajima, Y. Honda, O. Kitao, H. Nakai, T. Vreven, K. Throssell, J. A. Montgomery, Jr., J. E. Peralta, F. Ogliaro, M. J. Bearpark, J. J. Heyd, E. N. Brothers, K. N. Kudin, V. N. Staroverov, T. A. Keith, R. Kobayashi, J. Normand, K. Raghavachari, A. P. Rendell, J. C. Burant, S. S. Iyengar, J. Tomasi, M. Cossi, J. M. Millam, M. Klene, C. Adamo, R. Cammi, J. W. Ochterski, R. L. Martin, K. Morokuma, O. Farkas, J. B. Foresman, and D. J. Fox, *Gaussian 16 Revision B.01*, 2016. Gaussian Inc. Wallingford CT.

[100]   P. W. Atkins and R. S. Friedman, *Molecular Quantum Mechanics*, Oxford University Press, 5th ed., 2010.

[101]   G. Hong, E. Rosta, and A. Warshel, *Using the Constrained DFT Approach in Generating Diabatic Surfaces and Off Diagonal Empirical Valence Bond Terms for Modeling Reactions in Condensed Phases*, J. Phys. Chem. B, 110 (2006), pp. 19570–19574, DOI: 10.1021/jp0625199.

[102]   U. W. Schmitt and G. A. Voth, *Multistate Empirical Valence Bond Model for Proton Transport in Water*, J. Phys. Chem. B, 102 (1998), pp. 5547–5551, DOI: 10.1021/jp9818131.

[103]   Y. Mo and J. Gao, *An Ab Initio Molecular Orbital - Valence Bond (MOVB) Method for Simulating Chemical Reactions in Solution*, J. Phys. Chem. A, 104 (2000), pp. 3012–3020, DOI: 10.1021/jp994053i.

[104]   *The Nobel Prize in Chemistry 2013*. https://www.nobelprize.org/prizes/chemistry/2013/summary/.

[105]   S. C. L. Kamerlin and A. Warshel, *The Empirical Valence Bond Model: Theory and Applications*, WIREs Comput. Mol. Sci., 1 (2011), pp. 30–45, DOI: 10.1002/wcms.10.

[106] F. Jensen and P.-O. Norrby, *Transition States from Empirical Force Fields*, Theor. Chem. Acc., 109 (2003), pp. 1–7, DOI: 10.1007/s00214-002-0382-6.

[107] A. Warshel, *Dynamics of Reactions in Polar Solvents. Semiclassical Trajectory Studies of Electron-Transfer and Proton-Transfer Reactions*, J. Phys. Chem., 86 (1982), pp. 2218–2224, DOI: 10.1021/j100209a016.

[108] L. Mones, P. Kulánek, I. Simon, A. Laio, and M. Fuxreiter, *The Energy Gap as a Universal Reaction Coordinate for the Simulation of Chemical Reactions*, J. Phys. Chem. B, 113 (2009), pp. 7867–7873, DOI: 10.1021/jp9000576.

[109] L. Mones and G. Cyányi, *Topologically Invariant Reaction Coordinates for Simulating Multistate Chemical Reactions*, J. Phys. Chem. B, 116 (2012), pp. 14876–14885, DOI: 10.1021/jp307648s.

[110] T. J. F. Day, A. V. Soudackov, M. Cûma, U. W. Schmitt, and G. A. Voth, *A Second Generation Multistate Empirical Valence Bond Model for Proton Transport in Aqueous Systems*, J. Chem. Phys., 117 (2002), pp. 5839–5849, DOI: 10.1063/1.1497157.

[111] C. M. Maupin, K. F. Wong, A. V. Soudackov, S. Kim, and G. A. Voth, *A Multistate Empirical Valence Bond Description of Protonatable Amino Acids*, J. Phys. Chem. A, 110 (2006), pp. 631–639, DOI: 10.1021/jp053596r.

[112] R. Vuilleumier and D. Borgis, *Quantum Dynamics of an Excess Proton in Water Using an Extended Empirical Valence-Bond Hamiltonian*, J. Phys. Chem. B, 102 (1998), pp. 4261–4264, DOI: 10.1021/jp9807423.

[113] R. Vuilleumier and D. Borgis, *Transport and Spectroscopy of the Hydrated Proton: A molecular Dynamics Study*, J. Chem. Phys., 111 (1999), pp. 4251–4266, DOI: 10.1063/1.479723.

[114] Y.-T. Chang and W. H. Miller, *An Empirical Valence Bond Model for Constructing Global Potential Energy Surfaces for Chemical Reactions of Polyatomic Molecular Systems*, J. Phys. Chem., 94 (1990), pp. 5884–5888, DOI: 10.1021/j100378a052.

[115] A. Rodriguez and C. Tsallis, *A Generalization of the Cumulant Expansion. Application to a Scale-Invariant Probabilistic Model*, J. Math. Phys., 51 (2010), p. 073301, DOI: 10.1063/1.3448944.

[116] Y.-T. Chang, C. Minichino, and W. H. Miller, *Classical Trajectory Studies of the Molecular Dissociation Dynamics of Formaldehyde: $H_2CO \longrightarrow H_2+CO$*, J. Chem. Phys., 96 (1992), pp. 4341–4355, DOI: 10.1063/1.462826.

[117] H. B. Schlegel and J. L. Sonnenberg, *Empirical Valence-Bond Models for Reactive Potential Energy Surfaces Using Distributed Gaussians*, J. Chem. Theory Comput., 2 (2006), pp. 905–911, DOI: 10.1021/ct600084p.

[118] Y. Kim, J. C. Corchado, J. Villà, J. Xing, and D. G. Truhlar, *Multiconfiguration Molecular Mechanics Algorithm for Potential Energy Surfaces of Chemical Reactions*, J. Chem. Phys., 112 (2000), pp. 2718–2735, DOI: 10.1063/1.480846.

[119] O. Tishchenko and D. G. Truhlar, *Gradient-based Multiconfiguration Shepard Interpolation for Generating Potential Energy Surfaces for Polyatomic Reactions*, J. Chem. Phys., 132 (2010), p. 084109, DOI: 10.1063/1.3310296.

[120] S. C. L. Kamerlin, J. Cao, E. Rosta, and A. Warshel, *On Unjustifiably Misrepresenting the EVB Approach While Simultaneously Adopting It*, J. Phys. Chem. B, 113 (2009), pp. 10905–10915, DOI: 10.1021/jp901709f.

[121] J. L. Sonnenberg, K. F. Wong, G. A. Voth, and H. B. Schlegel, *Distributed Gaussian Valence Bond Surface Derived from Ab Initio Calculations*, J. Chem. Theory Comput., 5 (2009), pp. 949–961, DOI: 10.1021/ct800477y.

[122] K. F. Wong, J. L. Sonnenberg, F. Paesani, T. Yamamoto, J. Vanicek, W. Zhang, H. B. Schlegel, D. A. Case, T. E. Cheatham, III, W. H. Miller, and G. A. Voth, *Proton Transfer Studied Using a Combined Ab Initio Reactive Potential Energy Surface with Quantum Path Integral Methodology*, J. Chem. Theory Comput., 6 (2010), pp. 2566–2580, DOI: 10.1021/ct900579k.

[123] J. P. Perdew, A. Ruzsinszky, J. Tao, V. N. Staroverov, G. E. Scuseria, and G. I. Csonka, *Prescription for the Design and Selection of Density Functional Approximations: More Constraint Satisfaction with Fewer Fits*, J. Chem. Phys., 123 (2005), p. 062201, DOI: 10.1063/1.1904565.

[124] J. Steffen, *Reaktive Kraftfelder auf Basis quantenchemischer Rechnungen - Implementation und Anwendungen*, Master's thesis, University of Kiel, 2015.

[125] S. Trobro and J. Åqvist, *Mechanism of Peptide Bond Synthesis on the Ribosome*, Proc. Natl. Acad. Sci. U.S.A., 102 (2005), pp. 12395–12400, DOI: 10.1073/pnas.0504043102.

[126] S. Trobro and J. Åqvist, *Analysis of Predictions for the Catalytic Mechanism of Ribosomal Peptidyl Transfer*, Biochemistry, 45 (2006), pp. 7049–7056, DOI: 10.1021/bio605383.

[127] J. A. Rackers, Z. Wang, C. Lu, M. L. Laury, L. Lagardère, M. J. Schnieders, J.-P. Piquemal, P. Ren, and J. W. Ponder, *Tinker 8: Software Tools for Molecular Design*, J. Chem. Theory Comput., 14 (2018), pp. 5273–5289, DOI: 10.1021/acs.jctc.8b00529.

[128] G. A. Tribello, M. Bonomi, D. Branduardi, C. Camilloni, and G. Bussi, *PLUMED2: New Feathers for an Old Bird*, Comp. Phys. Comm., 185 (2013), pp. 604–613, DOI: 10.1016/j.cpc.2013.09.018.

[129] A. Grossfield, *WHAM: the Weighted Histogram Analysis Method*. http://membrane.urmc.rochester.edu/wordpress/?page_id=126.

[130] F. Neese, *The ORCA Program System*, WIREs Comput. Mol. Sci., 2 (2012), pp. 73–78, DOI: 10.1002/wcms.81.

[131] F. Neese, *Software Update: the ORCA Program System, Version 4.0*, WIREs Comput. Mol. Sci., 8 (2018), p. e1327, DOI: 10.1002/wcms.1327.

[132] *TURBOMOLE V6.2 2010, a Development of University of Karlsruhe and Forschungszentrum Karlsruhe GmbH, 1989-2007, TURBOMOLE GmbH, since 2007; Available From* http://www.turbomole.com.

[133] *CP2K: Open Source Molecular Dynamics*. https://www.cp2k.org/.

[134] J. Hutter, M. Iannuzzi, F. Schiffmann, and J. VandeVondele, *cp2k: Atomistic Simulations of Condensed Matter Systems*, WIREs Comput. Mol. Sci., 4 (2014), pp. 15–25, DOI: 10.1002/wcms.1159.

[135] K. Levenberg, *A Method for the Solution of Certain Non-Linear Problems in Least Squares*, Quart. Appl. Math., 2 (1944), pp. 164–168, DOI: 10.1090/qam/10666.

[136] D. W. Marquardt, *An Algorithm for Least-Squares Estimation of Nonlinear Parameters*, J. Soc. Indust. Appl. Math., 11 (1963), pp. 431–441, DOI: 10.1137/0111030.

[137] *Free vector graphic on Pixabay - Litter Disposal Person*. https://pixabay.com/vectors/litter-disposal-person-trash-can-44039/.

[138] D. G. Truhlar and C. J. Horowitz, *Functional Representation of Liu and Siegbahn's Accurate Ab Initio Potential Energy Calculations for H+H₂*, J. Chem. Phys., 68 (1978), pp. 2466–2476, DOI: 10.1063/1.436019.

[139] D. C. Clary, *Exchange Reactions of Hydrogen Halides with Hydrogenic Atoms*, Chem. Phys., 71 (1982), pp. 117–125, DOI: 10.1016/0301-0104(82)87011-0.

[140] G. C. Schatz and H. Elgersma, *A Quasi-Classical Trajectory Study of Product Vibrational Distributions in the OH+H₂ ⟶ H₂O+H Reaction*, Chem. Phys. Lett., 73 (1980), pp. 21–25, DOI: 10.1016/0009-2614(80)85193-1.

[141] M. Monge-Palacios, C. Rangel, J. C. Corchado, and J. Espinosa-Garcìa, *Analytical Potential Energy Surface for the Reaction with Intermediate Complexes NH₃+Cl ⟶ NH₂+HCl: Application to the Kinetics Study*, Int. J. Quantum Chem., 112 (2012), pp. 1887–1903, DOI: 10.1002/qua.23165.

[142] J. C. Corchado, J. L. Bravo, and J. Espinosa-Garcìa, *The Hydrogen Abstraction Reaction. I. New Analytical Potential Energy Surface Based on Fitting to Ab Initio Calculations*, J. Chem. Phys., 130 (2009), p. 184314, DOI: 10.1063/1.3132223.

[143] M. Monge-Palacios, C. Rangel, and J. Espinosa-Garcìa, *Ab Initio Based Potential Energy Surface and Kinetics Study of the OH+NH₃ Hydrogen Abstraction Reaction*, J. Chem. Phys., 138 (2013), p. 084305, DOI: 10.1063/1.4792719.

[144] J. Espinosa-Garcìa and J. C. Corchado, *Potential Energy Surface for a Seven-Atom Reaction. Thermal Rate Constants and Kinetic Isotope Effects for CH₄+OH*, J. Chem. Phys., 112 (2000), pp. 5731–5739, DOI: 10.1063/1.481148.

[145] J. Espinosa-Garcìa, C. Rangel, and J. C. Corchado, *Rate Constant Calculations of the GeH₄+OH/OD ⟶ GeH₃+H₂O/HOD Reactions Using an Ab Initio Based Full-Dimensional Potential Energy Surface*, Phys. Chem. Chem. Phys., 18 (2016), pp. 16941–16949, DOI: 10.1039/c6cp02986h.

[146] J. Espinosa-Garcìa, C. Rangel, and Y. V. Suleimanov, *Kinetics Study of the CN+CH₄ Hydrogen Abstraction Reaction Based on a New Ab Initio Analytical Full-Dimensional Potential Energy Surface*, Phys. Chem. Chem. Phys., 19 (2017), pp. 19341–19351, DOI: 10.1039/c7cp03499g.

[147] A. Chakraborty, Y. Zhao, H. Lin, and D. G. Truhlar, *Combined Valence Bond Molecular Mechanics Potential Energy Surface and Direct Dynamics Study of Rate Constants and Kinetic Isotope Effects for the H+C₂H₆ Reaction*, J. Chem. Phys., 124 (2006), p. 044315, DOI: 10.1063/1.2132276.

[148] D. F. Shanno, *Conditioning of Quasi-Newton Methods for Function Minimization*, Math. Comp., 24 (1970), pp. 647–656, DOI: 10.1090/s0025-5718-1970-0274029-x.

[149] K. Fukui, *The Path of Chemical Reactions - The IRC Approach*, Acc. Chem. Res., 14 (1981), pp. 363–368, DOI: 10.1021/ar00072a001.

[150] Hans C. Andersen, *Molecular Dynamics Simulations at Constant Pressure and/or Temperature*, J. Chem. Phys., 72 (1980), pp. 2384–2393, DOI: 10.1063/1.439486.

[151] Hans C. Andersen, *Rattle: A "Velocity" Version of the Shake Algorithm for Molecular Dynamics Calculations*, J. Comput. Phys., 52 (1983), pp. 24–34, DOI: 10.1016/0021-9991(83)90014-1.

[152] Yury V. Suleimanov, *Surface Diffusion of Hydrogen on Ni(100) from Ring Polymer Molecular Dynamics*, J. Phys. Chem. C, 116 (2012), pp. 11141–11153, DOI: 10.1021/jp302453z.

[153] *National Institute of Standards and Technology (NIST): Chemical Kinetics Database.* `https://kinetics.nist.gov/kinetics/index.jsp`.

[154] C. Riplinger and F. Neese, *An Efficient and Near Linear Scaling Pair Natural Orbital Based Local Coupled Cluster Method*, J. Chem. Phys., 138 (2013), p. 034106, DOI: 10.1063/1.4773581.

[155] C. Rieplinger, B. Sandhoefer, A. Hansen, and F. Neese, *Natural Triple Excitations in Local Coupled Cluster Calculations with Pair Natural Orbitals*, J. Chem. Phys., 139 (2013), p. 134101, DOI: 10.1063/1.4821834.

[156] E. Gonzalez-Lavado, J. C. Corchado, Y. V. Suleimanov, W. H. Green, and J. Espinosa-Garcìa, *Theoretical Kinetics Study of the O(^{3}P)+CH$_4$/CD$_4$ Hydrogen Abstraction Reaction: The Role of Anharmonicity, Recrossing Effects, and Quantum Mechanical Tunneling*, J. Phys. Chem. A, 118 (2014), pp. 3243–3252, DOI: 10.1021/jp5028965.

[157] S. Canneaux, B. Xerri, F. Louis, and L. Cantrel, *Theoretical Study of the Gas-Phase Reactions of Iodine Atoms (^{2}P$_{3/2}$) with H$_2$, H$_2$O, HI and OH*, J. Phys. Chem. A, 114 (2010), pp. 9270–9288, DOI: 10.1021/jp104163t.

[158] T. H. Dunning, Jr., *Gaussian Basis Sets for Use in Correlated Molecular Calculations. I. The Atoms Boron Through Neon and Hydrogen*, J. Chem. Phys., 90 (1989), pp. 1007–1023, DOI: 10.1063/1.456153.

[159] K. Lorenz, H. G. Wagner, and R. Zellner, *Rate Measurements for the Reactions H+I$_2$ ⟶ HI+I and H+HI ⟶ H$_2$+I by Lyman-α-Fluorescence*, Ber. Bunsenges. Phys. Chem., 83 (1979), pp. 556–560, DOI: 10.1002/bbpc.19790830603.

[160] M. A. ter Horst, G. C. Schatz, and L. B. Harding, *Potential Energy Surface and Quasiclassical Trajectory Studies of the CN+H$_2$ Reaction*, J. Chem. Phys., 105 (1996), pp. 558–571, DOI: 10.1063/1.471909.

[161] A. F. Wagner and R. A. Bair, *An Ab Initio Determination of the Rate Constant for H$_2$+CN ⟶ H+HCN*, Int. J. Chem. Kinet., 18 (1986), pp. 473–486, DOI: 10.1002/kin.550180406.

[162] Q. Sun, D. L. Yang, N. S. Wang, J. M. Bowman, and M. C. Lin, *Experimental and Reduced Dimensionality Quantum Rate Coefficients for H$_2$(D$_2$)+CN ⟶ H(D)CN+H(D)*, J. Chem. Phys., 93 (1990), pp. 4730–4739, DOI: 10.1063/1.458663.

[163] I. R. Sims and I. W. M. Smith, *Rate Constants for the Reactions CN(v=0), CN(v=1)+H$_2$,D$_2$ ⟶ HCN, DCN+H,D Between 295 and 768 K, and Comparisons with Transition State Theory Calculations*, Chem. Phys. Lett., 149 (1988), pp. 565–571, DOI: 10.1016/0009-2614(88)80384-1.

[164] A. Jacobs, M. Wahl, R. Weller, and J. Wolfrum, *Measurements of Absolute Rate Coefficients for the Reactions of CN Radicals with H$_2$O, H$_2$, and CO$_2$ in the Temperature Range 295 K ≤ T ≤ 1027 K*, Symp. Int. Combust. Proc., 22 (1989), pp. 1093–1100, DOI: 10.1016/S0082-0784(89)80119-5.

[165] X. Yu, S.-M. Li, J.-Y. Liu, Z.-F. Xu, Z.-S. Li, and C.-C. Sun, *Direct Dynamics Study on the Hydrogen Abstraction Reaction PH$_3$+H ⟶ PH$_2$+H$_2$*, J. Chem. Phys. A, 103 (1999), pp. 6402–6405, DOI: 10.1021/jp990367u.

[166] W. J. Hehre, R. Ditchfield, and J. A. Pople, *Self—Consistent Molecular Orbital Methods. XII. Further Extensions of Gaussian—Type Basis Sets for Use in Molecular Orbital Studies of Organic Molecules*, J. Chem. Phys., 56 (1972), pp. 2257–2261, DOI: 10.1063/1.1677527.

[167] R. Krishnan, J. S. Binkley, R. Seeger, and J. A. Pople, *Selfâ ̆ȐConsistent Molecular Orbital Methods. XX. A Basis Set for Correlated Wave Functions*, J. Chem. Phys., 72 (1980), pp. 650–654, DOI: 10.1063/1.438955.

[168] J. H. Lee, J. V. Michael, W. A. Payne, D. A. Whytock, and L. J. Stief, *Absolute Rate Constant for the Reaction of Atomic Hydrogen with Phosphine over the Temperature Range 209 to 495 K*, J. Chem. Phys., 65 (1976), pp. 3280–3283, DOI: 10.1063/1.433502.

[169] N. L. Arthur and I. A. Cooper, *Arrhenius Parameters for the Reactions of H Atoms with PH_3 and AsH_3*, J. Chem. Soc. Faraday Trans., 93 (1997), pp. 521–524, DOI: 10.1039/a606454j.

[170] M. E. Clarkson and H. O. Pritchard, *Partial State-to-State Calculation of the Infinite-Pressure Rate Constant for the Isomerization of Methyl Isocyanide*, Chem. Phys., 117 (1987), pp. 29–37, DOI: 10.1016/0301-0104(87)80094-0.

[171] F. W. Schneider and B. S. Rabinovitch, *The Thermal Unimolecular Isomerization of Methyl Isocyanide. Fall-Off Behavior*, J. Am. Chem. Soc., 84 (1962), pp. 4215–4230, DOI: 10.1021/ja00881a006.

[172] J. L. Collister and H. Q. Pritchard, *The Thermal Isomerisation of Methyl Isocyanide in the Temperature Range 120-320 °C*, Can. J. Chem., 54 (1976), pp. 2380–2384, DOI: 10.1139/v76-339.

[173] J.-F. Xiao, Z.-S. Li, Y.-H. Ding, J.-Y. Liu, X.-R. Huang, and C.-c. Sun, *Density Functional Theory and ab Initio Direct Dynamics Studies on the Hydrogen Abstraction Reactions of Chlorine Atoms with $CHCl_{3-n}F_n$ (n = 0, 1, and 2) and CH_2Cl_2*, J. Phys. Chem. A, 106 (2002), pp. 320–325, DOI: 10.1021/jp013405u.

[174] C. Lee, W. Yang, and R. G. Parr, *Development of the Colle-Salvetti Correlation-Energy Formula into a Functional of the Electron Density*, Phys. Rev. B, 37 (1988), pp. 785–789, DOI: 10.1103/PhysRevB.37.785.

[175] P. Goldfinger, G. Huybrechts, and G. Martens, *Elementary Rate Constants in Atomic Chlorination reactions. Part 2.-Experiments in Competitive Systems*, Trans. Faraday Soc., 57 (1961), pp. 2210–2219, DOI: 10.1039/tf9615702210.

[176] M. A. A. Clyne and R. F. Walker, *Absolute Rate Constants for Elementary Reactions in the Chlorination of CH_4, CD_4, CH_3Cl, CH_2Cl_2, $CHCl_3$, $CDCl_3$ and $CBrCl_3$*, J. Chem. Soc. Faraday Trans. 1, 69 (1973), pp. 1547–1567, DOI: 10.1039/f19736901547.

[177] M. G. Bryukov, I. R. Slagle, and V. D. Knyadzev, *Kinetics of Reactions of Cl Atoms with Methane and Chlorinated Methanes*, J. Phys. Chem. A, 106 (2002), pp. 10532–10542, DOI: 10.1021/jp0257909.

[178] K. Pei and H. Y. Li, *Ab Initio and Kinetic Calculations for the Reactions of Cl with SiH_nCl_{4-n} (n = 1, 2, 3, 4)*, J. Chem. Phys., 121 (2004), pp. 6738–6742, DOI: 10.1063/1.1788651.

[179] L. Ding and P. Marshall, *Kinetic Studies of the Reactions of Atomic Chlorine and Bromine with Silane*, J. Phys. Chem., 96 (1992), pp. 2197–2201, DOI: 10.1021/j100184a031.

[180] Q. Zhang, D. Zhang, S. Wang, and Y. Gu, *Ab Initio and Kinetic Calculations for the Reactions of H with $(CH_3)_{(4-n)}GeH_n$ (n = 1, 2, 3, 4)*, J. Phys. Chem. A, 106 (2002), pp. 122–129, DOI: 10.1021/jp012730e.

[181] D. F. Nava, W. A. Payne, G. Marston, and L. J. Stief, *The Reaction of Atomic Hydrogen with Germane: Temperature Dependence of the Rate Constant and Implications for Germane Photochemistry in the Atmospheres of Jupiter and Saturn*, J. Geophys. Res., 98 (1993), pp. 5531–5537, DOI: 10.1029/92je02806.

[182] N. L. Arthur, I. A. Cooper, and L. A. Miles, *Kinetic Isotope Effect for the Reaction of H Atoms with GeH_4 and GeD_4*, Int. J. Chem. Kinet., 29 (1997), pp. 237–243, DOI: 10.1002/(SICI)1097-4601(1997)29:4<237::AID-KIN1>3.0.CO;2-V.

[183] Y. Li, D. W. Brenner, X. Dong, and C. Sun, *Ab Initio Study of the Role of Entropy in the Kinetics of Acetylene Production in Filament-Assisted Diamond Growth Environments*, J. Phys. Chem. A, 110 (2006), pp. 132–140, DOI: 10.1021/jp054914p.

[184] Y. Ge, M. S. Gordon, F. Battaglia, and R. O. Fox, *Theoretical Study of the Pyrolysis of Methyltrichlorosilane in the Gas Phase. 1. Thermodynamics*, J. Phys. Chem. A, 111 (2007), pp. 1462–1474, DOI: 10.1021/jp065453q.

[185] Y. Ge, M. S. Gordon, F. Battaglia, and R. O. Fox, *Theoretical Study of the Pyrolysis of Methyltrichlorosilane in the Gas Phase. 2. Reaction Paths and Transition States*, J. Phys. Chem. A, 111 (2007), pp. 1475–1486, DOI: 10.1021/jp065455a.

[186] Y. Ge, M. S. Gordon, F. Battaglia, and R. O. Fox, *Theoretical Study of the Pyrolysis of Methyltrichlorosilane in the Gas Phase. 3. Reaction Rate Constant Calculations*, J. Phys. Chem. A, 114 (2010), pp. 2384–2392, DOI: 10.1021/jp911673h.

[187] C. Sosa and H. B. Schlegel, *Ab Initio Calculations on the Barrier Height for the Hydrogen Addition to Ethylene and Formaldehyde. The Importance of Spin Projection*, Int. J. Quantum Chem., 29 (1986), pp. 1001–1015, DOI: 10.1002/qua.560290435.

[188] A. F. Dodonov and G. K. Lavrovskaya, *Mass-Spectroscopic Determination of Rate Constants for Elementary Reactions. III. The Reactions $H+C_2H_4$, $H+C_3H_6$, and $H+n\text{-}C_4H_8$*, Kinet. Catal., 10 (1969).

[189] L. Teng and W. E. Jones, *Kinetics of the Reactions of Hydrogen Atoms with Ethylene and Vinyl Fluoride*, J. Chem. Soc. Faraday Trans. 1, 68 (1972), pp. 1267–1277, DOI: 10.1039/f19726801267.

[190] P. D. Lightfoot and M. J. Pilling, *Temperature and Pressure Dependence of the Rate Constant for the Addition of H to C_2H_4*, J. Phys. Chem., 91 (1987), pp. 3373–3379, DOI: 10.1021/j100296a054.

[191] J. T. Jodkowski, M.-T. Rayez, and J.-C. Rayes, *Theoretical Study of the Kinetics of the Hydrogen Abstraction from Methanol. 2. Reaction of Methanol with Chlorine and Bromine Atoms*, J. Phys. Chem. A, 102 (1998), pp. 9230–9243, DOI: 10.1021/jp980846d.

[192] J. V. Michael, D. F. Nava, W. A. Payne, and L. J. Stief, *Rate Constants for the Reaction of Atomic Chlorine with Methanol and Dimethyl Ether from 200 to 500 K*, J. Chem. Phys., 70 (1979), pp. 3652–3656, DOI: 10.1063/1.437957.

[193] P. D. Lightfoot, B. Veyret, and R. Lesclaux, *Flash Photolysis Study of the $CH_3O_2+HO_2$ Reaction Between 248 and 573 K*, J. Phys. Chem., 94 (1990), pp. 708–714, DOI: 10.1021/j100365a035.

[194] N. Kungwan and T. N. Truong, *Kinetics of the Hydrogen Abstraction $\cdot CH_3+Alkane \longrightarrow CH_4+Alkyl$ Reaction Class: An Application of the Reaction Class Transition State Theory*, J. Phys. Chem. A, 109 (2005), pp. 7742–7750, DOI: 10.1021/jp051799.

[195] F. S. Dainton, K. J. Ivin, and F. Wilkinson, *The Kinetics of the Exchange Reaction $CH_3+CH_4 \longrightarrow CH_4+CH_3$ Using 14C as Tracer*, Trans. Faraday Soc., 55 (1959), DOI: 10.1039/tf9595500929.

[196] N. L. Arthur and T. N. Bell, *An Evaluation of the Kinetic Data for Hydrogen Abstraction from Silanes in the Gas Phase*, Rev. Chem. Intermed, 2 (1978), pp. 37–74, DOI: 10.1007/BF03055540.

[197] Z.-F. Xu, S.-M. Li, Y.-X. Yu, Z.-S. Li, and C. C. Sun, *Theoretical Studies on the Reaction Path Dynamics and Variational Transition-State Theory Rate Constants of the Hydrogen-Abstraction Reactions of the $NH(X^3\Sigma^-)$ Radical with Methane and Ethane*, J. Phys. Chem. A, 103 (1999), pp. 4910–4917, DOI: 10.1021/jp984499j.

[198] M. Rohrig and H. G. Wagner, *A Kinetic Study about the Reactions of NH(X$^3\Sigma^-$) with Hydrocarbons. Part 1: Saturated Hydrocarbons and Acetaldehyde*, Ber. Bunsenges. Phys. Chem., 98 (1994), pp. 858–863, DOI: 10.1002/bbpc.19940980615.

[199] B. Jing, J.-y. Liu, Z.-s. Li, Y. Wang, L. Wang, H.-q. He, and C.-c. Sun, *Direct Dynamics Studies on the Hydrogen Abstraction Reactions CF$_3$O+CH$_4$(CD$_4$) $\longrightarrow$ CF$_3$OH(CF$_3$OD)+CCH$_3$(CD$_3$)*, Comput. Theor. Chem., 732 (2005), pp. 225–231, DOI: 10.1016/j.theochem.2005.07.018.

[200] A. D. Becke, *Becke's Three Parameter Hybrid Method Using the LYP Correlation Functional*, J. Chem. Phys., 98 (1993), pp. 5648–5652.

[201] P. J. Stephens, F. J. Devlin, C. F. Chabalowski, and M. J. Frisch, *Ab Initio Calculation of Vibrational Absorption and Circular Dichroism Spectra Using Density Functional Force Fields*, J. Phys. Chem., 98 (1994), pp. 11623–11627, DOI: 10.1021/j100096a001.

[202] N. R. Jensen, D. R. Hanson, and C. J. Howard, *Temperature Dependence of the Gas Phase Reactions of CF$_3$O with CH$_4$ and NO*, J. Phys. Chem., 98 (1994), pp. 8574–8579, DOI: 10.1021/j100085a042.

[203] C. Bourbon, C. Fittschen, J. P. Sawerysyn, and P. Devolder, *Temperature Dependence of the Gas Phase Reaction Rates of CF$_3$O with Methane, Ethane, and Isobutane*, J. Phys. Chem., 99 (1995), pp. 15102–15107, DOI: 10.1021/j100041a028.

[204] G. Bednarek, J. P. Kohlmann, H. Saathoff, and R. Zellner, *Temperature Dependence and Product Distribution for the Reaction of CF$_3$O Radicals with Methane*, Z. Phys. Chem., 188 (1995), pp. 1–15, DOI: 10.1524/zpch.1995.188.Part_1_2.001.

[205] C. Adamo and V. Barone, *Toward Reliable Density Functional Methods Without Adjustable Parameters: The PBE0 Model*, J. Phem. Phys., 110 (1999), pp. 6158–6170, DOI: 10.1063/1.478522.

[206] M. Ernzerhof and G. E. Scuseria, *Assessment of the Perdew-Burke-Ernzerhof Exchange-Correlation Functional*, J. Chem. Phys., 110 (1999), pp. 5029–5036, DOI: 10.1063/1.478401.

[207] S. Grimme, J. Anthony, S. Ehrlich, and H. Krieg, *A Consistent and Accurate Ab Initio Parametrization of Density Functional Dispersion Correction (DFT-D) for the 94 Elements H-Pu*, J. Chem. Phys., 132 (2010), p. 154104, DOI: 10.1063/1.3382344.

[208] R. Walsh and J. M. Wells, *The Kinetics of Reversible Diels-Alder Reactions in the Gas Phase. Part II. Cyclopentadiene and Ethylene*, J. Chem. Soc. Perkin Trans. 2, 2 (1976), pp. 52–55, DOI: 10.1039/P29760000052.

[209] J. H. Kiefer, S. S. Kumaran, and S. Sundaram, *Vibrational Relaxation, Dissociation, and Dissociation Incubation Times in Norbornene*, J. Chem. Phys., 99 (1993), pp. 3531–3541, DOI: 10.1063/1.466151.

[210] J. Müller, *Theoretical Investigations of Covalent Mechanochemistry* , PhD thesis, Christian-Albrechts Universität zu Kiel, 2017.

[211] J. Ribas-Arino and D. Marx, *Covalent Mechanochemistry: Theoretical Concepts and Computational Tools with Applications to Molecular Nanomechanics*, Chem. Rev., 112 (2012), pp. 5412–5487, DOI: 10.1021/cr200399q.

[212] L. Takacs, *The Historical Development of Mechanochemistry*, Chem. Soc. Rev., 42 (2013), pp. 7649–7659, DOI: 10.1039/C2CS35442J.

[213] G. Binnig and C. F. Quate, *Atomic Force Microscope*, Phys. Rev. Lett., 56 (1986), pp. 930–933, DOI: 10.1103/PhysRevLett.56.930.

[214] M. Grandbois, M. K. Beyer, M. Rief, H. Clausen-Schaumann, and H. E. Gaub, *How Strong Is a Covalent Bond?*, Science, 283 (1999), pp. 1727–1730, DOI: 10.1126/science.283.5408.1727.

[215] D. Schütze, K. Holz, J. Müller, M. K. Beyer, U. Lüning, and B. Hartke, *Pinpointing Mechanochemical Bond Rupture by Embedding the Mechanophore into a Macrocycle*, Angew. Chem. Int. Ed., 54 (2015), pp. 2556–2559, DOI: 10.1002/anie.201409691.

[216] J. Müller and B. Hartke, *ReaxFF Reactive Force Field for Disulfide Mechanochemistry, Fitted to Multireference Ab Initio Data*, J. Chem. Theory Comput., 12 (2016), pp. 3913–3925, DOI: 10.1021/acs.jctc.6b00461.

[217] M. Kudera, C. Eschbaumer, H. E. Gaub, and U. S. Schubert, *Analysis of Metallo-Supramolecular Systems Using Single-Molecule Force Spectroscopy*, Adv. Funct. Mater., 13 (2003), pp. 615–620, DOI: 10.1002/adfm.200304359.

[218] J. Ribas-Arino, S. Motoyuki, and D. Marx, *Unravelling the Mechanism of Force-Induced Ring-Opening of Benzocyclobutenes*, Chem. Eur. J., 15 (2009), pp. 13331–13335, DOI: 10.1002/chem.200902573.

[219] J. Wang, T. B. Kouznetsova, Z. Niu, M. T. Ong, H. M. Klukovich, A. L. Rheingold, T. J. Martinez, and S. L. Craig, *Inducing and quantifying forbidden reactivity with single-molecule polymer mechanochemistry*, Nature Chemistry, 7 (2015), pp. 323–327, DOI: 10.1038/nchem.2185.

[220] J. Steffen, J. Gamez, and B. Hartke, *Theoretical Investigation of Urethane Synthesis Based on EVB-QMDFF-RPMD*, in preparation.

[221] E. Delebecq, J.-P. Pascault, B. Boutevin, and F. Ganachaud, *On the Versatility of Urethane/Urea Bonds: Reversibility, Blocked Isocyanate, and Non-isocyanate Polyurethane*, Chem. Rev., 113 (2013), pp. 80–118, DOI: 10.1021/cr300195n.

[222] E. Sacher, *A re-Examination of the Polyurethane Reaction*, J. Macromol. Sci. B, 16 (1979), pp. 525–538, DOI: 10.1080/00222347908215180.

[223] A. A. Caraculacu and S. Coseri, *Isocyanates in Polyaddition Processes. Structure and Reaction Mechanisms*, Prog. Polym. Sci., 26 (2001), pp. 799–851, DOI: 10.1016/s0079-6700(00)00033-2.

[224] J. W. Baker and J. Gaunt, *4. The Mechanism of the Reaction of Aryl isoCyanates with Alcohols and Amines. Part III. The "Spontaneous" Reaction of Phenyl isoCyanate with Various Alcohols. Further Evidence Relating to the Anomalous Effect of Dialkylanilines in the Base-Catalysed Reaction.*, J. Chem. Soc., (1949), pp. 19–24, DOI: 10.1039/jr9490000019.

[225] J. R. Fischer, *Catalysis in the Preparation of Nitropolyurethanes*, Tetrahedron, 19 (1963), pp. 97–104, DOI: 10.1016/s0040-4020(63)80045-9.

[226] M. Ako and J. P. Kennedy, *Polyisobutylene-Based Urethane Foams*, Polym. Bull., 19 (1988), pp. 137–143, DOI: 10.1007/bf00257006.

[227] M. Sato, *The Rates of Reaction of 1-Alkenyl Isocyanates with Methanol*, J. Am. Chem. Soc., 82 (1960), pp. 3893–3897, DOI: 10.1021/ja01500a027.

[228] J. L. Han, C. H. Yu, Y. H. Lin, and K. H. Hsieh, *Kinetic Study of the Urethane and Urea Reactions of Isophorone Diisocyanate*, J. Appl. Polym. Sci., 107 (2008), pp. 3891–3902, DOI: 10.1002/app.27421.

[229] J. W. Baker and J. B. Holdsworth, *Kinetic Examination of the Reaction of Aryl Isocyanates with Methyl Alcohol*, J. Chem. Soc., (1947), pp. 713–126.

[230] A. E. Oberth and R. S. Brunner, *The Effect of Hydrogen Bonding on the Kinetics of the Urethane Reaction*, J. Phys. Chem., 72 (1968), pp. 845–855, DOI: 10.1021/j100849a013.

[231] G. Raspoet and M. T. Nguyen, *The Alcoholysis Reaction of Isocyanates Giving Urethanes: Evidence for a Multimolecular Mechanism*, J. Org. Chem., 63 (1998), pp. 6878–6885, DOI: 10.1021/jo9806411.

[232] M. Bertoldo, C. Cappelli, S. Catanorchi, V. Liuzzo, and S. Bronco, *Understanding the Accelerating Effect of ε-Caprolactam on the Formation of Urethane Linkages*, Macromolecules, 38 (2005), pp. 1385–1394, DOI: 10.1021/ma0480998.

[233] A. Y. Samuilov, L. A. Zenitova, Y. D. Samuilov, and A. I. Konovalov, *Quantum-Chemical Study on the Reaction of Phenyl Isocyanate with Linear Methanol Associates. Addition at the C=N Bond*, Russ. J. Org. Chem., 44 (2008), pp. 1316–1322, DOI: 10.1134/s107042800809011x.

[234] X. Y. Huang, W. Yu, and C. S. P. Sung, *Studies of Model Urethane Reactions and Cure in Polyurethanes by UV Absorption and Fluorescence Spectroscopy*, Macromolecules, 23 (1990), pp. 390–398, DOI: 10.1021/ma00204a007.

[235] L. Goerigk, A. Hansen, C. Bauer, S. Ehrlich, A. Najibi, and S. Grimme, *A Look at the Density Functional Theory Zoo with the Advanced GMTKN55 Database for General Main Group Thermochemistry, Kinetics and Noncovalent Interactions*, Phys. Chem. Chem. Phys., 19 (2017), pp. 32184–32215, DOI: 10.1039/c7cp04913g.

[236] N. Mardirossian and M. Head-Gordon, *Thirty Years of Density Functional Theory in Computational Chemistry: an Overview and Extensive Assessment of 200 Density Functionals*, Mol. Phys., 115 (2017), pp. 2315–2372, DOI: 10.1080/00268976.2017.1333644.

[237] F. Weigend and R. Ahlrichs, *Balanced Basis Sets of Split Valence, Triple Zeta Valence and Quadruple Zeta Valence Quality for H to Rn: Design and Assessment of Accuracy*, Phys. Chem. Chem. Phys., 7 (2005), pp. 3297–3305, DOI: 10.1039/b508541a.

[238] M. J. S. Dewar, E. G. Zoebisch, E. F. Healy, and J. J. P. Stewart, *Development and Use of Quantum Mechanical Molecular Models. 76. AM1: a New General Purpose Quantum Mechanical Molecular Model*, J. Am. Chem. Soc., 107 (1985), pp. 3902–3909, DOI: 10.1021/ja00299a024.

[239] J. J. P. Stewart, *Optimization of Parameters for Semiempirical Methods. I. Method*, J. Comp. Chem., 10 (1989), pp. 209–220, DOI: 10.1002/jcc.540100208.

[240] J. J. P. Stewart, *Optimization of Parameters for Semiempirical Methods. V. Modification of NDDO Approximations and Application to 70 Elements*, J. Mol. Model., 13 (2007), pp. 1173–1213, DOI: 10.1007/s00894-007-0233-4.

[241] S. Grimme, *Semiempirical Hybrid Density Functional with Perturbative Second-Order Correlation*, J. Chem. Phys., 124 (2006), p. 034108, DOI: 10.1063/1.2148954.

[242] F. A. Hamprecht, A. J. Cohen, D. J. Tozer, and N. C. Handy, *Development and Assessment of new Exchange-Correlation Functionals*, J. Chem. Phys., 109 (1998), pp. 6264–6271, DOI: 10.1063/1.477267.

[243] P. J. Wilson, T. J. Bradley, and D. J. Tozer, *Hybrid Exchange-Correlation Functional Determined from Thermochemical Data and Ab Initio Potentials*, J. Chem. Phys., 115 (2001), p. 9233, DOI: 10.1063/1.1412605.

[244] R. Miehlich, A. Savin, H. Stoll, and H. Preuss, *Results Obtained with the Correlation energy Density Functionals of Becke and Lee, Yang and Parr*, Chem. Phys. Lett., 157 (1989), pp. 200–206, DOI: 10.1016/0009-2614(89)87234-3.

[245] J. P. Perdew, *Generalized Gradient Approximation Made Simple*, Phys. Rev. Lett., 77 (1996), pp. 3865–3868, DOI: 10.1103/PhysRevLett.77.3865.

[246] J. P. Perdew, *Density-Functional Approximation for the Correlation Energy of the Inhomogeneous Electron Gas*, Phys. Rev. B, 33 (1986), pp. 8822–8824, DOI: 10.1103/PhysRevB.33.8822.

[247] A. D. Becke, *Density-Functional Exchange-Energy Approximation with Correct Asymptotic Behavior*, Phys. Rev. A, 38 (1988), pp. 3098–3100, DOI: 10.1103/PhysRevA.38.3098.

[248] A. D. Boese and J. M. L. Martin, *Development of Density Functionals for Thermochemical Kinetics*, J. Chem. Phys., 121 (2004), pp. 3405–3516, DOI: 10.1063/1.1774975.

[249] T. Yanai, D. Tew, and N. Handy, *A New Hybrid Exchange-Correlation Functional Using the Coulomb-Attenuating Method (CAM-B3LYP)*, Chem. Phys. Lett., 393 (2004), pp. 51–57, DOI: 10.1016/j.cplett.2004.06.011.

[250] T. M. Henderson, A. F. Izmaylov, G. Scalmani, and G. E. Scuseria, *Can Short-Range Hybrids Describe Long-Range-Dependent Properties?*, J. Chem. Phys., 131 (2009), p. 044108, DOI: 10.1063/1.3185673.

[251] Y. Zhao, N. E. Schultz, and D. G. Truhlar, *Exchange-Correlation Functional with Broad Accuracy for Metallic and Nonmetallic Compounds, Kinetics, and Noncovalent Interactions*, J. Chem. Phys., 123 (2005), p. 161103, DOI: 10.1063/1.2126975.

[252] Y. Zhao, N. E. Schultz, and D. G. Truhlar, *Design of Density Functionals by Combining the Method of Constraint Satisfaction with Parametrization for Thermochemistry, Thermochemical Kinetics, and Noncovalent Interactions*, J. Chem. Theory and Comput., 2 (2006), pp. 364–382, DOI: 10.1021/ct0502763.

[253] Y. Zhao and D. G. Truhlar, *The M06 Suite of Density Functionals for Main Group Thermochemistry, Thermochemical Kinetics, Noncovalent Interactions, Excited States, and Transition Elements: Two New Functionals and Systematic Testing of Four M06-Class Functionals and 12 Other Functionals*, Theor. Chem. Acc., 120 (2008), pp. 215–241, DOI: 10.1007/s00214-007-0310-x.

[254] J. Gamez, unpublished.

[255] D. L. Baulch, C. J. Cobos, R. A. Cox, P. Frank, G. Hayman, T. Just, J. A. Kerr, T. Murrells, M. J. Pilling, J. Troe, R. W. Walker, and J. Warnatz, *Evaluated Kinetic Data for Combustion Modeling. Supplement I*, J. Phys. Chem. Ref. Data, 23 (1994), pp. 847–1033, DOI: 10.1063/1.555953.

[256] D. L. Baulch, C. T. Bowman, C. J. Cobos, R. A. Cox, T. Just, J. A. Kerr, M. J. Pilling, D. Stocker, J. Troe, W. Tsang, R. W. Walker, and J. Warnatz, *Evaluated Kinetic Data for Combustion Modeling: Supplement II*, J. Phys. Chem. Ref. Data, 34 (2005), pp. 757–1397, DOI: 10.1063/1.1748524.

[257] J. Li, Z. Zhao, A. Kazakov, and F. L. Dryer, *An Updated Comprehensive Kinetic Model of Hydrogen Combustion*, Int. J. Chem. Kinet., 36 (2004), pp. 566–575, DOI: 10.1002/kin.20026.

[258] P. Dagaut and M. Cathonnet, *The Ignition, Oxidation, and Combustion of Kerosene: A Review of Experimental and Kinetic Modeling*, Prog. Energy Combust. Sci., 32 (2006), pp. 48–92, DOI: 10.1016/j.pecs.2005.10.003.

[259] S. G. Davis, A. V. Joshi, H. Wang, and F. Egolfopoulos, *An Optimized Kinetic Model of H_2/CO Combustion*, P. Combust. Inst., 30 (2005), pp. 1283–1292, DOI: 10.1016/j.proci.2004.08.252.

[260] T. J. Lane, D. Shukla, K. A. Beauchamp, and V. S. Pande, *To Milliseconds and Beyond: Challenges in the Simulation of Protein Folding*, Curr. Opin. Struct. Biol., 23 (2013), pp. 58–65, DOI: 10.1016/j.sbi.2012.11.002.

[261] S. Piana, J. L. Klepeis, and D. E. Shaw, *Assessing the Accuracy of Physical Models Used in Protein-Folding Simulations: Quantitative Evidence from Long Molecular Dynamics Simulations*, Curr. Opin. Struct. Biol., 24 (2014), pp. 98–105, DOI: 10.1016/j.sbi.2013.12.006.

[262] L.-P. Wang, A. Titov, R. McGibbon, F. Liu, V. S. Pande, and T. J. Martínez, *Discovering Chemistry with an Ab Initio Nanoreactor*, Nature chemistry, 6 (2014), pp. 1283–1292.

[263] S. Agrawalla and A. C. T. van Duin, *Development and Application of a ReaxFF Reactive Force Field for Hydrogen Combustion*, J. Phys. Chem. A, 115 (2011), pp. 960–972, DOI: 10.1021/jp108325e.

[264] C. Ashraf, A. Jain, Y. Xuan, and A. C. T. van Duin, *ReaxFF Based Molecular Dynamics Simulations of Ignition Front Propagation in Hydrocarbon/Oxygen Mixtures Under High Temperature and Pressure Conditions*, Phys. Chem. Chem. Phys., 19 (2017), pp. 5004–5017, DOI: 10.1039/C6CP08164A.

[265] M. Gao, Xiaoxia, and L. Guo, *Pyrolysis Simulations of Fugu Coal by Large-Scale ReaxFF Molecular Dynamics*, Fuel Process. Technol., 178 (2018), pp. 197–205, DOI: 10.1016/j.fuproc.2018.05.011.

[266] F. Castro-Marcano, M. F. Russo, Jr., A. C. T. van Duin, and J. P. Mathews, *Pyrolysis of a Large-Scale Molecular Model for Illinois No. 6 Coal Using the ReaxFF Reactive Force Field*, J. Anal. Appl. Pyrolysis, 109 (2014), pp. 79–89, DOI: 10.1016/j.jaap.2014.07.011.

[267] A. P. J. Jansen, *An Introduction to Monte Carlo Simulations of Surface Reactions*, arXiv Preprint, cond-mat/0303028 (2003), DOI: 10.1007/978-3-642-29488-4.

[268] A. Chatterjee and D. G. Vlachos, *An Overview of Spatial Microscopic and Accelerated Kinetic Monte Carlo Methods*, J. Comput.-Aided Mol. Des., 14 (2007), pp. 253–308, DOI: 10.1007/s10820-006-9042-9.

[269] E. M. Dietze and P. N. Plessow, *Kinetic Monte Carlo Model for Gas Phase Diffusion in Nanoscopic Systems*, J. Phys. Chem. C, 122 (2018), pp. 11524–11531, DOI: 10.1021/acs.jpcc.8b01816.

[270] M. Trochet, N. Mousseau, L. K. Béland, and G. Henkelman, *Off-Lattice Kinetic Monte Carlo Methods*, Springer, 2019, pp. 1–29.

[271] J. J. Lukken, *CARLOS: a General Purpose Program for the Simulation of Chemical Reactions Taking Place at Crystal Surfaces*. https://carlos.win.tue.nl/.

[272] L. Kunz and O. Deutschmann, *MoCKa - Monte Carlo Karlsruhe* . http://kmc-simulations.org/index.html.

[273] J. Hetherington, I. Christidi, R. Guichard, M. Stamakis, and M. Pineda, *Zacros - Advanced lattice-KMC made easy*. http://zacros.org/software.

[274] S. Lucas and P. Moskovkin, *Simulation at High Temperature of Atomic Deposition, Islands Coalescence, Ostwald and Inverse Ostwald Ripening with a General Simple Kinetic Monte Carlo Code*, Thin Solids Films, 518 (2010), pp. 5355–5361, DOI: 10.1016/j.tsf.2010.04.064.

[275] M. J. Hoffmann, M. Andersen, M. Bajdich, A. Garhammer, J. M. Lorenzi, and S. Matera, *kmos - kMC on Steroids: A Vigorous Attempt to Make Lattice Kinetic Monte Carlo Modeling as Fast as Possible* . http://mhoffman.github.io/kmos/.

[276] S. Plimpton, C. Battaile, M. Chandros, L. Holm, A. Thompson, V. Tikare, G. Wagner, E. Webb, X. Zhou, C. G. Cardona, and A. Slepoy, *Crossing the Mesoscale No-Man's Land via Parallel Kinetic Monte Carlo*, tech. rep., 2009.

[277] S. Plimpton, A. Thompson, and A. Slepoy, *SPPARKS Kinetic Monte Carlo Simulator*. `http://zacros.org/software`.

[278] M. Leetma and N. V. Skorodumova, *KMCLib: A General Framework for Lattice Kinetic Monte Carlo (KMC) Simulations*, Comp. Phys. Comm., 185 (2014), pp. 2340–2349, DOI: 10.1016/j.cpc.2014.04.017.

[279] M. Leetma and N. V. Skorodumova, *KMCLib 1.1: Extended Random Number Support and Technical Updates to the KMCLib General Framework for Kinetic Monte-Carlo Simulations*, Comp. Phys. Comm., 196 (2015), pp. 611–613, DOI: 10.1016/j.cpc.2015.06.016.

[280] L. J. Lauhon and W. Ho, *Direct Observation of the Quantum Tunneling of Single Hydrogen Atoms with a Scanning Tunneling Microscope*, Phys. Rev. Lett., 85 (2000), pp. 4566–4569, DOI: 10.1103/PhysRevLett.85.4566.

[281] J. Kua, L. J. Lauhon, W. Ho, and W. A. Goddard, III., *Direct Comparisons of Rates for Low Temperature Diffusion of Hydrogen and Deuterium on Cu(001) from Quantum Mechanical Calculations and Scanning Tunneling Microscopy Experiments*, J. Chem. Phys., 115 (2001), pp. 5620–5624, DOI: 10.1063/1.1396815.

[282] P. G. Sundell and G. Wahnström, *Quantum Motion of Hydrogen on Cu(001) Using First-Principles Calculations*, Phys. Rev. B, 70 (2004), p. 081403, DOI: 10.1103/PhysRevB.70.081403.

[283] P. G. Sundell and G. Wahnström, *Hydrogen Tunneling on a Metal Surface: A Density-Functional Study of H and D Atoms on Cu(001)*, Surf. Sci., 593 (2005), pp. 102–109, DOI: 10.1016/j.susc.2005.06.051.

[284] J. P. Perdew, K. Burke, and M. Ernzerhof, *Generalized Gradient Approximation Made Simple*, Phys. Rev. Lett., 77 (1996), pp. 3865–3868, DOI: 10.1103/PhysRevLett.77.3865.

[285] S. Goedecker, M. Teter, and J. Hutter, *Separable Dual-Space Gaussian Pseudopotentials*, Phys. Rev. B, 54 (1996), pp. 1703–1710, DOI: 10.1103/PhysRevB.54.1703.

[286] C. Hartwigsen, S. Goedecker, and J. Hutter, *Relativistic Separable Dual-Space Gaussian Pseudopotentials from H to Rn*, Phys. Rev. B, 58 (1998), pp. 3642–3662, DOI: 10.1103/PhysRevB.58.3641.

[287] M. Krack, *Pseudopotentials for H to Kr Optimized for Gradient-Corrected Exchange-Correlation Functionals*, Theor. Chem. Acc., 114 (2005), pp. 145–152, DOI: 10.1007/s00214-005-0655-y.

[288] J. VandeVondele and J. Hutter, *Gaussian Basis Sets for Accurate Calculations on Molecular Systems in Gas and Condensed Phases*, J. Chem. Phys., 127 (2007), p. 114105, DOI: 10.1063/1.2770708.

[289] T. E. Markland, S. Habershon, and D. E. Manolopoulos, *Quantum Diffusion of Hydrogen and Muonium Atoms in Liquid Water and Hexagonal Ice*, J. Chem. Phys., 128 (2008), p. 194506, DOI: 10.1063/1.2925792.

[290] S. Bhowmick, D. Bossion, Y. Scribano, and Y. V. Suleimanov, *The Low Temperature $D^+ + H_2 \longrightarrow HD + H^+$ Reaction Rate Coefficient: a Ring Polymer Molecular Dynamics and Quasi-Classical Trajectory Study*, Phys. Chem. Chem. Phys., 20 (2018), p. 26752, DOI: 10.1039/c8cp05398g.

[291] K. M. Hickson, J.-C. Loison, H. Guo, and Y. V. Suleimanov, *Ring-Polymer Molecular Dynamics for the Prediction of Low-Temperature Rates: An Investigation of the C(^{1}D)+H$_2$ Reaction*, J. Phys. Chem. Lett., 6 (2015), pp. 4194–4199, DOI: 10.1021/acs.jpclett.5b02060.

[292] M. P. Allen and D. J. Tildesley, *Computer Simulation of Liquids*, Oxford University Press, 2nd ed., 2017.

[293] R. Korol, N. Bou-Rabee, and T. F. Miller III, *Cayley Modification for Strongly Stable Path-Integral and Ring-Polymer Molecular Dynamics*, J. Chem. Phys., 151 (2019), p. 124103, DOI: 10.1063/1.5120282.

[294] H. M. Senn and W. Thiel, *QM/MM Methods for Biomolecular Systems*, Angew. Chem. Int. Ed., 48 (2009), pp. 1198–1229, DOI: 10.1002/anie.200802019.

[295] C. J. Cramer and D. G. Truhlar, *Implicit Solvation Models: Equilibria, Structure, Spectra, and Dynamics*, Chem. Rev., 99 (1999), pp. 2161–2200, DOI: 10.1021/cr960149m.

[296] A. Klamt, *The COSMO and COSMO–RS Solvation Models*, WIREs Comput. Mol. Sci., 1 (2011), pp. 699–709, DOI: 10.1002/wcms.56.

[297] R. Collepardo-Guevara, I. R. Craig, and D. E. Manolopoulos, *Proton Transfer in a Polar Solvent from Ring Polymer Reaction Rate Theory*, J. Chem. Phys., 128 (2008), p. 144502, DOI: 10.1063/1.2883593.

[298] T. F. Miller III, *Isomorphic Classical Molecular Dynamics Model for an Excess Electron in a Supercritical Fluid*, J. Chem. Phys., 129 (2008), p. 194502, DOI: 10.1063/1.3013357.

[299] R. Atkinson, *Kinetics and Mechanisms of the Gas-Phase Reactions of the NO3 Radical with Organic Compounds*, J. Phys. Chem. Ref. Data, 20 (1991), pp. 459–507, DOI: 10.1063/1.555887.

[300] W. N. Olmstead and J. I. Brauman, *Gas-Phase Nucleophilic Displacement Reactions*, J. Am. Chem. Soc., 99 (1977), pp. 4219–4228, DOI: 10.1021/ja00455a002.

[301] R. Collepardo-Guevara, Y. V. Suleymanov, and D. E. Manolopoulos, *Bimolecular Reaction Rates from Ring Polymer Molecular Dynamics*, J. Chem. Phys., 130 (2009), p. 174713, DOI: 10.1063/1.3127145.

[302] T. Yamamoto and W. H. Miller, *On the Efficient Path Integral Evaluation of Thermal Rate Constants Within the Quantum Instanton Approximation*, J. Chem. Phys., 120 (2003), pp. 3086–3099, DOI: 10.1063/1.1641005.

[303] P. Pulay and G. Fogarasi, *Geometry Optimization in Redundant Internal Coordinates*, J. Chem. Phys., 96 (1992), pp. 2856–2860, DOI: 10.1063/1.462844.

[304] S.-H. Lee, K. Palmo, and S. Krimm, *New Out-of-Plane Angle and Bond Angle Internal Coordinates and Related Potential Energy Functions for Molecular Mechanics and Dynamics Simulations*, J. Comp. Chem., 20 (1999), pp. 1067–1084, DOI: 10.1002/(SICI)1096-987X(19990730)20:10<1067::AID-JCC9>3.0.CO;2-V.

[305] V. Bakken and T. Helgaker, *The Efficient Optimization of Molecular Geometries Using Redundant Internal Coordinates*, J. Chem. Phys., 117 (2002), pp. 9160–9174, DOI: 10.1063/1.1515483.

All webpages have been accessed on November 30, 2019.

Curriculum Vitae

Personal Data

Name	Julien Steffen
Nationality	german
Date of birth	14/09/1991
Place of birth	Neumünster
Address	Waitzstraße 86, 24118 Kiel

Education

since 10/2015 — Doctoral candidate at *University of Kiel*, Germany
Topic: *Towards High-Quality Black-Box Chemical Reaction Rates with System-Specific Potential Energy Surfaces* with Prof. Dr. Bernd Hartke, Institute for Physical Chemistry

10/2013-09/2015 — Master of Science (Chemistry) studies at *University of Kiel*, Germany
Master's thesis: *Reaktive Kraftfelder auf Basis quantenchemischer Rechnungen - Implementation und Anwendungen* with Prof. Dr. Bernd Hartke, Institute for Physical Chemistry

10/2010-09/2013 — Bachelor of Science (Chemistry) studies at *University of Kiel*, Germany
Bachelor's thesis: *QM/MM-Simulation der Photodynamik von Chromophoren in Polymeren* with Prof. Dr. Bernd Hartke, Institute for Physical Chemistry

08/2002-06/2010 — School education at *Klaus Groth Schule Neumünster*, Abitur majoring in Mathematics and Chemistry

Awards

12/2013 — Award of the German Chemical Society (GDCh) for the Bachelor's thesis

06/2010 — Award of the German Chemical Society (GDCh) for the Abitur in Chemistry

Teaching Experience

10/2019-02/2020	Teaching assistant in Exercises *Mathematics for Chemists I*
03/2019-04/2019	Teaching assistant in Lab Course *Introduction to Theoretical Chemistry*
11/2018-12/2018	Lab course in the *compulsory elective core subject Theoretical Chemistry* with Sven Schultzke
10/2018-02/2019	Teaching assistant in Exercises *Mathematics for Chemists I*
10/2018	Teaching assistant in Exercises *Mathematics for Chemists (Pre-Course)*
08/2018	Voluntary short-term Lab course in Theoretical Chemistry with Michael Schulz
03/2018	Teaching assistant in Lab Course *Introduction to Theoretical Chemistry*
10/2017-02/2018	Teaching assistant in Exercises *Mathematics for Chemists I*
10/2017	Teaching assistant in Exercises *Mathematics for Chemists (Pre-Course)*
09/2017	Teaching assistant in Lab Course *Introduction to Theoretical Chemistry*
08/2017-09/2017	Advanced practical course in Theoretical Chemistry with Jennifer Müller
10/2016-02/2017	Teaching assistant in Exercises *Mathematics for Chemists I*
10/2016	Teaching assistant in Exercises *Mathematics for Chemists (Pre-Course)*
04/2016-09/2016	Teaching assistant in Exercises *Mathematics for Chemists II*
03/2016-05/2016	Advanced practical course in Theoretical Chemistry with Jan-Moritz Adam
10/2015-02/2016	Teaching assistant in Exercises *Mathematics for Chemists I*
10/2015	Teaching assistant in Exercises *Mathematics for Chemists (Pre-Course)*
04/2015-09/2015	Student assistant in Exercises *Mathematics for Chemists II*
10/2014-02/2015	Teaching assistant in *Perle tutorium Mathematics for Chemists I*
10/2014-02/2015	Teaching assistant in Exercises *Mathematics for Chemists I*
10/2014	Teaching assistant in Exercises *Mathematics for Chemists (Pre-Course)*
04/2014-09/2014	Student assistant in Exercises *Physical Chemistry II*
10/2013-02/2014	Teaching assistant in Exercises *Mathematics for Chemists I*
10/2013	Teaching assistant in Exercises *Mathematics for Chemists (Pre-Course)*
04/2013-09/2013	Student assistant in Exercises *Physical Chemistry II*

Posters, Talks and Cooperations

since 08/2017   Cooperation with *Covestro AG* on the topic *Kinetical Theory of Urethane Synthesis*.

08/2017   Poster at the *Congress of the World Association of Theoretical and Computational Chemists* (WATOC), Munich, Germany

03/2017   Talk at the Physics department, University of Kiel, Germany

03/2016   Poster at the *JCF Frühjahrssymposium*, Kiel, Germany

10/2015   Talk at *Software for Chemistry & Materials* (SCM), Amsterdam, Netherlands

List of Publications

1. J. Steffen, *A new class of reaction path based potential energy surfaces enabling accurate black box chemical rate constant calculations*, J. Chem. Phys., 150 (2019), 154105.

2. J. Steffen and B. Hartke, *Cheap but accurate calculation of chemical reaction rate constants from ab initio data, via system-specific, black-box force fields*, J. Chem. Phys., 147 (2017), 161701.

Acknowledgements

First and in particular I want to thank my supervisor Prof. Bernd Harte who made it possible to work on this topic (which he established) and to finish my PhD thesis. His relaxed and curious nature helped me a lot to feel comfortable during my work in the last years. He always kept his ears open for my questions or suggestions, some of the central ideas within this thesis originated either from a thought of him or developed during a fruitful exchange between us.

Further I want to thank Prof. Carolin König for accepting to be my second referee.

I would like to thank Jose Gamez of Covestro for the interesting (and continuing) cooperation on the field of polyurethane chemistry which widened my scientific horizon and gave some important stimuli for the overall forthcoming of my work.

Further I want to thank my colleagues who created a pleasant working environment that was also important to keep me motivated throughout the years. Several funny events on- and offside the work will be kept in good memory.

I am grateful to Bernd Hartke and the other proofreaders for the patient search of the many small mistakes and gaps within the text and for giving some suggestions for its overall improvement.

This whole work would of course not be possible without the steady support of my friends. I would like to thank Corvin, Atanur, Marco, Bente, Sven and many others for all the awesome and sometimes weird experiences we had together and that were crucial to endure some rather frustrating periods during this work.

Finally I want to thank my mother and my father who always were my most important support since I can remember. Without their steady interest, acceptance and motivation it would have been certainly impossible for me to go my way.

Declaration

I, Julien Steffen, hereby declare that the work presented in this thesis was done by me, under the supervision of Prof. Dr. Bernd Hartke, with no other help than the referenced sources in the text.

This is my first dissertation and the work has never been used in any other dissertation attempts. I have never been deprived of an academic title.

The dissertation complies to the good scientific practice rules as proposed by the German Research Foundation (DFG).

Kiel, December 03, 2019

JULIEN STEFFEN